



**National Library
of Canada**

**Bibliothèque nationale
du Canada**

Canadian Theses Service

Service des thèses canadiennes

Ottawa, Canada
K1A 0N4

NOTICE

The quality of this microform is heavily dependent upon the quality of the original thesis submitted for microfilming. Every effort has been made to ensure the highest quality of reproduction possible.

If pages are missing, contact the university which granted the degree.

Some pages may have indistinct print especially if the original pages were typed with a poor typewriter ribbon or if the university sent us an inferior photocopy.

Reproduction in full or in part of this microform is governed by the Canadian Copyright Act, R.S.C. 1970, c. C-30, and subsequent amendments.

AVIS

La qualité de cette microforme dépend grandement de la qualité de la thèse soumise au microfilmage. Nous avons tout fait pour assurer une qualité supérieure de reproduction.

S'il manque des pages, veuillez communiquer avec l'université qui a conféré le grade.

La qualité d'impression de certaines pages peut laisser à désirer, surtout si les pages originales ont été dactylographiées à l'aide d'un ruban usé ou si l'université nous a fait parvenir une photocopie de qualité inférieure.

La reproduction, même partielle, de cette microforme est soumise à la Loi canadienne sur le droit d'auteur, SRC 1970, c. C-30, et ses amendements subséquents.



National Library
of Canada

Bibliothèque nationale
du Canada

Canadian Theses Service Service des thèses canadiennes

Ottawa, Canada
K1A 0N4

The author has granted an irrevocable non-exclusive licence allowing the National Library of Canada to reproduce, loan, distribute or sell copies of his/her thesis by any means and in any form or format, making this thesis available to interested persons.

The author retains ownership of the copyright in his/her thesis. Neither the thesis nor substantial extracts from it may be printed or otherwise reproduced without his/her permission.

L'auteur a accordé une licence irrévocable et non exclusive permettant à la Bibliothèque nationale du Canada de reproduire, prêter, distribuer ou vendre des copies de sa thèse de quelque manière et sous quelque forme que ce soit pour mettre des exemplaires de cette thèse à la disposition des personnes intéressées.

L'auteur conserve la propriété du droit d'auteur qui protège sa thèse. Ni la thèse ni des extraits substantiels de celle-ci ne doivent être imprimés ou autrement reproduits sans son autorisation.

ISBN 0-315-55612-9

Canada

THE UNIVERSITY OF ALBERTA

**THE DESIGN AND CHARACTERIZATION OF A FOURIER
TRANSFORM SPECTROMETER FOR THE ULTRAVIOLET
AND VISIBLE REGIONS OF THE SPECTRUM.**

by

BRUCE RICHARD TODD



A Thesis

**Submitted To The Faculty Of Graduate Studies And Research
In Partial Fulfillment Of The Requirements For The Degree
Of Doctor Of Philosophy**

The Department of Chemistry

Edmonton, Alberta

Fall, 1989

THE UNIVERSITY OF ALBERTA

RELEASE FORM

NAME OF AUTHOR: Bruce Richard Todd

TITLE OF THESIS: The Design and Characterization of a Fourier Transform Spectrometer for the Ultraviolet and Visible Regions of the Spectrum.

DEGREE FOR WHICH THESIS WAS PRESENTED: Ph.D.

YEAR THIS DEGREE GRANTED: 1989

Permission is hereby granted to THE UNIVERSITY OF ALBERTA LIBRARY to reproduce single copies of this thesis and to lend or sell such copies for private, scholarly or scientific research purposes only.

The author reserves other publication rights, and neither the thesis nor extensive extracts from it may be printed or otherwise reproduced without the author's written permission.


.....
(signed)

Dept. of Chemistry,
2036 Main Mall,
University of British Columbia,
Canada. V6T 1Y6
(604) 228-2477

Date: *Sept. 18, 1989*
.....

THE UNIVERSITY OF ALBERTA
FACULTY OF GRADUATE STUDIES AND RESEARCH

The undersigned certify that they have read, and recommend to the Faculty of Graduate Studies and Research for acceptance, a thesis entitled THE DESIGN AND CHARACTERIZATION OF A FOURIER TRANSFORM SPECTROMETER FOR THE UV-VIS submitted by BRUCE RICHARD TODD in partial fulfillment of the requirements for the degree of Doctor of Philosophy.

.....*Gary Horlick*.....
Dr. G. Horlick (supervisor)

.....*John E. Bertie*.....
Dr. J. E. Bertie

.....*Dr. D. J. Harrison*.....
Dr. D. J. Harrison

.....*B. Kratochvil*.....
Dr. B. Kratochvil

.....*D. Routledge*.....
Dr. D. Routledge

.....*M. B. Denton*.....
Dr. M. B. Denton (external examiner)

Date: *Sept. 19, 1989*

To my parents.

Abstract

A Fourier Transform Spectrometer (FTS) designed specifically for use in the ultraviolet and visible (UV-VIS) regions of the spectrum has been fabricated and characterized.

This spectrometer is based upon a standard 90° Michelson interferometer configuration. The fixed and moving reflectors in the interferometer are planar. The moving mirror is designed for a maximum travel of 1.03 cm on either side of the position of Zero Path Difference. With this mirror travel, the minimum achievable full-width at one-half the maximum intensity (FWHM) of a spectral line is 0.30 cm⁻¹. Both simple spherical lens and folded Off-Axis-Parabolic mirror systems have been assessed as collimating and focussing optics. The aspheric, achromatic mirror systems have been found to provide superior collimation and focussing. The entrance collimation mirror system is particularly well-adapted to input of radiation via a fibre optic. To reduce the effects of instrumental apodization of the recorded interferogram, procedures for aligning the various optical components have been developed. To date, the best measured resolution is 0.63 cm⁻¹ (FWHM) of the Mg 285.213 nm peak from a Mg hollow cathode lamp.

In air the usable spectral band-width of this interferometer is from approximately 200 nm through the visible region of the spectrum. With evacuation or purging, the present optical components should allow for operation to approximately 180 nm.

The moving mirror is attached to an air-bearing/permanent magnet assembly. Twin wire coils provide the force by which the mirror is translated.

A zero-force servo system has been developed to maintain a constant mirror velocity. The velocity varies less than $\pm 0.4\%$ throughout an entire scan. The travel of the moving mirror is controlled via an absolute reference laser fringe counting system.

De-aliased spectra can be acquired using a frequency multiplied version of the reference laser fringe. The frequency multiplication is achieved via a digital Phase Locked Loop.

To reduce the effect of the multiplex disadvantage, A novel pre-dispersion system has been coupled with the interferometer. This pre-disperser is based upon the optical system of the LECO PLASMARRAY echelle spectrometer. Preliminary proof-of-concept studies have been successful.

Acknowledgements

I would like to acknowledge the encouragement and support of my supervisor, Dr. Gary Horlick, who allowed me a great deal of freedom in pursuing this doctorate in the manner in which I saw fit. In the same vein, I would like to acknowledge the support of Dr. Robert Jordan, the chairman of the department of chemistry at the University of Alberta during the latter stages of my tenure there.

The software required to manipulate the data acquired with this instrument was written by Dr. Greg King. This thesis would not have been possible without his efforts.

A number of individuals made my stay at the University of Alberta an utterly enjoyable academic and social experience. Rather than try to list them (and perhaps miss one or two) I will simply express my heartfelt gratitude to these people. You know who you are.

Finally, I would like to acknowledge the support of my parents John and Martina, and my sister and brother, Diane and Andrew.

TABLE OF CONTENTS

CHAPTER	PAGE
1. Introduction.....	1
1-1. The general methodology of FTS.....	1
1-2. An overview of optical FTS.....	8
1-2.1. FTS in the UV-VIS.....	12
1-3. The principles of optical FTS.....	32
1-3.1. Encoding with the Michelson interferometer.....	44
1-3.2 The interferogram and spectrum of chaotic light.....	63
1-3.3. Detection of the interferogram - Noise in FTS.....	76
2. Interferometer Optical System.....	86
2-1. Current interferometer design.....	88
2-2. Interferometer alignment procedure.....	92
2-2.1. Alignment of the mounting cube.....	98
2-2.2. Alignment of the beam-divider and moving mirror.....	101
2-2.3. Alignment of the reference laser optical path.....	106
2-2.4. Alignment of the entrance aperture and exit (O.A.P) mirror assemblies.....	117
2-2.5. Alignment of the source and detector.....	122
2-3. Resolution performance of the current optical system.....	124
3. Spectrometer Electronics Systems.....	149
3-1. Moving mirror constant velocity control system.....	152
3-1.1. Electro-mechanical control of the moving mirror velocity.....	154

3-1.2. Moving mirror feed-back control switching system.....	205
3-1.3. Moving mirror scan length control system.....	243
3-2. Digitization of the analog interferogram.....	296
4. Current Applications.....	355
5. Conclusions and Future Directions.....	365
REFERENCES	376
APPENDIX	PAGE
Spectrometer Control System Electronics.....	A1

LIST OF TABLES

TABLE	PAGE
3-1. Signals for feed-back switching and mirror scan length control.....	208

LIST OF FIGURES

FIGURE	PAGE
1-1. The Michelson interferometer.....	2
1-2. The truncated interferogram of a monochromatic source, and its spectrum. The instrumental line-shape of a FT spectrometer.....	6
1-3. A classical electromagnetic wave.....	34
1-4. Virtual source representation of the Michelson interferometer. Detected beams.....	51
1-5. Young's double slit experiment.	68
2-1. Schematic diagram of scanning Michelson interferometer system.....	89
2-2. Moving Mirror Assembly: moving sleeve vs. moving piston.....	91
2-3. Physical set-up for alignment of the mounting cube plus fixed mirror.....	99
2-4. Return and exit beam patterns due to multiple reflections.....	102
2-5. Physical set-up for alignment of the moving mirror and beam-splitter/compensator assemblies.....	105
2-6. Alignment of the reference laser periscope system.	107
2-7. Effect of tilt of the reference laser beam.....	109
2-8. Construction for the estimation of the magnitude of tilt of the reference laser beam.....	112
2-9. Physical set-up for alignment of the off-axis parabolic mirror assemblies.....	116
2-10. Physical set-up for alignment of the source.....	123
2-11. Calculated truncated interferogram of a monochromatic source. Calculated spectrum. Theoretical spectral line widths for truncated interferograms. (HeNe 632.8 nm reference laser.).....	126

2-12. Spectrum of a Mg hollow cathode lamp.	128
2-13. Different length interferograms of a Mg hollow cathode lamp.	131
2-14. Mg 285.213 nm lines from a hollow cathode lamp.	133
2-15. Calculated Gaussian envelope interferogram and spectrum.	135
2-16. Experimental 64K interferogram plus calculated Gaussian envelope.	137
2-17. Envelope of HeNe point source 64K interferogram.	138
2-18. Mg 285.213 nm line. Maximum resolution	141
2-19. Interferograms acquired with mirror and lens systems collimation.	143
2-20. Mg 285.213 nm lines for mirror and lens systems collimation.	145
2-21. Old and intermediate systems interferograms.	147
3-1. Spectrometer electronics systems.	150
3-2. Moving mirror scan control systems.	153
3-3. Simple model of the moving mirror.	155
3-4. A "closed loop" control system architecture.	159
3-5. Moving mirror electro-mechanical design.	165
3-6. Illustration of force exerted on current in a wire loop by an external magnetic field. a) Geometry of loop in field. b) Loop in homogeneous field. c) Loop in non-homogeneous field.	167
3-7. Illustration of the cylindrical symmetry of the loop/magnetic field geometry. (See text for details.)	169
3-8. Construction for the application of Gauss' law to a current loop in the external magnetic field of a permanent magnet.	171
3-9. Illustration of non-linearity of K_F for single loop system.	174
3-10. Approximate constancy of K_F via dual loop system. (See text for details.)	176

3-11. Electrical model of the electro-mechanical mirror drive assembly.....	181
3-12. Equivalent electrical circuit of the mirror drive electro-mechanical assembly. a) Time domain circuit. b) Laplace domain circuit.....	184
3-13. Two types of feed-back. a) bi-polar feed-back. b) Uni-polar feed-back. (See text for details.)	191
3-14. Simple schematic of moving mirror velocity control feed-back loop.....	194
3-15. Dual feed-back control system. (See text for details.)	195
3-16. a) Auxiliary coils. b) Bi-polar feed-back from coils.....	197
3-17. Moving mirror constant velocity control loop. Laplace domain representation.	201
3-18. Schematic description of MARK TIME and SCAN mode operation.	207
3-19. Auxiliary coils (coarse) and F/V (fine) feed-back loops in dual feed-back loop architecture.....	209
3-20. Block diagram and truth table of controllable reference, V_{REF1}	212
3-21. V_{EMF} and FWD/\overline{BWD} during turn-around sequences.	215
3-22. Schematic diagram of AD 451 frequency-to-voltage converter.....	218
3-23. Reference laser interferogram, FRINJ, and $ V_{e2} $	220
3-24. Window detector block diagram.....	222
3-25. Window detector comparator transfer characteristics. a) Lower threshold comparator. b) Upper threshold comparator. c) combined characteristic of window detector.	224
3-26. V_{REF1} , V_{EMF} , $ V'_{e2} $, and $EN1/\overline{EN2}$ during acquisition of fine feed-back.	228
3-27. $EN1/\overline{EN2}$, V_{EMF} , and $ V'_{e2} $ during a turn-around sequence.	231
3-28. Truth tables for the Window detector. (See text for details.)	233

3-29a. $ V'_{e2} $ and $EN1/\overline{EN2}$ during external disturbance.....	239
3-29b. $ V'_{e2} $ and $BWDACC/\overline{FWDACC}$ during external disturbance.	240
3-29c. $ V'_{e2} $ and V_{REF1} during external disturbance.	241
3-30. Fringe counting sequences during scan mode operation.....	244
3-31. White light and reference laser interferograms.	248
3-32. "Clipped" white light interferogram.....	251
3-33. Clipped and squared white light interferogram.	252
3-34. Processed white light interferogram and WLP.	253
3-35. Reference laser interferogram and $FRINJ_{W/H}$	255
3-36. Fringe counting during a typical turn-around sequence. a) Analog fringe. b) $FRINJ$. c) $FRINJ_{W/H}$	256
3-37. Typical turn-around counting sequences with $FRINJ$ for fringe counting. Determinate cases: a) Analog fringe voltage well above threshold when mirror stopped. b) Analog fringe voltage well below threshold when mirror stopped. (See text for details.).....	258
3-38. Turn-around counting sequence with $FRINJ$ for fringe counting. Indeterminate case: Analog fringe voltage just reaches threshold voltage when mirror is stopped. (See text for details.).....	261
3-39. Reference laser interferogram and $FRINJ_{W/H}$ during turn- around sequence. Minimum positive brackets.	265
3-40. Reference laser interferogram and $FRINJ_{W/H}$ during turn- around sequence. Minimum negative brackets.	266
3-41. Effect of off-setting V_{EMF} on timing of transition of FWD/\overline{BWD}	269
3-42. Effect of hysteresis on timing of transition of FWD/\overline{BWD}	270
3-43. Combined effect of off-setting V_{EMF} and hysteresis to produce delay of transition of FWD/\overline{BWD}	272

3-44. Reference laser interferogram and $\overline{\text{FWD/BWD}}$ during turn-around sequences.	273
3-45. Reference laser interferogram and \mathcal{V}_{EMF} during backward to forward turn-around sequence. Proper adjustment of off-set of raw \mathcal{V}_{EMF}	275
3-46. Reference laser interferogram and \mathcal{V}_{EMF} during forward to backward turn-around sequence. Proper adjustment of off-set of raw \mathcal{V}_{EMF}	276
3-47. Scan and turn-around counters block diagram.	278
3-48. $\text{FRINJ}_{\text{W/H}}$ and count streams $\text{FRINJ}_{\text{Px2}}$, FRINJ_{P} , and CFRINJ_{P}	281
3-49. Beginning of first half scan count to set-up mirror scan length. WL_{P} , $\text{FRINJ}_{\text{W/H}}$, and $\text{FRINJ}_{\text{Px2}}$	282
3-50. End of first half-scan count. Count out of scan counter. $\text{FRINJ}_{\text{Px2}}$, Q_{B} and Q_{A} of NCNTR , and $\text{NCNTR } \overline{\text{CNTOUT}}$	283
3-51. End of first half-scan count. Disabling of NCNTR DN input. Enabling of T/ACNTR UP input. $\text{FRINJ}_{\text{W/H}}$, $\text{FRINJ}_{\text{Px2}}$, FRINJ_{P} , and $\text{NCNTR } \overline{\text{CNTOUT}}$	285
3-52. Beginning of forward to backward turn-around sequence. Incrementing of T/A CNTR . $\text{NCNTR } \overline{\text{CNTOUT}}$, FRINJ_{P} , Q_{A} and Q_{B} of T/A CNTR	286
3-53. End of count-up during forward to backward turn-around sequence. Disabling of T/A CNTR UP input. $\overline{\text{FWD/BWD}}$, $\text{FRINJ}_{\text{W/H}}$, FRINJ_{P}	287
3-54. Beginning of count-down sequence during forward to backward turn-around sequence. Enabling of T/A CNTR DN input. $\overline{\text{FWD/BWD}}$, $\text{FRINJ}_{\text{W/H}}$, and CFRINJ_{P}	288
3-55. End of turn-around count during forward to backward turn-around sequence. Count out of T/A CNTR . CFRINJ_{P} , Q_{B} , Q_{A} and $\text{T/A CNTR } \overline{\text{CNTOUT}}$	290
3-56. End of forward to backward turn-around sequence. Beginning of first backward direction data acquisition scan. Disabling of T/A CNTR DN input. Enabling of NCNTR DN input. $\text{FRINJ}_{\text{W/H}}$, CFRINJ_{P} , and $\text{T/A CNTR } \overline{\text{CNTOUT}}$	291

3-57. End of first backward data acquisition scan. Disabling of NCNTR DN input. Enabling of T/ACNTR UP input. Beginning of count-up sequence of T/A CNTR. FRINJ _{W/H} , CFRINJ _p , and NCNTR CNTOUT.....	292
3-58. End of count-up during backward to forward turn-around sequence. Disabling of T/A CNTR UP input. FWD/ $\overline{\text{BWD}}$, FRINJ _{W/H} , CFRINJ _p	293
3-59. Beginning of count-down sequence during backward to forward turn-around sequence. Enabling of T/A CNTR DN input. FWD/ $\overline{\text{BWD}}$, FRINJ _{W/H} , and FRINJ _p	294
3-60. End of backward to forward turn-around sequence. Beginning of first forward direction data acquisition scan. Disabling of T/A CNTR DN input. Enabling of NCNTR DN input. FRINJ _{W/H} , FRINJ _p , and T/A CNTR CNTOUT.....	295
3-61. Summary of fringe counting for mirror scan length control. Set-up and acquisition of 8 point interferograms.....	300
3-62. Spectra of forward scan interferograms. a) 1 scan. b) 16 scans averaged.....	304
3-63. Spectra of backward scan interferograms. a) 1 scan. b) 16 scans averaged.....	305
3-64. Spectra of average interferograms. a) 16 forward scans. b) 16 backward scans. c) 8 forward+8 backward scans.....	307
3-65. Expansions of ~278.55-277.5 nm region of average spectra of Fig. 3-64. a) 16 forward scans. b) 16 backward scans. c) 8 forward+8 backward scans. Normalized peak heights. (See text for details.).....	308
3-66. Spectra of non-phase-shifted average (32 backward scans) interferograms.....	311
3-67. Averaging spectra vs. averaging interferograms. (See text for details.).....	312
3-68. Spectra of non-phase-shifted, and one fringe period phase-shifted interferograms.....	314
3-69. Averaging of phase-shifted spectra vs. spectrum of average of phase-shifted interferograms.....	316

3-70. Expansions of ~278.5-277.5 nm region of spectra of non-phase-shifted and phase-shifted average interferograms. Normalized peak heights. (See text for details.).....	317
3-71. Digital Phase Locked Loop frequency multiplication circuitry.....	325
3-72. FRINJ and 4x and 8x versions of ADC CLK.....	328
3-73. Lock-up of PLL at end of turn-around sequences. FRINJ and 4x version of ADC CLK.	333
3-74. Phase of input and output of PLL: 110 periods of FRINJ after turn-around sequences. FRINJ and 4x version of ADC CLK.....	335
3-75. Schematic spectra of sampled signals.....	337
3-76a. Spectrum of interferogram measured with R166 PMT and sampled with a frequency of 10 kHz.....	339
3-76b. Spectrum of Fig. 3-76a continued.....	340
3-77. Summary of aliasing in spectrum of interferogram measured with R166 PMT and sampled with a frequency of 10 kHz.....	342
3-78. Spectrum of interferogram measured with R166 PMT and sampled with a frequency of 40 kHz.....	343
3-79. Summary of aliasing in spectrum of interferogram measured with R166 PMT and sampled with a frequency of 40 kHz.....	345
3-80. Spectrum of an interferogram measured with R166 PMT and sampled at a frequency of 80 kHz.....	346
3-81. Summary of spectral regions of interferogram measured with R166 PMT and sampled at a frequency of 80 kHz.....	347
3-82. Expanded spectrum of interferogram of Mg HCL acquired with 8x version of ADC CLK. Vertical expansion = 512x. (See text for details.).....	348
3-83. Spectra of interferograms acquired with a) 1x, b) 4x, and c) 4x versions of ADC CLK.....	350
3-84. Spurious spectral features in spectrum of interferogram acquired with 8x version of ADC CLK.....	352

3-85. Expansions of ~287.5-277.5 nm region of aliased and de-aliased spectra. a) ADC CLK = 1x FRINJ. b) ADC CLK = 4x FRINJ. c) ADC CLK = 8x FRINJ. (See text for details.)	354
4-1. Practical resolution capability. Fe in an ICP.....	357
4-2. Practical resolution capability. As interfering with Cd. a) 16 K interferogram. b) 64K interferogram.....	358
4-3. A pre-dispersion configuration.....	362
4-4. Reduction of the multiplex disadvantage via pre-dispersion. a) No pre-dispersion. b) Pre-dispersion. (See text for details.).....	364
5-1. Alternative Michelson interferometer configurations. a) Separate optical paths. Tilt insensitive. b) Same optical paths. Tilt and shear insensitive.....	368
5-2. Post-dispersion configuration.....	372
5-3. Pre-dispersion without recombination. Fibre optic coupling.....	374

Appendix figures:

A-1. Moving mirror control system electronics.....	A3
A-2. Coarse feed-back module front panel.....	A4
A-3. Coarse feed-back board IC/module/connector assignments.....	A5
A-4a. Coarse feed-back board modules pin-outs.	A6
A-4b. Coarse feed-back board modules pin-outs.	A7
A-5. Coarse feed-back board block diagram.....	A8
A-6. Coarse feed-back board module inter-connections.	A9
A-7. Opto-switches and default logic.....	A10
A-8. Mark time and reference chooser modules circuitry.....	A11
A-9. Scan reference module circuitry.....	A12
A-10. Coarse feed-back error signal and direction modules circuitry.....	A13
A-11. Fine feed-back module front panel.	A14

A-12. Fine feed-back board IC/module test points/connector assignments.	A15
A-13a. Fine feed-back board modules pin-outs.	A16
A-13b. Fine feed-back board modules pin-outs.	A17
A-14. Fine feed-back board block diagram.	A18
A-15. Fine feed-back board modules inter-connections.	A19
A-16. $\pm 1\times$ Gain and error chooser modules.....	A20
A-17. Window detector and ripple remover modules circuitry.....	A21
A-18. Turn-around counter (T/A CNTR) board front panel.	A22
A-19. T/A CNTR board IC/test points/connector assignments.	A23
A-20. T/A CNTR board block diagram.....	A24
A-21. Count stream routing circuitry.	A25
A-22. T/A CNTR and miscellaneous T/A CNTR board logic.	A26
A-23. Scan counter (NCNTR) board front panel.....	A27
A-24. NCNTR board IC/connector assignments.....	A28
A-25. NCNTR board block diagram.....	A29
A-26. NCNTR board miscellaneous logic.....	A30
A-27. NCNTR circuitry.....	A31
A-28. ADC CLK frequency multiplication circuitry.....	A32

Chapter 1

Introduction

Optical Fourier Transform Spectroscopy (FTS) has a range of operation that roughly spans the spectral range extending from the vacuum ultraviolet to the far infrared regions of the electromagnetic spectrum. Presented in this thesis is the description of a spectrometer that has been specifically designed for use in the ultraviolet (UV), visible (VIS), and near-infrared (NIR) regions of the spectrum.

This introductory chapter is comprised of two sections. In the first section, the general methodology of optical FTS is outlined, and an overview of this field of study is presented. The second section consists of a more detailed description of the principles of optical FTS. Each section has been written with very little reference to the other section; hence, each may be read separately or together as desired.

1-1. The general methodology of optical FTS.

The key component of a typical optical FT spectrometer is the Michelson interferometer, illustrated in Fig. 1-1. The interferometer encodes the time varying behaviour of the magnitude of the electric field component of the incident radiation into a form that is physically detectable. Consider the case where the incident radiation is monochromatic with a wavelength λ .

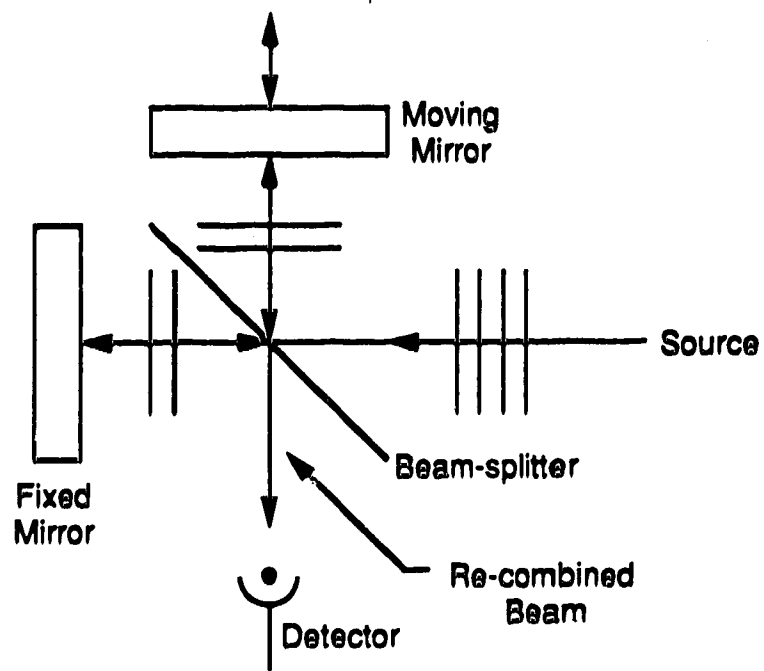


Figure 1-1. The Michelson interferometer.

The beam of incident radiation is divided to produce two beams that travel into the fixed and moving mirror arms of the interferometer. The two beams are reflected and recombined. The recombining beams interfere - the degree of interference being dependent upon the position of the moving mirror. When the optical path lengths between the two beams are equal the reflected beams interfere in a totally constructive manner. In this situation the moving mirror is said to be at the position of Zero Path Difference (ZPD). If the system was perfect, all of the source radiation would impinge upon the detector. A maximum would be detected. If the moving mirror was moved a distance $\lambda/4$ from the position of ZPD, the optical path difference between the two arms of the interferometer would then be $\lambda/2$. At the position of recombination (and at the detector) the two reflected beams would undergo total destructive interference. None of the source radiation would reach the detector. For any position of the mirror between ZPD and $\lambda/4$, varying degrees of interference are detected.

The usual operation of most FT spectrometers involves translation of the moving mirror with a constant velocity, such that the optical path difference between the two arms of the interferometer is varied in a constant fashion. For this case of constant velocity scanning (and a monochromatic source) the intensity of the radiation impinging upon the detector varies sinusoidally. This intensity oscillation is called the "interferogram" of the source radiation. The resulting detector output is also a sinusoid. The amplitude and frequency of the detector output waveform are directly proportional to those of the magnitude of the electric field component of the incident radiation.

The frequency of the output waveform is also directly proportional to the velocity of the moving mirror. By translating the mirror with a sufficiently low velocity, the frequency of the interferogram can be made low enough to allow it to be detected via conventional techniques.

For the case of polychromatic radiation, the interferogram has a complex time varying behaviour. Fourier transformation of the interferogram yields the frequency spectrum of the interferogram. With appropriate correction of the frequency (wavelength) axis of this spectrum, the spectrum of the source radiation is obtained.

Different spectrometer designs involve different schemes for scanning of the moving mirror. The mirror may be moved to only one side of ZPD, or it may be scanned symmetrically with equal travel on both sides of ZPD. These are often called "single-sided" and "double-sided" interferograms, respectively. If a perfect interferometer could be constructed, a double-sided interferogram would show symmetry about the position of ZPD. In this situation one-half of the interferogram would be redundant and need not be measured. The spectrum of the source could be correctly calculated from a single-sided interferogram. From the point of view of measurement time, the acquisition of single-sided interferograms is attractive. Unfortunately, except for some special cases with sources of limited spectral band-width, symmetric interferograms are rarely measured. Due to instrumental effects, measured interferograms are usually asymmetric. In this case it is no longer valid to assert that one-half of a double-sided interferogram is redundant.

It can be shown that the amplitude spectrum of an asymmetric double-sided interferogram is identical to that of the symmetric double-sided

interferogram that would be measured with a perfect interferometer [1]. Hence, for FTS applications, asymmetry of measured interferograms is unimportant if double-sided interferograms are acquired. It is still possible to acquire single-sided interferograms, but these must be corrected prior to Fourier transformation if they are to produce correct spectra.

The asymmetry of the interferogram can be treated as being the result of incorrect relative phases of the frequency components of the interferogram. Post-acquisition correction of single-sided interferograms is (in theory) possible and such phase correction procedures have been developed and applied [2]. Thus, a trade-off exists between the greater measurement time needed for acquisition of double-sided interferograms, versus the added calculational complexity involved in achieving the phase-corrected spectrum from asymmetric single-sided interferograms.

The instrumental line-shape of a perfect FT spectrometer is dependent upon the extent to which the moving mirror is scanned to either side of ZPD. This is illustrated in Fig. 1-2. Shown here are the interferogram and resultant spectrum of a monochromatic source. The interferogram is truncated because the moving mirror has a limited range of travel. As shown, the spectrum of a truncated sinusoid has a $\sin(2\pi\sigma)/2\pi\sigma$ wavenumber dependence ($\sigma = 1/\lambda$ cm⁻¹).

The spectral width $\Delta\sigma$, between the first two zero-crossings on either side of the principle maximum of the profile, is a figure of merit that is often used to describe the resolution capability of a particular Fourier transform spectrometer. If the maximum travel of the moving mirror is denoted by l , then $\Delta\sigma = 1/2l$. When the mirror has moved the distance l from the position

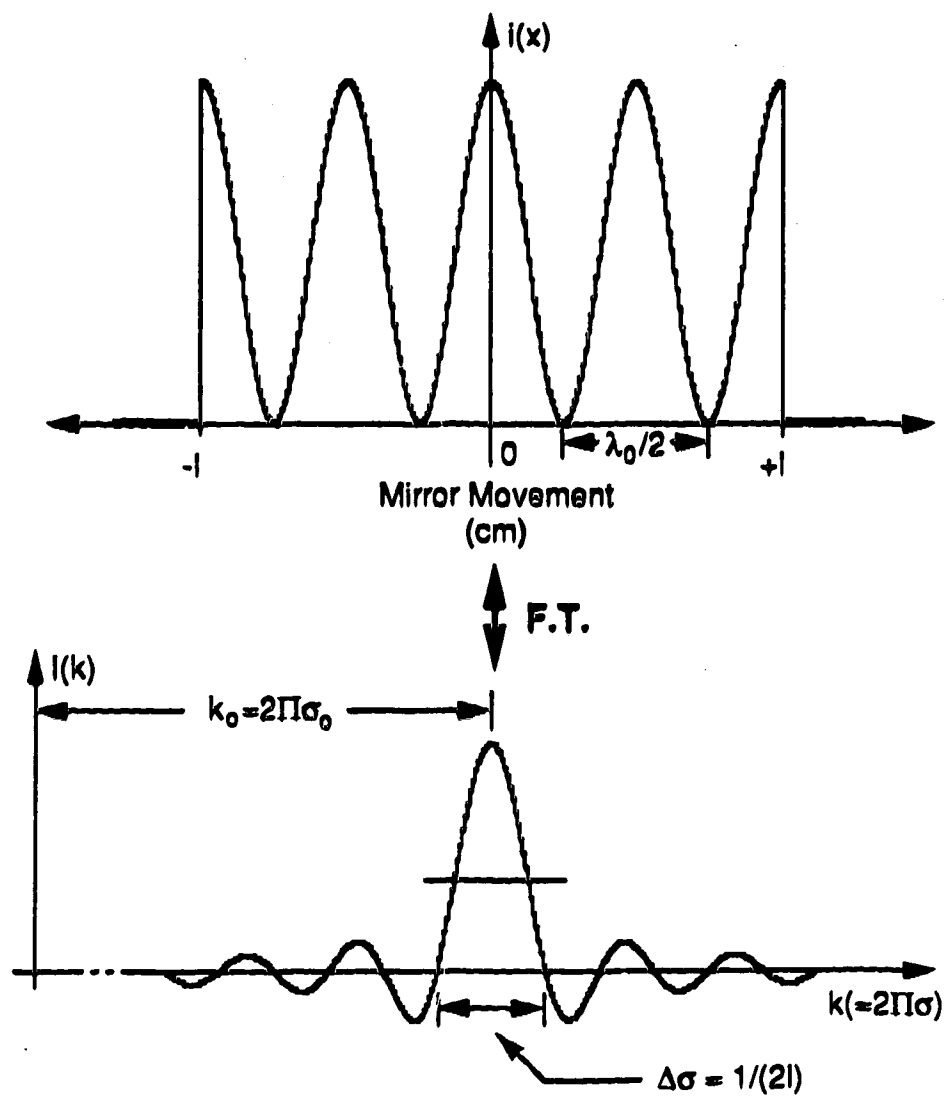


Figure 1-2. The truncated interferogram of a monochromatic source, and its spectrum. The instrumental line-shape of a FT spectrometer.

of ZPD, the optical path difference is $L = 2l$. Thus, $\Delta\sigma = 1/L$, where L is the maximum optical path difference achieved during a particular scan of the mirror. Clearly, $\Delta\sigma$ is inversely proportional to the length of mirror travel. Hence, to achieve greater resolution with an instrument of this type it is necessary to increase the distance that the mirror is translated away from the position of ZPD.

In many instances the performance of a spectrometer is defined by the full width of a spectral line at one-half of the peak intensity (particularly in the situation in which the spectral line-profile does not oscillate about the base-line i.e. a Gaussian line-profile). This is the criterion of resolution that is employed in this thesis. For the case of the $\sin(2\pi\sigma)/2\pi\sigma$ line-profile, the full width at half maximum (FWHM) $\Delta\sigma_{1/2} = 0.605\Delta\sigma$. The resolving power is defined to be $R = \sigma/\Delta\sigma_{1/2}$, where σ is the wavenumber corresponding to the peak intensity of the spectral feature of interest, and $\Delta\sigma_{1/2}$ is the FWHM of that peak. The spectra that are presented in this thesis are atomic emission spectra. The features in these spectra are narrow enough that to a good approximation the resolving power is also given by $R = \lambda/\Delta\lambda_{1/2}$.

It is important to note that a longer mirror movement does not automatically entail greater resolution. Any phenomenon that results in alteration of the envelope of the interferogram is a potential cause of broadening of the features in the resultant spectrum. In any given situation, the extent of broadening is dependent upon the relative widths of the source spectral features, and the instrumental line-shape that results from the alteration of the envelope of the interferogram. Truncation of the interferogram is a broadening phenomenon. If the optical system is imperfect, causing the envelope of the acquired interferogram to be altered,

the result will be poorer resolution than that which is dictated by the maximum travel of the moving mirror. If the mirror is moved well away from the position of ZPD, almost invariably the non-ideal nature of the instrument will be manifested in an interferogram envelope that decreases more rapidly (as the mirror is scanned away from ZPD) than is commensurate with the source spectral line-profiles. This phenomenon is known as "instrumental apodization". The effect of instrumental apodization is to limit the achievable resolution of an instrument to less than that which should be achievable on the basis of the maximum travel of the moving mirror. Hence, the elimination of instrumental apodization is of primary concern in the design of this type of spectrometer.

Typically, the detected interferogram is digitized with an analog to digital converter (ADC). It is important that digitization occur at equal, well-defined intervals of moving mirror travel. This is usually achieved by synchronizing digitization with the period (or some fraction of a period) of a reference interferogram. This reference interferogram is usually that of a HeNe laser operated at 632.8 nm. The digitized interferogram is input into a digital computer wherein the Fourier transform of the interferogram is calculated. The result, after suitable correction of the frequency axis, is the spectrum of the source radiation.

1-2. An overview of optical FTS.

For a number of years now, FTS has been the dominant spectroscopic analysis technique in the mid-infrared region. Currently, there are 9 instrument manufacturers who produce FT-IR instruments. At the most recent Pittsburgh conference in March 1989 there were seven sessions, over

five days, devoted to infrared analysis techniques. Only for very specialized applications did the presentations in these sessions not involve an FT-IR instrument. Clearly, this is an active area of research in which applications and instrumentation are continually being developed. An up-to-date view of this field is afforded in the book entitled, "Fourier Transform Infrared Spectroscopy", by P. R. Griffiths [3].

The majority of applications in this region involve the measurement of the absorption spectrum of a sample. Except for certain more esoteric applications (for instance time resolved spectroscopy on a short time scale) the advantages of FT-IR over comparable dispersive instruments are clear-cut. These include (in not necessarily the order of importance): 1) the multiplex (or Fellgett advantage), 2) the throughput (or Jacquinot) advantage, 3) the relative ease with which high resolution operation can be achieved, 4) the simultaneous acquisition of the continuous spectrum of the source radiation, and 5) absolute accuracy of the wave-length axis of the resultant spectrum (sometimes called the Connes advantage).

The multiplex advantage describes a comparison, based upon the achievable spectral signal-to-noise ratio (SNR), between a Fourier transform spectrometer and a comparable scanning dispersive instrument [4, 5]. Both instruments measure the spectrum of the source in a continuous fashion, over the same spectral range and with the same resolution. A resolution element of each spectrum is defined to be the band-width of the spectrum divided by the resolution of the spectrometer. Consider that there are M resolution elements in each spectrum.

During a particular measurement period the FT spectrometer continuously measures each resolution element throughout the entire measurement period. On the other hand, the scanning instrument measures any particular resolution element for only a fraction of the measurement time. Intuitively, it seems plausible that the SNR throughout the FT-derived spectrum should be greater than that in the spectrum acquired with the dispersive system, since each resolution element in the former is effectively integrated for a longer time than those in the latter.

Whether or not a multiplex advantage is realized is dependent upon the noise conditions under which the measurement of the interferogram is made. For most measurements of the interferograms of IR sources, the limiting noise is that of the detector. In such a "detector noise limited" situation a multiplex advantage is realized. In this situation, for equal measurement times the FT derived spectrum is expected to have a SNR that is $M^{1/2}$ times greater than that of an equivalent dispersive system.

The throughput advantage pertains to the situation that most FT-IR instruments can be configured with a large circular entrance aperture while comparable dispersive instruments employ slits that allow only a small fraction of the incident radiation to eventually reach the detector [6]. Greater throughput of the source radiation implies greater sensitivity.

In theory, all that is required to increase the resolution of a FT spectrometer is to lengthen the travel of the moving mirror. If the interferometer was illuminated with monochromatic radiation with a wavelength of $\lambda = 200$ nm, to achieve a resolving power of $R = 1 \times 10^6$ at 200 nm, the moving mirror would have to be moved a maximum distance $l =$

6.05 cm. Assuming that double-sided interferograms are being acquired, a total mirror travel of 12.1 cm would entail a relatively small interferometer system. To achieve the same resolving power with a dispersive system would require a significantly larger physical system. Interferometers with large maximum optical path differences have been constructed, resulting in resolving powers that would be impractical to achieve with dispersive systems. Some of these designs will be discussed shortly.

In theory, the wavelength axis of a spectrum acquired with a FT spectrometer is continuous across the measured spectral band-width. In practice, the Fourier transform of the interferogram is calculated by a digital computer. Thus, the wavelength axis is actually discrete, although for all intents and purposes it can be rendered continuous via appropriate interpolation techniques. A scanning dispersive spectrometer can produce a spectrum with a continuous wavelength axis. However, if a multiplex advantage exists the FT spectrometer would be the instrument of choice.

The calibration of the wavelength axis along the focal plane of a dispersive spectrometer can be a difficult and complex task. A source with a well-known wavelength can be used to calibrate a single point on the focal plane, but a number of sources are required to accurately calibrate the entire focal plane. In optical FTS the entire wavelength axis can be calibrated, via a calculation, if the wavelength of any single point on the axis is accurately known. The last point in the calculated spectrum corresponds to one-half of the frequency with which the interferogram was sampled. Since digitization of the interferogram is synchronized with the reference laser interferogram, the wavelength of this last point is directly related to that of the HeNe laser.

Hence, this well-known wavelength is typically used to calculate the wavelengths of all other points on the wavelength axis.

Until recently, FTS has largely been shunned as a candidate for many applications in the ultraviolet and visible regions of the spectrum. The major reason for this has been the anticipated presence of a multiplex disadvantage when the typical detectors of ultraviolet and visible radiation, photomultiplier tubes (PMTs) and/or photo-diodes (PDs), are employed in the measurement of the interferogram. The noise situation in FTS in the UV and VIS regions is considerably more complex than in the IR region. Even in the presence of a multiplex disadvantage, there are many other considerations to be made in the overall assessment of the applicability of this technique in these regions of the spectrum.

Another problem associated with operation in the ultraviolet and visible regions is that of aliasing of the spectrum. This is caused by undersampling of the analog interferogram during the process of digitization. The problem of aliasing and its solution are considered in detail in Chapter 3 of this thesis. At this point, suffice it to say that in contrast to the fundamental nature of the noise situation, aliasing in FTS UV-VIS is a technological problem that can be solved.

1-2.1. FTS in the UV-VIS.

In 1971, P. Luc and S. Gerstenkorn at the Laboratoire Aimé Cotton in Orsay Cedex, France, recorded, with high resolution, the atomic emission line spectrum of manganese [7]. The spectrometer that was employed in this study [8] was the second generation version of the first high resolution FT-IR

spectrometer built by J. Connes and P. Connes in 1968 [9]. As are the majority of the spectrometers presently being used in FTS UV-VIS, this instrument was based upon a Michelson interferometer.

To detect visible radiation, the spectrometer used by Luc and Gerstenkorn was equipped with PMT detectors. For double sided scans the maximum optical path difference was 1m. For an ideal interferometer, with zero instrumental apodization, this path difference corresponds to a resolving power (as defined above) of approximately 8.3×10^7 at 200 nm.

In 1978, these two researchers published a more comprehensive study aimed at assessing the capability of FTS in the UV-VIS - for both emission and absorption applications [10]. The spectrometer that was employed was an improved version of the one used in the previously cited study. The emission spectrum of Np was recorded with sufficient resolution to resolve the Doppler broadened profiles of the emission lines, and to resolve the hyperfine structure of the Np 237 isotope. The shortest reported wavelength of operation was approximately $28,866 \text{ cm}^{-1}$, or 346.43 nm. The absorption spectrum of iodine was also reported. The effective resolution was cited to be approximately 5×10^5 . Approximately 60,000 absorption bands in the region from $14,800$ to $20,000 \text{ cm}^{-1}$ (675.68 to 500.00 nm) were reported to have been recorded. In both of the above studies, the uncertainty in the assignment of peak wavenumbers was estimated to be approximately $\pm 0.001 \text{ cm}^{-1}$, or in the worst case $\pm 0.046 \text{ pm}$ at 675.68 nm. It was recognized that the accuracy of the assignment of peak wavelengths is affected by the signal-to-noise ratio (SNR) of the peak. For comparison purposes, if $\pm 0.001 \text{ cm}^{-1}$ performance could be achieved at 200 nm, this would correspond to an uncertainty in peak wavelength assignment of $\pm 4 \text{ fm}$.

The results of the above study clearly demonstrated the continuous wavelength coverage and wavelength accuracy capabilities of FTS in the near ultraviolet and visible regions of the spectrum. In addressing the question of a multiplex advantage or disadvantage, the authors stated that a multiplex disadvantage could be off-set by a gain due to the throughput advantage. In considering the situations of emission spectra (with strong and weak lines), continuous spectra, and narrow-band absorption spectra - the minimum overall gain over a comparable dispersive system was stated to be approximately unity. This was for the cases of weak emission lines, and strong absorption lines. An overall gain greater than unity was anticipated for continuous spectra and weak absorption lines. A gain much greater than unity was anticipated for strong emission lines.

During approximately the same period of time, researchers headed by J. W. Brault at the Kitt Peak National Observatory (KPNO) in Tucson, Arizona, and G. Horlick at the University of Alberta in Edmonton, Alberta, Canada were involved in the design and fabrication of a pair of FT spectrometers specifically designed to operate in the ultraviolet and visible regions of the spectrum. These two efforts represent a divergence in the field of FTS UV-VIS on the basis of the resolution capabilities of each instrument.

The KPNO spectrometer was specifically designed to be coupled to a solar telescope [11, 12]. For the most part, this instrument is a folded version of the original Connes spectrometer. An interesting feature of the design is that the interferometer consists of two moving reflector assemblies. These are translated in a push-pull fashion to reduce the physical space required to achieve a particular optical path difference. Since high resolution is required

for this application, the maximum optical retardation for double-sided scans was designed to be 1m. Later a demountable double passing system was developed to double the resolving power as required [13]. The optical system was designed to operate down to approximately 380 nm. This spectrometer was built primarily for the purpose of observing astronomical sources, and it has only been available to researchers on a limited basis. As will be discussed shortly, it has recently been coupled with laboratory sources in order to assess the analytical and spectrophysical capabilities of FTS UV-VIS. Prior to consideration of these studies, consider the approach of Horlick et al.

The overall aim of the work in the laboratory of G. Horlick has been to develop a simple, inexpensive, and reliable medium resolution FT spectrometer for routine analytical applications, and some specialized spectrophysical applications. It was recognized that for many studies, high resolving power is not necessary. In 1978, Yuen and Horlick reported the design and application of a modular Michelson interferometer capable of operation in the ultraviolet and visible regions [14, 15]. This instrument was designed to cover a band-width from approximately 180 nm (if purged or evacuated) to 3 μm . The maximum optical path difference over which data was acquired was 1.3263 mm. The maximum length of mirror travel was limited by the length of interferogram (in terms of the number of digitized points) that could be Fourier transformed by the standard laboratory computers available at that time. In the absence of instrumental apodization, this maximum optical path difference would produce an instrumental line-width equal to $\Delta\sigma = 7.72 \text{ cm}^{-1}$. The resolving power (as defined above) would be $R = 10,706$ for a FWHM of 18.7 pm at 200 nm. This is clearly a different resolution regime than that of the two spectrometers described above.

Due to instrumental apodization the full resolution capabilities of this instrument were not achieved. Nonetheless, this first generation instrument proved to be a valuable test-bed with which many of the facets of FTS UV-VIS could be explored. During the past decade, researchers in this laboratory have used this instrument to: 1) study the potential of FTS as the detection scheme in atomic emission spectroscopy, especially with an inductively coupled plasma (ICP) source [16-20], 2) investigate the potential of FTS in the NIR region [21], 3) study the noise situation when the interferogram is detected with a PMT or PD, as is the case in the UV and VIS regions [20, 22], 4) assess novel optical arrangements for reducing a multiplex disadvantage (if one exists) [18, 23], and 5) test novel hardware and software data manipulation implementations [19, 24, 25].

Even though many of the studies carried out by Horlick et al. during this period addressed phenomena that are not a function of resolving power of the spectrometer, interest in FTS UV-VIS as a routine analytical and spectrophysical tool seemed to wane in the early 1980s until the KPNO spectrometer was used in studies aimed at assessing these capabilities.

Initially, the KPNO spectrometer was used to measure the neutral atom excitation temperature of iron within an ICP [26]. The method that was employed involved measurement of the intensities of a number of emission lines of the same thermometric species, in this case iron. With the assumption that the iron was in at least local thermal equilibrium (LTE) within the plasma, a plot of $\ln(I\lambda_{nm}^2/g_m f_{mn})$ vs E_n produced what is known as a "Boltzmann plot". In these expressions, I is the measured intensity of the line of interest, λ_{nm} is the wavelength of the radiation emitted by the

transition from the upper energy state n to the lower state m , g_m is the statistical weight of the lower state, f_{mn} is the oscillator strength for the transition of interest, and E_n is the energy of the upper state. The slope of such a plot is equal to $-1/kT$, where k is the Boltzmann constant and T is the excitation, or Boltzmann, temperature. The advantage in using a FT spectrometer is that the peak intensities and wavelengths of a large number of the emission lines of the thermometric species of interest can be measured simultaneously and with a great degree of accuracy. This provides many points for the Boltzmann plot, thereby increasing the precision of the resultant value of the excitation temperature. Iron was picked as the thermometric species (as it typically is for these measurements) because the spectrum of iron is well-known, and a reasonably well-accepted set of "gf" values exist for iron.

In this study, the spectral band pass of the instrument was restricted to the wavelength region from 480 to 550 nm. The maximum optical path difference that was used in these experiments is unclear in this paper. The optical path difference is stated to be " ± 6.4 cm in the interferometer...(resulting) in resolution of 0.078 cm^{-1} ". This figure for the resolution ($\Delta\sigma$, that is the width of the instrumental line-profile at the first zero-crossings) is compatible with a maximum optical path difference of 12.8 cm. Hence, it is assumed here by the author of this thesis that the mirror movement was ± 6.4 cm. A resolution of 0.078 cm^{-1} corresponds to a wavelength resolution of $\Delta\lambda_{1/2} = 1.2 \text{ pm}$ at 500 nm.

The Fe(I) excitation temperatures for six viewing zones of the ICP were calculated. The minimum number of lines that could be used in a calculation was 4 while the maximum was 86. The limit on the number of lines that

could be used was determined either by the availability of gf values or the ability to identify Fe(I) lines within a given spectrum. The former is a literature problem while the latter might be related to a multiplex disadvantage. Nonetheless, this study clearly demonstrated the high spectral "information band-width" of FTS. It should be noted that this study did not rely heavily upon the high resolution capability of the KPNO spectrometer. In this type of study, resolving power is only necessary insofar as the spectral lines must be well enough separated that the peak intensities and wavelengths can be accurately measured.

The KPNO spectrometer was used by the same group of researchers to study the emission characteristics of argon in an argon ICP [27]. They reported the relative intensities and wavelengths of 109 emission lines within the NIR spectral region from 0.9 to 2.0 μm . The maximum optical path difference of the interferometer in this study was reported to be 12.48 cm; however, this figure is incompatible with the reported instrumental line width $\Delta\sigma = 0.040 \text{ cm}^{-1}$. It is assumed here that the quoted maximum optical path difference is actually the maximum distance between the two moving mirrors in this interferometer. This corresponds to the maximum travel of the moving mirror from ZPD in a standard Michelson interferometer, or one half of the maximum optical path difference. The accuracy of the measured wavenumbers of the spectral peaks was estimated to be within $\pm 0.001 \text{ cm}^{-1}$. The width (FWHM) of each of the spectral lines was also reported. Prior to this study, a preliminary study on the feasibility of ICP-FTS in the NIR region had been published by Stubbley and Horlick [21]. Both of these studies were of interest to many researchers since many non-metallic elements such as

oxygen, nitrogen, fluorine, chlorine, bromine, carbon, hydrogen, and sulfur emit in this region when excited within a ICP.

Still utilizing the KPNO spectrometer, L. M. Faires studied the effects of sample matrix on the detection limits in analytical ICP-FTS [28]. The conclusions of this study re-iterated those of a study performed by Stubbley and Horlick [18] - that a multiplex disadvantage may be present when the spectral band-width of a measurement contains a high intensity emission line of a matrix element. Reference was made to the illustration by Stubbley and Horlick that this effect can be reduced if the offending matrix element line is removed from the spectral band-pass prior to detection of the interferogram.

The high resolution capability of the KPNO instrument was used to measure the line-widths and profiles of 81 Fe(I) emission lines from an ICP [29]. The peak wavelengths of the observed lines extend from approximately 295 to 400 nm. The mirror movement was set to produce a theoretical instrumental line width $\Delta\sigma = 0.07 \text{ cm}^{-1}$. This corresponds to $\Delta\lambda_{1/2} = 0.61 \text{ pm}$ at 295 nm and 0.68 pm at 400 nm. Thus, in the absence of instrumental apodization, the resolving power across this spectral range is between approximately $R = 8 \times 10^5$ and 6×10^5 .

The emission lines of elements within an ICP are significantly broadened by physical processes such as collisions with other species in the emitting environment (collisional broadening), and motion of the emitting species relative to the detector of the emitted radiation (Doppler broadening). Collisional broadening results in a Lorentzian line-shape, while Doppler broadening results in a Gaussian line-profile. When both phenomena contribute significantly to the overall line-shape, a composite profile known

as the Voigt profile results. In the study cited above [29] the Lorentzian and Gaussian contributions to the observed line-shapes were analyzed. The Gaussian component was reported to be the dominant contribution, but the Lorentzian component was also significant. The reported widths (FWHM) of the lines range from 2.44 to 3.41 pm.

The KPNO spectrometer has been used to demonstrate the feasibility of FT-Raman spectroscopy [30]. In this experiment, the scattering light source was an Argon ion laser operated at 488.0 nm. The Raman spectrum of D₂ was measured. The major difficulty in performing FT-Raman is that the Rayleigh scattered radiation must be removed from interferogram before it is detected. Otherwise, almost certainly a multiplex disadvantage will exist such that the weak intensity Raman spectrum cannot be observed. This situation is similar to that of the previously described matrix effects in ICP-FTS. A half-wave plate was used to rotate the polarization of the output beam of the Argon ion laser such that the detected Rayleigh scattering could be minimized.

Currently, interest in FTS UV-VIS is running high. Since 1987 three new instruments designed specifically for use in the ultraviolet and visible regions have been designed and built. An upgraded version of the KPNO spectrometer has been designed and built by Brault at the Los Alamos National Laboratory (LANL) in Los Alamos, New Mexico. A commercial instrument designed specifically for FTS UV-VIS has been built by researchers headed by A. P. Thorne at Imperial College in London, England. This instrument is presently being manufactured and marketed by Chelsea Instruments Ltd. in London. The third new spectrometer has come out of the laboratory of G. Horlick. The design and characterization of this instrument is the subject of this thesis.

The LANL spectrometer represents the current state-of-the-art in optical FTS. The original design called for a maximum optical path difference of 2 m, a spectral band-width from 200 nm to $>20\text{ }\mu\text{m}$, and wavenumber accuracy of 0.0001 cm^{-1} [31]. In the absence of instrumental apodization, a maximum optical path difference of 2m would produce an instrumental line-width $\Delta\sigma_{1/2} = 0.003\text{ cm}^{-1}$, for a resolving power $R = 16.7 \times 10^6$ at 200 nm. As with the KPNO spectrometer, provision has been made to enable double passing of the interferometer such that twice the resolution can be obtained with the same maximum optical path difference. The projected wavenumber accuracy corresponds to a wavelength accuracy of 0.4 fm at 200 nm.

Intermediate reports from LANL give some indication of the achieved level of performance of this instrument. Resolution of 0.006 cm^{-1} ($\Delta\lambda_{1/2} = 1\text{ pm}$) has been reported for the 405.783 nm emission line of lead in a hollow cathode lamp (HCL) [32]. Preliminary studies have involved fundamental studies on He and Ne ICPs, emission from sulfide compounds, and high resolution IR studies [33]. Spectra are reported to have been acquired across a spectral band-width ranging from 210 nm to $10\text{ }\mu\text{m}$, and the highest resolution at the shortest wavelength was reported to be 0.56 pm at 250 nm [33].

Clearly, the theoretical resolving power of this spectrometer is extremely high. The push by the group of researchers involved at LANL and the KPNO project has been towards ever increasing resolution. At this point one might ask the question, "Is such high resolving power required for typical atomic emission spectroscopic applications?" It has been suggested as a rule-of-thumb that the instrumental line-width $\Delta\sigma$ should be at most one third of

the smallest physical line-width in the spectrum of interest [34]. This should allow resolution of the physical line-profiles. Three sources of current interest are the HCL, glow discharge lamp (GDL), and the ICP. The physical line-widths of a number of HCL emission lines have recently been measured with an echelle monochromator [35]. The reported values range from 0.41 to 0.96 pm. The same instrument was also used to measure the physical line-widths of a number of ICP emission lines. These reported values range between 1.4 and 6.0 pm. These are in the same range as those measured with the KPNO spectrometer [29]. Recently, the LANL spectrometer has been used to characterize the emission from a Grimm-type GDL [36]. The physical line-widths of four emission lines ranging from 371.9 to 425.4 nm, were measured under various operating conditions. The reported values range from 1.0 to 2.1 pm.

It has been suggested that for the ultraviolet and visible lines that are emitted by light to medium atomic mass elements, a maximum optical path difference of 5-7 cm should be sufficient to satisfy the rule-of thumb stated above [34]. This would produce a maximum instrumental line-width $\Delta\sigma_{1/2} = 0.12 \text{ cm}^{-1}$, or $\Delta\lambda_{1/2} = 1.9 \text{ pm}$ at 400 nm. Faires stated that [37] a maximum optical path difference of 5 cm corresponded to $\Delta\sigma = 0.1 \text{ cm}^{-1}$; however, the latter value is consistent with a maximum optical path difference of 10 cm, or a double-sided mirror travel of $\pm 5 \text{ cm}$. In this case, the maximum optical path difference would be 10 cm, and $\Delta\sigma_{1/2} = 0.0605 \text{ cm}^{-1}$, or $\Delta\lambda_{1/2} = 0.097 \text{ cm}^{-1}$ at 400 nm. This resolution capability might be adequate for the emission from lighter elements in an ICP. However, for emission from heavier elements in an ICP, and emission from HCLs, this is likely to be insufficient resolution.

As a worst case criterion of resolving power consider that it is decided to be able to resolve the physical line-profile of a 400 nm line with a line-width of 0.1 pm (FWHM). According to the above rule-of-thumb, this would require a maximum instrumental line-width $\Delta\lambda_{1/2} = 0.0333$ pm at 400 nm. This corresponds to $\Delta\sigma_{1/2} = 0.00208$ cm⁻¹ and therefore, a maximum optical path difference of 2.90 m. This would require a double-sided mirror travel of ± 1.45 m. This resolving power is within the resolution capabilities of the KPNO instrument if the interferometer is double-passed, and it should be well within the capabilities of the LANL spectrometer. Again, the caveat to be observed is that instrumental apodization must be absent to achieve this resolving power.

This criterion of resolving power is quite stringent - certainly for emission from an ICP. Since the physical line-widths in an ICP are typically between 1 and 10 pm, the maximum instrumental line-width might be set to $\Delta\lambda_{1/2} = 0.333$ pm at 400 nm. This corresponds to $\Delta\sigma_{1/2} = 0.0208$ cm⁻¹, requiring a maximum optical path difference of 29.0 cm, or a double-sided mirror travel of ± 14.5 cm. This regime of resolution capability is close to that for which the Chelsea spectrometer was designed.

The optical design of the Chelsea spectrometer [38] is similar in concept to the original Connes spectrometer [9]. The Chelsea instrument has been designed to operate down to 170 nm. The maximum travel of the moving mirror is ± 10 cm on either side of ZPD. Thus, the maximum optical path difference is 20 cm for a theoretical instrumental line-width $\Delta\sigma = 0.050$ cm⁻¹, and $\Delta\sigma_{1/2} = 0.030$ cm⁻¹. This corresponds to $\Delta\lambda_{1/2} = 0.48$ pm at 400 nm. According to the criterion stated above, this should allow resolution of the

physical line-profiles of lines with physical line-widths equal to 1.44 pm (FWHM) at 400 nm. The wavenumber accuracy has been reported to be reproducible to within $\pm 0.0006 \text{ cm}^{-1}$, or $\pm 2.4 \text{ fm}$ at 200 nm [38].

The Chelsea spectrometer has been coupled with an ICP to assess high resolution ICP-FTS [39]. Preliminary measurements of spectra of iron in an ICP have led to the conclusion that quantitative measurements of line intensities are optimal when the resolution of the spectrometer is set such that the lines are just fully resolved. The effects of source noise have also been studied with this instrument [40]. In this paper it is stated that the SNR of an emission line is independent of resolution until the physical line-profile of that line is just resolved. When the resolution is increased beyond this point the SNR of that line decreases. It is concluded that spectral interferences can be reduced (by increasing the resolution) with no sacrifice in SNR - until the instrumental line-width becomes less than the physical width of the line of interest.

The KPNO and LANL spectrometers are part of national research facilities that are available to researchers, for the most part, throughout the United States. The research mandate for these instruments is heavily biased towards fundamental astrophysical and spectrophysical studies. By virtue of cost and availability, these instruments are not readily available for the investigation and development of routine analytical procedures involving FTS in the UV-VIS. The Chelsea instrument has only recently become commercially available, and it is quite expensive (ca. £250,000 U.K.). For many routine analytical spectroscopic applications, the high resolution capability of the Chelsea instrument is not required.

As mentioned above, the approach of Horlick et al. has been to develop a simple, inexpensive, and reliable work-horse spectrometer with which many of the concepts of FTS UV-VIS may be elucidated. The original spectrometer [14, 15] suffered from significant instrumental apodization. During the period from 1978 to the present, the optical components comprising the interferometer have remained largely unchanged. The optical design is extremely simple, employing no compensation elements except for a compensator plate to negate the effect of dispersion of the beam-splitter substrate. For the current design it was felt that the optical components were still adequate for operation of this simple design in the ultraviolet and visible regions. Some surfaces had become suspect through aging, so these were refurbished and tested. The lack of compensating optical systems means that a great premium is placed upon effective alignment of the components of the interferometer, and maintenance of that alignment throughout the travel of the moving mirror. The large degree of instrumental apodization that was previously observed has been attributed to inadequate alignment of the interferometer. To remedy this, certain components of the interferometer have been re-designed to better enable alignment, and comprehensive, systematic alignment procedures have been developed and tested (where possible). In addition, criteria have been developed with which alignment of the interferometer can be judged.

The design of the present optical system of the interferometer, and the associated alignment procedures are presented in Chapter 2 of this thesis. With these improved procedures, the degree of instrumental apodization has been markedly reduced. The improvement in performance is large enough that many new proof-of-concept experiments may now be attempted.

The previous version of the electro-mechanical system with which the moving mirror was translated did not provide effective control of the velocity of the moving mirror. This caused spurious peaks to be introduced into acquired spectra [20]. An example will clarify how this occurred.

In this spectrometer, the output of the detector is typically band-width limited by a band-pass filter. This is to remove the dc-level of the interferogram plus any contribution due to stray light from the HeNe reference laser, and to reduce noise in the detected interferogram. It is usually desirable to have as narrow and well-defined a pass-band as possible. This entails sharp low and high frequency roll-offs of the filter transfer function. In the previous design, the moving mirror was translated with a velocity of 1.58 mm/s. This produced a reference laser interferogram with a frequency of 5 kHz. If the source was a Mg HCL, the 285.213 nm emission line would produce an approximately 11 kHz frequency component in the source interferogram. Typically, the output filter would be set for a pass-band from 8.5 to 17.5 kHz. The filter consists of a cascaded high and low pass filter. Each of these is an eighth order filter but for simplicity, consider that they are simple RC filters.

In the case of the high pass filter the -3 dB cut-off would be set to 8.5 kHz. The amplitude transfer function of this filter would be down 20 dB at 850 Hz, but it is essentially constant within the pass-band. If the velocity of the moving mirror was to change, the 11 kHz frequency component of the Mg 285 line would be frequency modulated across the pass-band of the filter. If the velocity modulation was sufficient to modulate the frequency of this component out of the pass-band, then this component would be amplitude

modulated due to the filter roll-offs. However, within the pass-band, frequency modulation would not be expected to produce significant amplitude modulation. Amplitude modulation would be undesirable since the spectrum of an amplitude modulated sinusoid is a peak at the frequency of the sinusoid, with side-bands symmetrically displaced on either side of that peak.

If the frequency of the 11 kHz component was not amplitude modulated, it might be expected that synchronization of sampling of the interferogram with the reference laser would negate the effect of frequency modulation of the interferogram. This would be the case if it was not for phase modulation of the interferogram as a result of the frequency modulation. Phase modulation arises because the roll-off of the phase transfer function of both filters extends into the pass-band. At 8.5 kHz, the phase of the output of the high pass stage has increased to 45° , at a rate of $45^\circ/\text{decade}$. Hence, when frequency modulated within the pass-band, the 11 kHz component of the Mg 285 line is phase modulated with respect to the reference laser interferogram.

Phase modulation is similar to frequency modulation in that the spectrum of a phase modulated sinusoid consists of an infinite number of symmetrically displaced side-bands whose amplitudes decrease as the displacement increases. Clearly, even minor modulation of the velocity of the moving mirror is undesirable since it can lead to the introduction of spurious spectral features. If the velocity is poorly controlled, this effect can be reduced by widening the band-width of the filter; however, attendant with this will be increased noise in the detection system. To avoid this trade-off, it has been decided to control the velocity of the mirror to as great a degree as

possible, thereby allowing the pass-band of the filter to be made as small as desired.

From 1978 until the present, minor modifications were made to the mirror drive electro-mechanical assembly, and the associated velocity and scan control electronics [41, 42]. However, even with these retro-fitted improvements the performance of the moving mirror drive remained inadequate. Therefore, it was decided to re-design, from the ground up, the electro-mechanical moving mirror assembly and associated electronics. The aim has been to achieve tight velocity control with absolute knowledge of the position of the moving mirror at all times during data acquisition. As described in Chapter 3 of this thesis, an effective velocity servo mechanism has been developed with which the velocity of the moving mirror is controlled to within approximately $\pm 0.4\%$ (a conservative estimate). The electronics of this system have been designed in a modular fashion, such that improved circuitry can be inserted into the design should that become desirable in the future.

A new scan control system has been designed whereby the position of the moving mirror is monitored at all times via counting of periods of the reference laser interferogram. As described in detail in Chapter 3, this absolute fringe counting system will ultimately enable highly efficient data acquisition with a duty cycle approaching 100%. The system is presently configured for a maximum double-sided scan length of $\pm 32,768$ periods of the reference laser interferogram. The scan control electronics are designed such that if it is desired in the future to increase the scan length, or acquire single-sided scans, these modifications could be easily achieved with a minimum re-designing of the system.

The current maximum double-sided mirror travel corresponds to a maximum optical path difference of 2.07 cm. In the absence of instrumental apodization, this mirror travel would produce an instrumental line-width $\Delta\sigma = 0.483 \text{ cm}^{-1}$, or $\Delta\sigma_{1/2} = 0.292 \text{ cm}^{-1}$. As mentioned previously, instrumental apodization has not been completely eliminated. As described in Chapter 2 of this thesis, the best resolution measured to date is $\Delta\sigma_{1/2} = 0.38 \text{ cm}^{-1}$, corresponding to a resolving power of 92,267 at 285.213 nm. The accuracy of the wavelength axis has been estimated to be approximately $\pm 1 \text{ pm}$ across the spectral range from 200 to 300 nm [43].

The FT spectrometer described in this thesis has only recently been completed. It is anticipated that the significantly improved performance of this instrument will allow workers within the research group of Horlick to perform studies such as the following.

FT-Raman will be studied. As with FTS UV-VIS in general, the application of this technique has suffered greatly from an expected severe multiplex disadvantage [44]. However, this technique is beginning to gain acceptance as evidenced by the growing number of researchers who are becoming involved in this area [45-51].

A number of absorption measurements will be studied with this instrument. Continuum flame atomic absorption using a FT spectrometer has been shown to be feasible [52], and studies regarding the usefulness of FTS for the measurement of UV-VIS molecular absorption are currently being conducted [53, 54].

Studies aimed at elucidating the nature of noise in FTS in the UV-VIS will be continued. It is anticipated that with the greatly improved capabilities of this current instrument, studies of the type performed by Marra and Horlick [20] can be extended by virtue of the significantly more controlled situation. This approach will be used to assess the effectiveness of various optical configurations (such as pre- and/or post dispersion) aimed at reducing the multiplex disadvantage. Preliminary work in this direction is presented in Chapter 4 of this thesis.

Currently, the sources under study within the research group of Horlick are the ICP, GDL, and HCL. In the same vein as the study by Faires et al. [26], relative line intensity measurements will enable Horlick et al. to determine various spectrochemical temperatures within these different sources. Currently, the preferred thermometric species is Fe; however, with this instrument other candidates, such as Cd, will be assessed.

The current version of this instrument will not be able to resolve the physical line-profiles of the majority of emission lines from the sources listed above. However, it will be possible to measure the line-profiles of certain highly broadened lines. For instance, from the line-width of the $H\beta$ line we will be able to determine electron densities within various regions of the plasma. It is anticipated that spectrophysical measurements such as those described here will aid significantly in the assessment and optimization of various designs of these sources.

In the future it may be decided to build a higher resolution instrument to actually measure line-profiles. This information would enable us to quantify the broadening processes such as collisional (pressure), Doppler, and

Stark broadening, that are occurring within these sources. By virtue of the modularity of the present design this would not be a particularly difficult or time-consuming task.

The continuous wavelength coverage, high wavelength axis accuracy, and ready availability of the data in a digitized form, render this instrument an almost ideal candidate for the measurement and tabulation of emission wavelength tables. This work has commenced [43].

The analytical capabilities of FTS in the UV-VIS are currently being characterized with this instrument. The multi-line capability enables one to choose the best line with which to analyze a sample. In addition, the use of more than one line from an element of interest provides added information that can be used to enhance the capability of detecting that element [43]. Already, methods for auto-qualitative and auto-semi-quantitative analyses have been developed and studied [43].

Finally, by virtue of the continuous wavelength information in the spectra, this instrument is a strong candidate for studies relating to the intelligent optimization of its performance, and instruments in general.

As a final point in this overview of FTS UV-VIS, it should be noted that a number of manufacturers of FT-IR spectrometers are beginning to explore the potential of FTS within, predominately, the visible and near-infrared regions of the spectrum. A number of the studies cited within the first chapter of this thesis were performed on commercial instruments [48-51, 52-54, 64]. For the most part, these instrument manufacturers are interested in the assessment and development of FT-Raman in the NIR region, and FT molecular spectroscopy within the visible region. Both of these

measurements would be expected to suffer from a multiplex disadvantage; however, it is clear that other aspects of the experiment are being considered by researchers interested in these applications. Where once FTS in the UV and VIS regions was shrugged off as being non-competitive with dispersive systems, members of the analytical spectroscopy community are now starting to realize that the comparison is complex, and in certain cases FTS UV-VIS can out-perform equivalent dispersive instruments.

The first part of this chapter has been written to provide the reader with an introduction to the optical FTS method and provide an overview of this area of study such that the present work can be put into perspective. The next section of this chapter provides a more detailed description of the physical principles that are involved in this experiment. This description is approached from the point of view of the characterization of the optical radiation that is emitted by excited gaseous atoms; however, the principles described herein are quite general.

1-3. The principles of optical FTS.

The operation of an optical Fourier transform spectrometer is most easily explained in terms of the classical electromagnetic picture of light. In fact, the Michelson interferometer that is employed in this type of spectrometer will be shown to be analogous to the physical set-up of Young's double slit experiment, the classic experiment by which the wave nature of light is demonstrated.

Each atom in the source of radiation that is to be characterized is considered to be an elementary radiator. Each of these elementary radiators

emits an electromagnetic wave that propagates away from the atom at the speed of light $c = 2.99792458 \times 10^8$ m/s [55]. As a starting point, consider that an elementary radiator started to emit an infinity of time ago and that it will continue to emit for an infinity of time, hence.

An electromagnetic wave consists of an electric field and magnetic field component. These are described by vectors which at any given point in time or space are both directed perpendicular to each other and to the direction of propagation. In many instances the directions of these vectors change as the wave propagates. However, the wave illustrated in Fig. 1-3 is linearly polarized, therefore the planes of vibration of the electric and magnetic field components are constant. With the direction of propagation defined to be the z-axis in a right-handed coordinate system, the electric field is always, at all points in time and space, directed along the x-axis.

Since the elementary radiator has been emitting for an infinity of time, the spatial extent of the wavetrain is infinite along the direction of propagation. At any point z' along the direction of propagation, the magnitude of the electric field component varies sinusoidally with time. Since the wavetrain has infinite spatial and temporal extent, this is by definition a monochromatic electromagnetic wave. Note that monochromaticity requires that the magnitude of the electric field component vary in a purely sinusoidal fashion, with no change in the amplitude over time or space.

For simplicity this will be considered to be collimated radiation, therefore this is a plane wave. The electric and magnetic field components

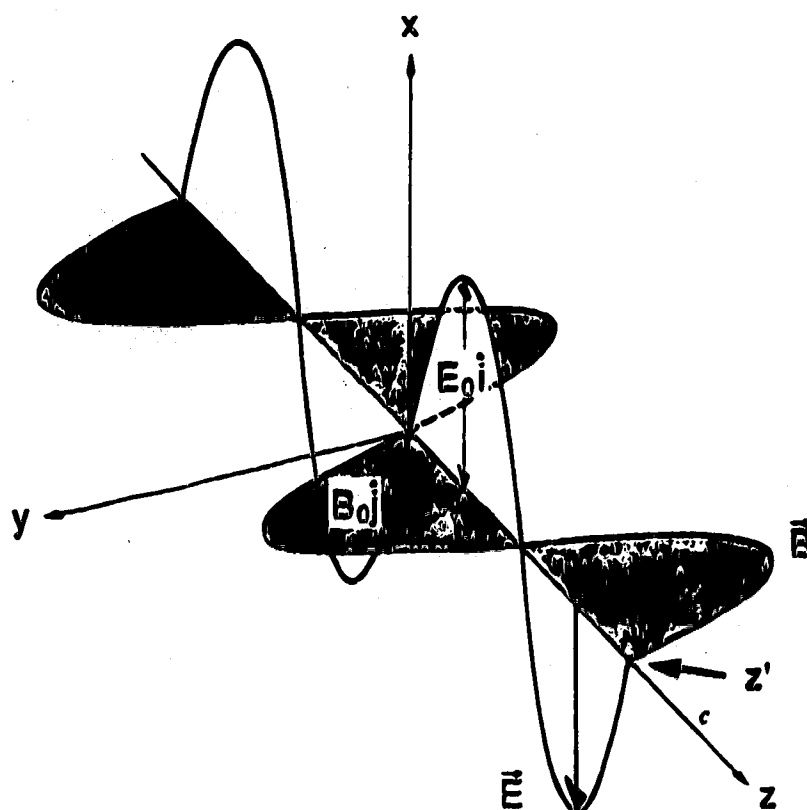


Figure 1-3. A classical electro-magnetic wave.

have magnitudes that are constant across infinite planes that are at all points perpendicular to the direction of propagation.

In the following discussions, the electromagnetic wave that is emitted by one of these elementary radiators will be considered to be the smallest unit of electromagnetic radiation. Larger disturbances will consist of the superposition of a number of these elementary wavetrains. For now the length of time over which the radiators emit is considered to be infinite; however, in later discussions this time will be finite.

Referring again to Fig. 1-3, at the point z' the electric field component of the radiation from one of these elementary radiators can be expressed as:

$$\vec{E}(z',t) = \vec{E}_0 \cos(k_0 z' - \omega_0 t + \epsilon) \quad \text{Eq. 1-1}$$

where

$\vec{E}_0 = \hat{i} E_0$ = electric field amplitude vector,

k_0 = radian spatial frequency,

ω_0 = radian temporal frequency, and

ϵ = phase relative to the position z' .

Since these various quantities will be used interchangeably throughout the thesis, then for completeness:

$k_0 = 2\pi\sigma_0$, where σ_0 = spatial frequency, or, wavenumber,

$\sigma_0 = 1/\lambda_0$, where λ_0 = spatial period, or, wavelength,

$\omega_0 = 2\pi\nu_0$, where ν_0 = temporal frequency, and

$\nu_0 = 1/T_0$, where T_0 = temporal period.

Consider that a source contains a number, N , of these elementary radiators. These radiators emit N wave trains, all of which have the same direction of propagation, polarization, and frequency of oscillation of the electric field component magnitude.

Since these wavetrains travel through the same region of space they superpose to produce a composite electromagnetic wave. All of the wave trains have the same polarization, therefore the superposition of the waves is achieved with a simple scalar addition. The electric field component of the resultant wave is given by [56],

$$E(z',t) = \sum_{i=1}^N E_{0i} \cos(k_0 z' + \epsilon_i - \omega_0 t) \quad \text{Eq. 1-2.}$$

The magnitude of the resultant electric field component oscillates with the same frequency as the individual components. However, depending upon phase shifts ϵ_i of the individual components, the amplitude of the resultant sinusoidal oscillation can be any value between zero and

$$\sum_{i=1}^N E_{0i}.$$

For the purposes of illustration, we will assume here that the wavetrains are all in phase. This situation is akin to a source of laser radiation. To simplify matters further, let the individual amplitudes of the electric field component magnitudes be equal. Then, $E_0 = NE_{0i}$.

At distances far away from the source, the magnitude of the electric field component of a particular electromagnetic radiation is c (the speed of light) times the magnitude of the magnetic field component. Hence, the detection of electromagnetic radiation typically involves the interaction of the electric field component with the matter of the detecting system.

Consider the following "thought experiment." An electric field detector with a negligible response time is placed at some point z' along the direction of propagation. The output of the detector is connected to a very fast oscilloscope.

The trace on the screen of the oscilloscope would be a sinusoid with a constant amplitude E_0 and period T_0 . As an example, let the radiation have a wavelength of 200 nm. From the screen of the oscilloscope, the period would be measured to be $T_0 = 6.671281904 \times 10^{-16}$ s. Thus, the frequency of oscillation of the electric field component at the position of the stationary detector would be calculated to be $\nu_0 = 1.49896229 \times 10^{15}$ Hz.

In this experiment we've chosen to measure the electric field component of the radiation field. In this simple hypothetical situation, the detector directly measures the time varying behaviour of the magnitude of the electric field component of the radiation. Depending upon the nature of this detector, it might have been possible to measure the polarization of the radiation relative to the the laboratory frame of reference. However, since the argument will be constrained to the situation of identical polarization for all of the elementary wavetrains, the effect of polarization will not be considered. What information regarding the source of this radiation could be inferred

from this measurement, and how should that information be presented for interpretation?

First, consider the time domain presentation of the information, i.e. the oscilloscope output. The magnitude of the resultant electric field varies in a purely sinusoidal fashion, no matter how long we observe the oscilloscope screen. From this it can be inferred that the length of the constituent wavetrains must be long, relative to the length of time over which the output is observed. Also, there must be a fixed phase relationship between the elementary wavetrains during the measurement period. Hence, it can be concluded that the radiation from this source is coherent.

Consider that the phases of the constituent wavetrains vary in a random manner over the length of the measurement time. Even if the length of time over which the radiators emit is long in comparison to the measurement time, random shifts in phase could be introduced via interactions of the radiators with each other and with other species within the source. The elementary wavetrains would only be coherent in phase for the short time between interactions. Since the phase of the radiators varies in a random fashion, then as indicated by Eq. 1-2, the magnitude of the resultant electric field fluctuates in a random fashion. This random fluctuation would be observed on the oscilloscope screen.

Thus, depending upon the nature of the source, the trace on the output oscilloscope could range from a pure sinusoid, to a complex randomly varying fluctuation with time. This will be discussed in greater detail further on in this chapter; however, suffice it to say that any departure of the oscilloscope trace from the pure sinusoid could be recognized as being the

result of: 1) the finite life-time during which a given radiator emits a continuous wavetrain, 2) interaction of the radiators with other species in the source environment, 3) random motion of the radiators relative to the point of detection, or 4) interaction of the radiators with other electric or magnetic fields within the source environment.

As described above, for the simple case of coherent radiation the amplitude, frequency and phase of the magnitude of the resultant electric field component could be directly measured from the trace on the oscilloscope screen. An amplitude and phase spectrum of the radiation could be plotted. The former would consist of an infinitely narrow line (i.e. a δ -function) with a length equal to the measured amplitude. The line would be positioned at the measured frequency of oscillation of the electric field component magnitude. Similarly, the phase spectrum would consist of a single point representing the phase at the measured frequency of the radiation. These spectra could then be taken to an independent observer for interpretation.

The independent observer, having no prior knowledge of the time varying behaviour of the radiation, would be able to conclude that the measured radiation was coherent. This would be apparent from the discrete nature of the spectra. Such a spectrum can only be produced by a harmonically pure sinusoid of infinite extent. If the spatial and/or temporal extent of a pure sinusoid is limited, the resulting spectrum still consists of a single line centered at the frequency of the sinusoid. Now however, the line has a finite spectral width. This is a statement of a general property of functions of time and their frequency spectra. The width of a spectrum of a particular function of time is inversely proportional to the temporal extent of

that function. For instance, truncation in the time domain causes broadening in the frequency domain.

From the conclusion that the measured radiation was coherent, the independent observer would be able to draw the same inferences regarding the environment of the source radiators, as did the observer of only the time information. In this simple example, presentation of the data as a time or frequency domain representation has no effect upon the interpretation of the measurement. However, the situation is not always so simple.

Consider that a number of sources produce coherent radiation such as that described above. The radiation from each source is the superposition of the emission from a number of elementary radiators. The only difference between these radiations is the frequency with which the magnitude of the electric field component oscillates, and the amplitude of each oscillation. These sources are combined, such that the radiation that is detected at the point z' is the superposition of the component source radiations.

The trace on the screen of the oscilloscope is no longer a simple sinusoidal waveform. Instead, it is now the superposition of a number of pure sinusoids with differing amplitudes, frequencies, and phases. On the basis of simple observations of this time varying waveform, conclusions of the type drawn in the previous example would be difficult to achieve. In order that a similar type of reasoning can be followed, we must be able to separately examine each of the component radiations that make up the resultant superposition. This is nothing less than the usual desire (perhaps necessity) of human beings to linearize a problem to allow linear, piece-by-piece, interpretation.

The information that we seek is encoded within the resultant electric field component of the radiation. It is encoded, or multiplexed, in the form of a superposition of sinusoids of varying frequencies, amplitudes, and phases. The question to be asked is, "Knowing the manner in which the individual units of information are multiplexed, how does one decode, or demultiplex, this composite form to recover the individual units?"

Traditionally, optical spectroscopists have expended a great deal of time and effort pursuing methods by which superpositions of electromagnetic radiation can be separated in a manner that allows individual components to be identified and studied. In the early stages of this field of study this separation was achieved *physically* - first with prisms and then later with diffraction gratings. In both of these cases the frequency information is spatially dispersed. Detection of the electric field component of the dispersed radiation, at strategic positions in space, provides the desired decoded information. Note that in this decoding strategy more than one detector is required. An alternative decoding scheme involving only one detector has been known to be feasible for some time. However, it has only recently become technologically practical to employ this methodology.

It is possible to mathematically decode the frequency component information in the signal that is detected by this single hypothetical detector. This could be achieved via a Fourier series decomposition of the detected function of time. As will be explained, this is feasible in this special case because the superposition function of time is periodic by virtue of the discrete nature of the frequency components of that function.

The theory of Fourier series decomposition begins with the premise that any arbitrary periodic function of time can be represented as a sum (perhaps infinite) of sinusoids with appropriate amplitudes, frequencies, and phases. Recognizing the orthogonality of sinusoidal functions, relationships are easily derived that allow one to determine which frequency components are required, and with what amplitude and phase, in order to produce the periodic function of time of interest. In effect, the procedure interrogates the time varying waveform as to its constituent frequency components. By virtue of the initial premise that the time function is comprised of a sum of frequency components, the result is a discrete spectrum of the required amplitudes of each component. In addition, a discrete spectrum of the required phases of each component is produced.

If this procedure was applied to the function of time that was measured by the hypothetical detector, the result would be an amplitude and phase spectrum of the source radiation. The amplitude spectrum would consist of a number of infinitely narrow lines positioned at the frequencies of oscillation of the electric field component of each of the component radiations. The length of each line would be proportional to the amplitude of the electric field oscillation of each component. The amplitude and phase spectra for each component can now be interpreted separately. Thus, the multiplexed time domain information has been transformed into demultiplexed frequency domain information.

This example describes a so-called " Multiplex" technique. In this case, the signal that is initially detected contains the information in a multiplexed form. Knowing the process of encoding, the signal may be appropriately

decoded to produce the desired individual, interpretable, units of information. This can be contrasted with the previously described "Dispersive" techniques wherein the physical situation is arranged to provide demultiplexing prior to detection. Note that with a multiplex technique only one detector is required, whereas with a dispersive system a number of detectors are required. As will be described, either type of technique has its own particular set of advantages or disadvantages and, in a sense, the two techniques are complementary.

Consider again for a moment the situation in which the detected radiation is emitted from a number of incoherently phased oscillators. Due to the random fluctuations of the magnitude of the resultant electric field component, the trace on the screen of the oscilloscope would likewise vary randomly. It would be very difficult for an observer of this time-varying signal to draw any conclusions as to the nature of the source of this radiation. Perhaps the only conclusion that could be reached is that the source was emitting incoherent radiation at the time of detection.

If, however, the spectrum of the detected function of time could be obtained, the result would be a single broadened line centered at the frequency of the radiation. The random fluctuations seen in the time varying output signal are (in this case) caused by random variations in the relative phases of the constituent wavetrains. This process is functionally equivalent to truncation of the wavetrains - a line-broadening phenomenon. If a number of spectra were obtained, the extent of broadening in each spectrum would follow a particular statistical distribution. If a large number of these spectra were averaged, the result would be an average spectral line profile with a characteristic line-width. Both the spectral line-shape and width can be

used to quantitatively assess many of the physical processes that occur within sources of atomic emission. To a human being possessing a reasonably typical view of reality, this information would not be available from the time-domain signal. Clearly, for our present purposes this signal must be transformed into the corresponding frequency domain signal. As will be described, the technique of Fourier series decomposition can be generalized to allow its application to arbitrary aperiodic functions of time. All that is required is to measure the time varying behaviour of the magnitude of the electric field component of the radiation field of interest. It is this measurement wherein the "rub" lies.

As indicated above, radiation with a wavelength of 200 nm has an electric field component whose magnitude oscillates with a frequency on the order of 10^{15} Hz. This is orders of magnitude higher than the frequency response of even the fastest detectors of light that are currently available. Thus, it is unlikely that there is any hope of directly measuring the time varying behaviour of a field of optical radiation. A further encoding step is required.

1-3.1. Encoding with the Michelson interferometer.

In order that the mathematical techniques of Fourier analysis may be employed in the decoding step, the result of further encoding should be a signal in which the time varying behaviour of each frequency component of the encoded signal is directly and uniquely related to that of the corresponding frequency component in the resultant electric field of the radiation that is to be characterized. For instance, if each frequency component could be made to produce an electrical signal with the same

relative amplitude (relative to the other electric field component amplitudes) and phase, and with a proportionate frequency that is much lower than that of the optical electric field, then when these individual frequency components were combined in a superposition fashion the result would be a physically measurable signal whose time varying behaviour would be directly related to that of the electric field of the radiation. Exactly this encoding step is achieved through the use of a Michelson interferometer.

Prior to the discussion of this encoding step, consider for a moment the actual manner in which optical radiation is typically detected. Since the description of the encoding step that is to follow is most easily approached from the classical wave picture of light, the detection of light will be approached from this perspective as well.

Currently, optical radiation is typically detected with either a photomultiplier tube (PMT), or a photo-diode (PD). The frequency responses of either of these types of detectors are orders of magnitude lower than that which would be required to directly detect the temporal variations of the light impinging upon them. At low light levels the particle description of light is manifested in the ability of these detectors to count photons. However, when viewing a more intense source, the output of detectors such as these is a steady time invariant signal. For either description of the incident radiation, this is the result of a detector that is too slow. For the purposes of illustration, it is this situation that we are interested in.

As mentioned above, it is the electric field component of the radiation that interacts with the matter of the detection system. These detectors, being slow in relative terms, integrate this interaction over time. The energy that is

carried by an electromagnetic wave across a unit area, as a function of time, is described by the Poynting vector of the wave. Physical detectors respond to this energy but they average it over time. Thus, these detectors respond to the power that crosses a unit area through which the wave passes. This power per unit area is called the "irradiance" and it is found by integrating the time varying Poynting vector with respect to time. The irradiance is also more commonly called the "intensity." Although this might offend some, this is the term that will be used to describe the quantity of the field that the physical detector measures.

In a vacuum, the intensity of an electromagnetic wave with an electric field component \vec{E} (this is the total electric field component, which may be the superposition of a number of other components) is given by [56]

$$I = \epsilon_0 c \langle \vec{E} \cdot \vec{E} \rangle \text{ w/m}^2 \quad \text{Eq. 1-3}$$

where

ϵ_0 = the permittivity of free space, and,

c = the speed of light in a vacuum.

The term in angle brackets in Eq. 1-3 is the time average of the time varying magnitude of the electric field component of the electromagnetic wave. For the trivial case of the plane monochromatic wave described by Eq. 1-1, the intensity is given by $I = \epsilon_0 c E_0^2 / 2$, where E_0 is the amplitude of the sinusoidally varying electric field component of the radiation.

From this small discussion there are two important points to note: 1) from a classical point of view a physical detector produces a signal that is

proportional to the time average of the (time varying) magnitude of the electromagnetic radiation, and 2) if the intensity of a radiation field is reduced by $1/2$, then the magnitude of the electric field component of that radiation is reduced by $1/\sqrt{2}$.

The Michelson interferometer is named after A.A. Michelson, the man who invented it ca. 1881 [57]. The manner in which this instrument encodes the frequency information of a radiation field into a readily detectable form is best described with reference back to Fig. 1-1.

The Michelson interferometer is one of a class of interferometers known as "amplitude-splitting interferometers." The incident radiation impinges upon a partially reflecting surface such that part of the radiation is transmitted towards a fixed mirror while the rest is reflected towards a mirror that is translatable, that is, the moving mirror.

The amplitudes of the electric and magnetic field vectors of the radiation in each arm are some fraction of those of the incident radiation. For the purposes of illustration it is assumed that the beam-splitting surface transmits and reflects 50% of the incident intensity, regardless of wavelength. Thus, the magnitude of the electric field of the radiation that enters either arm of the interferometer is $1/\sqrt{2}$ times that of the incident radiation.

As well, for clarity it is assumed that this surface does not require a transmitting substrate for support. In actual practice such a substrate is required. Consequently, an identical plate is placed in the moving mirror arm of the interferometer (in this particular arrangement). This equalizes the optical path length that each beam traverses in travelling to its respective

mirror and then back to the point of splitting. This can be seen in the actual design described in Chapter 2 of this thesis.

The Michelson interferometer depicted here is configured with the plane of the beam-splitter set at 45° , relative to the planes of the incident wave-fronts. Plane reflectors are indicated in the two arms of the interferometer. For proper operation, the planes of these mirrors must be accurately set to be at 45° , relative to the plane of the beam-splitter. Other arrangements are possible, with various arrangements of reflectors at different angles. However, the configuration shown is that which is employed in the instrument described in this thesis. Again, this is described in detail in Chapter 2.

Consider now the situation in which the wave-fronts of the radiation that is incident upon the beam-splitter are planar (with the indicated orientation) and the magnitude of the electric field component varies sinusoidally with time at any point along the direction of propagation. In other words, collimated monochromatic radiation is incident upon the interferometer. This radiation can be considered to be either a single wavetrain from an isolated elementary radiator, or the superposition of N of these wavetrains from a group of radiators that are emitting coherently. Again, since the radiation is monochromatic, the magnitude of the electric field component is a sinusoidal variation of infinite spatial and temporal extent. The wavelength of the radiation is λ .

As the incident radiation impinges upon the beam-splitting surface, 50% is transmitted through the beam-splitter to enter the fixed mirror arm of the interferometer, while the other 50% is reflected into the moving mirror

arm. The two beams travel to their respective mirrors at which point they are reflected back towards the point at which the beam was split. The mirrors in each arm of the interferometer can be thought of as a pair of coherent sources of radiation. During the ideal beam-splitting process two beams with identical polarizations, a fixed phase difference, the same frequency, and equal amplitudes are produced.

The two beams do not have identical phases because the beam that entered the moving mirror arm underwent a reflection while the other was transmitted. On the way back through the point at which the splitting occurred, the fixed mirror arm beam is reflected towards the detector while that from the moving mirror arm is transmitted. If the correct geometry of the optical components is maintained, the two beams are brought together in the same region in space. That is, they are recombined and will interfere if possible. During the splitting and recombination processes each beam is transmitted once and reflected once. Thus, when the two are recombined, the phase difference that was introduced during splitting is removed.

Upon returning to the beam-splitter, one-half of the moving mirror beam is transmitted towards the detector while the other half is reflected back towards the source. The same is true for the fixed mirror beam wherein 50 % of this beam is transmitted back towards the source. These beams are recombined in the same manner as the output beam. However, since the moving mirror beam underwent two reflections while the fixed mirror beam was transmitted twice, the phase shift between the two recombined beams due to reflections does not cancel as in the output beam. If it is assumed that the reflection/transmission phase shift is zero for the output beam, through conservation of energy considerations there must be a

reflection/transmission phase shift of π radians between the components of the recombined beam that returns back to the source.

If the conditions are correct for interference between the recombining beams, the result is a spatial redistribution of the intensity of the incident radiation. By virtue of the incident radiation, a certain number of joules of energy cross the area of the entrance aperture per second. If the conditions are correct for total constructive interference between the re-combined beams that travel towards the detector, then (with monochromatic incident radiation) this beam contains all of the incident intensity. Therefore, the two beams that recombine to head back towards the source must interfere in a completely destructive fashion such that the intensity that returns to the source is zero. Conversely, if the conditions are correct for totally destructive interference at the output, all of the incident radiation must return towards the source. In summary, if the beam-splitting/recombination process introduces any phase difference between the two beams that re-combine and travel towards the detector, the two beams that recombine and travel back towards the source must be shifted by the same amount plus or minus π radians.

Clearly, by virtue of the above discussion we can treat this ideal Michelson interferometer as a system of two pairs of collinear sources of coherent radiation. This is illustrated in Fig. 1-4. Shown in this figure is the pair of sources that represent the beams that re-combine and travel to the detector. The source S_1 represents the moving mirror arm of the interferometer. It emits radiation whose electric field component is designated as \vec{E}_1 . Similarly, S_2 , representing the fixed mirror arm, emits radiation that has an electric field component \vec{E}_2 . The optical path lengths that the two beams travel to reach the detector are X_1 and X_2 , respectively.

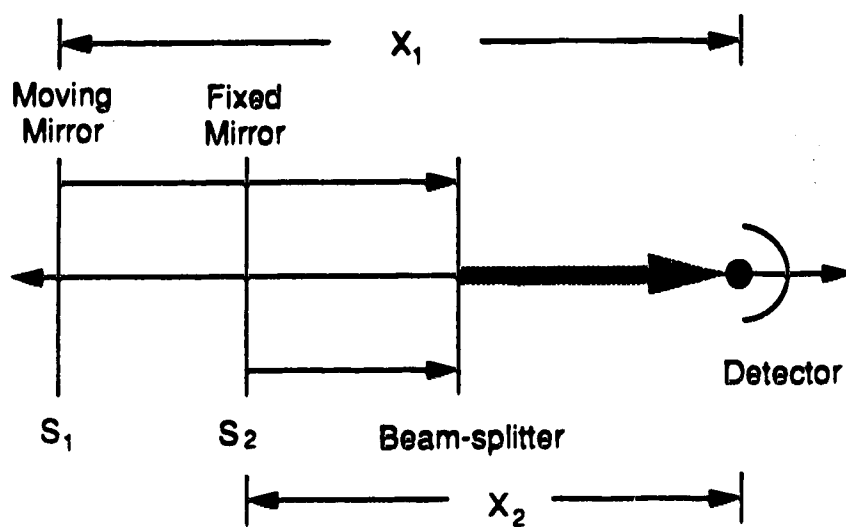


Figure 1-4. Virtual source representation of the Michelson Interferometer. Detected beams.

The two sources that represent the beams that re-combine and travel back towards the source are equivalent to the above two, except that one source emits radiation whose electric field oscillation is π radians out of phase with that emitted by the other source.

The electric field components of the radiation from the two sources S_1 and S_2 , at the position of the detector, are as follows:

$$\vec{E}_1 = \vec{E}_{01} \cos(k_0 X_1 - \omega t) , \text{ and}$$

$$\vec{E}_2 = \vec{E}_{02} \cos(k_0 X_2 - \omega t)$$

The electric field at the point of the detector is the superposition of \vec{E}_1 and \vec{E}_2 . That is,

$$\vec{E} = \vec{E}_1 + \vec{E}_2 .$$

The detector responds to the intensity of the radiation, which, by Eq. 1-3 is proportional to the square of the magnitude of the electric field component of the radiation. The intensity of the radiation at the position of the detector is therefore,

$$I = \epsilon_0 c \langle \vec{E} \cdot \vec{E} \rangle$$

where

$$\vec{E} \cdot \vec{E} = |\vec{E}_1|^2 + |\vec{E}_2|^2 + 2 (\vec{E}_1 \cdot \vec{E}_2) .$$

Hence,

$$I = \epsilon_0 c \left[\langle |\vec{E}_1|^2 \rangle + \langle |\vec{E}_2|^2 \rangle + 2 \langle \vec{E}_1 \cdot \vec{E}_2 \rangle \right] \quad \text{Eq. 1-4.}$$

Thus,

$$I = I_1 + I_2 + I_{12} \quad \text{Eq. 1-5.}$$

From Eq. 1-5, it can be seen that the overall intensity of the radiation at the position of the detector is the sum of three terms. The term I_{12} is the component of the intensity at the detector that is due to interference between radiation from the two sources representing the arms of the interferometer. The first two terms represent the intensity of the radiation emitted by either source. That is, if S_2 was turned off (i.e. if the path of the light through the fixed mirror arm was blocked), then the intensity of the radiation at the position of the detector would be equal to I_1 . In this situation I_{12} would be zero since interference cannot occur with only one beam from the one source.

The interference term I_{12} is particularly interesting. The time average in this term, namely $\langle \vec{E}_1 \cdot \vec{E}_2 \rangle$, is (for this situation) the so-called "first order correlation function" for the two imaginary sources S_1 and S_2 . The extent to which this quantity is not zero is an indication of the coherence of the two fields of radiation that are emitted by the two sources. This will be considered in greater detail further on in this discussion.

As a result of the perfect 50% reflection and transmission properties of the beam-splitter, the amplitudes and polarizations of \vec{E}_1 and \vec{E}_2 are the same. During the beam-splitting/re-combination process, the magnitude of the electric field of the radiation is reduced by $1/\sqrt{2}$ on each of the two passes. Therefore, the magnitude of the electric field component of the radiation that

is emitted by either S_1 or S_2 is $1/2$ of that of the incident radiation (which means that the intensity of the light from either of these sources is one quarter of that of the incident light). Hence, $E_{01} = E_{02} = 1/2 E_0$, where E_0 is the amplitude of the electric field component of the incident radiation. The first two terms of Eq. 1-5 are equivalent and it is easy to show that $I_1 + I_2 = 1/2 I_0$ where I_0 is the intensity of the incident radiation.

It is also easy to show that the third term of Eq. 1-5 (the interference term) is equal to:

$$I_{12} = \frac{1}{2} I_0 \cos[k_0(X_1 - X_2)]$$

and therefore, the intensity of the radiation that reaches the detector, as a function of optical path difference $X = X_1 - X_2$, is given by:

$$I_D = \frac{1}{2} I_0 [1 + \cos(k_0 X)] \quad \text{Eq. 1-6a.}$$

Similarly, the intensity of the radiation that returns to the source can be expressed as:

$$I_s = \frac{1}{2} I_0 [1 + \cos(k_0 X + \pi)] \quad \text{Eq. 1-6b.}$$

These two equations state that the intensity of the radiation that reaches the detector, or of that which is reflected back towards the source, is dependent upon the optical path difference between the two arms of the interferometer. With respect to this optical system, this intensity that varies as a function of optical retardation is called an "interferogram." Clearly, two interferograms are generated by the Michelson interferometer, one that is detected and one that travels back to the source. Again, due to the phase

shifts that are introduced via reflections and transmissions, the two interferograms are 180° out-of-phase with each other. In this optical arrangement the interferogram that travels back towards the source is for the most part inaccessible; however, in other configurations it can be detected. This can be useful for some applications. An example of this is given in Chapter 5 of this thesis.

The intensity of the detected radiation is dependent upon the optical path difference between the two arms of the interferometer. Does Eq. 1-6a make sense from an intuitive point of view? If the moving mirror is positioned such that the distances of the two mirrors from the point of beam-splitting are equal, then each beam that enters an arm of the interferometer has to travel the same distance from the beam-splitter, to its respective mirror, and then back to the beam splitter. Therefore, when the two beams are recombined at the beam splitter they are in phase. Total constructive interference occurs and the intensity at the detector is maximized. From Eq. 1-6a, this situation is that in which the optical path difference is zero. As indicated by this equation the intensity at the detector is the maximum that it can be. The condition in which the optical path difference is zero is called the condition of Zero Path Difference (ZPD). Depending upon the source, this can be a special situation.

If the moving mirror is moved away from the position of ZPD, through a distance of $\lambda/4$, the beam that enters the moving mirror arm has to travel twice $\lambda/4$ more than the beam that enters the fixed mirror arm - to return to the point of splitting. Hence, the phase of the moving mirror beam lags that of the fixed mirror beam by $\lambda/2$. When the two beams are recombined total destructive interference occurs. The intensity at the detector is

zero. This is also predicted by Eq. 1-6a. For a given change in the physical position of the moving mirror, the optical path difference changes by twice this amount. Thus, the optical path difference after this $\lambda/4$ movement of the moving mirror is $\lambda/2$. Since $k_0 = 2\pi/\lambda_0$, the cosine term in Eq. 1-6a is equal to -1, therefore the intensity at the detector is zero.

If the moving mirror is translated with a constant velocity, the optical path difference changes linearly. From Eq. 1-6a it can be seen that this will result in a detected intensity that varies sinusoidally. For a given wavelength of incident radiation the period of the sinusoidally varying intensity will be dependent upon the velocity of the moving mirror.

For a given velocity of the moving mirror, the period of the interferogram is directly related to the frequency of oscillation of the electric field component of the incident radiation. Thus, the time varying behaviour of the interferogram is directly related to that of the electric field component of the incident radiation. If the electric field component has a complex time dependence, this is faithfully reflected in the time-varying portion of the interferogram.

Since X_2 is fixed and X_1 is variable, in theory the optical path difference $X = X_1 - X_2$ can take any value between $X = \pm\infty$. If the mirror has a velocity V_M , then the optical path variation as a function of time is $X(t) = 2V_M t$, where it is understood that t varies between $t = \pm\infty$. The zero of time is recognized to be the instant that the moving mirror is in the ZPD position. Substituting the time varying optical path difference into Eq. 1-6a results in the following equation for the intensity at the detector as a function of time:

$$I_D(t) = \frac{1}{2} I_0 [1 + \cos(2\pi f_0 t)] \quad -\infty < t < +\infty \quad \text{Eq. 1-7a}$$

where

$$f_0 = \frac{2V_M}{\lambda_0} = \frac{2V_M}{c} v_0 \quad \text{Eq. 1-7b.}$$

Note that f_0 is the frequency of oscillation of the interferogram and that it is related to the wavelength of the incident radiation.

In the interferometer that is described in this thesis, the mirror is translated with a constant velocity equal to approximately 3.2 mm/s. Monochromatic radiation with a wavelength of 200 nm would produce a sinusoidally varying interferogram which oscillates with a frequency of approximately 32 kHz. With currently available technology, this is an easily detectable intensity oscillation.

Monochromatic radiation with a wavelength of 400 nm would produce a 16 kHz interferogram. If these two radiations were combined, the resultant interferogram would be an intensity oscillation that would be the superposition of a 32 and 16 kHz interferogram. This time-varying behaviour would be reproduced in the ac-component of the detected signal. When this was Fourier analyzed, the result would be an amplitude and phase spectrum in which only the frequency axis would have to be corrected, by a constant multiplicative factor.

In the above example, the interferogram that is produced from the 2-component radiation would be the same as that which would be produced if each component was incident upon the interferometer at different times,

followed by addition of the two separate interferograms to produce the composite interferogram. This allows us to generalize Eq. 1-7a in the following manner.

The interferogram that is produced when the incident radiation consists of a number of mono-chromatic frequency components, each having the wavelength λ_i , is simply the sum of the interferograms of each component. That is,

$$I_D(t) = \frac{1}{2} \sum_i I_i + \frac{1}{2} \sum_i I_i \cos(\omega_i t),$$

where, I_i is the intensity of the i^{th} component of the incident radiation, and ω_i is the angular frequency of oscillation of the interferogram of the i^{th} component.

Physically, spectral distributions are never discrete. Let $I(\nu)$ be the function that describes the intensity of the radiation that is emitted by the source as a function of the optical frequency. That is, $I(\nu)$ is the intensity spectrum of the source. Then, $I(\nu)d\nu$ is the intensity that is emitted with a frequency between ν and $\nu+d\nu$. The total intensity that impinges upon the interferometer is the integral of $I(\nu)$ over all values of ν .

$I(\nu)d\nu$ is the intensity that is emitted with a frequency between ν and $\nu+d\nu$. This portion of the intensity produces a frequency component in the interferogram with a proportional intensity and a frequency that lies between f and $f+df$. This infinitesimal frequency increment is related to the optical frequency increment via Eq. 1-7b. Therefore, let $I_D(\omega)d\omega$ be the measured intensity whose frequency of oscillation in the interferogram lies between ω

and $\omega + d\omega$. Then, for a continuous spectral distribution of intensity, the measured interferogram can be expressed as,

$$I_D(t) = \frac{1}{2} \int_0^\infty I(v) dv + \frac{1}{2} \int_0^\infty I_D(\omega) \cos(\omega t) d\omega \quad -\infty < t < +\infty \quad \text{Eq. 1-8.}$$

Note that the first term on the right hand side of Eq. 1-8 corresponds to one half of the incident intensity. This produces a time invariant dc-level in the measured interferogram. Hence, it has not been expressed in terms of the interferogram radian frequencies, ω .

Since the spectral distribution of the intensity of the incident radiation is now considered to be a continuous function of frequency, the measured interferogram is also continuous. Since it is no longer periodic, the simple procedure of Fourier series de-composition cannot be applied to decode the desired spectral information from the interferogram. Instead, a continuous form of Fourier analysis must be employed. That is, the Fourier integral transform must be used.

The Fourier integral transform results from consideration of the Fourier series de-composition of a periodic function of time, as the period is made to approach infinity in the limit. The result is a pair of integrals that operate on a function in one domain (time or space) to produce the corresponding function that describes the original function in a reciprocal domain (temporal or spatial frequency). For one dimension, the corresponding integral pairs that we are interested in are as follows:

$$\mathcal{F}\{g(t)\} = G(\omega) = \int_{-\infty}^{\infty} g(t) \exp[i\omega t] dt \quad \text{Eq. 1-9a,}$$

$$\mathcal{F}^{-1}\{G(\omega)\} = g(t) = \frac{1}{2\pi} \int_{-\infty}^{\infty} G(\omega) \exp[-i\omega t] d\omega \quad \text{Eq. 1-9b,}$$

and,

$$\mathcal{F}\{f(x)\} = F(k) = \int_{-\infty}^{\infty} f(x) \exp[ikx] dx \quad \text{Eq. 1-10a,}$$

$$\mathcal{F}^{-1}\{F(k)\} = f(x) = \frac{1}{2\pi} \int_{-\infty}^{\infty} F(k) \exp[-ikx] dk \quad \text{Eq. 1-10b.}$$

When a periodic or non-periodic function of time, $g(t)$, is operated on by the Fourier integral of Eq. 1-9a, the result is the function $G(\omega)$ that represents the radian frequency component content of $g(t)$. Therefore, $G(\omega)$ is the spectrum of $g(t)$. The inverse Fourier transform relationship is given by Eq. 1-9b, wherein $g(t)$ is recovered from the spectrum $G(\omega)$.

The Fourier transform pair of Eq. 1-10a and 1-10b relate the spatial and radian spatial frequency domains in the same manner as the time/frequency pair.

Consider once again Eq. 1-8. This describes the interferogram that would be obtained if the source had a continuous spectrum. Since the first term on the right hand side is time-invariant, it does not provide any information (within the context of this experiment). Therefore, it is not considered in the following discussion.

The second term on the right hand side of Eq. 1-8, that is,

$$I_D(t) = \frac{1}{2} \int_0^{\infty} I_D(\omega) \cos(\omega t) d\omega \quad -\infty < t < +\infty \quad \text{Eq. 1-11,}$$

represents the superposition of the component intensities with a time varying behaviour that is directly related to that of the resultant electric field component of the incident radiation. This produces a signal at the output of the detector that is a (potentially) complex function of time.

Consider the result of applying an inverse Fourier transformation, via Eq. 1-9b, to the interferogram spectral density function, $I_D(\omega)$. For a perfect interferometer of the type being considered here, the interferogram that is produced is an even function of optical path difference X . Hence, it is also an even function of time. With this in mind it is easy to show that the mathematical spectrum of the interferogram, given by the Fourier transform of the interferogram, is also even, stretching from $\omega = -\infty$ to $\omega = +\infty$. Hence, from Eq. 1-9b, the inverse transform of $I_D(\omega)$ is given by,

$$\mathcal{F}^{-1}\{I_D(\omega)\} = \frac{1}{2\pi} \int_{-\infty}^{\infty} I_D(\omega) \exp[-i\omega t] d\omega.$$

Since $I_D(\omega)$ is even, it can be shown that,

$$\mathcal{F}^{-1}\{I_D(\omega)\} = \frac{1}{\pi} \int_0^{\infty} I_D(\omega) \cos(\omega t) d\omega.$$

Comparing this equation with Eq. 1-11, it is clear that,

$$I_D(t) = \frac{\pi}{2} \mathcal{F}^{-1}\{I_D(\omega)\},$$

and therefore,

$$\mathcal{F}\{I_D(t)\} = \frac{\pi}{2} \mathcal{F}\{\mathcal{F}^{-1}\{I_D(\omega)\}\} = \frac{\pi}{2} I_D(\omega).$$

From the above discussion it can be seen that the interferogram is the inverse Fourier transform of a spectral density function that is functionally equivalent to that of the source radiation, except that the entire range of the function has been shifted to lower frequencies. In other words, the Fourier transform of the interferogram is the spectrum of the interferogram. This spectrum is equivalent to the intensity spectrum of the source, except that the frequency axis is incorrect by a constant dividing factor. The intensity spectrum of the source is achieved by correcting the frequency axis. The required multiplicative factor can be determined from Eq. 1-7b. In practice, the frequency axis is actually calibrated. The method by which this calibration is achieved is discussed in detail in Chapter 2 of this thesis.

It should be noted that the same result could be obtained through consideration of the interferogram as a function of optical path difference, and a spectral density that is a function of radian spatial frequency [1].

At this point one might ask whether or not information has been lost in this encoding procedure. Certainly, for the case of monochromatic incident radiation the time varying behaviour of the magnitude of the electric field component of that radiation is accurately reflected in the time-varying behaviour of the interferogram. However, a truly monochromatic field of radiation is an idealization. In certain applications some lasers approach this ideal; however, the majority of light sources are, to a greater or lesser degree, incoherent. As described previously, the time varying behaviour of the magnitude of the electric field component of incoherent radiation is complex. Direct measurement of the electric field would ultimately allow quantitative conclusions to be drawn regarding the nature of

the source of the radiation. Does the interferometric encoding process allow for the same conclusions to be drawn? Consider the interferogram that would be produced with incoherent radiation incident upon the Michelson interferometer.

1-3.2. The interferogram and spectrum of chaotic light

The radiation from a source of atomic emission is at best quasi-monochromatic. An isolated line from the spectrum of such a source has a finite width. Consider the wavetrain that is emitted from an isolated elementary (atomic) radiator. What physical processes can cause the wavetrain to be of limited spatial and/or temporal extent?

First and foremost, the life-time of atomic radiative states are limited in duration. A typical radiative life-time could be on the order of 10^{-8} s [58]. Hence, in loose terms, the wavetrain that is emitted by the radiator could be considered to be approximately 3 m in length. Consider that a source of atomic emission contains N identical elementary radiators that have a radiative life-time of 10^{-8} s. The wavetrains that are emitted by these radiators are identical in terms of amplitude and phase. However, due to the random nature of the emission process, the relative phases of the wavetrains vary randomly with time.

The electric field component of one of the emitted wavetrains can be described as in Eq. 1-1; however, for convenience a complex form will be used here. The state of polarization of each electric field component is not important since a randomly varying polarization is functionally equivalent to random phase in the overall superposition. Hence, the magnitude of the

electric field component of the radiation emitted by one of these elementary radiators, at the point z' , is given by,

$$E(z',t) = E_{0i} \exp[i(k_0 z' - \omega_0 t + \varepsilon(t))]$$

where $\varepsilon(t)$ is the randomly varying phase. Note that the random shifting of phase occurs in a discontinuous fashion. The phase remains constant with a particular value for a random length of time after which the phase shifts abruptly to another value that is completely unrelated to the previous value.

The superposition of the electric field components of N of these identical radiators is,

$$E(z',t) = \sum_{i=1}^N E_{0i} \exp(-i\omega_0 t) \exp(i[k_0 z' + \varepsilon_i(t)])$$

which, with the stipulation that these are identical radiators and therefore $E_{01} = E_{02} \dots = E_{0i} = E_0$, rearranges to yield

$$E(z',t) = E_0 \exp(-i\omega_0 t) \sum_{i=1}^N \exp(i\phi_i(t)) \quad \text{Eq. 1-12.}$$

The first part of Eq. 1-12, is simply the time-varying behaviour of the magnitude of the electric field of a single wavetrain. The sum term contains the random phase information. The exponential term, $\exp(i\phi_i(t))$, can be considered to be a radial vector with unit magnitude and a direction ϕ that varies randomly in the fashion described above. The sum term is therefore a sum of vectors with equal magnitudes and randomly varying directions. Hence, the resultant vector has a magnitude and direction that vary in a random fashion. The magnitude and direction of the resultant vector are defined to be $a(t)$ and $\delta(t)$, respectively. Thus,

$$a(t)\exp(i\delta(t)) = \sum_{i=1}^N \exp(i\phi_i(t)) \quad \text{Eq. 1-13.}$$

From Eq. 1-13 one can see that the maximum value of the magnitude of the resultant vector is N . This is a special case in which all of the unit vectors have the same direction. If this was the case, then by Eq. 1-12, the amplitude of the electric field component would be NE_0 . Similarly, the minimum value that the magnitude of the resultant vector can be is zero, such that at that particular instant in time, the amplitude of the electric field would be zero. Since both of these cases are special cases, the probability of their occurrence is very low. The probability that the magnitude of the resultant vector has a value between a and $a+\delta a$ is given by [59]

$$P(a)da = \frac{2}{N} a \exp\left[-\frac{a^2}{N}\right] da.$$

This is the so-called Rayleigh distribution. From this equation, it is found that the most probable value for the magnitude of the resultant is $\sqrt{N/2}$, and the average value is \sqrt{N} . Thus, the amplitude of the electric field component of radiation that is described in this fashion varies randomly between 0 and NE_0 , with a most probable value of $\sqrt{N/2} E_0$. The average of many measurements of the instantaneous value of the electric field amplitude would be $\sqrt{N} E_0$. By virtue of the random nature of the amplitude of the electric field, radiation that is described in this manner is called "chaotic light".

Since the long time average of the amplitude of the electric field is $\sqrt{N} E_0$, the long time average of the magnitude squared of the electric field can be expressed as,

$$\langle E(z',t)^2 \rangle = \frac{1}{2} N E_{0i}^2.$$

Therefore by Eq. 1-3, the intensity of radiation from a chaotic source consisting of N identical elementary radiators is

$$I = \frac{1}{2} \epsilon_0 c N E_{0i}^2 \quad \text{w/m}^2.$$

The very first situation that we considered was the case of radiation from a source containing N identical oscillators emitting in phase. In this case the intensity of the resultant coherent radiation was found to be

$$I = \frac{1}{2} \epsilon_0 c N^2 E_{0i}^2 \quad \text{w/m}^2.$$

Thus, for a source containing N elementary radiators, if the radiators emit chaotically the intensity of the emitted radiation will be less than if the radiators emit coherently.

We have already seen how coherent light is encoded into an interferogram by the Michelson interferometer. The interferogram of coherent light is completely deterministic, being entirely predictable on the basis of well-defined parameters. However, the interferogram of chaotic light is not expected to be so deterministic. How then, is the statistical nature of light from a chaotic source (i.e. an atomic emission source) manifested in the interferogram of that radiation.

A problem that is analogous to this has been extensively treated by the methods of coherence theory. As mentioned earlier, the Michelson interferometer can be considered in terms of two pairs of virtual sources, each

pair emitting coherent radiation. We are only interested in the pair that lead to the detected interferogram, that is, S_1 and S_2 of Fig. 1-4.

These two sources are analogous to the two slits in the physical set-up of Young's double slit experiment. This set-up is illustrated in Fig. 1-5. For simplicity, instead of two slits the configuration consists of two pin-holes. This arrangement constitutes a wave-front splitting interferometer, as opposed to the amplitude-splitting Michelson interferometer. Since a single wave-front covers both pin-holes, these become secondary sources of coherent radiation in the same sense that the beam-splitter produces two coherent beams. Interference is observed on a distant screen. The degree to which the beams from the two sources interfere at the point of observation on the screen is dependent upon the path difference that the two beams must travel to reach that point. This path difference is analogous to that which is introduced in the Michelson interferometer by changing the position of the moving mirror.

The intensity of the radiation at a point \vec{r} on the screen can be expressed as [60],

$$I(\vec{r}) = I_1 + I_2 + 2u_1^*u_2 \operatorname{Re}\langle E^*(\vec{r}_1,t_1) E(\vec{r}_2,t_2) \rangle \quad \text{Eq. 1-14,}$$

In this expression the complex form of the magnitude of the electric field component has been used. $E(\vec{r}_2,t_2)$ is the magnitude of the electric field component at the position r_2 (i.e. at the second pin-hole) at the time t_2 . The u_1 and u_2 factors depend upon the geometry of the experiment. In terms of the Michelson interferometer, these would be reflection and transmission coefficients.

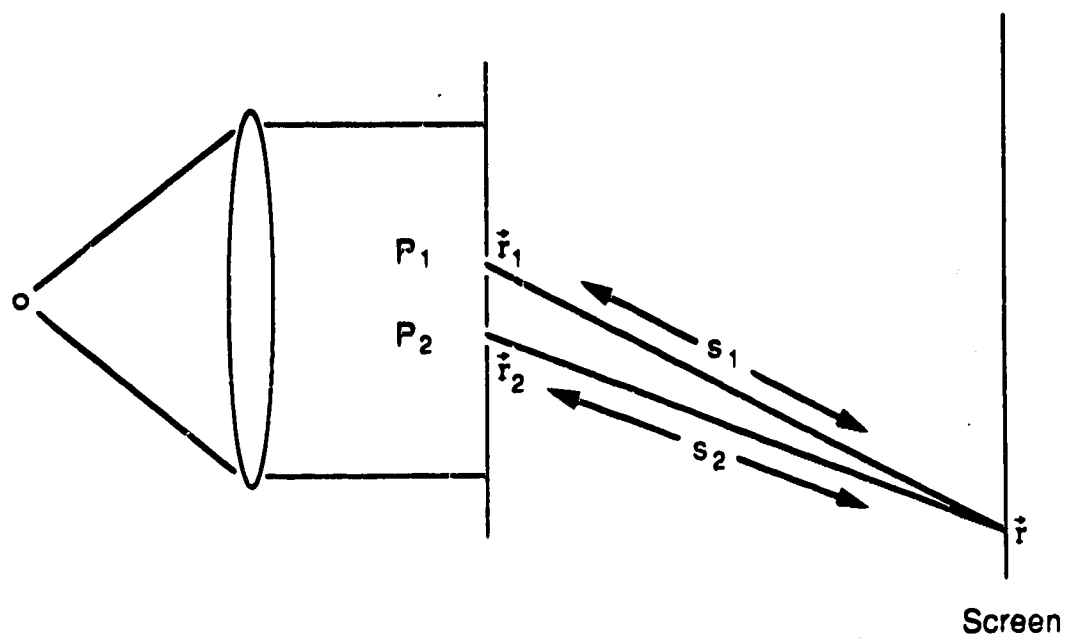


Figure 1-5. Young's double slit experiment.

The form of Eq. 1-14 is very similar to that implied by Eq. 1-4 and 1-5. As mentioned earlier, the interference term is of interest. For this slightly more general case the time average is given by,

$$\langle E^*(\vec{r}_1, t_1) E(\vec{r}_2, t_2) \rangle \quad \text{Eq. 1-15.}$$

Eq. 1-15 is called the first-order correlation function of the fields at the points in space and time, (\vec{r}_1, t_1) and (\vec{r}_2, t_2) . At a particular point on the screen a certain intensity is observed. The amount of interference that occurs will be related to both the particular path difference that the light from the two sources has to travel and the degree of coherence of the source.

The times at which the radiation that is interfering on the screen left each pin-hole are given by, $t_1 = t - s_1/c$ and $t_2 = t - s_2/c$. In theory, at any given instant in time the radiations that leave the two slits are identical. Hence, they are coherent. Consider the situation illustrated in Fig. 1-5. The radiation that leaves the pin-hole P_1 travels further, to reach the point of observation, than does that which leaves P_2 . Hence, radiation that was emitted from P_1 at the time t_1 interferes with radiation that left P_2 some time after t_1 (i.e. at t_2). Consider the case where the source radiation is coherent, comprised of the superposition of infinite length wavetrains from a large number of coherently phased radiators. Thus, this is the ideal case of purely monochromatic radiation.

Since the incident radiation is monochromatic, the radiation that leaves each pin-hole is also monochromatic. The magnitude of the electric field component of either of the radiations oscillates sinusoidally with an infinite spatial (along the direction of propagation) and/or temporal extent.

Thus, all points on the wave-fronts of these radiations are correlated. Any phase difference between points is due to the relative geometry of the points. Consequently, all points on the observation screen are correlated. Interference occurs at all points, subject to the geometry of the path differences from the pin-holes to the points on the screen.

If the distance from the pin-holes to the screen was increased, all points on the screen would remain correlated. This is because the resultant electric field oscillation has an infinite spatial extent along the direction of propagation.

Consider the situation in which the incident radiation is the emission from an isolated atomic elementary radiator. Due to the finite life-time of the radiative state, the emitted wavetrain has limited spatial extent. Previously, a typical value for the length of the wavetrain was cited to be approximately 3m. In addition, the emitting process is random, therefore the time intervals between successive emissions of the radiation are random. Imagine that the screen is positioned a distance of 1m from the pin-holes. The radiator emits and a wavetrain passes through the pin-holes. The two wavetrains that are emitted from the slits are coherent. At most points where the two radiations impinge upon the screen, interference occurs. The degree of interference will be mostly dependent upon path difference.

Now consider that the screen is moved further than 3 m from the pin-holes. For some positions on the screen the impinging radiation will be correlated and interference will occur. At other positions, where the path length difference is large, the wavetrains from each pin-hole (that strike the screen simultaneously) will be from different incident wavetrains. Since

different wavetrains are emitted at random times, these two wavetrains will not be correlated at all. No interference will occur. This situation can be seen to be analogous to the situation in which this same source radiation is incident upon the Michelson interferometer and the moving mirror is moved a large distance from the position of ZPD. The wavetrains that recombine and head to the detector are from different incident wavetrains. Therefore they are not correlated and no interference is observed.

Finally, consider that the incident radiation is chaotic light as described previously. Such light is considered to be chaotic by virtue of the random emission process which causes the phases of the constituent wavetrains in the overall superposition to vary randomly. If the magnitude of the electric field component of the radiation could be measured at two points in time very close to each other, it is unlikely that the phases of all of the component wavetrains would have changed during that period. Hence, the magnitude of the electric field at these points in time is still relatively well-correlated. For any given source, there is a characteristic interval of time over which the magnitude of the electric field component doesn't change in a random fashion (to any great extent). This time interval is called the "coherence time", τ_c .

Radiation from each of the pin-holes impinges upon the screen at the point of observation. As described previously, the light leaving P_1 to strike the screen at the point of observation left at the time t_1 . The light leaving from P_2 to hit the same point on the screen at the same time, left P_2 at the later time (for the purposes of illustration) t_2 . If the difference in time $t_{21} = t_2 - t_1$ is sufficiently short, then the two radiations striking the screen will be correlated and interference will occur. However, if t_{12} is much longer, i.e.

longer than the coherence time of the source, the two radiations are completely uncorrelated and no interference occurs.

This description of the effect of coherence length on the degree of interference can be applied to the Michelson interferometer. Consider that the moving mirror is positioned at the point of ZPD. With reference to Fig. 1-4, the two virtual sources S1 and S2 are the same distance from the point of detection. By virtue of the beam-splitting process, these sources are coherent. Since the optical distances to the detector are equal, at any given instant in time the two radiations that are impinging upon the detector must have left the two sources at the same time. These radiations are fully correlated, hence interference results.

If the moving mirror is moved away from the beam-splitter, the optical path length in the moving mirror arm of the interferometer is longer than that in the fixed mirror arm. The distance that the radiation emitted from S1 travels to reach the detector is now further than that from S2. At any given instant in time the radiation from S2 is re-combined with radiation that is delayed with respect to the radiation with which it is fully correlated (i.e. at the time of beam-splitting). If this delay is less than the correlation time, the two radiations that recombine are at least partially correlated and interference occurs. If however, the delay is greater than the correlation time, the two radiations are completely uncorrelated and no interference results. This means that, depending upon the coherence length of the source radiation, the interference that produces the interferogram at the detector should decrease as the moving mirror is moved in either direction away from the position of ZPD. Hence, for a given length of travel of the moving mirror, and two sources, the time varying portion of the interferogram of the source with the

shorter coherence length will die away more quickly as the mirror is moved away from the position of ZPD.

The term "visibility" is used to describe the extent of the interference that is occurring, in the case of the Young experiment at various points on the observation screen, and with the Michelson interferometer at different points of optical path difference (i.e. different moving mirror positions). In the Young experiment, the maxima and minima of the interference pattern on the screen constitute the so-called interference fringe pattern. Thus, for the Young experiment the visibility of the fringe pattern is defined to be

$$V(\vec{r}) = \frac{I_{\max} - I_{\min}}{I_{\max} + I_{\min}}$$

where I_{\max} is the intensity at a maximum and I_{\min} is the intensity at the next adjacent minimum. For the case of a perfect coherent source, the incident radiation would be perfectly monochromatic and the fringe pattern would consist of a sinusoidal variation of the intensity across the screen. A given peak would be followed by an adjacent minimum with zero intensity. Therefore, at that point the fringe visibility would be unity. With monochromatic light the visibility would be unity all the way across the screen. Departures from unity visibility correspond to departures from monochromaticity. For completely incoherent light, the visibility is zero.

It is clear from the above discussion that the coherence length of the source radiation affects the level of interference in both experiments. To reiterate an important point, the coherence length of the radiation from a source is greatly dependent upon the statistical physical processes that occur within the environment of the elementary radiators. Thus it is no surprise

that the fringe visibility (that is, its functional form) can provide a great deal of information as to the statistical processes that are occurring within the source. This is especially so for the Michelson interferometer.

So far, the chaotic light that we have considered has been something akin to "natural" light. That is, radiation from a source in which no broadening phenomena, other than that due to the radiative process itself, are occurring. The finite width of an isolated line from the spectrum of such a source is the minimum achievable line-width. This is the natural line-width. The natural line-profile (the resonance profile) is mathematically described by the Lorentzian function. The full-width at half the maximum value (FWHM) of the line is designated as γ .

It can be shown [60] that the fringe visibility in the Young's double aperture experiment, in which the source radiation is chaotic with a Lorentzian line-shape, is given by

$$\mathcal{V}(\vec{r}) = \frac{I_{\max} - I_{\min}}{I_{\max} + I_{\min}} = \frac{2u_1^* u_2 \exp(-\gamma |s_1 - s_2| / c)}{|u_1|^2 + |u_2|^2} \quad \text{Eq. 1-15}$$

where γ is the FWHM of the Lorentzian line profile. Ignoring the geometric factors u_1 and u_2 , one can see from this equation that as the difference between the two paths s_1 and s_2 increases the fringe visibility (that is, the interference) decreases exponentially. As described previously, this decrease in the level of interference is due to the chaotic nature of the source radiation, as described by the coherence length.

Note that the FWHM of the spectral line-profile plays a role in the decay of the fringe visibility. This is to be expected since a small value of γ can be interpreted as meaning that the wavetrains that are emitted by the

elementary radiators are longer than those that would be emitted if γ was larger. Longer wavetrains result in a longer time interval over which the magnitude of the electric field component is reasonably deterministic, that is, the coherence time is longer. In light of this, it is not surprising that the coherence time of a source is often defined to be the reciprocal of the FWHM of a spectral line of the source radiation. In this case, the coherence time is $1/\gamma$.

Source radiation with a different spectral line-profile produces a fringe pattern whose visibility is described by a different function. For instance, it can be shown [60] that the fringe visibility for source radiation that has a Gaussian line-profile will be described by a Gaussian function itself. The Gaussian spectral profile is the result of particular statistical physical processes within the source. It is interesting to note that by observing the visibility, the spectral line-profile can be ascertained without actually measuring the spectrum of the radiation (a measurement, in fact, carried out by Michelson).

Eq. 1-15, is easily modified for the case of the Michelson interferometer. The factors u_1 and u_2 would be replaced by reflection and transmission coefficients. The distances from the pin-holes to the screen, s_1 and s_2 , would be replaced by X_1 and X_2 , the optical path lengths from the virtual sources to the detector. Thus, the visibility (or envelope) of the interferogram is related to the spectral line-profile of the radiation that is incident upon the interferometer. It is easy to show [1] (see also Fig. 2-15) that the spectral line-profile is the Fourier transform of the visibility function. That is, if just the envelope of the interferogram was measured, the line-profile (but not the frequency of the line) could be obtained by Fourier transformation of the envelope.

In summary, the interferogram of quasi-monochromatic radiation (i.e. an isolated line from a source of atomic emission) consists of an intensity oscillation that decays as the mirror is moved away from the position of ZPD. The information regarding the frequency of the radiation is encoded into the under-lying oscillation of the interferogram. The information regarding the various physical processes occurring within the source is encoded into the shape of the envelope of the interferogram.

From an instrumental point of view, this last point is of paramount importance. In a typical experiment, the interferogram of a source is acquired and then Fourier transformed to produce the spectrum of the source. The line-shape information is encoded within the shape of the envelope of the interferogram. Any alteration of the shape of the envelope, as a result of an instrumental effect (i.e. an instrumental apodization of the interferogram), will alter the resultant spectral line-profile. This is undesirable from a fundamental studies and resolution perspective. This problem is more acute when one is working with the short wavelengths of the UV region. These considerations, with respect to the design of the Michelson interferometer for this system, are the subject of Chapter 2.

1-3.3. Detection of the interferogram - Noise in FTS.

In the UV-VIS regions, the interferogram is typically detected with a photo-multiplier tube (PMT). This is a different situation than in the IR region, wherein Bolometers, Golay cells, IR photo-diodes, etc. are employed. The key difference between these detectors and a PMT is that the latter is far more sensitive. This creates an interesting situation with respect to the noise

that is associated with the measurement of an interferogram, and consequently, the noise within the final spectrum.

Although the discussion of the Michelson interferometer was more easily approached from the wave picture of light, the following discussion is approached from the photon picture.

The problem of noise in FTS can be viewed from the communications perspective of amplitude modulation of a carrier wave. The amplitude of a sinusoid (the carrier wave) is modulated by a time-varying signal wave. The signal wave has its own characteristic spectrum. It is well known that the spectrum of the modulated carrier wave consists of a peak corresponding to the carrier, and two replicates of the signal wave spectrum symmetrically located on either side of the carrier peak. The important point is that modulation of the amplitude of a sinusoid introduces symmetrically displaced spectral features. Consider the interferogram of a monochromatic source.

The intensity oscillation at the detector is a pure sinusoid. If this is detected with no alteration of the amplitude, the resultant spectrum will consist of only one peak. If however, the amplitude of the interferogram is modulated by noise, the spectrum of the noise is symmetrically distributed on either side of the peak. White noise is considered to be composed of an infinite range of frequency components with random amplitudes and phases. If the amplitude of the interferogram was modulated with white noise, that noise would be evenly distributed into the base-line of the resultant spectrum. In this case, the noise would be the same at all points on the interferogram. If the interferogram was signal averaged, the noise would be

reduced at all points in the interferogram. Consequently, the noise would be reduced at all points in the spectrum. However, now consider the case where the noise associated with the measurement of the interferogram is directly related to the intensity of the interferogram.

PMTs are sensitive enough to count photons. Consider that a noiseless PMT counts photons from a light source for a time T . This experiment is carried out repeatedly, such that eventually a relative frequency histogram of the counts could be plotted. It would be found that the counts followed a Poisson distribution. This could be expressed as

$$P_m(T) = \frac{\bar{m}^m}{m!} \exp(-\bar{m})$$

where $P_m(T)$ is the probability of counting m photons during the counting time T . \bar{m} is the mean number of photons counted. The standard deviation of such a distribution is proportional to the square root of the mean number of photons. The standard deviation of this distribution represents the minimum noise that could be achieved in a measurement of the intensity of chaotic light. This fundamental noise of a radiation field is called "photon noise". This is also sometimes called "shot noise".

Clearly, the noise increases as the mean number of photons, or intensity, increases. However, since the noise is proportional to the square root of the mean number of photons, increased intensity represents an increased signal-to-noise ratio (SNR). The SNR is given by the average value of a signal divided by the standard deviation of the signal. For instance if the mean number of photons was increased from 10 to 100, the SNR would increase from 3.16 to 10. This is an important point with respect to optical

dispersive systems. In this case, the frequency information is decoded spatially. For the case of narrow-line emission spectra, typically only the peaks are detected. It is desirable to have the maximum possible intensity at any particular detector since this will achieve the maximum SNR in the measurement of that spectral line. However, the situation is different for optical FTS.

As described above, the fundamental noise in a radiation field is photon noise. This is the minimum noise that we could expect to achieve if a perfect PMT was employed. Photon noise is proportional to the square root of the signal intensity, therefore the noise in the interferogram of a monochromatic source is not the same at all points on the interferogram. At the peaks of the interferogram the intensity is greatest, therefore in absolute terms the noise is greatest. At the minima, the noise is lower. The SNR is not the same throughout the interferogram. The maxima have higher SNR than do the minima.

The photon noise modulates the amplitude of the pure sinusoid of the noiseless interferogram. Hence, upon Fourier transformation the noise is distributed into the base-line of the spectrum. However, since the amplitude modulation of the noiseless interferogram is not the same at all points in the spectrum, the situation is similar to that in which a carrier is modulated by a signal with a complex spectrum. The noise is not evenly distributed into the base-line of the spectrum.

With a dispersive system, two adjacent emission lines are spatially separated and measured. The noise associated with the measurement of one line does not affect that of the other line. The measurement of a line with a

large intensity has no effect upon the measurement of an adjacent line with a small intensity (naturally, the problem of stray light is being neglected here). However, consider the situation in which an interferogram consists of the superposition of two monochromatic components, one of which has a large intensity, the other a small intensity.

The form of the noiseless interferogram would be dominated by the interferogram of the large intensity component. The interferogram would consist of a large sinusoidal variation upon which a small ripple oscillated. Fourier transformation of the noiseless interferogram would produce a spectrum with a large and small intensity peak. If the noise associated with the measurement of the interferogram was white, such noise would be evenly distributed throughout the interferogram. In any given scan, the small ripple might be indistinguishable from the noise in the interferogram. In that case, the interferogram would appear to be a noisy sinusoid. If the interferogram was signal averaged, the noise level would decrease until eventually the ripple would become distinguishable throughout the entire interferogram. The small peak would then be observable in the resultant spectrum. Note that in this case, the presence of the large intensity component has no effect upon the measurement of the small intensity component.

If the noise associated with the measurement of the interferogram was photon noise, each component of the interferogram would contribute a proportionate amount of noise. The greatest contribution to the overall noise would be that due to the large intensity component. This noise would not be evenly distributed throughout the interferogram. The noise associated with the measurement of the high intensity regions of the interferogram would be

greater than that of the low intensity regions. After extensive signal averaging, the small ripple might be evident in the small intensity regions, but still obscured by the noise in the high intensity regions. Until the ripple was readily observable throughout the entire interferogram, the small intensity peak would not be correctly observed within the final spectrum. Clearly, the presence of the large intensity component greatly affects the measurement of the small component.

If the noise associated with the measurement of the interferogram has some other direct proportionality with respect to the interferogram intensity, the situation can worsen. For instance, if the noise is directly proportional to the interferogram intensity (instead of just proportional to the square root), the noise associated with the measurement of the interferogram is dominated even more strongly by the noise associated with the measurement of the large intensity component. Again, this can be thought of in terms of the noise associated with the large amplitude component being distributed into the base-line of the spectrum in a complex fashion, causing the small intensity peak to be obscured.

This situation in which the measurement noise is dominated by the presence of a large intensity component in the interferogram, to the detriment of all other components, is often called the "multiplex disadvantage." It is a potential problem in optical FTS whenever the noise associated with the measurement of the interferogram has a direct dependence upon the intensity of the interferogram.

When FTS is applied in the IR, the detectors are so insensitive that they do not respond to the photon nature of the radiation in the

interferogram. Consequently, the noise associated with these detectors is, for the most part, not dependent upon the intensity of the interferogram. Thus, the measurement of the interferogram is made under "detector-noise limited" conditions. In this situation it can be shown that in comparing dispersive and multiplex systems, a "multiplex advantage" is realized.

The existence of a multiplex advantage was first noted by P. Fellgett in 1951 [4]. Consequently, this phenomenon has come to be known as the Fellgett advantage. If both a multiplex and dispersive spectrometer are used to characterize a particular spectral band-width over a particular measurement time, the multiplex advantage describes any increase in the SNR of the multiplex derived spectrum when the two measured spectra are compared. In this case, the dispersive system that is compared is a scanning system in which the spectrum of the source is scanned across a single detector.

If a dispersive and multiplex system have the same spectral resolution, and both characterize the same spectral band-width, the number of spectral resolution elements, M , is given by the band-width divided by the resolution. The total detection time is T . This is the time required to scan the spectrum across the detector, or to acquire the interferogram. When the measurement of the interferogram is detector noise limited a multiplex advantage is realized, in that the SNR of the multiplex-derived spectrum is \sqrt{M} times greater than that of the dispersive-derived spectrum.

When the noise associated with the measurement of the interferogram is dependent upon the intensity of the interferogram, the measurement is said to be "signal noise limited". As described above, the functional dependence of the noise on the intensity can take several forms. Depending

upon the relationship, the noise will be distributed throughout the spectrum in different ways. The potential existence of a multiplex disadvantage has been a significant factor in the reluctance of researchers to apply this technique in the UV-VIS.

Studies concerning the distribution of noise within spectra, under detector noise limited situations, have been undertaken within this laboratory. S. Marra has studied this problem, using as investigative tools the standard deviation, average and SNR spectra of populations of replicate interferograms [20,22]. For the most part, noise was found to be largely distributed in the immediate vicinity of the spectral peaks. As expected, the spectral distribution of the noise was very clearly found to be dependent upon the nature of the spectrum. As a result of the strong spectral dependence of the noise, some lines in a spectrum can exhibit a multiplex advantage, while some suffer a multiplex disadvantage. This has led T. Hirschfeld to coin the phrase "distributive multiplex advantage" to describe this situation [61].

In many situations of practical interest, the source noise may dominate the measurement of the interferogram. This is noise over and above the photon noise of the source. Typically, this is "flicker noise". The effects of flicker noise on the resultant spectrum of the source radiation are being studied by a number of researchers. Both theoretical [62] and experimental [40] assessments of this situation have been undertaken. This problem can be particularly acute because the flicker noise of the source radiation often increases linearly as the intensity of the source is increased. The effect is equivalent to the situation in which the noise in the measurement is linearly related to the interferogram intensity. By virtue of the often observed narrow frequency spectrum of flicker noise, this situation is particularly amenable to

treatment on the basis of the model of amplitude modulation of a carrier wave.

Due to the seriousness and prevalence of the flicker noise problem, a number of researchers are investigating methods of improving the situation. Either the source can be improved [63] with respect to its noise characteristics, or the method of acquiring the interferogram can be altered [64].

Once the photons of the interferogram impinge upon the PMT, the best situation that can be realized is that of photon noise and perhaps, some form of a distributive multiplex advantage. As described above, if most of the photons are due to large intensity components, the noise situation is dominated by these components. To reduce the noise due to these contributions, such that small components can be measured, one has to remove the photons due to the large components. This implies some sort of filtering of the source radiation prior to entry into the interferometer. This approach has been investigated within this laboratory by E.A. Stubbley [18, 23]. Some success was achieved. As will be described in Chapter 4, further experiments are currently under way with an improved system employing the current version of the Michelson interferometer system.

A novel approach, directed towards achieving a detector noise limited situation when a PMT is used as the detector, has recently been put forth by R.R. Williams [65]. In this methodology, the interferogram is acquired with a step-scan interferometer. The time over which the detected signal is integrated is varied in accordance with the intensity of the interferogram. High intensity points of the interferogram are integrated for a longer time than are those of low intensity. In this way, the distribution of the noise in

the interferogram is made equal, regardless of the intensity. This is the same situation as a detector noise limited situation. In this manner, Williams expects to realize a multiplex advantage.

As far as the author is aware, once the noise is encoded within the interferogram, there is no way of reducing it within the spectrum. However, it may turn out that the techniques of Bayesian spectral analysis might allow for post acquisition improvement of the SNR in the spectrum [66].

In summary, the noise situation for measurements of interferograms in the UV-VIS is complex. The situation has not been completely characterized as yet, especially with respect to the existence of a multiplex advantage or disadvantage. Studies concerning this problem are continuing. By virtue of potential military applications, the detection of IR radiation is an active area of research. It is interesting to note that as IR detectors improve, the field of FT-IR creeps closer to the noise dilemmas facing FTS in the ultraviolet and visible regions. Consequently, these studies take on greater potential significance.

Chapter 2

Interferometer Optical System

In this spectrometer, the key optical element is the Michelson interferometer. As described in Chapter 1, the interferometer enables us to measure a signal whose time varying behaviour is directly related to that of the electric field component of the incident radiation. Then, knowing the temporal characteristics of the source radiation, the Fourier transform can be employed to calculate the frequency, or wavelength spectrum of that radiation.

This idea is not new. However, the application of this technology to the ultraviolet and visible regions of the spectrum has occurred only rarely. Some of the reasons for this were discussed in Chapter 1. A practical problem of significant importance is that of the fabrication and assembly of optical components into a system that is to operate in the ultraviolet and visible regions of the spectrum, wherein the wavelengths are relatively short.

This spectrometer has been designed to span an optical band-width ranging from approximately 200 nm to 2.5 μm . In future, the short wavelength end may be reduced by evacuating, or purging, the optical path. The maximum resolution is designed to be $\Delta\sigma_{1/2} = 0.29 \text{ cm}^{-1}$. As described in Chapter 1 of this thesis, to achieve this resolution the moving mirror must be moved at least 1.04 cm on either side of ZPD. In practice, even with this

length of mirror travel, the achievable resolution may be less than anticipated. Any instrumental effect that causes the envelope of the source interferogram to decay faster than that dictated by the natural (or broadened) line-shape of the source radiation, that is, any instrumental apodization of the interferogram, will cause the lines in the resultant spectrum to be broadened, thereby reducing the resolution of the instrument.

The major causes of instrumental apodization are: 1) the presence of off-axis rays of incident radiation, and 2) mis-alignment of the moving mirror of the interferometer.

Off-axis rays occur as a result of poor collimation of the source radiation due to poor optics, and/or the necessity to collimate the light from a source of finite size.

If the moving mirror is only slightly mis-aligned with respect to the fixed mirror and beam-splitter, the intensity grand maximum of the interferogram may be close to optimal. However, as the mirror is moved further away from the beam-splitter the effect of any slight mis-alignment becomes more significant. As a result, the intensity of the interferogram at positions of larger optical retardation is less than it should be, based upon the line-shape and line-width of the source.

Instrumental apodization is, for the most part, a technological problem. In order to reduce the magnitude of this problem, certain components in the interferometer have been re-designed and/or further developed. Concomitant with these developments has been the design of a comprehensive procedure for the alignment of the components in the optical path of the interferometer. As will be described in this chapter, these

developments have resulted in significantly less instrumental apodization of the source interferogram.

2-1. Current interferometer design.

Fig. 2-1 is a schematic diagram of the present interferometer system. A good deal of the system hardware has been modified to aid in alignment, while the moving mirror electro-mechanical assembly and the detector assembly have been completely re-designed.

The collimation optics consist of either a single plano-convex quartz lens, or an off-axis parabolic mirror assembly. The lens system has the advantage of extreme simplicity, but also the disadvantages of significant chromatic and spherical aberration. The off-axis parabolic assembly, while more complex and difficult to implement, is a significantly better collimation system as it is both achromatic and aspheric. This latter system is essentially identical to that which is employed as the exit focussing optics.

The beam splitter/compensator assembly is situated within a machined aluminum mounting cube. Also attached to this cube is the fixed mirror mount. This mount is designed to allow very fine adjustment of the angle of the plane of the fixed mirror. These three components have not been significantly altered, and they are described in detail, elsewhere [14] .

As mentioned previously, the moving mirror electro-mechanical assembly has been completely re-designed. One of the key design changes has been to de-couple the drive assembly from the mounting cube. This allows for greater flexibility in the alignment of the moving mirror. Previous mirror drive designs were mounted directly onto the cube, relying upon

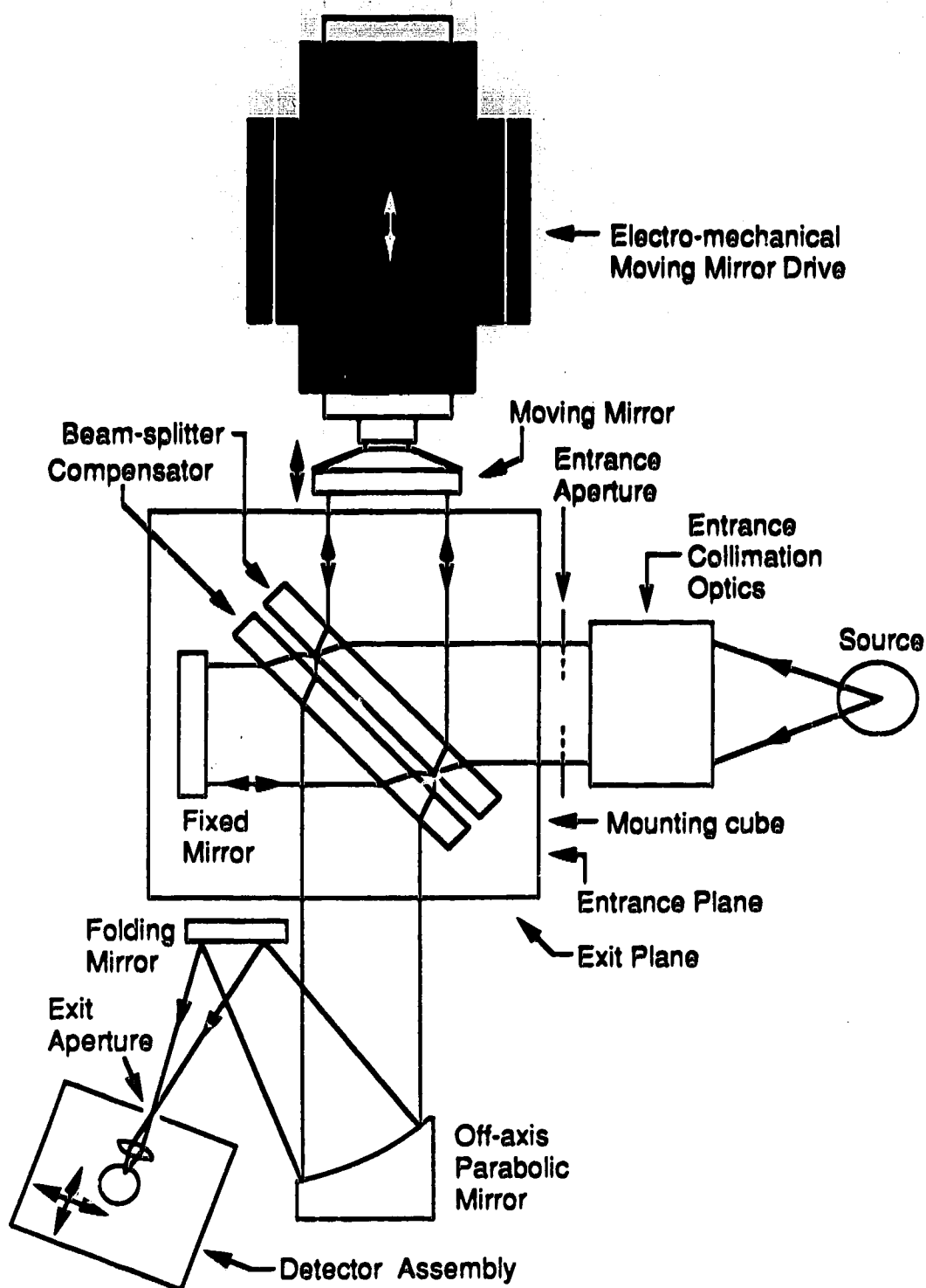


Figure 2-1. Schematic diagram of scanning Michelson interferometer system.

machining accuracy during the fabrication process to achieve the correct alignment. This has proven to be inadequate to meet the tight tolerances required for operation with the short wavelengths of the UV region of the spectrum.

Shown in part a) of Fig. 2-2 is a side-view schematic of the present electro-mechanical assembly. The moving mirror is attached to an air-bearing assembly (Dover S/N 1335 Dover Instrument Corp. P.O. Box 100, 5 Walkup Drive, Westboro, Mass 01581 (617) 366-1456) which provides essentially friction-free movement of the mirror. This air-bearing assembly consists of a 6 in. long x 2.5 in. wide x 1.25 in. thick piston, and a sleeve with strategically positioned gas outlets on its inner surface (and a hose nipple for gas inlet). Both the sleeve and the piston are manufactured from so-called, "hard-coat aluminum", such that the surfaces are as hard as sapphire, as stated by the manufacturer. The quoted linear accuracy of this assembly is 0.000004 in. per in. of linear travel.

In previous versions of the interferometer, the air-bearings that were employed were all cylindrical in design [15, 23]. With such a design there is the possibility of rotation of the moving mirror. If the surface of the mirror and the axis of the bearing were not perpendicular to each other, the effect of this rotation would be to modulate the optical path length in the moving mirror arm of the interferometer. With this rectangular design, rotation of the mirror is not a significant consideration.

An obvious design choice is whether to move the piston while holding the air-bearing sleeve in a fixed position, or vice versa. In previous designs [15, 23], the piston of the air-bearing was driven electromagnetically. A

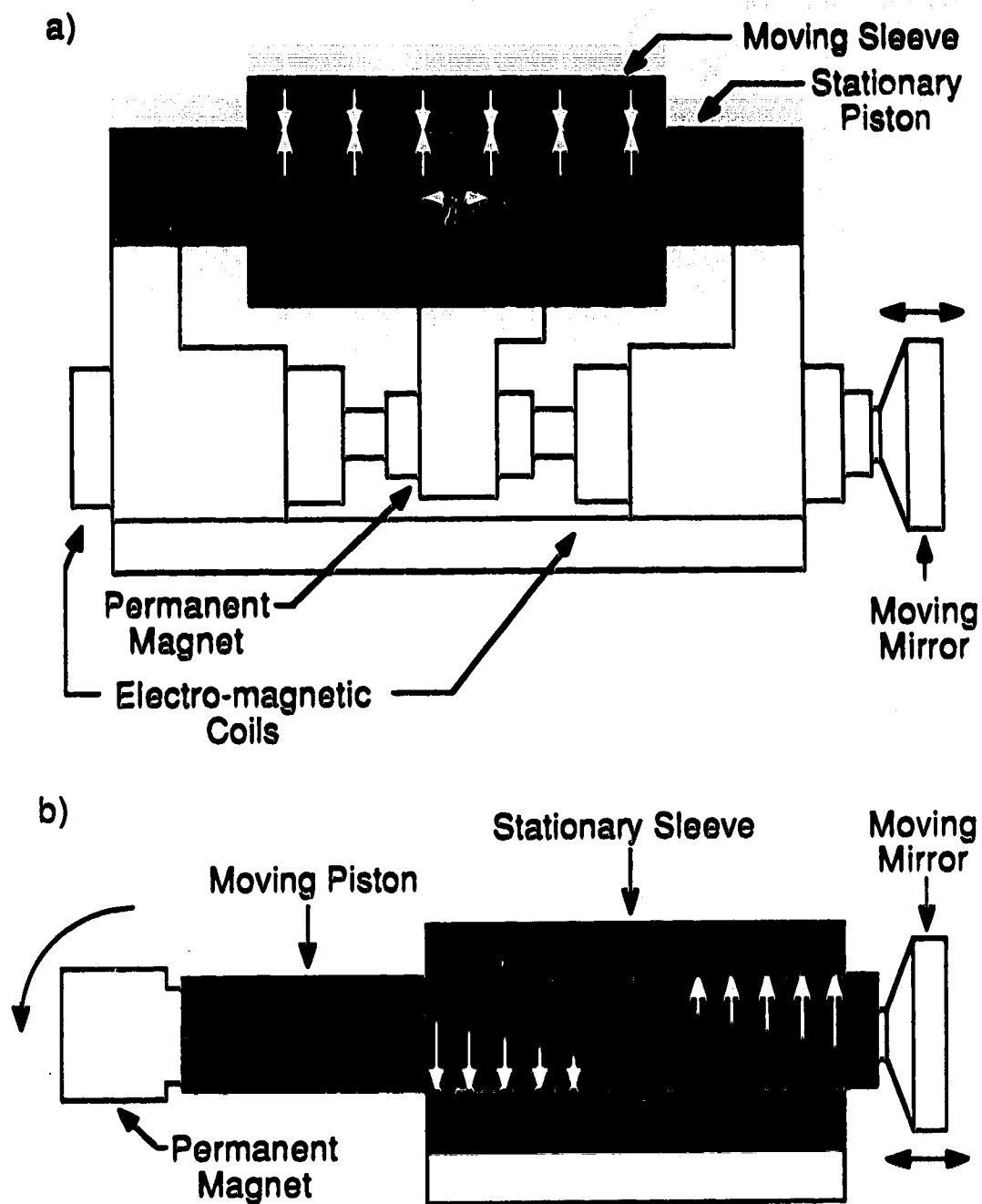


Figure 2-2. Moving Mirror Assembly: moving sleeve vs. moving piston.

permanent magnet was attached to one end of the piston while the moving mirror was attached to the other end. The permanent magnet was located within an electromagnetic coil (or set of coils) and movement of the mirror was effected by setting up an electric current in the coils. (The symmetric design was also employed, that is, a fixed magnet and moving coil.) This situation is illustrated in part b) of this figure. Here the magnet and mirror are attached to the moving piston while the sleeve of the air-bearing is held stationary. As indicated in part a) of this figure, in the present design the mirror is still driven electromagnetically, however, the magnet and mirror are attached to the movable sleeve while the piston is held fixed. The rationale behind this choice is as follows.

The gas film between the sleeve and the piston is on the order of one-thousandth of an inch thick (as inferred from feeler gauge measurements of the clearance between the unfloated sleeve and piston). The gas film is compressible. Once the moving mirror has been correctly aligned, it is essential that the same alignment be maintained throughout the travel of the mirror. Hence, it is important that the forces that compress the gas (i.e. those that are exerted by the inner surface of the sleeve and the surface of the piston) remain constant during the entire stroke of the mirror. If this is the case, then the thickness of the gas film will remain constant, and so too will the alignment of the moving mirror. This situation is illustrated in part a) of Fig. 2-2. The arrows of equal length represent (admittedly, in a highly simplistic manner) the equal forces that are exerted on the gas film.

As illustrated in part b) of this figure, for the situation of the moving piston, the forces exerted on the gas film would be highly dependent upon the relative positions of the sleeve and the piston. One would expect the mirror

to experience a position-dependent tilt as a result of the torque introduced by the asymmetry of masses in the system. The tilt, and subsequent misalignment of the moving mirror, would be worse near the ends of the travel of the mirror. Clearly, this is a source of instrumental apodization of the interferogram.

In the limit of the above scenario, the gas film could be compressed to an extent that would be sufficient to cause the two surfaces of the sleeve and piston to make contact, thereby destroying the friction-less aspect of the system. Even with the servo-system described in Chapter 3, this situation would cause modulation of the velocity of the mirror resulting in the introduction of spurious spectral features into the final spectrum.

Referring back to Fig. 2-1, the re-combined wavefronts of the source radiation are focussed onto the detector by an off-axis parabolic mirror assembly. This consists of an off-axis parabolic mirror element and, due to space constraints, a secondary planar folding mirror.

As mentioned previously, this mirror system is identical to that which is used to collimate the source radiation. This assembly was implemented previously [14] , however, with limited success due to alignment difficulties. Eventually, it was moth-balled in favor of a simpler single quartz lens system. As with the entrance optics, it is desirable to implement this mirror assembly since it is achromatic and aspherical. Recently, upon re-assessment of the alignment procedures, modifications to the hardware have been effected, and an alternative alignment procedure has resulted in the successful implementation of these mirror assemblies.

The detector assembly has been re-designed to better enable alignment of the detector at the focal point of the exit optics. As with the moving mirror assembly, the previous design of the detector housing was mounted directly onto the mounting cube. Again, accurate machining was relied upon to provide alignment accuracy. In the present design the detector assembly is decoupled from the mounting cube, and the detector housing is mounted onto an X-Y-Z alignment stage. This has greatly improved the facility with which the detector can be aligned in the exit focal plane.

For operation in the UV region of the spectrum, the mirrored optical components require special optical coatings. The reflectance of a pure bare aluminum coating decreases to approximately 75% at 200 nm. This would allow reasonable operation in the near-UV; however, pure Al oxidizes rapidly and this oxide layer absorbs in the UV. Hence, the short wavelength reflectance would decrease over time. Mirrors that are over-coated with a protective, oxide preventing, SiO layer, have markedly reduced reflectance below 350 nm. The short wavelength reflectance of Al can be enhanced by the application of dielectric film layers (typically a proprietary process), with a final over-coat of MgF_2 . This can result in better than 80% reflectance at 200 nm [67]. At the very least the mirrored surfaces throughout the present version of the interferometer are over-coated with MgF_2 , and when possible, UV-enhanced coatings have been specified.

Ideally, during passage from the source to the detector, the wavefronts of the source radiation are converted from spherical (for the case of a point source) to planar, and then back to spherical. That is, the light is first collimated, then reflected at planar surfaces, and finally focussed onto the

detector. Along the way the wavefronts are also divided and re-combined by the beam-splitter. Due to the short wavelengths involved in operation in the UV, the achievement and maintenance of high quality wavefronts requires that the optical surfaces in use be fabricated to within tight tolerances.

The classification of optical surfaces varies between manufacturers. With respect to optical flats, for use as substrates for plane mirrors or beam-splitters, a typical test is to compare the test surface with a reference surface that is known to be flat to better than the desired flatness of the test piece. Collimated light from a source such as a HeNe laser ($\lambda = 632.8 \text{ nm}$) produces an interference pattern due to the microscopic air wedge between the two surfaces. Any curvature (global or localized) of the lines of the interference pattern indicate that the test surface is not an accurate copy of the reference surface. In other words, the test surface is not flat. The curvature of the lines is quantified in terms of fractions of the test source wavelength, in this case $632.8 \text{ nm}/x$.

For operation in the infrared region of the spectrum, the mirrors in an interferometer will usually be specified to be flat to within $\lambda/4$, or 158.2 nm . For $1 \text{ }\mu\text{m}$ wavelength radiation, this represents a deviation from planarity that is less than one sixth of a wavelength. However, for 200 nm radiation, the curvature of the surface is almost one wavelength in magnitude. Clearly, the 200 nm wavefront would undergo far greater deviation upon reflection from this surface than would the $1 \text{ }\mu\text{m}$ radiation.

As a result of these considerations, the plane surfaces throughout the present version of this interferometer have been specified to be at least $\lambda/20$, over the entire aperture of the surface. It should be noted that a mirror that is

specified to be $\lambda/20$ over the entire surface is usually better than this over a small portion of the surface. The entrance aperture of the present system is typically 1 cm, or less. Hence, the planarity of the surfaces throughout this restricted optical path can be expected to be better than $\lambda/20$. Wherever possible, the planar optical surfaces of the interferometer (and associated external optical systems) have been tested for flatness, and if necessary, the surfaces have been stripped of their coatings, re-worked, and re-coated. This work was performed in the University of Alberta Optics Facility.

Spherical and aspherical optical surfaces are more difficult to characterize than are planar surfaces. Again, due to the shorter wavelengths in the UV, such non-planar surfaces must meet more stringent specifications than would those for use in the IR. The off-axis parabolic mirrors in the entrance and exit optical assemblies are state-of-the art optical elements (OAP-024-02, Space Optics Research Laboratories, 7 Stuart Rd., Chelmsford, Mass. 01824 U.S.A., (617) 256-4511.) The aperture is 5.08 cm (2 in.) with a 16.76 cm (6.6 in.) focal length. The focus is off-set from the innermost edge of the mirror by 6.10 cm (2.4 in.). The surface is specified to be accurate to within a maximum peak-to-peak deviation of $\lambda/8$ at 632.8 nm. It would be significantly more convenient if the element were taken from a point higher up on a parabola, such that the angle of a ray from the center of the aperture to the focal point would be closer to 90° . However, the author has been assured by a private manufacturer [68] of optical equipment that such an optic would be prohibitively difficult (if not impossible) to produce with this $\lambda/8$ surface accuracy. These mirror substrates were purchased uncoated. They were coated with pure aluminum, followed by a MgF_2 over-coat, at the University optics facility.

2-2. Interferometer alignment procedure.

The alignment procedure that will be described in this section involves alignment of the interferometer with respect to an external axis. This axis is the optical axis of the optical rail-bed upon which the interferometer rests. Such a reference axis would be the corner-stone of the usual strategy for alignment of the interferometer into a complex system of optical components. For instance, if a source was later aligned to the reference optical axis, at this point it would be assumed that the source was also aligned to the interferometer. The choice of the distance of the source from the entrance plane would be based upon a knowledge of the focal length of the collimating optics.

Recognizing that the interferometer is a symmetric optical system, a more modular approach to the problem of alignment of the interferometer within a complex system can be considered. The interferometer has its own internal optical axis whose interesting features begin and end on two focal points, one for the entrance collimating optics and the other for the exit focussing optics.

Consider that the components of the interferometer have been correctly aligned. If a point source was placed at the entrance focal point, the light from that source would be focussed at the exit (detector) focal point. Conversely, if the point source was positioned at the exit focal point, the light travelling back through the interferometer would be focussed at the entrance focal point. A source, or any other optical element for that matter, could be positioned very easily at the entrance focal point, thereby aligning the

element with the optical axis of the interferometer at the correct point along the axis. This situation is analogous to having a lens which could be back-lit with a point source such that the primary focal point could be visualized and aligned with the optical axis of another element. Thus, even though the interferometer is being aligned to a reference optical axis, this is only a matter of convenience. This axis is defined by the beam of a HeNe alignment laser, but the beam from any similar laser would do, regardless of where it was situated.

2-2.1. Alignment of the mounting cube.

Fig. 2-3 is a schematic diagram of the physical set-up for alignment of the mounting cube with respect to the external axis. The desired results of this procedure are to orient the mounting cube such that 1) the entrance plane is perpendicular to the direction of the incident beam and 2) the aperture of the entrance plane is co-axial with the external axis. It is then assumed that, within typical machining tolerances, the other three planes of the mounting cube are either parallel or perpendicular to the external axis as defined by the incident beam. This is considered to have been achieved when the reflected beam returns upon the incident beam.

As indicated in part a) of this figure, the beam of the alignment laser passes through two pin-hole apertures. The first is used to reduce the exit aperture of the laser. This makes it easier to determine when the return beam is aligned with the incident beam. The second aperture is used to define the center of the entrance plane of the interferometer.

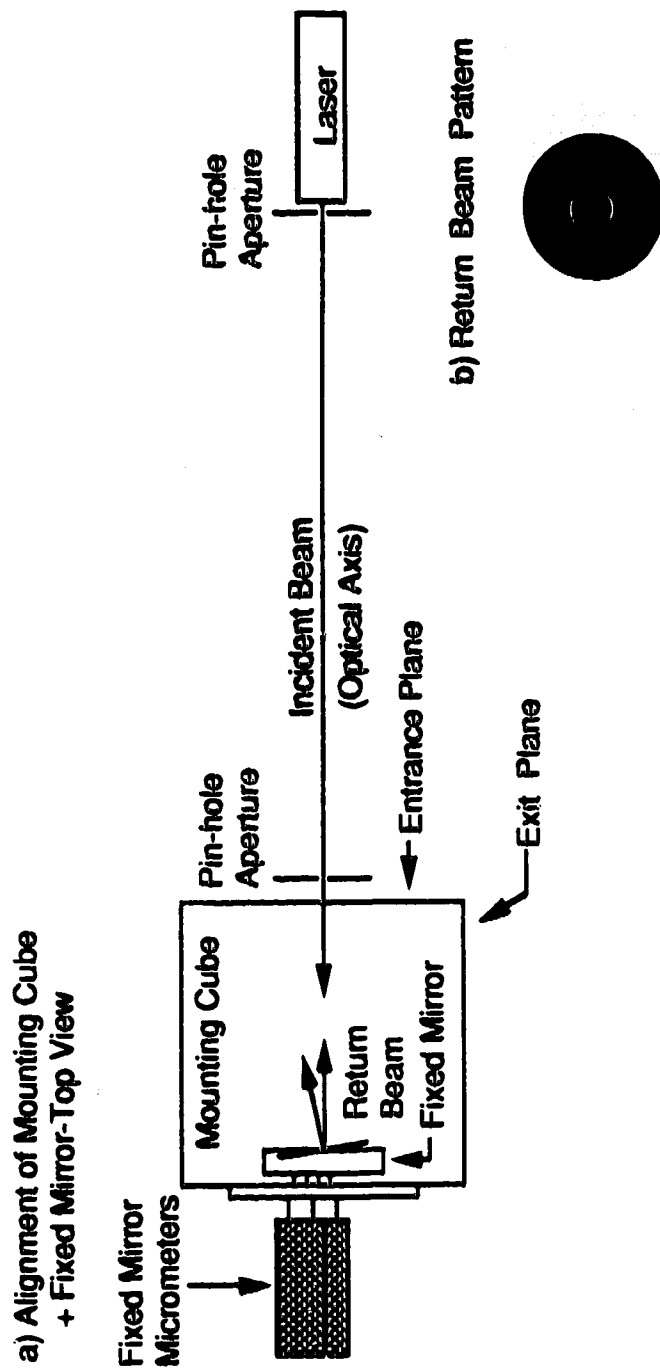


Figure 2-3. Physical set-up for alignment of the mounting cube plus fixed mirror.

Two criteria must be met for the reflected beam to return to the laser exit aperture: 1) the interferometer must be aligned such that the incident beam travels along the central axis of the entrance plane of the cube, and 2) the plane of the fixed mirror must be perpendicular to the direction of the incident beam. If this second criterion is satisfied, and if the entrance plane of the mounting cube is parallel to the plane of the fixed mirror, then the entrance plane is also perpendicular to the external axis. The pattern generated by the return beam when these criteria are satisfied, is shown in part b) of Fig. 2-3. Due to the small size of the apertures, diffraction rings are observed.

The fixed mirror mount is designed such that the plane of the fixed mirror can be adjusted with respect to the plane of the mounting flange of the assembly, and hence, with respect to the planes of the mounting cube itself. The plane of the mirror is adjusted to be as nearly parallel to the plane of the mounting flange as is possible. This is achieved by aligning, via usual machinists' techniques, the plane of the adjustable mirror holder such that it is parallel with the plane of the mounting flange. It is then assumed that the surface of the mirror is parallel with the plane of the holder, which is parallel with the plane of the mounting flange. When the assembly is mounted to the mounting cube it is assumed that the fixed mirror is now parallel to the entrance plane face of the cube.

This initial alignment is not designed for great accuracy. Many assumptions are being made with respect to machining and fabrication accuracy. This procedure appears to be accurate enough for the alignment of the mounting cube with respect to the external axis. Refinements could be developed to better ensure that the plane of the fixed mirror is parallel to the

entrance plane of the mounting cube. So far, it does not appear that this is necessary. The final adjustment of the fixed mirror is achieved interferometrically.

2-2.2. Alignment of the beam divider and moving mirror.

Once the mounting cube is properly aligned, the next step is to align the beam-splitter and the moving mirror with respect to the external axis. Before describing this procedure, consider for a moment the passage of the incident alignment beam as it is divided by the beam-splitter/compensator assembly. This is illustrated in Fig. 2-4.

As shown (qualitatively) in this figure, the beam-splitter partially reflects the incident alignment beam towards the moving mirror, while the remainder is transmitted towards the fixed mirror. In this figure, the fixed mirror beam is blocked.

As the beam enters the quartz of the beam-splitter optical flat, it is refracted at an angle of approximately 28° relative to the normal axis of the surface. After the first reflection at the partially reflecting surface, the reflected portion of the beam traverses the beam-splitter flat, reaching the first surface with an angle of incidence of 28° . With this angle of incidence (and the refractive index change from quartz to air) there is significant reflection at this internal surface. This internally reflected beam traverses the beam-splitter flat and is partially reflected at the beam-dividing surface. It is as if the internally reflected beam is another incident beam that is displaced from the true incident beam. With the fixed mirror arm not blocked, this internal

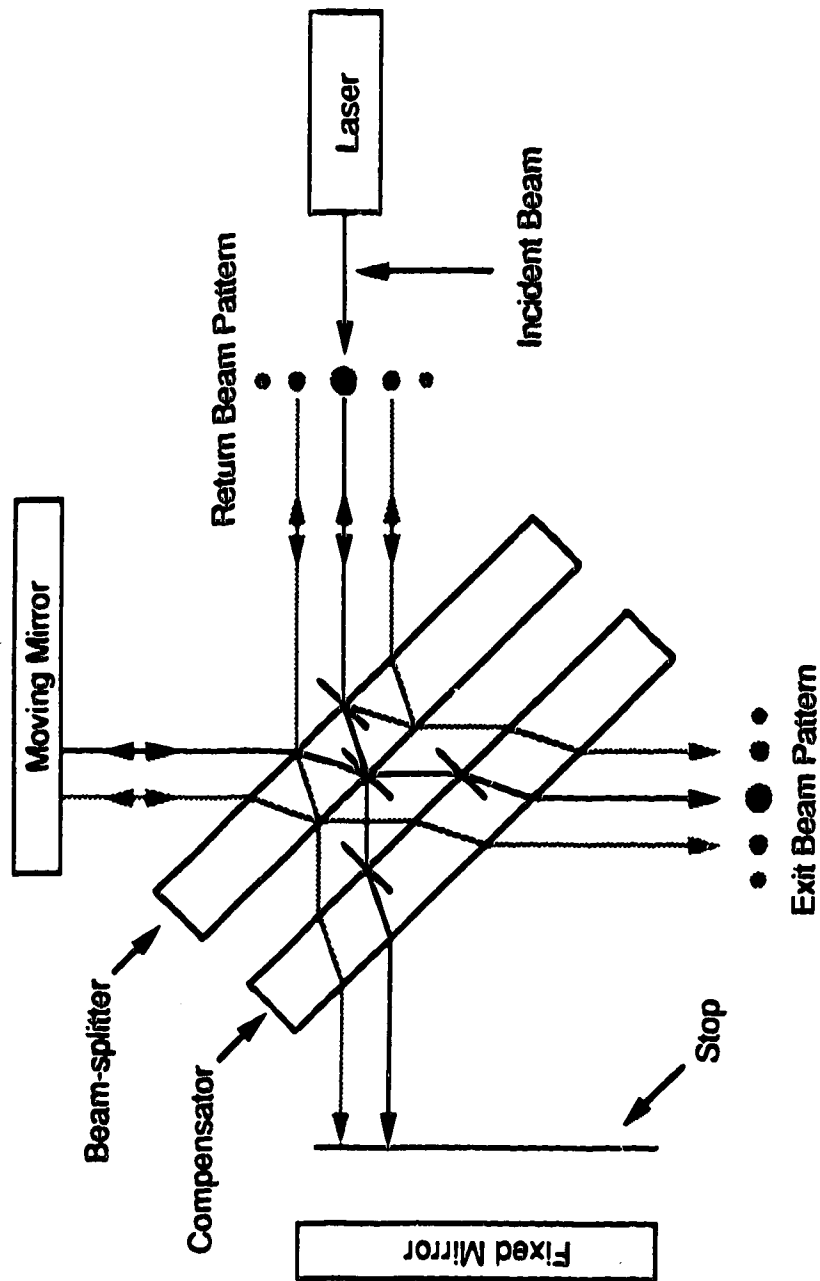


Figure 2-4. Return and exit beam patterns due to multiple reflections.

beam undergoes division and re-combination in the same manner as the incident beam, except that the re-combined output beam is displaced from , and of lesser maximum intensity than, the incident beam.

As a result of other single and multiple internal reflections there are a number of ways in which displaced exit and return beams are generated. These are seen as smaller intensity beams that are displaced from the main incident beam. The pattern of exit and return beams is shown in Fig. 2-4. Due to the symmetry of the system, there is a central main beam (due to the incident beam) and pairs of auxiliary beams, on either side of the main beam, due to reflections. The main beam defines the internal optical axis of the interferometer.

For the incident beam, two re-combined beams are formed. One beam is transmitted in the direction of the exit plane of the interferometer, while the other is reflected back in the direction of the source. The same is true for the internally reflected beam. Since it appears to be a displaced source of lesser intensity, the return and re-combined beams are both displaced from the position of the incident beam.

If the moving mirror optical path is blocked, while that of the fixed mirror is clear, a similar pair of beam patterns is observed. If both optical paths are unblocked, and if the fixed and moving mirrors are mis-aligned with respect to re-combination, then a pair of return beam patterns is observed. Similarly, a pair of patterns would be observed at the exit plane of the interferometer. When the two mirrors are properly aligned for re-combination, the pairs of patterns become superimposed such that single return beam and exit plane patterns are observed. When it is time to adjust

the fixed mirror interferometrically, this provides a convenient method with which to roughly align the plane of the fixed mirror for re-combination.

The physical set-up for alignment of the moving mirror is illustrated in Fig. 2-5. Again the path to the fixed mirror is blocked. The desired result of this procedure is that the planes of the beam-splitter and fixed mirror will be oriented at 45° and 90° to the external axis, respectively. This is the preferred arrangement for operation with the present design of the mounting cube. If this situation is achieved, the exit beam will leave the mounting cube with a direction perpendicular to that of the external axis.

The beam splitter and the moving mirror could be oriented at some angle other than 45° to each other. As long as the fixed mirror was adjusted to make the same angle with respect to the beam-splitter, effective re-combination would still take place. However, the angle of the exit beam would no longer be 90° with respect to the direction of the incident beam. This situation would require far more flexibility in the positioning and alignment of the exit focussing optics than is presently built into the system.

The beam-splitter and moving mirror are aligned in an iterative fashion such that the return beam is superimposed on the incident beam. An alignment target is positioned along the axis of the exit plane aperture. As mentioned above, in this design the exit plane axis has been chosen to be at 90° to the entrance plane axis. Several situations can occur.

If the beam-splitter and moving mirror are oriented at 45° with respect to each other, but mis-aligned with respect to the incident beam, then the return beam will not be superimposed upon the incident beam.

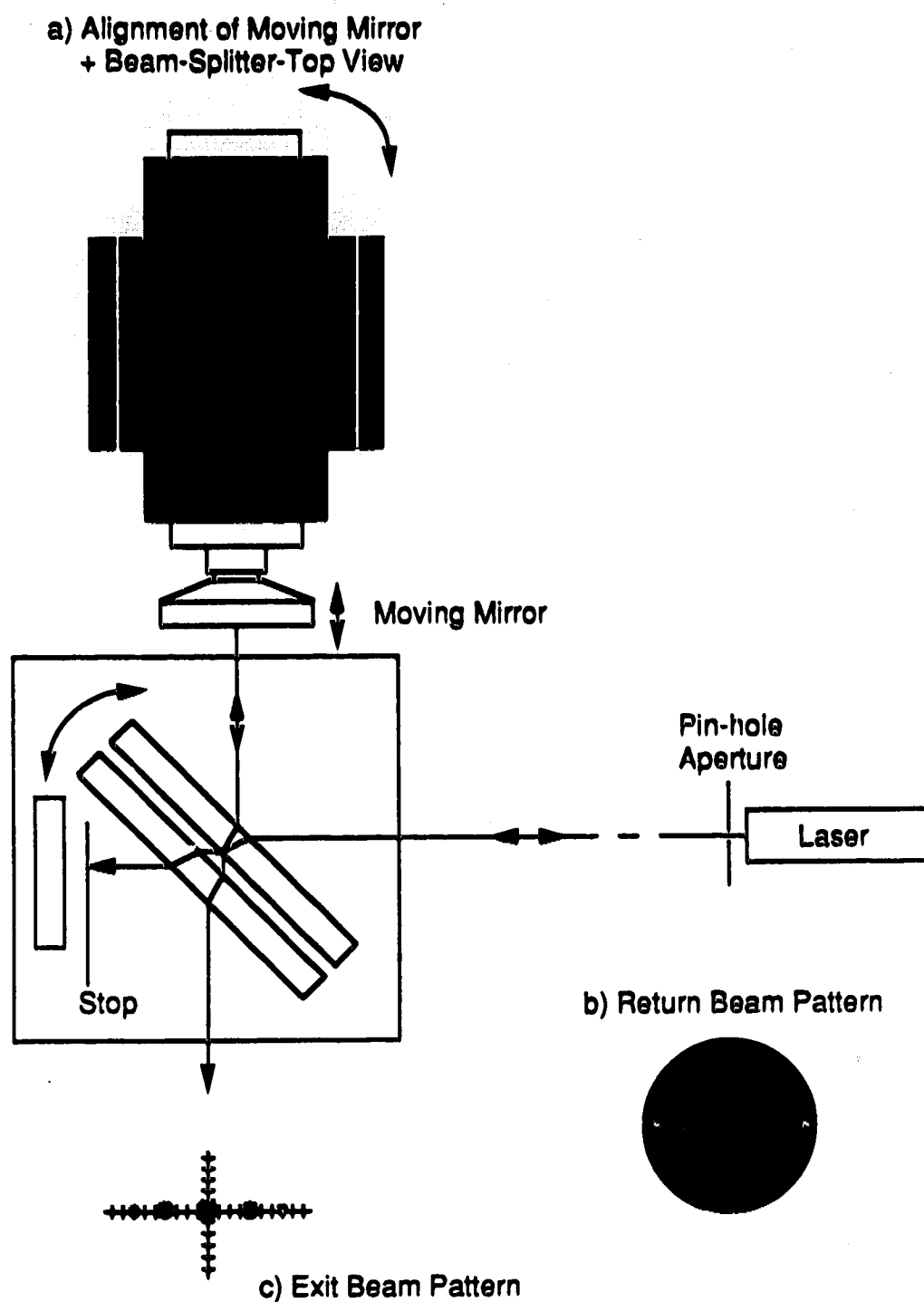


Figure 2-5: Physical set-up for alignment of the moving mirror and beam-splitter/compensator assemblies.

If the beam splitter and moving mirror are aligned such that the return beam is super-imposed upon the incident beam, but the beam splitter is not at 45° to the incident beam, then the moving mirror cannot be at 90° to the incident beam and hence, the exit beam will not strike the target correctly. Thus, only when the desired 45° orientation is achieved will the return beam be superimposed upon the incident beam, and the exit beam will hit the target appropriately, as indicated in parts b) and c) of Fig. 2-5.

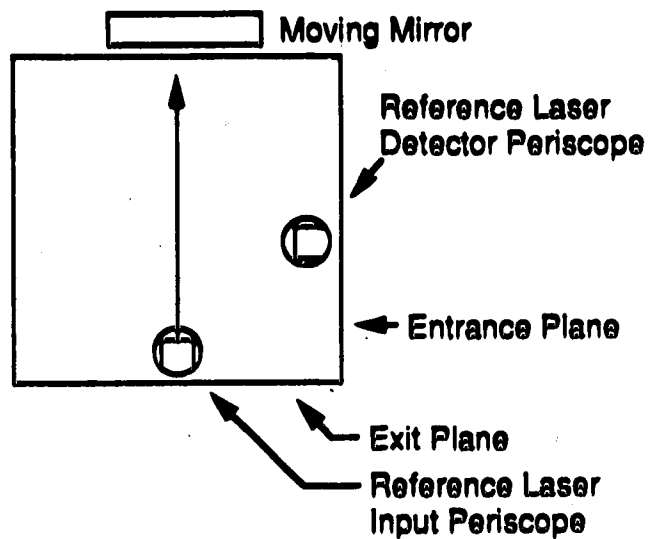
The beam-splitter and moving mirror are adjusted, iteratively, at various points in the moving mirror travel. This is done with the air-bearing floated, otherwise there may be some play in the tilt of the moving mirror due to the clearance between the sleeve and piston of the air-bearing.

The moving mirror assembly is strongly fixed at this time. The beam-splitter assembly is not fixed yet. The next step is to align the reference laser through the reference laser input periscope. This is illustrated in Fig. 2-6.

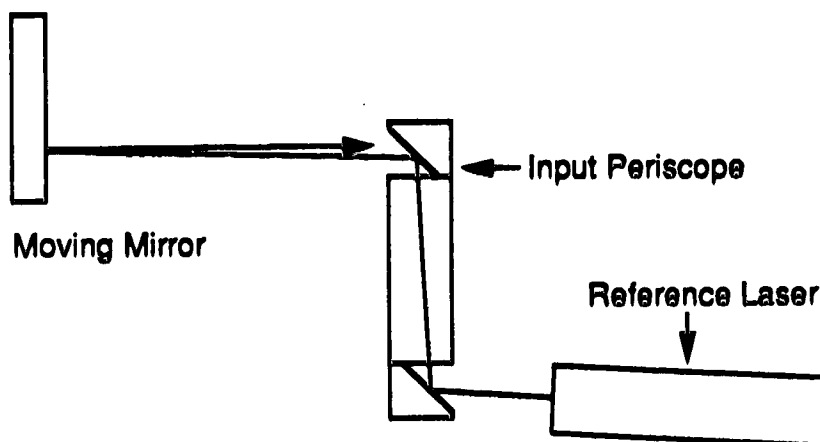
2-2.3. Alignment of the reference laser optical path.

The periscope system by which the reference laser is brought into the interferometer is described elsewhere [14]. The moving mirror assembly has been locked into position and the beam-splitter is removed. Removing the beam-splitter is only necessary due to the configuration of the present system. In future designs it should be reasonably simple to design the reference laser optical path such that the beam-splitter does not have to be removed to align the reference laser. As shown in part a) of this figure, the reference laser beam travels backwards through the interferometer. This is purely a matter of convenience with the present system configuration.

a) Top View



b) Side View



c) Input Periscope-Front View

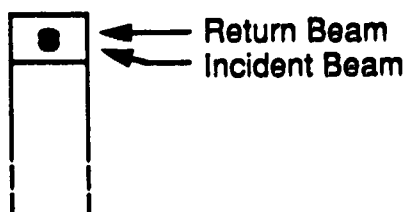


Figure 2-6. Alignment of the reference laser periscope system.

Ideally, the reference laser should be oriented such that the beam is parallel to the optical axis of the interferometer, that is, perpendicular to the plane of the moving mirror. However, if this was the case, then upon reflection the beam would return and re-enter the laser cavity. Typically, feed-back of this type into the laser cavity causes gross fluctuations of the output intensity. To circumvent this problem, the laser is slightly tilted, as illustrated in parts b) and c) of this figure. As a result, the return beam is offset and does not enter the cavity. The effect of this is to introduce a determinate error into the calibration of the wavelength axis of spectra obtained with this instrument. The means by which this occurs is shown in Fig. 2-7.

Illustrated in part a) of this figure is the situation in which the reference laser is directed perpendicular to the plane of the moving mirror. The reference beam is divided at the partially mirrored beam-splitter surface. The beam that enters the moving mirror arm of the interferometer travels a distance d , first through the quartz of the beam-splitter substrate, then through air to reach the moving mirror. The total geometric path length that the beam must travel to reach the recombination point on the beam-splitter is twice this distance. If the position of the mirror is changed by an amount Δx , then the geometric path length is changed by the amount, $2\Delta x$. Hence, for the intensity of the reference interferogram to be modulated through one period, the mirror must move through a distance equal to $\lambda/2$, where λ is the wavelength of the reference laser.

In the discussion of interference upon re-combination at the beam-splitter it is the optical path length, rather than the geometric path length,

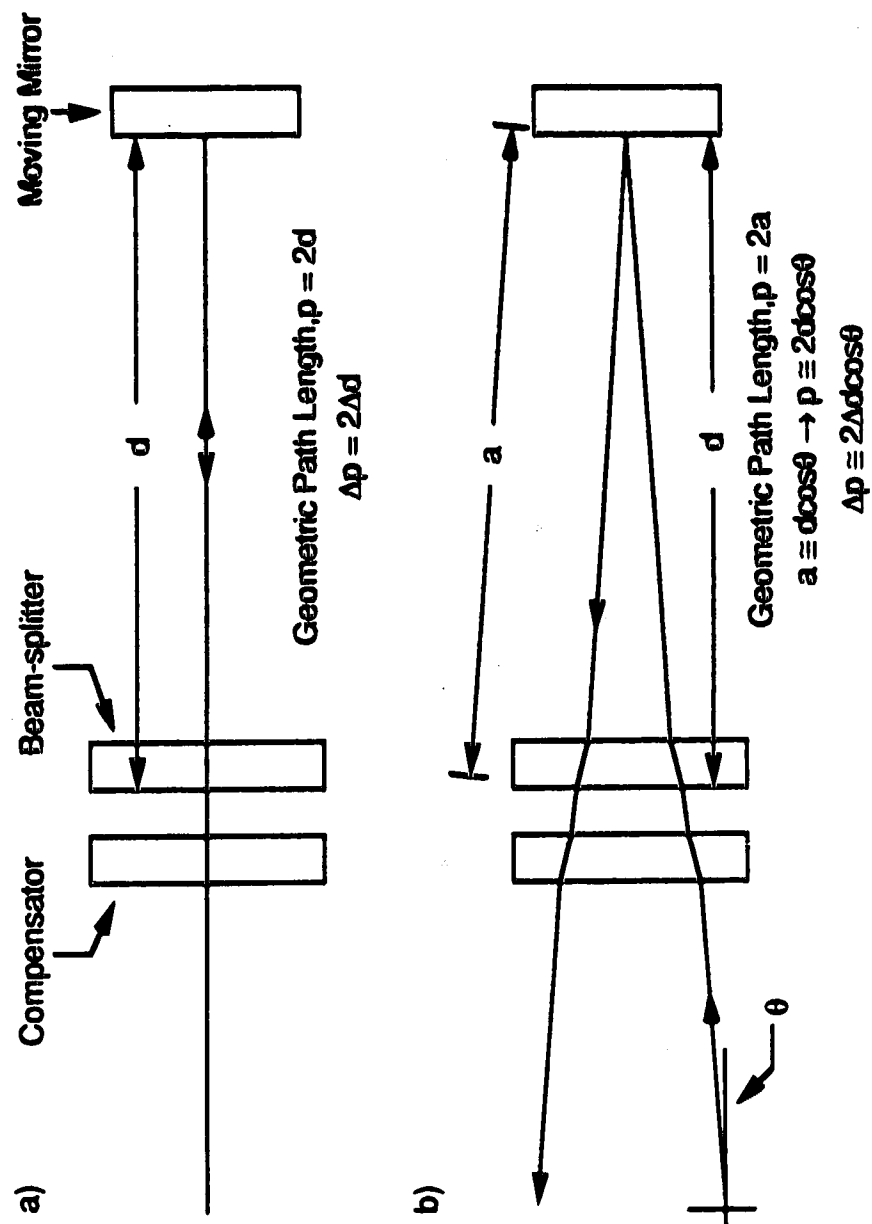


Figure 2-7. Effect of tilt of the reference laser beam.

that should be considered. The optical path length takes into account the refractive index of the various media that the beam travels through. However, for the purposes of this discussion, the optical path length will be taken to be equal to the geometric path length.

Illustrated in part b) of this figure is the situation in which the laser is slightly tilted such that the reflected beam does not return upon itself. If the laser is tilted by an amount θ , then for a change in the position of the mirror equal to Δx , the geometric path length is changed by the amount $2\Delta x \cos\theta$. For the intensity of the reference interferogram to be modulated through one period, the mirror must move through a distance of $\lambda/2\cos\theta$. This is a larger interval of movement than that for the case where the beam is aligned with no tilt. Thus, it is as if a laser with a longer wavelength is being used for the reference source. With this in mind, consider the use of a Michelson interferometer to determine the wavelength of a laser that is aligned (with no tilt) along the interferometer optical axis.

In this discussion, changes in the angle of the reference beam, due to refraction by the beam-splitter and compensator optical flats, are being neglected. As will be shown, for the present configuration of the system, θ is small. For an incident beam with near-normal incidence, the deviation due to refraction is small, that is, the angles of incidence and refraction are almost equal. Since the angle, θ , will be estimated from the distance between the exit and return beam spots on the reference laser periscope, and the distance from these spots to the moving mirror, this neglect of the refraction along the path of the beam will be seen to provide a worst case estimate of the angle at which the laser is tilted.

For illustration purposes, the source is a continuous wave HeCd laser with a wavelength of 325.129 nm [69]. The wavelength of the HeNe reference laser will be taken to be 632.81646 nm [69]. Since the wavelength of the source is less than that of the reference, the period of the interferogram of the source would be observed to be shorter than that of the reference. With both the source and reference beams aligned with no tilt, the period of the interferogram of the source would be measured to be equal to 0.513781 of the period of the reference interferogram. Therefore, the wavelength of the source is equal to this fraction of the reference wavelength, or 325.129 nm. Consider now the situation in which the reference beam is tilted 10° from horizontal.

The interval of mirror movement that is required to modulate the intensity of the reference interferogram through one period is now equal to $0.32128934 \mu\text{m}$. The period of the source interferogram would be measured to be 0.505820 of the period of the reference. If the reference wavelength was taken to be 632.81646 nm, then the source wavelength would be calculated to be 320.091 nm. Clearly, this result is grossly in error. However, in this illustrative example, the amount of tilt of the reference beam is known. Hence, an effective wavelength could be calculated for use in the source wavelength calculation. For example, with a tilt of 10° , the effective reference wavelength would be calculated to be 642.57868 nm. Since the source wavelength is known to be 0.505820 of the reference wavelength, with this effective reference wavelength, the source wavelength would be correctly calculated to be 325.029 nm. The actual tilt of the reference beam in the present system is certainly less than 10° . The magnitude of the tilt is estimated with the aid of the construction shown in Fig. 2-8.

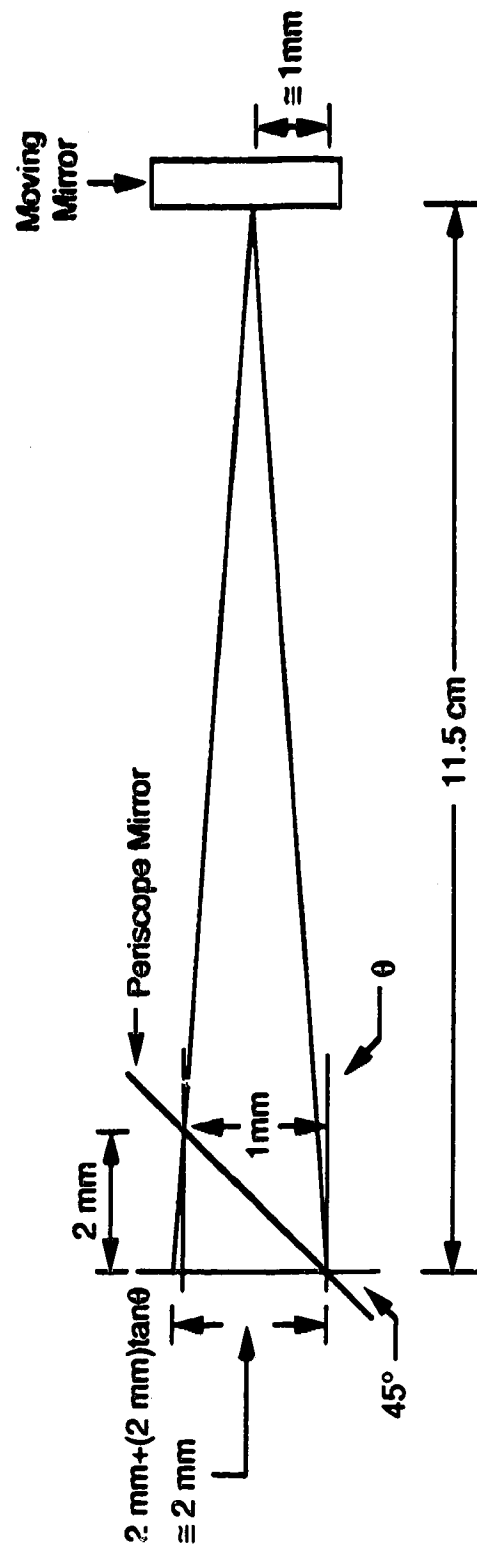


Figure 2-8. Construction for the estimation of the magnitude of tilt of the reference laser beam.

The beam that returns to the periscope mirror is estimated to be displaced from the exit beam by, at most, 2 mm. This is observed with the beam splitter in place. Since the beam-splitter/compensator causes further divergence due to refraction, the actual displacement of the return beam is less than that which is observed. Hence, the angle of tilt is less than that which is calculated from this construction. The distance from the exit beam to the moving mirror, when the moving mirror is situated as far from the periscope as possible, is approximately 11.5 cm. It can be seen from this figure that the angle of tilt is approximately equal to the inverse tangent of $0.1/11.5$, or 0.49821161° . The values for the two numbers in this calculation are estimates. For illustration purposes, the precision of the numbers has been set to be arbitrarily high.

In the same manner as described above, if the tilt of the reference beam was not accounted for, the source wavelength would be calculated to be 325.017 nm. If the amount of tilt was accounted for, then the effective wavelength of the reference would be calculated to be 632.84038 nm. With this value for the reference wavelength, the calculation would proceed to the correct answer.

The example above is a general description of the use of a Michelson interferometer as a so-called "wavemeter" to determine the wavelength of, perhaps, a tuned laser. However, in the application for which this system has been designed, the source interferogram is a complex superposition of many wavelength components. The spectrum of the interferogram is obtained via spectral analysis; in this case through a numerical Fourier transform. The wavelength axis of the calculated spectrum is calibrated via a calculation that is analogous to that described above. If the reference laser is tilted, the effect

on the accuracy of the wavelength axis of the spectrum is the same as that described above.

In actual operation of the system, when the value 632.81646 nm is used for the wavelength of the reference laser, as expected, the wavelengths corresponding to the peaks of well-characterized emission lines are slightly in error. Typically, wavelengths will be in error by approximately -8 pm [43]. Experimental factors, other than the slight tilt of the reference laser beam, also affect the calibration of the wavelength axis. For instance, the wavelength of the HeNe reference laser is subject to thermal drift due to thermally induced changes in the laser cavity dimensions. At this time, rather than attempting to control all of the various phenomena that can contribute to erroneous wavelength axis calibration, a method of calibration that incorporates the method of correction described above has been developed [43].

The wavelength axis is calibrated by determining the effective value of the reference laser wavelength that will give the correct result in the calculation of the wavelength of the peak of a well-known emission line. Specifically, this procedure is repeated with four iron lines whose wavelengths span a wide spectral band-width and are well-known. From this, an average effective reference wavelength is calculated. This wavelength is then used to calibrate the wavelength axis of subsequent calculated spectra. The achieved performance of this wavelength calibration procedure is described in detail elsewhere. [43] In general, the wavelength accuracy of the present system is within ± 1 pm. Clearly, the effect of tilting the reference beam in the entrance periscope is correctable.

It is of interest to note that a typical value for the effective wavelength of the reference laser is 632.8445 nm. If tilt of the reference beam was the only factor to be accounted for, this effective wavelength would correspond to a tilt of approximately 0.54° . This is in reasonable agreement with the value obtained above, via the construction of Fig. 2-8 and the associated estimated values. From this a tentative conclusion is that the dominant effect causing error in the calibration of the wavelength axis is the tilt of the reference laser. It would appear that the reference laser and the interferometer optics are reasonably stable with respect to the usual causes of instrumental drift.

For greater accuracy and precision, the obvious strategies for improvement would be to enclose and control the environment of the interferometer system, and acquire a reference laser with greater stability with respect to wavelength and intensity. Also, an alternative optical design might incorporate corner-cube, or cat's-eye, retroreflectors. With this type of design, the reference beam need not return into the laser cavity. Hence, there would be no need to tilt the reference laser.

At this point the moving and fixed mirrors, the beam-splitter/compensator, and the reference laser optical path have all been aligned. The white light optical path does not require any special alignment procedure. Typical machining accuracy has proven to be adequate for this task. With the present configuration, the entrance and exit off-axis parabolic mirror assemblies are aligned prior to attachment to the mounting cube. The physical set-up by which this is achieved is diagrammed in Fig. 2-9.

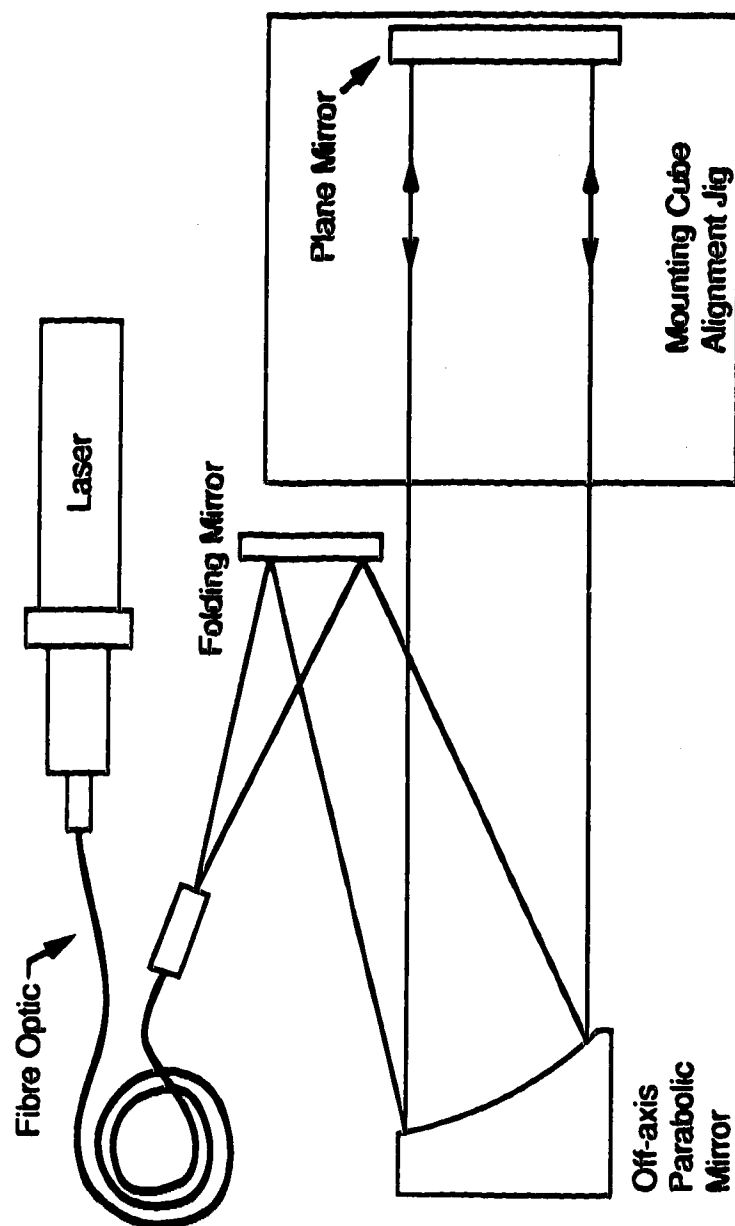


Figure 2-9. Physical set-up for alignment of the off-axis parabolic mirror assemblies.

2-2.4. Alignment of the entrance and exit off-axis parabolic mirror assemblies.

The light from a HeNe laser is focussed onto an optical fibre with a diameter of approximately 0.5 mm. The output end of the fibre is a reasonable approximation of a rather intense point source. Admittedly, the solid angle of emittance of this source is restricted. However, so far no applications that require any greater solid angle have been encountered. This is a highly useful tool for many alignment applications. The small physical size of the output end allows for great flexibility in the positioning of this point source.

This point source is approximately positioned at the focal point of an off axis parabolic (O.A.P.) mirror assembly. The assembly is mounted onto a replicate of the mounting cube that is used in the interferometer. As indicated in this figure, a plane mirror is mounted onto the alignment cube. Within typical machining tolerances, the plane of this mirror is parallel to the plane of the alignment cube to which it is attached. The O.A.P. assembly collimates the spherical wavefronts of the point source, producing planar wavefronts. Upon reflection at the mirror, the planar wavefronts are focussed by the O.A.P. assembly. This results in a spot on the source plane. Clearly, with reference to this figure, one can see that when the planes of the wavefronts are parallel to the plane of the mirror, then, the return beam spot will be superimposed upon the point source. The O.A.P. housing allows for adjustments to be made to the position of the off-axis parabolic mirror element. The mirror is adjusted until the return spot is superimposed on the output end of the optic fibre. At the same time, the axial position of the point source is adjusted to minimize the return beam spot size. This roughly aligns the end of the fibre optic to the focal point of the assembly.

The plane mirror is removed, and the roughly collimated beam is projected onto a target located approximately 3 m from the alignment cube. The target consists of 2 in. diameter circle. If the point source was perfectly collimated, the beam would exactly fill such a circle. However, some divergence in the equatorial plane has been observed, such that the spot at this distance has an elliptical shape.

This elliptical beam cross-section is suggestive of some astigmatism in the optical system. In commercially available collimation systems [70] that are analogous to this set-up, the secondary mirror is not perfectly planar. Instead it has a computer optimized aspheric profile to correct for aberrations. As well, many such systems employ some sort of spatial filtering to further enhance the beam quality.

As a result of the reasonably small aperture size that is typically in use in this system, the aberration described above is not considered (for the present) to be serious. When the circular target is placed within a meter of the alignment cube, the collimated beam very closely approximates a circular beam. Since travel through the interferometer constitutes an optical path length of less than 20 cm, the amount of divergence in this distance is unlikely to be significant, from an interferometric point of view.

The off-axis parabolic mirror element mount has been modified to allow for rotation of the mirror. The mirror is rotated until the principal axis of the elliptical beam shape is parallel to the tangential plane. The position of the point source on the axis of the assembly is adjusted, if necessary, such that the collimated beam appropriately fills the target.

The plane mirror is once again mounted onto the alignment cube and, if necessary, the angle of the off-axis parabolic mirror is adjusted to re-align the return spot with the point source. The plane mirror is again removed and the off-axis parabolic mirror is rotated, if necessary, while viewing the beam shape on the circular target. These two procedures are iterated until the return spot is superimposed upon the output end of the fibre optic, and the beam has the correct shape as indicated by the circular target.

The entrance and exit O.A.P. assemblies are aligned in this manner. With the assumption that the interferometer mounting cube is very similar to the alignment cube, when these assemblies are attached to the former, they will be correctly aligned. Admittedly, it is desirable that this adjustment be performed in situ while the assemblies are mounted to the actual mounting cube. With the present system this is difficult to achieve; however, in the future, this can be achieved with suitable modifications. In fact, the projected next generation alignment procedure will most likely incorporate the O.A.P. assemblies in the role of an auto-collimator such that the fixed and moving mirrors can be aligned. The beam-splitter/compensator assembly will then be aligned interferometrically. In brief, the procedure might be as follows.

The entrance O.A.P. assembly is mounted at the entrance plane of the interferometer mounting cube. The laser point source is used to align the assembly via the same procedure as that described above. In this case, a planar mirror is mounted such that the plane of the mirror is as parallel as possible to the fixed mirror plane of the mounting cube.

The fixed mirror is mounted onto the cube. The angle of the plane of the fixed mirror is adjusted until the return spot is superimposed upon the

point source. The plane of the fixed mirror is now aligned such that it is parallel to the collimated wavefronts of the entrance O.A.P assembly. Note that in this situation, there is no alignment with respect to an external axis. The interferometer components are being aligned with respect to the internal optical axis.

The exit O.A.P assembly is mounted onto the exit plane of the cube, and aligned as described above. The moving mirror is then aligned, again, by superimposing the return spot onto the point source. This is performed for all points in the travel of the mirror. It should be possible to modify the moving mirror assembly such that the angle of the plane of the moving mirror can be adjusted, independent of the air-bearing assembly.

The procedure described above should be more effective for aligning the plane of the moving mirror than that which is based upon viewing the return of the external axis alignment beam. In the latter procedure, since it is desirable that the moving mirror be centered on the optical axis of the interferometer, the external axis beam strikes the mirror close to its center. The deviation of the return beam, per unit of angular deviation of the plane of the moving mirror, is less than it would be if the beam were to strike the mirror closer to the edge. Thus, the return beam procedure, in its present implementation, is in its least sensitive configuration. With a procedure that is based upon reflection of the collimated point source light, all points of the mirror must be perpendicular to the axis of the O.A.P. Clearly, the criteria for correct alignment of the mirror are much more stringent in this latter procedure, than in the former.

The beam-splitter/compensator assembly is aligned interferometrically. The present design of this assembly is currently under modification to allow for minute adjustment of both the angle and tilt of the plane of the beam-splitter/compensator with respect to the planes of the fixed and moving mirrors.

With the point source positioned at the focal point of the entrance O.A.P. assembly, the beam-splitter orientation is adjusted until an interference pattern is observed on a screen placed at the exit plane of the mounting cube, that is, before focussing by the exit O.A.P. assembly. If the light from the point source was perfectly collimated, and if the dividing and reflection processes proceeded perfectly, then the beams from the two arms of the interferometer would re-combine with the same degree of interference over the whole cross-section of the beam. In other words, observed on the screen would be a homogeneous distribution of light whose intensity would be determined by the position of the moving mirror in its travel. Since the system is not perfect, the actual pattern will be significantly more complex; however, the position of the beam-splitter/compensator that is required to produce interference will be clearly identifiable.

With unfinished components of this modified system, some preliminary observations have been made. The observed interference pattern consists of a symmetric pair of hyperbolae whose axes are set at right angles. Symmetry indicates correct alignment. Over the typical aperture size of 1 cm, the degree of interference is essentially constant. The observed pattern most likely results from the previously mentioned suspected astigmatism of the entrance O.A.P. assembly. In order to achieve a larger useful aperture, it

would appear that the O.A.P. assemblies will have to be corrected for aberrations.

2-2.5. Alignment of the source and detector.

The alignment of the detector and the source to the interferometer internal axis proceeds in the same manner for both alignment procedures. Prior to alignment of the detector the fixed mirror, or the beam-splitter/compensator, is adjusted to produce interference, as viewed on the screen at the exit plane.

The point source is positioned at the focal point of the entrance O.A.P. assembly, and the aperture of the detector assembly is positioned, via the X-Y-Z stage, at the focal point of the exit O.A.P. assembly. This is usually achieved by observing the output signal of the detector as the detector entrance aperture is manipulated in the focal plane of the exit O.A.P. assembly.

The point source is then positioned in the entrance aperture of the detector assembly. This is illustrated in Fig. 2-10. The light from the point source is collimated and then focussed at the focal point of the entrance O.A.P. assembly. This provides an extremely convenient alignment beam with which to position the source. The source (or position of the source that is to be sampled) is placed at the focal point of this beam.

It is important to note that the interferometer may now be treated as a simple autonomous optical element. It is simply an "interferometer module". The optical axis of the rail bed upon which the interferometer is

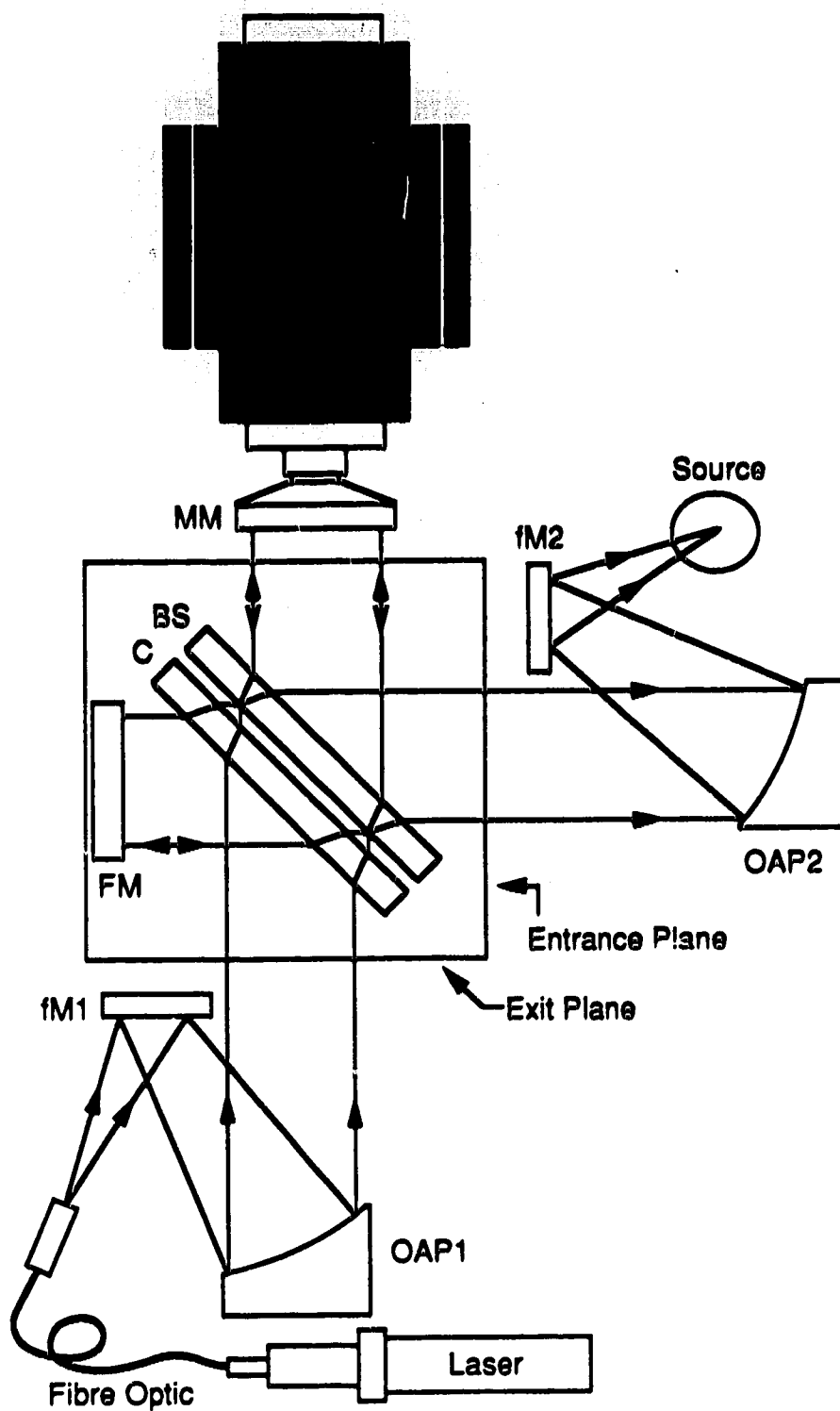


Figure 2-10. Physical set-up for alignment of the source.

situated is now irrelevant with respect to the alignment of the interferometer. A source that is well removed from the optical axis could be easily aligned with respect to the interferometer, simply by placing it at the focal point of the beam from the entrance O.A.P. assembly.

2-3. Resolution performance of the current optical system.

In assessing the resolving power of a dispersive spectrometer, one might observe the spectrum that is produced from a narrow line source such as a laser or atomic emission discharge source. The effects that the instrument has on the measurement must be characterized from the spectrum; there is little other information available. Typically, the profiles of the lines in the spectrum are studied. Since instrumental effects are convolved into the spectrum, simple observation of the line profiles often does not allow for intuitive assessment of these effects. The situation is, however, quite different for an interferometric spectrometer of the type being described here.

With such a spectrometer, instrumental effects are often very easily recognized in the acquired interferogram. An effect that causes the line profiles in the spectrum to change appears in the interferogram in a multiplicative fashion. This is often intuitively obvious. Hence, to assess the resolving performance of this instrument it is worth looking at interferograms, as well as the resultant spectra, of various sources.

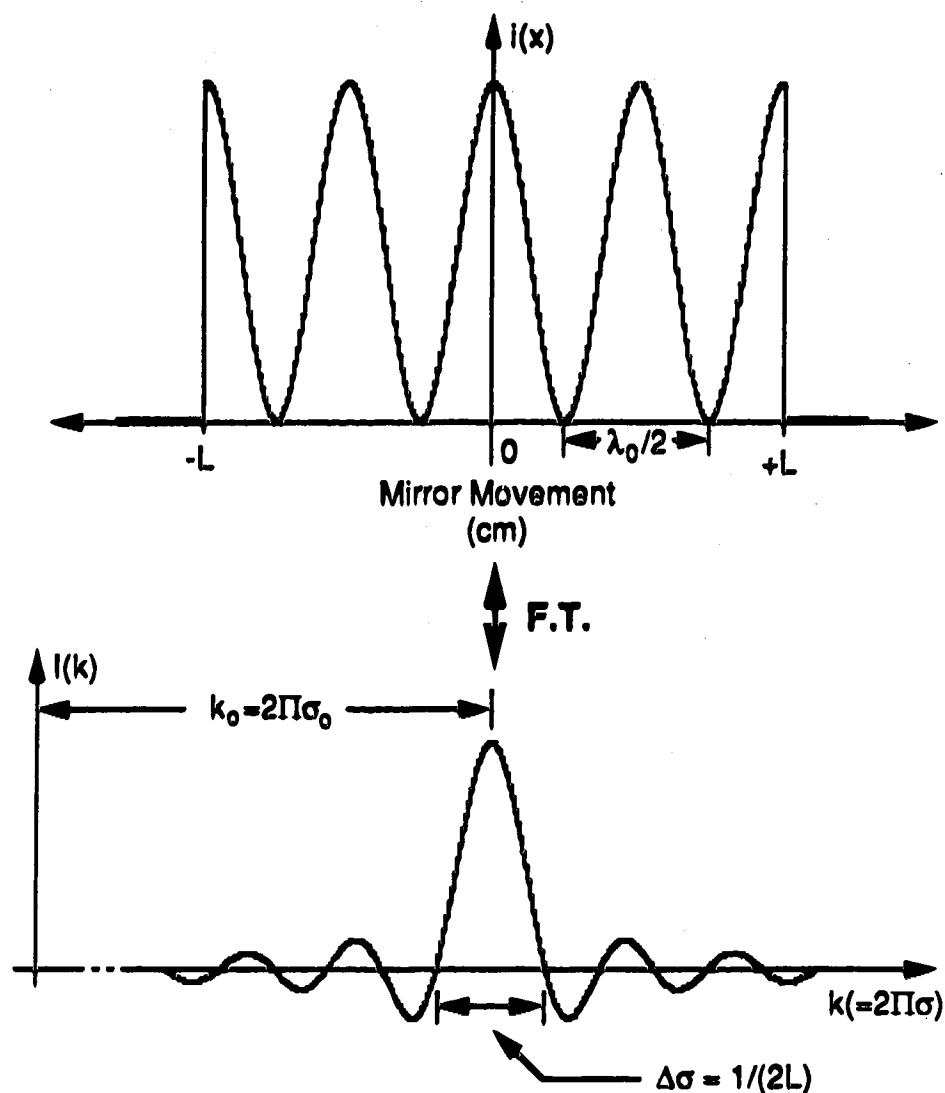
The moving mirror in this interferometer design moves through a limited travel. If the optical system was perfect, the final spectrum might, or might not, show an effect due to the abrupt truncation of the interferogram

from which the spectrum was derived. The effect of truncation becomes more pronounced for sources of narrow band radiation, such as atomic emission sources, while the spectra derived from broad band continuum sources may not be significantly affected by truncation of the interferogram. Consider the case in which the interferogram of an ideal monochromatic source is acquired.

An ideal monochromatic source has a spectrum that consists of an infinitely narrow spectral line situated at the wavenumber of the source $\sigma_0 = 1/\lambda_0$. If the interferogram of such a source was measured with a perfect interferometer of the type being considered here, the result would be a truncated sinusoid with a perfectly constant amplitude. Regardless of the length of travel of the moving mirror, the amplitude of the interferogram would not change throughout the scan.

A calculated truncated sinusoidal wave, and its spectrum, are shown in Fig. 2-11. The spectrum consists of a spectral line centered on $\sigma_0 = 1/\lambda_0$. However, instead of an infinitely narrow line (i.e. a δ -function) the line has a finite width and a $\sin\sigma/\sigma$ profile. The wavelength interval between the first two zero-crossings on either side of the maximum is defined, in this case, to be the spectral line-width. As indicated, the line-width is inversely proportional to the length of the interferogram. In the limit, as the interferogram approaches infinite length, the line-width approaches zero.

A truly monochromatic source is an idealization. The closest approximations to such a source are lasers, and some sources of atomic emission.



Interferogram Length (2L)		$\Delta\sigma(\text{cm}^{-1})$
No. of Periods of Reference Int'gm.	cm	
4096	0.130	7.69
8192	0.259	3.86
16384	0.518	1.93
32768	1.037	0.97
65536	2.074	0.48

Figure 2-11. Calculated truncated interferogram of a monochromatic source. Calculated spectrum. Theoretical spectral line-widths for truncated interferograms. (HeNe 632.8 nm reference laser.)

Under ideal conditions, the radiation that is emitted as a result of electronic transitions in atoms has a natural line-width that is determined by the fundamental physics of the particular emitting species. In the case of a laser, the optical configuration, in combination with lasing action, produces radiation with a line-width that is significantly less than the natural line-width of the emitting transition. Thus, for many purposes a laser provides an excellent approximation of a monochromatic source.

Typical sources of atomic emission rarely produce radiation that approaches the natural line-width of the emitting transitions. The emitting species in these sources are usually excited in the gas phase (often in a plasma environment). As a result, many line broadening processes occur. For example, collisions with other species during emission, interaction of the emitting species with an electric field, and translational motion of the emitting species with respect to an observer; all of these cause broadening of the lines in the emitted radiation. These are termed, respectively, collisional, Stark, and Doppler broadening. These processes notwithstanding, in many situations atomic emission sources can provide essentially monochromatic radiation.

A highly developed and studied atomic emission source is the Hollow Cathode Lamp (HCL). Under appropriate conditions, the only broadening that is assumed to be affecting the output line-width and profile is Doppler broadening. For the purposes of observing the resolution performance of this spectrometer, a Mg HCL is particularly suitable.

The spectrum of a Mg HCL is shown in Fig. 2-12. As can be seen, the spectrum is dominated by a line at 285.213 nm. The next most significant

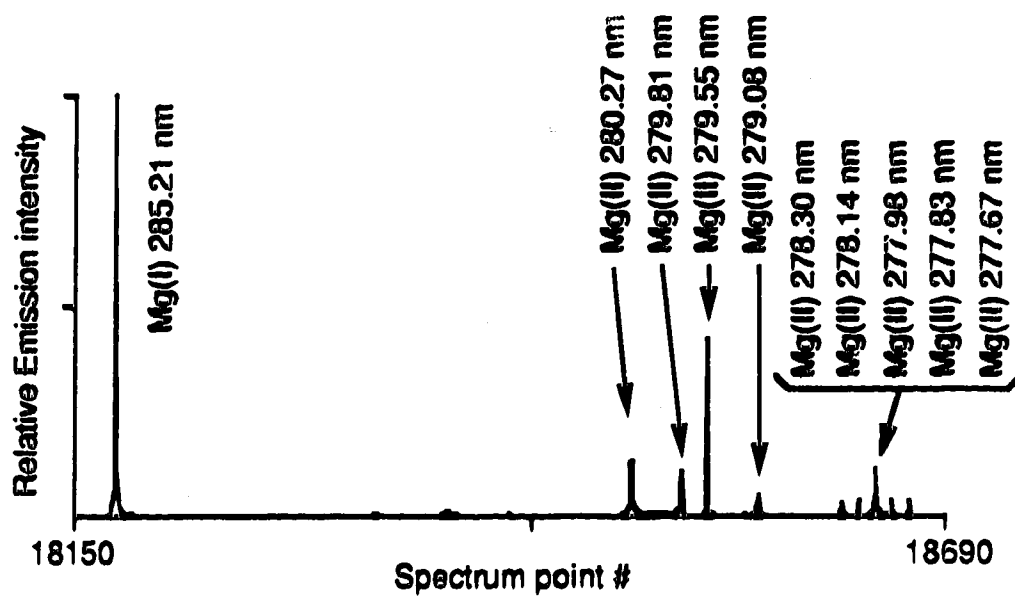


Figure 2-12. Spectrum of a Mg hollow cathode lamp.

contribution is a line at 279.55 nm. Typically, this line has a maximum intensity that is one half that of the 285.213 nm line. Since these two lines are due to atomic and ionic emission, respectively, the ratio of their intensities is highly dependent upon the excitation conditions within the source. This is manifested in the strong dependency of this ratio upon the lamp current.

The spectrum of radiation from a Mg HCL essentially consists of two lines. Consider for a moment that these two lines are infinitely narrow and of equal intensity. The interferogram of this radiation would be the superposition of two sinusoids with equal amplitudes but different frequencies. Hence, the interferogram would be an amplitude modulated sinusoid. It is easy to show that the wavelength of the sinusoid is given by $\lambda = 2\lambda_1\lambda_2/(\lambda_1+\lambda_2)$. Similarly the wavelength of the modulation of the amplitude is given by $\lambda_m = 2\lambda_1\lambda_2/(\lambda_1-\lambda_2)$. With $\lambda_1 = 285.213$ nm and $\lambda_2 = 279.55$ nm, $\lambda = 282.353$ nm, and $\lambda_m = 28.159$ μ m. Thus, the interferogram would oscillate through one period as the mirror was translated through 0.141177 μ m, and the amplitude of the interferogram would be modulated through one period as the mirror was translated through 28.259 μ m. For this case of infinitely narrow lines, the interferogram would not decay as the optical path difference was increased.

If this interferogram was measured with an interferometer with significant instrumental apodization, the envelope of the interferogram would be seen to decay slowly with respect to optical path difference. Thus, the envelope of the interferogram would consist of a rapid variation due to the spectrum of the source, and a slowly varying component due to the instrumental apodization. Therefore, even though this would not be a monochromatic source, viewing the envelope over large intervals of optical

path difference would still allow one to assess the extent of instrumental apodization of the interferogram. In this example, the two wavelength components were assumed to have equal amplitudes. In the Mg HCL the two wavelength components have unequal amplitudes. This is a more difficult case to treat mathematically; however, the case of equal amplitudes represents the worst case situation regarding the superposition of two sinusoids.

The spectral lines from a HCL have finite widths. The envelope of the interferogram of two such lines, if measured with a perfect interferometer, would decay slowly relative to the modulation resulting from the superposition of the two wavelength components. Depending upon the limit of the moving mirror travel, the decay of the envelope due to finite spectral line-widths must be accounted for in assessing instrumental apodization.

One might ask why the resolution is not characterized with a laser as the source. Indeed, this would be the ideal situation; however, since this instrument is designed for use in the UV, it is desirable that the resolution be tested with respect to UV radiation. Thus, a Continuous Wave (CW) UV laser would be required. At present these are not readily available. Use of a visible CW laser such as a HeNe laser would not provide an accurate assessment of the resolution in the UV, although, as will be shown, some useful information can be gleaned from the use of such a source.

Shown in Fig. 2-13 are typical interferograms of a Mg HCL. Parts a), b), and c) are interferograms in which the total moving mirror travel was, respectively, 4096, 8192, and 16384 periods of a HeNe reference laser interferogram. As indicated in the table at the bottom of Fig. 2-11, these correspond to 0.130, 0.259, and 0.518 cm, of total travel of the moving mirror.

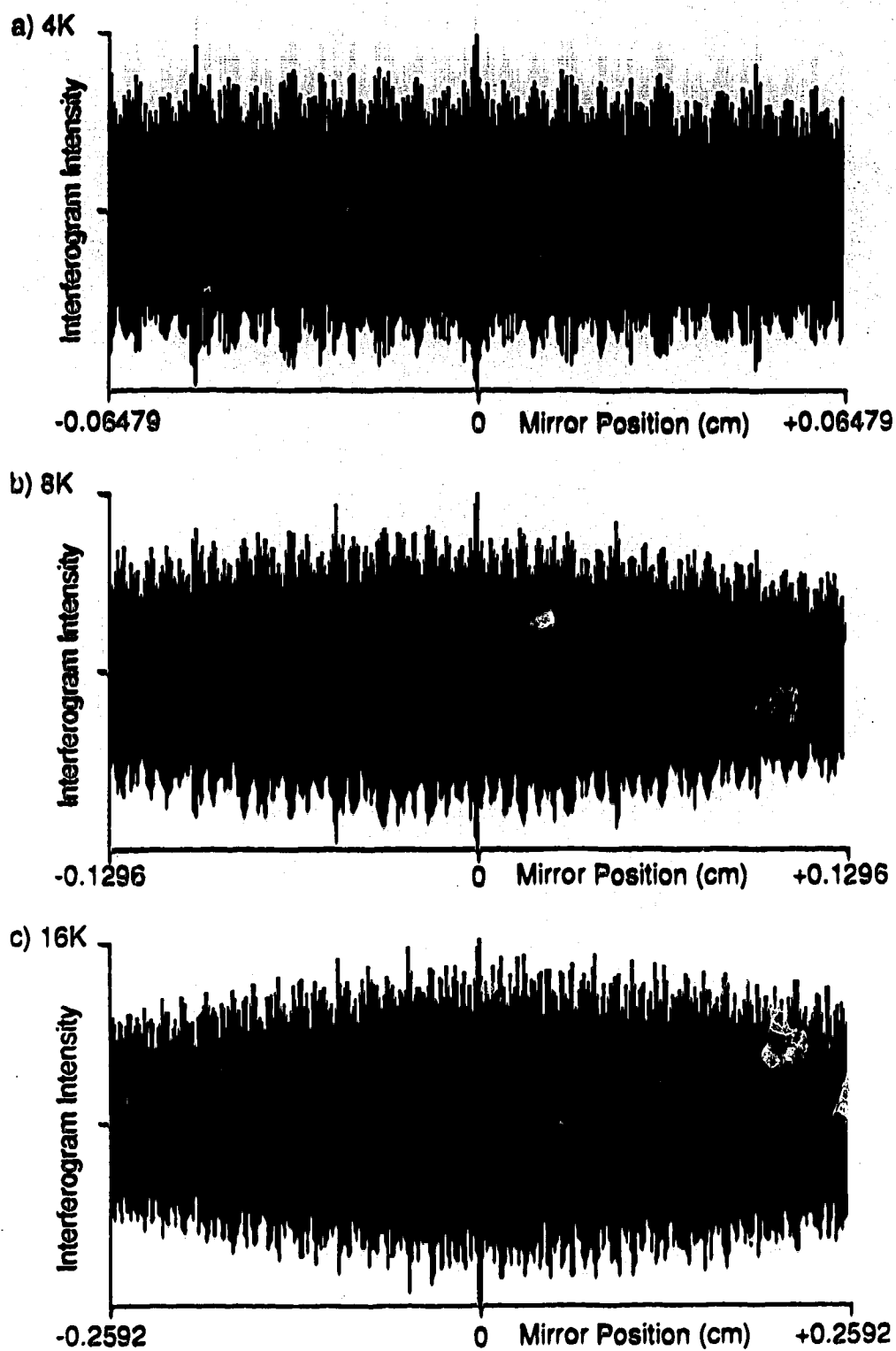


Figure 2-13. Different length interferograms of a Mg hollow cathode lamp.

With reference to the envelopes of these interferograms, one can see that all three are strongly truncated. The envelope of the 4K interferogram is essentially constant across the travel of the mirror. However, the envelopes of the 8K and 16K interferograms show some decay as the mirror moves away from the position of the middle of the interferogram. This is due to either the natural line-width of the HCL source, or instrumental effects, that is, instrumental apodization.

The Mg 285.213 nm lines from the spectra derived from these three interferograms are shown in parts a), b) and c) of Fig. 2-14, respectively. As expected, since the 4K interferogram is strongly truncated and shows little decay of the envelope, the line profile of the 285.213 nm line in the spectrum is very similar to that shown in Fig. 2-11. Both the shape and width of the profile agree well with the calculated profile. This is strong evidence that, at least for a 4K interferogram, there is little instrumental apodization of the interferogram.

For the 8K and 16K interferograms, the shapes and widths of the 285.213 nm profiles deviate from the calculated version. This is due to the decay of the envelopes of the interferograms. As mentioned above, this is due to either an instrumental effect (i.e. tilt of the moving mirror), or the natural line shape of the source. To assess this, consider the line profile of the Mg 285.213 nm line emitted by a Mg HCL of this type.

For these measurements, the HCL was operated with a lamp current of 10 ma. Under this condition, it is assumed that the dominant source of broadening of the emitted radiation is Doppler broadening, resulting in a Gaussian frequency distribution given by [71],

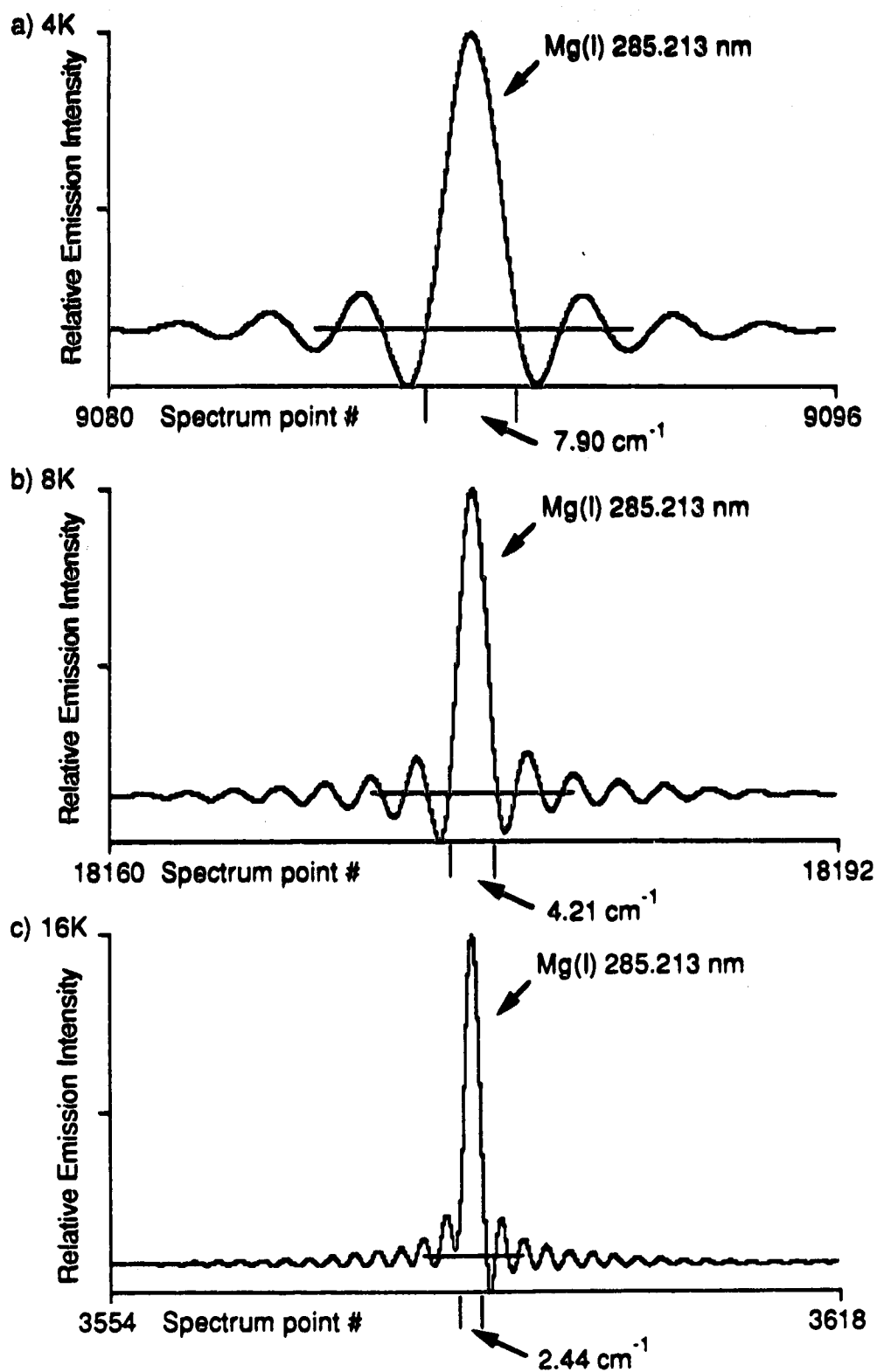


Figure 2-14. Mg 285.213 nm lines from a hollow cathode lamp.

$$I(\sigma) = I_0 \exp \left[- \left(\frac{2(\sigma - \sigma_0)}{\Delta\sigma_D} \sqrt{\ln 2} \right)^2 \right],$$

where $\Delta\sigma_D$ is the full-width at half the maximum (FWHM) intensity, I_0 , of the profile. This spectral line, and the interferogram from which it would be derived, are shown in Fig. 2-15.

As indicated in this figure, the Gaussian profile of the spectral line is a direct consequence of the Gaussian shape of the envelope of the interferogram. As expected, the width of the spectral line is inversely proportional to the width of the envelope of the interferogram. In the limit, an interferogram with an envelope of infinite width would result in a spectrum with infinitely narrow lines.

Two expressions for the product of the widths of the functions in the reciprocal domains are given at the bottom of this figure. The expressions for the intensity of the interferogram are functions of the optical retardation, X . At any given mirror position, x , the optical retardation at that position is $2x$. When this is accounted for, the equation at the bottom of the figure (inside the box) is produced. This equation relates the width of the interferogram, in terms of mirror movement, to the width of the spectral line, in wavenumbers. Again, these are full-widths at half maximum.

Hasegawa and Haraguchi have measured the width of the 285.213 nm line of a commercial Mg HCL, operating with a lamp current of 10 ma, to be $\Delta\lambda_D = 0.95$ pm ($\Delta\sigma_D = 0.12$ cm⁻¹) [35]. The interferogram from which such a spectral line would be derived should have $\Delta x_D = 3.7$ cm. Hence, if the interferogram of this source was detected with a perfect interferometer, then,

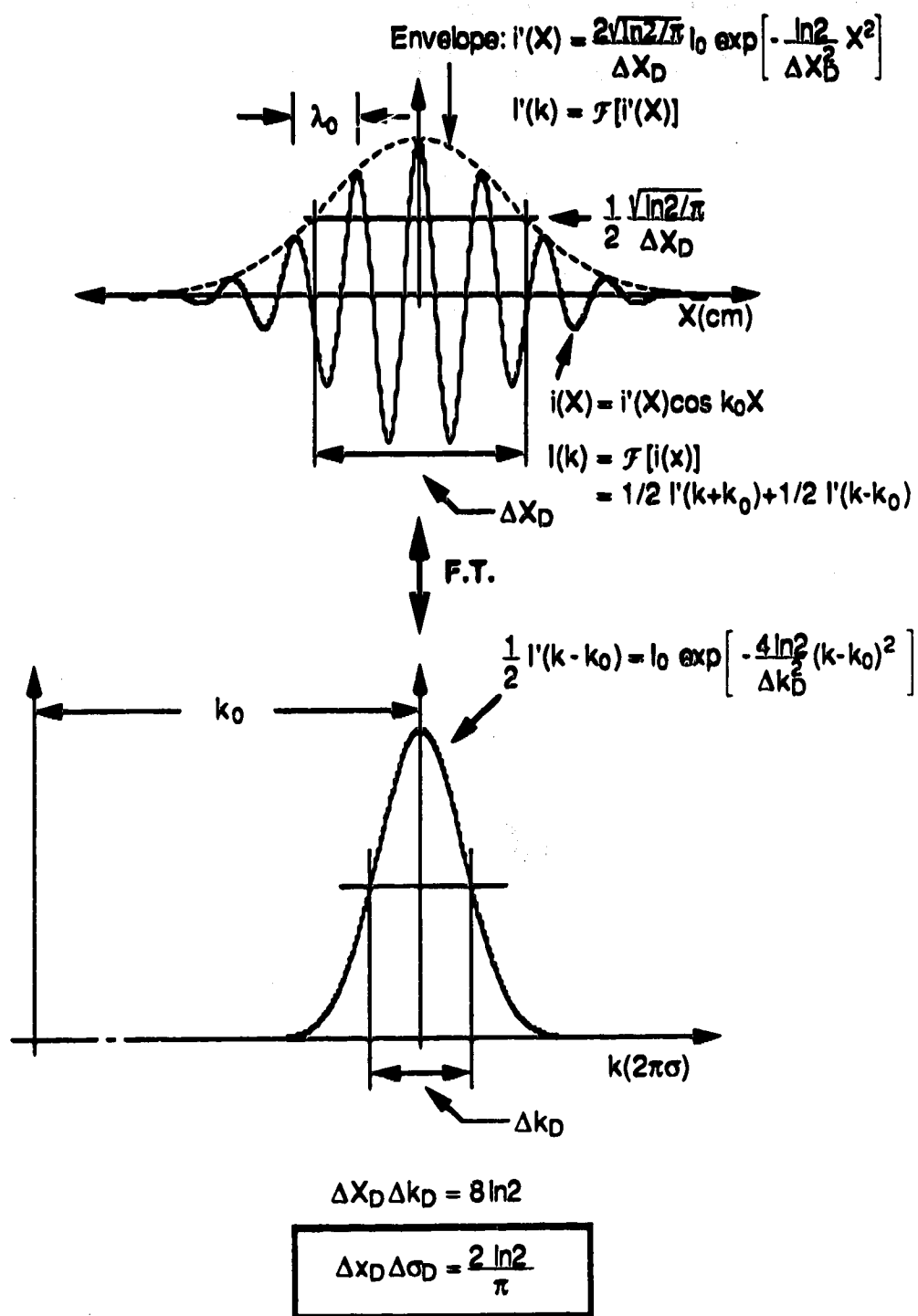


Figure 2-15. Calculated Gaussian envelope interferogram and spectrum.

after the mirror had travelled ± 1.9 cm from the position of the middle of the interferogram, the envelope of the interferogram would have decreased to one half of the maximum value.

With this calculated value for the approximate FWHM of the interferogram envelope, it is difficult to assess whether or not the observed decay of the 8K and 16 K interferograms of Fig. 2-13 is due to instrumental broadening. However, the situation is very clear-cut for the interferogram shown in Fig. 2-16.

The interferogram in this figure was acquired over ± 1.037 cm (or 65536 periods of the reference laser interferogram) of mirror travel. This is the maximum mirror travel of the present system. Superimposed upon the interferogram is the Gaussian envelope profile with a FWHM = 3.7 cm. Due to the great number of points present in the interferogram, it is difficult to assess the maximum intensity of the interferogram in this figure. However, for the purposes of this discussion, the envelope of the interferogram is readily discernible.

Clearly, the envelope of the experimental interferogram decays significantly faster, as the mirror moves away from the position of the middle of the interferogram, than does the calculated envelope. With the assumption that this calculation reflects, to within a reasonable approximation, the actual nature of the Mg HCL source radiation, then it can be concluded that the decay of the experimental interferogram envelope is due almost entirely to instrumental effects.

This conclusion is further strengthened by the data presented in Fig. 2-17. This figure is a normalized plot of the magnitude of the envelope of the

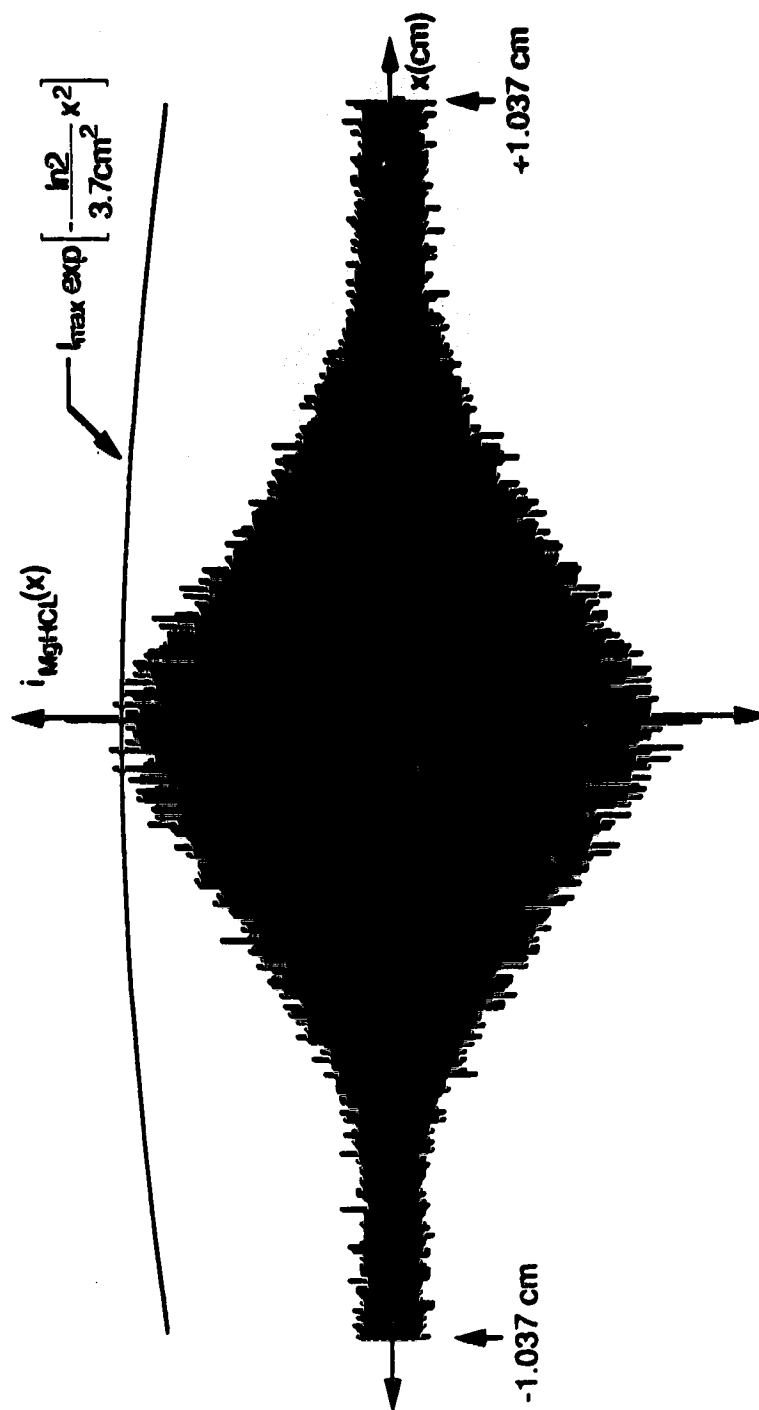


Figure 2-16. Experimental 64K interferogram plus calculated Gaussian envelope.

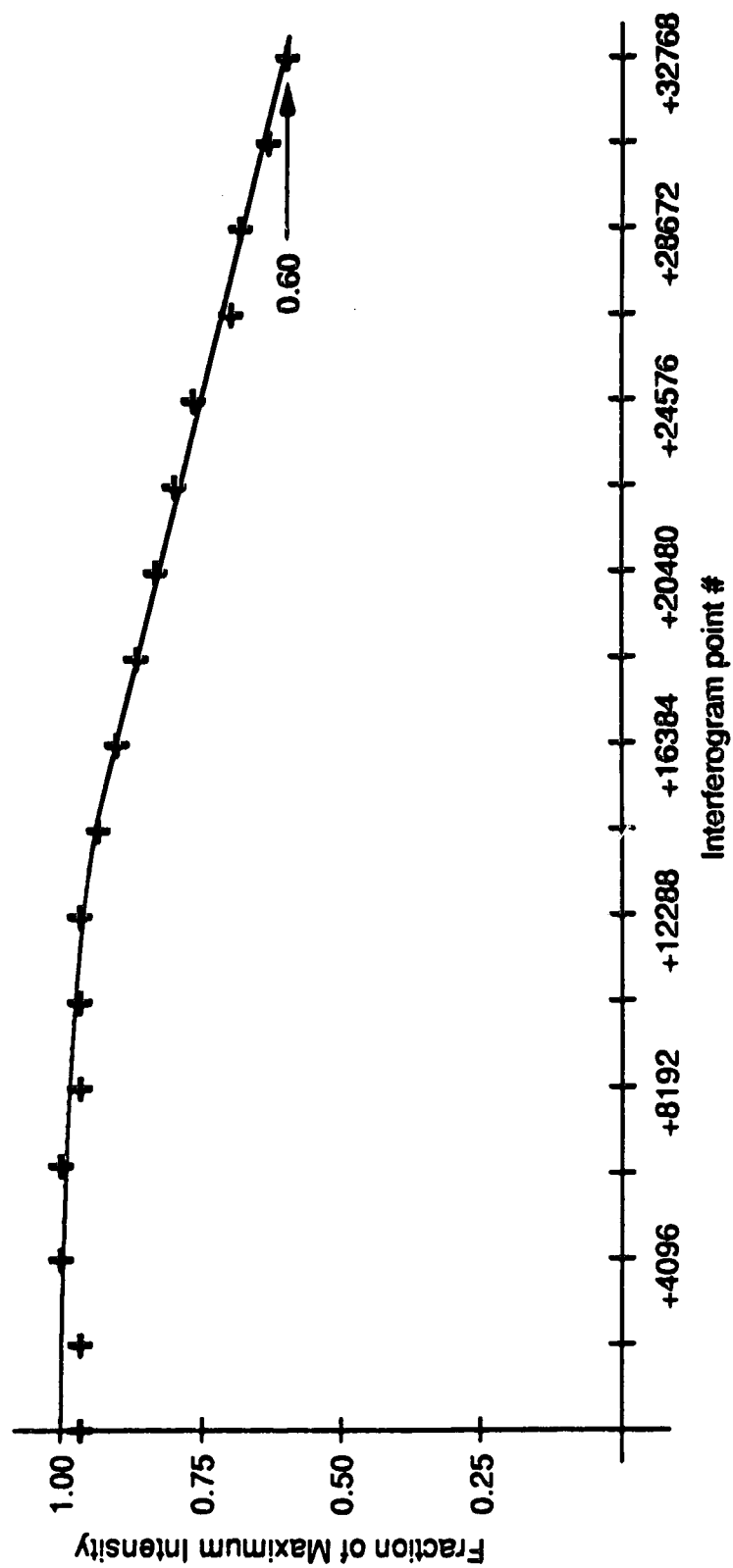


Figure 2-17. Envelope of HeNe point source 64K interferogram.

interferogram of the HeNe laser plus fibre optic point source that is usually employed for alignment of the interferometer. This experimental set-up probably represents the best case situation with respect to minimum instrumental apodization.

The wavelength of this source is significantly longer than those involved in the HCL tests, therefore misalignments such as moving mirror tilt, that might have been significant for the previous experiments, will be less significant in this situation. As well, since the source is laser radiation, the FWHM of the true interferogram is expected to be significantly greater than the longest travel of the moving mirror, thereby providing an approximately monochromatic source for the test. A value for the spectral line-width of the particular laser that was employed in this test was unavailable. However, this laser is an identical model to that which is used as the reference laser. At the positions of maximum mirror travel, the envelope of the reference laser interferogram decays to 0.92 of the maximum value at the middle of the mirror travel. Hence, the source line-width should play only a small role in the overall decay of the envelope of the interferogram, over the maximum travel of the mirror. Finally, this source is easily aligned with respect to the optical axis of the interferometer, because it is typically used to define this optical axis.

As can be seen from this figure, at the ends of the mirror travel the envelope of the interferogram decays to approximately 60% of the maximum value at the middle of the mirror travel. This is a clear indication of the extent of what is probably the minimum apodization of an interferogram that is caused by instrumental effects. This data suggests that for interferograms comprising a total mirror movement of 16384 periods of the reference laser,

instrumental apodization is not a significant problem. However, due to the wavelength of the source, this conclusion has an appended caveat.

Again, with reference to Fig. 2-17, as the mirror moves outwards in its travel, the envelope of the interferogram decreases slowly at first, and then almost linearly with mirror position. This is further evidence that this is an instrumental effect since this envelope shape would not produce a physical spectral line profile.

From the preceding discussions, it is clear that the optical components being used in the present system, and/or the procedures by which these components are aligned, are not adequate to allow for the realization of the maximum resolution that is possible with an instrument of this design.

As a result of the instrumental apodization of the interferogram of Fig. 2-16, the effect of truncation on the resultant spectrum is lessened. In fact it is just this strategy that is employed in the mathematical apodization of a strongly truncated interferogram. The Mg 285.213 nm line from the spectrum of this interferogram is shown in Fig. 2-18.

The profile of this spectral line has little, if any, $\sin\sigma/\sigma$ character. Without fitting an equation to the line it is difficult to say what the functional form of the line profile is. Judging from the interferogram it is most likely that the line profile is something akin to a Voigt profile, that is, a hybrid of Gaussian and Lorentzian profiles.

Currently, the bench-mark of resolution performance that is employed within this laboratory is the FWHM of this Mg 285.213 nm line in the spectrum of this Mg HCL. From this figure this is seen to be equal to 0.63 cm^{-1} .

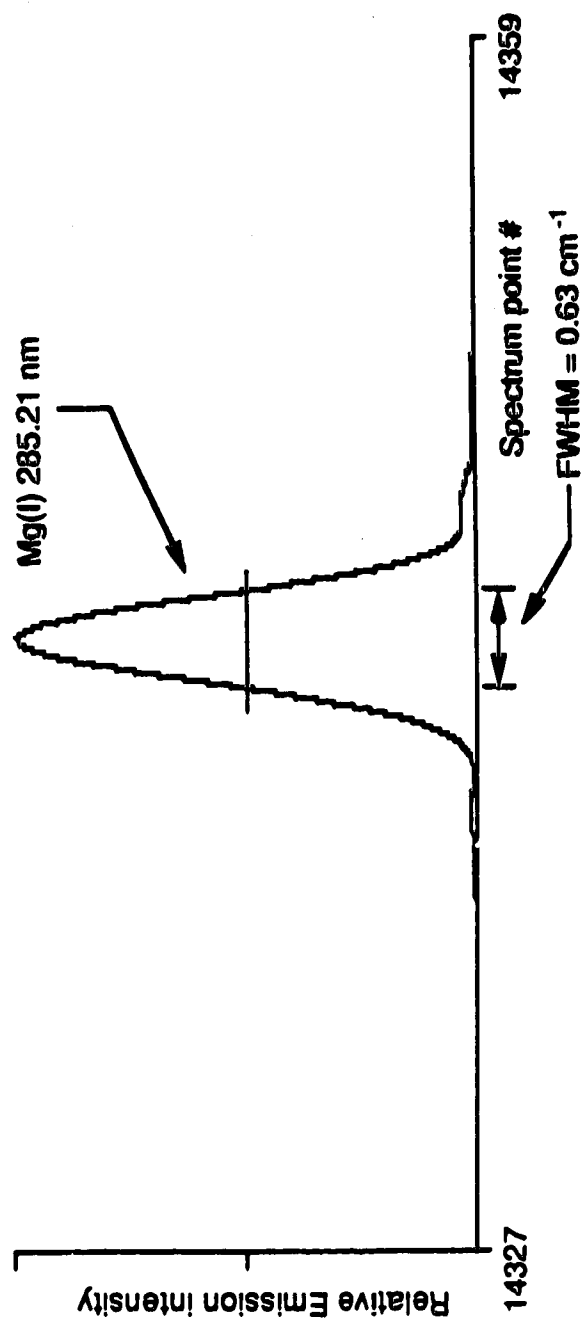


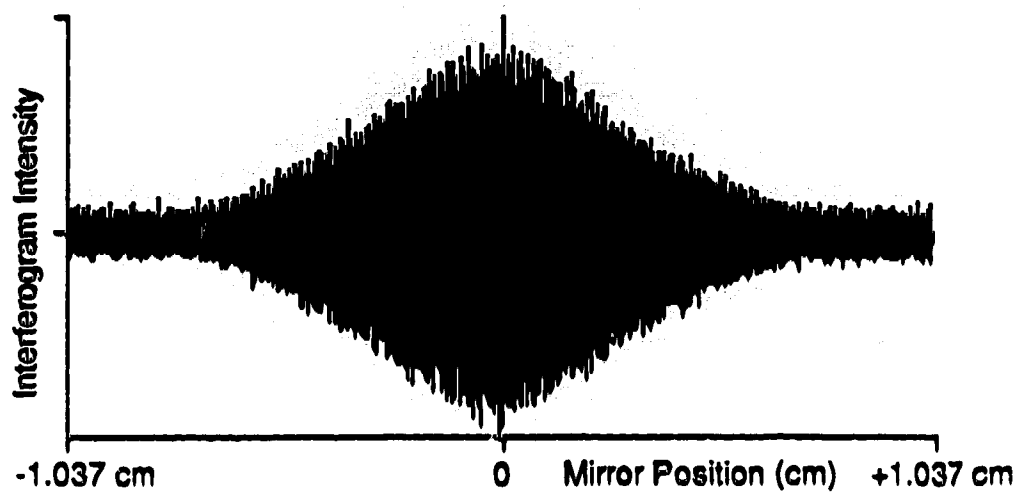
Figure 2-18. Mg 285.213 nm line. Maximum resolution.

The interferogram from which this spectrum was derived was acquired over the maximum mirror travel (total travel 2.074 cm) of this version of the instrument. The entrance aperture during this measurement was 8mm. From the experiments described previously, in which the collimation of the HeNe alignment point source was assessed (albeit qualitatively) interferometrically, it has been judged that with this small an aperture, even UV radiation should be well-collimated. The detector aperture was matched to the diameter of the central fringe (at 285.213 nm) in the focal plane of the interferometer. The diameter of this fringe was calculated to be 1.24 mm [14] . A 1.0 mm detector aperture was used for this measurement. Since this aperture is smaller than the calculated value for the central fringe diameter, some loss of sensitivity can be expected; however, the visibility of the interferogram, and hence, the resolution in the spectrum, should not be affected.

With the above points in mind, it's considered that this measurement was acquired under the highest resolution conditions for the present version of the instrument. The value, 0.63 cm^{-1} , for the FWHM of this line is the best resolution that we have obtained with this instrument. This value corresponds to a resolving power (defined as $R = \sigma / \Delta\sigma_{1/2}$) of $R = 55,653$. At 200 nm if $\Delta\sigma = 0.63 \text{ cm}^{-1}$, then $R = 79,365$. In terms of wavelengths, at 200, 250 and 350 nm, respectively, $\Delta\lambda = 2.52, 3.94$, and 5.67 pm .

The interferogram of Fig. 2-16 was obtained with the O.A.P mirror assembly as the entrance collimator. This is repeated for convenience in part a) of Fig. 2-19. The interferogram of part b) of this figure is analogous to that of part a), except that the former was obtained with a simple bi-convex quartz

a) Mirror Collimation



b) Lens Collimation

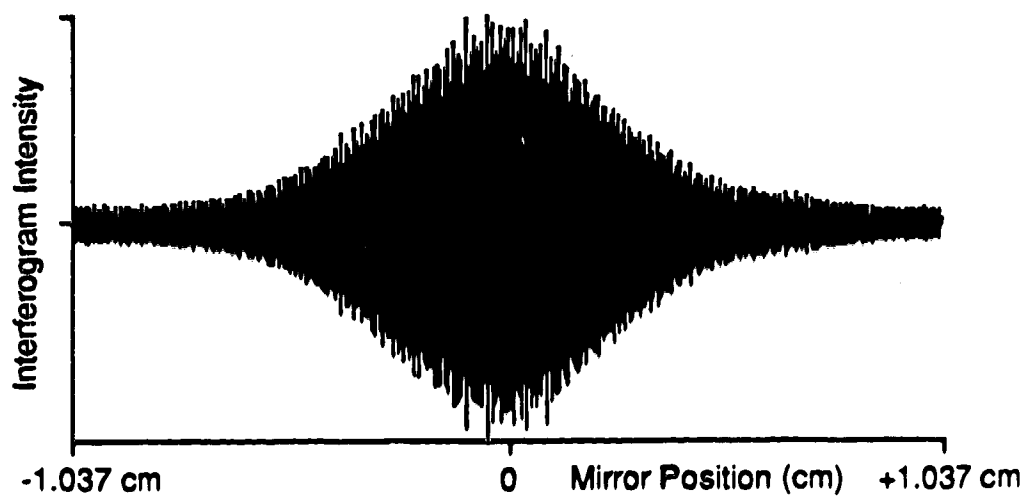


Figure 2-19. Interferograms acquired with mirror and lens collimation systems.

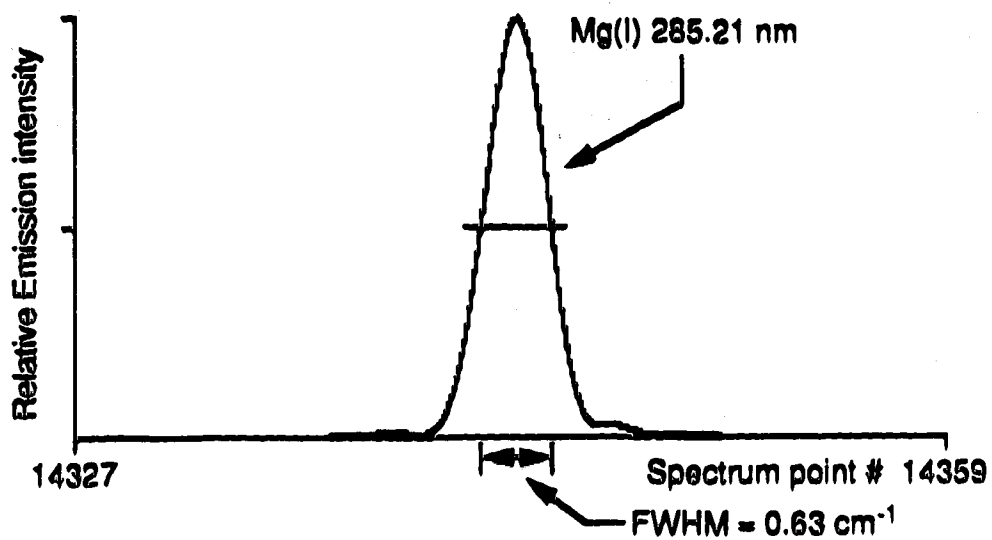
lens as the entrance collimation optics. It appears that the envelope of the interferogram acquired with the lens system decays slightly faster than does that of the mirror system, suggesting that the resolution should be poorer for the lens system.

The Mg 285.213 nm lines from the spectra derived from these two interferograms are shown in Fig. 2-20. The spectrum of Fig. 2-18 is repeated in part a), for convenience. Shown in part b) is the spectrum from the interferogram acquired with the lens system. As indicated, the FWHM of the lens system peak is greater than that of the mirror system. As expected, the lens system is not as effective at collimating the source radiation, hence the resolution is lower in this case.

It should be noted that when the O.A.P. mirror assembly was used, the radiation region of the HCL was focussed onto a 1 mm quartz rod. This was used as a light pipe, a necessity due to the constricted geometry of the O.A.P. assembly and the length of the glass envelope of the HCL. This is a better approximation of a point source than is the entire radiation region that is directly collimated via the quartz lens. Hence, better collimation with the mirror system is the result of not only the asphericity of the mirror system, but also the smaller effective source size. This suggests that coupling the interferometer to the source via a high quality quartz fibre optic should result in the highest performance with regard to resolution and flexibility in the positioning of the source with respect to the interferometer.

Further comparisons of spectra obtained with the lens and mirror entrance collimation systems indicated that, indeed, there was significant chromaticity in the FWHM values of the spectral peaks of the spectra

a) Mirror Collimation



b) Lens Collimation

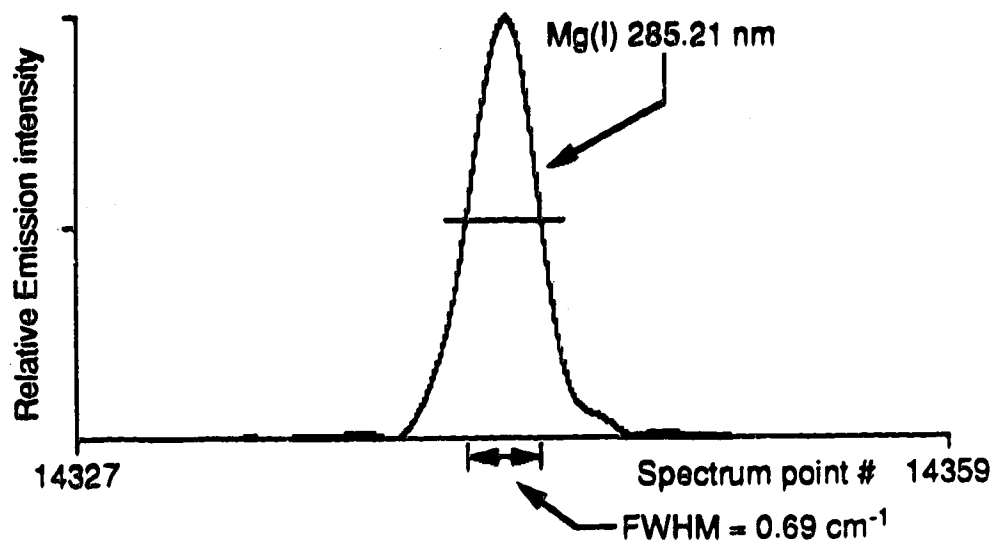


Figure 2-20. Mg 285.213 nm lines acquired with mirror and lens collimation systems.

obtained with the lens. That is, the resolution was a function of wavelength, with the shorter wavelength peaks being wider than the longer wavelength ones.

Finally, to illustrate the improvements in performance that have been achieved through the changes and procedures described in this chapter, consider the interferograms shown in Fig. 2-21. Shown in part a) is an interferogram acquired with the previous version of the interferometer, wherein the moving mirror assembly was still attached to the mounting cube. This is the interferogram of radiation from an inductively coupled plasma (ICP), into which a 100 ppm Mg solution was nebulized. This interferogram was acquired over a mirror travel consisting of 4096 periods of the reference laser interferogram. As can be seen, the envelope of the interferogram decreases rapidly as the mirror moves away from the center of its travel. Although the spectral lines in the radiation from an ICP can be expected to be significantly broader than those from a HCL, this is clearly a case of serious instrumental apodization.

The interferogram of part b) of this figure was obtained with most of the present system, except that both the entrance collimating and exit focussing optics were simple single quartz lens systems, and the HeNe laser alignment point source had not yet been developed. Since the point source was not available, the source had to be aligned, with respect to the interferometer, in a much cruder fashion. As can be seen, in comparison with the interferogram of part b) of Fig. 2-19, the envelope of the interferogram obtained with the intermediate system decays significantly faster than that obtained with the present system. The Mg 285.213 nm line of

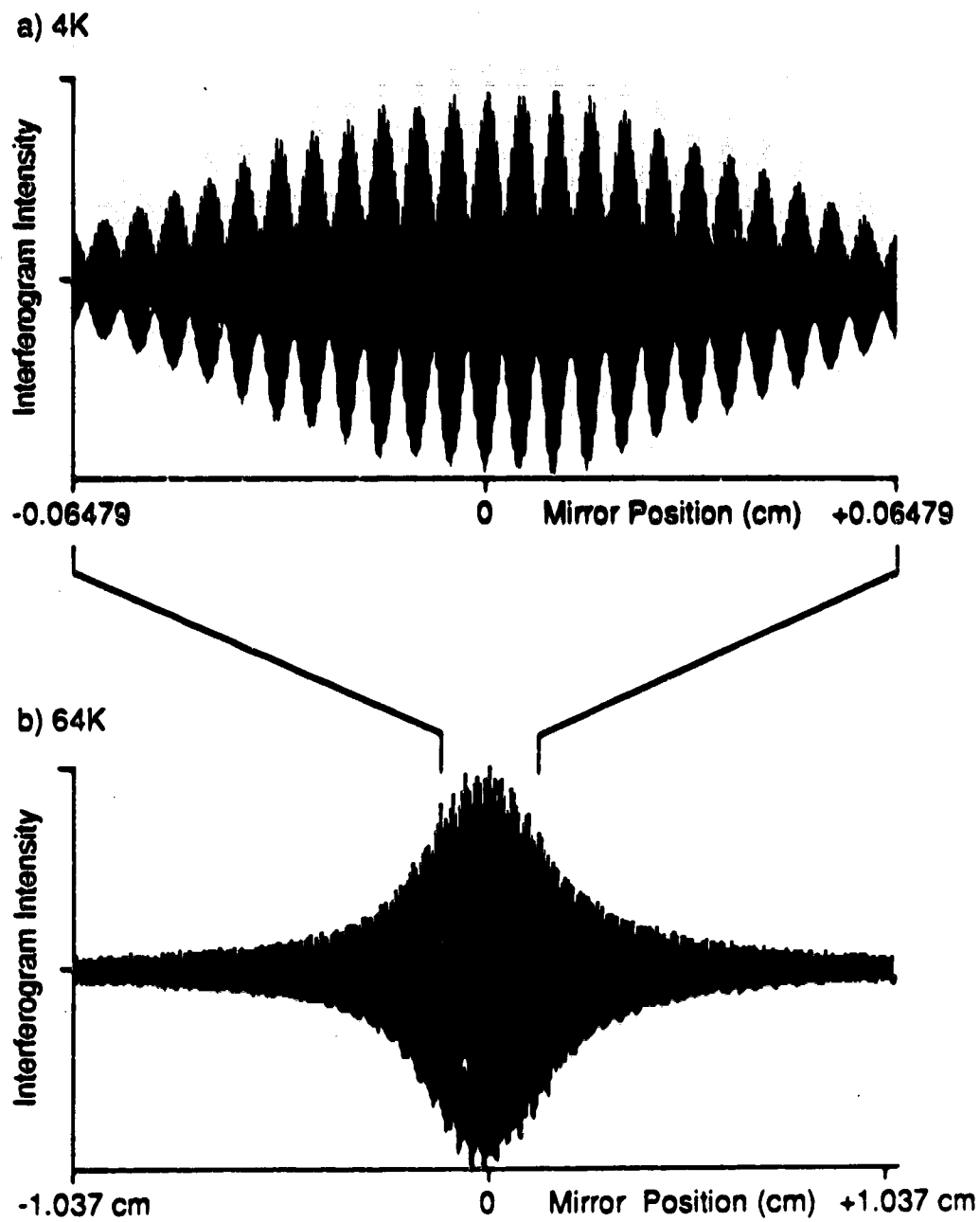


Figure 2-21. Old and intermediate systems interferograms.

the intermediate system interferogram has a FWHM of approximately 1 cm^{-1} , which as expected, is greater than that obtained with the present system.

Thus, with the present optical system, the achievable resolution, based upon the FWHM of the spectral peaks, is approximately $0.6 - 0.7\text{ cm}^{-1}$. With respect to instrumental apodization, the instrument has been greatly improved; however, this is still a problem of significant magnitude. For many of the intents and purposes that this instrument has been designed for, the present amount of instrumental apodization is unimportant, in practice. In many cases, it would be desirable to apodize the interferogram to reduce the effect of truncation of the interferogram. Instrumental apodization achieves this physically.

If it was desired to use this instrument to investigate fundamental spectrophysical properties such as line-shapes, widths, hyper-fine structure, and so on, then the problem of instrumental apodization would have to be either eliminated through improvement of the design, or corrected for through more comprehensive characterization of the problem. In either case, however, for the typical line-widths of the sources of interest such as HCLs or ICPs, the effect of truncation of the interferograms would then become the dominant instrumental effect. The author is unaware of any manner in which this problem can be alleviated, other than by lengthening the travel of the moving mirror. It might be argued that with regard to significant effort to further improve the system, thereby reducing instrumental apodization, these efforts would be better expended on a new design with a longer mirror travel.

Chapter 3

Spectrometer Electronics Systems

As is the case with the optical systems comprising the interferometer, the electronics required for the operation of this UV-VIS Fourier transform spectrometer are similar in concept to, yet somewhat more sophisticated than, those required for an equivalent IR spectrometer.

Fig. 3-1 is a block diagram of the electronics systems required for the operation of this spectrometer. The moving mirror of the interferometer is scanned to produce an interferogram of the source radiation. This is typically detected with a photomultiplier tube (PMT), then digitized for input into a micro-computer for transformation, processing, display, and so on.

These electronics systems have been designed with the following goals in mind. The velocity of the moving mirror must be precisely controlled such that it remains as constant as possible during the data acquisition portion of a mirror scan.

The maximum travel of the moving mirror is designed to be equal to 65,536 periods of the reference laser interferogram. The source interferogram is to be digitized in a symmetric fashion, that is, during the longest mirror scan the mirror should travel, to either side of the mid-point of the source interferogram, $\pm 32,768$ periods of the reference laser interferogram. The system should be configured such that data from successive scans, or at least every second scan, can be signal averaged. To achieve these ends, the present

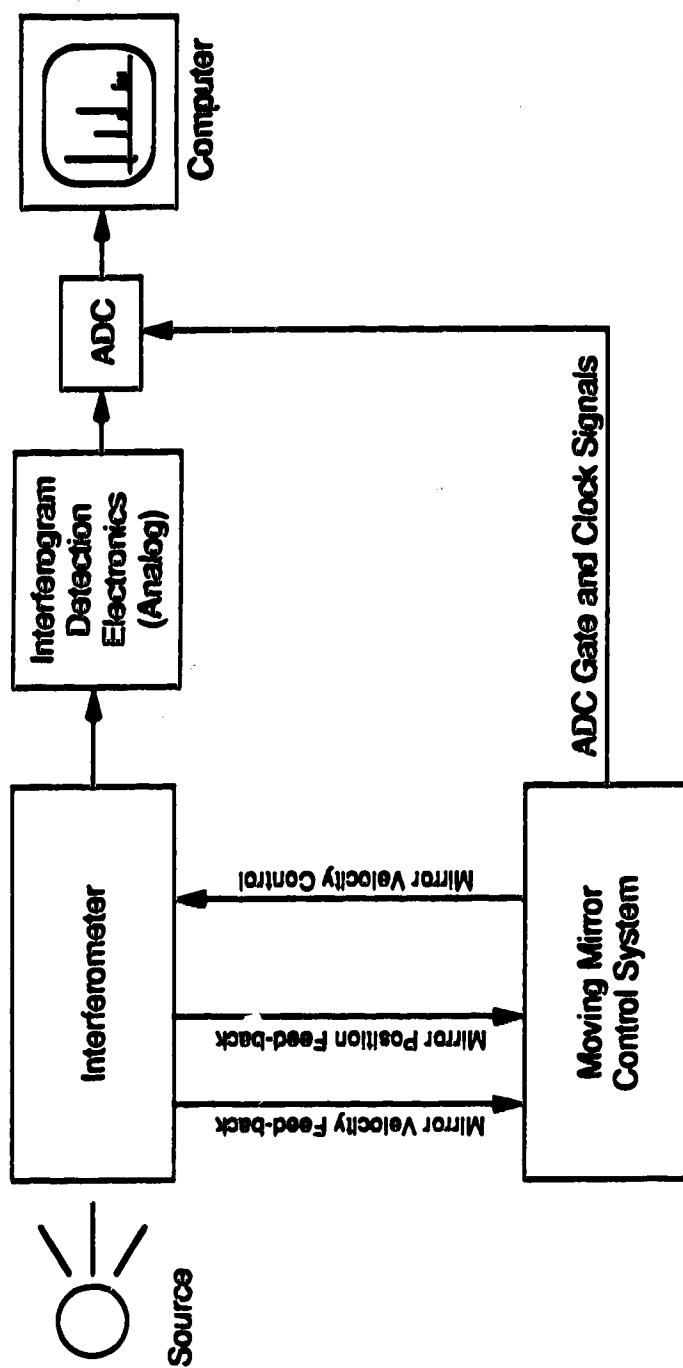


Figure 3-1. Spectrometer electronics systems.

system has been designed such that the position of the mirror, relative to a reference point, is known at all times.

Finally, as will be discussed in detail, there are certain situations in which the source interferogram is not sampled correctly during the digitization process; that is, aliasing occurs. Depending upon the situation, this may not be a problem. However, for some experiments this is unacceptable. Electronics have been designed such that the problem of aliasing can be alleviated, when necessary.

The heart of the overall system is the moving mirror control system. It performs several roles. It controls scanning of the moving mirror, maintaining a highly constant mirror velocity. This is achieved through continuous polling of mirror velocity feed-back signals that are generated by interferometer sub-systems.

This system controls the length of travel of the moving mirror. Again, sub-systems of the interferometer generate signals that are used by the control system, in this case, to determine the precise position of the mirror with respect to a well-defined reference point. With this information, the control system, at the appropriate time, signals the moving mirror actuating mechanism to reverse the direction of mirror movement.

The information as to the position of the moving mirror is used by the by the control system to digitize the analog interferogram at specific desired positions of optical retardation.

For the most part, the vital statistics of both the analog and digital interferogram detection electronics are determined by the velocity of the

moving mirror. The present design employs a mirror velocity of approximately 0.32 cm/s. This results in modulation of the HeNe reference laser ($\lambda = 632.8\text{nm}$) at a frequency of 10 kHz. A 180 nm wavelength component in the source radiation (neglecting air absorption) would produce an intensity modulation with a frequency of approximately 35 kHz. Hence, the analog detection electronics must have an upper frequency band-width limit that is significantly greater than 35 kHz. To correctly digitize a signal with frequency components up to 35 kHz, according to the Nyquist sampling criterion, the sampling frequency must be at least 70 kHz.

The criteria involved in the choice of the system micro-computer, and the implementation of that machine, have been discussed elsewhere [43].

In this chapter, the design and/or characterization of the systems required for control of the moving mirror, and digitization of the analog source interferogram, are presented.

3-1. Moving mirror constant velocity control system.

Illustrated in Fig. 3-2 are the systems required to control the moving mirror of the interferometer. Feed-back signals are generated by sub-systems of the interferometer. These are used by the control system to produce the signal with which the mirror velocity is controlled. This control signal, being low-level in nature, requires amplification in a power stage to become an effective actuating signal.

The sub-systems of the interferometer provide two different signals that are indicative of the velocity of the mirror. One of these is based upon the electro-motive force that is produced as a permanent magnet, attached to

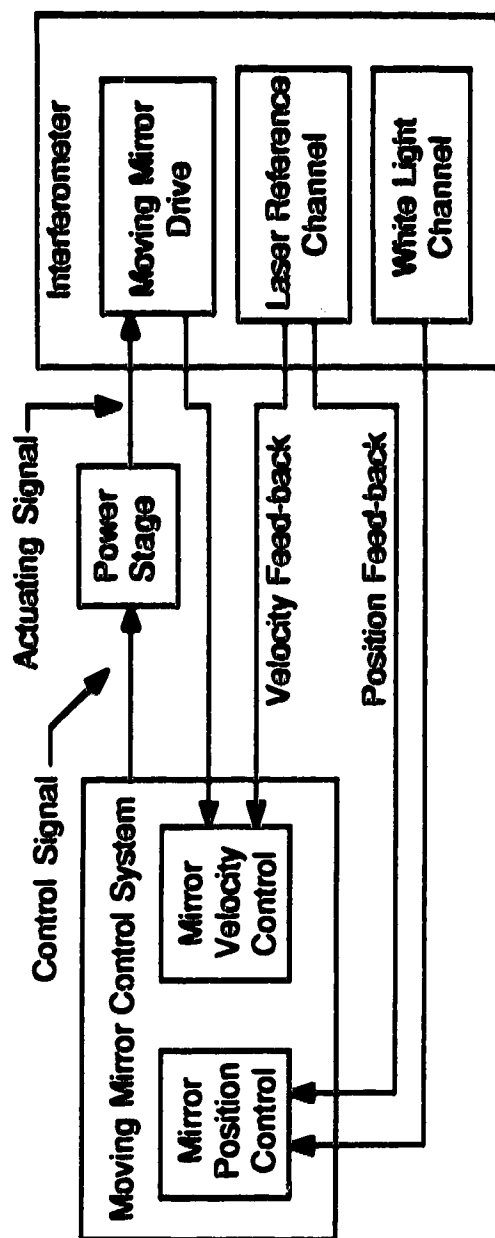


Figure 3-2. Moving mirror scan control systems.

the moving mirror assembly, is moved axially within a set of wire coils. The other feed-back signal is based upon observation of the temporal period of the reference laser interferogram. These two signals are, in a sense, complementary. It turns out that the former signal is well-suited for control of the mirror velocity as the direction of travel is reversed, while the latter is better suited for constant velocity control during the data acquisition portion of each scan. The control system has been designed such that either feed-back can be switched into action at appropriate times during a mirror scan.

The reference laser and white light channels of the interferometer provide the information that is necessary to keep track of the position of the mirror within its travel. The white light interferogram provides a well-defined reference point within the mirror travel. Since the period of the reference laser interferogram represents a well-defined interval of mirror movement, the position of the mirror, with respect to the white light reference point, is continually up-dated by counting periods of the reference laser interferogram. With this continuous knowledge of the position of the mirror, the control system precisely controls the length and positioning of each scan of the mirror.

3-1.1. Electromechanical control of the moving mirror velocity.

The design of the present mirror velocity control system was developed from consideration of the simple mechanical system illustrated in Fig. 3-3, a frictionless system in which a body of mass M is acted upon by an applied force F .

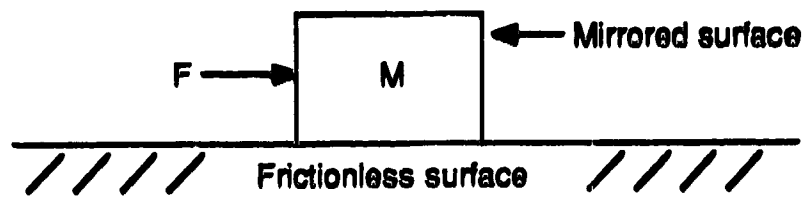


Figure 3-3. Simple model of the moving mirror.

Consider the application of a 1 nt force at $t = 0$ s., with the mass initially at rest. The mass accelerates according to Newton's first law of motion, and continues to accelerate as long as the force is applied. When the force is removed, since there are no frictional forces, the mass coasts with a constant velocity. It is important to note that since $F = M \, dV/dt$, an instantaneous change in the velocity would require an infinite force. Hence, the velocity of the mass cannot change instantaneously.

Mathematically, the velocity of the mass in this simple system is given by Eq. 3-1. A brief note is required first on the symbol convention that is in use in this section of the thesis. Functions of time are denoted in plain text type. Functions of the Laplace variable, s , are written in bold-face type.

$$V_M(t) = \frac{1}{M} \int_{t_0}^t F(t') dt' + V_M(t_0) \quad \text{Eq. 3-1.}$$

A 1 nt force applied at $t = 0$ s, then removed at $t = t_1$ s, is given by

$$F(t) = 1 \text{ nt } [u(t) - u(t-t_1)] \quad \text{Eq. 3-2}$$

where $u(t)$ is the usual Heaviside unit step function.

Eq. 3-2 is substituted into Eq. 3-1 and the integration is performed (a simple procedure in this case) to determine the velocity of the mass as a function of time. Initially, the mass is at rest. Since the velocity cannot change instantaneously, $V_M(0^+) = V_M(0^-) = 0$ m/s. Therefore, with this initial condition, the velocity of the mass is given by,

$$V_M(t) = \frac{1}{M} t \quad 0 \leq t \leq t_1 \quad \text{Eq. 3-3 a.}$$

$$V_M(t) = \frac{1}{M} t_1 \quad t \geq t_1$$

Eq. 3-3 b.

Eq. 3-3a and 3-3b describe the velocity of the mass before and after the time t_1 , when the force is removed. Before t_1 , the constant applied 1 nt force causes the velocity to change linearly. When the force is removed, the velocity remains constant.

The use of some form of gas bearing allows for the construction of a system in which there is essentially zero friction. Thus, one might envision a moving mirror drive in which a mass/mirror is accelerated to some desired velocity, at which time the accelerating force is removed. The mirror would then coast at the desired velocity. The force required to accelerate the mass to the appropriate velocity, in a given amount of time, would be calculated on the basis of the measured mass. This magnitude of force would be applied for the necessary time and then shut-off. It would then be assumed that the mass was moving with the desired velocity.

For this system, the mass of interest is $M = 1.22$ kg. The desired velocity is 0.0032 m/s; therefore, from Eq. 3-3b, the time required to reach this velocity is, $t_1 = 3.8$ ms. A 1 nt force is certainly realizable, hence this calculation gives an idea of the time frame in which we're working.

A system such as that described above is an example of a so-called "open-loop" system. At no time in the operation of the system is the velocity measured. With such an open-loop system, any sort of external disturbance can alter the velocity of the mass, away from the desired value. If, however, the velocity is continuously monitored, deviations from the desired value can be recognized and an appropriate force applied to accelerate or decelerate

the mass, accordingly. This is a description of a "closed loop" feed-back control system. Such a system to control the velocity of a mass is illustrated in Fig. 3-4. In this system the input is a reference force. The output is the velocity of the mass/mirror. It is instructive to consider the servo action of this control loop.

The output velocity is fed-back for comparison with the reference input. In the feed-back path there is a velocity-to-force conversion to make the feed-back and reference signals compatible for comparison. Practically, the reference signal could be a dc-voltage level. Since there would be a voltage-to-velocity conversion in the feed-forward path, a velocity-to-voltage conversion would be required in the feed-back path.

Consider the situation in which the mass is initially at rest, and the reference force is a 1 nt step at $t = 0$ s. Since the velocity of the mass cannot change instantaneously, $V_M(0^+) = V_M(0^-) = 0$ m/s. Since the velocity is zero, $F_F(0^+) = F_F(0^-) = 0$ nt. Therefore, $F_E(0^+) = 1$ nt. The mass starts to accelerate in response to the application of the 1 nt error force. As the mass accelerates, the feed-back signal increases until eventually the velocity is such that, $F_F = 1$ nt. At this point, $F_E = 0$ nt, and the mass coasts with a constant velocity. Should there be a disturbance that decelerates the mass, then this would cause F_F to decrease below 1 nt. The error force, F_E , then increases above the 0 nt level, thereby accelerating the mass until F_F is once again 1 nt. Similarly, if the mass is accelerated as a result of an external disturbance, F_E becomes less than 0 nt, causing the mass to be decelerated until the error force is once again zero.

It is important to note that the servo action of this control loop occurs about a zero error force level. When the mass is moving with the correct

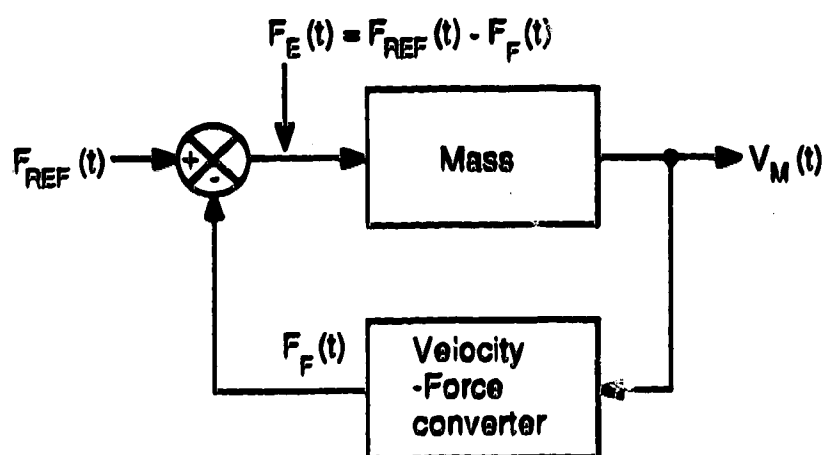


Figure 3-4. A "closed loop" control system architecture.

velocity, no force is being applied. Assuming that external disturbances are the exception and not the rule, this means that the actuating mechanism which produces the error force is active for only a small percentage of the time that the loop is operating.

Previous mirror drive designs within this research group [15, 23] employed an air bearing design incorporating springs, against which an applied force would work. Constant velocity was achieved when the applied force was equal to the spring force. Hence, this design required that the applied force be ON as long as a constant velocity was required. In these designs, as in the present design, the applied force was produced electromagnetically, with a force being applied to the mass only when there was current flowing through a wire coil. Obviously, the power requirements of the previous designs were much greater than those of the present design, as current was flowing in the coil for a much greater percentage of the time.

Also, from a purely mechanical point of view, the use of springs precludes mechanical isolation of the mass from its surroundings. The use of a gas bearing provides a large degree of isolation; however, coupling springs to the moving portion of the bearing destroys that isolation. Vibrations are then transmitted directly to the moving mass, perturbing its velocity. Another more subtle point is that the spring force is approximately linearly dependent upon the extent to which the spring is compressed or extended. This means that the force that must be applied to achieve the desired velocity must change in accordance with the spring force. The dynamic range of the power stage that produces the coil drive current becomes a much more critical consideration, since saturation of any of the elements around a control loop will almost certainly lead to loop oscillation.

The role of feed-back in a loop such as that illustrated in Fig. 3-4 is to correct for external disturbances. It is desirable that the control system respond to external disturbances as quickly as possible. By virtue of the fact that the output of the loop is the velocity of the mass, and that this cannot be changed instantaneously, there is a fundamental limit to the speed with which this control system can effect corrections. The mathematical description of this control system provides insight into the physical parameters that affect the time varying behaviour of the velocity of the mass in this system.

The velocity output of this control loop is related to the reference input by a simple differential equation.

$$\frac{dV_M(t)}{dt} + \frac{K}{M} V_M(t) = \frac{1}{M} F_{REF}(t) \quad \text{Eq. 3-4.}$$

In this equation M is the mass and K is the constant of proportionality relating the feed-back force to the output velocity. Eq. 3-4 is easily solved via the Laplace transform method. Given that the Laplace transform of a function of time can be defined as follows,

$$\mathcal{L}\{g(t)\} = G(s) = \int_0^\infty g(t) e^{-st} dt$$

then,

$$\mathcal{L}\left\{\frac{dV_M(t)}{dt}\right\} = sV_M(s) - V_M(0) \quad \text{Eq. 3-5.}$$

Eq. 3-4 is transformed, using Eq. 3-5, to produce Eq. 3-6, below.

$$sV_M(s) - V_M(0) + \frac{K}{M} V_M(s) = \frac{1}{M} F_{REF}(s) \quad \text{Eq. 3-6.}$$

With the mass initially at rest, rearrangement of Eq. 3-6 results in Eq. 3-7, which relates the output velocity to the input reference force.

$$V_M(s) = \frac{1}{M} \left[\frac{1}{\frac{K}{M} + s} \right] F_{REF}(s) \quad \text{Eq. 3-7.}$$

One can (in principle) calculate the time varying behaviour of the velocity of the mass by first transforming the reference force from the time domain to the s-domain. Then the appropriate algebraic manipulations are performed, after which the resulting equation for $V_M(s)$ is inverse transformed into the time domain to produce $V_M(t)$.

If the mass is initially at rest, and the reference force input is a 1 nt step at $t = 0$ s, then

$$F_{REF}(t) = 1nt \, u(t) .$$

The Laplace transform of this unit step function is simply,

$$F_{REF}(s) = 1nt \, \frac{1}{s} \quad \text{Eq. 3-8.}$$

When Eq. 3-8 is substituted into Eq. 3-7, followed by a partial fraction decomposition, the result is Eq. 3-9, below.

$$V_M(s) = \frac{1}{K} \left[\frac{1}{s} - \frac{1}{s + \frac{K}{M}} \right] \quad \text{Eq. 3-9}$$

Since,

$$\mathcal{L}\{u(t)\} = \frac{1}{s} \quad \text{and} \quad \mathcal{L}\{e^{-at}\} = \frac{1}{s+a}$$

the inverse transform of Eq. 3-9 can be obtained by inspection. Hence,

$$V_M(t) = \frac{1}{K} \text{ m/s} [1 - e^{-t/\tau}] \quad \text{for } t \geq 0 \quad \text{Eq. 3-10}$$

where $\tau = M/K$.

From Eq. 3-10, it can be seen that for a unit step input, the velocity of the mass increases exponentially from zero to $V_M(\infty) = 1/K$ m/s. The time constant, τ , governs the speed with which the mass reaches the final velocity. Mathematically, the velocity of the mass stops changing only when an infinite amount of time has passed. However, after five τ periods of time have elapsed, the velocity will have reached 99.3% of its final value. Practically, the process is then complete, and the velocity is considered to be constant. It should be noted that the application of an instantaneous unit step reference force results in an instantaneous unit step error force. During operation of the loop, there will be error forces generated due to external disturbances that change the velocity of the mass. It is unlikely that any of these error signals will have anywhere near the magnitude of a 1 nt step, nor can they be as abrupt. Hence, this unit step response should be a good worst case characterization of the time behaviour of the velocity of the mass.

Obviously, it is desirable to have the loop respond to disturbances as fast as possible. Therefore, it is necessary to reduce the time constant. Since $\tau = M/K$, this can be achieved by decreasing the mass, M . This is intuitively obvious.

Increasing K will also decrease the time constant. However if K is increased, the final velocity of the mass is reduced. With a larger K , a smaller velocity corresponds to 1 nt of force, which is fed-back and compared with the 1nt reference force. The condition of zero error force is therefore reached more quickly. If K was increased to decrease the time constant, a larger reference force would have to be applied to achieve the desired final velocity.

In the present system, the desired final velocity is $V_M(\infty) = 0.0032$ m/s. With a 1nt step reference force, the required value of K would be 312.5 nt-s/m. Since the mass of interest is, $M = 1.22$ kg, the time constant of the system is $\tau = 3.8$ ms. Hence, starting from rest, the mirror would reach the desired velocity in approximately 19 ms. This is slower than the analogous open loop case; however, there is now feed-back control in the system. This would be a worthwhile compromise.

The present mirror drive design is illustrated in Fig. 3-5. Friction-free movement is provided by the air bearing. As outlined in Ch.2, it was decided to move the sleeve of the air bearing, rather than the piston. The mass M , is comprised of the air bearing sleeve, the permanent magnet assembly, and the mirror. Their total mass is 1.22 kg.

Accelerating or decelerating forces are applied to the mass via the interaction of the magnetic field of the permanent magnet with the current in the coils. The permanent magnet is an approx. 1 in. square by 1/2 in. thick cube of a Nd/Fe/B alloy. (Magnet Sales and Mfg. Co., 11250 Playa Ct., Culver City, CA90230). Pole faces of mild steel extend into the central regions of the

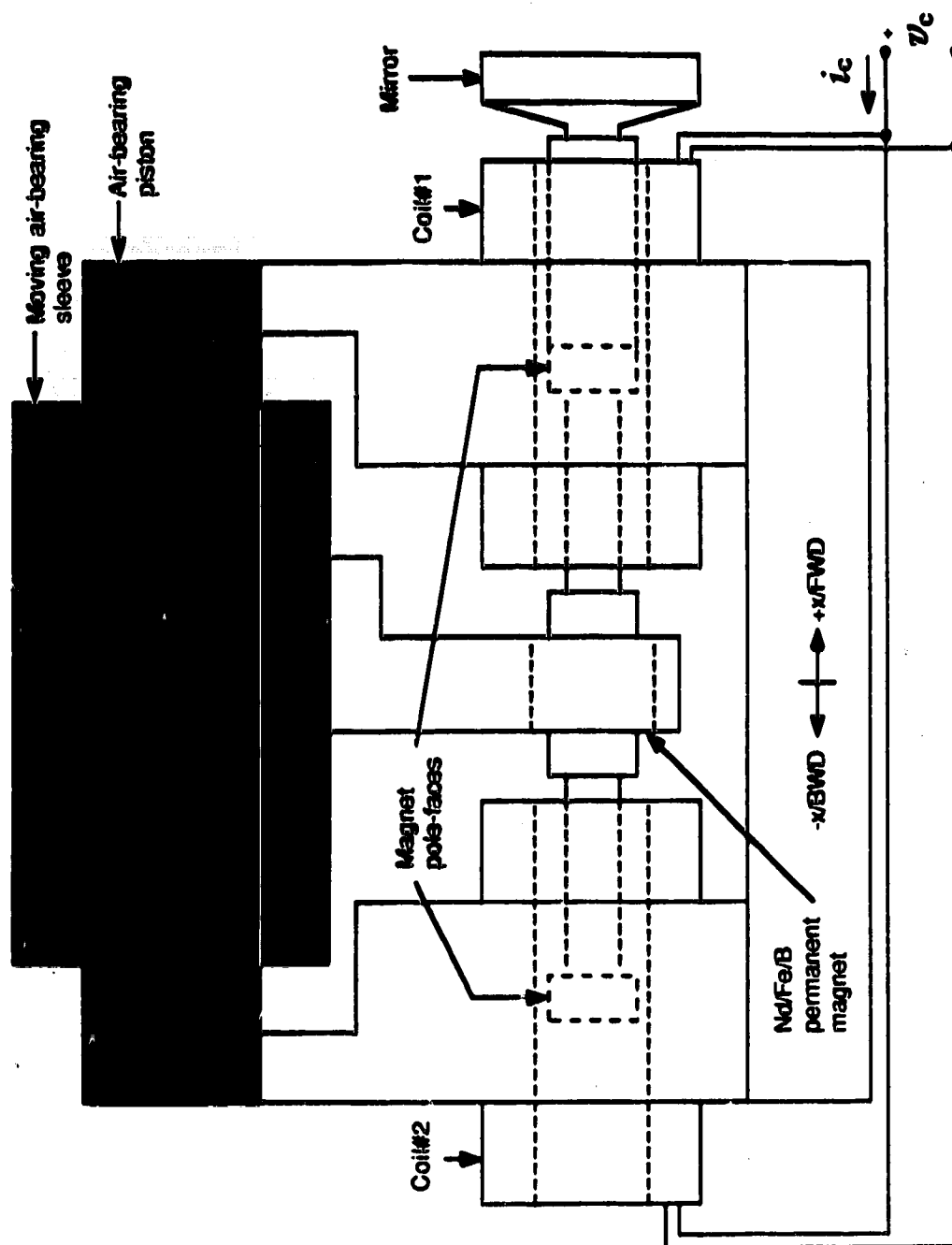


Figure 3-5. Moving mirror electro-mechanical design.

coils. The coils are (essentially identical) simple solenoids wound from AWG 22 magnet wire (Belden #8051). Each coil is 6.9 cm in length, with inner and outer winding diameters of 2.3 and approx. 3.6 cm, respectively. Each winding layer (except the outermost) contains 100 turns. There are 8 full layers, plus one partially filled, such that there are approximately 810 loops of wire in each coil.

The electromagnetic interaction that produces a force on the mass is illustrated in Fig. 3-6. It is well-known that magnetic fields exert forces on moving charges. If these charges are moving on average in a particular direction within a wire, the field exerts a net force on the wire.

For a wire loop carrying a constant current I , immersed in a magnetic field, the force experienced by an infinitesimal section of the loop (which is considered to be straight) is given by Eq. 3-11, below.

$$d\vec{F} = I (d\vec{l} \times \vec{B}) \quad \text{Eq. 3-11}$$

$d\vec{l}$ points in the direction of current flow through the infinitesimal element. \vec{B} is tangent to the line of force that passes through the infinitesimal element. Shown in part a) of Fig. 3-6 is a single loop of wire carrying a dc current, I . The loop is co-axial with a magnetic field such as that which would be present if a permanent magnet were nearby along the $+x$ axis. Consider for a moment the special case where the magnetic field through the loop is spatially uniform and directed along the loop axis. This is the case in part b) of Fig. 3-6.

On the basis of Eq. 3-11, an infinitesimal element of the loop experiences an infinitesimal force that is directed radially inward or outward,

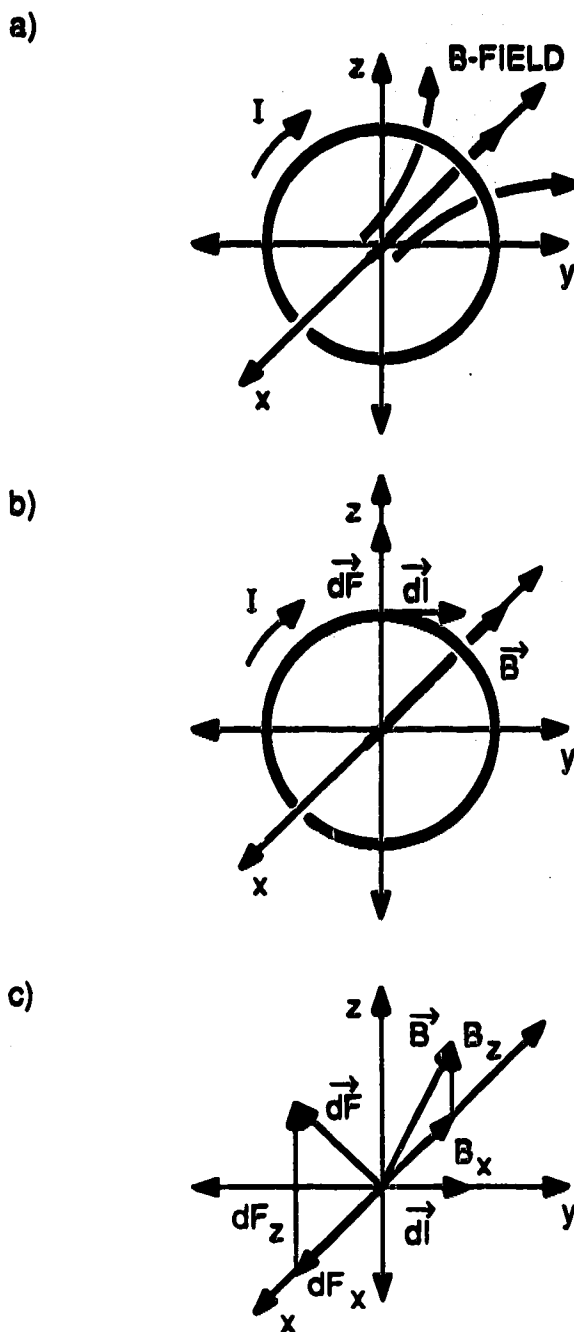


Figure 3-6. Illustration of force exerted on current in a wire loop by an external magnetic field. a) Geometry of loop in field. b) Loop in homogeneous field. c) Loop in non-homogeneous field.

the direction depending upon the direction of the current in the loop, and the polarity of the magnetic field. Integrating these infinitesimal forces around the loop yields zero net force on the loop.

Consider now, however, that the loop is situated within a non-homogeneous field. Each infinitesimal element now experiences a force (with a direction perpendicular to the B -vector at that point) as illustrated in part c) of this figure. These infinitesimal forces do not sum up to zero as the integration is performed, therefore the loop experiences a net force due to the magnetic field of the permanent magnet. In this case, there is a net force in the x -direction.

The magnet exerts a force on the loop and the loop exerts an equal and opposite force on the magnet. If the loop is held fixed and the magnet is free to move, the magnet will accelerate along the x -axis in response to this force. Assuming that the polarity of the field is not changed, the direction of acceleration of the magnet depends upon the direction of current flow within the loop.

The configuration of the loop and applied magnetic field shown in Fig. 3-6 is cylindrically symmetric about the x -axis. As a result the radial components (i.e. the components in the yz plane) of the forces applied to the infinitesimal elements around the loop, sum up to zero. This is shown in parts b) and c) of Fig. 3-7, for the simple case of a point on the loop where the B -vector has no y -component. Clearly, the z - (radial) components of the forces experienced by the infinitesimal elements of the loop cancel, while the x - components add. This is the case for all of the elements around the loop. Therefore, when the integration is performed to add up the forces around the

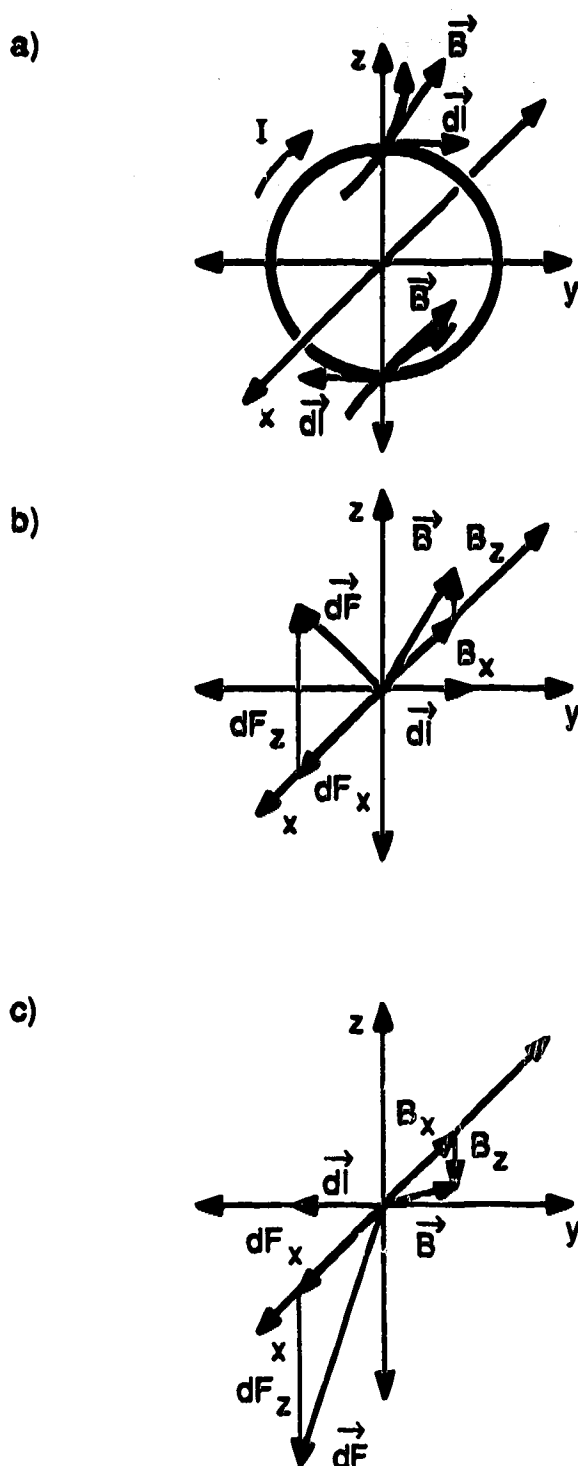


Figure 3-7. Illustration of the cylindrical symmetry of the loop /magnetic field geometry. (See text for details.)

loop, the result is a net force on the loop that is in the direction of the x-axis only.

The actual value of the x-component of the infinitesimal force shown in Fig. 3-6 is $dF_x = IB_z dl$. The component vector $dF_x \hat{i}$ is perpendicular to the component vector $B_z \hat{k}$ at this point. From the cross product relationship of Eq. 3-11, the infinitesimal force at any point on the loop is directed perpendicular to the B-vector at that point. The same applies for the components of the force and magnetic field vectors. At any point around the loop, the sum of the y and z components of the B-vector produces another vector with a direction that is perpendicular to the x-axis (i.e. a radial component vector situated in the yz plane). Naming this vector $B_\perp (= B_y \hat{j} + B_z \hat{k})$, it is then easy to show that for any point around the loop,

$$dF_x = I B_\perp dl$$

Eq. 3-11.

To derive an equation for the force on the loop in the x-direction [72], an expression for B_\perp is needed. This is achieved through the application of Gauss' law to the gaussian surface indicated in Fig. 3-8.

Shown in part a) of this figure is the co-axial configuration of the (North) pole face of a permanent magnet, and a current carrying loop. In part b) the loop is displaced in the negative x direction by an amount, dx . One can see that less magnetic field flux passes through the loop in the displaced position. Some of the flux that originally passed through the area of the loop now passes through the ribbon that connects the two faces of the pill-box surface. Since the displacement of the loop is infinitesimal, these lines of force must be perpendicular to the x-axis. Thus, the lines of force that pass

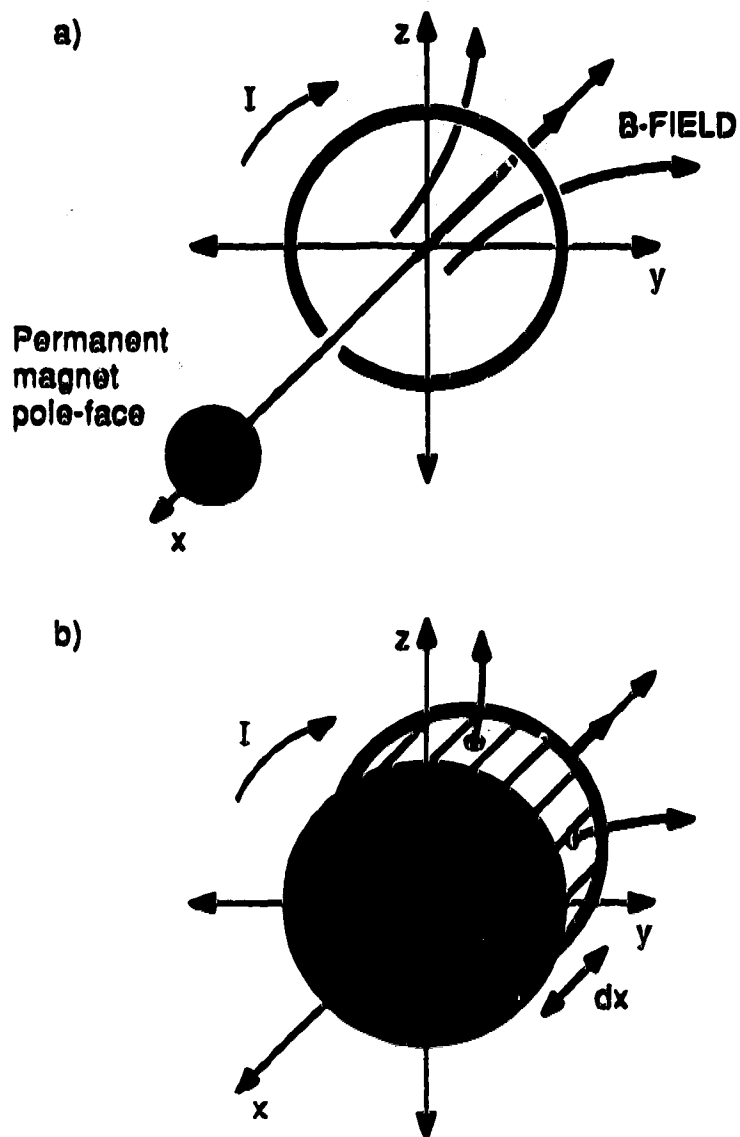


Figure 3-8. Construction for the application of Gauss' law to a current loop in the external magnetic field of a permanent magnet. (See text for details.)

through the ribbon represent the radial component of the magnetic field at any point along the loop. As described previously, it is just this component that is responsible for the force exerted on the loop. Application of Gauss' law to find the flux passing through the ribbon results in the following expression,

$$\oint B_{\perp} dl = \frac{\partial \Phi}{\partial x}.$$

Integrating Eq. 3-11 gives the force on the loop in the x-direction.

$$F_x = I \oint B_{\perp} dl = I \frac{\partial \Phi}{\partial x} \quad \text{Eq. 3-12.}$$

In an analogous manner, expressions for the forces in the y and z directions can be derived, but these are equal to zero by virtue of the cylindrical symmetry of the system. Also, note that the force on the loop of wire does not depend upon the magnetic field that is set up by the flow of current within the loop. The "self-flux" due to this current does not change as the loop is displaced, therefore it does not contribute to the force on the loop.

The force on the magnet is equal and opposite to that exerted on the loop, i.e.

$$F = -I \frac{\partial \Phi}{\partial x}.$$

(The x subscript is dropped from here on in since this is the only net force on the loop.) If there are N loops in a coil, then the force on the magnet is,

$$F = -N I \frac{\partial \Phi}{\partial x} = [N (-\frac{\partial \Phi}{\partial x})] I = K_F I$$

therefore,

$$K_F = N \left(- \frac{\partial \Phi}{\partial x} \right)$$

Eq. 3-13.

Eq. 3-13 is valid only if the N loops of the coil are wound so tightly that they occupy the same region in space. Then the flux through each turn is the same. This is not the case for the real solenoids in use; however, these equations will not be used for quantitative calculations. They are useful to provide a qualitative understanding of the mechanism of operation of the drive, and to indicate possible modifications to improve performance.

K_F is called the force constant. It relates the force applied to the magnet to the current flowing in the coil. Consider the situation illustrated in Fig. 3-9.

The magnet is held fixed and the loop can translate along the x -axis. The lines of magnetic force diverge from the x -axis in a non-linear manner. As the loop is translated along the x -axis, away from the pole-face, the flux that passes through the loop decreases non-linearly. Therefore, $\partial \Phi / \partial x$ is a non-linear function of x . Hence, $K_F = K_F(x)$. This means that for a constant loop current, the force that is applied to the magnet is dependent (in a highly non-linear manner) upon the the relative positions of the pole-face and loop.

It is desirable that K_F be constant, regardless of the relative positions of the pole-face and loop. K_F is a gain factor in the feed-forward path. It is involved in the loop gain of the control system. The output signal of this type of control system is fed-back to the input through a feed-back gain stage. This produces the error signal, which is fed through the feed-forward gain stage(s) to produce the output. Gain stages in the feed-forward and feed-back

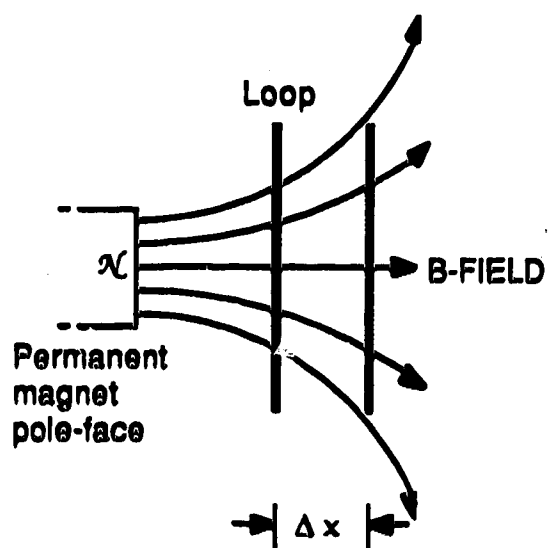


Figure 3-9. Illustration of non-linearity of K_F for single loop system.

portions of the loop must satisfy specific amplitude and phase constraints, in order that the loop be stable. These constraints are determined through consideration of the loop as a whole. Should the characteristics of one (or more) of the element(s) in the loop change significantly, the possibility of loop oscillation arises. With a highly variable K_F , it is possible that the loop would be stable over some limited range of the magnet travel, becoming oscillatory outside of this range. Oscillation of this system involves high speed traversing of the mass, back and forth between the limits of its travel. Obviously, these oscillations can be destructive and are to be avoided.

With a single loop (coil)+permanent magnet electro-mechanical assembly, the value of K_F would be highly dependent upon the position of the magnet within its overall travel. As described earlier in this section, the present design employs a pair of solenoid coils. The main reason for this is to achieve the desired invariance of K_F . This is illustrated in Fig. 3-10.

In part a) of this figure, the magnet is situated, at rest, in the middle of its travel. The directions of current flow in the loops are such that loop #1 pulls the magnet, while loop #2 pushes it. (The currents in the loops are equal in magnitude.) The force on the magnet is the sum of the forces due to the two loops. This force has some particular magnitude, depending upon the current in the loops.

In part b) of this figure the magnet is situated, at rest, closer to loop #1 than it is to loop #2. Depending upon the position of the North pole face relative to that of the loop, $\partial\Phi_1/\partial x$ has either increased or decreased. (Depending upon the configuration of the pole-face and loop, $\partial\Phi_1/\partial x$ can have a maximum as a function of distance of the loop from the pole face.) Assume

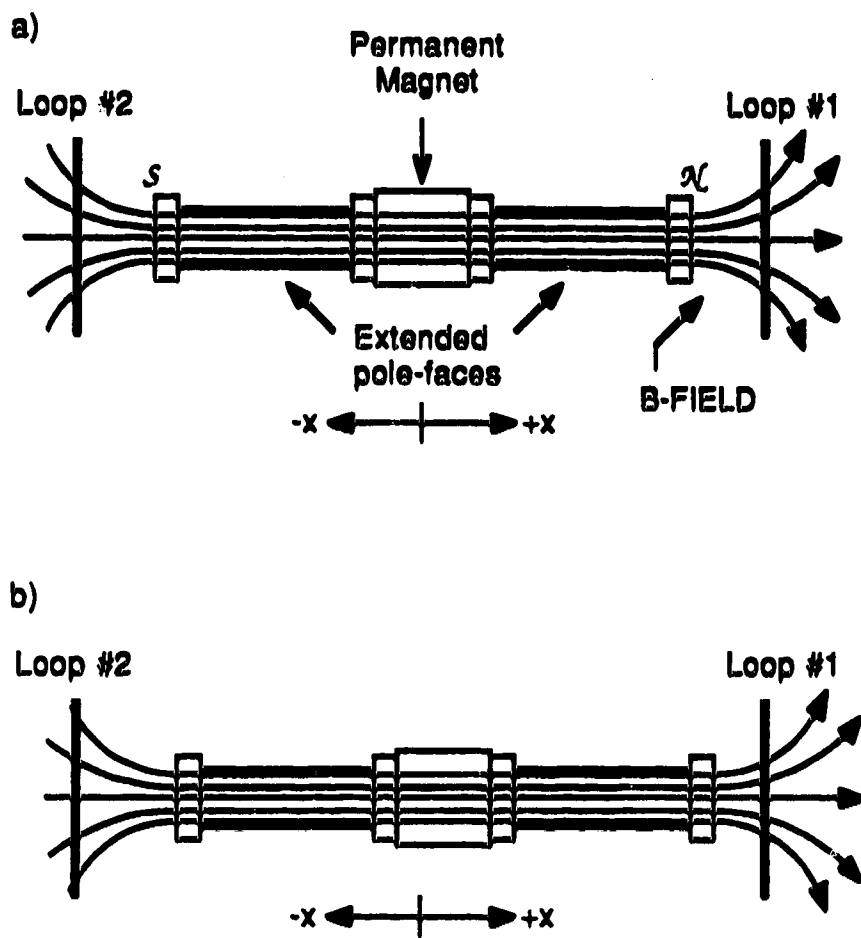


Figure 3-10. Approximate constancy of K_F via dual loop system.
(See text for details.)

that $\partial\Phi_1/\partial x$ has decreased. Then, the force on the magnet due to loop #1 has decreased, by a certain amount. However, due to the symmetry of the arrangement of the pole-faces, in moving the North pole-face closer to loop #1, the South pole-face has been moved away from loop #2, by an equal amount. Assuming that $\partial\Phi_2/\partial x$ has the same functional form as $\partial\Phi_1/\partial x$, in moving the pole face away from the loop, $\partial\Phi_2/\partial x$ will have increased to some extent. (Due to the non-linearity of $\partial\Phi/\partial x$, the increase in $\partial\Phi_2/\partial x$ will not be as large as the decrease in $\partial\Phi_1/\partial x$.) The force due to loop #2 is now larger.

Since the force on the magnet is the sum of the forces due to the two loops, the decrease in the force due to loop #1 has been, at least partially, compensated for by the increase in the force due to loop #2. Clearly, with this push-pull arrangement of two loops, the value of K_F is no longer as strongly dependent upon the position of the magnet within its travel.

As indicated in Fig. 3-5, the pole-faces are extended into the middle region of each coil. This, also, is to aid in attaining a constant K_F .

From Eq. 3-13, the force on the magnet, due to a coil, is proportional to the number of loops in the coil. Assuming that the loops to the rear of a pole-face do not make an appreciable contribution to the force applied by a coil (due to the low permanent magnet flux density in these regions), then the force on the magnet is proportional to the number of loops of a coil that are in front of a pole face. As can be seen from Fig. 3-5, as the magnet is moved in the $+x$ -direction, the pole-face situated in coil #1 moves deeper into that coil. The number of loops of the coil that are in front of the pole face has decreased, and therefore, the force on the magnet due to coil #1 has decreased. Conversely, the pole face inside coil #2 has moved in the $+x$ -direction.

Subsequently, there are more loops of coil #2 in front of this pole-face. The force due to coil #2 has increased, thereby off-setting the decrease in force due to coil #1.

Experiments were performed on different pole face/coil configurations to achieve a design with a K_F that is both as constant, and as large in magnitude, as possible. A large K_F eases the power requirements of the stage that has to produce the coil current.

The force applied to the mass per unit current was measured for a number of designs. This was done for different current levels, and at different points in the travel of the mass. Obviously, the design achieving the best results is the one that is in use at present. It should be noted that some compromises had to be made in the design. It was necessary to include in the design the facility to attach a mirror to one of the pole-faces. This constrained the possible pole face designs. The other pole-face was then made to be the same in the interests of symmetry.

K_F was measured to be 2.4 nt/A. This value was observed to deviate by no more than $\pm 5\%$ over the whole range of mass travel. The deviation from constancy is slightly asymmetric. This is most likely due to the asymmetry of the pole faces that is introduced by attachment of the mirror to one end, and also the fact that the two coils are not exactly identical.

A "next generation" mirror drive has been partially fabricated. This design is analogous to the one presently in use; however, improved performance is expected due to several design modifications. The new design has significantly greater symmetry with respect to the coils/magnet geometry, and the mass of the magnet plus mirror assembly is approximately an order

of magnitude less than that of the present design. Intuitively, the advantages of this last point seem obvious. The detailed implications of a smaller mass, on the system performance, will be discussed in a following section.

Consider again the single wire loop shown in part a) of Fig. 3-9. With the loop fixed and the magnet free to move, as the magnet moves towards the loop, the flux seen by the loop changes with time. Hence, an electromotive force is induced within the loop. Mathematically, the production of the e.m.f. is described by Faraday's law of induction, given below [73].

$$\varepsilon = -\frac{\partial\Phi}{\partial t},$$

$$\varepsilon = -\left[\frac{\partial\Phi}{\partial x} \frac{dx}{dt} + \frac{\partial\Phi}{\partial y} \frac{dy}{dt} + \frac{\partial\Phi}{\partial z} \frac{dz}{dt} \right].$$

As the magnet moves towards the loop along the x-axis, there is no change in the relative positions of the loop and the magnet in either the y or z directions. Therefore, dy/dt and dz/dt in the above expression both equal zero. The magnet moves with a velocity V , therefore the loop and magnet change their relative positions in the x-direction at this rate. Thus,

$$\varepsilon = -\frac{\partial\Phi}{\partial x} \frac{dx}{dt} = -\frac{\partial\Phi}{\partial x} V.$$

For N loops occupying the same region in space,

$$\varepsilon = N \left(-\frac{\partial\Phi}{\partial x} \right) V = K_B V.$$

Therefore,

$$K_B = N \left(-\frac{\partial\Phi}{\partial x} \right)$$

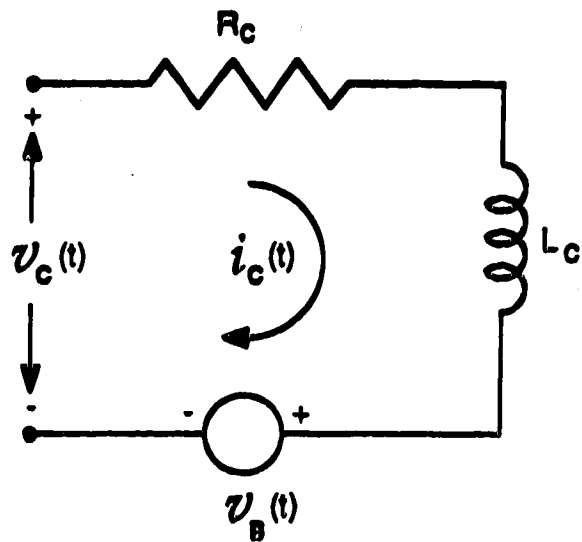
Eq. 3-14.

K_B is the back e.m.f. constant. It relates the e.m.f. generated in the coil to the velocity of the magnet. (By the same argument used for K_F , with a single loop design $K_B = K_B(x)$.) It can be seen that equations 3-13 and 3-14 are identical.

K_B was measured for the present design. The e.m.f. generated with different magnet velocities was measured. An average value of $K_B = 2.38$ v/m/s, was obtained. As expected, this value is close to the measured value of K_F . As with K_F , the values of K_B obtained at various points in the mass travel were observed to have less than $\pm 5\%$ variation.

The step response of the control system shown in Fig. 3-4 is a simple exponential rise. The error force in this system can be applied instantaneously, as a step. However, an electro-mechanical design, such as that described above, cannot apply a force to the mass instantaneously. The force is proportional to the current in the coils. Due to the inductance of the coils, the current cannot change instantaneously, therefore neither can the applied force. The following "ball-park" calculations were done to provide an estimate of the possible performance of this design, and to indicate parameters which can be altered to improve this performance.

The coils are modelled as illustrated in Fig. 3-11. There is a series resistance and inductance associated with the coils. As well, the power stage "sees" an impedance that is proportional to the back e.m.f. that is generated in the coils due to the movement of the magnet. Consider the application of a 1v step at $t = 0$ s, with the mass initially at rest. Since the velocity of the mass cannot change instantaneously, $V_B(0^+) = V_B(0^-) = 0$ v. As well, due to the inductance of the coils, $i_C(0^+) = i_C(0^-) = 0$ A. Since no current is flowing



$R_c (\Omega)$	$L_c (\text{mH})$	$K_F (\text{nt/A})$	$K_B (\text{v-s/m})$
2.06	1.53	2.4	2.38

Figure 3-11. Electrical model of the electro-mechanical mirror drive assembly.

$V_R(0^+) = 0v$, therefore $V_L(0^+) = 1v$. Current starts to flow in the coils, and the magnet starts to accelerate, causing the back e.m.f. to increase. The generated e.m.f. opposes the coil current. If the magnet travel is long enough, the magnet eventually reaches a velocity such that $V_B = 1v$. At this point the back e.m.f. completely opposes the flow of current in the coils, and the mass now coasts with a constant velocity. Hence, the application of a 1 v step input results in the mass moving with a constant velocity.

While the mass is moving with a constant velocity, if an external agent was to cause the mass to decelerate, V_B would decrease below 1v. The coil current would then increase, causing the mass to accelerate until the back e.m.f. was once again 1v. In a similar manner, an increase in the velocity would cause the coil current to decrease, thereby decelerating the mass until $V_B = 1v$. Clearly, negative feed-back is inherent in this type of electro-mechanical mirror drive.

The feed-back in this system arises as a result of the back e.m.f. that is generated when the magnet pole-faces move through the coils. For the case where K_B is constant throughout the travel of the magnet,

$$V_B(t) = K_B V_M(t) .$$

Therefore,

$$\frac{dV_B(t)}{dt} = K_B \frac{dV_M(t)}{dt} .$$

With K_F constant, the force applied to the mass is a simple function of the coil current.

$$F(t) = K_F i_C(t) = M \frac{dV_M(t)}{dt}$$

Equating and rearranging the above two equations yields an expression relating the coil current to the back e.m.f.

$$i_C(t) = \frac{M}{K_F K_B} \frac{dV_B(t)}{dt} = \frac{M}{K_F^2} \frac{dV_B(t)}{dt}.$$

Comparing this equation with the expression relating the current and voltage of a capacitor,

$$i(t) = C \frac{dV(t)}{dt}$$

leads to the definition of the "electro-mechanical capacitance",

$$C_c = \frac{M}{K_F^2} \quad \text{Eq.3-15.}$$

Therefore,

$$i_C(t) = C_C \frac{dV_B(t)}{dt} \quad \text{Eq.3-16.}$$

As can be seen from Eq. 3-16, the generation of the back e.m.f. is analogous to the charging or discharging of a capacitor. This means that this electro-mechanical system can be modelled as a series RLC circuit, as indicated in part a) of Fig. 3-12. Using this well known equivalent circuit, the mathematical description of the time varying behaviour of this system is easy to obtain.

Consider once again the application of the 1v step at $t = 0$ s, with the mass initially at rest. Since it is the time varying behaviour of the velocity of the mass that is of interest, the system will be solved for the back e.m.f. as a

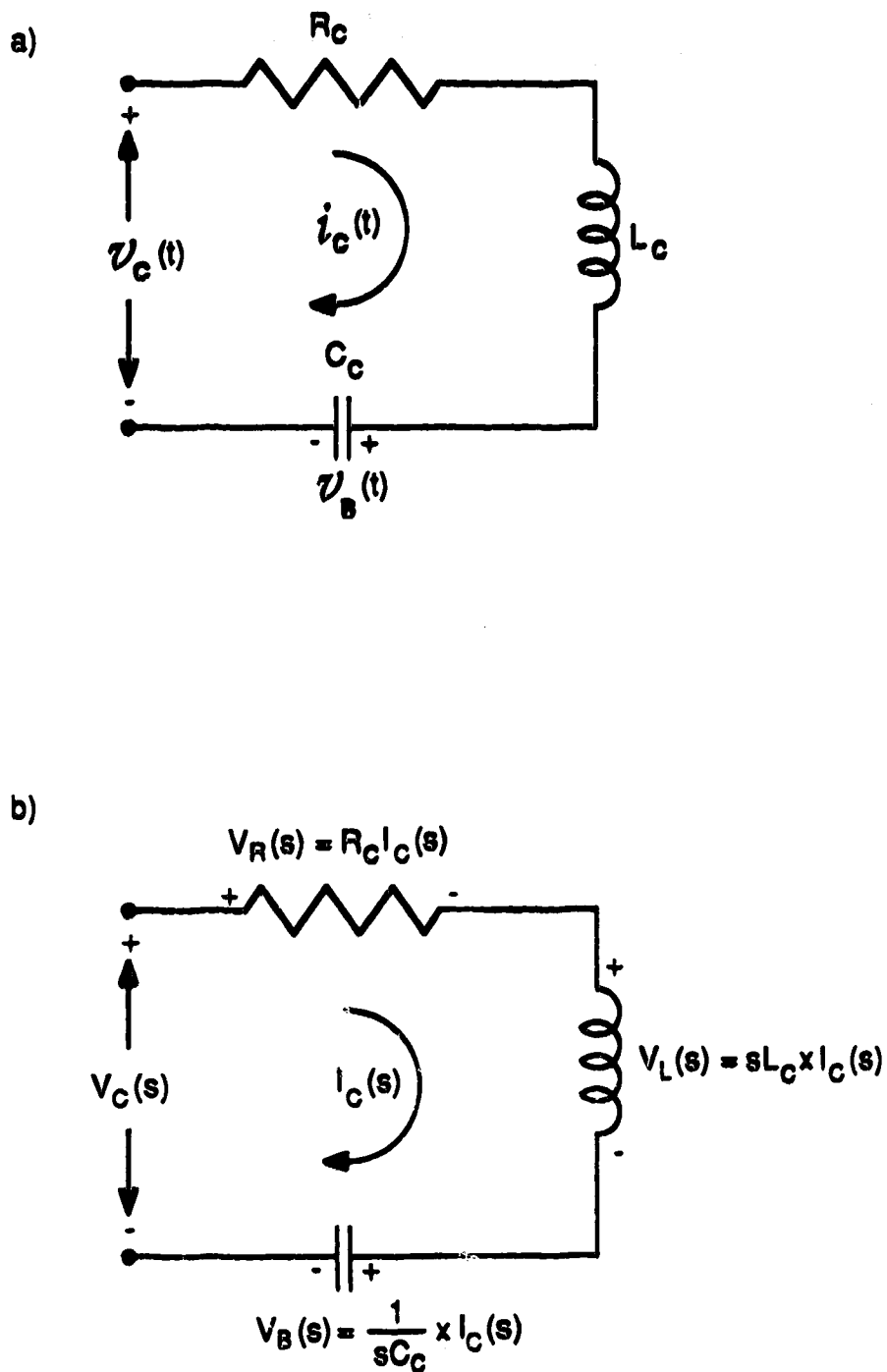


Figure 3-12. Equivalent electrical circuit of the mirror drive electro-mechanical assembly. a) Time domain circuit. b) Laplace domain circuit.

function of time. With the assumption that K_B is constant, the velocity is then simply related to the back e.m.f. This system will be solved in the same manner as the closed loop system illustrated in Fig. 3-4.

The Laplace transform relating the output back e.m.f. to the input applied voltage can be obtained through the application of simple voltage division to the s-domain representation of the circuit, shown in part b) of Fig. 3-12. This representation is achieved by performing separately the Laplace transforms of the current-voltage relationships of the elements in the circuit. Both the inductor and capacitor have derivatives in these relationships, hence the presence of the s variable. Note that this representation is only valid for zero inductor current and capacitor voltage initial conditions.

The Laplace transform relating the output to the input is as follows;

$$V_B(s) = \left[\frac{1/L_C C_C}{s^2 + R_C/L_C s + 1/L_C C_C} \right] V_C(s).$$

Defining the un-damped natural frequency, ω_n , as

$$\omega_n = \sqrt{\frac{1}{L_C C_C}}$$

and the damping ratio, ζ ,

$$\zeta = \frac{R_C}{2} \sqrt{\frac{C_C}{L_C}}$$

and substituting these into the above equation results, after suitable rearrangement, in the following equation.

$$V_B(s) = \left[\frac{\omega_n^2}{s^2 + 2\zeta\omega_n s + \omega_n^2} \right] V_C(s)$$

Eq.3-15a.

Since $V_C(t) = 1v u(t)$, then $V_C(s) = 1/s$, therefore the Laplace transform of the output back e.m.f. is given by

$$V_B(s) = \frac{1}{s} \left[\frac{\omega_n^2}{s^2 + 2\zeta\omega_n s + \omega_n^2} \right] v. \quad \text{Eq. 3-15b.}$$

The form of the inverse transform of Eq. 3-15b is dependent upon the value of ζ , the damping ratio. If $\zeta = 0$ (no damping in the system) then $V_B(t)$ and therefore the velocity of the mass, is oscillatory. The system is said to be un-damped. For $0 < \zeta < 1$, $V_B(t)$ will be a damped sinusoid. Thus, the velocity will rise and over-shoot the final value, then continue to oscillate in a damped sinusoidal fashion. The oscillations die out over time and eventually the final value is reached. This is an under-damped system. For $\zeta \geq 1$, $V_B(t)$ rises in a bi-exponential fashion. This is an over-damped system. If $\zeta = 1$, the system is said to be critically damped. In this case, the velocity rises exponentially, at the greatest rate of the over-damped exponential responses.

Note that ζ is dependent upon the values of the coils' series resistance and inductance, R_C and L_C . These can be altered by various means such as changing the gauge of the wire used and/or changing the number of turns in each coil. As well, ζ is a function of the electromechanical capacitance, C_C . This is a function of the mass, M , and the force constant, K_F , both of which can be varied with relative ease. Hence, in principle, the time behaviour of this type of system can be adjusted and optimized in future designs.

For this system, $C_C = M/K_F^2 = 0.21F$. Using the values indicated in Fig. 3-11, the undamped natural frequency and damping factor are calculated to be $\omega_n = 56 \text{ rad/s}$ and $\zeta = 12$. Since $\zeta \gg 1$, the system is strongly over-damped. For this case, the inverse transform of Eq.3-15b is given by [74],

$$V_B(t) = 1v + \frac{\omega_n}{2\sqrt{\zeta^2-1}} [\tau_1 e^{-t/\tau_1} - \tau_2 e^{-t/\tau_2}] v$$

Eq. 3-16a,

where,

$$\tau_1 = \frac{1}{\omega_n [\zeta + \sqrt{\zeta^2 - 1}]} = 7.5 \times 10^{-4} \text{ s}$$

, and,

$$\tau_2 = \frac{1}{\omega_n [\zeta - \sqrt{\zeta^2 - 1}]} = 0.43 \text{ s}.$$

Examination of Eq. 3-16a indicates that the velocity of the mass increases in a bi-exponential fashion. τ_1 and τ_2 are the time constants governing the two decaying exponential terms. However, because $\tau_1 \ll \tau_2$, other than for times that are small relative to τ_1 , the time behaviour of the velocity of the mass is dominated by the longer time constant, τ_2 . It can be shown [74], that the approximate response of the system is given by the exponential rise,

$$V_B(t) = 1v. (1 - e^{-t/\tau_2}) \quad \text{for } t \geq 0$$

Eq. 3-16b.

With $K_B = 2.38 \text{ v-s/m}$,

$$V_M(t) = 0.42 (1 - e^{-t/\tau_2}) \text{ m/s for } t \geq 0$$

Eq. 3-17.

Thus, to a good approximation, in response to a $1v$ step input, the velocity of the mass rises exponentially to $V_M(\infty) = 0.42 \text{ m/s}$, in $5\tau_2 = 2.2 \text{ s}$. This velocity would produce a reference laser output with a frequency of approximately 1.3 MHz. For a 10 kHz reference laser output, the velocity should be approximately 0.32 cm/s. For this system to achieve this value as the final

velocity, the input should be a 7.7 mv step, rather than a 1v step input. Then the coefficient multiplying Eq.3-17 would be, 0.32 cm/s. Note that, even though the final velocity is much lower than that for the 1v input, it still takes approx. $5\tau_2 = 2.2$ s to achieve this velocity.

Ultimately, this electro-mechanical system was designed to be used within a control system as illustrated in Fig. 3-4. However, one might question why it is necessary to put the assembly within a loop at all? There is already negative feed-back as a result of the generated back e.m.f. In response to a step input, the velocity of the mass rises to the desired value. The back e.m.f. then provides the feed-back to maintain a constant velocity.

One might envision a very simple mirror drive system requiring only this electro-mechanical assembly, and a stable reference voltage source whose polarity can be switched when desired. To start scanning, the reference is stepped up to the appropriate level. The mass then accelerates until it reaches the desired velocity. The mass moves with a constant velocity until the time at which it should be turned around. At this point, the reference is stepped through zero to the appropriate value of opposite polarity. The mass decelerates to zero velocity, and then accelerates to the correct velocity in the opposite direction. Repeated scanning of the mirror would result from repeated reference polarity reversals.

A mirror drive of this type is certainly possible. With the present electro-mechanical assembly, however, there are several problems that would first have to be overcome. Probably the most serious is that this present version of a dual coil architecture is not perfect with respect to the constancy of K_B .

As the mass travels through its range of motion there is a maximum change in K_B of $\pm 5\%$. This change in K_B would cause the velocity of the mirror to change over the length of a scan. As described above, when a 1v step is applied, the back e.m.f. rises from zero to a final value of 1v. At this point the mass moves with a constant velocity. The feed-back in the system operates to maintain a constant back e.m.f. If K_B decreases as the mass moves along, the back e.m.f. that opposes the 1v reference signal decreases as well. Current flows in the coils to increase the velocity until the e.m.f. is once again 1v. If K_B continues to decrease, then the velocity of the mass will increase continuously. (If K_B increases, the velocity of the mass decreases.) Since it is important to maintain a constant velocity throughout a scan, the variation in K_B for this version of the electro-mechanical assembly is unacceptable.

A second problem associated with the use of this version of the electro-mechanical assembly is the fact that it is a highly over-damped system. As indicated by the above calculation, in response to a step input, the time required to reach the final velocity would be approximately 2.2 s. In relative terms, the system is sluggish. It should be expected that with this slow a response, the ability of the system to respond to external disturbances such as vibrations would be poor.

The present version of the electro-mechanical assembly is unsuitable for use in this simple mirror system design. As will be described in later sections of this chapter, it is presently being successfully employed in a somewhat more complex design. Before leaving consideration of this simple design, one final point should be made.

A highly desirable aspect of the nature of the feed-back in this design is that it is bi-polar. This means that negative feed-back is maintained regardless of the direction of motion of the mass. As described above (and as will become clearer in subsequent sections of this chapter), the mirror drive design is greatly simplified as a result of this type of feed-back.

It is also possible to have a system with uni-polar feed-back. In this case there is negative feed-back during movement of the mass in one direction, and positive feedback when moving in the other direction. There is no control over the velocity of the mass during operation in a positive feed-back mode.

Bi-polar and uni-polar feed-back are illustrated in parts a) and b), respectively, of Fig. 3-13. The signals $V_{REF}(t)$, $V_F(t)$, and $V_E(t)$ are voltages that are analogous to $F_{REF}(t)$, $F_F(t)$, and $F_E(t)$, respectively, from Fig. 3-4. The reference voltage steps between $\pm 1v$.

In part a) of this figure, at the time when the reference is stepped through zero, the feed-back voltage has attained a value of 1 v. When the reference is stepped to -1v, the error voltage steps down to -2v. Due to the fact that the velocity of the mass cannot change instantaneously, the feed-back voltage remains momentarily at a value of 1v. The waveforms in part a) are exactly analogous to those that would be observed for the voltage across a capacitor within a simple series RC circuit, in response to an ac-coupled square wave.

The negative error voltage produces a negative force on the mass, causing it to decelerate in the forward direction (accelerate in the backward

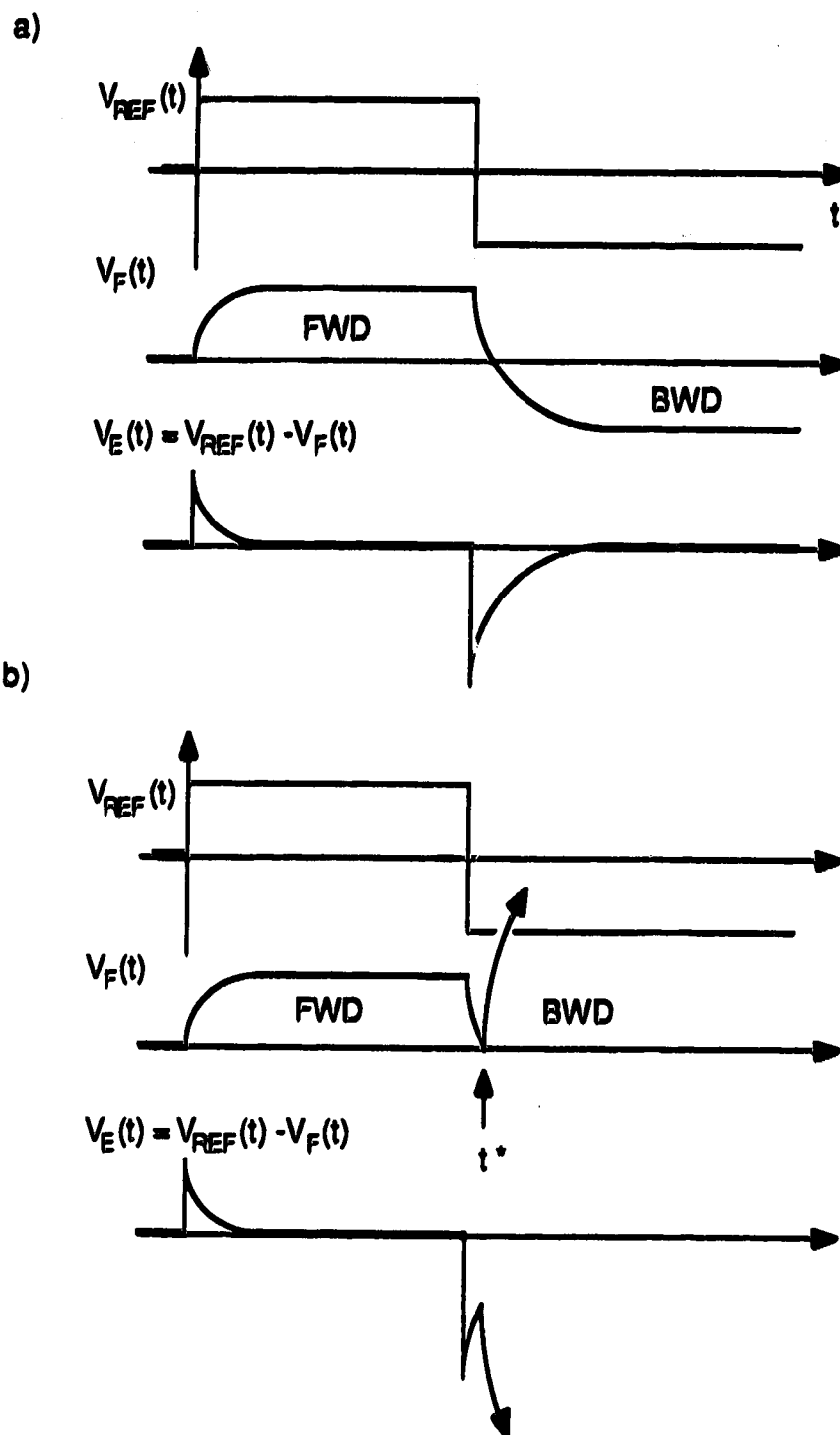


Figure 3-13. Two types of feed-back. a) Bi-polar feed-back.
b) Uni-polar feed-back. (See text for details.)

direction), stop, and then accelerate in the backward direction. As the mass accelerates in the backward direction, the feed-back voltage increases negatively such that eventually the error voltage becomes zero and the mass moves with the correct velocity.

The key aspect of bi-polar feed-back, leading to successful operation for both directions of mass movement, is that the feed-back voltage correctly indicates acceleration or deceleration of the mass and the direction in which this is happening. For example, the back e.m.f. generated in the coils of the electro-mechanical assembly increases positively in response to an acceleration in the forward direction. It increases negatively for an acceleration in the backward direction. When the mass is moving in the forward direction, an increase in velocity causes an increase in the feed-back signal. The error voltage becomes slightly negative to decelerate the mass back to the correct velocity. When moving in the backward direction, an increase in the velocity causes a decrease (increase negatively) in the feed-back signal. The error voltage becomes slightly positive to decelerate (with respect to backward movement) the mass.

In part b) of this figure, the feed-back signal correctly indicates acceleration or deceleration only for forward motion of the mass. An acceleration in either direction produces an increase in the feed-back signal. As indicated in this part of the figure, negative feed-back is maintained during forward motion. However, when the reference voltage is stepped to -1 v, positive feed-back occurs just as the mass starts to move in the backward direction. This point is indicated by t^* along the time axis. At this point, as the mass accelerates in the backward direction, the feed-back voltage starts to increase (with bi-polar feed-back it would be starting to decrease through

zero). Rather than the error voltage continuing to increase towards zero, it starts to decrease, thereby accelerating the mass in the backward direction. As the mass accelerates, the feed-back voltage increases, causing the error voltage to decrease further. The mass is accelerated even more in the backward direction. This process continues and very quickly "snow-balls". Subsequently, control of the velocity of the mass is completely lost.

In order that uni-polar feed-back can be employed it is necessary to be able to sense the direction of motion of the mass. Once this is known, the polarity of the feed-back can be toggled appropriately. This adds, significantly, to the overall complexity of the mirror drive system.

The electro-mechanical assembly illustrated in Fig. 3-5 is presently being employed in the control loop shown schematically in Fig. 3-14. (This loop is analogous to that shown in Fig. 3-4.) The output of the loop is the velocity of the mass (mirror). A velocity-to-voltage feed-back element produces the feed-back voltage, $V_F(t)$. This is compared with a reference voltage, $V_{REF}(t)$, to produce the error voltage, $V_E(t)$. The error voltage is applied to the input of a power stage to produce the control (or coil) voltage, $V_C(t)$. This produces the coil current, $i_C(t)$, with which the velocity of the mass is controlled.

The actual system architecture is shown in greater detail in Fig. 3-15. Two feed-back loops are indicated in this drawing. The present system utilizes two velocity-to-voltage conversion schemes in the feed-back path. Each has its own advantages and disadvantages. As shown, the system is set up such that one can switch between the two types of feed-back as desired. Of

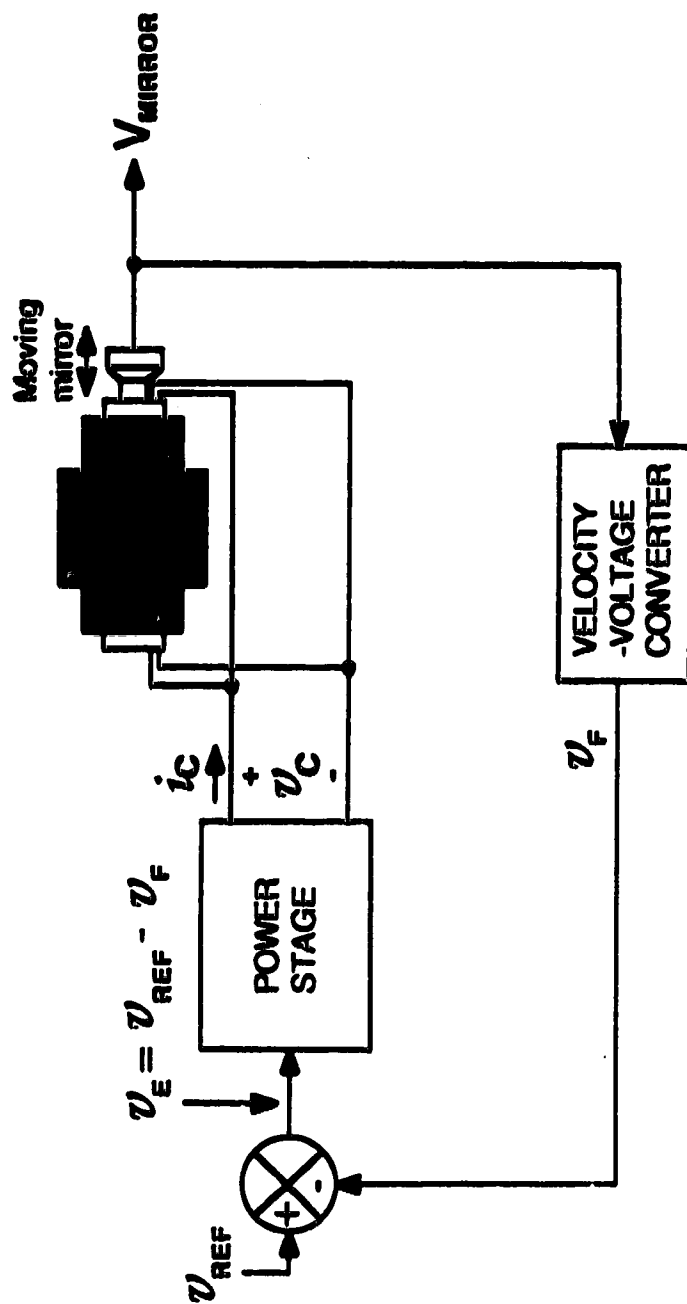


Figure 3-14. Simple schematic of moving mirror velocity control feed-back loop.

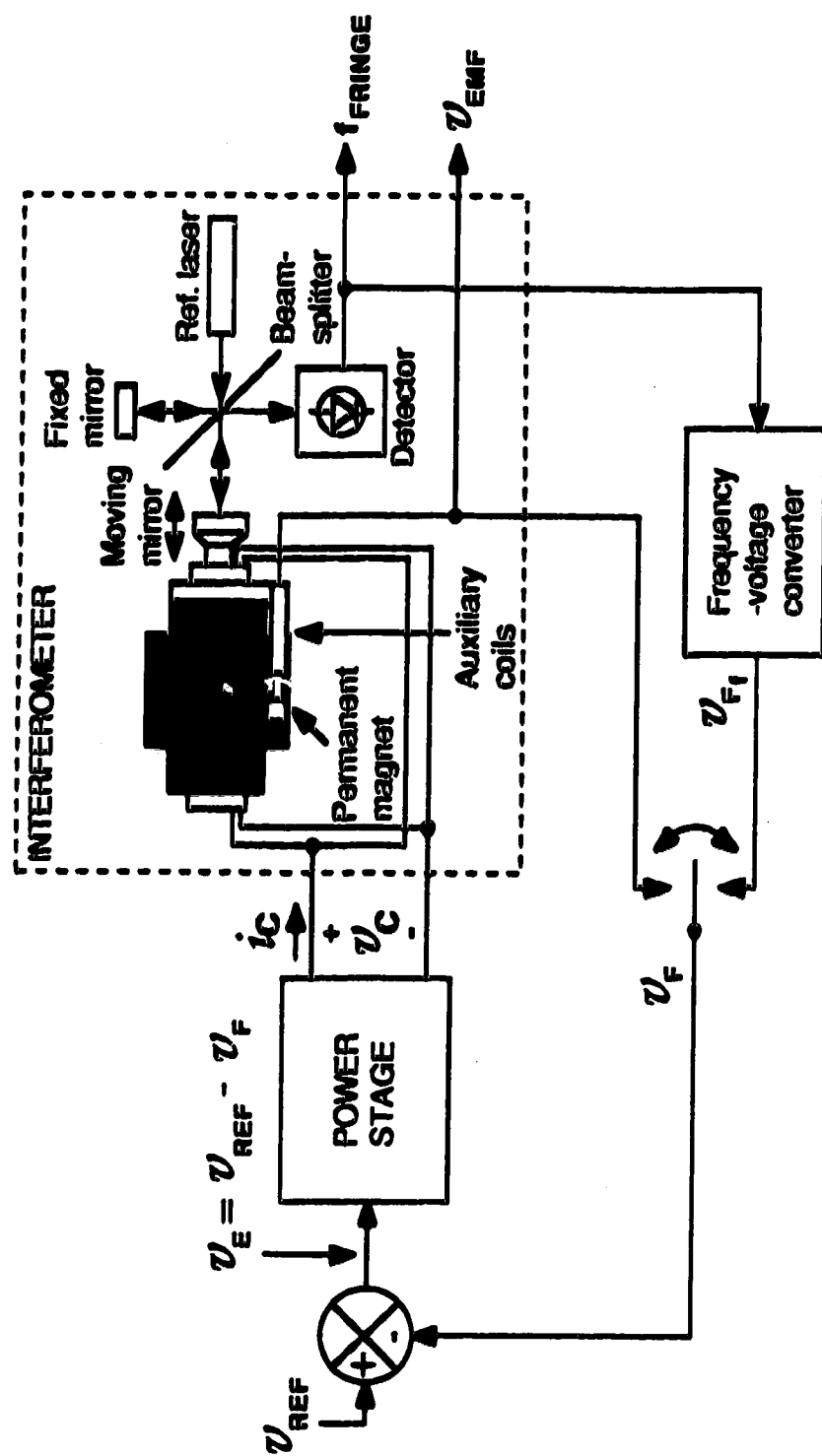


Figure 3-15. Dual feed-back control system. (See text for details.)

the two feed-back elements, one provides bi-polar feed-back, while the other provides uni-polar feed-back.

Bi-polar feed-back is provided by a set of so-called "auxiliary coils." These are illustrated in part a) of Fig. 3-16. The permanent magnet from inside a 2" teflon magnetic stirring bar is attached to the moving sleeve of the air bearing. Consequently, the magnet moves with the same velocity as the mass of interest. The magnet is mounted on the end of an extending rod such that it is approximately symmetrically located within the auxiliary coils, which are mounted to the fixed air-bearing piston. There is no mechanical contact between the magnet and the coils. This would introduce friction and provide a path for coupling vibrations to the mass.

The auxiliary coils are essentially a smaller version of the main drive coils except that they are being used as linear generators rather than as motors. The two coils are approximately identical simple solenoids wound from AWG 28 magnet wire (Alkenex-N. Canadian General Electric.). Each coil is 2 cm in length, with inner and outer winding diameters of approximately 9 and 8 cm, respectively. Each winding layer (except the outermost) contains approximately 60 turns. There are approximately 600 turns in each coil.

The two coils are connected in the same manner as the drive coils. In part a) of this figure, the direction of the current generated by movement of the magnet through the coils in the forward direction is indicated. For the coil adjacent to the north pole of the magnet, according to Lenz's law, movement of the magnet in the +x-direction will induce a current with the

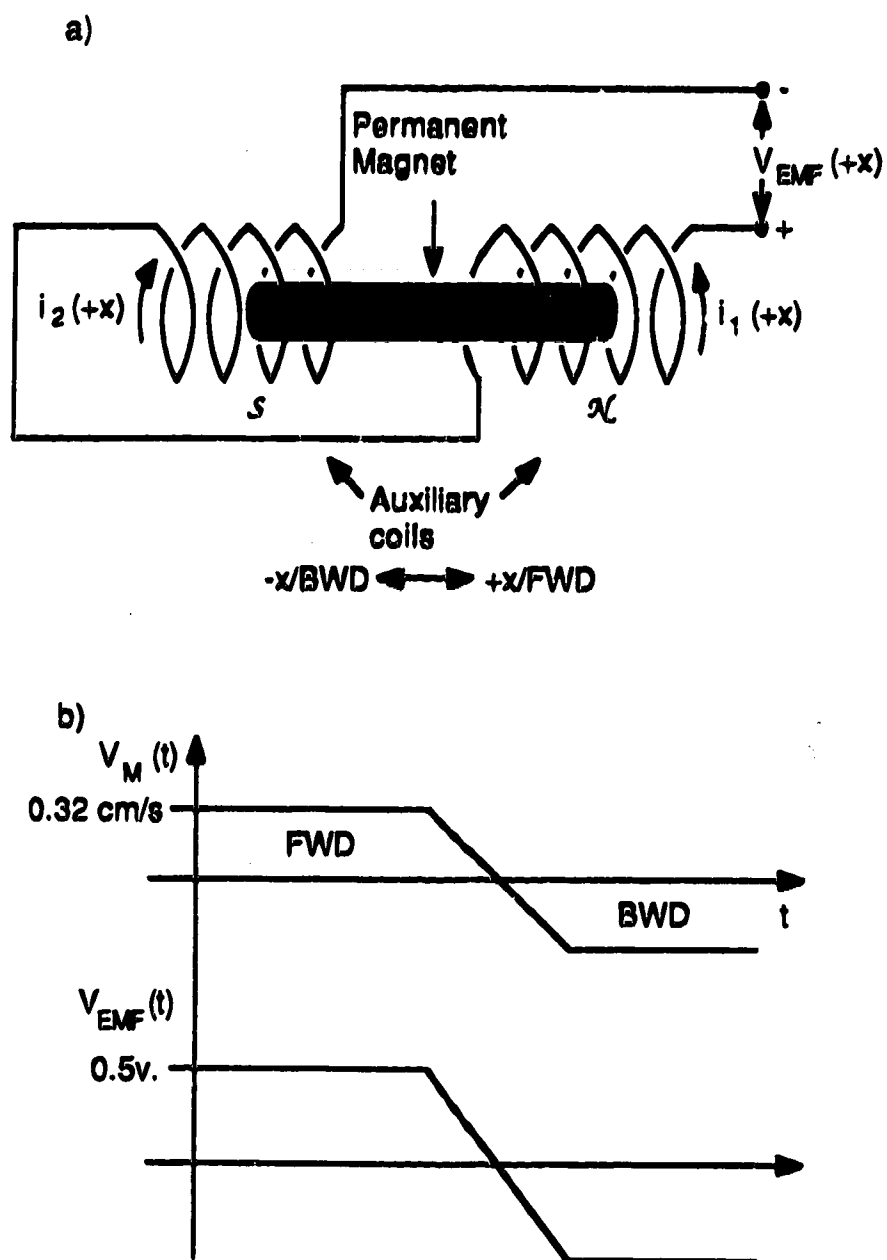


Figure 3-16. a) Auxiliary coils. b) Bi-polar feed-back from coils.

direction shown. The coil adjacent to the south pole of the magnet is connected such that it produces a current in the same direction.

Originally, these coils were designed and built to provide a signal that would indicate the direction of movement of the mass (by the e.m.f. polarity). A double coil system was used to provide twice the e.m.f. per unit mass movement. However, it was recognized that the bi-polar nature of the e.m.f. generated could provide a useful feed-back signal, especially during the turn-around phase of the mass travel. This bi-polar feed-back is shown schematically in part b) of this figure.

As indicated, a velocity of 0.32 cm/s produces an output signal $V_{EMF} = 0.5$ v. As with the drive coils, due to the dual coil architecture, the e.m.f. (i.e. K_B) does not vary as much during travel of the mass at constant velocity as it would with a single coil system. As a result of the original anticipated use for these coils, the attention paid to the symmetry of the system was minimal. With greater care in design and fabrication, it is anticipated that coils could be produced in which the e.m.f. would be essentially constant, for a constant velocity, over the entire travel of the mass. (Recently, the author has learned of a commercial version of the auxiliary coils. These are manufactured by Transducer Systems, Inc. and are available from Servo Systems Inc. as Stock No. PR-235. The travel of this device is 8.6 cm, and the e.m.f. per unit velocity is specified to be 1.77 v/m/s, with $\pm 3\%$ variation of the e.m.f. throughout the travel, for a constant velocity.)

The second feed-back loop shown in Fig. 3-15 has a frequency-to-voltage (F/V) converter in the feed-back path. This is used to convert the HeNe reference laser output frequency into a proportional voltage. Since the

reference laser output frequency is proportional to the mirror velocity, this element performs a velocity-to-voltage conversion. However, because the process of producing the reference laser output occurs in the same manner for either direction of mirror movement, this velocity-to-voltage conversion provides uni-polar feed-back. Regardless of the direction of movement of the mass, the output of the F/V increases when the velocity of the mass increases.

The F/V feed-back, although uni-polar, provides a very high quality feed-back signal with which to control the mass velocity. If the optical components of the interferometer are correctly aligned, and as long as the length of mirror travel is much less than the coherence length of the reference laser, the reference laser output is a slowly decaying damped sinusoid, with a non-zero average value. If the dc-level of such a signal is removed, the frequency of occurrence of zero-crossings is constant as long as the mirror velocity is kept constant, regardless of the position of the mirror in its travel.

One can see that the feed-back provided by the reference laser plus F/V converter system is in a sense complementary to that of the auxiliary coils. F/V feed-back can be used to produce a highly constant velocity that does not change as the mass traverses its limits. Being uni-polar in nature, though, it renders the system susceptible to positive feed-back for one direction of mass travel. With the auxiliary coils it is difficult to produce a system in which the velocity of the mass does not change throughout the travel of the mass. However, by virtue of its bi-polar nature, this feed-back is perfect for maintaining control of the mass during the turn-around phase.

As indicated in Fig. 3-15, a switch is provided with which the feed-back element of the control loop can be changed back and forth between the auxiliary coils and the F/V converter system. Thus, either of the two feed-back systems can be used as desired. The mode of operation of the present version of the mirror drive system is to utilize auxiliary coils feed-back during the start-up and turn-around phases of the mass travel. For the rest of a scan when data is to be acquired, the F/V feed-back loop is in operation.

During auxiliary coils operation, the reference voltage is changed to reverse the motion of the mass. The speed with which the auxiliary coils loop responds to a change in the reference voltage is of great interest. The dynamics of the auxiliary coils loop have been calculated with reference to Fig. 3-17. Shown in this figure are the Laplace transforms of the various signals around the control loop, as well as the equations (transfer functions) relating them to one another.

For the highly over-damped electromechanical assembly, Eq. 3-15a relates the Laplace transform of the coil back e.m.f., $V_B(s)$, to that of the coil voltage, $V_C(s)$. This expression involves two time constants, one of which is much greater than the other, therefore the following approximate transfer function can be used.

$$V_B(s) = \frac{1}{1 + s\tau_2} V_C(s)$$

Where τ_2 is given by,

$$\tau_2 = \frac{1}{\omega_n [\zeta - \sqrt{\zeta^2 - 1}]} = 0.43 \text{ s.}$$

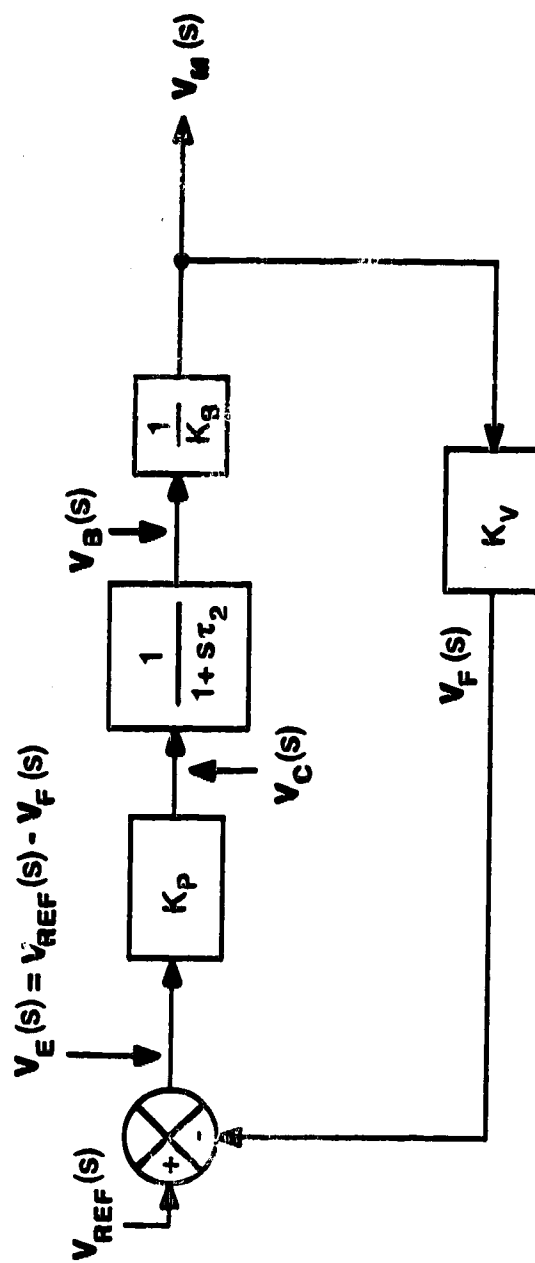


Figure 3-17. Moving mirror constant velocity control loop. Laplace domain representation.

Following the error voltage through the feed-forward path results in the overall feed-forward transfer function,

$$G(s) = \frac{V_M(s)}{V_E(s)} = \frac{K_P}{K_B} \frac{1}{1 + s\tau_2}$$

Eq. 3-18a.

The feed-back transfer function, for either the auxiliary coils or the F/V system, is a simple proportional constant,

$$H(s) = \frac{V_F(s)}{V_M(s)} = K_V$$

Eq. 3-18b.

A few points should be noted here. First, in this approximate analysis it is being assumed that the proportional constants, K_B , K_P , and K_V are not functions of the complex frequency variable, s . In other words, these "gain stages" have infinite frequency responses. As well, with respect to K_V , this is the overall constant of proportionality that relates the output velocity to the feed-back voltage. This includes all of the various gains up to and including the comparison step in which the final feed-back voltage is subtracted from the reference voltage.

For this type of simple loop, with $G(s)$ and $H(s)$ as the feed-forward and feed-back transfer functions respectively, the transfer function relating the output velocity to the input reference voltage is given by,

$$\frac{V_M(s)}{V_{REF}(s)} = \frac{G(s)}{1 + G(s)H(s)}$$

Eq. 3-19.

Substituting Eq. 3-18a and Eq. 3-18 b into Eq. 3-19 results in the approximate system transfer function,

$$\frac{V_M(s)}{V_{REF}(s)} = \frac{K_P}{K_B + K_P K_V} \left[\frac{1}{1 + s\tau_2} \right]$$

Eq. 3-20a,

where,

$$\tau'_2 = \frac{\tau_2}{1 + K_p K_V / K_B} \quad \text{Eq. 3-20b.}$$

For the present system, the numerical values of the constants in the above two equations are listed below.

$$K_p = 48.$$

$$K_B = 2.38 \text{ v-s/m.}$$

$$K_V = 5.3 \times 10^2 \text{ v-s/m.}$$

In the denominator of Eq. 3-20a, the product $K_p K_V$ ($= 2.5 \times 10^4$) is much greater than K_B , hence Eq. 3-20 is given approximately by,

$$V_M(s) = \frac{1}{K_V} \left[\frac{1}{1 + s\tau'_2} \right] V_{REF}(s) = 1.9 \times 10^{-3} \text{ m/s-v} \left[\frac{1}{1 + s\tau'_2} \right] V_{REF}(s)$$

Eq. 3-21a.

Substituting the numerical values into Eq. 3-20b results in the following value for the system time constant,

$$\tau'_2 = 9.4 \times 10^{-5} \tau_2 = 4.0 \times 10^{-5} \text{ s.} \quad \text{Eq. 3-21b.}$$

Eq. 3-21a is the Laplace transform of an exponential rise, with the time constant $\tau'_2 = 40 \mu\text{s}$. In response to a 1v step in the reference input, the velocity of the mass would rise exponentially to a final velocity of 0.19 cm/s in a time $5\tau'_2 = 200 \mu\text{s}$. Since a final velocity of 0.32 cm/s is required to produce a 10 kHz reference laser output, the reference voltage would have to

be stepped up to approximately 1.7 v. The time required to achieve this final velocity would still be the same.

It can be seen that in comparison with the response of the electromechanical system by itself, the control loop employing this system responds much faster to a step change in the reference level. Again, since the velocity cannot change instantaneously, a step change in the reference voltage is equivalent to a step change in the error voltage. An external disturbance cannot cause a step in the error voltage because the velocity of the mass cannot be changed instantaneously. Thus, externally induced error voltages will rise slowly in comparison with the abrupt increase that results from a step reference change. Hence, this is a reasonable worst case calculation of the time response of the system.

For the case of F/V feed-back, K_v ranges from approximately 1.6×10^3 to 3.5×10^3 v-s/m. For the minimum K_v the time constant for the system, as given by Eq. 3-20b, is $\tau'_2 = 1.3 \times 10^{-5}$ s. With the assumption that most mechanical vibrations in buildings should occur with frequencies less than 1 kHz, i.e. a 1 ms period, it is expected that the speed of response of the F/V feed-back system should be adequate in correcting for vibrational disturbances coupled from the floor of the room to the mass. This is indeed the case. However, for acoustic disturbances there is a greater effect on the mirror velocity. A sharp clap of the hands will cause a significant modulation of the frequency of the reference laser output. This is probably caused by a compressional wave in the air impinging upon the mirror surface. Since a clap is a sharp, discontinuous sound, there should be a significant high audio frequency content in the compressional wave striking the mirror surface. Assuming that the audio band extends out to 25 kHz., a disturbance with this

frequency has a period of 4×10^{-5} s. Clearly, even when under F/V feed-back, this type of disturbance occurs too fast for effective correction by the loop. Hence, for this system, a good deal of attention should be paid to protecting the system (i.e. with enclosures) from acoustic frequency vibrations coupled through the air, whereas mechanical vibrations coupled through the supporting structure should be of lesser concern.

3-1.2. Moving mirror feed-back control switching system.

As mentioned previously, due to the complementary nature of the auxiliary coils and F/V feed-back signals, one or the other of these is employed at any given time during operation of the system. Hence, it is necessary to be able to switch, at will, between these two feed-back loops. Described in this section are the methods by which the feed-back is switched. The actual generation of the control signals to do this will be described in a later section.

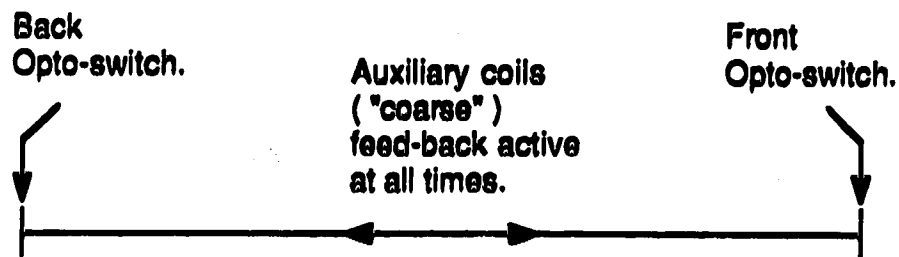
A note is required on the symbol conventions used in this section. The auxiliary coils and F/V feed-back loops will often be referred to as "coarse" and "fine" feed-back, respectively. The notation for analog electrical quantities [75] is illustrated by the following example. $v_{EMF} = V_{EMF} + v_{emf}$; here v_{EMF} is the sum of a dc-component, V_{EMF} , and an ac-component, v_{emf} . Digital signals are denoted by bold face upper-case letters. A line over the signal indicates negation. As an example, FWD/\overline{BWD} is a digital signal that indicates if the mirror is moving in the forward, or backward direction. When this signal is a 1 or HI, the drive is moving in the forward direction. When the mirror is moving in the backward direction, $FWD/\overline{BWD} = 0$, or LO.

The signals involved in the operation of the coarse and fine feed-back loops, and those required to control the switching between the two loops, are indicated in Fig. 3-18. Although the description of the operation of the feed-back switching system has been simplified for clarity, it is anticipated that a glossary of the signals involved will be helpful. These signals, as well as those required for scan length control, are described in Table 3-1.

The basic operation of the feed-back switching system involves switching the error signal, V_E , (which provides input to the power stage) between the coarse and fine feed-back error signals, V_{E1} and V_{E2} , respectively. The sub-scripts indicate that the coarse feed-back loop is designated as loop #1, while the fine feed-back loop is loop #2. The switching between the two loops is ultimately controlled by the logic level of $EN1/\overline{EN2}$. When HI, $EN1/\overline{EN2}$ chooses the coarse feed-back error signal, when LO, the fine feed-back loop is chosen. The rest of the signals shown in Fig. 3-18 are involved in ensuring correct operation of the two feed-back loops during the time that either loop is chosen to be active.

The moving mirror control system is configured for two modes of operation. The first mode, shown in part a) of Fig. 3-19, is called the MARK TIME mode. This mode is invoked when the system is powered up. When operating in this mode, the drive is always under coarse feed-back control with the Mark Time Reference or, V_{REFM} , as the reference for the loop. This reference is bi-polar, the polarity being changed in a step fashion at the end of the mirror travel, as indicated by the triggering of one of a pair of opto-switches. These opto-switches are set outside of the maximum desired data

a) MARK TIME mode.



b) SCAN mode.

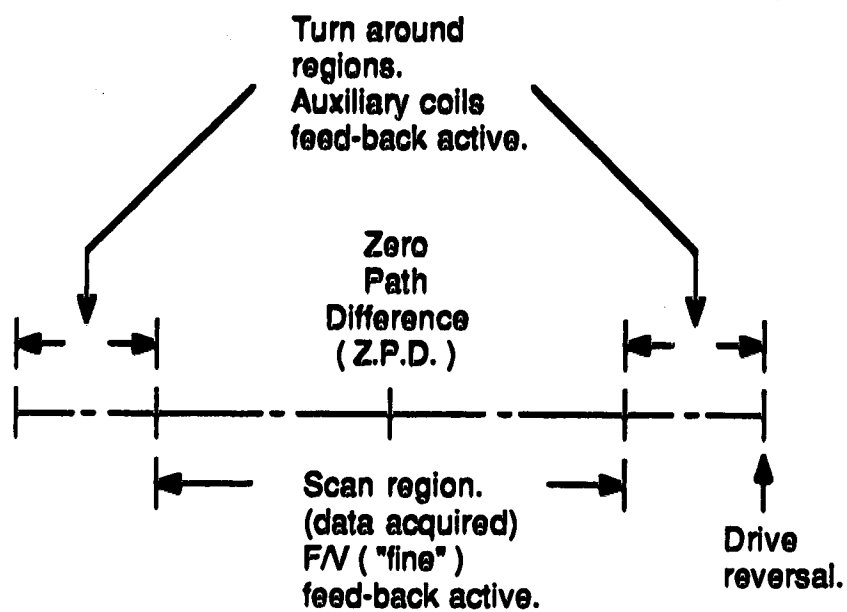


Figure 3-18. Schematic description of MARK TIME and SCAN mode operation.

SIGNAL	FUNCTION
V_E	System feed-back control error signal.
V_{E1}	Coarse feed-back loop error signal.
V_{E2}	Fine feed-back loop bi-polar error signal.
EN1/EN2	HI = enable coarse feed-back loop. LO = enable fine feed-back loop.
SCAN/MK.TIME	HI = Scan mode operation. LO = mark time mode operation.
V_{REFM}	Reference for coarse feed-back loop during mark time mode operation.
FNTBLKD	HI to LO when front opto-switch blocked.
BCKBLKD	Same as above for back opto-switch.
V_{REF1}	Controllable reference for coarse feed-back loop during scan mode operation.
V_{EMP}	Output of auxiliary coils. Feed-back signal for coarse feed-back loop.
V_{REF2}	Fine feed-back loop reference signal.
$ V_{E2} $	Fine feed-back loop uni-polar error signal.
$ V_{E2}' $	Output of ripple remover circuit.
DEFAULT	HI = no effect. LO = asynchronously invoke mark time mode operation.
ZERO	LO = asynchronously set V_{REF1} to zero to stop mirror while coarse feed-back loop is enabled.
RAMP/CONSTANT	HI = V_{REF1} ramps. LO = V_{REF1} remains constant.
OUTSIDE/INSIDE	HI = $ V_{E2}' $ is outside window of window detector. LO = inside window.
LWR	LO = $ V_{E2}' $ is less than lower threshold of window detector.
BWDACC/FWDACC	HI = V_{REF1} ramps for backward acceleration when under coarse feed-back loop control. LO = vice versa.
DIR	HI = move forward. LO = move backward.
T/A	LO = asynchronously initiates turn-around sequence.
FWD/BWD	HI = mirror moving forward. LO = mirror moving backward.
WLP	White light pulse signal.
FRINJ	Square wave version of reference laser interferogram.
FRINJW/H	Square wave version of reference laser interferogram - with hysteresis.
FRINJ _{Pz}	Pulse version of FRINJ. Pulses every rising edge.
CFRINJ _P	Pulse version of FRINJ. Pulses every falling edge.
FRINJ _{Px2}	Pulses for both edges of FRINJ.
T/A CNTR CNTOUT	LO pulse signals turn-around count is finished.
NCNTR CNTOUT	LO pulse signals scan count is finished.

Table 3-1. Signals for feed-back switching and mirror scan length control.

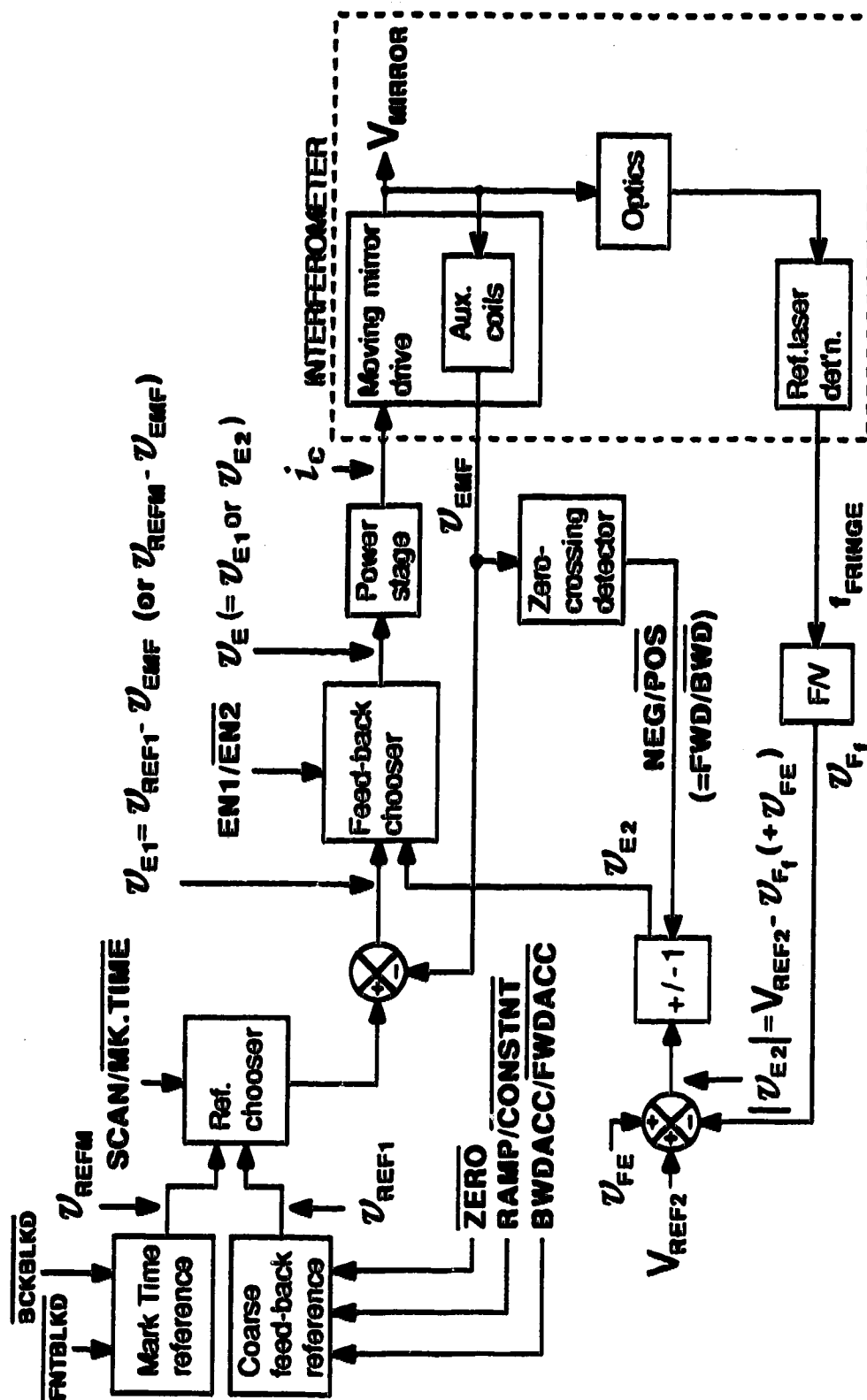


Figure 3-19. Auxiliary coils (coarse) and F/V (fine) feed-back loops in dual feed-back architecture.

acquisition scan length. Thus, in the mark time mode the mirror cycles back and forth between the opto-switches under auxiliary coil feed-back control.

When the system is powered down, the drive coils are "crow-barred" by a latchable relay. This short circuit across the coils ensures that voltage transients do not cause the mirror to be moved in an un-controlled manner, perhaps causing damage, when the system is powered up. The system powers up in the mark time mode such that when the crow-bar is removed, the mirror accelerates smoothly into the mark time cycle.

The second mode of operation is called the SCAN mode. This mode can be invoked once the system is up and operating in the mark time mode. Referring to Fig. 3-18, when the signal $\overline{\text{SCAN/MK.TIME}}$ is switched from LO to HI, the mirror continues to cycle in the mark time mode until the next time that $\overline{\text{BCKBLKD}}$ goes LO, indicating that the back opto-switch has been blocked. At this point the system switches into the scan mode. The reference for the coarse feed-back loop is changed from V_{REFM} to V_{REF1} . (Even though both of these references are used in the coarse feed-back loop, the latter is called the coarse feed-back reference since it is in use most of the time.) The mirror is stopped, and then accelerated in the forward direction under coarse feed-back, until fine feed-back is acquired. The system is now operating in the scan mode. As illustrated in part b) of Fig. 3-19, fine feed-back is in operation during the data acquisition portion of a scan. At the end of data acquisition, the feed-back is switched to the coarse feed-back loop to start a turn-around sequence. After the turn-around is complete, control is switched back to the fine feed-back loop.

Referring once again to Fig. 3-18, this drawing shows, schematically, the system with which feed-back is switched from fine to coarse, and back again. Consider first the scan mode operation of the auxiliary coils loop.

During scan mode operation, the coarse feed-back loop is active during the drive reversal portions of each scan. The reference for the coarse feed-back loop, throughout all scan mode operation, is V_{REF1} . This reference is designed to be programmable. By varying V_{REF1} , the velocity of the mirror can be changed. This is required during both the start-up phase of the initial scan, and turn-around sequences at the ends of each scan.

The design of this controllable reference is shown in greater detail in Fig. 3-20. The basic design consists of an 8-bit counter (2 x 74161) that feeds an 8-bit digital-to-analog converter (DAC-08). The output square wave from a voltage-to-frequency converter (not shown), set to an output frequency of approximately 1.8 kHz, is connected to the CLK input of the reference module. This clock signal is gated via associated logic to the clock input of the counter. If the square wave reaches the clock input, the counter counts up or down, causing the number being fed to the DAC to increase or decrease. This causes the output of the DAC to increase or decrease, within maximum limits of $\pm 5v$. If the square wave is locked out from the counter clock input, the output of the DAC remains constant. Thus, by appropriately gating the CLK square wave input, the output of the DAC can be made to ramp up, ramp down, or remain constant. (Because the frequency of the CLK signal is constant, the counter output changes linearly. Therefore, the DAC output, or V_{REF1} , during changes is a ramp.) As indicated in this drawing, there are

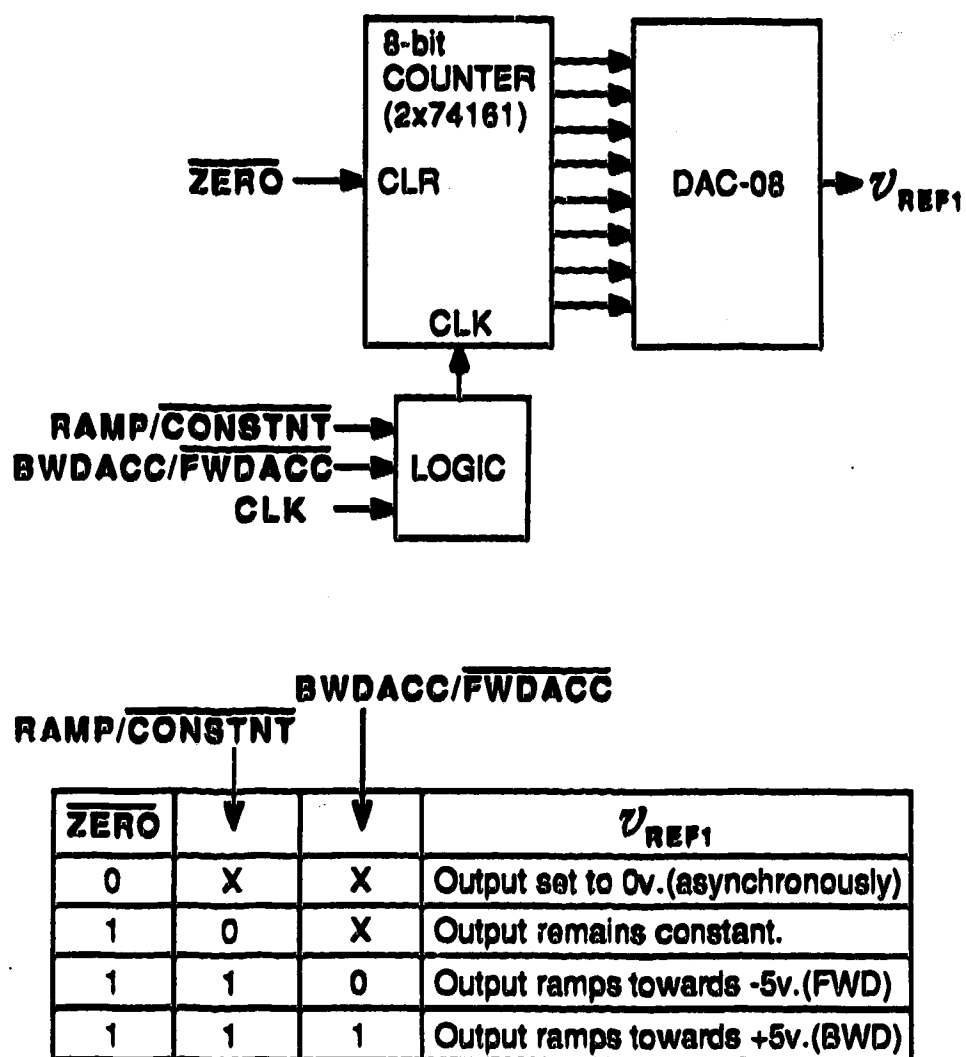


Figure 3-20. Block diagram and truth table of controllable reference, V_{REF1}

three signals that are used to control the gating of the CLK signal. These are summarized in the truth table at the bottom of this figure.

When $\overline{\text{ZERO}}$ goes LO, V_{REF1} is set to 0v, asynchronously. This stops the mirror dead. This is used during the acquisition of the first scan. This is the scan that starts when the back opto-switch is triggered for the first time since scan mode operation has been invoked. The mirror is stopped and then accelerated in the forward direction to begin the first scan of scan mode operation.

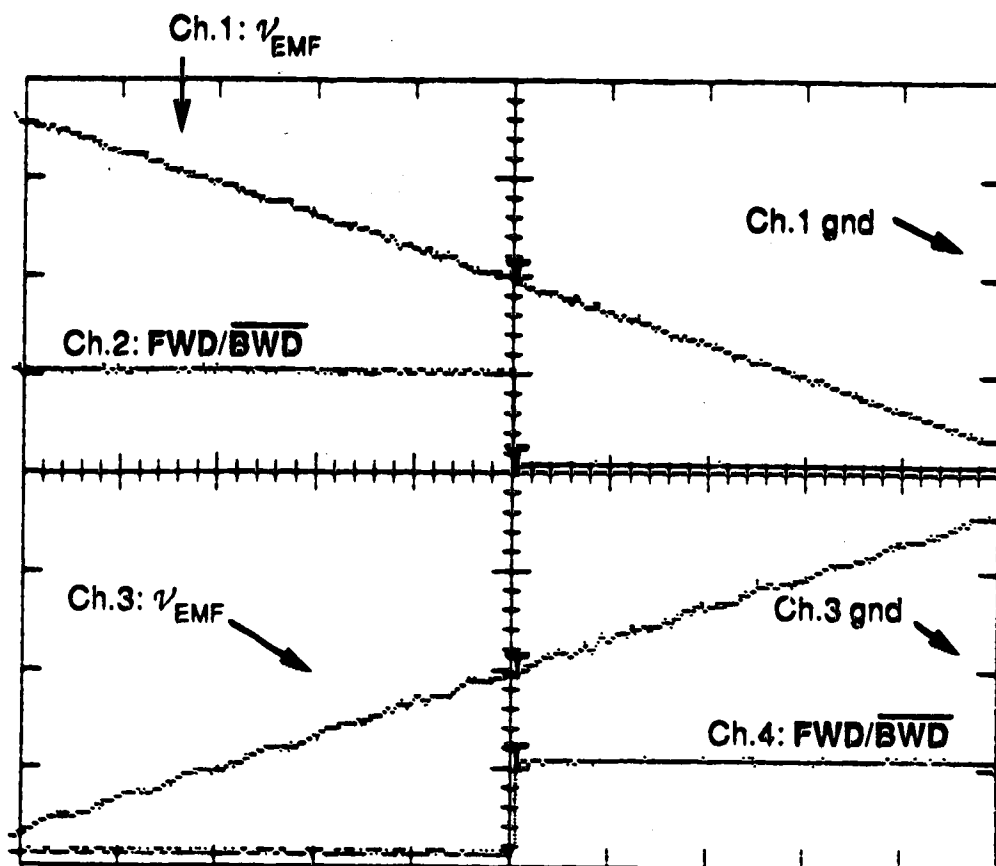
If the logic level at the $\text{RAMP}/\overline{\text{CONSTANT}}$ input is LO, the coarse feed-back reference remains constant. This condition locks out the CLK input from the counter clock input. If this signal is HI while the system is under coarse feed-back control, then the reference ramps and, consequently, the mirror velocity changes linearly. If $\text{RAMP}/\overline{\text{CONSTANT}}$ is HI when $\text{BWDACC}/\overline{\text{FWDACC}}$ is LO, then the reference ramps in the direction that accelerates the mirror in the forward direction. This would be the case when it is desired to change the direction of motion from backward to forward. (The way the system is set up, the ramp in this case decreases from a positive voltage towards -5v.) The opposite case is when $\text{BWDACC}/\overline{\text{FWDACC}}$ is HI. The mirror is then accelerated in the backward direction.

Referring back to Fig. 3-18, the signal generated by the auxiliary coils, V_{EMF} , is fed back to a difference amplifier to produce the coarse feed-back error voltage, V_{E1} . The polarity of V_{EMF} can be used to indicate the direction of mirror movement. As well, in principle, the point in time at which V_{EMF} crosses the 0 v level is the time when the mirror is stationary. To detect the polarity and transition of this signal, V_{EMF} is fed into a comparator with a

zero volt reference level, that is, a zero-crossing detector. The input, V_{EMF} , and output, FWD/\overline{BWD} , of this comparator are shown in Fig. 3-21. V_{EMF} is shown in the top trace as the direction of mirror travel is reversed from forward to backward motion. Indicated in the second trace is the transition of FWD/\overline{BWD} , as V_{EMF} traverses the zero volt level. The lower two traces are analogous to the above two, except that here the drive is reversing direction from backward to forward motion.

As indicated in Fig. 3-18, FWD/\overline{BWD} is connected to a $\pm 1x$ gain stage in the fine feed-back loop. This input is called NEG/\overline{POS} . This stage reverses the polarity of the fine feed-back uni-polar error voltage, $|V_{E2}|$. This solves the problem caused by the uni-polar nature of the F/V feed-back, that is, stability of the loop for one direction of movement, and instability in the other direction. The output of the $\pm 1x$ gain stage, V_{E2} , maintains negative feed-back for both directions of mirror movement.

At this point one might ask why it is necessary to use the auxiliary coils feed-back at all, if negative feed-back can be set up for both directions of mirror movement with the F/V loop. Attempts to do this met with some success; however, problems with positive feed-back still arose. With a feed-back polarity switching architecture, the time at which the polarity is switched is critical. If the polarity is changed before the drive has stopped, then the feed-back switches over to positive feed-back in the direction in which the drive is already moving. Instead of the drive decelerating to zero velocity, it would then start accelerating in the uncontrolled positive feed-back fashion. Conversely, if the polarity was switched after the mirror had stopped and was accelerating in the opposite direction, positive feed-back would be in operation until the polarity was changed. There would be a certain period of



Trigger: Ch.2 and Ch.3 (- slope for Ch.1/Ch.2, + slope for Ch.3/Ch.4)
 Time base: 5 ms/div
 Vert. gain: Ch.1/Ch.3: 200mv/div
 Ch.2/Ch.4: 5v/div

Figure 3-21. V_{EMF} and $\overline{FWD/BWD}$ during turn-around sequences.

time during which positive feed-back is in action. Once the polarity was changed the drive would then be under negative feed-back control, and in principle, it should eventually attain the correct velocity. If it had over-shot the correct velocity, then it would have to be decelerated. Suffice it to say that the level of control during the turn-around could range from no control to a momentary loss of control unless the polarity was switched at precisely the moment that the mirror was stopped during the turn-around. It was found that with this feed-back polarity switching system, positive feed-back occurred far too frequently, and in some cases this could result in destructive oscillation of the mass. At the very least, these oscillations would cause the moving mirror to become severely mis-aligned with respect to the fixed mirror and the beam-splitter.

The auxiliary feed-back system, with bi-polar feed-back, is inherently stable as the velocity changes through the zero level. There is nothing special about zero velocity, and in fact the drive will remain motionless if the coarse feed-back reference voltage is set to zero. It is anticipated that this condition would be rather difficult to achieve with the polarity switching system. Thus, due to the inherent "fool-proof" nature of the auxiliary coils feed-back, and because the polarity switching system is fine once the velocity is significantly away from zero, the mirror drive system has evolved into the present hybrid design.

The general strategy, then, is that fine feed-back is switched into operation only when the velocity of the mirror is close to that which is desired for data acquisition. At all other times the coarse feed-back system is in operation. Since this system has been implemented, there have been no instances of the gross oscillations that were seen previously.

The desired velocity for the present system is approximately 0.32 cm/s. While in the scan mode, whenever the velocity of the mirror is close to this value, the system switches into fine feed-back. To determine that the velocity is within a prescribed set of limits on either side of this velocity, the uni-polar error voltage, $|V_{E2}|$, is observed. Prior to the detailed discussion of this process, the generation of $|V_{E2}|$ has to be considered.

$|V_{E2}|$ is the output of a commercially available frequency-to-voltage converter, the Analog Devices AD451J. A schematic [76], is shown in Fig. 3-22. The important points about the architecture of this module are as follows. First, the precision charge dispenser outputs bursts of charge which are integrated by the capacitor, C_C . The higher the input frequency, the greater the number of charge packets per unit time, and therefore, the larger the integrated voltage across the capacitor. Although there is filtering of the voltage across the capacitor, there is still an ac ripple on the output signal of the module. The magnitude of this ripple can be significant. It is inversely proportional to the input frequency, therefore to have minimum ripple the input frequency should be as high as possible.

The second point of interest with respect to this module is that the output can be off-set. In normal operation, the output increases from 0 to 10v as the input frequency changes from dc to whatever the full scale frequency is set to be. Usually this feed-back signal would then be subtracted from a reference to produce a uni-polar fine feed-back loop error signal. However, as indicated in the schematic, pin #4 of the module is connected to the summing point input of the second amplifier, A2. This allows the output to be off-set downwards by an amount equal to the value of the fine feed-back

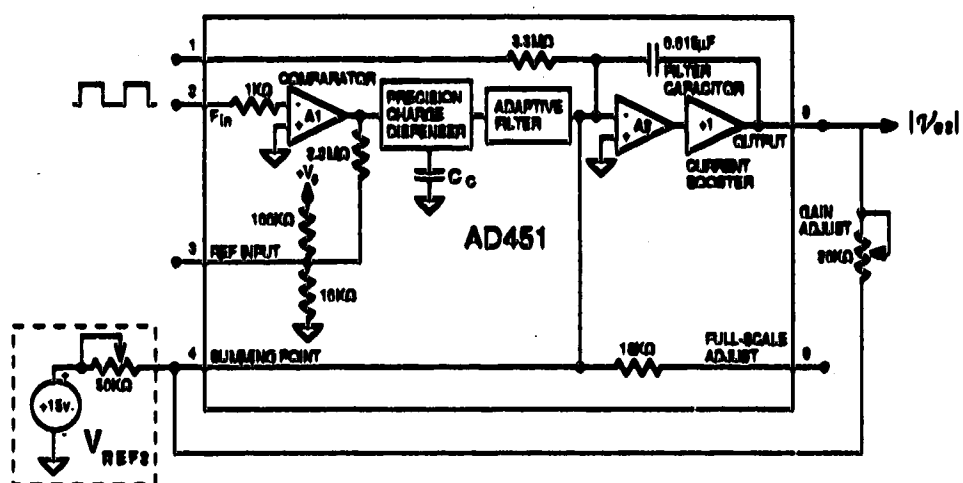
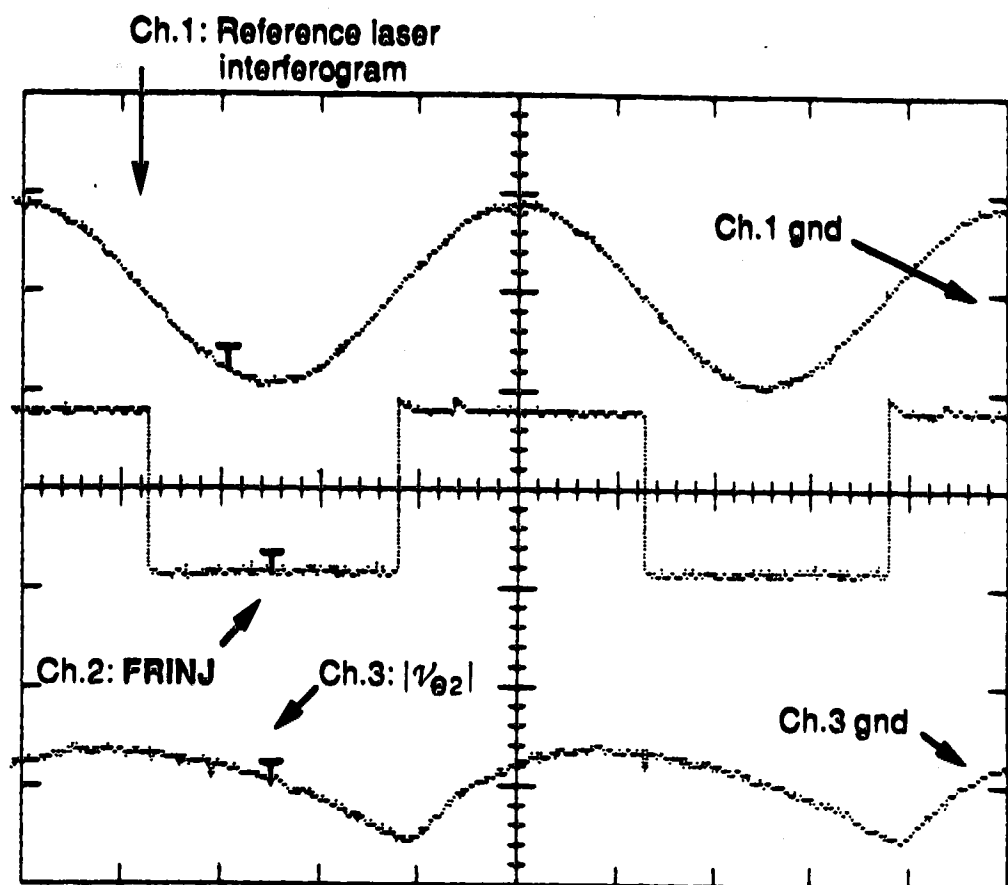


Figure 3-22. Schematic diagram of AD 451 frequency-to-voltage converter.

reference voltage, V_{REF2} . The value of the reference then sets the input frequency at which the output will equal zero. When the fine feed-back loop is in operation, the velocity of the mirror will be kept constant at the velocity required to produce a reference laser output at this frequency. The output, $|V_{E2}| = V_F - V_{REF2}$, where V_F is the output of the F/V with no off-set, is uni-polar. If used in the fine feed-back loop, as is, the system would be stable for only one direction of mirror movement. As described above, when this is multiplied by ± 1 , the result is the bi-polar error voltage, V_{E2} .

In Fig. 3-23, the digital oscilloscope traces of three signals are shown. These were obtained during fine feed-back operation, with a reference laser output frequency of 10 kHz. The top trace is the analog reference laser output from the detection photo-diode. The second trace is the digital output from a comparator into which the above reference laser fringe has been input, in an ac-coupled fashion. This square wave output is the input for the AD451J. The reference voltage for the comparator is zero volts, hence this is a zero-crossing detector. If the mirror changes velocity, the frequency of the reference laser output changes. Accordingly, the frequency of the square wave representation of the analog signal changes. This digital signal is called the FRINJ, making reference to the fact that it is derived from the reference laser fringe. The bottom trace in this figure is the output, $|V_{E2}|$, of the AD451J during fine feed-back operation, with a FRINJ frequency of approximately 10 kHz. The vertical scale is expanded. An approximately 200 mv ripple with twice the frequency of the FRINJ input can be seen.

As mentioned before, the only time that fine feed-back may be operational is when the mirror velocity is close to the desired value required for data acquisition scanning. When this is the case, the uni-polar fine feed-



Trigger: Ch.2

Time base: 20 $\mu\text{s}/\text{div}$

Vert. gain: Ch.1: 5v/div

Ch.2: 2v/div

Ch.3: 200mv/div

Figure 3-23. Reference laser interferogram, FRINJ, and $|\psi_{\theta 2}|$.

back error signal, $|V_{E2}|$, has a magnitude very close to zero, as is indicated in Fig. 3-23. The present system is set up such that when the dc-level of $|V_{E2}|$ is within approximately ± 75 mv of zero volts, fine feed-back can, and will, be activated during the data acquisition portion of a scan. To sense when $|V_{E2}|$ is within this window about the zero volt level, an electronic circuit called (appropriately enough) a "window detector" is employed. This circuit is central to the operation of the feed-back switching system.

The window detector being used in the present system is illustrated schematically in Fig. 3-24. (Ignore for the moment the associated logic blocks in the diagram.) Since the ripple on $|V_{E2}|$ is approximately 200 mv., a circuit called a "ripple remover" is employed to reduce the ripple to approximately 15 mv.

The ripple remover circuit is not simply a low pass filter. Rather, in this circuit the gain for the dc-component of the input signal is +1, while for the ac-component it is subtracted from itself to produce a net ac-gain of zero. Originally, it was thought that with this circuit the ripple on $|V_{E2}|$ could be removed, and this cleaner version would then be used in the fine feed-back loop. This is desirable, since a ripple on the error voltage of the loop produces a slight modulation of the velocity of the mirror, which in turn causes modulation of the frequencies of the various wavelength components in the measured interferogram. This can lead to the introduction of spurious spectral features in the final spectrum. It was hoped that this circuit would remove the ripple with much less phase shifting and time delaying of the error signal than would be possible with a simple low pass filter. This was not the case, however, and when the circuit was tried within the fine feed-back loop, the result was an oscillation of the mirror. Nonetheless, the ripple

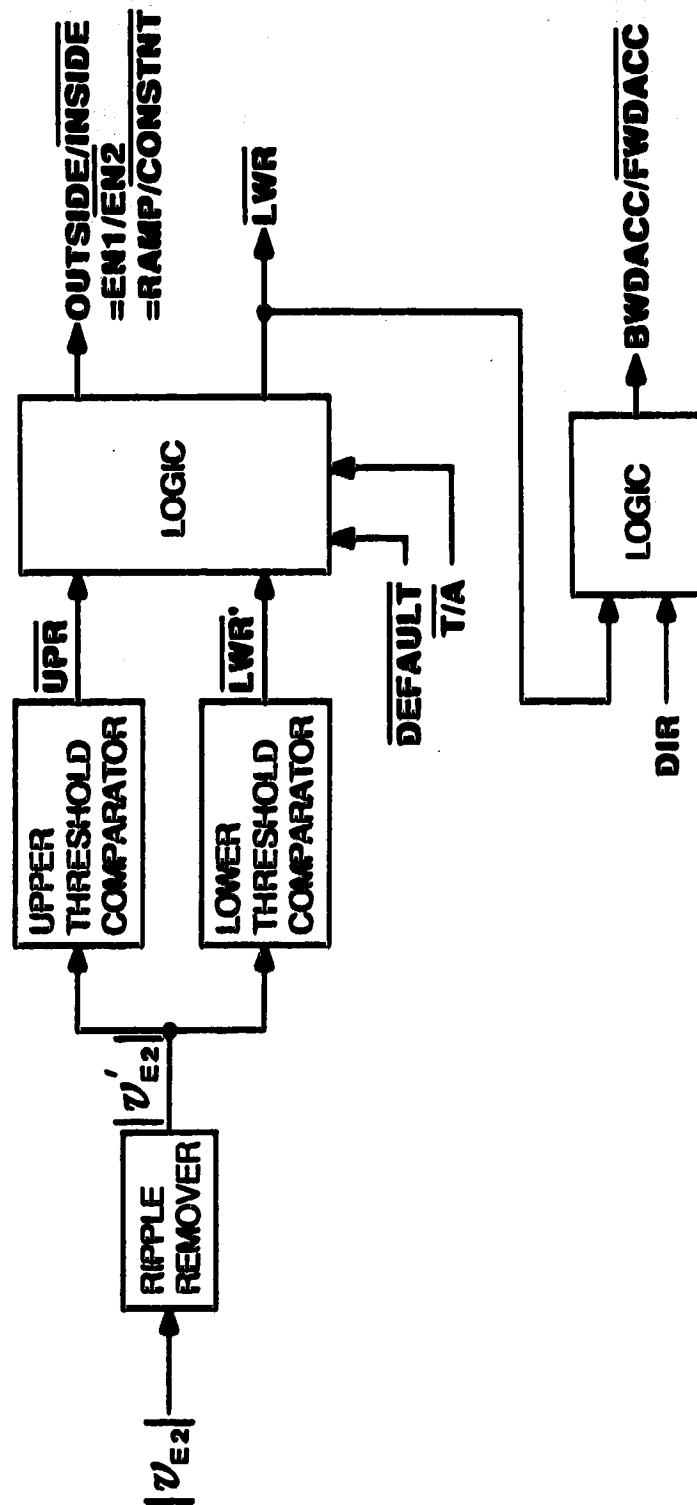


Figure 3-24. Window detector block diagram.

remover output is fine for use with the window detector, although a simpler low pass filter would probably suffice.

The output of the ripple remover, $|V_{G2}'|$, is simultaneously fed into two comparators denoted the upper and lower threshold comparators, respectively. The input/output transfer characteristics are depicted graphically in Fig. 3-25 a) and b). Consider that of the lower threshold comparator, shown in part a) of this figure.

As evidenced by the presence of a hysteresis loop, this is the transfer characteristic of a comparator circuit in which positive feed-back is being employed. Hysteresis reduces "chatter" of the comparator output. Chatter consists of spurious level changes of the comparator output due to noise on the input that causes the input voltage to traverse, more than once, the switching threshold level. In a circuit with hysteresis, the output of the comparator can change state only if the input voltage traverses the appropriate threshold voltage level with the correct direction of change (i.e. increasing or decreasing through the threshold). As indicated in part a) of this figure, when the output voltage is 0v, the output changes state only when the input voltage increases through the threshold voltage, V_{LT} . If the input then decreases to traverse V_{LT} again, the output does not change state. Only when the input decreases through the lower threshold indicated in the figure does the output change from +5v to 0 v. If the input then increases through this lower threshold, the output does not change state until V_{LT} is once again traversed.

After the first time that the input voltage has crossed V_{LT} , then, even if noise causes it to re-traverse this threshold, as long as it does not cross the

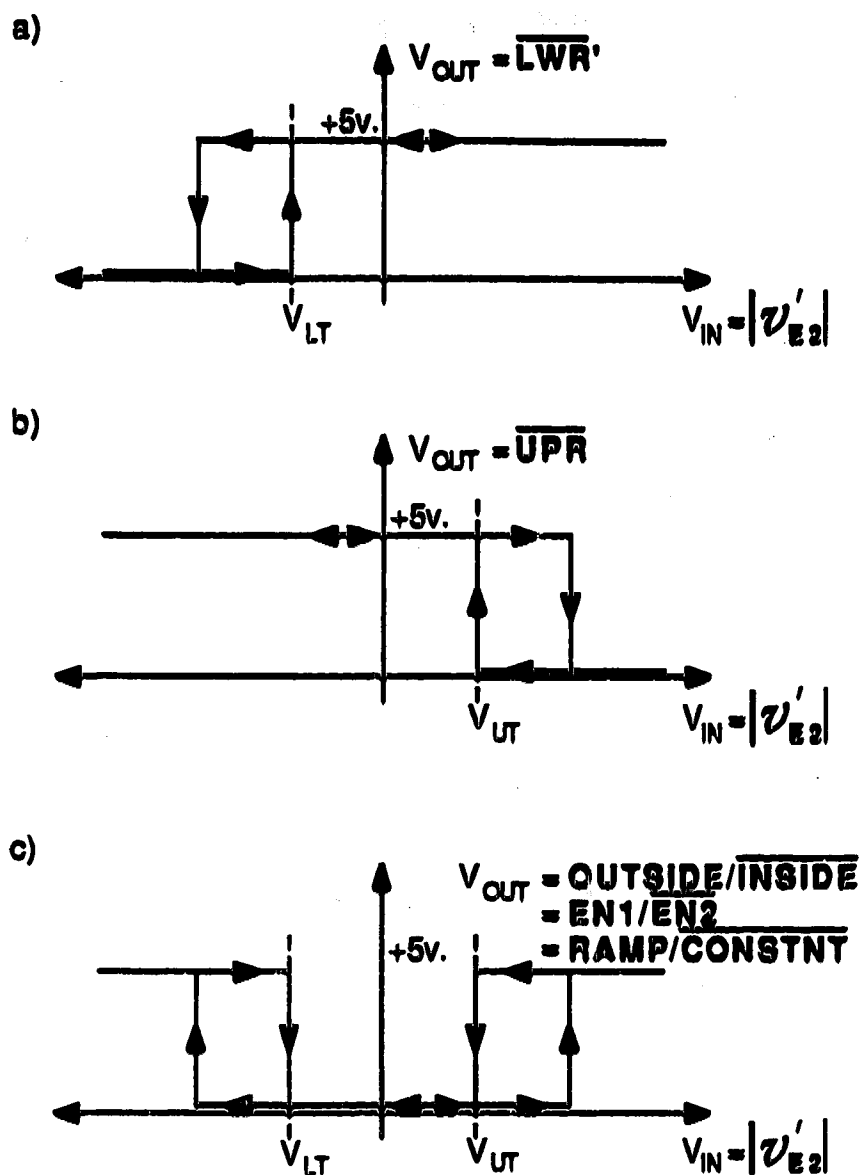


Figure 3-25. Window detector comparator transfer characteristics.
 a) Lower threshold comparator. b) Upper threshold comparator. c) Combined characteristic of window detector.

lower threshold the output will not change state spuriously. Since the input to the window detector is $|V_{E2}'|$, multiple traverses of each particular threshold voltage level could result from the residual ripple on $|V_{E2}'|$. As described above, hysteresis prevents the output from chattering when this signal is used as input. In addition, the positive feed-back in the circuit causes the comparator to switch very quickly and forcefully when the appropriate threshold voltages have been traversed. This is desirable when the input is a slowly varying signal such as $|V_{E2}'|$.

The lower threshold voltage, V_{LT} , is set to be approximately -50 mv. If the input $|V_{E2}'|$ is greater than V_{LT} , then the output of the lower threshold comparator, \overline{LWR} , is +5v. The hysteresis loop has a width of approximately 25 mv. If the input decreases through $V_{LT} - 25 \text{ mv} = -75 \text{ mv}$, the output changes from +5v to 0v. If the output is 0v, and the input increases through V_{LT} , then the output changes from 0v to +5v. Note that due to the hysteresis, for this last case the output does not change state as the input increases through the threshold at -75 mv.

The transfer characteristic of the upper threshold comparator is similar to that of the lower, except that the output, \overline{UPR} , changes state from LO to HI when the input decreases through the upper threshold voltage, $V_{UT} = 50 \text{ mv}$. These two transfer characteristics are "summed", via the associated logic, to produce the characteristic shown in part c) of this figure. This is the transfer characteristic of the window detector, with hysteresis. If the output, $\overline{\text{OUTSIDE/INSIDE}}$, is HI, and the input, $|V_{E2}'|$, decreases through the +50 mv threshold, then the output changes from HI to LO. In other words, $\overline{\text{OUTSIDE/INSIDE}}$, undergoes a 1→0 transition when the error voltage enters the window from above. Similarly, if the error voltage enters the window

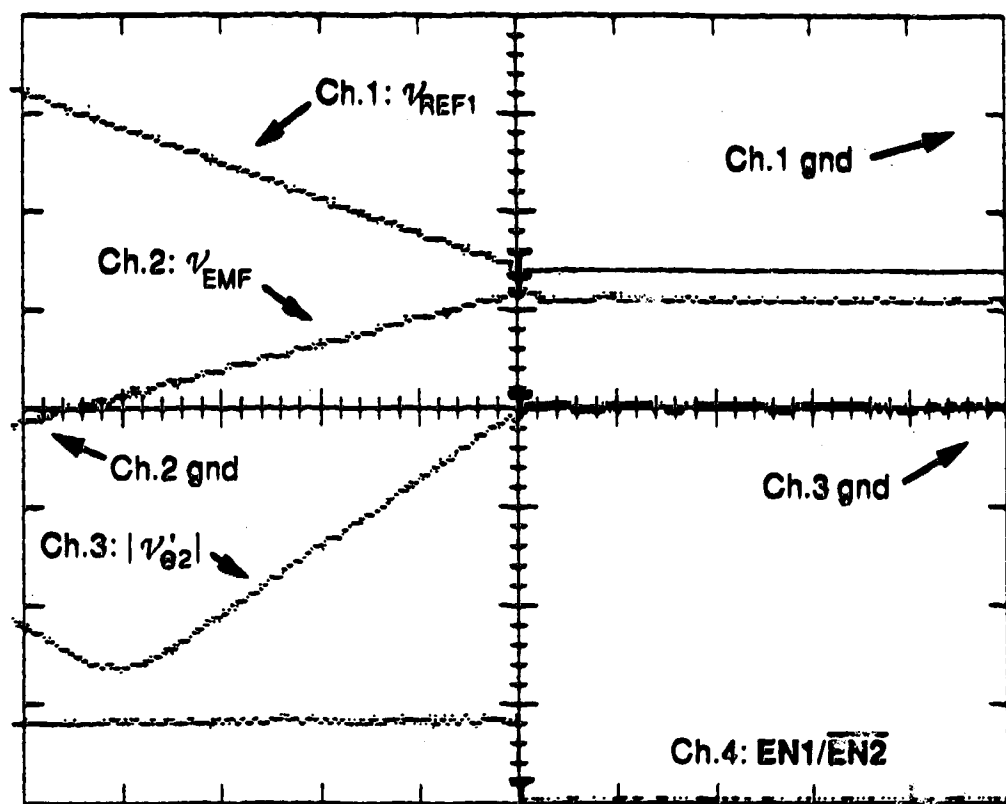
from below, OUTSIDE/INSIDE again undergoes a $1 \rightarrow 0$ transition. When the error voltage leaves the ± 50 mv window and increases through the $+75$ mv threshold, the output changes from $0 \rightarrow 1$. Similarly, when $|V_{E2}'|$ decreases through the -75 mv threshold, OUTSIDE/INSIDE is again cleared LO.

The sensitivity of the F/V converter is set somewhere between 1.6×10^3 and 3.5×10^3 v-s/m. Consider the case where the mirror is moving in the forward direction under fine feed-back. Since the fine feed-back reference is constant, any changes in the error signal are due to changes in the F/V feed-back signal caused by changes in the mirror velocity. Take as a worst case, an F/V sensitivity equal to 1.6×10^3 v-s/m. An increase of the error voltage to $+75$ mv corresponds to a change in the velocity of the mirror of $\Delta V_M \approx 4.6 \times 10^{-5}$ m/s. This is an estimate of the largest velocity change that would cause the system to switch from fine to coarse feed-back. At present, the velocity of the mirror under fine feed-back is 0.32 cm/s. The above change in velocity, 4.6×10^{-3} cm/s, is equal to 1.4% of this velocity. Thus, one can say that when the system is operating properly, and is maintaining fine feed-back throughout the complete data acquisition portion of a scan, the velocity doesn't vary by more than $\pm 1.4\%$. If it did the system would switch into coarse feed-back. This calculation provides a coarse estimate of the degree of velocity control while under fine feed-back control. During fine feed-back operation, $|V_{E2}'|$ is actually observed to vary only approximately ± 10 mv from zero. Following the same calculation as above, this corresponds to a fine feed-back controlled velocity that does not vary by more than $\pm 0.2\%$.

During scan mode operation, fine feed-back is in operation until a turn-around sequence is initiated. At this point, control is switched to the coarse feed-back loop. The coarse feed-back loop reference voltage, V_{REF1} , is

ramped in the direction of decreasing mirror velocity. The drive decelerates, stops, and then accelerates in the opposite direction. The coarse feed-back reference ramps towards whatever value is required to reach the desired scan velocity. During the turn-around, fine feed-back isn't active in the loop, but $|V_{H2}'|$ is active; and it is an indication of the velocity of the mirror. After the direction of motion has been reversed, the coarse feed-back reference continues to ramp. Eventually, $|V_{H2}'|$ enters the window. At this point control is switched back to the fine feed-back loop. As control is switched, fine feed-back is acquired. As soon as the acquisition is complete, the ramp of the coarse feed-back reference is stopped. This leaves V_{REF1} at whatever voltage it happened to attain during the turn-around sequence. When the next turn-around is initiated, the system again switches to coarse feed-back control. Assuming that there are no gross asymmetries in the mirror drive electro-mechanical assembly, the value of the coarse feed-back reference should be very close to that which is required by the coarse feed-back control loop to produce the velocity at which the mirror is already moving. In this way, the transition from fine to coarse feed-back occurs smoothly. This is to keep the coarse feed-back reference from being some value that would dictate a very different velocity than the present fine feed-back velocity. If this were to happen, then upon switching the coarse feed-back loop would experience what would be, effectively, a step change in the coarse feed-back reference.

The re-acquisition of fine feed-back, at the end of a backward to forward turn-around sequence, is shown in Fig. 3-26. The top trace is the coarse feed-back reference, V_{REF1} , ramping downward while the system is under coarse feed-back control. This decelerates the drive in the backward direction, causing the drive to stop and then accelerate in the forward direction. This



Trigger: Ch.4
 Time base: 10 ms/div
 Vert. gain: Ch.1: 2v/div
 Ch.2: 500mv/div
 Ch.3: 500mv/div
 Ch.4: 5v/div

Figure 3-26. V_{REF1} , V_{EMF} , and $|V'_{\theta 2}|$ during acquisition of fine feed-back.

can be seen in the second trace. This is the output of the auxiliary coils, V_{EMF} , as it ramps upward following the ramp of V_{REF1} . The third trace is the fine feed-back error signal, $|V_{E2}'|$. It can be seen that it first decreases, and then increases back towards the zero volt level. The decrease is due to the mirror decelerating in the backward direction. The minimum in the trace corresponds to the point at which the mirror has stopped. Note that the minimum does not occur at exactly the same point in time as does the zero-crossing of V_{EMF} . In principle, there should not be any lead or lag between these points on these two signals. This is due to amplifier and comparator, input and output, voltage off-sets. For this application, this situation is not critical.

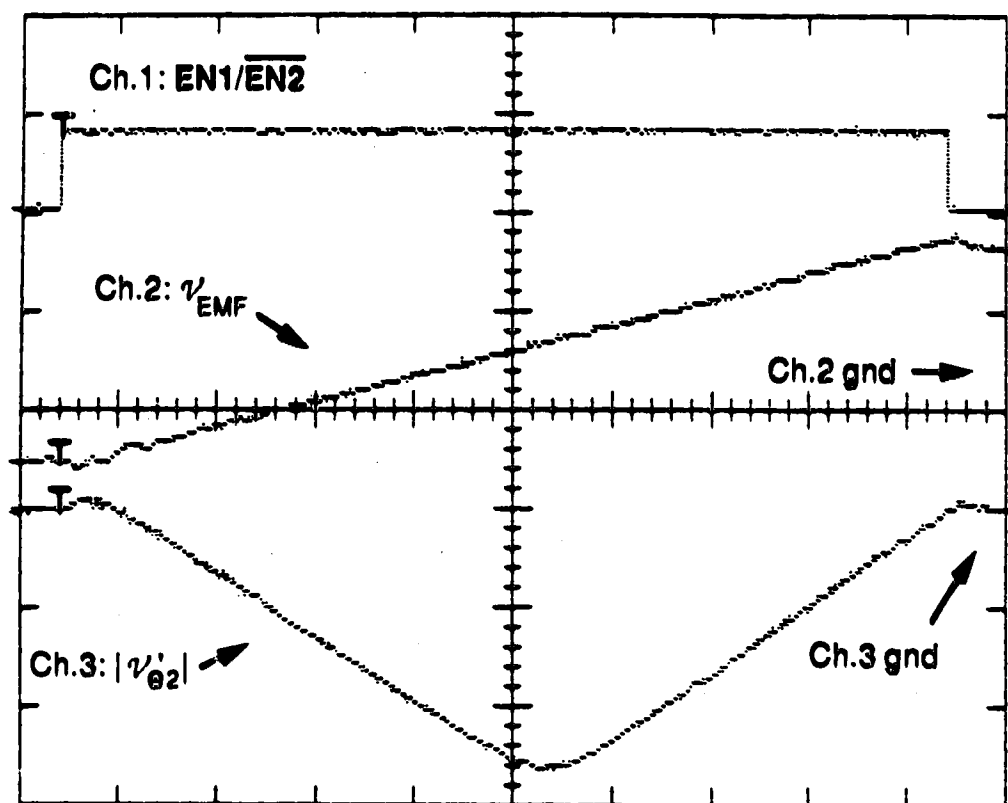
The increase in $|V_{E2}'|$ is the result of the acceleration of the mirror in the forward direction. As expected, since the velocity of the mirror is changing linearly, $|V_{E2}'|$ increases linearly. When the error signal enters the window at -75mv., the digital signal $OUTSIDE/\overline{INSIDE}$ undergoes a 1 \rightarrow 0 transition. This signal, shown in the bottom trace, indicates when the fine feed-back velocity has been reached in the forward direction.

$OUTSIDE/\overline{INSIDE}$ is also used to control the switching between the two feed-back loops. In this feed-back switching capacity, $OUTSIDE/\overline{INSIDE}$ is routed to the, $EN1/\overline{EN2}$, input of the feed-back switching circuitry. As mentioned previously, when this line is HI, coarse feed-back is enabled. When $EN1/\overline{EN2}$ is LO, the system operates under fine feed-back. From this figure it can be seen that once the fine feed-back error voltage is within the window, control is switched from the coarse to fine feed-back loop. This then shuts off the ramping of V_{REF1} , to maintain the appropriate value for the next turn-around.

The first attempts at switching the feed-back loops met with limited success. Often, the system would hang up at the threshold voltage of the window detector, switching back and forth between coarse and fine feed-back. The combination of introducing hysteresis into the window detector, and continuing the ramp of V_{REF1} until $|V_{E2}'|$ has entered the window, has resulted in flawless operation.

A full turn-around sequence is shown in Fig. 3-27. The signal, $\overline{T/A}$ (to be discussed in the scan length control section of this chapter), initiates the backward to forward turn-around by setting $EN1/\overline{EN2}$ to 1. This pulls the system out of fine feed-back and switches control to the coarse feed-back loop. The direction of mirror travel is reversed under coarse feed-back, as indicated by V_{EMF} in the second trace of this figure. When $|V_{E2}'|$ enters the window through the -75 mv threshold, $OUTSIDE/\overline{INSIDE} = EN1/\overline{EN2}$ undergoes a $1 \rightarrow 0$ transition that switches control back to the fine feed-back loop and shuts off the coarse feed-back ramp. As seen in this figure, the whole turn-around process takes approximately 90 ms. The forward to backward turn-around sequence is essentially identical except that during coarse feed-back operation, V_{REF1} ramps upward, causing V_{EMF} to ramp downward. This turn-around sequence also takes approximately 90 ms to complete.

As described above, all that is required to reverse the direction of mirror travel is to switch over to coarse feed-back control and ramp the coarse feed-back reference appropriately. The switch to coarse feed-back, and the subsequent re-acquisition of fine feed-back in the opposite direction, are both controlled by $EN1/\overline{EN2}$. The associated logic blocks in Fig. 3-24 impose certain conditions on this control signal.



Trigger: Ch.1
 Time base: 10 ms/div
 Vert. gain: Ch.1: 2v/div
 Ch.2: 500mv/div
 Ch.3: 500mv/div

Figure 3-27. $EN1/\overline{EN2}$, V_{EMF} , and $|V'_{\theta 2}|$ during a turn-around sequence.

Part a) of Fig. 3-28 is the truth table for the overall window detector system. The input, $\overline{\text{DEFAULT}}$, has not been mentioned until now. This signal invokes the system default condition of mark time mode operation. When the system is operating in this mode, $\overline{\text{DEFAULT}}$ is LO. After the signal $\text{SCAN}/\overline{\text{MK.TIME}}$ is switched from 0→1 to initiate scan mode operation, $\overline{\text{DEFAULT}}$ stays LO until the back opto-switch has been triggered. At this point it is set HI, and the system operates in the scan mode. When $\overline{\text{DEFAULT}}$ is HI, it has no effect on the scan mode operation of the system. However, a number of events can occur which may cause the mirror to overshoot its scan mode limits of travel, such that it eventually triggers one of the opto-switches. At this point $\overline{\text{DEFAULT}}$ goes LO, and the system reverts, unconditionally, to the mark time mode. In this mode coarse feed-back is always active, therefore, $\text{EN1}/\overline{\text{EN2}}$ is simultaneously set HI.

The outputs of the upper and lower threshold comparators, $\overline{\text{UPR}}$ and $\overline{\text{LWR}}$, respectively, act upon the window detector output as described previously. To re-iterate, if either of these signals is cleared LO, then $|V_{E2}'|$ is outside of the window and therefore $\text{OUTSIDE}/\overline{\text{INSIDE}}$ is set HI. If both signals are HI, then $|V_{E2}'|$ is inside the window and $\text{OUTSIDE}/\overline{\text{INSIDE}}$ is LO. Thus, since $\text{OUTSIDE}/\overline{\text{INSIDE}} = \text{EN1}/\overline{\text{EN2}}$, fine feed-back is enabled when $|V_{E2}'|$ is within the window, otherwise coarse feed-back is enabled.

It was mentioned earlier that the signal, $\overline{\text{T/A}}$, initiates the turn-around sequence. It can be seen from this truth table that when it is set HI, there is no effect on the window detector output. When it is cleared LO, however, $\text{EN1}/\overline{\text{EN2}}$ is asynchronously set HI. This pulls the system out of fine feed-back, switching it into coarse feed-back for a turn-around sequence. $\overline{\text{T/A}}$ remains LO until the transition on $\text{FWD}/\overline{\text{BWD}}$ (either a rising or falling

a)

DEFAULT				OUTSIDE/INSIDE = EN1/EN2 = RAMP/CONSTNT	
↓	\overline{UPR}	\overline{LWR}	$\overline{T/A}$	↓	\overline{LWR}
0	X	X	X	1	X
1	1	0	1	1	0
1	1	1	1	0	1
1	0	1	1	1	1
1	X	X	0	1	0

b)

DIR	\overline{LWR}	↓	BWDACC/FWDACC
0	0	1	DIR=0 → MOVE MIRROR BWD
0	1	0	DIR=1 → MOVE MIRROR FWD
1	0	0	
1	1	1	

Figure 3-28. Truth tables for the Window Detector.
(See text for details.)

edge) indicates that the turn-around is half over. At this point, $\overline{T/A}$ goes high to release the window detector from its effect. The window detector is then free to re-acquire fine feed-back in the opposite direction.

When a turn-around sequence is initiated, the ramp of the coarse reference must increase or decrease in accordance with the direction in which the mirror is moving. As described earlier, the $BWDACC/\overline{FWDACC}$ input of the coarse feed-back reference module controls the direction in which the reference ramps. $BWDACC/\overline{FWDACC}$ is derived from the signals DIR and \overline{LWR} .

The signal DIR dictates to the system the direction of mirror movement during scan mode operation. As indicated in the truth table in part b) of this figure, when $DIR = 0$ the mirror is to move in the forward direction. When $DIR = 1$, the system is to move in the backward direction. The signal \overline{LWR} is a slightly altered version of the lower threshold comparator output, $\overline{LWR'}$.

From the truth table in part a) of this figure, \overline{LWR} is the same as $\overline{LWR'}$ except that \overline{LWR} is cleared LO in response to $\overline{T/A}$ going LO. Thus, if $|V_{E2}'|$ is within the ± 75 mv window, then \overline{LWR} is HI. If $|V_{E2}'|$ decreases out of the bottom of the window, through the -175 mv threshold, \overline{LWR} undergoes a $1 \rightarrow 0$ transition. If $|V_{E2}'|$ increases out of the top of the window, \overline{LWR} remains LO. As an error signal, $|V_{E2}'|$ is uni-polar. Hence, for either direction of mirror travel, if $|V_{E2}'|$ crosses the lower threshold, thereby causing \overline{LWR} to go LO, this is an indication that the mirror is moving too slowly. Hence, if \overline{LWR} is HI, then the mirror is either moving with the correct velocity (as indicated by $OUTSIDE/\overline{INSIDE} = 0$), or too rapidly (as indicated by

OUTSIDE/INSIDE = 1). Note that if $\overline{T/A}$ is cleared LO, this clears \overline{LWR} . To the system it appears that the the mirror is moving too slowly. From the truth table in part b) of this figure, $\overline{BWDACC/FWDACC}$ is the exclusive-NOR output of **DIR** and \overline{LWR} . Consider the changes of these signals during the turn-around sequences of scan mode operation.

Assume that the mirror is moving in the forward direction. At some point in the recent past, **DIR** was set HI. The system is under fine feed-back control with $|v_{g2}'|$ within the window. Therefore $\overline{LWR} = 1$, and since **DIR** = 1, $\overline{BWDACC/FWDACC}$ is HI.

To initiate a turn-around sequence, $\overline{T/A}$ is cleared LO. This clears \overline{LWR} . Simultaneously, the signal that clears $\overline{T/A}$ ($\overline{NCNTR\ CNTOUT}$, to be discussed in the scan length control section of this chapter) also clears **DIR**. **DIR** = 0 indicates to the system that the mirror is to be moved in the backward direction.

At this point, as far as the system is concerned the situation is that the mirror is supposed to be moving in the backward direction. Because \overline{LWR} has been cleared LO (falsely) by the clearing of $\overline{T/A}$, the system also perceives that the velocity in the backward direction is too low. (Forgive the anthropomorphization. It aids in clarifying the operation of the system.) The appropriate action, then, since the mirror is supposed to be moving in the backward direction, and at present its velocity in that direction is too low, is to accelerate the mirror in the backward direction. Since at the initiation of the turn-around sequence, both **DIR** and \overline{LWR} were cleared LO, $\overline{BWDACC/FWDACC}$ remained high. Thus, if coarse feed-back was enabled,

the mirror would accelerate in the backward direction under this feed-back control.

When $\overline{T/A}$ went LO, $EN1/\overline{EN2}$ was set HI. Hence, coarse feed-back was enabled with the coarse feed-back reference ramping for backward acceleration. As the drive initially decelerates in the forward direction, $|V_{E2}'|$ decreases out of the bottom of the window. Half-way through the turn-around sequence, $\overline{T/A}$ is re-set HI. Since at this point, $|V_{E2}'|$ is well out of the window, \overline{LWR} remains LO. After the mirror has stopped and is accelerating in the backward direction, $|V_{E2}'|$ increases towards the lower threshold of the window detector. When it enters the window detector from below, \overline{LWR} is set HI, causing $EN1/\overline{EN2}$ to be cleared LO. Fine feed-back is acquired in the backward direction. This completes the turn-around sequence.

At the back end of the mirror travel a similar sequence of events occurs. When $\overline{T/A}$ signals a turn-around, DIR is set HI, and \overline{LWR} is once again cleared LO. This is an indication that the drive should be moving in the forward direction, and that its velocity is too low. This calls for an acceleration in the forward direction, accordingly $BWDACC/\overline{FWDACC}$ is cleared LO. The mirror accelerates in the forward direction under coarse feed-back. \overline{LWR} eventually increases past the lower threshold of the window detector, and fine feed-back is acquired in the forward direction.

Consider now what happens while the mirror is moving in the forward direction under fine feed-back control, and an external disturbance decelerates the mirror such that $|V_{E2}'|$ decreases out of the bottom of the window. During the last turn-around sequence, DIR was set HI, indicating to the system that the mirror is to move in the forward direction.

While $|V_{E2}'|$ was inside the window, \overline{LWR} was HI, and therefore, $\overline{BWDACC/FWDACC}$ was HI. When $|V_{E2}'|$ leaves through the bottom of the window, \overline{LWR} goes LO, and coarse feed-back is enabled. The mirror is moving too slowly in the forward direction. As \overline{LWR} is cleared, $\overline{BWDACC/FWDACC}$ is also cleared LO. Thus, as coarse feed-back is enabled, the coarse feed-back reference starts to ramp in the direction for acceleration in the forward direction. This ramping starts from the value of the reference that was required to accelerate the mirror under coarse feed-back, up to the fine feed-back velocity, during the last backward to forward turn-around sequence. As the mirror is accelerated under coarse feed-back, $|V_{E2}'|$ is driven back into the window until eventually, if it is possible, $|V_{E2}'|$ enters the window and fine feed-back is re-acquired. At this point \overline{LWR} is set HI, causing $\overline{BWDACC/FWDACC}$ to be once again set HI.

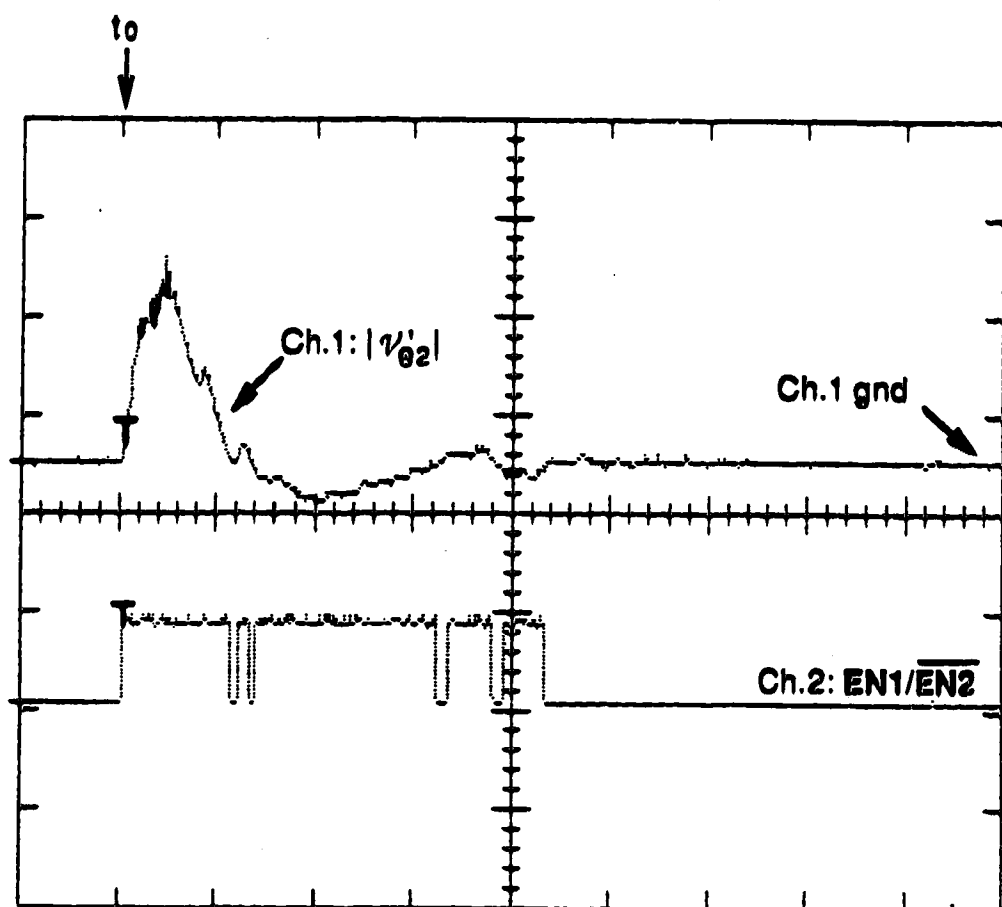
If an external disturbance accelerates the mirror, then $|V_{E2}'|$ increases out of the top of the window. Coarse feed-back is enabled but since $|V_{E2}'|$ increased through the upper threshold voltage, \overline{LWR} has remained unchanged as HI. To the system, the fine feed-back error signal has left the window, but not through the bottom, therefore it must have left through the top. Thus, the mirror is moving with too high a velocity in the forward direction. $\overline{BWDACC/FWDACC}$ has remained HI such that when coarse feed-back is enabled, the coarse feed-back reference starts to ramp for deceleration in the forward direction(acceleration in the backward direction). The coarse feed-back decelerates the mirror until $|V_{E2}'|$ enters the window once again from above. Fine feed-back is then re-acquired.

The sequences of events described above are illustrated in Figs 3-29 a,b, and c. These were obtained with the present system while the mirror was moving in the forward direction under fine feed-back control. In Fig. 3-29a, the top trace is $|V_{E2}'|$. $|V_{E2}'|$ is initially constant, with a value of zero, indicating that the mirror is moving with the fine feed-back velocity. In the bottom trace, $EN1/\overline{EN2}$ is initially LO, indicating that fine feed-back is in operation.

At time t_0 the mirror is accelerated by an external disturbance. $|V_{E2}'|$ initially increases out of the window. As a result, $EN1/\overline{EN2}$ is set HI, and coarse feed-back is enabled. As indicated in Fig. 3-29b, while $|V_{E2}'|$ is greater than zero (indicating that the velocity is too high) $BWDACC/\overline{FWDACC}$ remains HI. During this time the coarse feed-back reference ramps upward to decelerate the mirror in the forward direction. This is seen in the bottom trace of Fig. 3-29c. V_{REF1} ramps upward while $|V_{E2}'|$ is above zero volts.

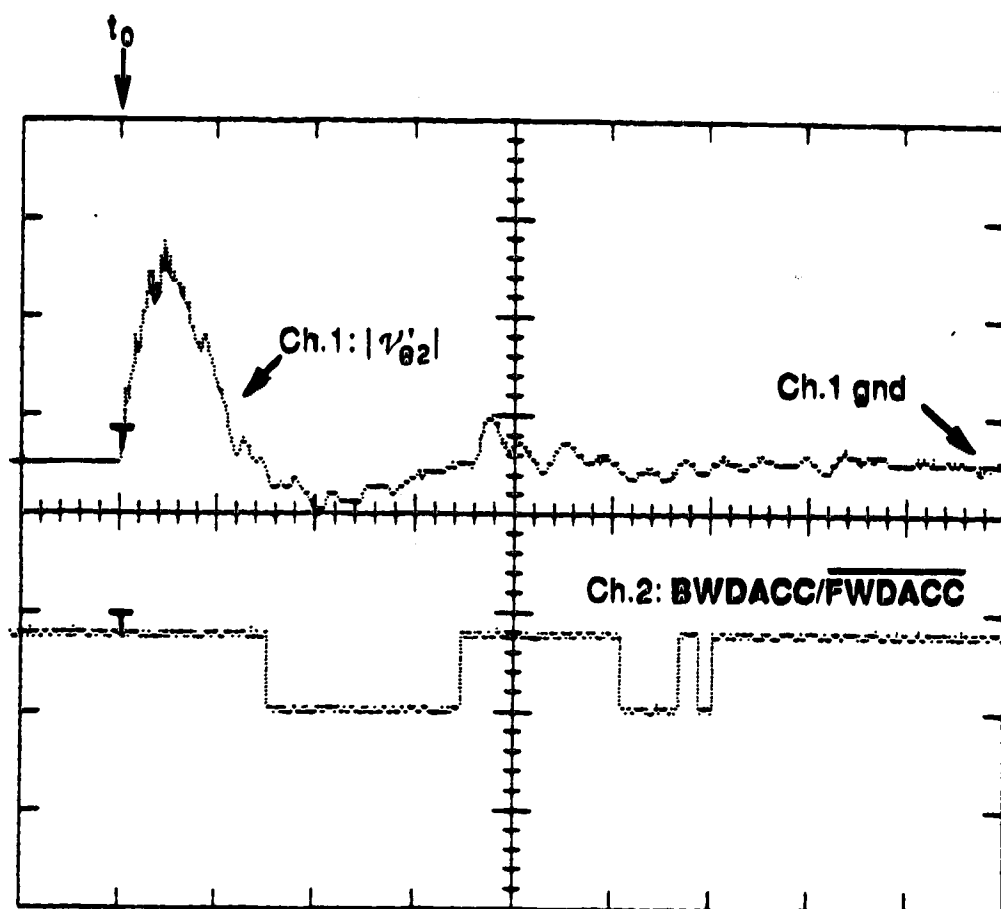
Referring back to the upper trace of Fig. 3-29a, coarse feed-back decelerates the mirror, driving $|V_{E2}'|$ back into the window. Some overshoot is observed as $|V_{E2}'|$ dips below zero volts. Coarse feed-back is once again enabled and, as evidenced in Figs. 3-29b and c, $BWDACC/\overline{FWDACC}$ is cleared LO, causing V_{REF1} to ramp downward to accelerate the mirror in the forward direction. As $|V_{E2}'|$ oscillates in and out of the window, the action of the coarse feed-back is to accelerate or decelerate the mirror such that this fine feed-back error signal is driven back into the window.

When moving in the backward direction, the same type of feed-back switching occurs during the response to a large enough external disturbance.



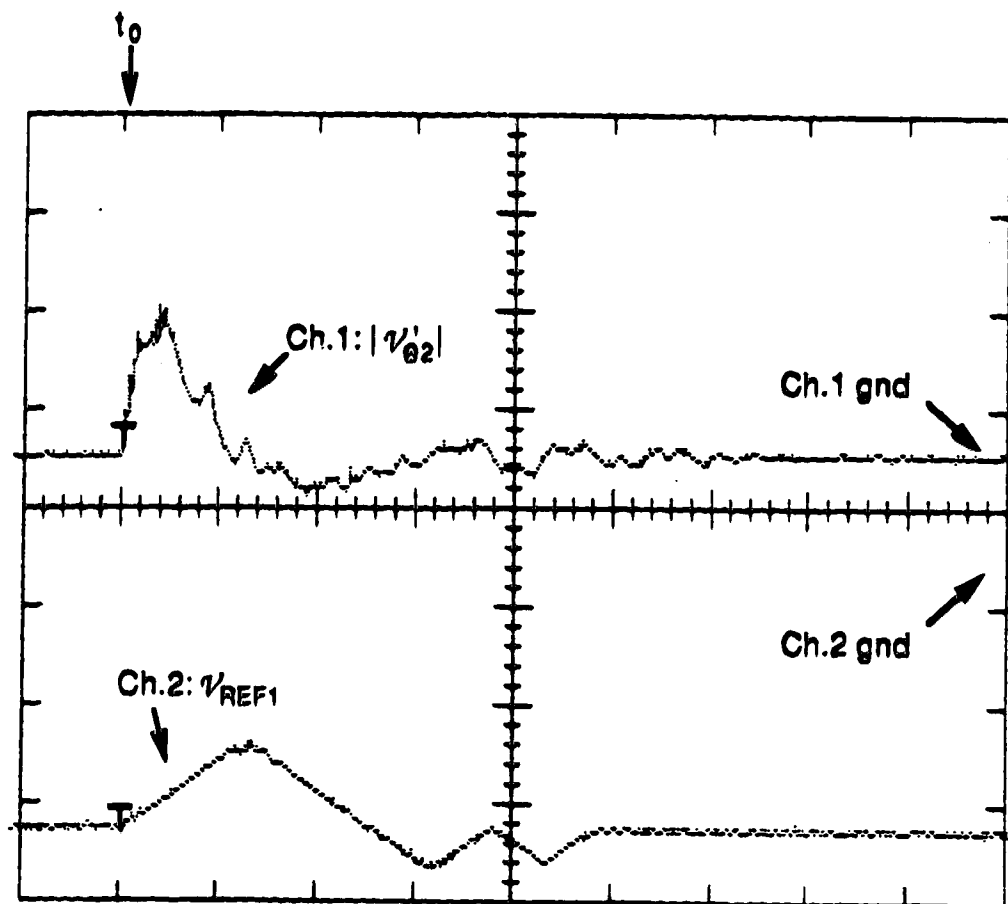
Trigger: Ch.2
 Time base: 10 ms/div
 Vert. gain: Ch.1: 1v/div
 Ch.2: 5v/div

Figure 3-29a. $|V'_{\theta 2}|$ and $EN1/\overline{EN2}$ during external disturbance.



Trigger: $\overline{\text{EN1/EN2}}$
 Time base: 10 ms/div
 Vert. gain: Ch.1: 1v/div
 Ch.2: 5v/div

Figure 3-29b. $|v'_{\theta 2}|$ and $\overline{\text{BWDACC/FWDACC}}$ during external disturbance.



Trigger: $\overline{EN1/EN2}$
 Time base: 10 ms/div
 Vert. gain: Ch.1: 1v/div
 Ch.2: 5v/div

Figure 3-29c. $|V'_{\theta 2}|$ and V_{REF1} during external disturbance.

In summary, the feed-back switching system is designed such that if the fine feed-back error signal ever leaves the window, coarse feed-back is enabled to drive the system back towards re-acquisition of fine feed-back. During turn-around sequences, coarse feed-back is enabled, and false signals are applied to the system such that it appears that the mirror is moving too slowly in the opposite direction. The coarse feed-back then drives the system towards re-acquisition of fine feed-back in the opposite direction of movement.

While in the data acquisition portion of a scan, the present feed-back switching system is in its most stable configuration when the mirror is moving in a particular direction under fine feed-back control. Any other condition is non-stable. If an external agent moves the system away from this stable condition, then when the agent is removed, the system drives back towards the re-acquisition of fine feed-back in that particular direction.

In a previous version of the feed-back switching system, when in the scan mode, coarse feed-back was enabled only during the turn-around portion of the scan. The method of re-acquiring fine feed-back after the turn-around was basically the same as the present system, involving the window detector in the same manner. During the data acquisition portion of the scan, however, fine feed-back was active, regardless of the value of $|V_{E2}'|$. By virtue of the servo-action of the fine feed-back loop, the system was still in a stable configuration when the mass was moving with the fine feed-back velocity. However, if a disturbance momentarily caused the direction of mirror movement to be reversed, it was often observed that the mirror would then accelerate up to the correct fine feed-back velocity in the opposite direction. Thus the previous system had more than one stable configuration.

In principle, with the present system such a drive reversal cannot occur and indeed has not been observed to date.

3-1.3. Moving mirror scan length control system.

To control the scanning of the mirror during scan mode operation, the position of the mirror at any given time must be known. In the present system, this is achieved by first defining a reference point within the travel of the mirror. At some point in time, the mirror is situated at this reference position. As the mirror is moved away from the reference position, periods of the reference laser interferogram are counted. In this fashion, the position of the mirror is known at all times to within one period of the reference fringe.

Periods of the reference laser interferogram are signalled by detecting the zero-crossings of the ac-coupled fringe signal. Zero-crossings occur every half period of the fringe; hence, starting from a particular zero-crossing, the next zero-crossing occurs when the mirror has moved $0.1582 \mu\text{m}$. In the present system whole periods of the fringe are counted, therefore every second zero-crossing is counted. Thus, the mirror position count is up-dated every $0.3164 \mu\text{m}$ of mirror movement.

The scheme that is employed in the present system to keep track of the fringe period number with respect to a reference point is illustrated in the flow diagram of Fig. 3-30. The diagrams on the left side of this figure illustrate the positions of mirror travel at which the various events described on the right occur. For convenience, only a portion of the moving mirror

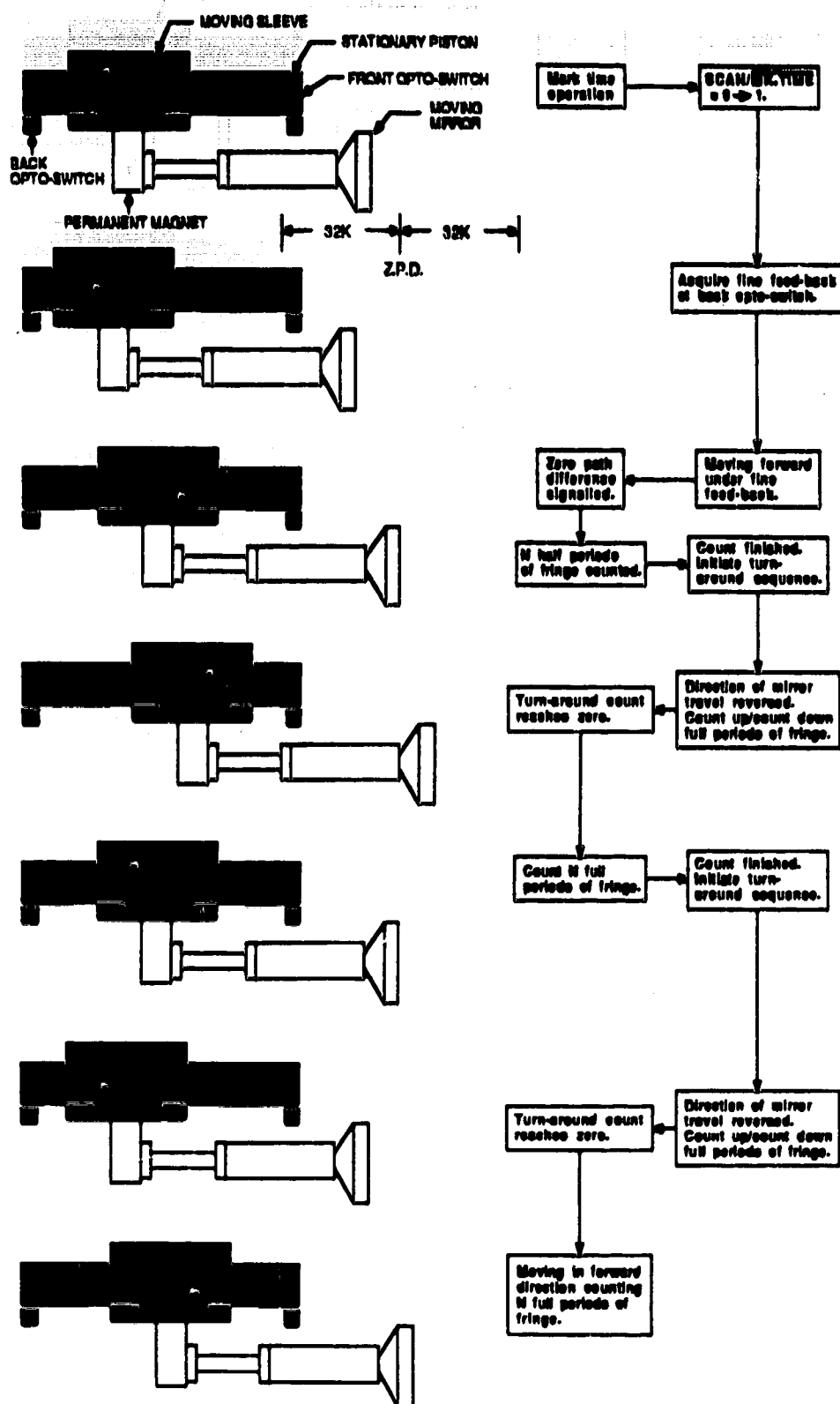


Figure 3-30. Fringe counting sequences during scan mode operation.

assembly is shown. Not shown are the drive coils, and one of the permanent magnet pole faces.

As indicated in this figure, the mirror travels a maximum of 32,768 full periods of the reference fringe to either side of the reference position for a full travel of 2.07 cm. In this system, the reference point is located very nearly at the position of Zero Path Difference (ZPD). At this point, the optical path lengths in the fixed and moving mirror arms of the interferometer are equal. For a continuum source, this is the position at which the grand maximum (central burst) of the interferogram occurs. ZPD defines the center of a symmetric double-sided interferogram.

Consider that the system has been successfully powered up and is operating in the mark time mode. The mirror is cycling back and forth between the two opto-switches, under coarse feed-back control. To initiate scan mode operation, $\overline{\text{SCAN/MK.TIME}}$ is set HI. The mirror continues cycling under coarse feed-back until the next time that the back opto-switch is blocked. When this occurs, the mirror is stopped, and then accelerated in the forward direction under coarse feed-back control. Eventually, fine feed-back is acquired. Thus, at this point the mirror is moving forward under fine feed-back control.

Eventually, the mirror traverses the position of ZPD. This point is signalled, and a counter begins counting out one-half of a data acquisition scan. To do this, every half period of the fringe is counted. If the number of half periods counted is, N , then upon completion of this count the mirror will have moved, $N \times 0.1582 \mu\text{m}$, from the position of ZPD. At this point $\overline{\text{T/A}}$ is cleared LO to initiate a turn-around sequence.

During the turn-around sequence, full periods of the fringe are counted as the mirror is decelerated in the forward direction, stopped, and then accelerated in the backward direction. These fringe periods are counted with an up/down counter such that periods can be added to, or subtracted from, the turn-around count. Starting from zero at the time when $\overline{T/A}$ goes LO, the turn-around count increases until the end of forward travel (i.e. the mirror has stopped) is indicated by the 1→0 transition of FWD/\overline{BWD} . After this, fringe periods are subtracted from the turn-around count. In this way, the turn-around count re-traces the steps in mirror movement that occurred during the first half of the turn-around sequence.

When the turn-around count reaches zero, the mirror has returned to the point at which the turn-around sequence was started. Thus, the position of the mirror with respect to the position of ZPD is still known, even after the direction of mirror travel has been reversed. As a result, the reference position signal can now be ignored. It is only required to symmetrically position data acquisition scans about the ZPD position.

When the turn-around counter reaches zero, the scan counter begins to count N complete fringe periods in the backward direction. The mirror moves $N \times 0.3164 \mu\text{m}$, at which point $\overline{T/A}$ is again cleared LO to initiate another turn-around sequence. Since the scan counter has been counting full periods, the mirror will have moved twice the distance that it did during the first scan count, in which half periods of the fringe were counted. Hence, half of the count is finished when the position of ZPD is reached, and the second half is completed after traversing this position. Therefore, the scan is symmetric about the position of ZPD.

The backward to forward turn-around sequence is counted in the same manner as the previous one. When the turn-around count reaches zero, the scan counter again counts N full periods of the fringe. When this is complete, a turn-around sequence is initiated. The system continues in this cycle during scan mode operation.

The reference position in the present system is defined by the "white light" signal. This is the maximum of the interferogram of a tungsten filament light bulb. Since this maximum occurs very close to the position of Z.P.D., the white light signal essentially defines the middle position of a data acquisition scan.

Typical white light and HeNe reference laser interferograms are shown in Fig. 3-31. The tungsten bulb, being a continuum source, is broad in the time domain and therefore narrow in the frequency domain. The opposite is true for the narrow line-width laser source. Note that the grand maximum of the white light interferogram doesn't line up exactly with a peak in the reference fringe. (Due to the relatively long coherence length of the laser radiation, it is difficult to discern which of the maxima is the grand maximum.) In principle, the grand maxima of the two interferograms should line up since ZPD should occur at the same mirror position for all wavelengths.

The most significant cause of the observed phase difference is probably the fact that the optical axis of the white light signal passes through the top of the beam-splitter, while that of the laser passes through the bottom. When the fixed mirror is adjusted slightly to maximize the white light (or source) interferogram, the optical path of the laser can be changed in the opposite

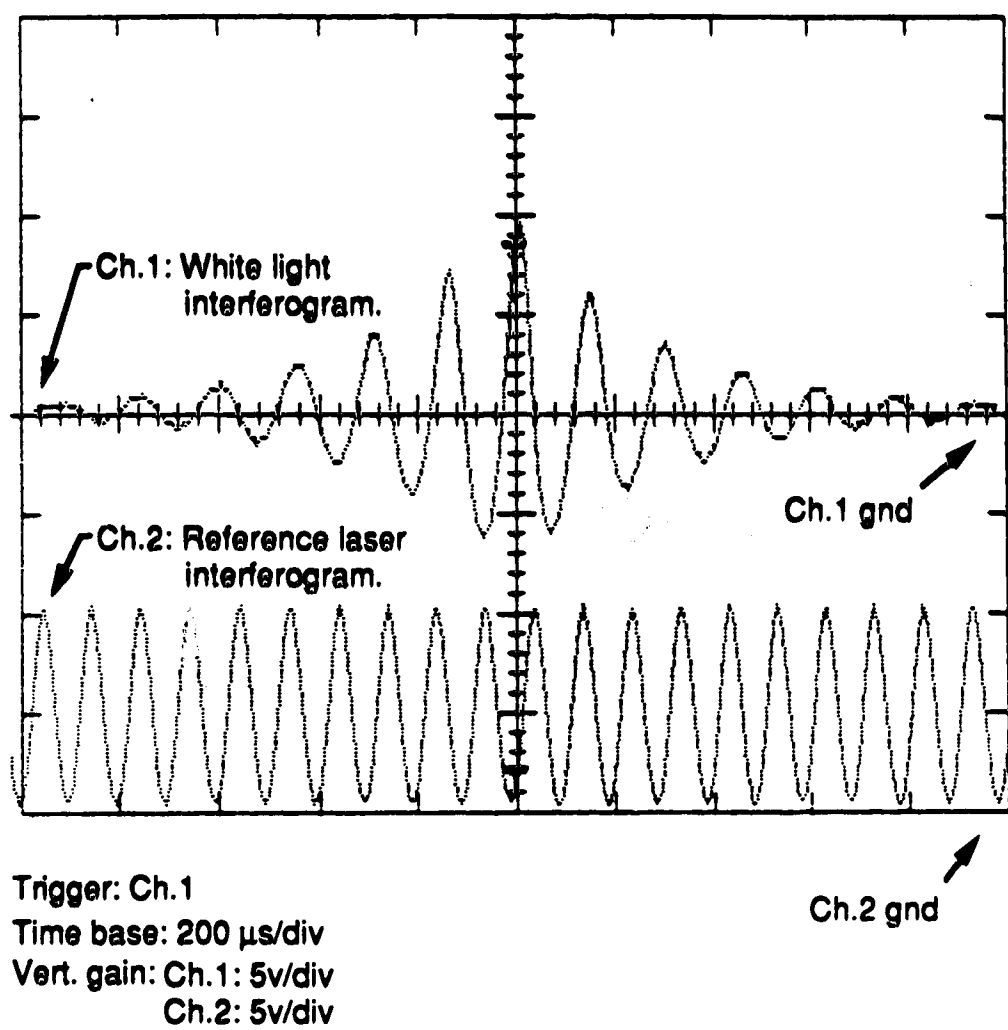


Figure 3-31. White light and reference laser interferograms.

direction to that of the white light. That is, if the top of the fixed mirror is tilted forward, the optical path of the white light is slightly shortened, while that of the laser is slightly lengthened. If this adjustment is not too great, the effect is to shift the phases of the two interferograms relative to each other. As well (but probably to a lesser extent), dispersion of the beam-splitter, coupled with the slightly un-equal thicknesses of the beam-splitter and compensator, could contribute to this phenomenon.

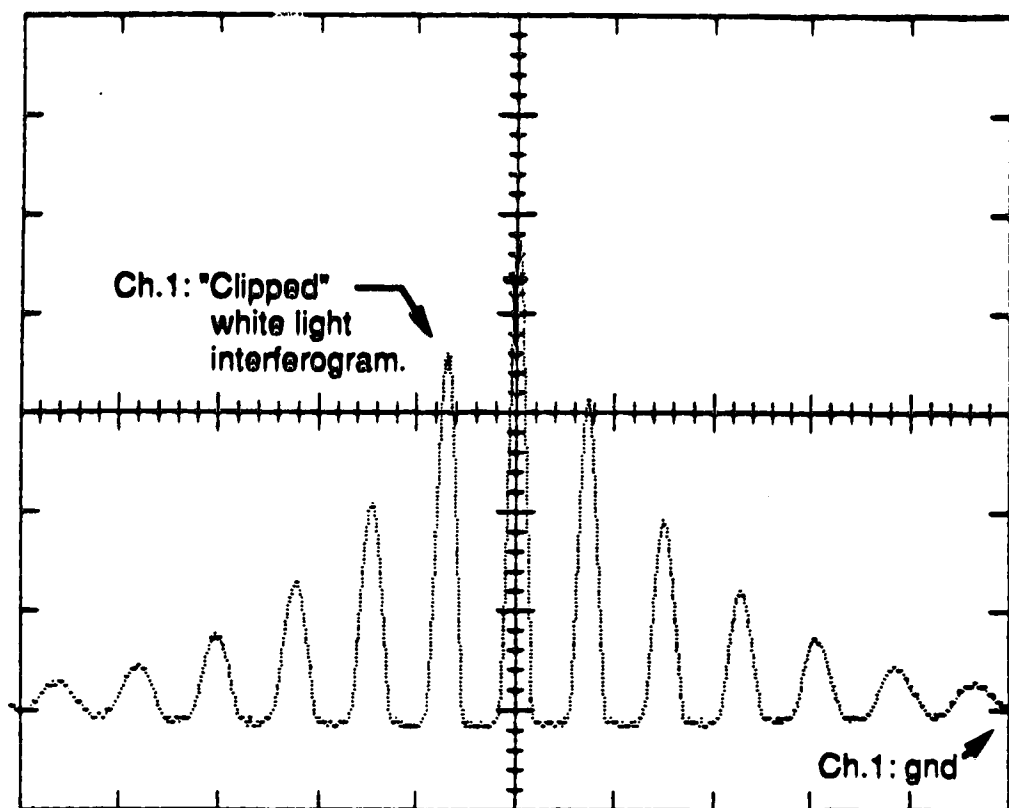
The difference in phase between the white light and laser does not present a problem. What is important is that the phase difference between the signal and reference laser interferograms remains constant during signal averaging. (After the initial set-up scan, the white light can be ignored.) As a result of thermal drift of the optical hardware, the position of ZPD for the signal interferogram could shift with respect to the scan defined by the fringe counting. This would be equivalent to signal averaging interferograms with drifting phases with respect to the position of Z.P.D., and hence with respect to each other.

The white light interferogram is used to produce a digital signal which indicates that the position of ZPD has been reached. One method of achieving this [15] has been to input the white light into a comparator circuit. The threshold voltage is set high enough that the comparator fires at a voltage close to that of the grand maximum of the white light interferogram. However, as indicated in Fig. 3-31, there are two peaks, with large relative amplitudes, on either side of the grand maximum. If the overall magnitude of the white light interferogram changes due to drift, or fixed mirror adjustment to maximize the signal interferogram, then the situation can arise wherein these peaks also cause the comparator to fire. This confuses the

detection of the position of ZPD. To remedy this situation, the white light interferogram in the present system is processed to increase the height of the grand maximum relative to that of the side peaks.

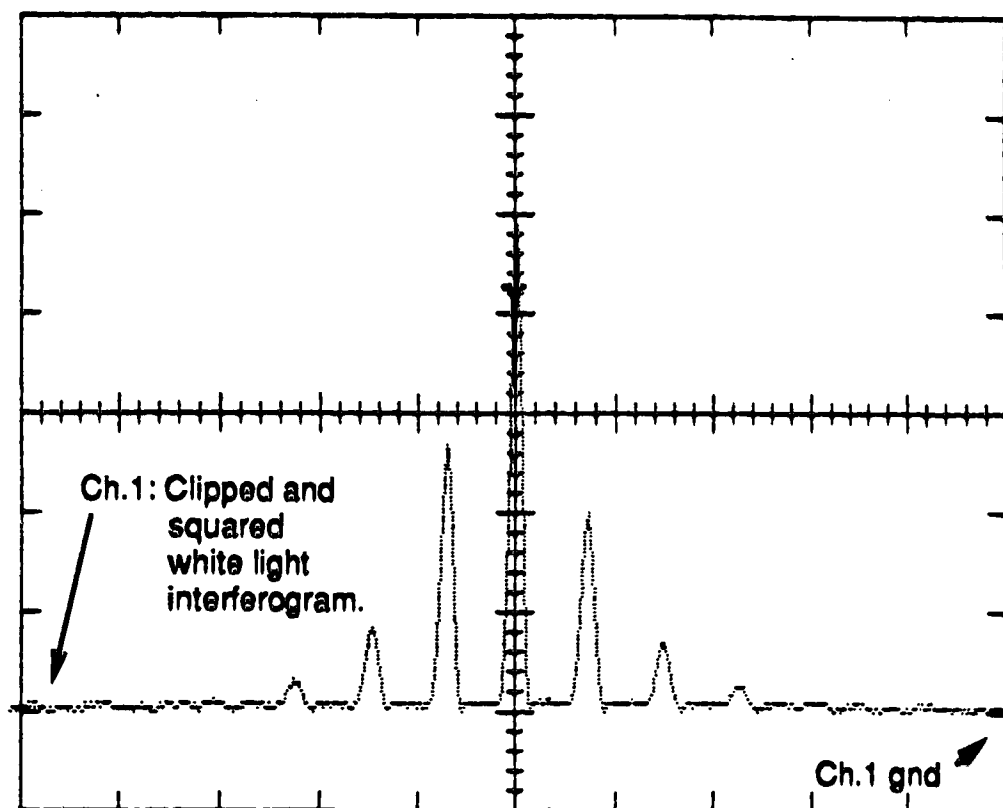
In the first level of processing, the white light signal is ac-coupled and the negative portion of the signal is removed with a diode clipping circuit. As shown in Fig. 3-32, the grand maximum has an amplitude of approximately 9v., while the two side peaks are approximately 6.4 and 7 v in height. Simply amplifying the white light signal increases the difference between the heights of the grand maximum and the side peaks, but to further increase this difference, a monolithic analog multiplication circuit (EXAR 2208 CP) is used to square the clipped output. The output of the squaring circuit is shown in Fig. 3-33. Now, the grand maximum still has an amplitude of approximately 9 v (the output is normalized to the maximum value of the input), but the side peaks are approximately 5.4 and 4 v. This signal is input into a comparator with a threshold voltage of 7 v. The amplitude of the side peaks would have to increase by at least 1.5 v to cause spurious firings of the comparator. This situation has not been observed to date with the present system. The comparator output is input into a monostable multi-vibrator to produce the digital pulse, WL_p , shown in Fig. 3-34.

The signal that is used for fringe counting is a square wave representation of the reference laser interferogram. This is produced in a manner similar to that described previously for the production of the signal, FRINJ. It has been found that the rate of change of the reference laser fringe is large enough that no hysteresis is required in producing FRINJ. Hysteresis in producing FRINJ is undesirable, as this signal is used as the input for the F/V



Trigger: Ch.1
Time base: 200 μ s/div
Vert. gain: Ch.1: 2v/div

Figure 3-32. "Clipped" white light interferogram.



Trigger: Ch.1
Time base: 200 μ s/div
Vert. gain: Ch.1: 2v/div

Figure 3-33. Clipped and squared white light interferograms.

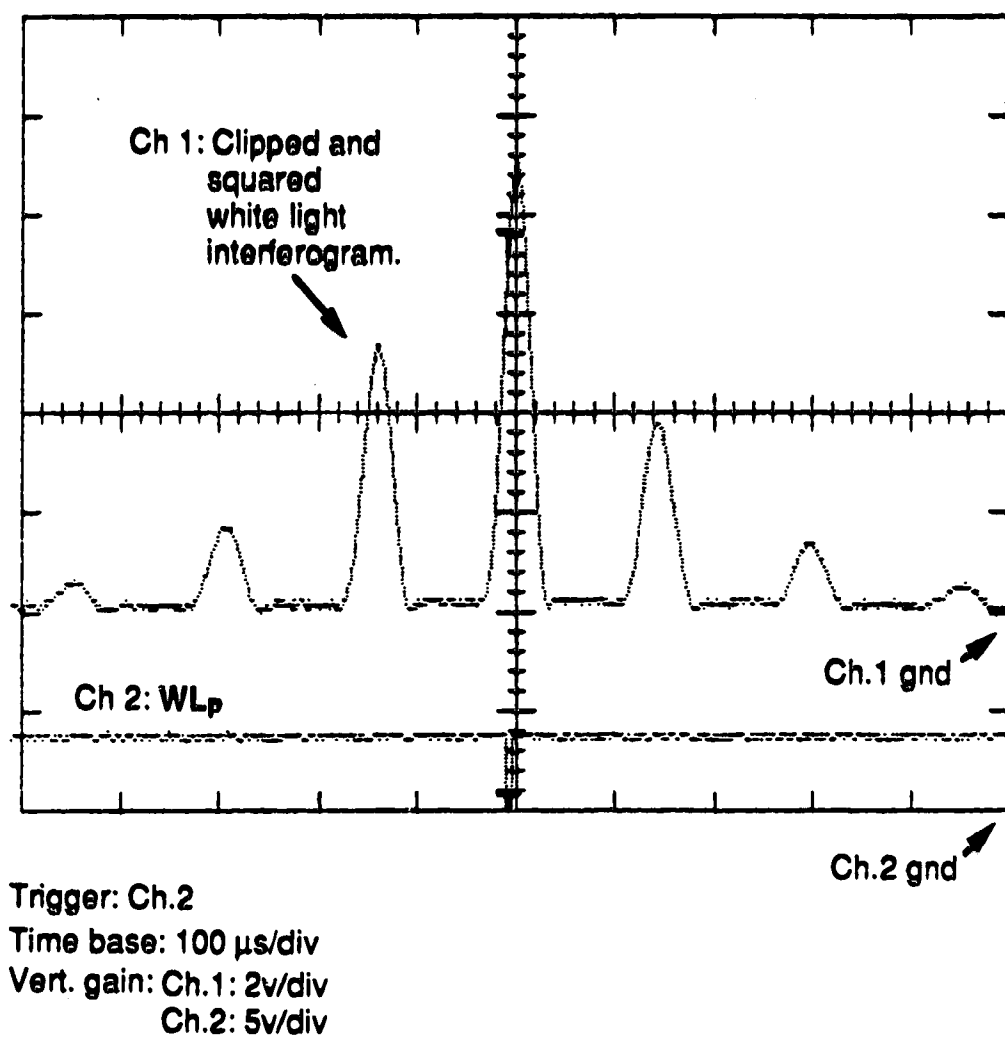
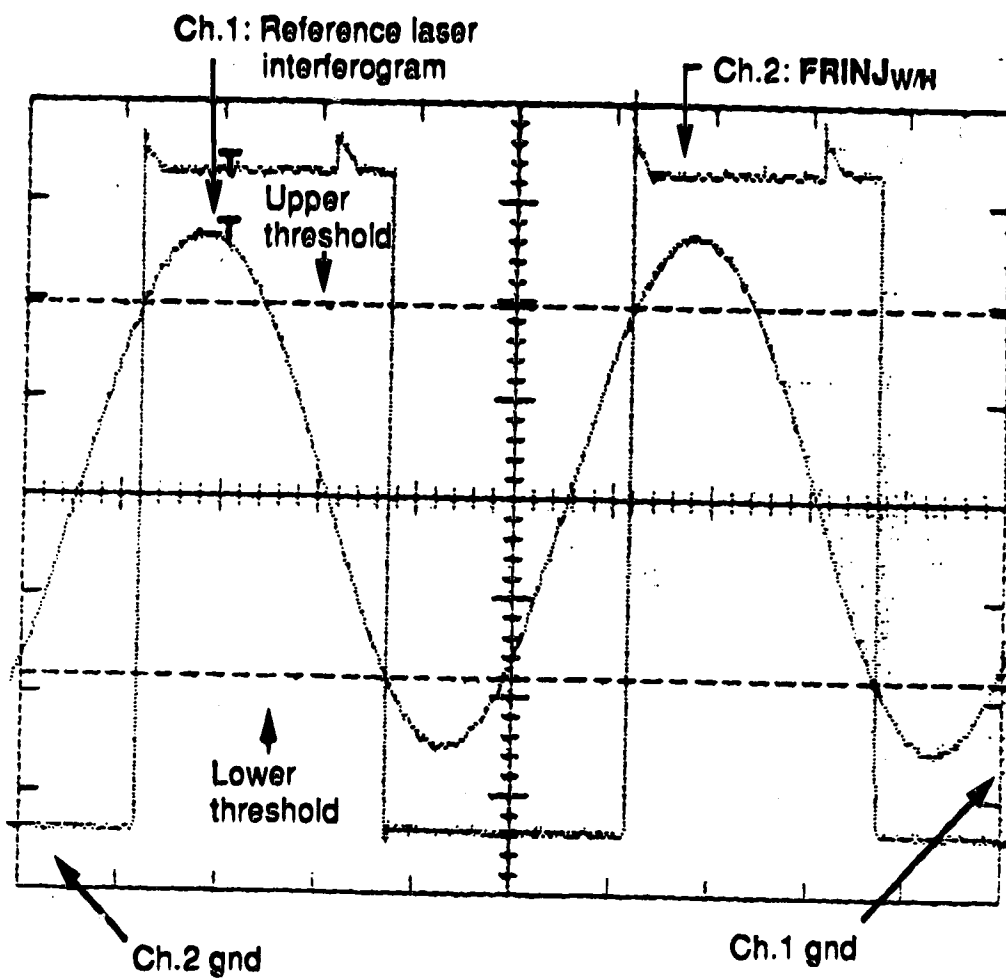


Figure 3-34. Processed white light interferogram and WL_p.

converter in the fine feed-back loop, and to generate the ADC clock. However, **FRINJ** is unsuitable for use in the fringe counting system. Instead, a square wave representation of the dc-coupled analog fringe is generated using a comparator circuit in which hysteresis is employed. This signal, designated as, **FRINJ_{W/H}**, is shown in Fig. 3-35. The center of the hysteresis loop is set at the dc level of the dc-coupled analog fringe input. The width of the hysteresis loop is approximately 6.25 v. As indicated in this figure, due to the hysteresis, **FRINJ_{W/H}** lags the analog fringe signal. The lag is the same for both directions of mirror travel. Since **FRINJ** is in phase with the analog fringe, the effect of the hysteresis in the circuit is to delay the transitions of **FRINJ_{W/H}** with respect to those of **FRINJ**. The need for hysteresis lies in the nature of the turn-around sequence at the end of each data acquisition scan.

The analog fringe, **FRINJ**, and **FRINJ_{W/H}** during a forward to backward turn-around sequence are illustrated schematically in Fig. 3-36. Shown in part a) of this figure is a calculated version of the analog fringe during reversal of the direction of mirror travel. Since the frequency of the fringe is directly proportional to the velocity of the mirror, the fringe during drive reversal is a frequency modulated sine wave. The frequency of the fringe is modulated from 10 kHz to zero, and back to 10 kHz. In this diagram, the distance over which the mirror travel is reversed is abbreviated. In actual operation, approximately 150 periods of the analog fringe are required to turn the drive around. This is a distance of approximately 47 μm .

The dc-level of the fringe is indicated. Upon ac-coupling, this becomes the zero level for the signal. **FRINJ**, as it would be produced by a zero crossing detector, is shown in part b). It can be seen that if **FRINJ** were generated by a perfect zero-crossing detector with no hysteresis or delays, rising transitions



Trigger: Ext.1: WL_p (+slope)

Time base: $20 \mu s/div$

Vert. gain: Ch.1: $2v/div$

Ch.2: $500 mv/div$

Figure 3-35. Reference laser interferogram and $FRINJ_{w/h}$.

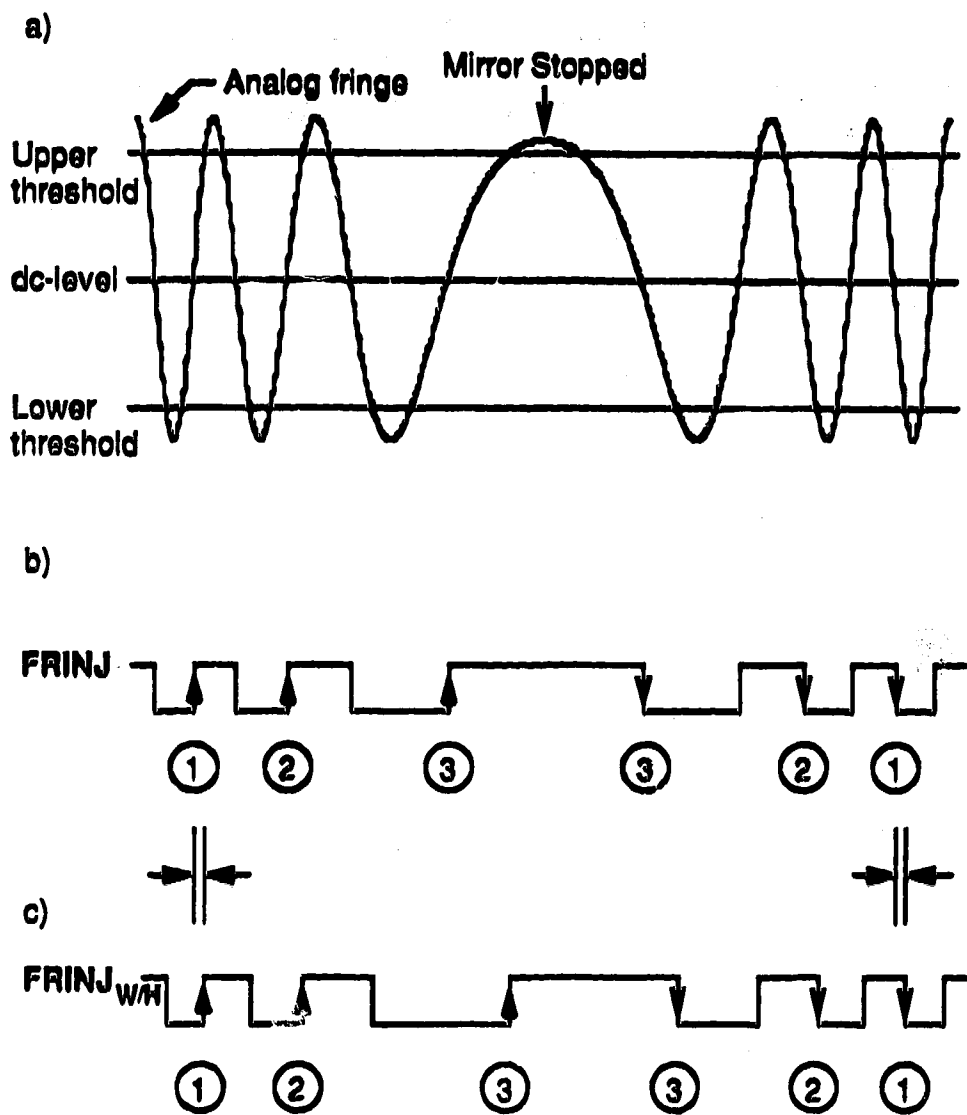


Figure 3-36. Fringe counting during a typical turn-around sequence.
a) Analogfringe. b) FRINJ. c) FRINJ_{W/H}.

that occurred during forward movement would correspond to falling edges generated while the mirror moved backwards. Thus, to know when the mirror has returned to the position of optical retardation at which the forward to backward turn-around sequence was started, the turn-around counter should increment on rising edges before the mirror has stopped, and decrement on falling edges afterwards.

$FRINJ_{W/H}$ is shown in part c) of this figure. Note the delay of the transitions of $FRINJ_{W/H}$, with respect to those of $FRINJ$. The delay is the same before and after the drive has been reversed. As a result of the hysteresis, the positions of optical retardation that produce rising edges during movement in one direction, do not correspond exactly to those which produce falling edges while the mirror moves in the opposite direction. As will be shown, this is not a problem. $FRINJ_{W/H}$ is used for fringe counting, while $FRINJ$ is used to generate the ADC clock. After a turn-around sequence, $FRINJ_{W/H}$ does not return to exactly the position at which the turn-around was started. $FRINJ$, however, does.

A more detailed illustration of the turn-around counting scheme during a forward to backward turn-around sequence is shown in Fig. 3-37. Both the analog fringe and $FRINJ$ are shown in parts a) and b) of this figure. As mentioned previously, $FRINJ_{W/H}$ is used for fringe counting. For the situations illustrated here, hysteresis is not required and the fringe counting scheme can be adequately described using $FRINJ$. This will aid in clarifying the need for hysteresis.

The turn-around sequence shown in Fig. 3-36 is continuous in time, from left to right on the page. Half of the trace is redundant. To save space

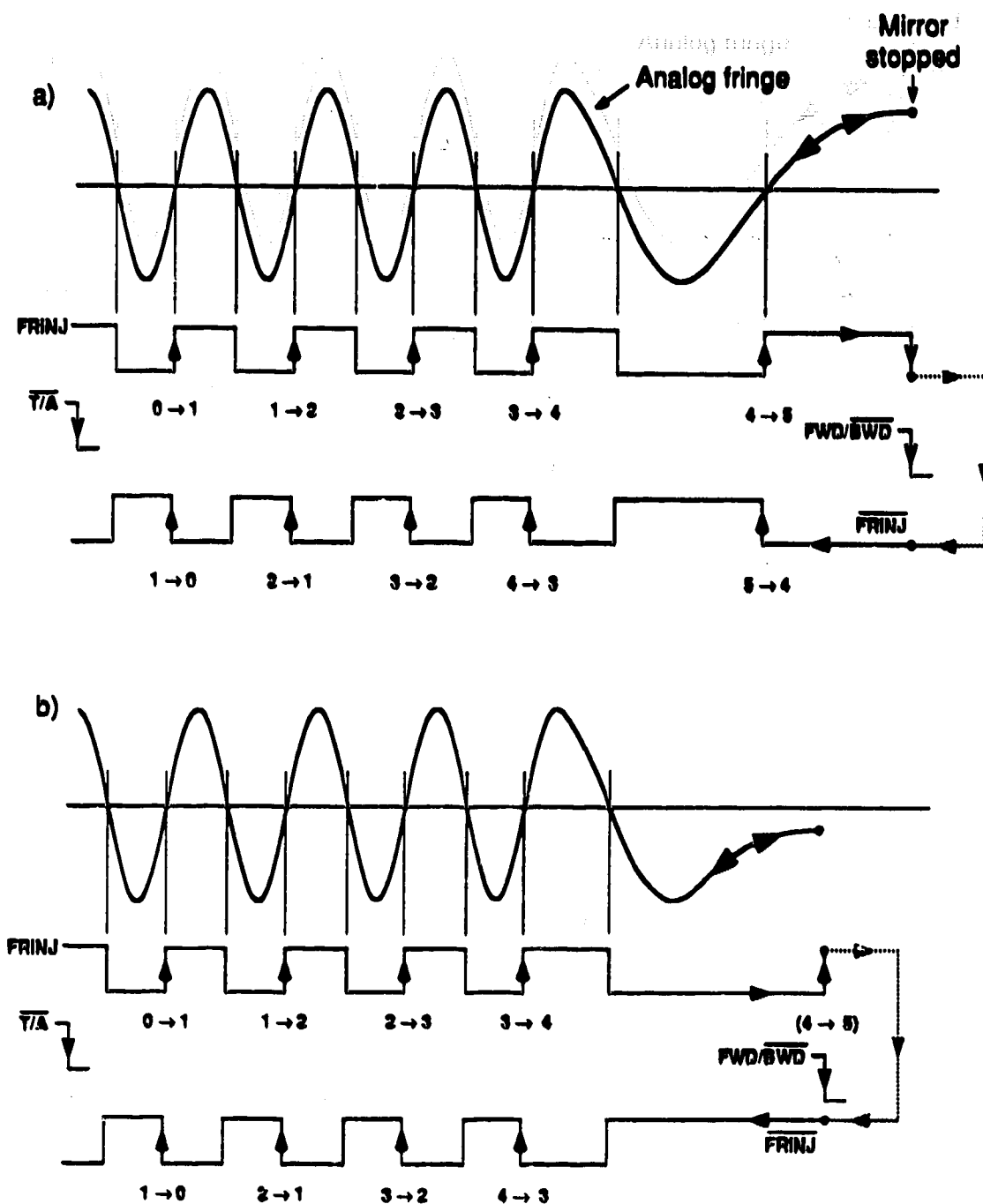


Figure 3-37. Typical turn-around counting sequences with FRINJ for fringe counting. Determinate cases: a) Analog fringe voltage well above threshold when mirror stopped. b) Analog fringe voltage well below threshold voltage when mirror stopped. (See text for details.)

and improve detail, the two analog fringes in Fig. 3-37, are continuous from left to right, and then from right to left. A complete turn-around sequence consists of tracing the analog fringe from left to right; then re-tracing from right to left. The digital representations of the analog fringe are separated into forward and backward parts. A complete turn-around sequence is followed by tracing the upper representation of FRINJ from left to right, and then tracing the lower one from right to left. In subsequent diagrams in this thesis, drive reversals are represented in this manner.

In part a) of Fig. 3-37, the turn-around sequence is initiated by the clearing of $\overline{T/A}$. In the present system, the digital counters that are used for fringe counting are triggered by rising edges at their clock inputs. Thus, on the first rising edge of FRINJ, the turn-around counter increments from 0→1. Subsequent rising edges increment the counter until the count increments from 4→5. Shortly after this count, the mirror stops moving, as indicated by the dot on the trace. In principle, at this point FWD/\overline{BWD} undergoes a 1→0 transition, signalling that the drive has stopped. This is the signal that the turn-around counter should now decrement on falling edges of FRINJ. After the direction of mirror motion has been reversed, the falling edges of FRINJ correspond to the rising edges that occurred while the mirror was moving in the forward direction. By complementing FRINJ, the falling edges are turned into rising edges. Therefore, after the transition of FWD/\overline{BWD} , the turn-around counter is decremented with \overline{FRINJ} as the clocking input. As can be seen from this part of the figure, the turn-around counter reaches zero at the mirror position at which the turn-around count was started.

In part b) of this figure, a slightly different turn-around sequence is illustrated. In this case, the last transition of FRINJ, before that of

$\overline{\text{FWD/BWD}}$ is a falling edge. Note that when FWD/BWD fires, the complementing of FRINJ produces a rising edge. Such edges that occur due to the complementing of FRINJ should not be (and are not) counted. The brackets of the increment, (4→5), signify that this edge is not counted. As can be seen, the turn-around counter reaches zero at the position of optical retardation at which the turn-around sequence was initiated. In this situation, the turn-around count only reaches a value of 4 before the counter is decremented.

The timing of the transition of FWD/BWD is critical to the success of this fringe counting scheme. For turn-around counting to be successful, each rising edge of FRINJ that has been counted before the mirror has stopped has to be subtracted on the way back as the mirror accelerates in the opposite direction. In the situations illustrated in Fig. 3-37, the transitions of FWD/BWD with respect to the transitions of FRINJ are well-characterised. The turn-around counting proceeds correctly for both sequences. This is usually the case. However, if the fringe voltage just reaches the threshold voltage as the mirror is being stopped, the timing of the edges of FRINJ with respect to FWD/BWD becomes indeterminate. In this case, turn-around counting will often proceed incorrectly. This is illustrated in Fig. 3-38.

Represented in this figure is the situation in which the analog fringe voltage reaches the zero volt level (the threshold voltage level) at the same time as forward motion of the mirror is stopped. The transition of FWD/BWD , with respect to the time at which the mirror has stopped moving, is subject to some variation. Consequently, the relative timing of the transitions of FRINJ and FWD/BWD , is unknown in this situation. In this figure, the point at which the mirror has stopped moving is greatly

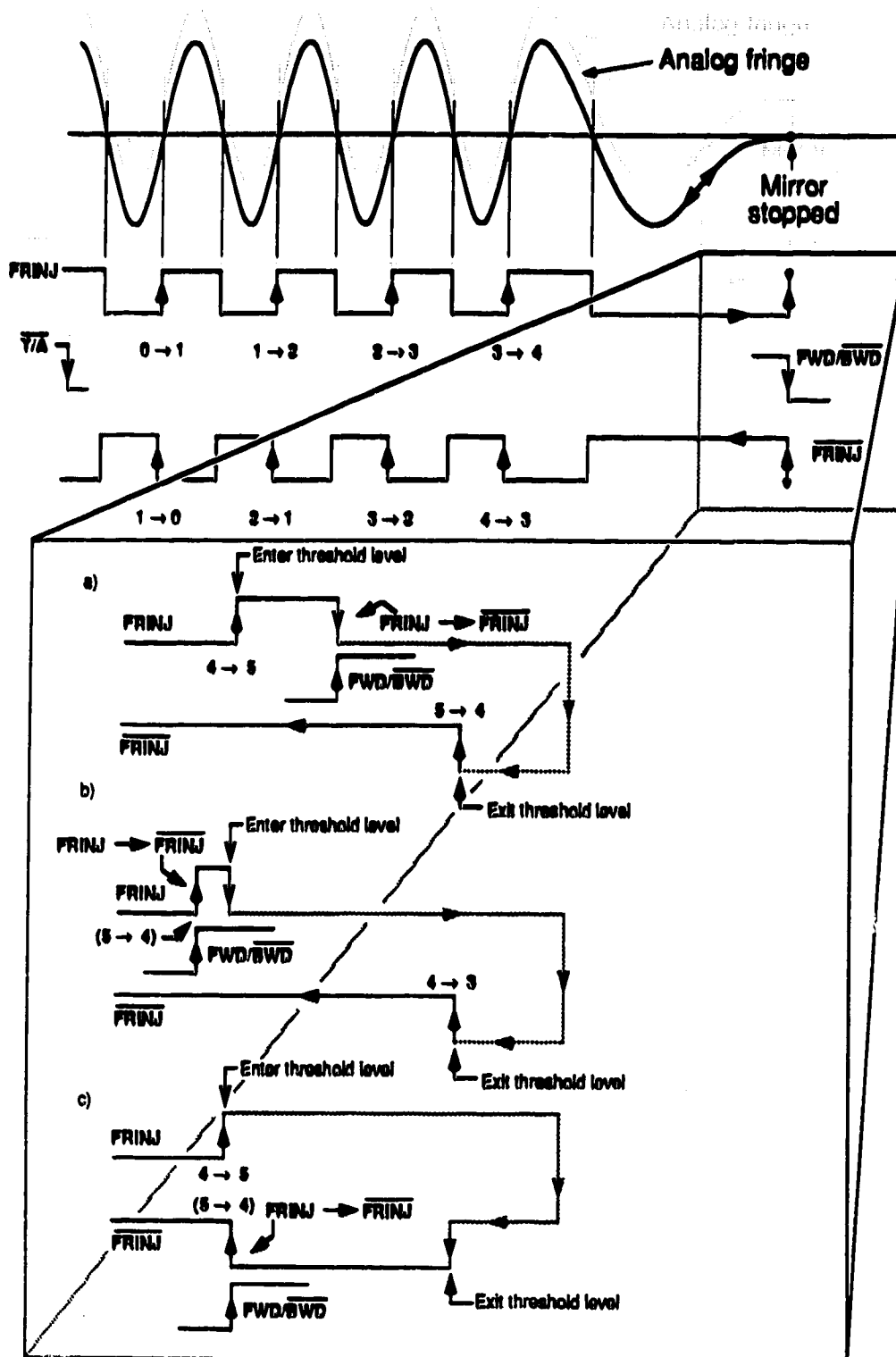


Figure 3-38. Turn-around counting sequence with **FRINJ** for fringe counting. Indeterminate case: Analog fringe voltage just reaches threshold voltage when mirror is stopped. (See text for details.)

expanded with respect to the time scale. The events illustrated should be occurring on the nano- to micro-second time scale. Three of a number of possible timing sequences are illustrated.

In part a) of this figure, the analog fringe voltage has entered the threshold region of the comparator before the transition of FWD/\overline{BWD} has occurred. This final increment brings the fringe count to a value of 5. While the mirror is stationary, FWD/\overline{BWD} fires. This complements $FRINJ$. As the mirror starts to move in the backward direction, the analog fringe voltage moves out of the zero volt threshold region. This causes a $1 \rightarrow 0$ transition of $FRINJ$; however, the turn-around counter is by this time decrementing on \overline{FRINJ} . Therefore, this rising edge decrements the turn-around count by one, and the rest of the count occurs correctly.

In part b) of this figure, the transition of FWD/\overline{BWD} occurs a short period of time before the analog fringe voltage enters the threshold region. After this point the turn-around counter is decremented on \overline{FRINJ} . The rising transition that occurs as a result of complementing $FRINJ$ is ignored by the counter. When the mirror accelerates in the backward direction, the analog fringe voltage leaves the threshold region, and the resultant rising transition decrements the counter by one count. This is too soon for correct turn-around counting. The turn-around counter reaches zero one full period of the fringe before it should. The interferogram that is digitized on this backward scan is one period of the fringe out of phase with respect to the properly digitized interferograms it is to be averaged with.

In part c), the mirror has been stopped, and is now moving in the backward direction at the time when FWD/\overline{BWD} fires. The analog fringe

voltage enters and leaves the threshold region before the transition of FWD/\overline{BWD} occurs. As can be seen, an extra increment results. Therefore, when the turn-around count is decremented, the mirror will have to travel one extra period of the fringe until the count reaches zero. Again, this introduces a one fringe period phase shift into the interferogram that is digitized on this backward scan.

As illustrated in the examples of Fig. 3-38, a potential problem exists if $FRINJ$ is used as the turn-around counter clock signal, when the analog fringe voltage just reaches the threshold voltage as the mirror is being stopped. The crux of this situation is as follows.

In the examples shown so far, it can be seen that two criteria must be met for correct turn-around fringe counting. When the mirror is decelerating to a stop, the last edge (before the mirror has come to a complete stop) of the digital representation of the analog fringe must occur before the transition of FWD/\overline{BWD} . During acceleration of the mirror in the opposite direction the first edge that occurs must do so after the transition of FWD/\overline{BWD} . In other words, these two transitions must bracket the transition of FWD/\overline{BWD} . For this reason, these two transitions are collectively called the "bracket" of the turn-around count. A positive bracket consists of a rising transition followed by a falling one. A negative bracket is the opposite of this.

In the sequences shown in Fig. 3-37, since the analog fringe voltage is not close to the threshold voltage (after having just crossed it) when the mirror is stopped, the brackets of these sequences are wide. Thus, some leeway is afforded in the timing of the transition of FWD/\overline{BWD} . However, as illustrated in the sequences shown in Fig. 3-38, when the analog fringe

voltage barely crosses the threshold voltage as the mirror is being stopped, the resulting brackets are closely spaced in time. As described above, the situation arises that the transition of FWD/\overline{BWD} can occur outside of the bracket, resulting in erroneous counting. It is possible, through the use of hysteresis, to set a limit on the minimum width of the bracket of the turn-around sequence. This is shown in Fig. 3-39 and Fig. 3-40.

These two figures are digital oscilloscope traces of the analog fringe voltage and $FRINJ_{W/H}$ during two separate backward to forward turn-around sequences. Shown in these figures are the minimum positive and negative brackets, respectively. FWD/\overline{BWD} was used to trigger the oscilloscope. This is indicated by the "T" on the traces. Clearly, the transition of FWD/\overline{BWD} occurs well within the brackets.

As mentioned previously, due to hysteresis in the circuit, the output changes state only when the input satisfies two criteria. Not only must a threshold level be traversed, but this must be done in the appropriate direction. Hence, $FRINJ_{W/H}$ is set HI when the analog fringe voltage increases through the upper threshold. When the fringe voltage decreases through this threshold, the output remains HI. In Fig. 3-39, as the mirror stops, the fringe voltage just exceeds the upper threshold voltage level. The output of the comparator goes HI. As the direction of mirror movement is reversed, the fringe voltage re-crosses the upper threshold; however, the output remains HI. If hysteresis was not in effect, when the fringe voltage re-crossed the threshold, a falling edge would occur, resulting in a very narrow bracket. However, because of the hysteresis in the circuit, the next transition of the pair comprising the bracket for this turn-around occurs when the fringe voltage next decreases through the lower threshold. A shorter time between

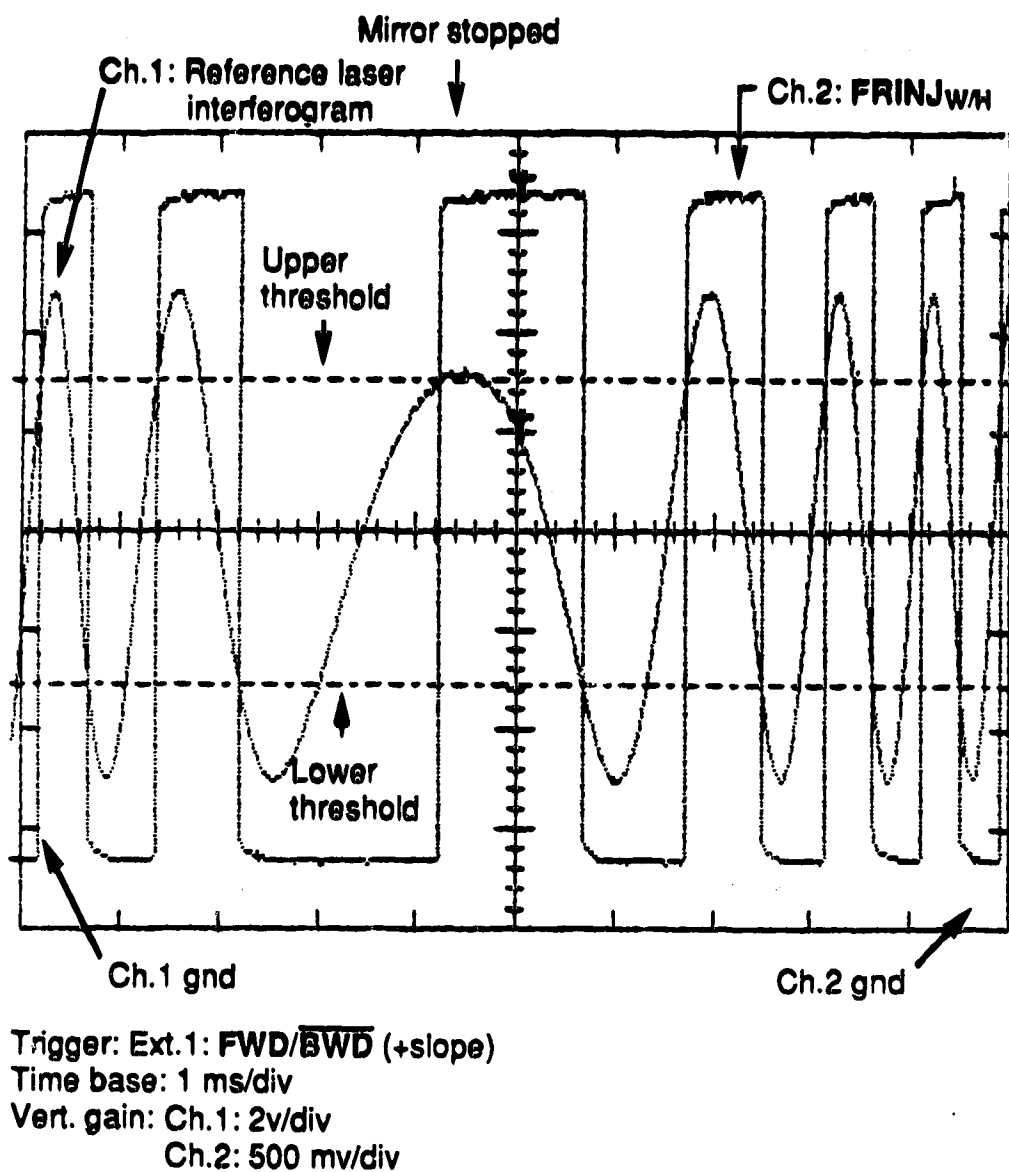


Figure 3-39. Reference laser interferogram and $FRINJ_{w/H}$ during turn-around sequence. Minimum positive brackets.

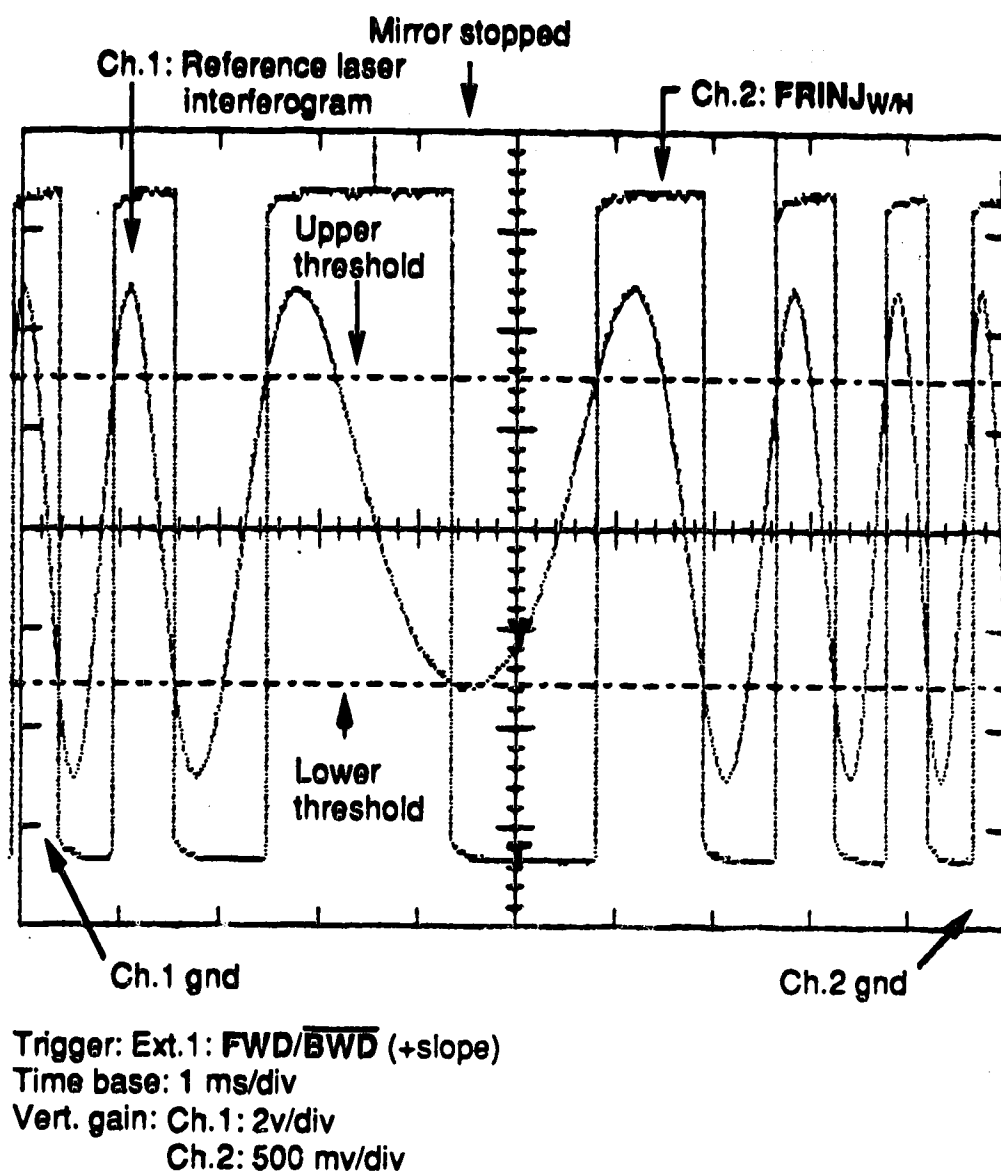


Figure 3-40. Reference laser interferogram and $\text{FRINJ}_{w/h}$ during turn-around sequence. Minimum negative brackets.

the transitions of the bracket cannot occur. Thus, the difference between the two threshold voltages (i.e. the width of the hysteresis loop) determines the minimum width of the brackets of this type of turn-around sequence. The symmetric situation, to produce a negative bracket, is shown in Fig. 3-40.

An important point to note in these figures is that the effect of the hysteresis is to delay the transitions of $FRINJ_{W/H}$ with respect to the zero-crossings of the analog fringe. This delay is maximized during the time when the mirror is being stopped. Since the mirror is moving slowly, it takes more time for the fringe voltage to increase or decrease from the level of, say, a zero-crossing to that of one of the threshold voltages.

For correct fringe counting, the transition of FWD/\overline{BWD} must occur within the brackets of the turn-around. Due to the hysteresis in the system, the brackets of turn-around sequences are delayed. If the transition of FWD/\overline{BWD} occurs at exactly the point at which the mirror has stopped moving, then, in order that this edge occurs within the brackets, it must also be delayed. Thus, the timing of the transition of FWD/\overline{BWD} , with respect to the point in time at which the mirror is stationary, is an important consideration in this system. FWD/\overline{BWD} is the output of a comparator whose input is a processed version of V_{EMF} . In order that the transition of FWD/\overline{BWD} can be delayed, the input signal is off-set, and hysteresis is introduced into the comparator circuit. (Note that the hysteresis being discussed here is not that which is used to impose a lower limit on the minimum turn-around bracket size. In this situation, hysteresis ensures that the switching of FWD/\overline{BWD} occurs without chatter, and introduces a delay into this transition with respect to the time at which the mirror is stopped.)

The effect of hysteresis on the timing of FWD/\overline{BWD} is illustrated in Fig. 3-41. The ideal situation would be if the comparator could be operated without hysteresis. As shown in part a) of this figure, with a simple zero-crossing detector without hysteresis, the transition of FWD/\overline{BWD} wouldn't be delayed in any respect for either direction of turn-around sequence. In this situation, the transition of FWD/\overline{BWD} could be precisely controlled with a circuit such as a variable delay monostable multi-vibrator. However, by virtue of the fact that V_{EMF} is a reasonably noisy signal, and since the rate of change of this signal is low in the region of zero velocity, hysteresis has to be added to the circuit to minimize multiple firings of the comparator output,

The comparator output is either +5 v or 0 v. The threshold voltages are fractions of the two possible output levels. The lower threshold voltage is a fraction of 0 v, or 0 v. The upper threshold voltage is a fraction of 5 v. In the present system, the upper threshold is set at approximately 0.5 v. As shown in part b) of this figure, the output of the comparator undergoes a 1 \rightarrow 0 transition when V_{EMF} decreases through the zero volt level. However, to cause a rising transition, V_{EMF} must increase to a voltage greater than approximately 0.5 v. This takes time. Thus, for a backward to forward turn-around sequence, the rising edge of FWD/\overline{BWD} is delayed with respect to the time of zero velocity.

V_{EMF} is the amplified version of the back e.m.f. that is generated in the auxiliary coils. The effect of introducing an off-set into V_{EMF} is indicated in Fig. 3-42. In part a) of this figure, V_{EMF} is off-set by a positive voltage. The result is that the rising transition of FWD/\overline{BWD} leads the point of zero velocity, while the falling transition is delayed. The symmetric situation is

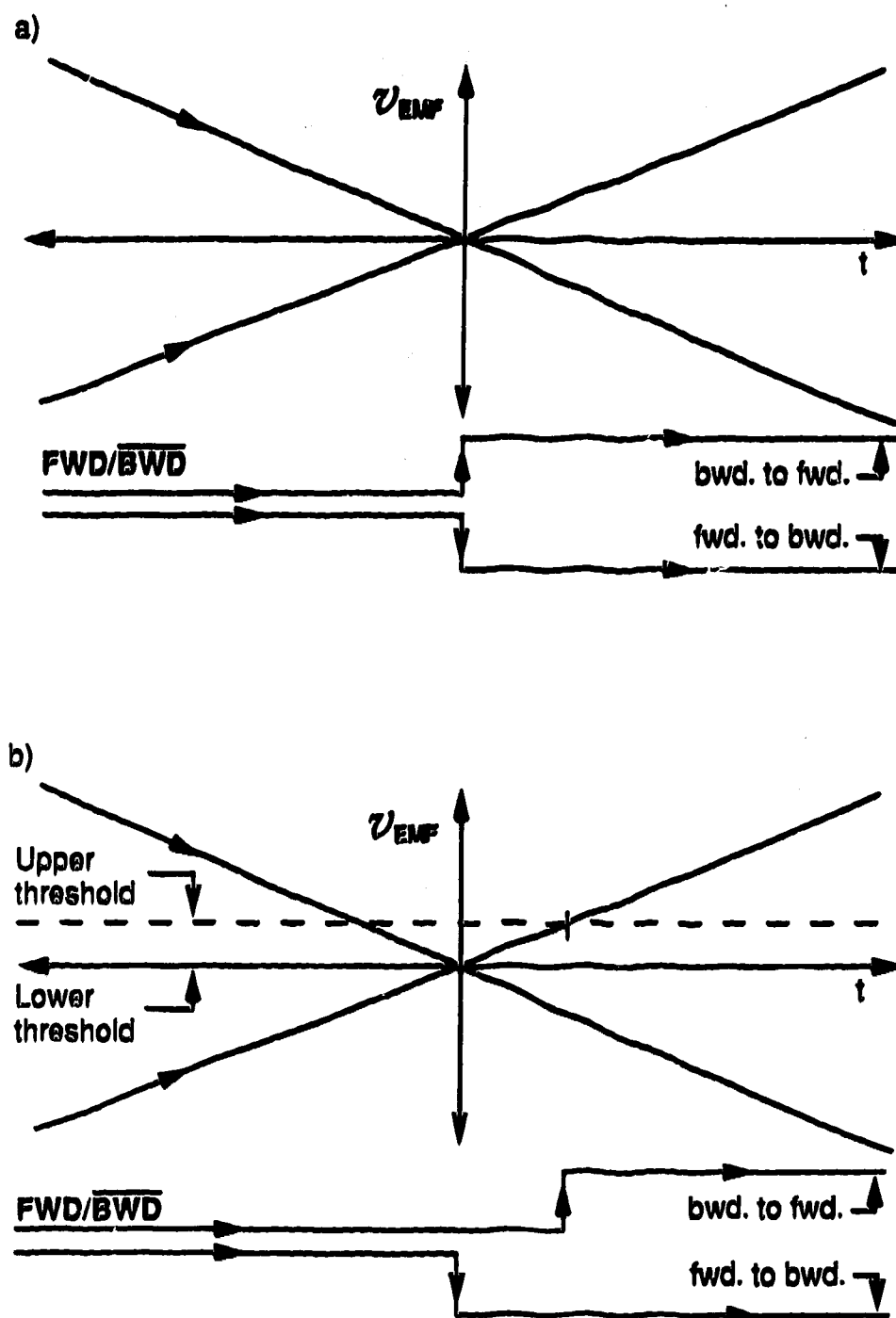


Figure 3-41. Effect of hysteresis on timing of transition of FWD/BWD.

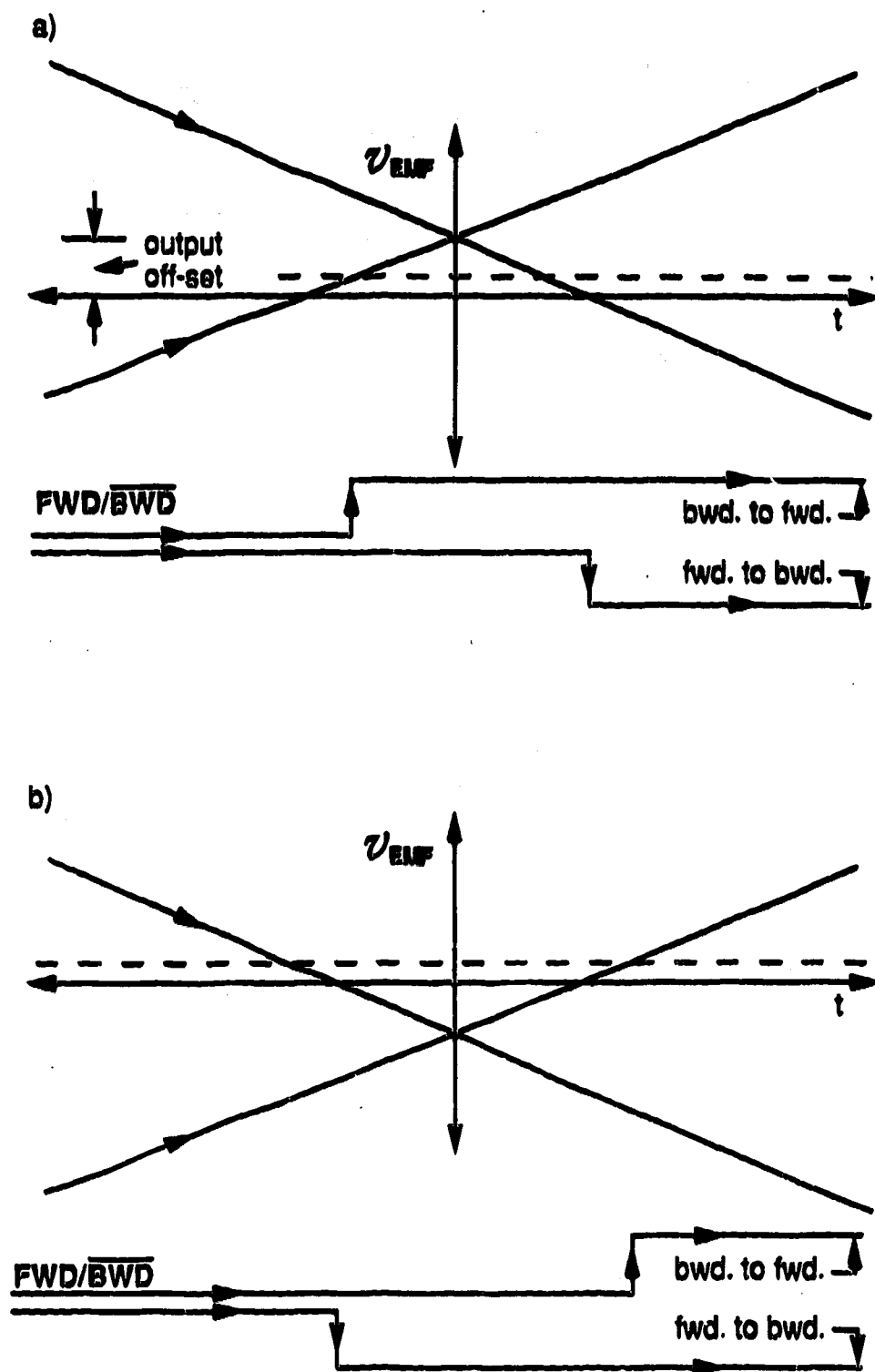


Figure 3-42. Effect of off-setting v_{EMF} on timing of transition of FWD/BWD.

shown in part b) of this figure. If the off-set is negative, the falling transition leads the time of zero mirror velocity, and the rising transition is delayed.

In part a) of this figure, it can be seen that by raising the upper threshold level of the comparator, the lead introduced into the rising transition, as a result of the positive off-set, can be over-come by the delay caused by hysteresis. This is the scheme that is employed in the present system. With a positive off-set, the falling edge of FWD/\overline{BWD} is already delayed. The off-set is adjusted until the falling transition is situated, comfortably, within the brackets of successive forward to backward turn-around sequences. The rising transition of FWD/\overline{BWD} is then delayed by changing the level of the upper threshold of the comparator. This is achieved by changing the width of the hysteresis loop. The fraction of the output that is fed back to the input, is adjusted until the rising transition occurs well within the brackets of successive backward to forward transitions. The desired result of these adjustments is illustrated in Fig. 3-43. For clarity, the difference between the delays has been exaggerated. The lengths of time of the actual delays are much more similar, as indicated in Fig. 3-44.

In the present system, the raw back e.m.f. that is generated by the auxiliary coils is amplified to produce V_{EMF} . This is used in the coarse feedback loop, and to produce FWD/\overline{BWD} . In the latter capacity, V_{EMF} is somewhat noisy, with a slow rate of change with respect to time. Since we are interested in the nature of V_{EMF} only in the vicinity of zero volts, the time rate of change can be increased through amplification, without worrying about saturation of the amplifier. This, in conjunction with some filtering of the higher frequency noise components, results in a cleaner signal for use as input into the comparator circuit. Thus, V_{EMF} is input into an op-amp with

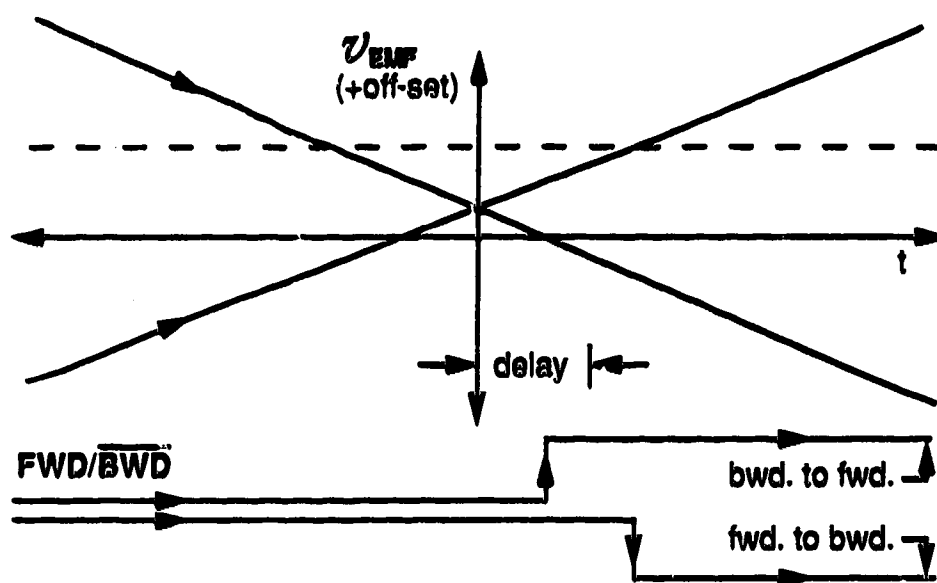
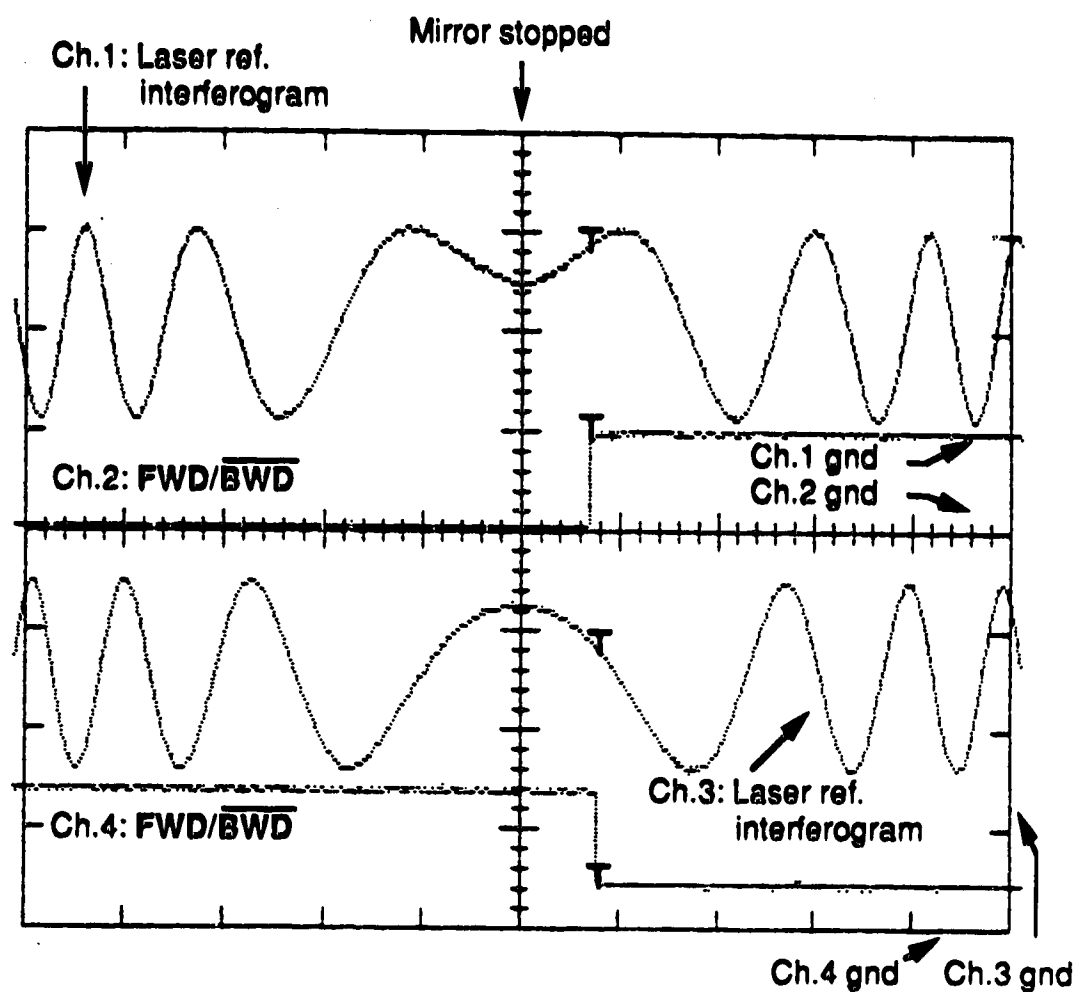


Figure 3-43. Combined effect of off-setting V_{EMF} and hysteresis to produce delay of transition of FWD/BWD.



Trigger: Ch.2 (+ slope for Ch.1/Ch.2, - slope for Ch.3/Ch.4)

Time base: 1 ms/div

Vert. gain: All channels 5v/div

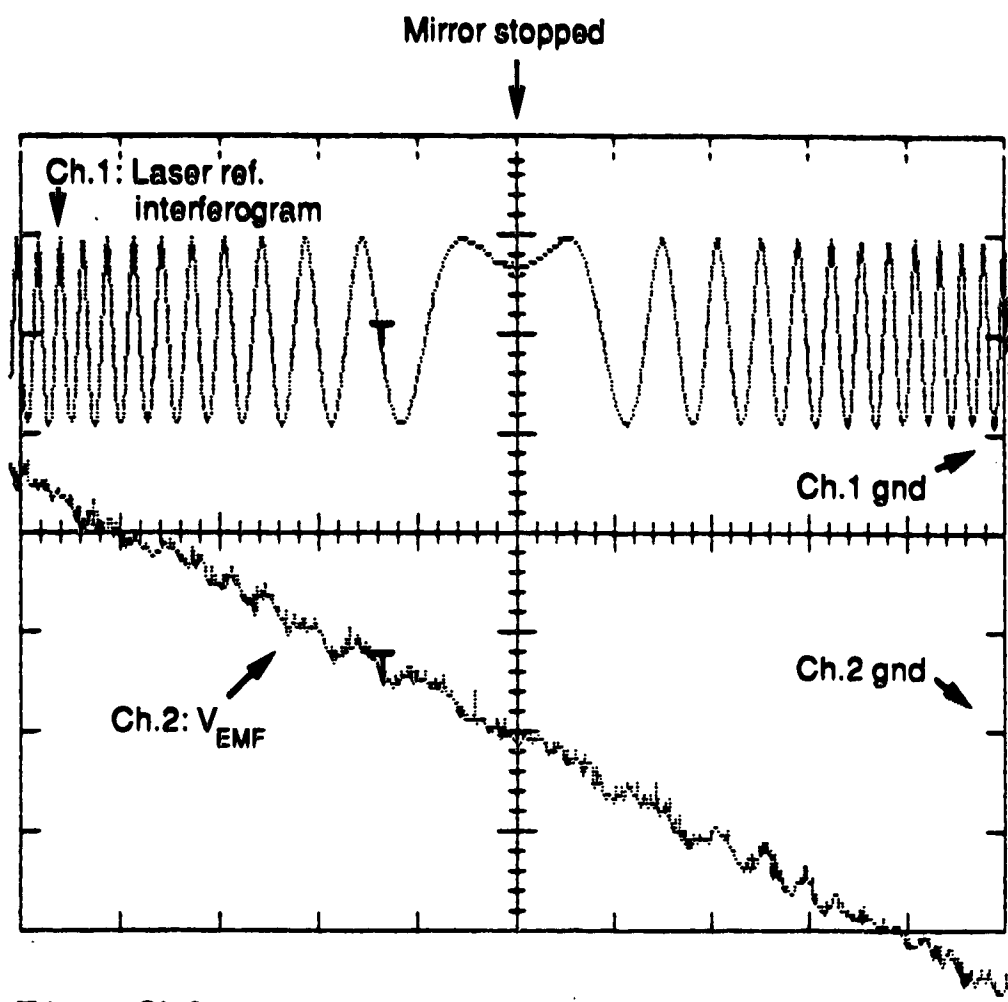
Figure 3-44. Reference laser interferogram and $\overline{\text{FWD/BWD}}$ during turn-around sequences.

closed loop gain of approximately 100, and with a small capacitor across the feed-back loop to shunt high frequency components to virtual ground. This version of V_{EMF} is input into the comparator to produce FWD/\overline{BWD} .

Since the positioning of the transition of FWD/\overline{BWD} with respect to the brackets of the turn-around sequences is critical to correct fringe counting, the adjustment procedure is presented here. The off-set of V_{EMF} is nulled such that the zero-crossing, for both directions of drive reversal, corresponds to the time of zero mirror velocity, as indicated by the center of symmetry of the analog fringe. These conditions are shown in Fig. 3-45 and Fig. 3-46. This is achieved by adjusting a potentiometer that is situated on the lid of the auxiliary coils module.

During adjustment of the timing of the transitions of FWD/\overline{BWD} the off-set of V_{EMF} is no longer adjusted; rather, the off-set of the afore-mentioned op-amp is adjusted to change the delay of the falling transition. This off-set is controlled via the off-set null adjustment inputs of the op-amp. The small potentiometer on the front panel of the coarse feed-back module is used to make this adjustment. Counterclockwise rotation increases the off-set, thereby increasing the delay of the falling edge.

The output of this op-amp is connected through a resistor into the non-inverting input of a comparator. The output is fed back to the input through a feed-back resistor. In this way, positive feed-back occurs and hysteresis is established. Changing the value of the input resistor relative to that of the feed-back resistor changes the fraction of the output voltage that is fed back to the input. As a result, the level of the upper threshold is changed to introduce more, or less, delay into the timing of the rising transition of



Trigger: Ch.2
 Time base: 2 ms/div
 Vert. gain: Ch.1: 5v/div
 Ch.2: 50 mv/div

Figure 3-45. Reference laser interferogram and V_{EMF} during backward to forward turn-around sequence. Proper adjustment of off-set of raw V_{EMF} .

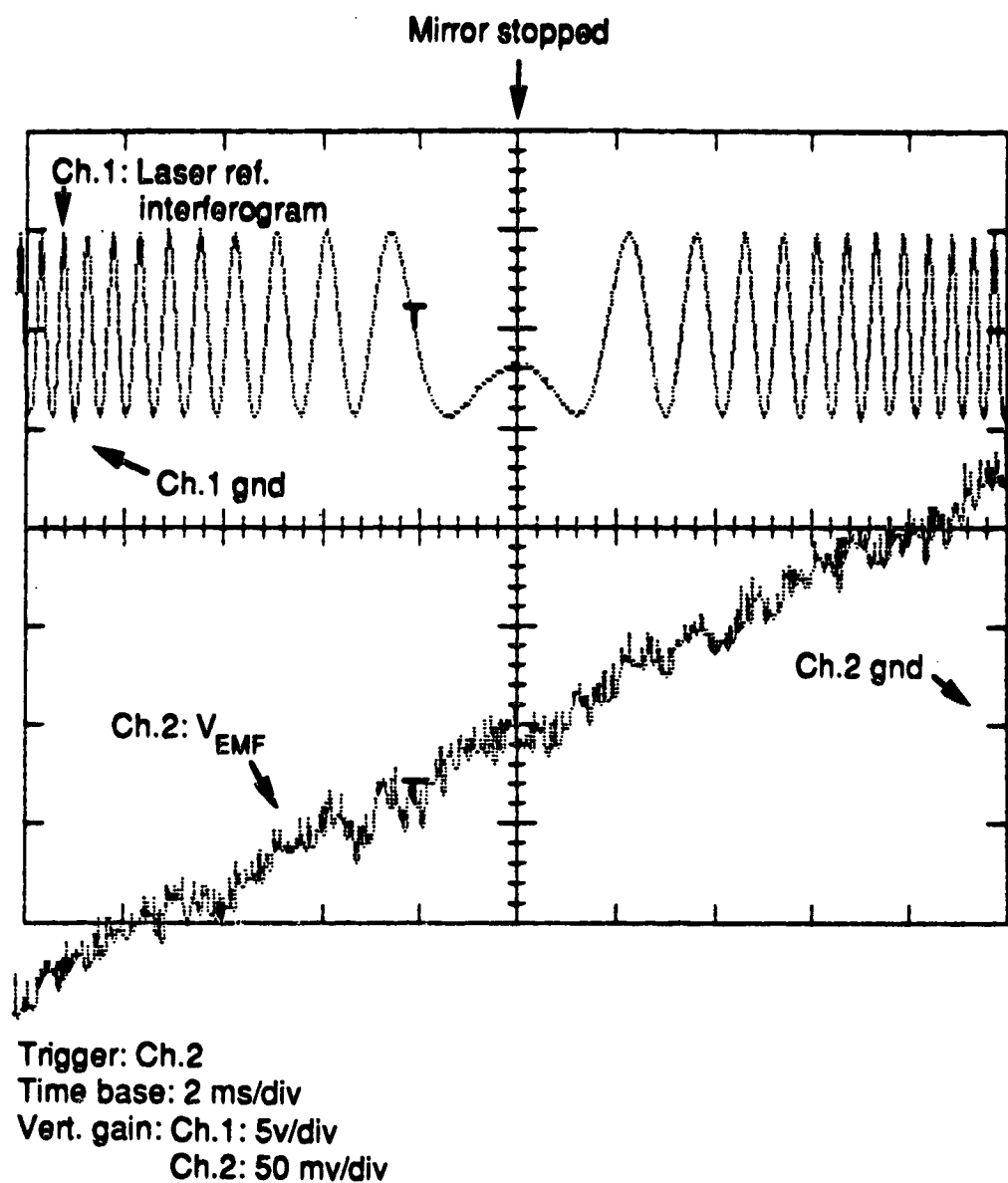


Figure 3-46. Reference laser interferogram and V_{EMF} during forward to backward turn-around sequence. Proper adjustment of off-set of raw V_{EMF} .

FWD/BWD. The amount of hysteresis is adjusted to achieve approximately equal delays, of appropriate magnitude, of the two transitions of **FWD/BWD**. Again, this is illustrated in Fig. 3-44.

Fig. 3-47 is a block diagram of the fringe counting system that is used for mirror scan length control. In the present configuration of this system, two counters are employed; one for counting fringes during the data acquisition portion of each scan and another for counting fringes during the turn-around portion of a scan. Accordingly, these counters are termed the scan and turn-around counters, respectively. These counters are also often referred to as NCNTR and T/A CNTR, respectively.

For proper operation, these counters must be activated at the appropriate times during the cycle of mirror travel, with the correct edge of **FRINJ_{W/H}** made available for counting. In the present system, the method by which this is achieved is to generate three separate counting streams. These are gated such that at any given time, one of the streams is connected to either the down count input of the scan counter, or the up or down count inputs of the turn-around counter. The down count input of the scan counter is designated NCNTR DN input. Similarly, the two inputs of the turn-around counter are often referred to as the T/A CNTR UP and T/A CNTR DN, inputs.

The general operation of this system is as follows. During the data acquisition portion of a scan, the scan counter counts down on the appropriate edge of **FRINJ_{W/H}**. When the count reaches zero, the scan counter (NCNTR) produces the signal **NCNTR $\overline{\text{CNTOUT}}$** . This signal clears

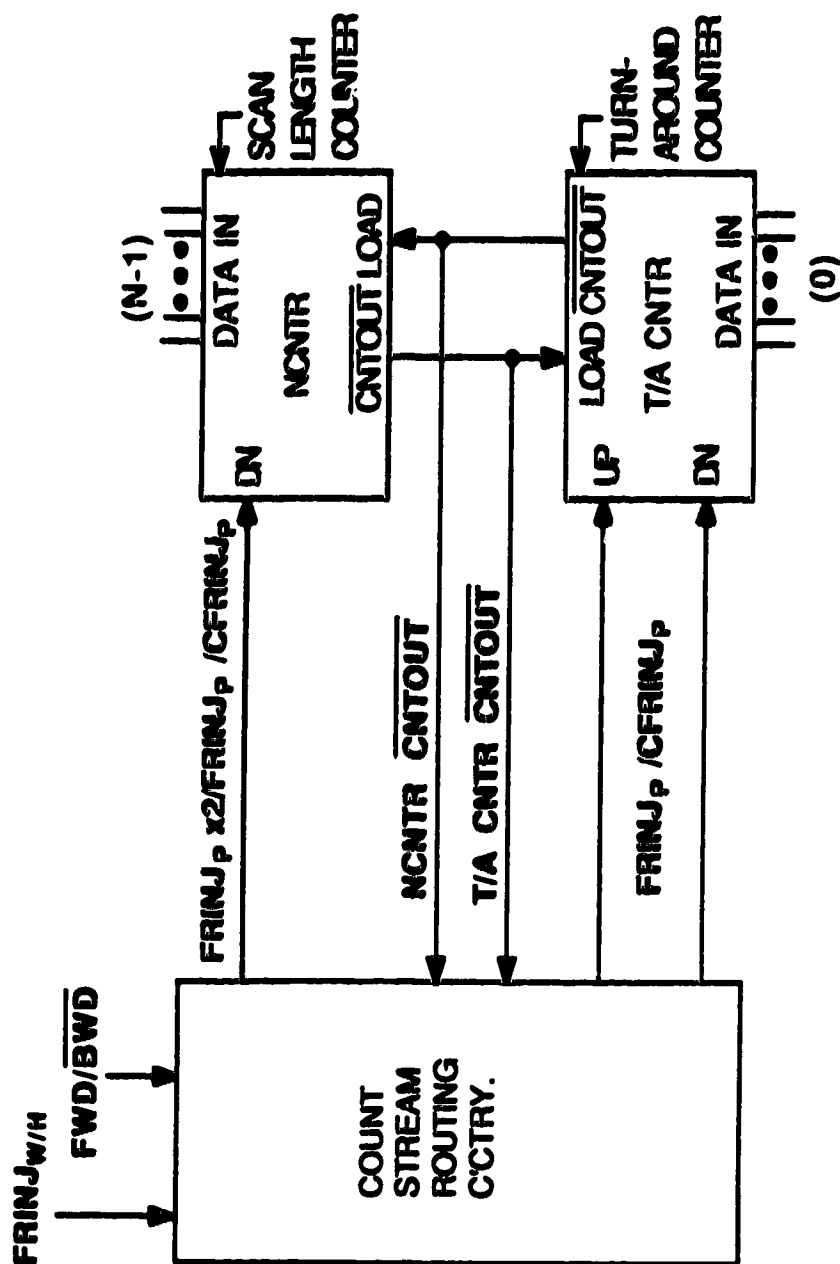


Figure 3-47. Scan and turn-around counters block diagram.

any count in the turn-around counter, and signals the routing circuitry to switch the count stream to the up count input of the turn-around counter.

The T/A CNTR starts incrementing on the appropriate edge of $FRINJ_{W/H}$, until the transition of FWD/\overline{BWD} occurs. This signals the routing circuitry that the mirror has stopped moving. The routing circuitry removes the count stream from the up input of the T/A CNTR, and applies the complement count stream to the down count input of the turn-around counter. The T/A CNTR decrements on the appropriate edge of $FRINJ_{W/H}$, until a count out occurs, at which point the signal T/A CNTR \overline{CNTOUT} is produced. This signal loads the appropriate number (for a particular scan length) into the scan counter, and signals the routing circuitry to switch the appropriate count stream to the down count input of the scan counter. The scan counter counts out and the cycle continues.

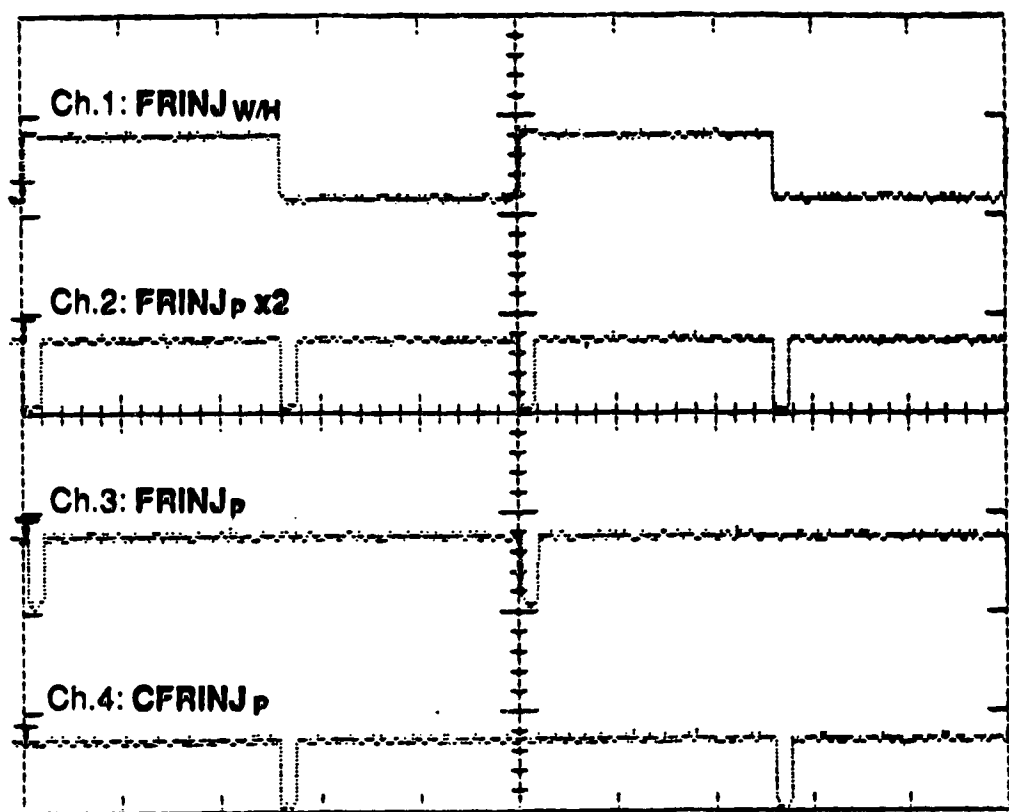
When the mirror is moving in the forward direction, both counters count rising edges of $FRINJ_{W/H}$. During movement in the backwards direction, the rising edges of $\overline{FRINJ_{W/H}}$ are counted. These are the falling edges of $FRINJ_{W/H}$. A special case is the first half scan after the white light position has been sensed. In this case, both edges of $FRINJ_{W/H}$ are counted to define one-half of the data acquisition scan range.

Easily combined, and gated, count streams are generated by triggering edge sensitive, mono-stable multivibrators with the edges of $FRINJ_{W/H}$. One of these circuits is set to trigger on rising edges; the other triggers on falling transitions. The output of the former circuit is designated, $FRINJ_p$. It reproduces the rising edges of $FRINJ_{W/H}$. ("P", in these designations stands for "pulse.") The output of the second monostable, $CFRINJ_p$, represents the

falling edges of $FRINJ_{W/H}$. (The "C" in the designation $CFRINJ_P$ indicates that this is derived from the complement of $FRINJ_{W/H}$.) For the special case of the first half scan after the position of ZPD has been passed, $FRINJ_P$ and $CFRINJ_P$ are combined to produce $FRINJ_{Px2}$. In this signal, a pulse is produced for both edges of $FRINJ_{W/H}$. $FRINJ_{Px2}$ is used only once during scan mode operation. It is routed to the scan counter during the first scan in the forward direction to set the front end limit on the data acquisition scan length. After this, $FRINJ_{Px2}$ is inactive until the next time that scan mode operation is invoked. These three signals, along with $FRINJ_{W/H}$ for comparison, are shown in the digital oscilloscope traces of Fig. 3-48.

During forward direction movement of the mirror, the active count stream is $FRINJ_P$. When moving backwards, $CFRINJ_P$ is active. The status of FWD/BWD controls which of these count streams is active. The enabling or disabling of each of the three counter inputs, and the routing of either of the count streams to the active input, is controlled by the two signals designated as $NCNTR \overline{CNTOUT}$ and $T/A \overline{CNTR \overline{CNTOUT}}$. Both of these are $1 \rightarrow 0 \rightarrow 1$ pulses that are output by either the scan counter or the turn-around counter, respectively, when the counter reaches zero.

Consider the operation of the fringe counting system from the point at which the mirror passes through the ZPD position of optical retardation, on the first scan in scan mode operation. As shown in Fig. 3-49, after the digital white light pulse has occurred, the scan counter down count input is enabled, with $FRINJ_{Px2}$ as input. The scan counter counts down at twice the frequency of $FRINJ_{W/H}$, until zero is reached. At this point, $NCNTR \overline{CNTOUT}$ is pulsed LO. The timing of the falling edge of $NCNTR \overline{CNTOUT}$ is important. As indicated in Fig. 3-50, this edge does not occur immediately after the least

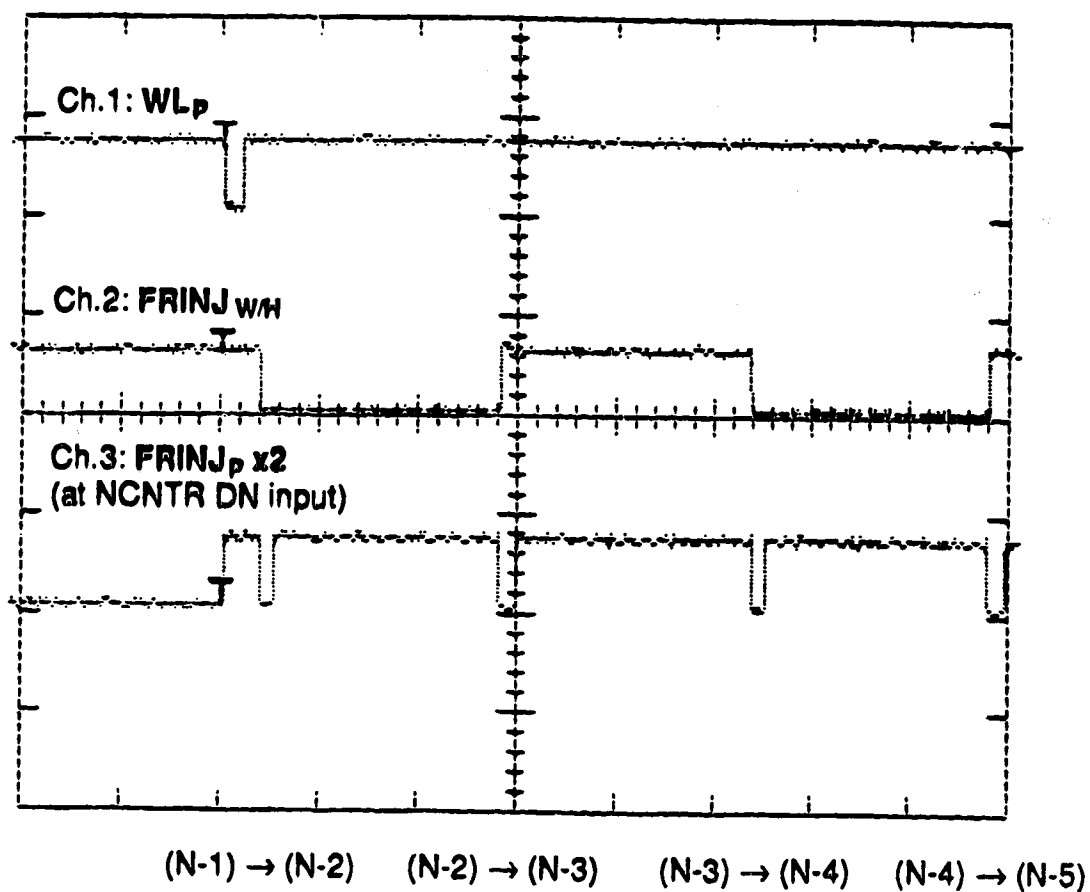


Trigger: Ch.1

Time base: $20 \mu\text{s}/\text{div}$

Vert. gain: All channels $5\text{v}/\text{div}$

Figure 3-48. $\text{FRINJ}_{W/H}$ and count streams $\text{FRINJ}_P \times 2$, FRINJ_P , and CFRINJ_P .

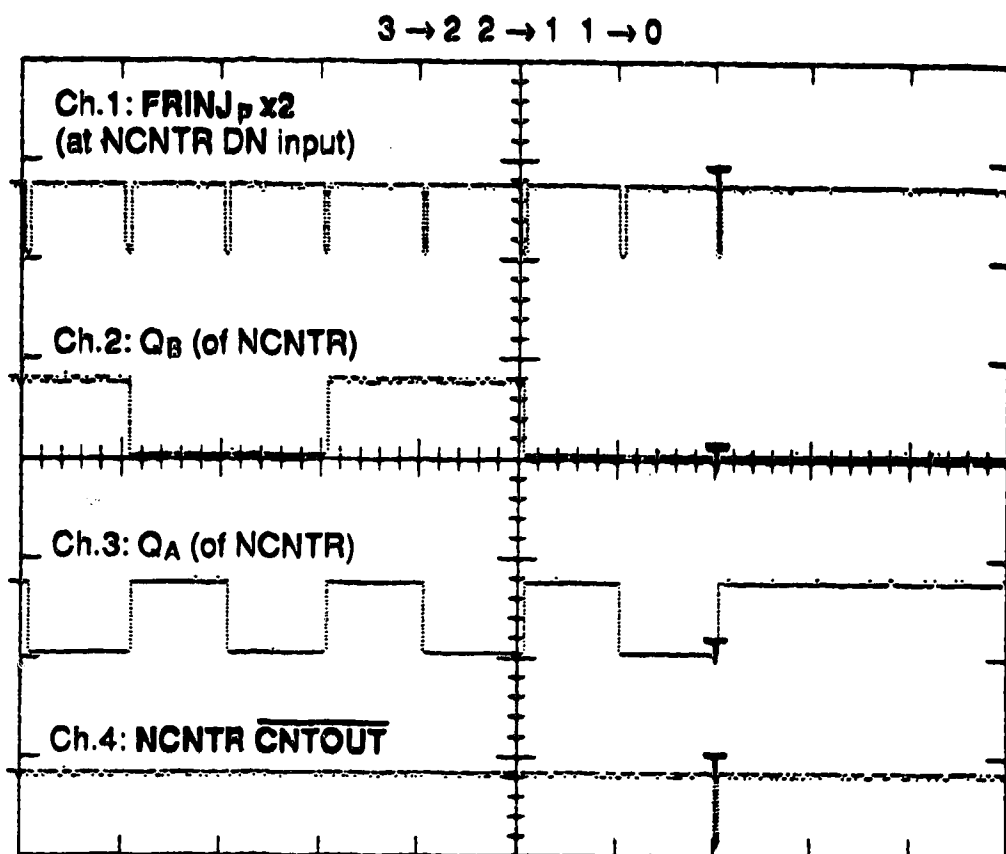


Trigger: Ch.1

Time base: 20 $\mu s/div$

Vert. gain: All channels 5v/div

Figure 3-49. Beginning of first half-count to set-up mirror scan length.
 WL_P , $FRINJ_{W/H}$, $FRINJ_P \times 2$.



Trigger: Ch.4

Time base: 100 μs /div

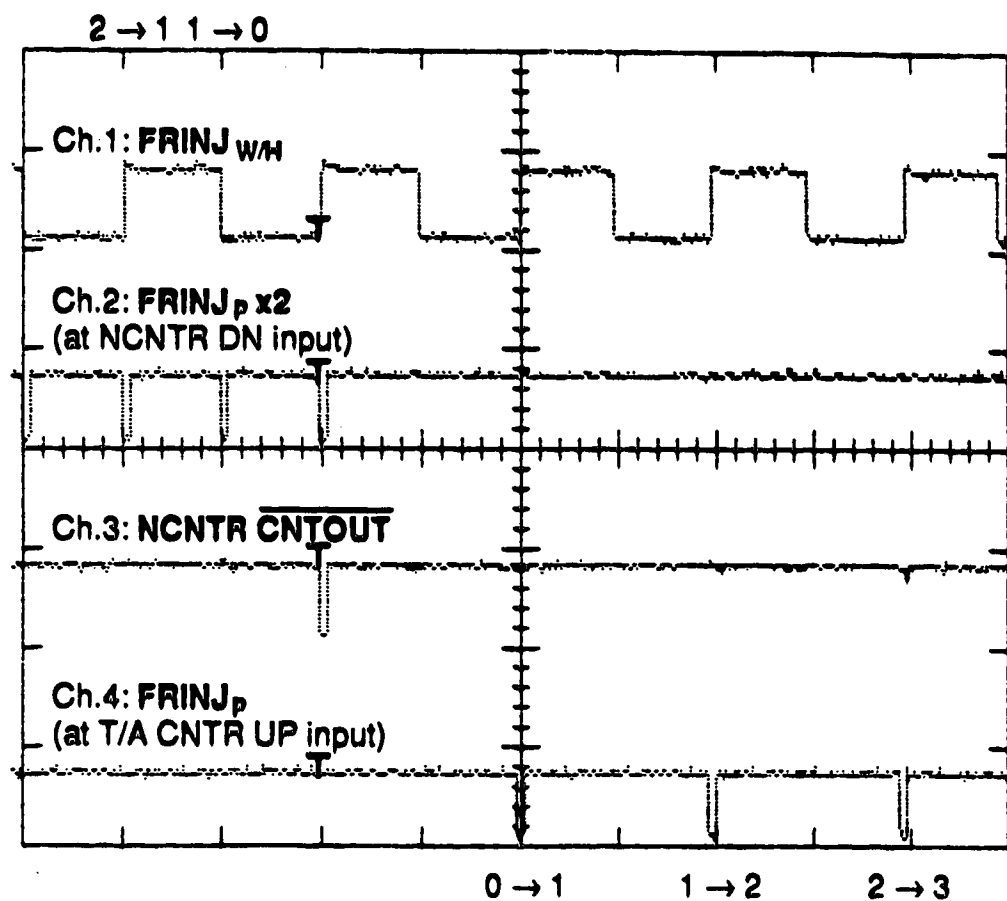
Vert. gain: All channels 5v/div

Figure 3-50. End of first half-scan count. Count out of scan counter.
 $FRINJ_P \times 2$, Q_A , Q_B of NCNTR and NCNTR \overline{CNTOUT} .

significant bit, Q_A , of the count is cleared LO for the 1→0 decrement. Instead, $\text{NCNTR } \overline{\text{CNTOUT}}$ is cleared LO on the next falling edge of the count stream input. For $\text{FRINJ}_{p \times 2}$, this next edge occurs after one-half period of $\text{FRINJ}_{W/H}$. (In Fig. 3-50, what is labelled as $\text{FRINJ}_{p \times 2}$ is actually FRINJ_p . However, the situation is identical when $\text{FRINJ}_{p \times 2}$ is used except that the pulses occur every 50 μs rather than every 100 μs .) The next rising edge of the count stream re-sets this signal. Since the count stream inputs consist of pulses, $\text{NCNTR } \overline{\text{CNTOUT}}$ is also a pulse. For both the scan and turn-around counters, when counting either FRINJ_p , or CFRINJ_p , the pulse of $\text{NCNTR } \overline{\text{CNTOUT}}$ occurs one full period of $\text{FRINJ}_{W/H}$ after the 1→0 decrement of the count has occurred.

When $\text{NCNTR } \overline{\text{CNTOUT}}$ is pulsed LO, the up count input of the turn-around counter is enabled, and FRINJ_p is re-routed from the scan counter input, to this input. This is shown in Fig. 3-51. When $\text{NCNTR } \overline{\text{CNTOUT}}$ was pulsed LO, the turn-around counter output was set to zero, as indicated in Fig. 3-52. On the first rising edge of FRINJ_p at the turn-around counter input, the LSB of the counter, Q_A , is set HI for the first increment of the turn-around count.

The LO pulse of $\text{NCNTR } \overline{\text{CNTOUT}}$ clears T/A. A forward to backward turn-around sequence is initiated. The drive begins to decelerate and the turn-around counter continues to increment until $\text{FWD}/\overline{\text{BWD}}$ is cleared LO. As shown in Fig. 3-53 and Fig. 3-54, when this transition occurs, the up count input is disabled while the down count input is enabled. When $\text{FWD}/\overline{\text{BWD}}$ is cleared LO, the count stream becomes CFRINJ_p . This is routed to the down count input to decrement the turn-around count as the mirror is accelerated in the backwards direction.

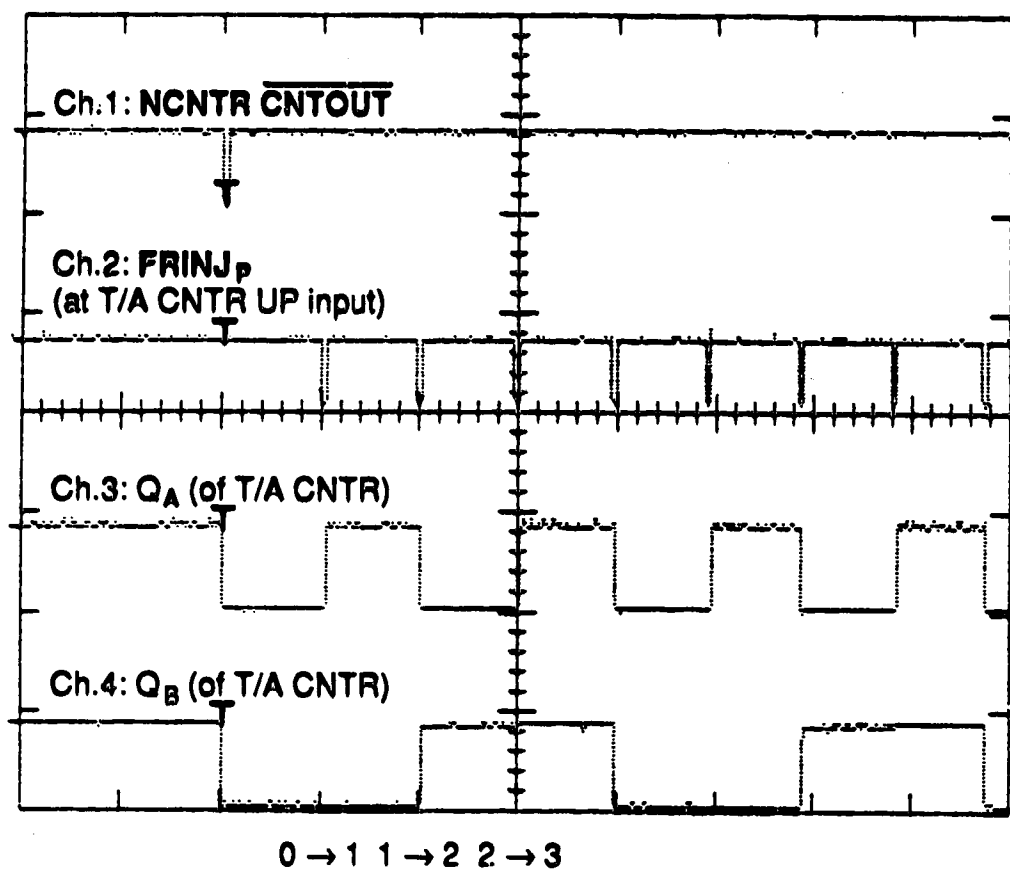


Trigger: Ch.3

Time base: 50 $\mu\text{s}/\text{div}$

Vert. gain: All channels 5v/div

Figure 3-51. End of first half-scan count. Disabling of NCNTR DN input. Enabling of T/A CNTR UP input. $\overline{\text{FRINJ}}_{w/h}$, $\overline{\text{FRINJ}}_p \times 2$, $\overline{\text{FRINJ}}_p$, and $\overline{\text{NCNTR CNTOUT}}$.

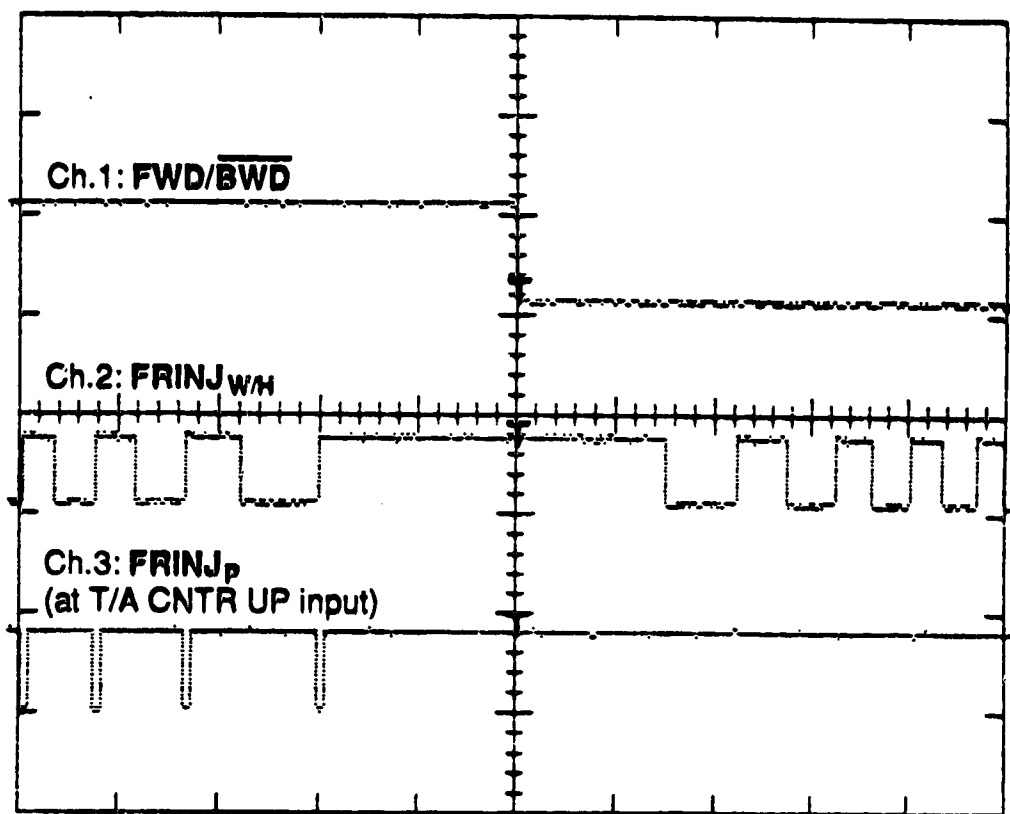


Trigger: Ch.1

Time base: 100 μ s/div

Vert. gain: All channels 5v/div

Figure 3-52. Beginning of forward to backward turn-around sequence. Incrementing of T/A CNTR. NCNTR CNTOUT, FRINJ_P, Q_A, and Q_B of T/A CNTR.



(X-2) → (X-1)

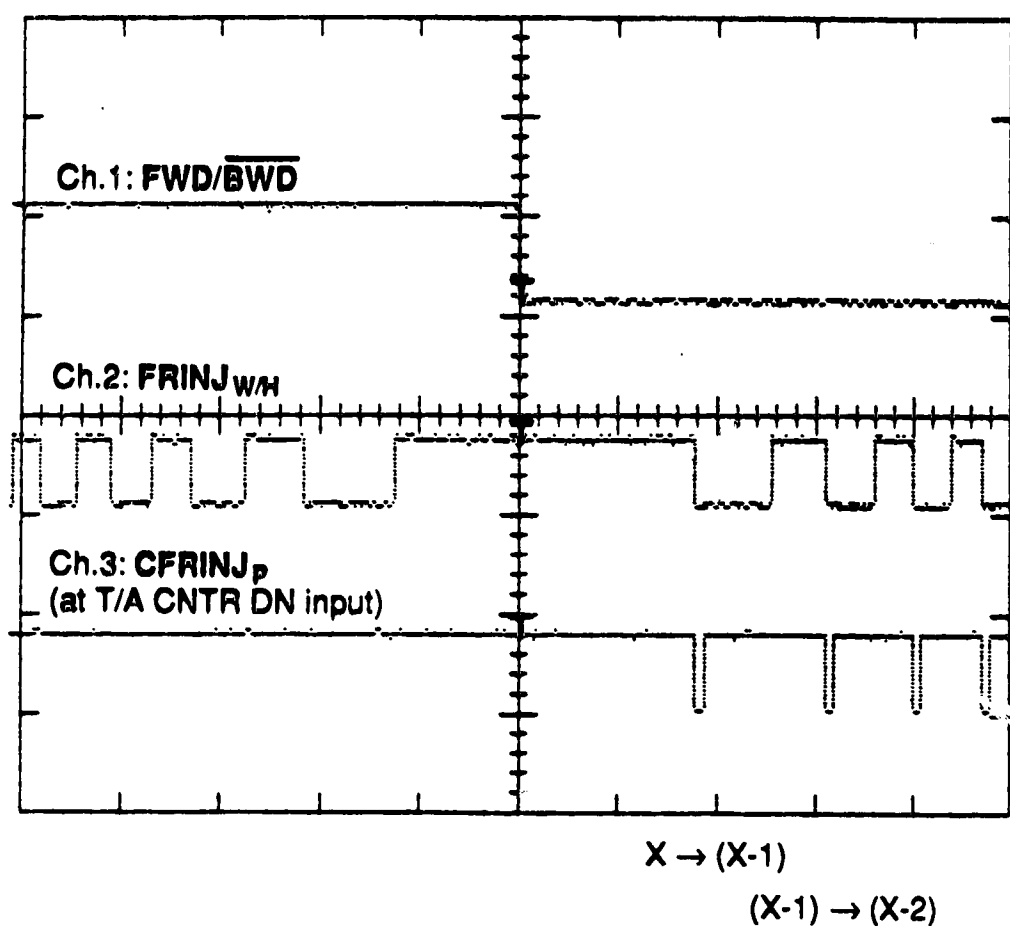
(X-1) → X

Trigger: Ch.1

Time base: 1 ms/div

Vert. gain: All channels 5v/div

Figure 3-53. End of count-up during forward to backward turn-around sequence. Disabling of T/A CNTR CNTR UP input. **FWD/BWD**, **FRINJ_{W/H}**, **FRINJ_P**.



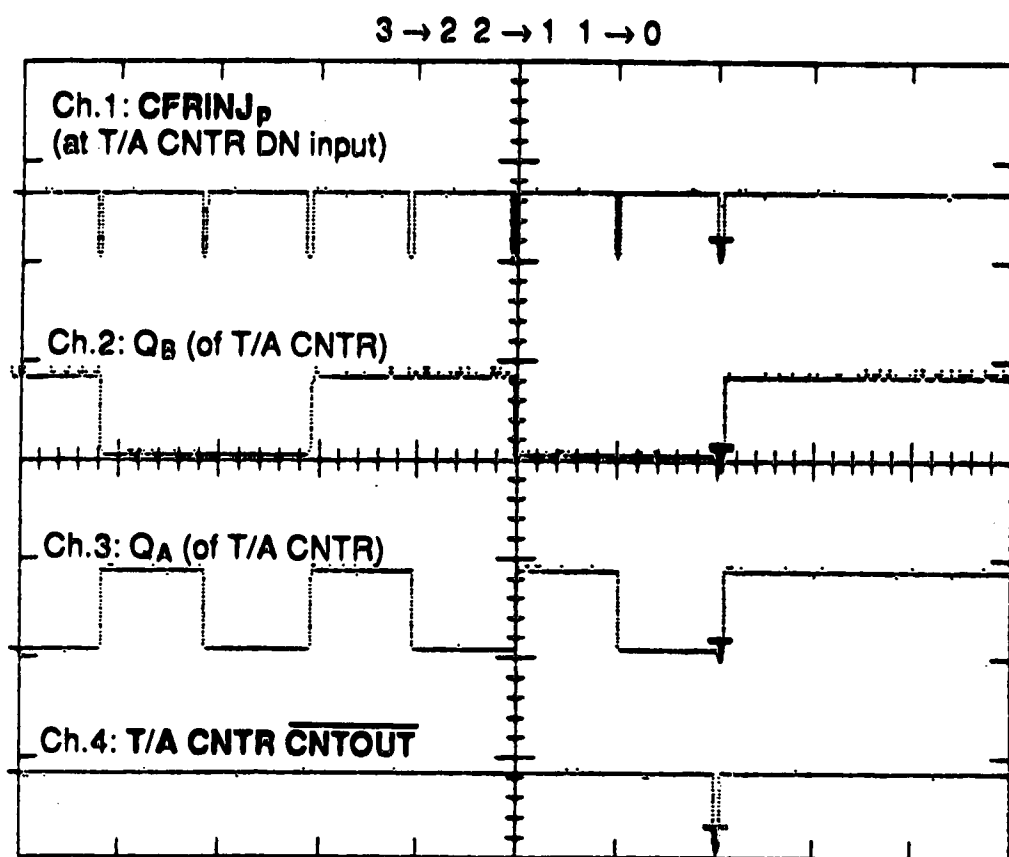
Trigger: Ch.1
 Time base: 1 ms/div
 Vert. gain: All channels 5v/div

Figure 3-54. Beginning of count-down sequence during forward to backward turn-around sequence. Enabling of T/A CNTR DN input. $\overline{\text{FWD/BWD}}$, $\text{FRINJ}_{W/H}$, and CFRINJ_p .

The turn-around counter decrements until zero is reached. As indicated in Fig. 3-55, one period of $\overline{\text{FRINJ}}_{\text{W/H}}$ after the 1→0 decrement has been clocked, T/A CNTR CNTOUT is pulsed LO. This falling edge sets the count of the scan counter to the value N-1. As shown in Fig. 3-56, the down count input of the turn-around counter is disabled, and CFRINJ_p is routed to the newly enabled down count input of the scan counter. On the next rising edge of CFRINJ_p , the scan counter begins to decrement from the value, N-1. This is the beginning of the first data acquisition scan in the backwards direction.

The sequence illustrated in Fig. 3-57 to Fig. 3-60 illustrates: 1) the counting out of the scan counter on CFRINJ_p to finish the backward direction data acquisition scan, 2) the counting up/counting down of the turn-around counter during the backward to forward turn-around, and 3) the start of counting of the first forward direction data acquisition scan, by the scan counter. The cycle of fringe counting is completed when on the forward scan, the scan counter reaches zero, and NCNTR CNTOUT pulses LO. The first data acquisition scan in the forward direction would then be complete, and another forwards to backwards turn-around sequence would be initiated.

By counting periods of the reference laser interferogram, the scan mode travel of the mirror is precisely controlled. Assuming that the electronics and optical systems are stable, the absolute positions in the travel of the mirror at which zero-crossings of the fringe occur should be reproducible. The fringe counting system provides an identity for each of these positions. Once each position has a "name", that position can be returned to on a repetitive basis during mirror scanning. These well-characterized positions in the travel of the mirror are used to trigger digitization of the source interferogram, as described in the next section of this chapter.

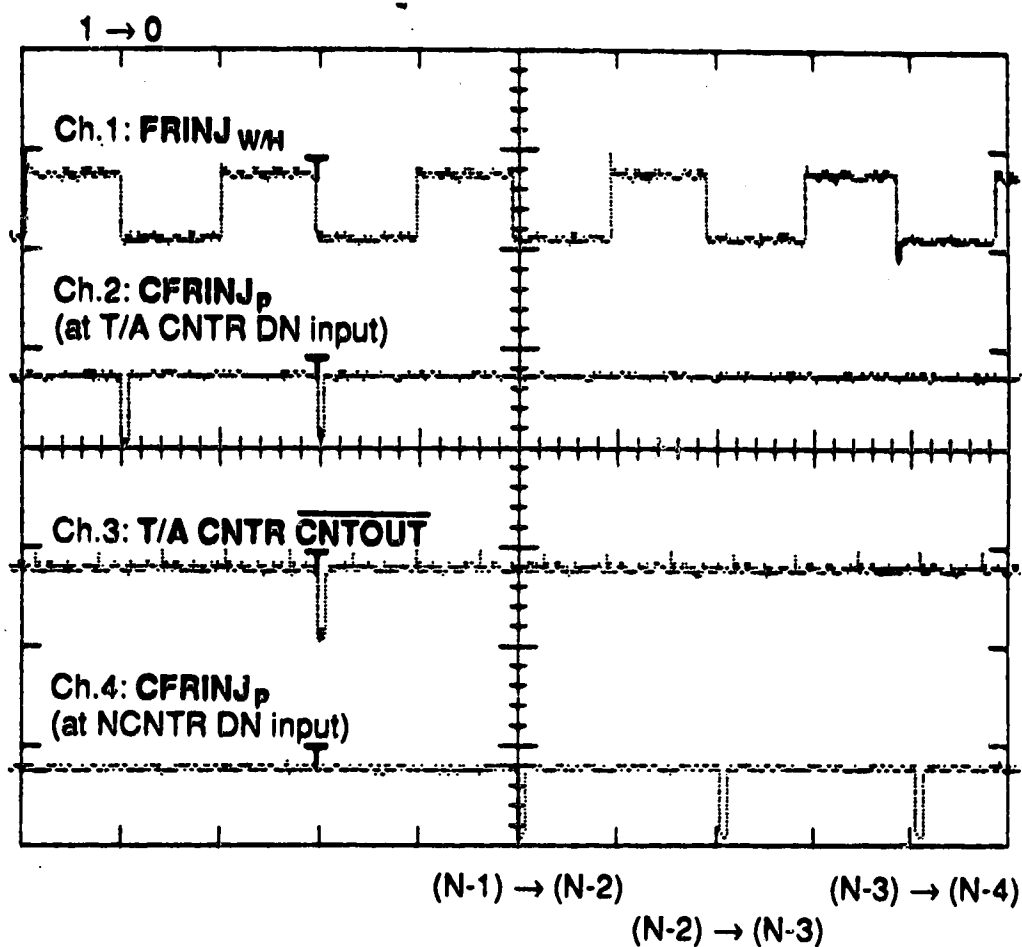


Trigger: Ch.4

Time base: 100 $\mu\text{s}/\text{div}$

Vert. gain: All channels 5v/div

Figure 3-55. End of turn-around count during forward to backward turn-around sequence. Count-out of T/A CNTR. CFRINJ_p , Q_A , Q_B , and T/A CNTR $\overline{\text{CNTOUT}}$.

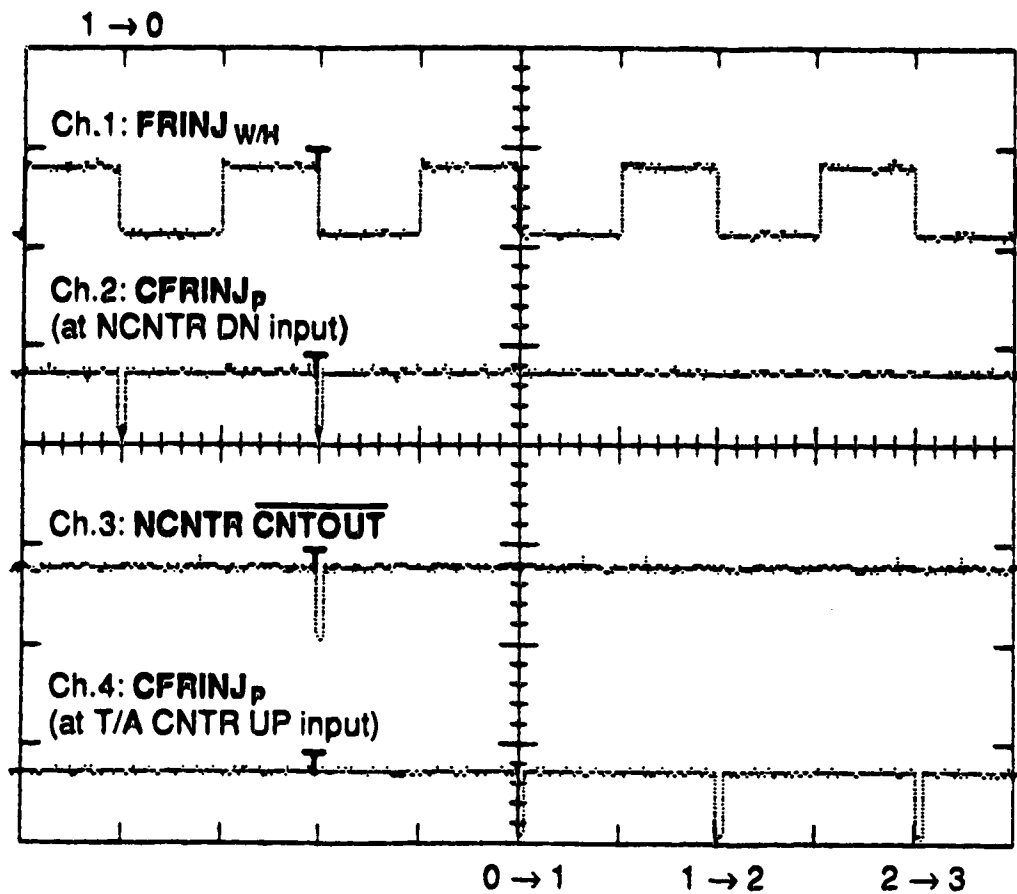


Trigger: Ch.3

Time base: 50 $\mu\text{s}/\text{div}$

Vert. gain: All channels 5v/div

Figure 3-56. End of forward to backward turn-around sequence.
Beginning of first backward direction data acquisition scan.
Disabling of T/A CNTR DN input. Enabling of $\overline{\text{NCNTR DN}}$
input. $\overline{\text{FRINJ}}_{w/H}$, CFRINJ_p , and $\overline{\text{T/A CNTR CNTOUT}}$.

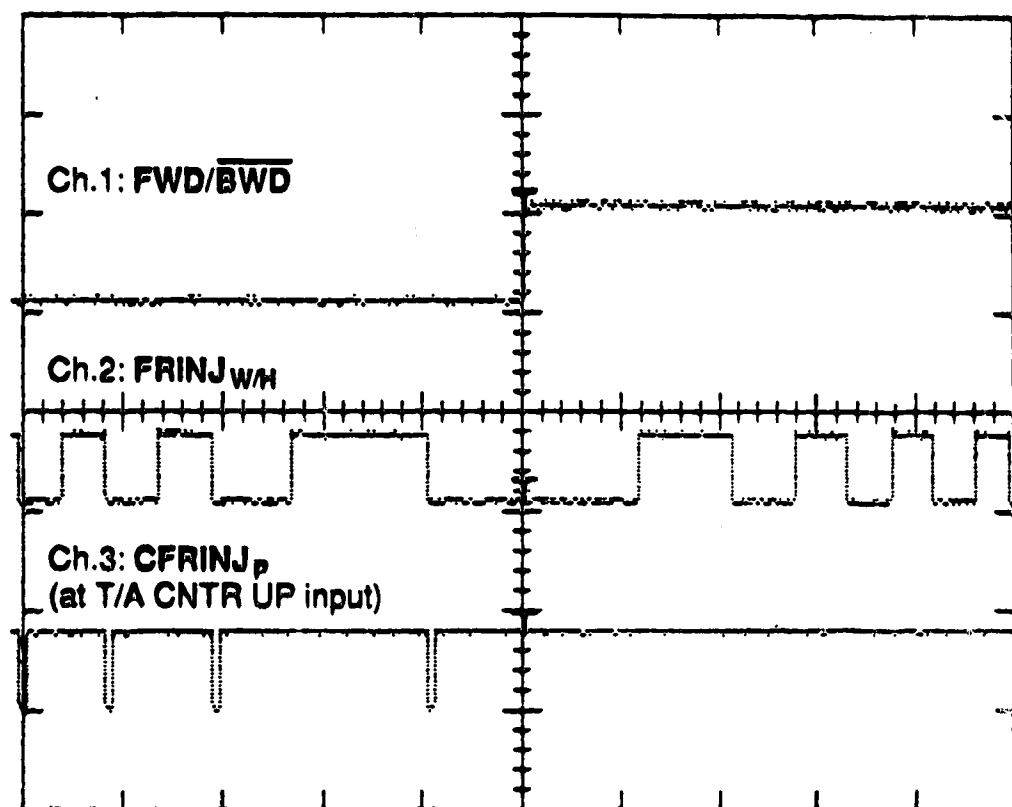


Trigger: Ch.3

Time base: 50 $\mu\text{s}/\text{div}$

Vert. gain: All channels 5v/div

Figure 3-57. End of first backward data acquisition scan. Disabling of NCNTR DN input. Enabling of T/A CNTR UP input. Beginning of count-up sequence of T/A CNTR. $\overline{\text{FRINJ}}_{w/H}$, CFRINJ_p , and NCNTR CNTOUT .



(X-2) \rightarrow (X-1)

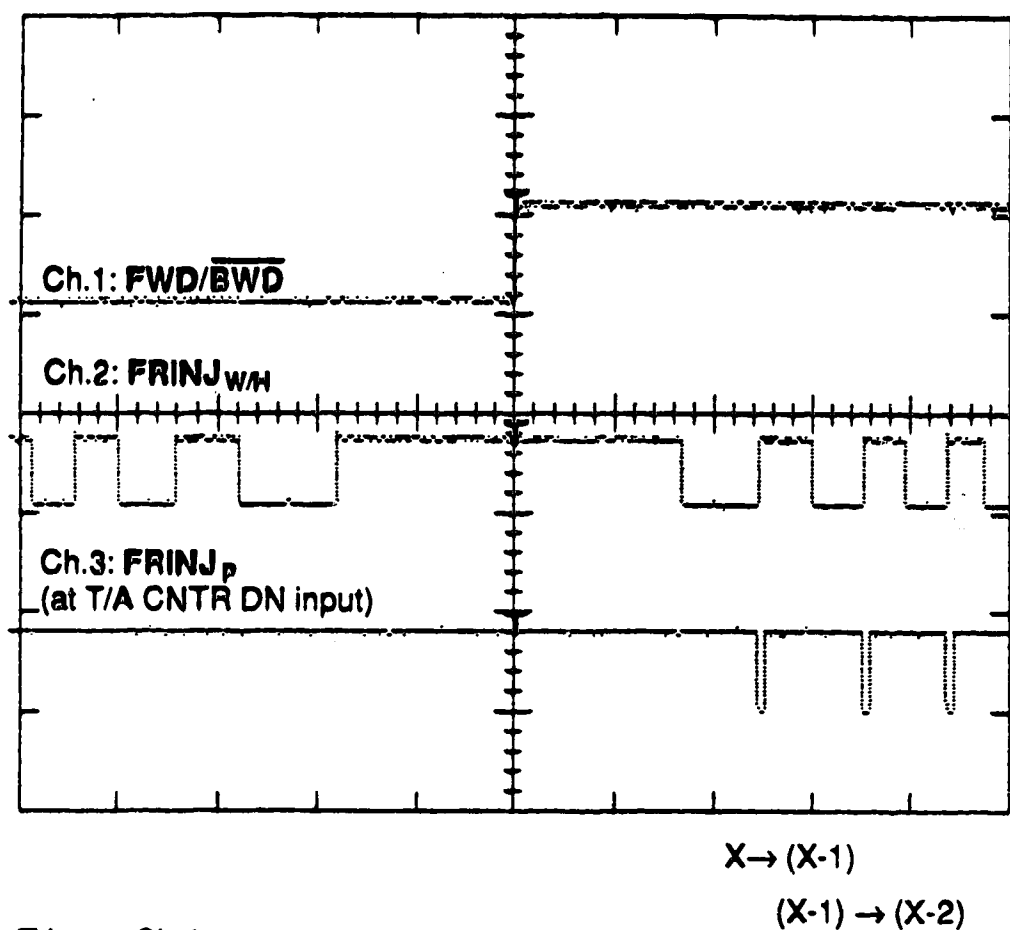
(X-1) \rightarrow X

Trigger: Ch.1

Time base: 1 ms/div

Vert. gain: All channels 5v/div

Figure 3-58. End of count-up during forward to backward turn-around sequence. Disabling of T/A CNTR CNTR UP input. $\overline{\text{FWD/BWD}}$, $\text{FRINJ}_{W/H}$, CFRINJ_P .



Trigger: Ch.1
 Time base: 1 ms/div
 Vert. gain: All channels 5v/div

Figure 3-59. Beginning of count-down sequence during forward to backward turn-around sequence. Enabling of T/A CNTR DN input. $\overline{\text{FWD/BWD}}$, $\text{FRINJ}_{W/H}$, and FRINJ_P .

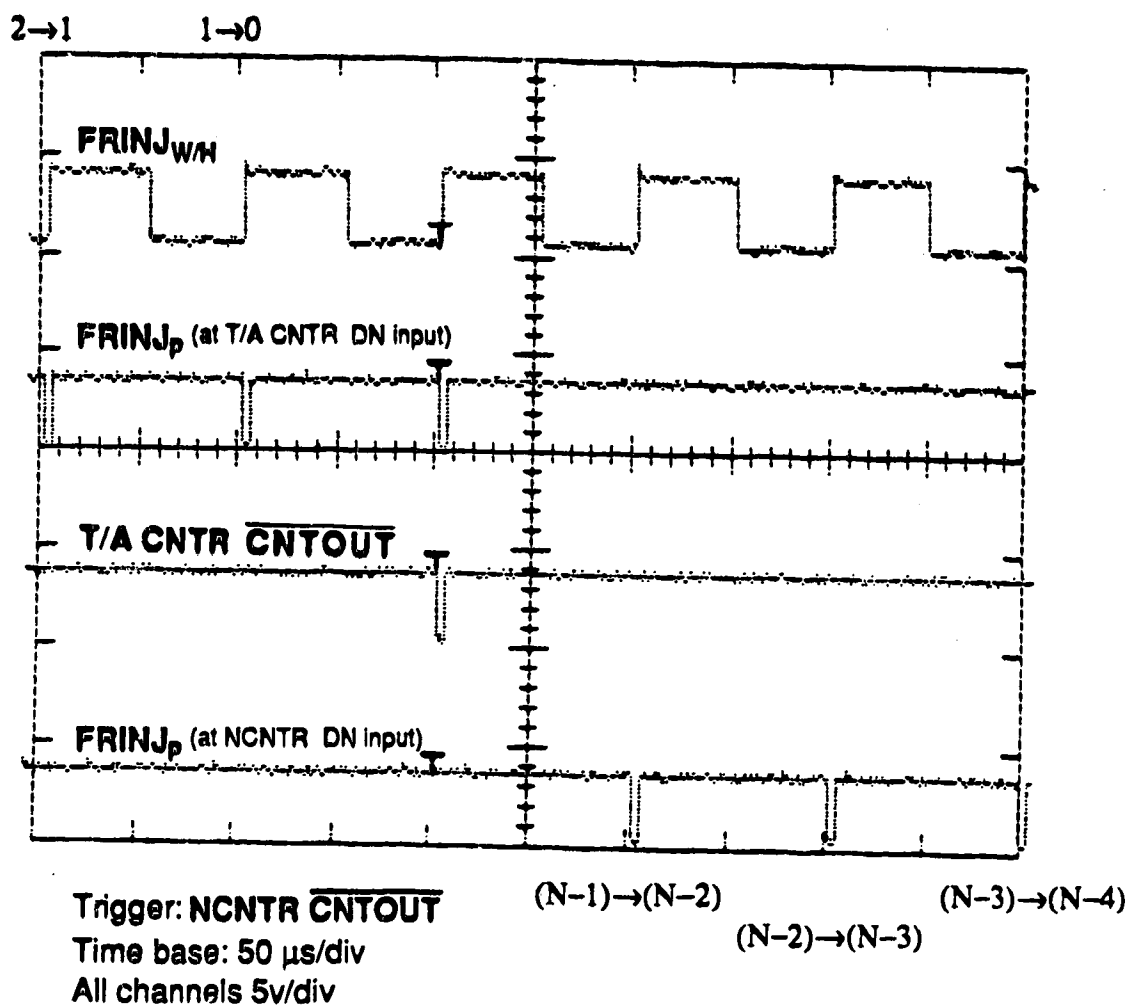


Figure 3-60. End of backward to forward turn-around sequence.
 Beginning of first forward direction data acquisition scan.
 Disabling of T/A CNTR DN input. Enabling of NCNTR
DN input. FRINJ_{W/H}, FRINJ_P, and T/A CNTR CNTOUT.

3-2. Digitization of the analog interferogram.

In the present system, the markers of mirror travel are the transitions of FRINJ. Strictly speaking, it is the transitions of FRINJ_{W/H} that are counted to control scanning of the mirror. However, with respect to digitization of the source interferogram, the system ADC is triggered by the transitions of FRINJ. Since only every second transition of FRINJ is important, the markers are spaced with 0.3164 μm between them.

In the present scheme of digitization of the source interferogram, it is desirable that digitization occur at equally spaced positions of optical retardation. Digitization of the source interferogram is achieved with a particular "sampling interval" or "sampling period". The former pertains to the increment of mirror travel between digitizations, while the latter is the period of time between digitizations. The two are related through the velocity of the mirror.

Consider for a moment the nature of the reference laser interferogram. Due to the finite line-width of the reference laser, the fringe amplitude decreases as the mirror moves away from the position of ZPD. The magnitude and shape of the damping depends upon the laser line-shape, as determined by the physical processes occurring within the lasing medium. The frequency of the fringe, as defined by the period (temporal or spatial) between zero-crossings, is related solely to the wavelength of the laser radiation.

With the Michelson interferometer used in this system, zero-crossings occur as the mirror moves through increments of $\lambda/4$, where λ is the wavelength of the reference laser. As long as the wavelength of the laser

remains constant, the distance that the mirror travels between zero-crossings remains constant throughout the entire travel of the mirror. The transitions of $FRINJ$ are triggered by the zero-crossings of the fringe, therefore the use of $FRINJ$ to clock the ADC ensures that the source interferogram is digitized at equal increments of optical retardation.

It would be undesirable to use a signal such as $FRINJ_{W/H}$ to trigger the ADC. As the mirror moves away from the position of Z.P.D., the period of $FRINJ_{W/H}$ increases as the amplitude of the fringe decreases. Thus, if this signal was used to digitize the source interferogram, the increment of optical retardation between digitizations would increase as the mirror approached the ends of its travel.

It was mentioned in the first section of this chapter that $FRINJ$ is also used as the input for the F/V converter in the fine feed-back loop. $FRINJ_{W/H}$ would not be suitable for maintaining a constant mirror velocity during fine feed-back operation. The fine feed-back loop operates such that the period of the input to the F/V converter is kept constant. As described above, the period of $FRINJ_{W/H}$ increases as the mirror moves away from the position of ZPD. With $FRINJ_{W/H}$ as the input into the F/V converter, as the mirror approaches either end of its travel, the fine feed-back loop must increase the velocity of the mirror to keep the period of $FRINJ_{W/H}$ constant. Thus, in this situation, the mirror is not moved with a constant velocity. With $FRINJ$, however, the distance through which the mirror moves to produce a pair of transitions is the same throughout the travel of the mirror. If the length of time between transitions is kept constant, the mirror moves with a constant velocity, throughout the whole travel of the mirror.

Each point in a digitized interferogram represents the source intensity at a given position of optical retardation. From the point of view of signal averaging, it is important that corresponding points within a set of replicate interferograms be digitized at the same position of optical retardation. In other words, point #1 of the first replicate interferogram is digitized at a position of optical retardation, x_1 . After this forward scan is finished, the direction of mirror movement is reversed. After the subsequent backward scan, the drive is again reversed, and the first point of the second replicate interferogram is digitized at the position of optical retardation, x_2 . These two points, x_1 and x_2 , comprise a pair of corresponding points. For correct signal averaging, these two positions at which the interferogram is digitized should be the same. (The same is true for all the pairs of corresponding points in the two interferograms.) This is achieved with the present system of counting periods of the analog fringe.

The fringe counting system described in the last section of this chapter provides a method by which the transitions of $FRINJ_{W/H}$ are identified and labelled with respect to the reference position of ZPD. The transitions of $FRINJ$ lead those of $FRINJ_{W/H}$ as a result of the hysteresis used in the production of the latter. Each transition of $FRINJ$ is associated with one (and only one) of the transitions of $FRINJ_{W/H}$. In this way, each position of optical retardation that is marked by a particular transition of $FRINJ$ can be repeatedly recognized during the cycle of mirror scanning. An example will clarify this point.

A transition of $FRINJ$ occurs just after a transition of $FRINJ_{W/H}$. This latter transition is identified by the fact that it represents a position of optical

retardation that is a reproducible number of fringe periods away from the position of ZPD. This associated transition of FRINJ is given a name, say, "Point #1." This is now a well-characterized position in the travel of the mirror at which digitization is to occur. When the mirror passes through this position, the transition of FRINJ triggers the ADC, producing one point (Point #1) of the digital representation of the source interferogram. The mirror moves through this position of optical retardation and continues on in the cycle of scan mode operation. Some time later, the mirror approaches this point in optical retardation again. This position was previously known as Point #1. If the fringe counting system is working properly, this position is still identified as Point #1. If the optical and electronic systems are stable, digitization of the interferogram occurs, again, at exactly the same position of optical retardation at which it occurred the last time the mirror passed through. If the same conditions are met for all of the positions at which digitizations are performed, then two replicate interferograms that can be correctly signal averaged are produced.

The digitization of 8-point interferograms is illustrated in Fig. 3-61. The cycle of fringe counting described in the previous section of this chapter is summarized in this figure. The sequence starts with the first scan of scan mode operation (i.e. the first scan after fine feed-back was acquired at the back opto-switch) in which the mirror scan length is defined by counting FRINJ_{px2} .

The relationship between fringe counting and the digitization of the source interferogram is clearly shown in this figure. $\text{FRINJ}_{w/H}$ is not shown; however, the edges of the count streams represent the edges of this signal. FRINJ is used to generate the signal, ADC CLK. The falling edges of this

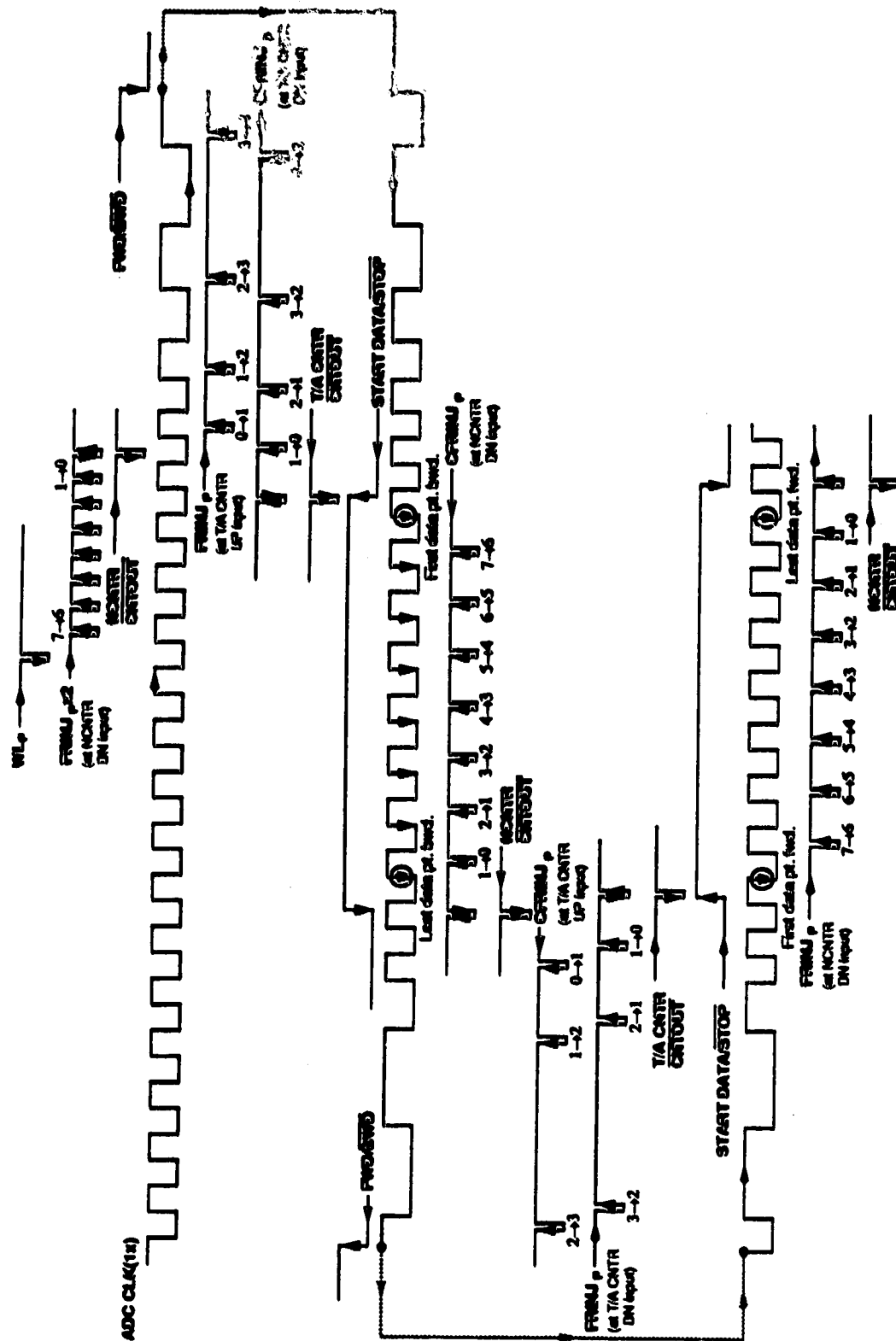


Figure 3-61. Summary of fringe counting for mirror scan length control. Set-up and acquisition of 8 point interferograms.

signal are used to trigger the ADC during digitization of the analog interferogram. As will be described later in this section, ADC CLK can take one of three forms. It is either a 1x, 4x, or 8x frequency multiplied version of FRINJ. All three of these versions of ADC CLK are in phase with FRINJ. The edges of FRINJ lead those of the count streams, therefore the edges of ADC CLK also lead those of the count streams. The 1x version of ADC CLK is shown in this figure. Note the delay of the count stream transitions relative to those of ADC CLK.

Obviously, during the first half scan that is used to define the scan length, no data is acquired. However, after the first forward to backward turn-around sequence is complete, the system is then set up for data acquisition.

Falling edges of ADC CLK trigger the ADC if the signal $\text{START DATA}/\overline{\text{STOP}}$ is HI. The latter is cleared or set, respectively, by the falling transitions of $\text{NCNTR } \overline{\text{CNTOUT}}$ and $\text{T/A CNTR } \overline{\text{CNTOUT}}$. After the first turn-around sequence (once again exaggerated in its brevity) $\text{T/A CNTR } \overline{\text{CNTOUT}}$ is pulsed LO. This sets $\text{START DATA}/\overline{\text{STOP}}$ HI. On the next falling edge of ADC CLK, the analog interferogram is digitized, and the first point of the first digitized interferogram is obtained. Subsequent falling edges of ADC CLK produce data points in the interferogram. The scan counter starts to count down from the value N-1, which is equal to 7 in this case. When zero is reached, $\text{NCNTR } \overline{\text{CNTOUT}}$ is pulsed LO. This clears $\text{START DATA}/\overline{\text{STOP}}$, thereby halting digitization of the analog interferogram. An 8-point interferogram is acquired in this manner. The backward to forward turn-around sequence commences, and when complete, $\text{T/A CNTR } \overline{\text{CNTOUT}}$ is pulsed LO. Again, this sets $\text{START DATA}/\overline{\text{STOP}}$, and the next falling edge of ADC CLK triggers the ADC. It can be seen that, in

principle, the point in optical retardation at which this digitization is carried out is the same point at which the last digitization was triggered while moving in the backwards direction. In other words, data point #8 of the first digitized interferogram corresponds to point #1 in this interferogram. Clearly, with this scheme of fringe counting, the possibility exists for signal averaging forward and backward direction interferograms on a point by point basis.

A requirement of such a signal averaging scheme is that the detection of zero-crossings of the fringe, the generation of falling edges of FRINJ, and the subsequent digitization of the source interferogram all occur in as short a period of time as possible. If there is a delay between the time at which the fringe signal goes through a zero-crossing, and the time when digitization at that zero-crossing is completed, then digitization of the forward scan interferograms does not occur at exactly the same positions of optical retardation as for the backward scan interferograms. Although in this situation, forward and backward scan interferograms can be averaged amongst themselves, the two sets of interferograms should not be averaged together.

From an efficiency point of view, it is desirable to be able to average forward and backward scan interferograms. This maximizes the data acquisition duty cycle. It also means that only one Fourier transformation need be performed. This can be a time consuming step, depending upon the particular computing machine being used to calculate the spectrum. In the present system, an Apple® MACII computer is implemented. With state-of-the art software, the time required to calculate the transform of a 65,536 point interferogram is approximately 90 s [43]. If forward scan and backward scan

interferograms cannot be averaged together, the two average forward and backward scan interferograms could be transformed separately, and then the two magnitude spectra could be averaged to produce one final average spectrum.

To assess the feasibility of signal averaging successive scan interferograms, consider the spectra shown in Figures 3-62, 3-63 and 3-64. These are spectra of a magnesium hollow cathode lamp (HCL) source, obtained under identical experimental conditions, except that different signal averaging schemes were employed. All three spectra were digitized with the 1x version of ADC CLK, therefore the sampling interval is $0.3164 \mu\text{m}$. This corresponds to a sampling frequency of approximately 10 kHz. The total travel of the mirror during the data acquisition portion of each scan was 0.52 cm. Thus, each interferogram consists of 16,384 data points.

Part a) of Fig. 3-62 is a spectrum calculated from a single interferogram that was obtained during a forward direction data acquisition scan. The spectrum in part b) of this figure was derived from the average of sixteen replicate forward direction interferograms. Qualitatively, viewing both the positions and relative heights of the peaks, these spectra appear to be very similar. As expected, the averaged spectrum is clearly less noisy than the single scan spectrum. The small peaks on either side of the 285.21 nm peak of the single scan spectrum are due to a slight random modulation of the moving mirror velocity. Due to the random nature of the modulation, these peaks are reduced by signal averaging, as evidenced in this figure.

The two spectra shown in Fig. 3-63 are analogous to those of Fig. 3-62, except that these spectra were calculated from backward scan interferograms.

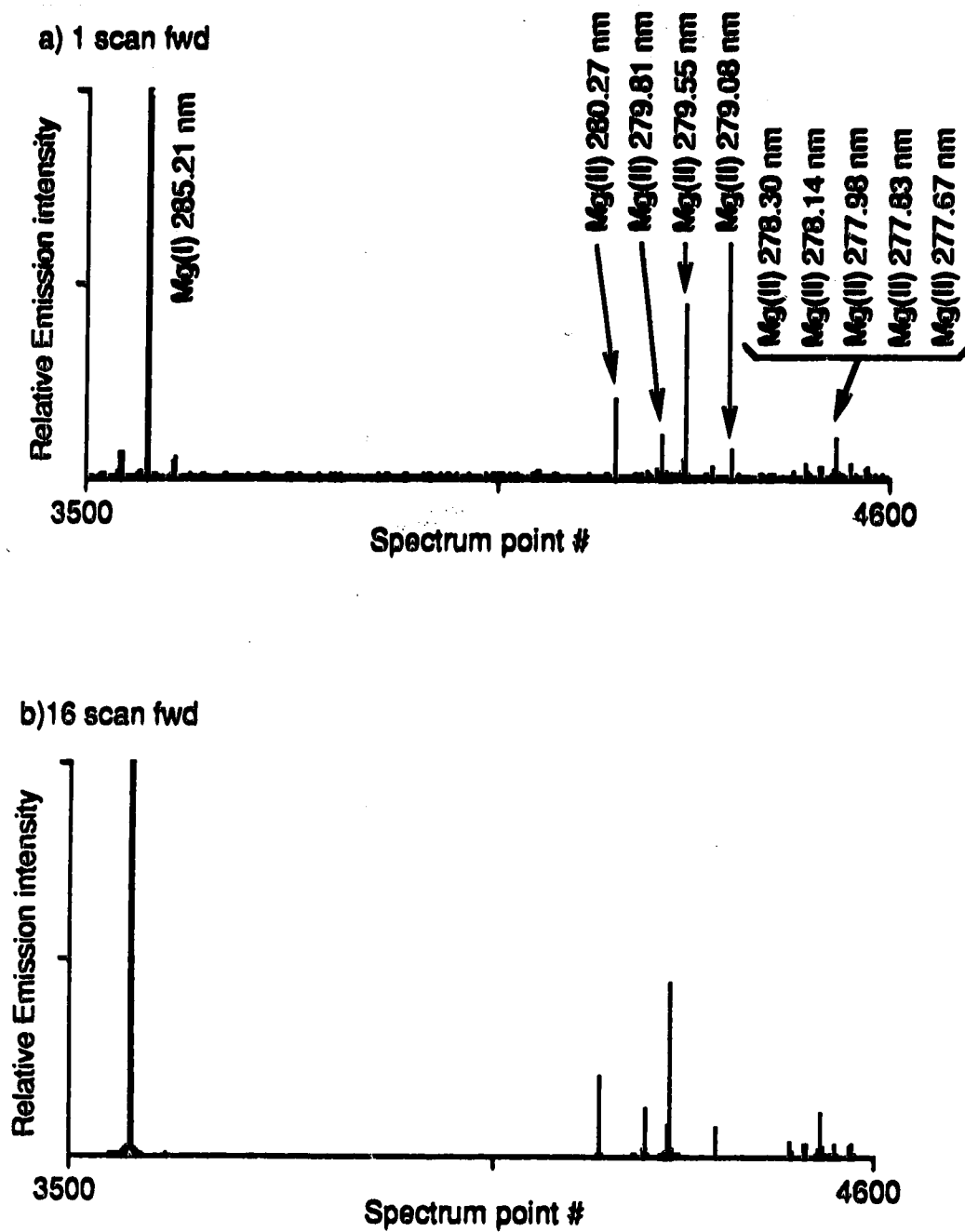
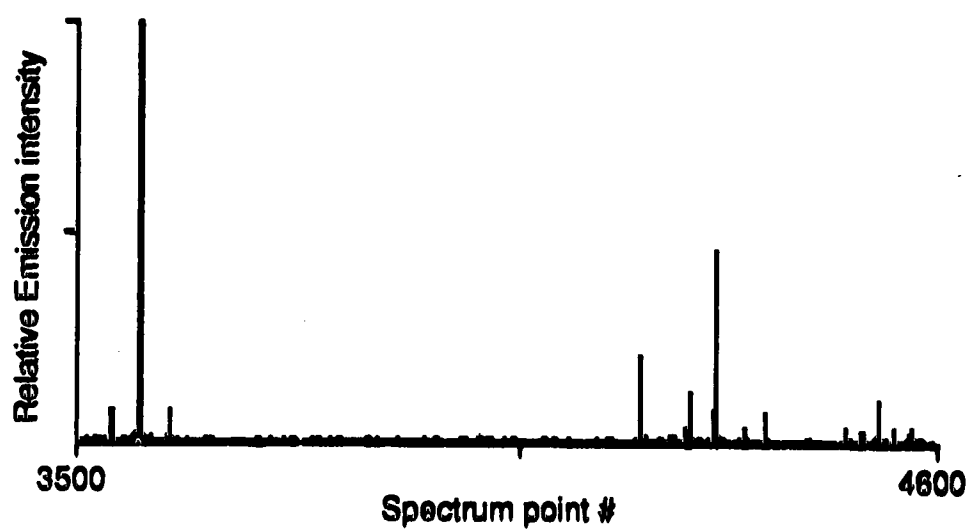


Figure 3-62. Spectra of forward scan interferograms. a) 1 scan.
b) 16 scans averaged.

a) 1 scan bwd



b) 16 scan bwd

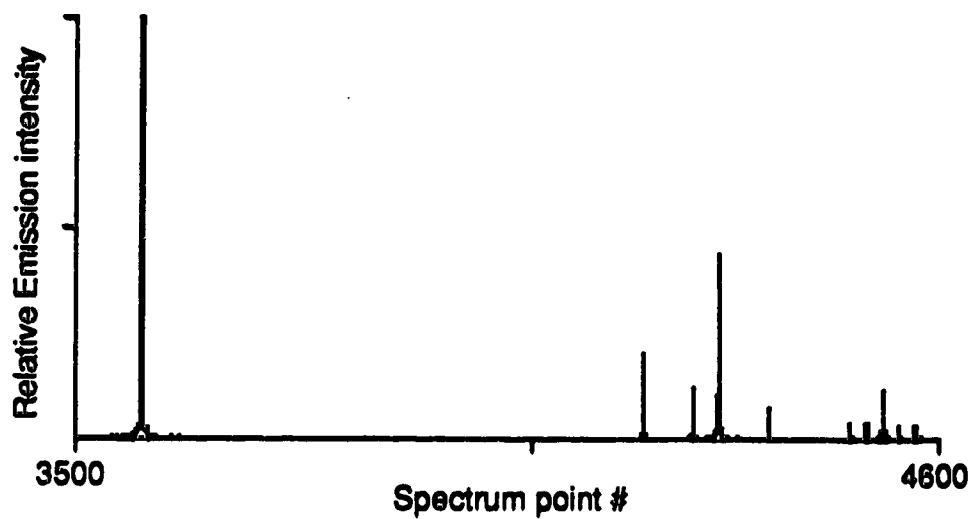


Figure 3-63. Spectra of backward scan interferograms. a) 1 scan.
b) 16 scans averaged.

Again, qualitatively, these two spectra appear to be very similar, and they agree well with those of Fig. 3-62.

These forward and backward scan average spectra are shown in parts a) and b) of Fig. 3-64, respectively. Shown in part c) is the spectrum derived from an interferogram that is the average of 16 successive scans, that is, 8 forward and 8 backward scans. The intensities of the major peaks of the three spectra are included in this figure. It can be seen that although the heights for a given peak vary between spectra, within a given spectrum the trends in peak height are the same for all three spectra. The discrepancies between spectra are most likely due to fluctuations in the intensity of the source. The Mg HCL source was operated in an open loop fashion, with no feed-back to stabilize the output intensity. From this data it would appear that signal averaging successive scan interferograms may be feasible with this system.

The regions of the three average spectra from approximately 278.5 to 277.5 nm have been expanded and zero-filled (64 x) to produce Fig. 3-65. Parts a), b), and c), are derived from the 16 forward, 16 backward, and 8 forward/8 backward scans average spectra, respectively. Qualitatively, with respect to the shape and positioning of the spectral lines, there is very good agreement among the three spectra.

Also included in this figure are the peak height ratios for each peak. The height of each peak has been divided by the height of the peak at 285.21 nm in each spectrum. The fluctuations in the values for any given peak are not consistent. For the peak at 278.30 nm, the normalized intensity for the 8 forward/8 backward scan spectrum is well removed from the two values for the forward and backward scan spectra. However, for the peak next to this

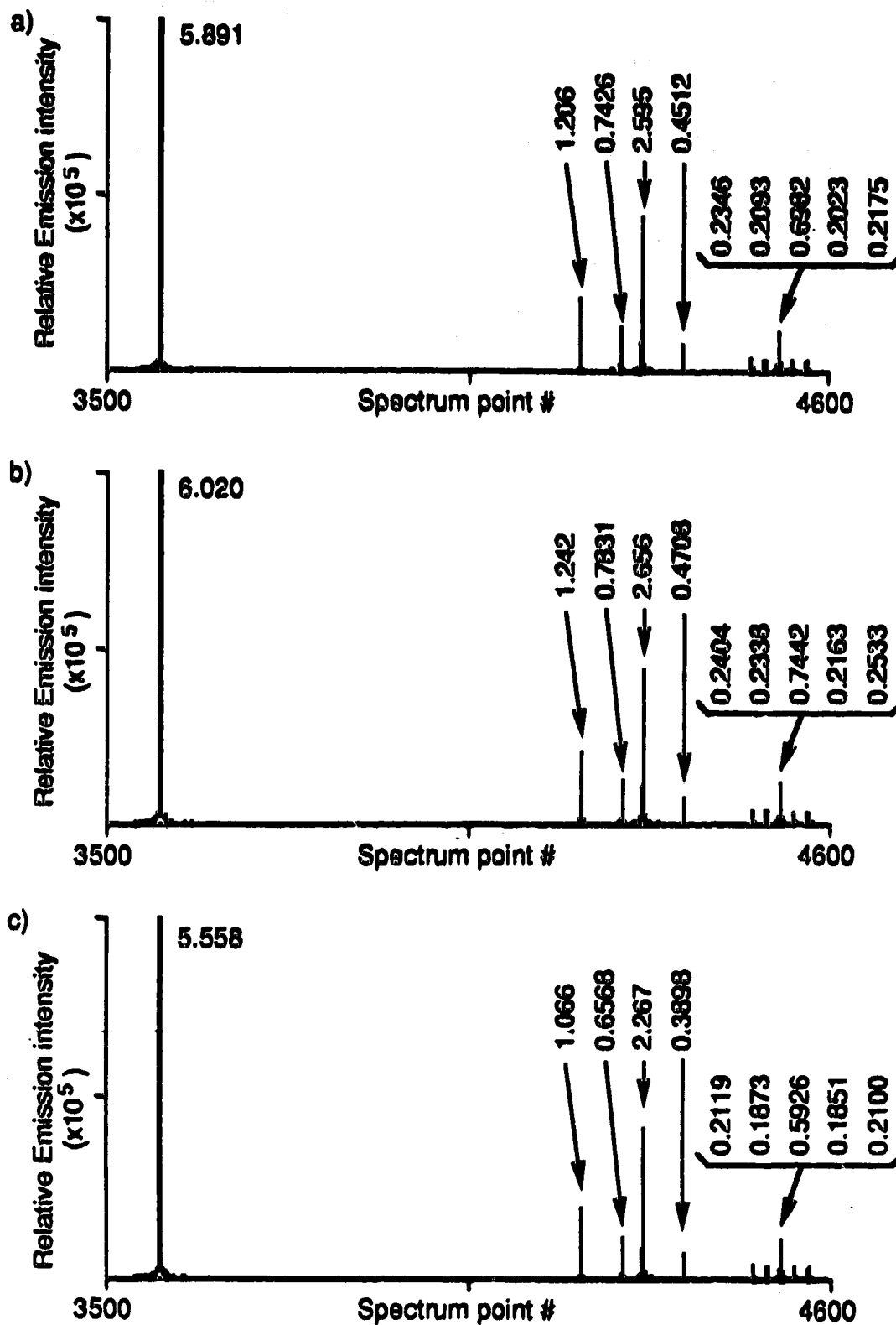


Figure 3-64. Spectra of average interferograms. a) 16 forward scans. b) 16 backward scans. c) 8 forward + 8 backward scans.

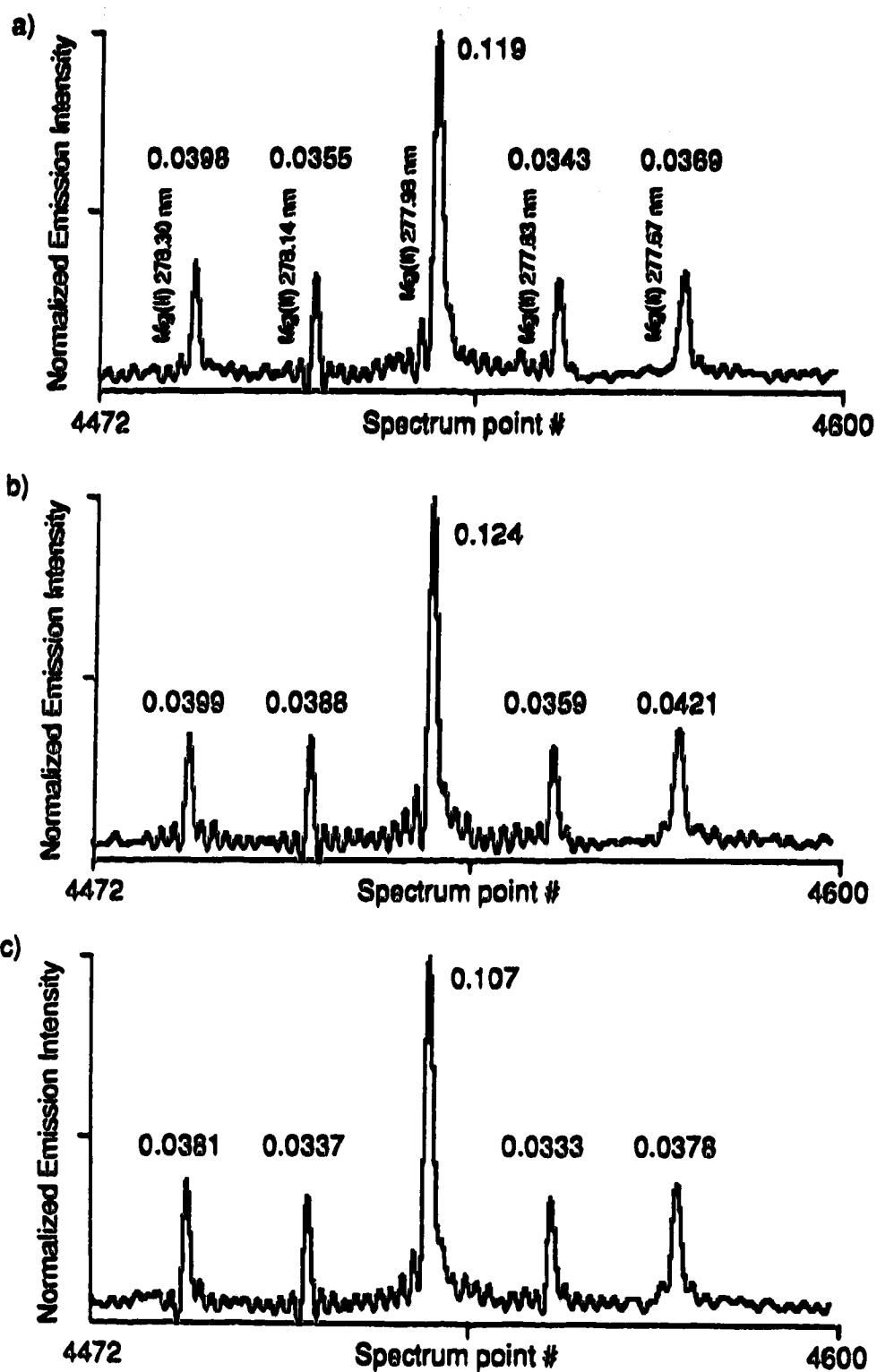


Figure 3-65. Expansions of ~278.5-277.5 nm region of average spectra of Fig. 3-64. a) 16 forward scans. b) 16 backward scans. c) 8 forward + 8 backward scans. Normalized peak heights. (See text for details.)

one at 278.14 nm, the value for the backward spectrum is in disagreement with those of the other two spectra. Certainly, there are no conclusive discrepancies between these three spectra that could be construed as arising from signal averaging phase shifted interferograms during the successive scan averaging process.

From the spectra presented in Figs. 3-64 and 3-65, a tentative conclusion can be reached that signal averaging interferograms in both directions does not appreciably affect the quality of the spectrum that is obtained. The fluctuations in peak heights and peak height ratios may well be due to drift in the excitation conditions of the source. A more detailed study would require a highly stable, or well stabilized source.

It is important to note that with the present system it should only be possible to average interferograms which are acquired with the 1x version of ADC CLK . To do this with the 4x or 8x versions of ADC CLK, additional electronic hardware would be required. As digital signal processing becomes more sophisticated and readily available, the need and advantages of successive scan interferogram averaging will become less significant.

Consider the situation in which successive backwards direction interferograms are being signal averaged. As mentioned earlier, if the falling transition of FWD/\overline{BWD} does not occur within the bracket of a turn-around, the next interferogram that is acquired in the backward direction will be shifted in phase relative to the previously acquired backward scan interferograms. If fringe counting then proceeds correctly, all of the subsequent backward scan interferograms will be shifted by one fringe period.

The effect is to have shifted the position of the data acquisition scan by one fringe period.

Interferograms that differ in phase by one fringe period should not be signal averaged. The effects of this on the resultant spectrum are shown in Figs. 3-66 to 3-70.

Shown in parts a) and b) of Fig. 3-66 are two spectra, S1 and S2, of a Mg HCL source. The wavelength assignments in these spectra are the same as those indicated in Fig. 3-62. These spectra were calculated from two average interferograms, I1 and I2, respectively. I2 was acquired directly after I1. Both of these interferograms consist of 16,384 data points, acquired with the 1x version of ADC CLK. In both cases, 32 successive backward scan interferograms were averaged. During data acquisition, it was ensured that fringe counting occurred properly. As evidenced in this figure, S1 and S2 are very similar in nature. Differences between corresponding peak heights in the two spectra are considered to be due to drift of the HCL source output intensity.

The Fourier transform is a linear transform. If a set of replicate interferograms are transformed to produce a set of replicate spectra, then the average of these spectra should be identical to the spectrum that is calculated from the average of the replicate interferograms. This is illustrated in Fig. 3-67.

The spectrum $S(I1+I2)$, shown in part a) of this figure, was calculated from an interferogram that is the average of the two 32 scan, non-shifted, average interferograms, I1 and I2. The spectrum shown in part b) of this figure, $S1+S2$, is the average of the two spectra, S1 and S2, that were calculated

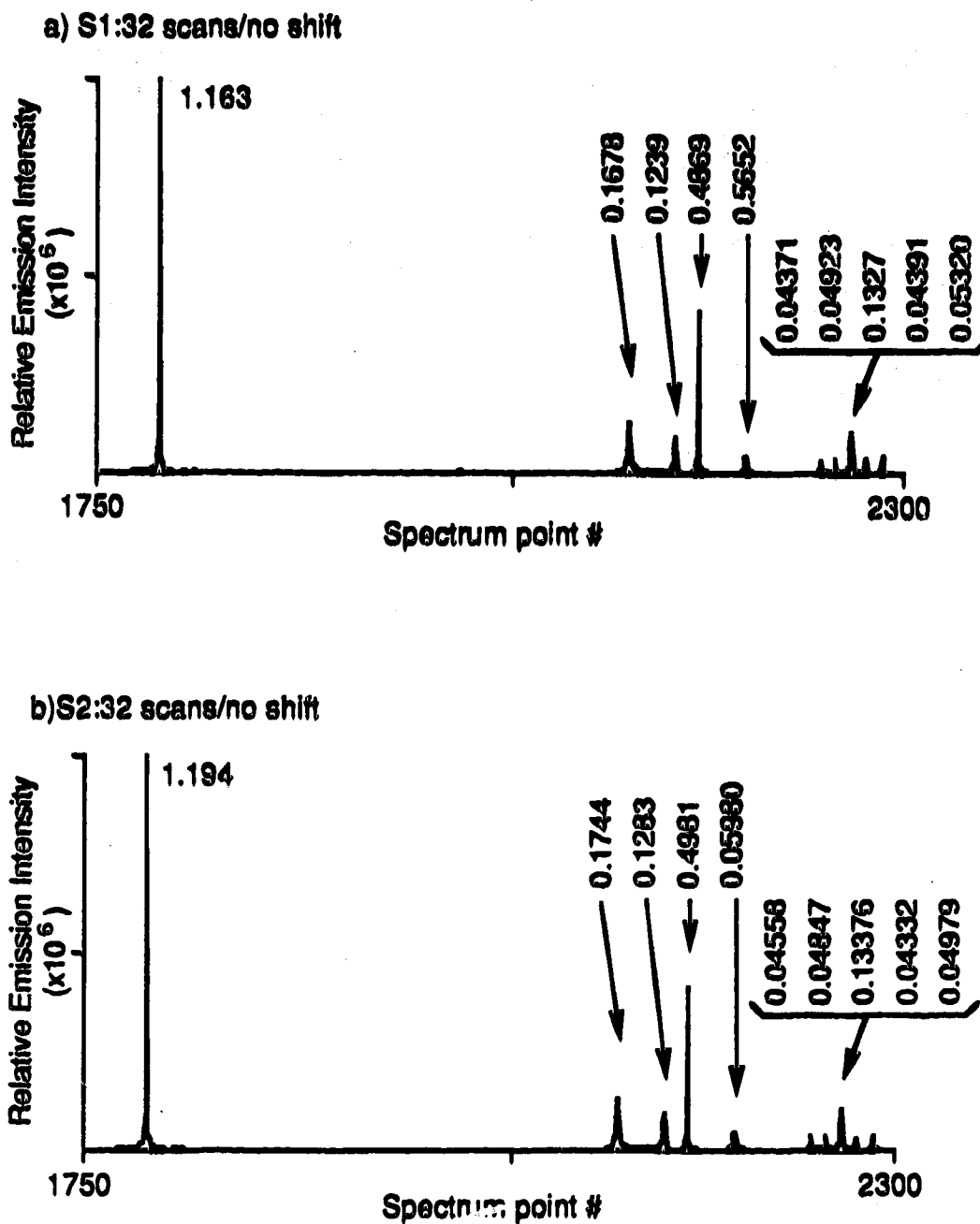


Figure 3-66. Spectra of non-phase-shifted average (32 backward scans) interferograms.

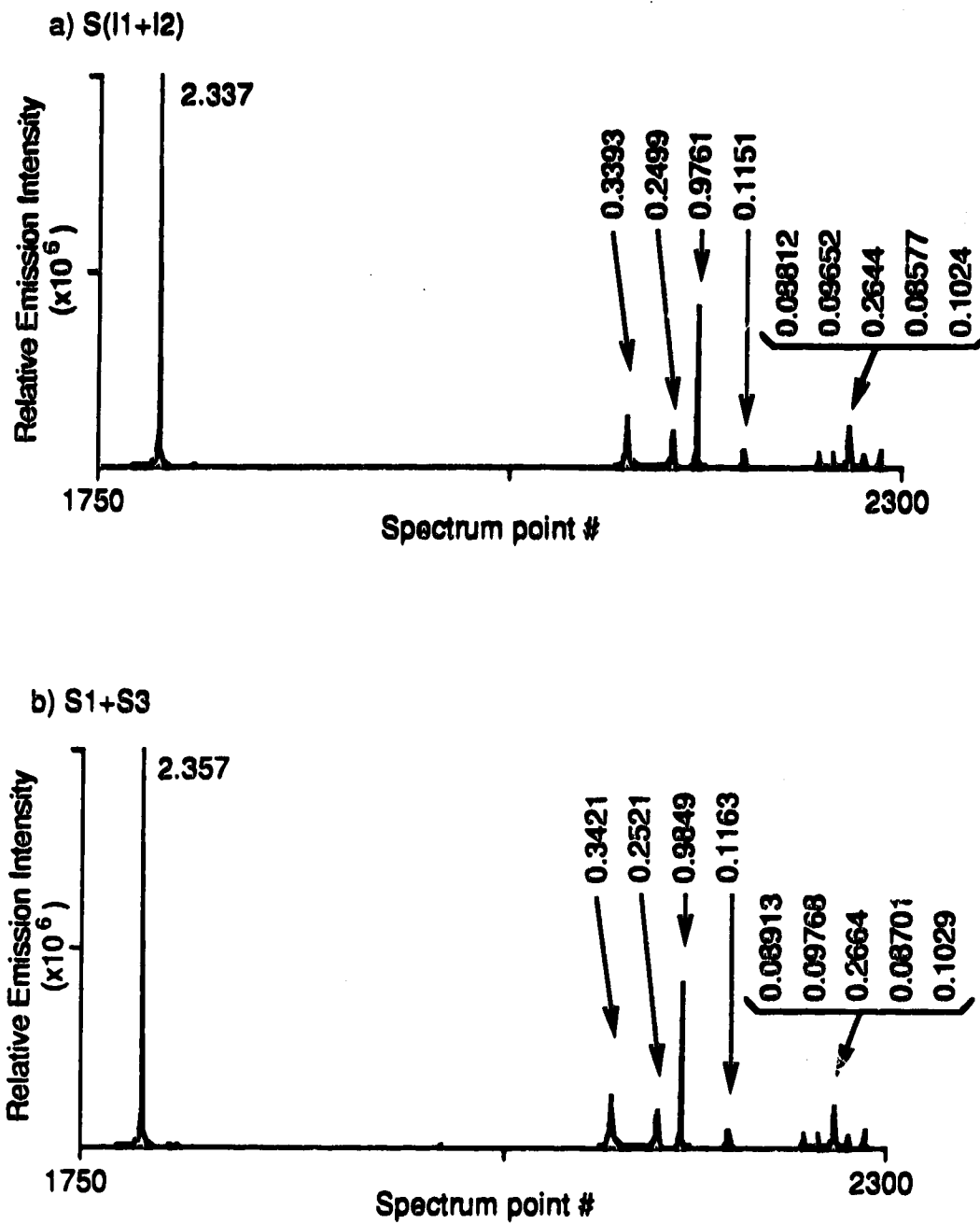


Figure 3-67. Averaging spectra vs. averaging interferograms.
(See text for details.)

from I1 and I2. It can be seen that, as expected, these two spectra are very similar. This result indicates that I1 and I2 do not differ appreciably in phase.

Incorrect operation of the fringe counting system was simulated by delaying the transitions of **START DATA/STOP** by one fringe period. 32 replicate interferograms were acquired under this condition. These were averaged to produce the interferogram I3. I3 was transformed to produce S3, as shown in part b) of Fig. 3-68. For convenience, S1 of part a) of Fig. 3-66 is reproduced in part a) of this figure. Thus, these two spectra were calculated from interferograms that are phase shifted, relative to each other, by one period of the fringe.

It can be seen that the introduction of a one fringe period phase shift has little effect upon the nature of the resultant spectrum. S1 and S3 are very similar. This is not surprising. Although the phase spectra for the two interferograms would be expected to be quite different, the amplitude spectra should show very little difference for this small a relative phase shift. The effect of this shift is to slightly alter the truncation of the interferogram. In this system, symmetric truncation is strived for. Asymmetric truncation results in distorted spectral line-shapes. Since these interferograms are 16,384 fringe periods in length, a shift of one period of the fringe in either direction has little absolute effect upon the truncation of the interferogram. Thus, in this situation, there is a negligible effect upon the peak intensities and/or the spectral line shapes. However, if the phase shift was a large enough number of fringe periods, the result would be a spectrum with highly distorted line-shapes.

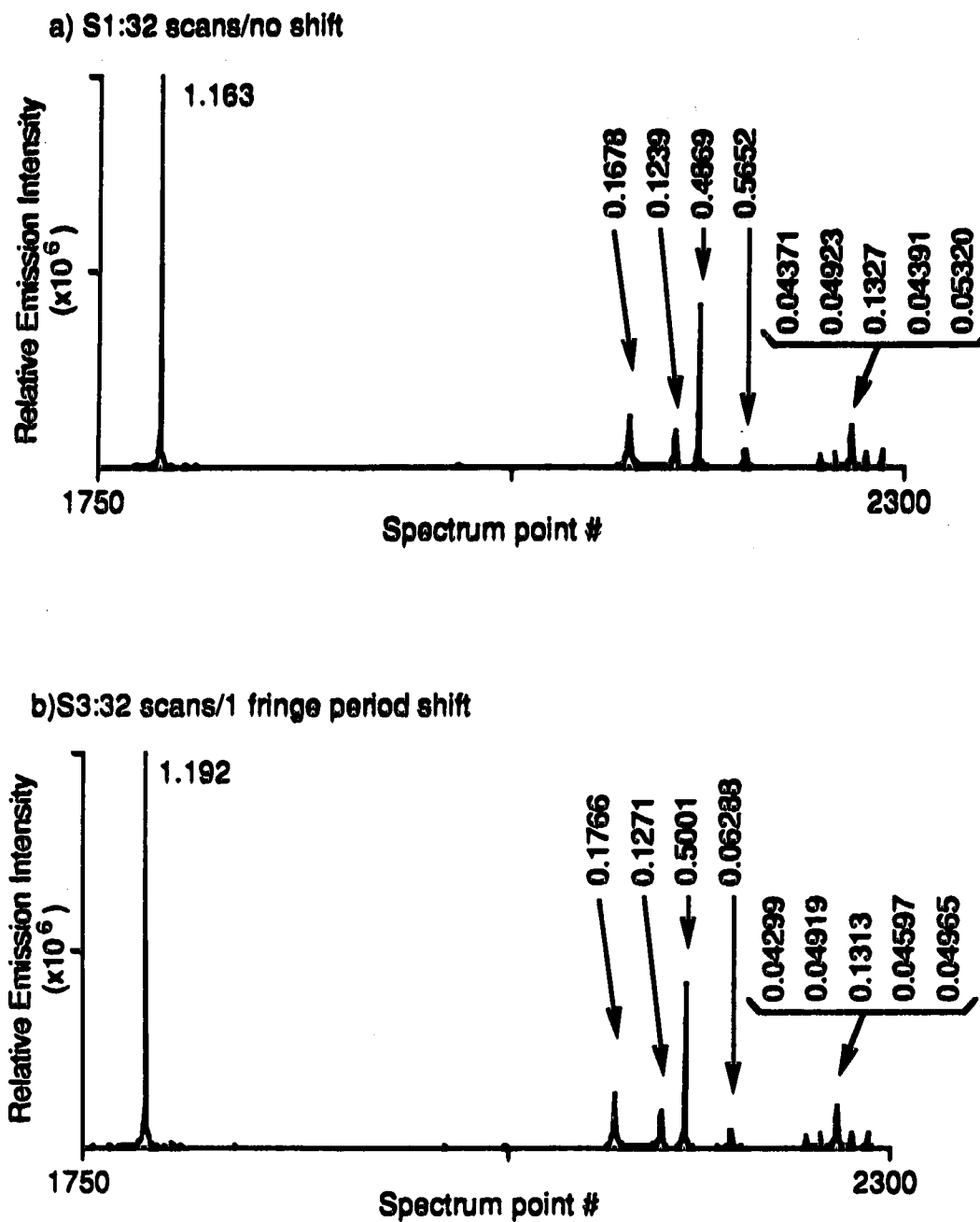


Figure 3-68. Spectra of non-phase-shifted, and one fringe period phase-shifted interferograms.

Even though they were derived from a non-shifted and shifted pair of interferograms, S_1 and S_3 of Fig. 3-68, could be averaged to produce a spectrum that is very similar to that which would be obtained from a correctly averaged 64 scan interferogram. The average of these spectra, S_1+S_3 , is shown in part a) of Fig. 3-69. This spectrum agrees well with $S(I_1+I_2)$ in part a) of Fig. 3-67. However, if the non-shifted and shifted interferograms, I_1 and I_3 , are averaged and then transformed, the resultant spectrum, $S(I_1+I_3)$, has markedly different peak height values than those in the correctly averaged situation. $S(I_1+I_3)$ is shown in part b) of Fig. 3-69. Clearly, when compared with those of $S(I_1+I_2)$, the peak heights of $S(I_1+I_3)$ are significantly in error.

Portions of $S(I_2+I_2)$ and $S(I_1+I_3)$ are shown, expanded (and zero-filled $64 \times$), in Fig. 3-70, parts a) and b), respectively. The regions shown range from 277.5 to 287.5 nm. The ratios of the respective peak heights to that of the 285.21 nm line in each spectrum are indicated. Qualitatively, the shape of the spectral lines in these two spectra do not differ appreciably. Again, since the truncation of the interferogram is not being strongly affected in this situation, it is not unreasonable that the spectral line-shapes are largely unaffected by this incorrect averaging procedure.

However, the peak height ratios are significantly different. Those of $S(I_1+I_2)$ are in reasonable agreement with those indicated in Fig. 3-65. The discrepancies could be attributed to drift of the source (especially with respect to excitation conditions) and the larger number of replicates that were averaged in this study. The peak height ratios of $S(I_1+I_3)$ are in serious disagreement with all of the spectra of Fig. 3-65, and that of part a) of this figure. Clearly, averaging interferograms that are shifted in phase by one full

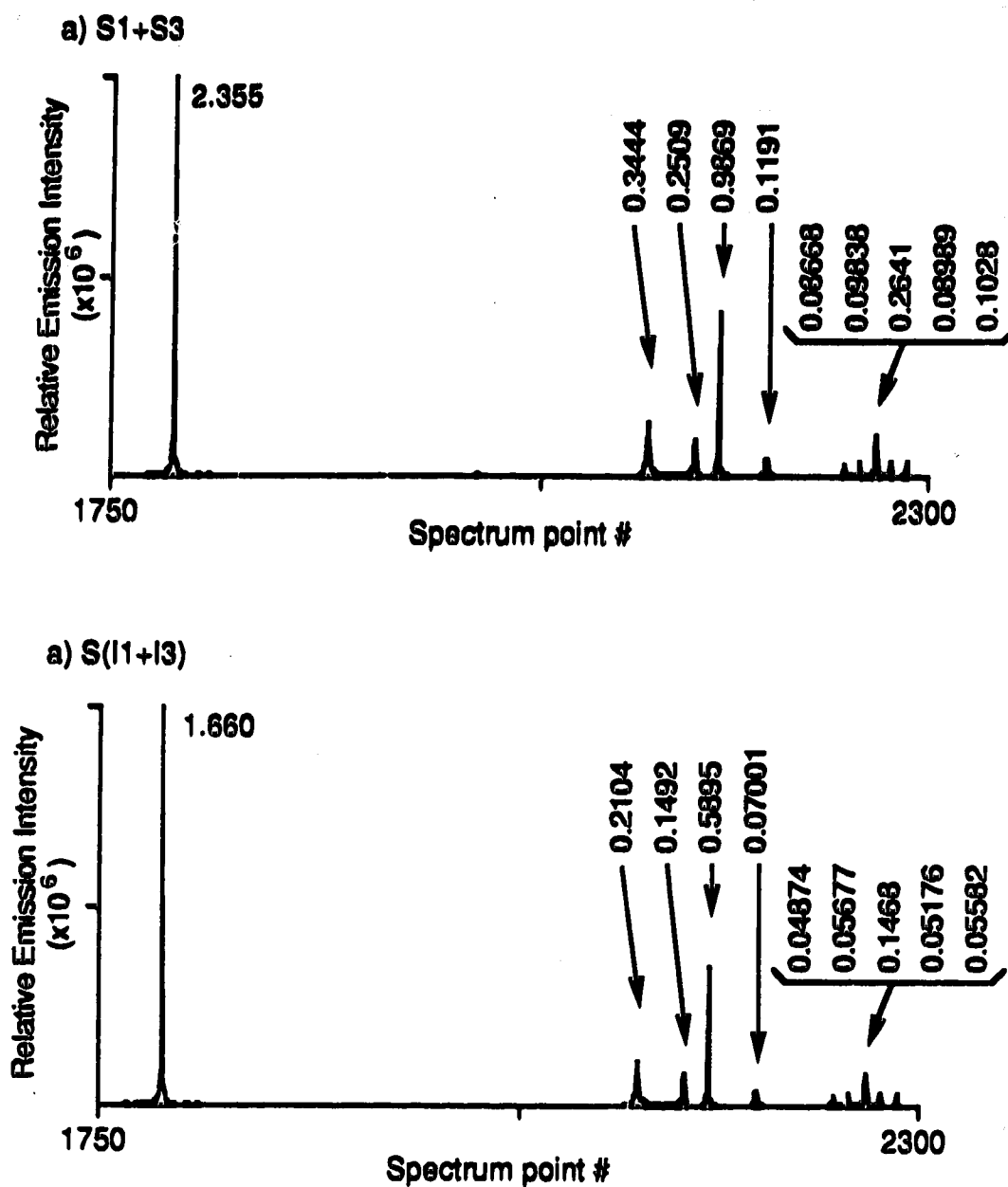
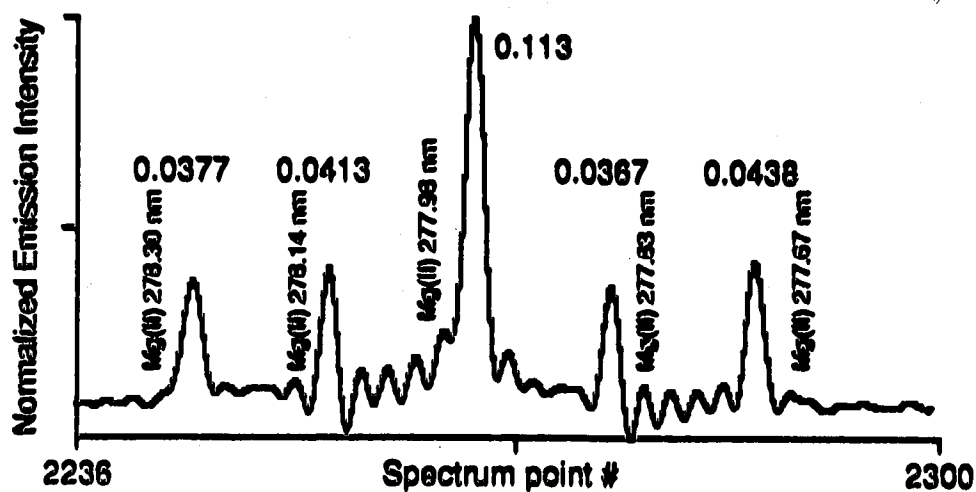


Figure 3-69. Averaging of phase-shifted spectra vs. spectrum of average of phase-shifted interferograms.

a) S(I1+I2)



b) S(I1+I3)

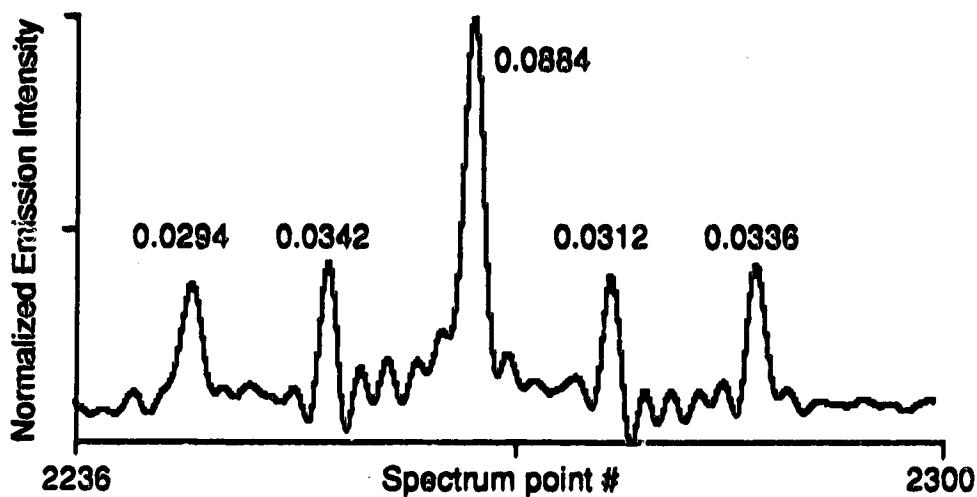


Figure 3-70. Expansions of ~278.5-277.5 nm region of spectra of non-phase-shifted and phase-shifted average interferograms. Normalized peak heights. (See text for details.)

period of the fringe results in significantly incorrect intensities in the final spectrum. Thus, for correct signal averaging of interferograms, it is essential that the fringe counting system operate properly.

In calculating the incorrectly averaged interferogram, half of the replicate interferograms that were included in the sum were shifted by one fringe period. This is the worst case situation. The number of phase shifted replicates could be smaller than half of the total. Obviously, in this case the effect on the spectrum would be less. In the case where only a few interferograms were shifted, the effect might be negligible. To assess this situation a more stable source would be required such that small discrepancies between spectra could be recognized.

When the fringe counting system is operating properly, full fringe period phase shifts do not occur. At present, the operation of the fringe counting system is assessed by counting periods of the fringe from the beginning of a forward scan up to the position of ZPD. Assuming that the relative phases of the fringe and the white light signal are stable, then, if the fringe counting system is working correctly, the start of this count should occur, repeatedly, at the same number of fringe periods from the white light signal. Hence, during correct operation, the same count results scan after scan. In the current version of the system, this count is displayed continuously. In this way the operator can monitor if the fringe counting system is working properly. (In the event that the value of this count drifts, the usual course of action is to adjust the position of FWD/BWD as described previously.) At the present time the system stability is such that it is not uncommon for the count to remain constant throughout hours of operation.

When it does change it is often the result of drifting of the phase difference between the fringe and the white light signal.

Consider for a moment the process of digitizing the interferogram of a laser of wavelength, λ . The interferogram of such a source would be a slowly decaying sinusoid, the extent of the decay being related to the coherence length of the laser. The intensity of the interferogram is modulated through one period as the mirror moves through a distance of $\lambda/2$. To correctly digitize this signal, at least 2 samples should be acquired per period of the interferogram. This means that digitization should occur at intervals of $\lambda/4$ of mirror movement. If the system was set up for digitization on this interval, the interferograms from other sources would be correctly digitized as long as the radiation from these sources had no wavelength components that were shorter than λ . The interferograms of such components would be sampled less than twice per period. As an example, with the present system, the shortest wavelength of source radiation that we are interested in is approximately 180 nm. To go much lower into the vacuum UV region would require different optical materials and/or coatings for windows, mirrors, beam-splitters, etc. 180 nm is a reasonable worst case figure for the present version of this instrument. To correctly sample the 180 nm component in an interferogram, the sampling interval must be set to 0.045 μm .

Since the mode of operation of this Fourier transform spectrometer is to acquire data during constant velocity scanning of the moving mirror, the interferogram is acquired as a time varying signal. This is to distinguish between this system and others in which the mirror is held stationary at a

given sampling position during which time signal averaging is performed, followed by a step to the next sampling position.

At present, the mirror moves with a velocity of 0.3164 cm/s. A 180 nm wavelength component appears in the interferogram as a 35.16 kHz frequency component. In terms of the usual Nyquist sampling criterion, to correctly sample an interferogram whose highest frequency component is 35.16 kHz, the sampling frequency must be at least twice this frequency, or 70.32 kHz. This is indeed the case when a sampling interval of 0.045 μm of mirror movement is used. With the present mirror velocity, the mirror moves through the sampling increments of 0.045 μm in 14.2 μs . That is, digitization of the interferogram occurs with a frequency of 70.31 kHz.

From the above, a convenient spatial Nyquist sampling criterion could be stated as follows. In order to correctly sample the interferogram of the radiation from a source in which the shortest wavelength component is λ , the sampling interval must be less than or equal to $\lambda/4$ of mirror movement.

In the present system, the sampling interval is 0.3164 μm , as determined by the wavelength of the HeNe reference laser. With this sampling interval, an interferogram produced by source radiation in which the shortest wavelength is 1.266 μm would be correctly sampled. If the incident radiation contained shorter wavelengths (as would be the case with atomic emission sources), these would be incorrectly sampled. In the final spectrum, these shorter wavelength components would appear as longer wavelength components. That is, these shorter wavelength components would be folded back, or "aliased", into longer wavelength regions of the spectrum. In some situations aliasing is more of a nuisance than a major

problem. This is often the case with line spectra of limited band-width. In other situations, for instance with broad band continuum sources, aliasing becomes unacceptable.

For sources with wavelengths as short as 180 nm, in order to completely eliminate aliasing the sampling interval must be reduced to 0.045 μm . For this system, this can be achieved in a number of ways.

In the present system, the sampling interval is defined by the mirror travel between every second zero crossing. Thus, by using every zero crossing to trigger the ADC, the sampling interval is reduced to 0.1582 μm . With this sampling interval the low wavelength end of non-aliased operation becomes 632.8 nm. For our purposes, the sampling interval must be reduced further.

The simplest and most straight-forward method to further reduce the sampling interval would be to use a reference laser with a shorter wavelength than that of the HeNe laser presently in use. Ideally, what is required is a CW laser with a wavelength of 180 nm. With such a laser, zero crossings would occur as the mirror moved through 0.045 μm . Clocking the ADC on every zero-crossing would result in the required sampling interval. This idea is fine in principle; however, in practice a whole new set of technological problems would be introduced in attempting to incorporate a laser with this short a wavelength into this system. The quality of the necessary optical components would have to be very high. Alignment throughout the optical path would be difficult, and the optical path would most likely have to be evacuated or purged. Furthermore, a strong presupposition here is that such a CW laser would be commercially available at a reasonable price.

Using a shorter wavelength laser might be a viable alternative for the situation in which it is only desired to reduce the sampling interval to approximately one quarter of its present value. When the optical detector is a R166 PMT, only a limited band-width of wavelength components in the source radiation are detected. This is because the R166 PMT has a limited spectral sensitivity, responding only over the wavelength range from approximately 180 to 300 nm. Since wavelength components above 300 nm are not detected, this region of the final spectrum is empty. Thus, the wavelength components from 180 to 300 nm can be aliased to longer wavelengths in the final spectrum without over-lap problems. With a sampling interval of 0.090 μm , a 180 nm wavelength component in the source radiation would be sampled only once per period. All of the wavelength components up to and including 360 nm would be under-sampled, and therefore aliased to longer wavelengths. The region from 180 to 360 nm would be symmetrically folded back about an axis at 360 nm. All of the components between 180 and 360 nm would appear between 360 and 540 nm, with 540 nm corresponding to the aliased 180 nm. Again, this region from 360 to 540 nm is empty, hence, there are no over-lap problems. Since the R166 PMT does not respond appreciably to radiation with wavelengths above 300 nm, the final spectrum would consist of a band from 420 to 540 nm.

If a HeCd laser, with a wavelength of 325 nm, was used as the reference laser, the sampling interval would be reduced to 0.0813 μm (if every zero-crossing was used to clock the ADC). With a R166 PMT, the 180-300 nm wavelength region would appear from 350 to 470 nm (with 470 nm corresponding to 180 nm) in the final spectrum. In the event that operation of an instrument of this sort was to be limited to this type of band-limited

operation, the use of a He Cd laser would be a viable solution to the problem of aliasing. It should be noted that HeCd lasers are substantially more expensive than HeNe lasers, the prices being ca. \$3000-\$7000 (US) and \$300 (US), respectively. A more general, less expensive method of reducing the sampling interval is desirable.

If a reference laser with a shorter wavelength is used, the sampling interval is directly reduced. That is, the zero-crossings that are used to clock the ADC are a direct indication of smaller intervals of mirror movement. An indirect method of indicating intervals of movement that are smaller than the interval between zero-crossings of the HeNe fringe, is to divide up the interval of time required to traverse the positions of zero-crossings

In the present system, the time between zero crossings is 50 μ s, but since every second zero-crossing is used to clock the ADC, the time between digitizations is 100 μ s. Since the mirror moves with a constant velocity, time elapsed and distance travelled are related in a simple fashion. With the assumption that the velocity is constant, 12.5 μ s after detection of the last digitizing zero-crossing, the mirror has travelled one-eighth of the distance to the next digitizing zero-crossing. Thus, the mirror has moved a distance of 0.03955 μ m. This is a small enough interval of mirror movement that if the signal that 12.5 μ s has passed was used to clock digitization, non-aliased operation with wavelengths as short as approximately 160 nm would be ensured.

A simple method of reducing the sampling interval, then, would be to build a cascade of 7 mono-stable multi-vibrator circuits, the output of the first being used as the input of the second, and so on. The input for the first circuit

is FRINJ. When the mirror moves through a zero-crossing to produce a falling edge of FRINJ, this transition triggers the first mono-stable whose delay is set for $12.5 \mu\text{s}$. After $12.5 \mu\text{s}$ has elapsed, a falling transition is generated at the output of this circuit. This clocks the ADC and triggers the second mono-stable. The process is repeated such that the next digitization occurs $25 \mu\text{s}$ after the last digitizing zero-crossing. This continues down the cascade of mono-stables such that digitizations occur every $12.5 \mu\text{s}$, resulting in non-aliased operation. The process is repeated on each falling edge of FRINJ.

This scheme is elegant in its simplicity, however it is an open loop situation with no capability for corrective action in the event that a disturbance to the system occurs. For instance, an absolute pre-requisite for the successful operation of this system is that the velocity remains constant with a well-known value. If the velocity changes, the time between zero crossings will no longer be $100 \mu\text{s}$. After a zero crossing, 7 samples are taken at $12.5 \mu\text{s}$ intervals. This no longer evenly divides the period between zero crossings. It is important that the source interferogram be digitized at equal intervals of optical retardation. This criterion would not be satisfied in this situation. Rather than implementing this simple open loop system, a phase locked loop circuit (with feed-back) has been constructed. In this manner, the period of FRINJ is actively divided into equal increments of time.

The phase locked loop (PLL) circuit that has been implemented is illustrated, schematically, in Fig. 3-71. The input reference signal for the loop is FRINJ. The loop is set up to synthesize an output square wave with a frequency that's four times that of FRINJ. In this way, the period of FRINJ is divided into four equal intervals, each being $25 \mu\text{s}$ in duration. The output of

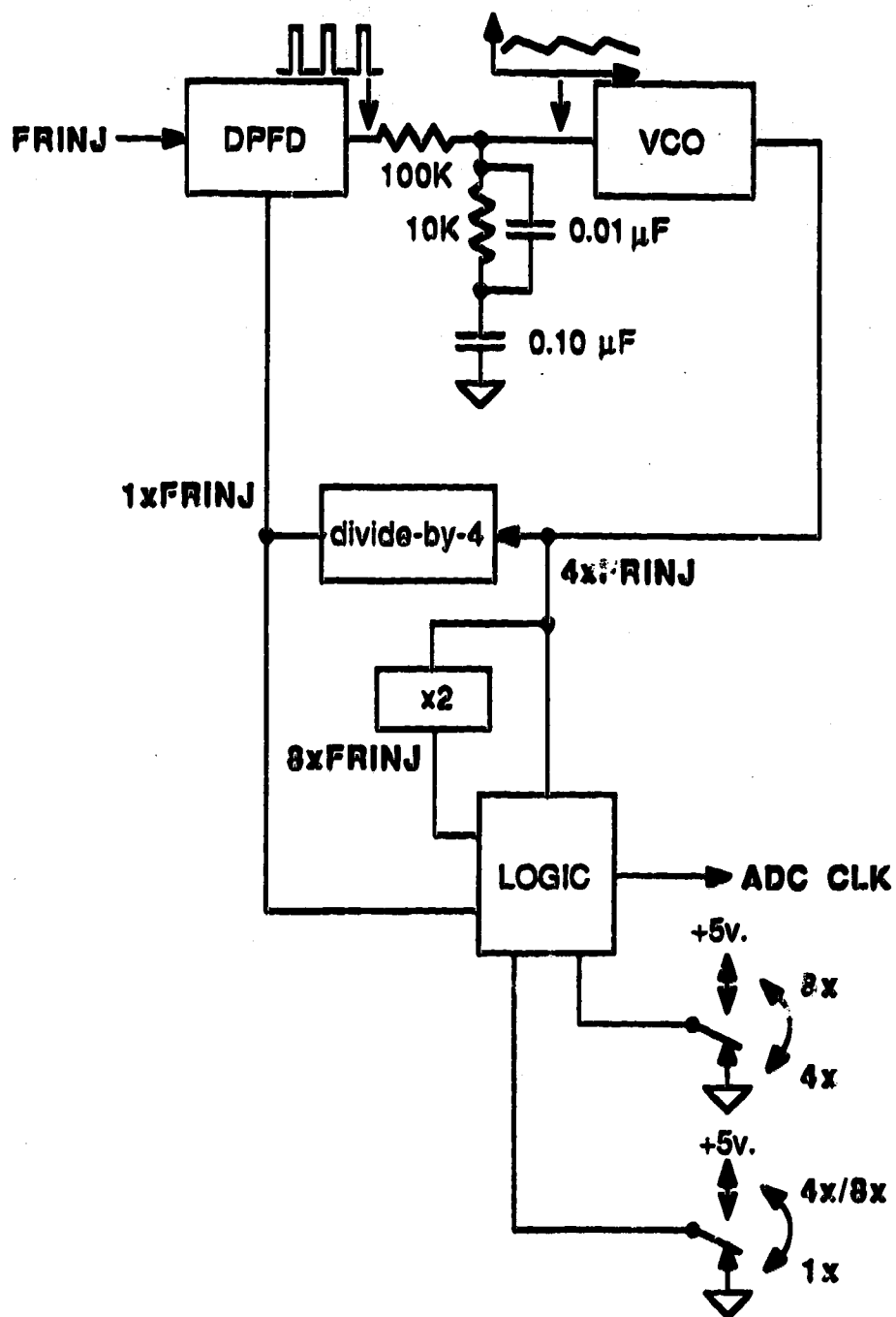


Figure 3-71. Digital Phase Locked Loop frequency multiplication circuitry.

the loop is fed-back and compared with the input. If the period of FRINJ changes as a result of an external disturbance, the loop tracks the changes in the period to maintain four equal increments per period.

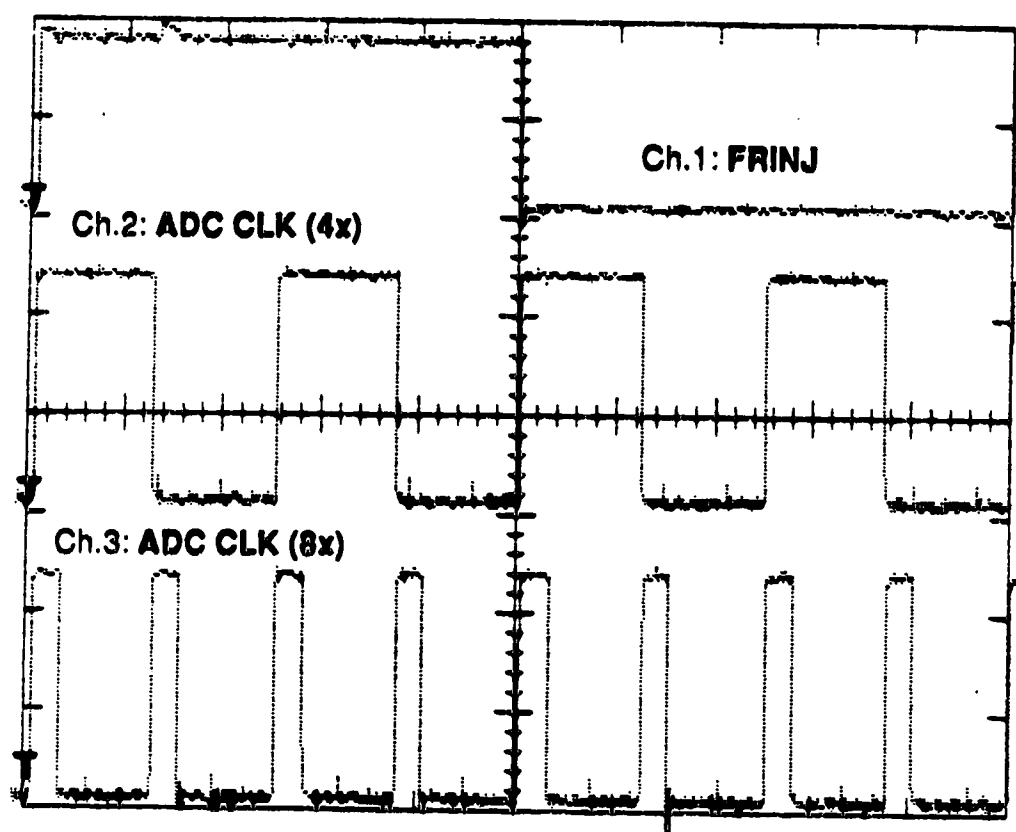
This circuit of Fig. 3-71 is based upon the CD 4046 (RCA) monolithic phase locked loop integrated circuit. On this chip there are two phase detectors. One of these is a Digital Phase-Frequency Detector (DPFD). This type of phase detector is particularly suitable for use in square wave frequency synthesis applications. The most important characteristic of this detector is that it doesn't lock onto harmonics of the input signal. During turn-around sequences, the frequency of FRINJ is modulated from 10 kHz to dc and back up to 10 kHz. Other phase detectors are prone to locking onto a harmonic of the input signal during such a modulation of the input frequency. In this case, the period of FRINJ could be divided by 8, 12, 16, etc., intervals. Clearly, in this application, this is unacceptable. It should be noted that during constant velocity scanning of the mirror, FRINJ has a very tightly controlled frequency. Data is acquired only during the time when the frequency is constant. What happens to the output of the loop during the major portion of the turn-around sequence is of no consequence. The conditions under which the loop has to operate are highly controlled. Thus, the loop architecture can be optimized for this very specific application, with few compromises.

The DPFD receives as inputs the reference signal, FRINJ, and a 4 times frequency divided version of the output square wave. The output of the DPFD is connected to a low pass filter which is in turn connected to the input of a Voltage Controlled Oscillator (VCO). The frequency of the square wave output of the VCO increases or decreases as the output voltage of the filter

increases or decreases. The output of the VCO is fed into a divide-by-four counter. The output of this counter is input into the DPF to close the feed-back loop. The feed-back loop keeps the frequencies and phases of FRINJ and the feed-back square wave equal. Therefore, the output of the VCO is equivalent to FRINJ, with each period divided into four equal intervals.

The 4 times period divided version of FRINJ is a square wave. This is input into a pair of mono-stable multivibrators with associated logic. In a manner analogous to the production of FRINJ_{px2}, pulses are produced for each transition of the 4 times divided signal. This produces an 8 times period divided version of FRINJ. This architecture was implemented rather than switching the divide-by-N counter in the feed-back path between divide-by-4 and divide-by-8. In this way the loop operation could be optimized without the design compromises that would be needed for the generation of two different output frequencies.

The three versions of FRINJ are designated as 1x, 4x, or 8x. These are all input into switching logic, the output of which is designated ADC CLK. This can be chosen to be any one of the three versions of FRINJ. The 4x and 8x versions of ADC CLK are shown, along with FRINJ for comparison, in Fig. 3-72. (The 1x is simply a reproduction of FRINJ.) Note that the rising edge of FRINJ is concurrent with rising edges of both the 4x and 8x versions. Since the frequency of FRINJ is not exactly 100 μ s, the period of the 4x ADC CLK is not exactly 25 μ s. It is however, one quarter of the period of FRINJ. Also, the duty cycle of the 4x version waveform is not exactly 50 %. The HI portion is slightly less than the LO portion. This doesn't affect sampling with the 4x version since this asymmetry is constant and, therefore, the falling transitions still occur at equal intervals. However, since the falling edges of the 8x



Trigger: Ch.1

Time base: 10 μ s/div

Vert. gain: All channels 2v/div

Figure 3-72. FRINJ and 4x and 8x versions of ADC CLK.

version of ADC CLK are generated by both transitions of the 4x version, the sampling interval of the former is slightly frequency modulated. This could introduce spurious peaks into the final spectrum; however, it is expected that this modulation is so small as to be negligible.

The 4x version of ADC CLK is usually chosen when a R166 PMT is in use, the 8x when fully non-aliased operation is required, and the 1x when high resolution of a well-known spectrum is desired. (With the 1x version fewer data points are required as the mirror is moved through longer travel for increased resolution.)

The output of the DPF_D is a tri-state output. Rising edges of FRINJ connect the output of the DPF_D to +5 v. Rising edges of the feed-back signal connect the output to ground. When the rising edges of both signals occur simultaneously, the output is in a high impedance state. Consider the situation in which FRINJ is suddenly turned ON at the reference input of the DPF_D, with a dc-level output from the VCO.

The first rising edge of FRINJ connects the output of the DPF_D to +5 v. The filter integrates this step input such that the input to the VCO ramps towards +5 v. The VCO starts to output a square wave with an increasing frequency. The first rising edge of the feed-back square wave connects the output of the DPF_D to 0 v. The ramp to the VCO input starts to decrease until the next rising edge of FRINJ connects the output of the DPF_D to +5 v. Since the rising edges of FRINJ occur more rapidly per unit time than do those of the feed-back signal, the output of the filter ratchets upward. Eventually, the edges of FRINJ and the feed-back square wave occur simultaneously. The two waveforms have the same frequency and are in phase. The output of the

DPFD is now in the high impedance state. This maintains the filter output, and hence the VCO output, constant. If the edges of FRINJ start to lead those of the feed-back signal, either through a change in frequency and/or phase, +5 v pulses occur at the filter input. When these pulses are integrated, the increase in the filter voltage causes the VCO to increase in frequency, thereby re-synchronizing the edges of the two signals. Conversely, if the edges of the feed-back signal were to lead those of FRINJ, the input of the filter would be connected, in a pulsed fashion, to ground. This would cause the output of the filter to decrease, thereby decreasing the frequency of the VCO output square wave. Again, this re-synchronizes the edges of the two signals.

In this example, when FRINJ is turned ON, a maximum time of one period of FRINJ is required until the feed-back loop starts to take corrective action. The actual amount of time required for the feed-back signal to become synchronized with FRINJ is substantially longer than one period of FRINJ. This feed-back system is most likely, to a first approximation, a second order feed-back loop. A detailed analysis of the feed-back loop has not been performed; however, it is expected that the response of this loop would be exponential or damped sinusoidal in nature.

The response of the loop is determined, for the most part, by the loop filter. The filter that is being used in the present design is a passive type that was developed, for the most part, through trial and error. The performance of various filters was judged on the basis of minimum ripple on the filter output, with acceptable time response of the loop.

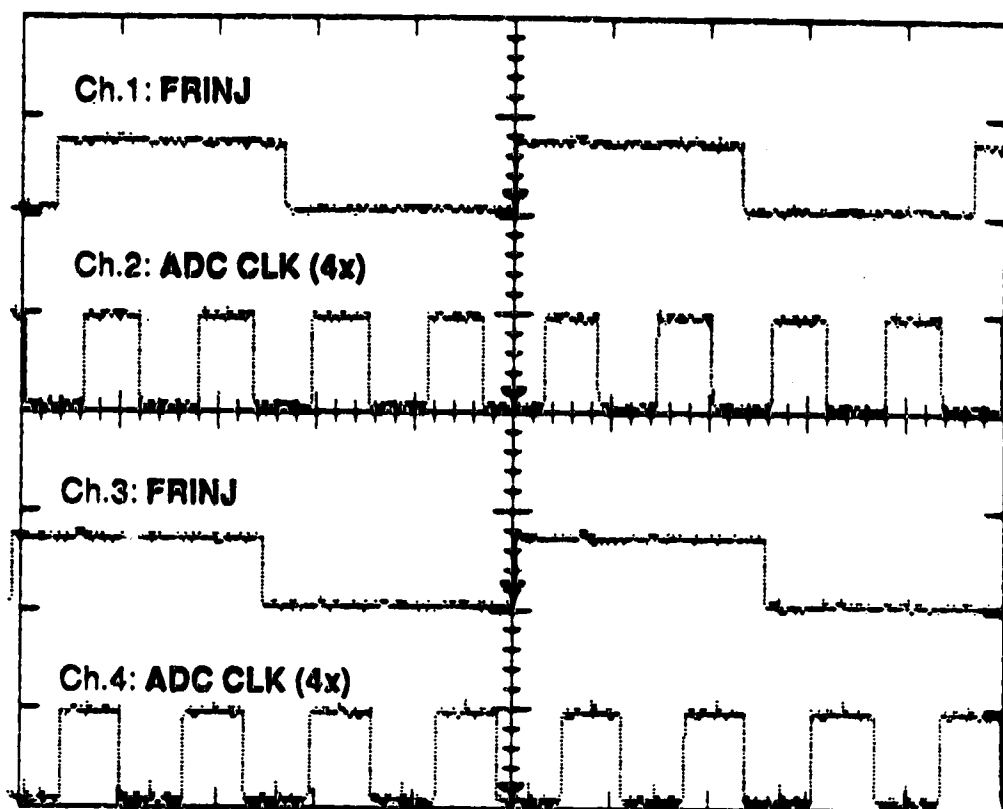
The output of the DPFD is in the form of pulses. These are integrated to produce the input for the VCO. If the filter output responds too quickly to

changes at its input, the filter output will have a significant ac component. This phenomenon is well known in the field of communications as "carrier feed-through." This term refers to the case where a PLL circuit is used to demodulate a frequency modulated carrier frequency. In this case the carrier would be FRINJ. Usually the de-modulated output is taken from the filter output. In the situation where there is no modulation of the carrier, as should be the case with FRINJ, the output of the de-modulator (the filter output) should be a dc-level. Thus, the spectrum of the de-modulated output should contain only a peak at zero frequency. However, if there is an appreciable ripple due to the carrier, this shows up in the spectrum of the output. In de-modulation applications, the spectrum of the carrier shows up in the spectrum of the de-modulated signal output, hence the name carrier feed-through.

In this application the PLL circuit is not used for de-modulation; however, ripple on the filter output is of concern. When applied to the VCO input, this ripple causes the VCO output square wave to be frequency modulated. This is a highly undesirable situation because it means that the period divided version of FRINJ would be frequency modulated with respect to FRINJ and therefore, more importantly, with respect to the source interferogram. If this divided version of FRINJ is used to clock the ADC, the situation is equivalent to digitizing a source interferogram that is frequency modulated. Therefore, it is important that the source interferogram be digitized at equal intervals of optical retardation. Each line in the source interferogram will produce the spectrum of a frequency modulated frequency component. This introduces many spurious peaks into the final spectrum. (The situation is worse for the larger peaks in the spectrum.)

Carrier feed-through is controlled by adjusting the loop filter parameters. The optimization of the loop filter is a compromise between slow integration for low carrier feed-through, and fast response of the loop to changes of the input frequency. For a given filter, the output ripple decreases as the input frequency is increased. With a previous version of the mirror drive, the fringe frequency was set to 5 kHz, or half of the present value of 10 kHz. With this higher fringe frequency it is easier to attain reasonable time response with low ripple at the VCO input. This has been the first consideration in the filter design.

As mentioned before, the loop output is important only during the constant velocity data acquisition portion of a scan. During this time the frequency of FRINJ never strays very far from 10 kHz, therefore the loop does not require extremely fast response. However, the response cannot be too slow or the frequency of the feed-back signal will lag behind that of FRINJ, well after the frequency of FRINJ has stopped changing through a turn-around sequence. Shown in Fig. 3-73 are FRINJ and the 4x version of the ADC CLK. These traces were triggered on the falling transition of $\overline{T/A\ CNTR\ CNTOUT}$ at both ends of a 16,384 FRINJ periods scan. At this point in the turn-around sequence, the ramp of the velocity of the mirror has ceased. The frequency of FRINJ is no longer changing. It can be seen that FRINJ leads the 4x version of ADC CLK. The PLL circuit is still in the process of servo-ing the feed-back square wave to match FRINJ in both frequency and phase. This illustrates the compromise between the need for low carrier feed-through, and reasonable speed of response of the loop.



Trigger: Triggered on first edge of **FRINJ** after pulse of **T/A CNTR CNTOUT**.
 Ch.1/Ch.2: BWD to FWD. Ch.3/Ch.4: FWD to BWD

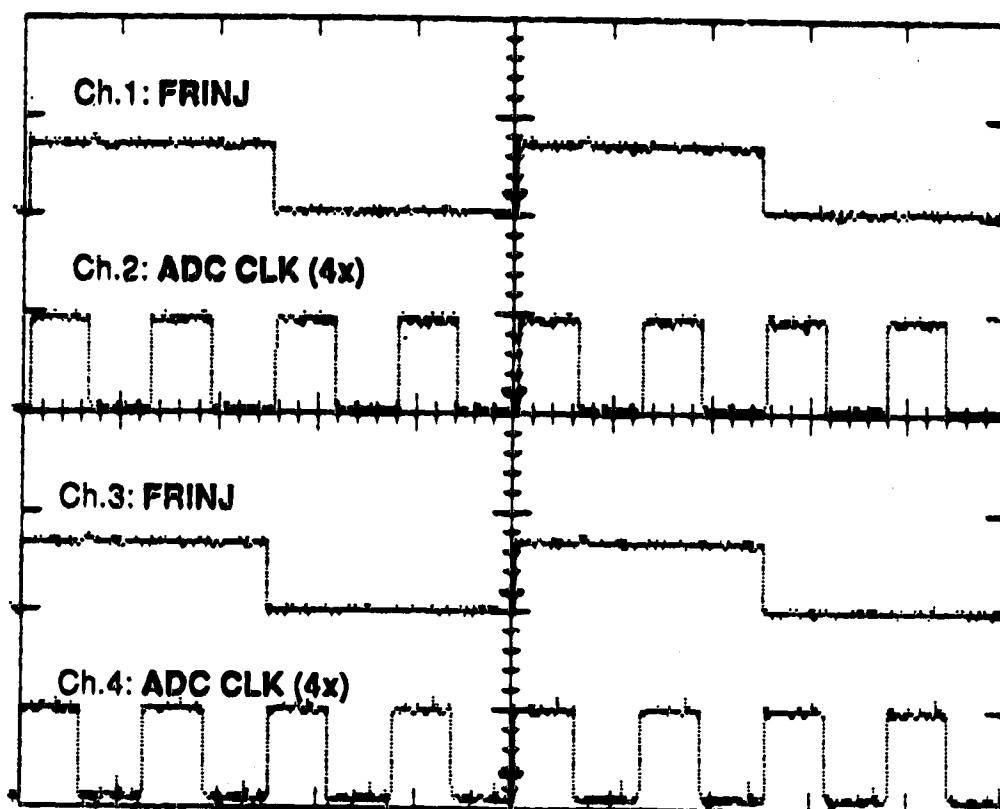
Time base: 10 μs/div

Vert. gain: All channels 5v/div

Figure 3-73. Lock-up of PLL at end of turn-around sequences. **FRINJ** and 4x version of **ADC CLK**.

The traces of Fig. 3-74 were triggered 110 FRINJ periods after the falling transition of T/A CNTR CNTOUT. FRINJ and the 4x version are now in phase. During these 110 periods of the fringe, the 4x version of ADC CLK is slightly frequency modulated. Since the frequency modulation consists of ramping the frequency of the feed-back square wave up to match that of FRINJ, the modulation does not go through even one period during these 110 periods of FRINJ. Hence, the frequency of this modulation is very low. Spurious peaks that might be introduced into the final spectrum would be situated almost right under the peaks. It is expected that the instrumental line width would obscure these side-bands, even if they were of suitable amplitude to be seen. Since this slight modulation occurs during only approximately 110 fringe periods out of 16,384, it is not expected to pose any problems. If, however, the loop was made more sluggish, spurious side-bands could well appear. The situation would also be expected to be worse for shorter interferograms.

Before exhibiting the attained spectral performance of this PLL system, the aliasing scheme in this experiment will be explicitly illustrated. In this thesis, a R166 PMT is used almost exclusively to detect the source interferogram. The aliasing scheme for the system with this detector will be described here. For most of the few cases in this thesis where a detector with a broader range of spectral sensitivity is used, for instance a 1P28 PMT, these interferograms are acquired with a sampling interval of $0.03955 \mu\text{m}$ of mirror movement (8x version of ADC CLK) to produce non-aliased spectra. For the remaining cases of broad-band PMT spectra, the aliasing that would occur with a 0.6328 or $0.1582 \mu\text{m}$ sampling interval of optical retardation (1x and 4x



Trigger: Triggered 110 periods of FRINJ after pulse of T/A CNTR CNTOUT.
 Ch.1/Ch.2: BWD to FWD. Ch.3/Ch.4: FWD to BWD

Time base: 10 μ s/div

Vert. gain: All channels 5v/div

Figure 3-74: Phase of input and output of PLL: 110 periods of FRINJ after turn-around sequences. FRINJ and 4x version of ADC CLK.

versions of ADC CLK, respectively) is as described in detail by G. Horlick et al [16].

Thus far the sampling of the interferogram has been approached from the point of view of the increments of mirror movement at which the interferogram is sampled. This defines the spatial sampling period. However, in practice the interferogram is acquired as a time varying signal that is sampled with a particular frequency. For convenience, the detailed description of aliasing in this system will be considered in the more usual fashion involving functions of time and their frequency spectra.

The origin of aliasing can be illustrated in the manner of Fig. 3-75. Shown in this figure is a function of time $f(t)$ and its amplitude spectrum, $|F(j2\pi f)|$. When the time function is digitized, the sampled function $f_s(t)$ results. It is easy to show that the spectrum of the sampled function consists of replicates of the spectrum of the un-sampled function. These replicates are centered on integral multiples of the sampling frequency, f_s . This is for the case of delta function sampling. If the pulses in the sampling train have finite width, the over-all spectrum has a $\sin(x)/x$ envelope. This isn't of concern here.

As is evident in this figure, when the amplitude spectrum of a sampled signal is calculated, there is much redundancy. Only the region from zero frequency to one half of the sampling frequency is of interest. This region should contain only one half of one replicate of the amplitude spectrum of the non-sampled signal. As long as the highest frequency component in the signal, f_H , is less than $f_s/2$, there will be no over-lap of replicates of the un-sampled spectrum. That is, the signal is correctly sampled if the sampling

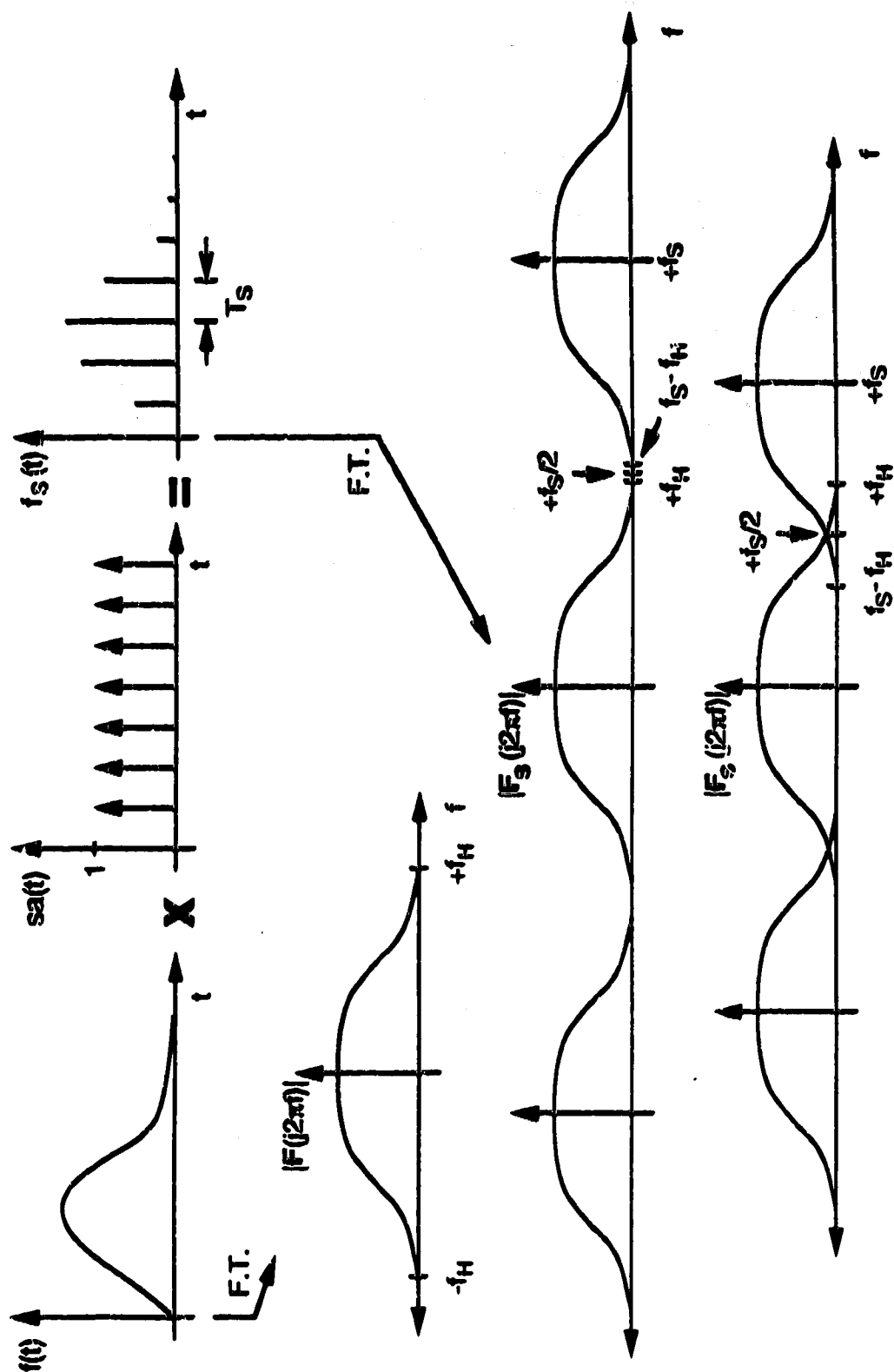


Figure 3-75. Schematic spectra of sampled signals.

frequency is twice the frequency of the highest frequency component in the un-sampled signal. Again, this is Nyquist's sampling criterion. As illustrated, aliasing occurs if the sampling frequency is too low, such that frequency components of other replicates over-lap into the region of interest.

For the purposes of this illustration, the frequency of FRINJ is assumed to be 10.000 kHz. Thus, the 4x and 8x sampling frequencies are 40.000 and 80.000 kHz. The wavelength of the HeNe laser is taken to be 632.8 nm. With these values, the highest frequency component present in the source interferogram, neglecting air absorption, has a frequency of 35.156 kHz, corresponding to a 180.00 nm wavelength component.

Assuming that the spectral sensitivity of the R166 PMT cuts off at 300.00 nm, the lowest frequency component in the source spectrum has a frequency of 21.093 kHz. With this detector, the spectrum of the interferogram is band-width limited to a spectral range from 21.093 to 35.156 kHz. Hence, the spectrum of the interferogram is represented in the following set of figures by a band-pass transfer function.

Fig. 3-76a and 3-76b are schematic representations of a portion of the spectrum that would result if an interferogram was detected with a R166 PMT, and sampled at a rate of 10 kHz. For clarity, replicates of the spectrum of the un-sampled interferogram are shown successively down the figure. The shaded portion of the spectrum is the region of interest from 0-5 kHz. For the replicates that are centered on $\pm f_s$ and $+2f_s$, no frequency components are aliased into the 0-5 kHz region. However, as indicated in Fig. 3-76b, frequency components of the replicate that is centered on $-2f_s$ folds frequency components from approximately 21-25 kHz into the region from 1-5 kHz. As

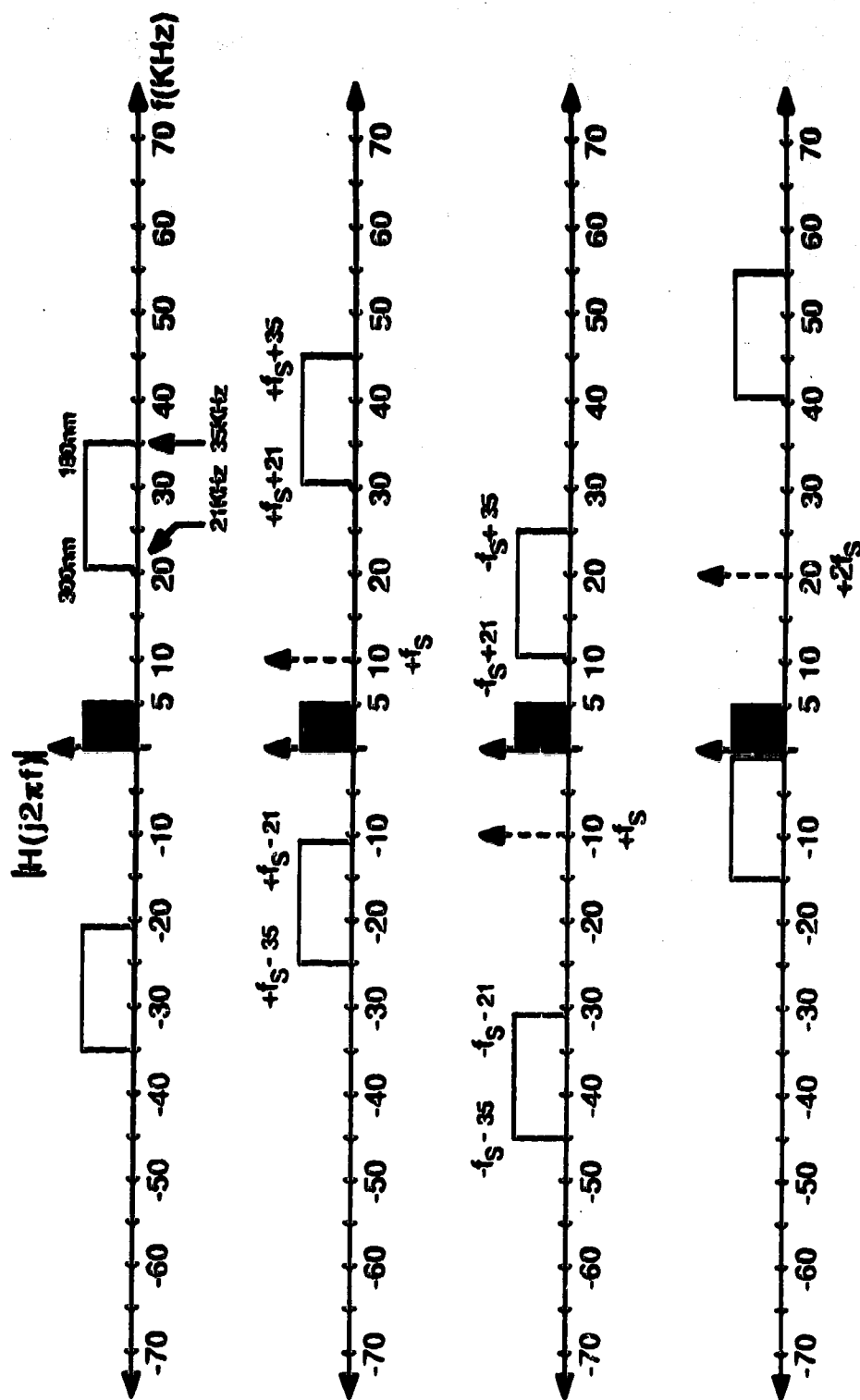


Figure 3-76a. Spectrum of interferogram measured with R166 PMT and sampled with a frequency of 10kHz.

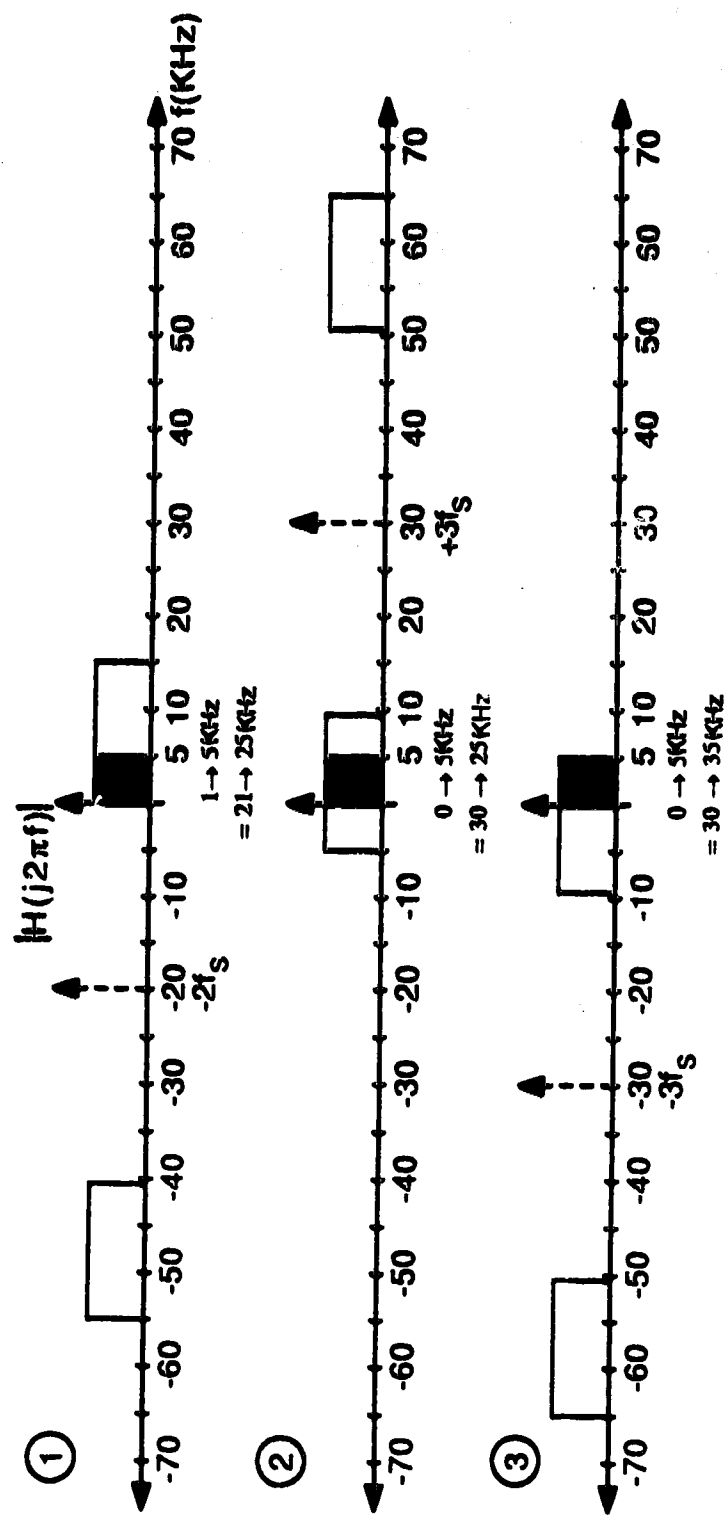


Figure 3-76b. Spectrum of Fig. 3-76a cont'd.

well, the replicate centered about $+3f_s$ folds frequency components from approximately 30-25 kHz into the region from 0-5 kHz. Finally, the replicate that is centered about $-3f_s$ aliases frequency components from 30-35 kHz into the region from 0-5 kHz. These aliases are summarized in Fig. 3-77.

4 regions of aliasing can be recognized. Region 1 extends across the actual frequency region 1.093-5.000 kHz. Aliased into this region are frequencies from the region 21.093-25.000 kHz. This frequency range corresponds to the range of wavelength components from 300.00 to 253.12 nm. Thus, the wavelength of a peak in this region of the final spectrum could be erroneously assigned. The other aliases are summarized in the same manner in this figure.

Fig. 3-78 is analogous to Fig. 3-76, except in this case the interferogram that was measured with the R166 PMT is assumed to be sampled at 40 kHz. The spectrum of the un-sampled interferogram does not fall within the region of interest from 0 to 20 kHz. However, the replicate spectrum that is centered on $+f_s$ aliases the complete spectrum from 35 to 21 kHz into the region from 5-19 kHz. From 0 to 5 kHz there is no spectral information. This region corresponds to wavelength components that are less than 180 nm. Since the roll-off of the spectral sensitivity of the R166 PMT is not as sharp as is indicated schematically, the region from approximately 19 to 20 kHz could contain some spectral information of wavelengths longer than 300 nm. It is clear from this figure that none of the replicate spectra that are centered on other integral multiples of the sampling frequency could alias frequency components into the region of interest.

For $\lambda_{\text{HeNe}} (= \lambda_{\text{REF}}) = 632.8 \text{ nm}$ and $f_{\text{FRINGE}} = 10.000 \text{ KHz}$:

300.00 nm \longrightarrow 21.093 KHz

180.00 nm \longrightarrow 35.156 KHz

① f_{ACTUAL} (KHz): 1.093 \longrightarrow 5.000

f_{ALIAS} (KHz): 21.093 \longrightarrow 25.000

λ_{ALIAS} (nm): 300.00 \longrightarrow 253.12

② f_{ACTUAL} (KHz): 0.000 \longrightarrow 5.000

f_{ALIAS} (KHz): 30.000 \longrightarrow 25.000

λ_{ALIAS} (nm): 210.93 \longrightarrow 253.12

③ f_{ACTUAL} (KHz): 0.000 \longrightarrow 5.000

f_{ALIAS} (KHz): 30.000 \longrightarrow 35.000

λ_{ALIAS} (nm): 210.93 \longrightarrow 180.80

④ f_{ACTUAL} (KHz): 4.844 \longrightarrow 5.000

f_{ALIAS} (KHz): 35.156 \longrightarrow 35.000

λ_{ALIAS} (nm): 180.00 \longrightarrow 180.80

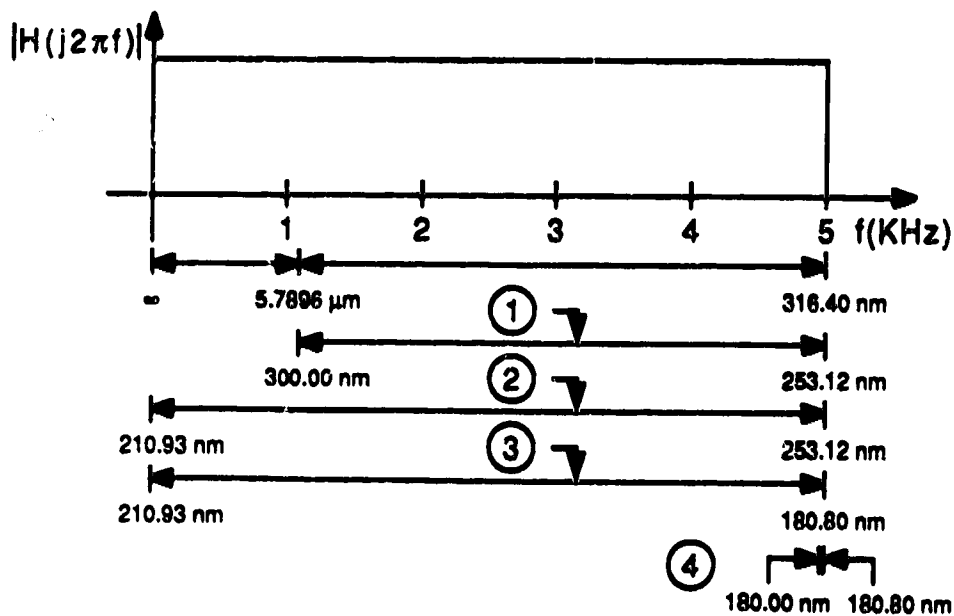


Figure 3-77. Summary of aliasing in spectrum of interferogram measured with R166 PMT and sampled with a frequency of 10 kHz.

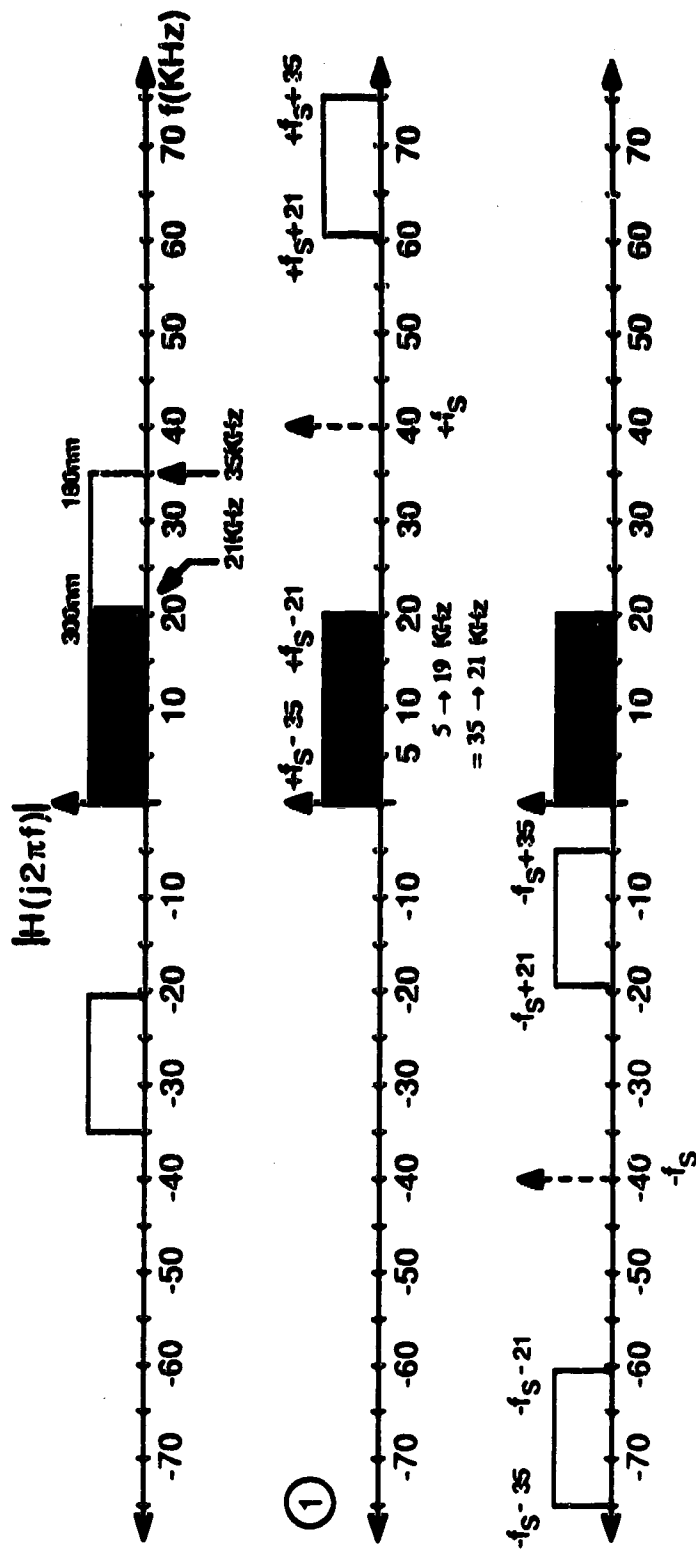


Figure 3-78. Spectrum of interferogram measured with R166 PMT and sampled with a frequency of 40 kHz.

The aliasing of an interferogram that is detected with a R166 PMT and sampled with the 4x version of ADC CLK is summarized in Fig. 3-79. There is no aliasing problem in this situation. Only one alias occurs such that the final spectrum is reversed but not mixed together.

When the 8x version of CLK is used to clock the ADC, the result is non-aliased operation for interferograms that contain wavelength components down to 180 nm. (Actually, this extends down to approximately 160 nm.) As indicated in Fig. 3-80, when the interferogram is detected with a R166 PMT the larger portion of the region of interest of the final spectrum does not contain any spectral information. The non-aliased operation with the 8x version of ADC CLK is summarized in Fig. 3-81.

As mentioned previously, carrier feed-through can create frequency modulation side-bands on either side of strong peaks in the spectrum. If the feed-back signal slightly lags the FRINJ input, the output of the DPF (input to the filter) is a series of +5 v pulses. The rising edges of FRINJ set the output of the DPF to +5 v, therefore the period between these pulses is 100 μ s. Thus, the ripple on the output of the filter has a period of 100 μ s since it results from integration of a pulse train with a period of 100 μ s. This means that the fundamental frequency at which the VCO is frequency modulated is 10 kHz. If there is any appreciable carrier feed-through in this system, side-band peaks that are separated from large peaks by ± 10 kHz will be seen in the spectrum.

Shown in Fig. 3-82 is a section of the spectrum of a Mg HCL source. The interferogram from which the parent spectrum was obtained consists of 65,536 data points acquired with the 4x version of ADC CLK. 64

f_{ACTUAL} (KHz): 0.000 \rightarrow 4.884

f_{ALIAS} (KHz): 40.000 \rightarrow 35.156

λ_{ALIAS} (nm): 158.20 \rightarrow 180.00

(Beyond R166 PMT spectral response. No aliased frequencies)

① f_{ACTUAL} (KHz): 4.884 \rightarrow 18.907

f_{ALIAS} (KHz): 35.156 \rightarrow 21.093

λ_{ALIAS} (nm): 180.00 \rightarrow 300.00

f_{ACTUAL} (KHz): 18.907 \rightarrow 20.000

f_{ALIAS} (KHz): 21.093 \rightarrow 20.000

λ_{ALIAS} (nm): 300.00 \rightarrow 316.40

(Beyond R166 PMT spectral response. No aliased frequencies)

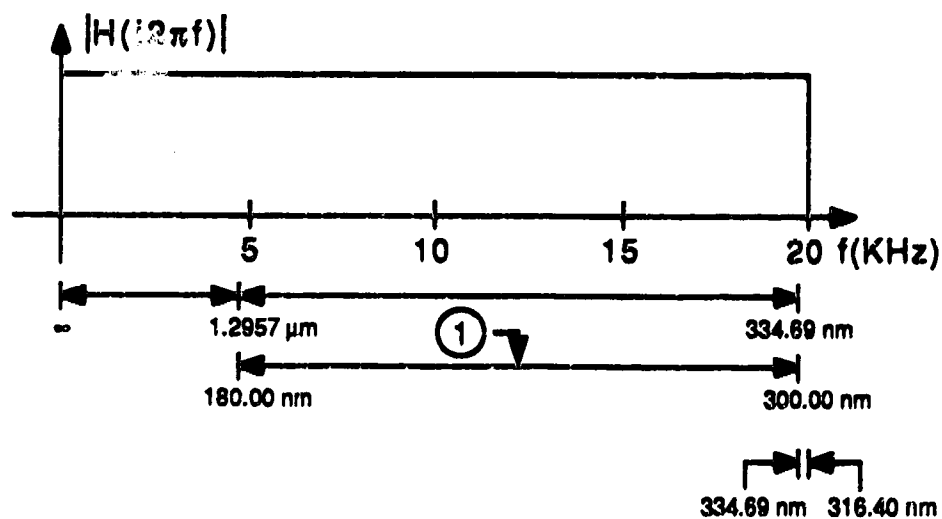


Figure 3-79. Summary of aliasing in spectrum of interferogram measured with R166 PMT and sampled with a frequency of 40 kHz.

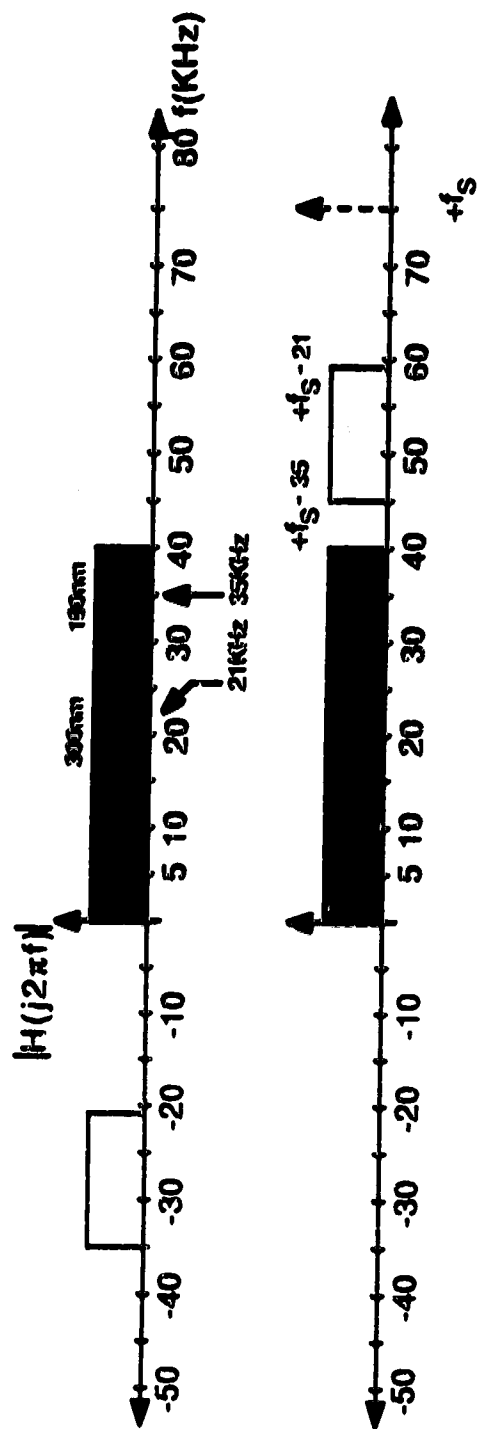


Figure 3-80. Spectrum of an interferogram measured with R166 PMT and sampled at a frequency of 80 kHz.

f_{ACTUAL} (KHz): 0.000 \rightarrow 21.093
 λ range (nm): $\infty \rightarrow$ 300.00
 (Outside R166 PMT spectral response band.)

f_{ACTUAL} (KHz): 21.093 \rightarrow 35.156
 λ range (nm): 300.00 \rightarrow 180.00

f_{ACTUAL} (KHz): 35.156 \rightarrow 40.000
 λ range (nm): 180.00 \rightarrow 158.20
 (Outside R166 PMT spectral response band.)

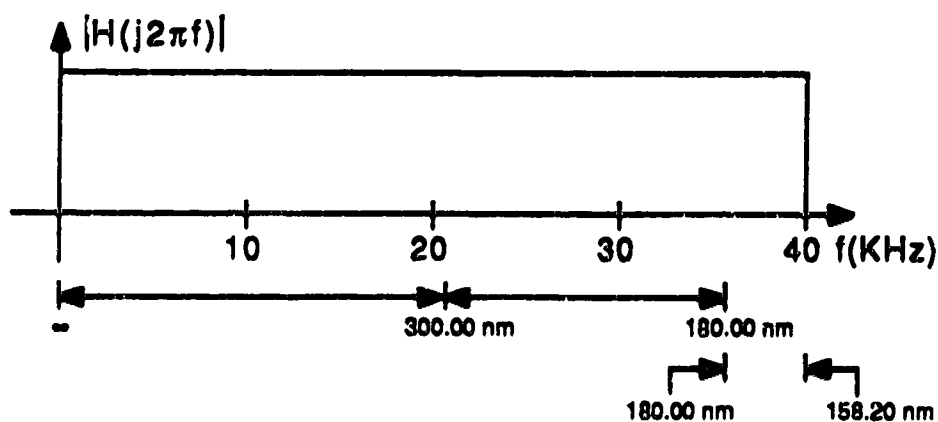


Figure 3-81. Summary of spectral regions of interferogram measured with R166 PMT and sampled at a frequency of 80 kHz.

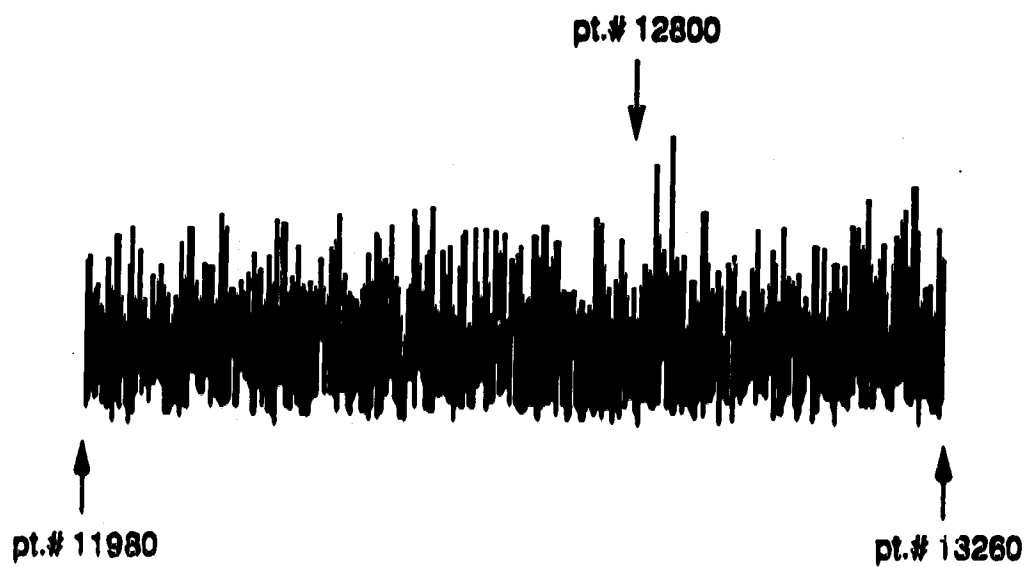


Figure 3-82. Expanded spectrum of interferogram of Mg HCL acquired with 8x version of ADC CLK. Vertical expansion = 512x.
(See text for details.)

interferograms were averaged to reduce the noise in the base-line of the spectrum.

The parent spectrum is comprised of 32,768 points that extend from 0 to (approximately) 20 kHz. The largest peak is situated at point #29184. This corresponds to the Mg 285.213 nm line. A span of 10 kHz corresponds to a span of 16,384 points in this spectrum. If there is significant carrier feed-through, side-bands would appear at $\pm 16,384$ points either side of # 29184. Clearly, only the -16,384, or point #12800, side-band would fall within the region of interest. A region of this spectrum containing point # 12800 is shown, with a 512x vertical expansion. It is difficult to state unequivocally that any side-band is in present within this spectrum. This is strong evidence that there is very little carrier feed-through with this PLL implementation.

It should be noted that side-bands were certainly in evidence with previous versions of this design. The problem of carrier feed-through was especially prominent when the frequency of FRINJ was set to 5 kHz.

During signal averaging, the ripple due to FRINJ is coherent in phase from scan to scan. Therefore this is not a problem that is reduced via signal averaging. In fact, the interferogram from which the above spectrum was derived was the average of 64 scans. When side-bands were seen previously, it was often necessary to signal average extensively to bring them out of the noise of the base-line.

Shown in Fig. 3-83 are portions of the spectra of a Mg HCL source. The interferograms from which parts a), b), and c) were calculated were digitized with the 1x, 4x, and 8x versions of ADC CLK, respectively. The interferograms all consist of 64 signal averaged scans. For parts a) and b) the

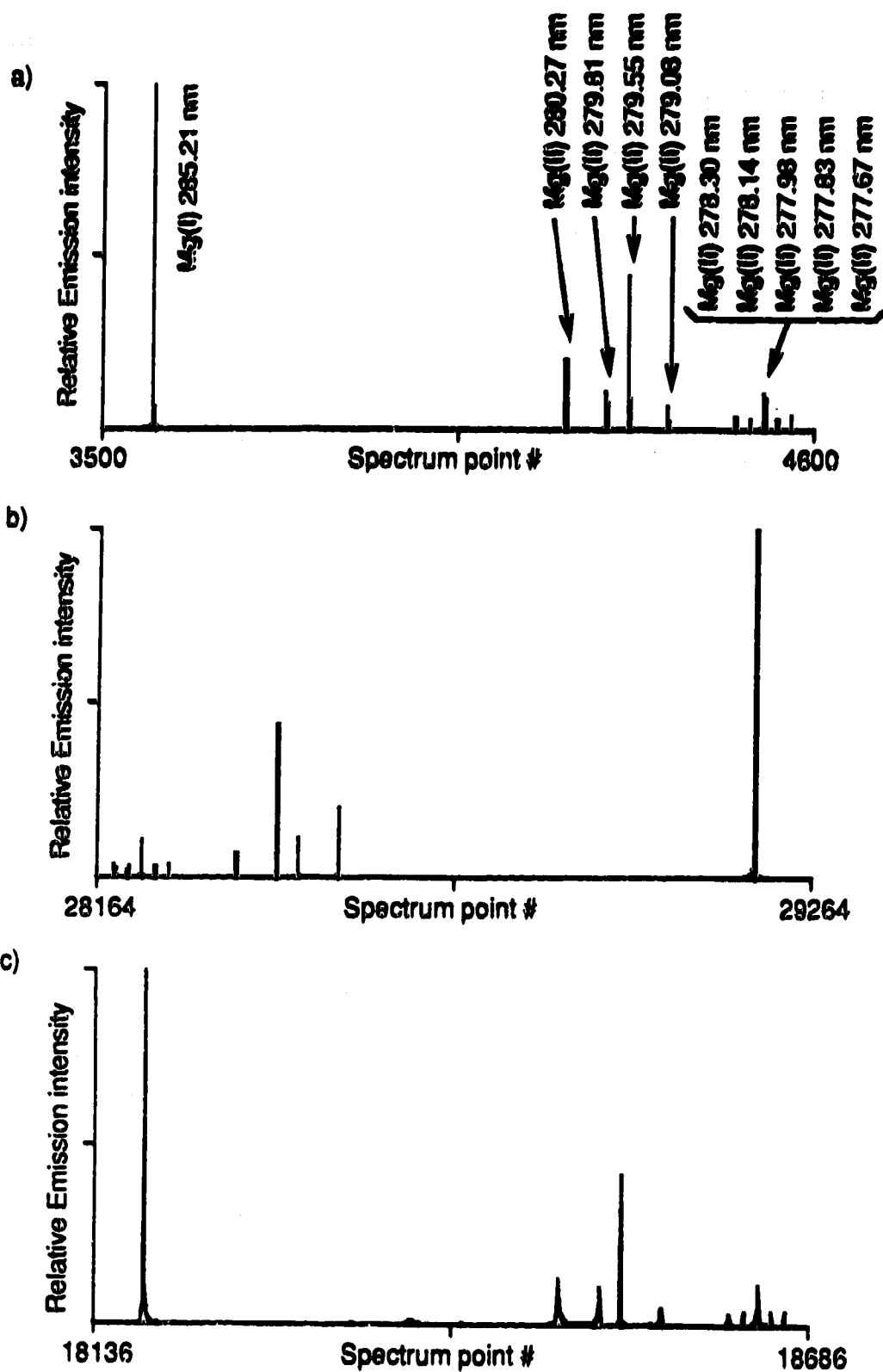


Figure 3-83. Spectra of interferograms acquired with a) 1x, b) 4x, and c) 8x versions of ADC CLK.

length of the mirror travel was 16,384 periods of the reference fringe. Thus, these spectra have equivalent spectral resolution. The interferogram acquired with the 4x version of ADC CLK consists of 65,536 points. Since the present computing system can transform an interferogram consisting of a maximum of 65536 points, when the 8x version of ADC CLK is used, the maximum mirror travel is 8192 periods of the fringe. This is the case for the spectrum of part c). Consequently, the spectral resolution in this spectrum is one half of that in the other two.

The prominent peaks in the spectrum range from 285.21 to 277.67 nm, or from 22.187 to 22.789 kHz. With reference to Fig. 3-77, this range of frequencies is aliased back into region 1 of the 1x aliasing scheme; with the 285.21 nm peak at the low frequency end of the aliased range. As indicated in Fig. 3-79, this range of frequencies appears in region 1 of the 4x aliasing scheme, after folding over one time around an axis at 20 kHz. The lower end of the aliased frequency range appears at the higher frequency end of the spectrum. Hence, the spectrum obtained with the 4x version of ADC CLK is reversed with respect to that obtained with the 1x version. When the 8x version of ADC CLK is used, non-aliased operation results. The range of frequencies appears correctly in the spectrum.

Qualitatively, the spectra of Fig. 3-83 appear to be very similar. The peak height ratios do not appear to be out of order; however, in the the 8x spectrum there appears to be a spurious spectral feature approximately mid-way between the 285.21 and 280.27 nm peaks.

The region around the 285.21 nm peak has been expanded. The result is shown in Fig. 3-84. Clearly, there appears to be a pair of side-bands with a

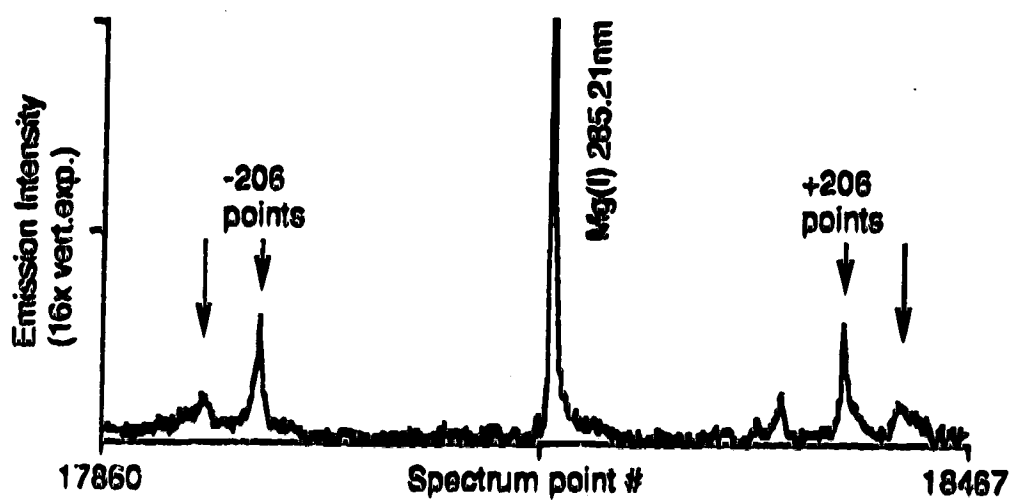


Figure 3-84. Spurious spectral features in spectrum of interferogram acquired with 8x version of ADC CLK.

separation of ± 205 points on either side of the peak. This corresponds to a frequency separation of approximately ± 250 Hz. At present, the origin of these is unknown. In a frequency or amplitude modulation type of scenario, the spectrum of the modulating signal appears in the side-bands. In this case it appears that the modulating signal is somewhat more complex than a simple fixed frequency sinusoid.

In Fig. 3-85, the regions containing the lines from 277.67 to 278.30 nm have been expanded. As well, the ratios of the individual peak heights, relative to that of the 285.213 nm peak height for each spectrum, are shown.

Parts a) and b) were taken from the 1x and 4x spectra. The wavelength axis reverses, and when this is taken into account, there is reasonable agreement between the peak height ratios for the two spectra. However, the peak height ratios in the 8x spectrum are somewhat different from those of the other two spectra. It appears that the 8x system not only introduces spurious side-band structures into the spectrum, but that it also introduces error into the observed spectral intensities.

From the data presented in Figs. 3-83 to 3-85, it appears that operation with the 4x version of ADC CLK does not appreciably affect the acquisition of an interferogram. When the experimental situation allows for the use of a R166 PMT as the detector, or some form of optical band-width limiting, the 4x version of ADC CLK should provide un-confused, de-aliased, operation. However, if the situation dictates fully de-aliased operation (i.e. acquisition of the interferogram of a broad-band continuum source), then the use of the 8x version of ADC CLK must be approached with some caution. Both spurious spectral features and erroneous spectral intensities may result.

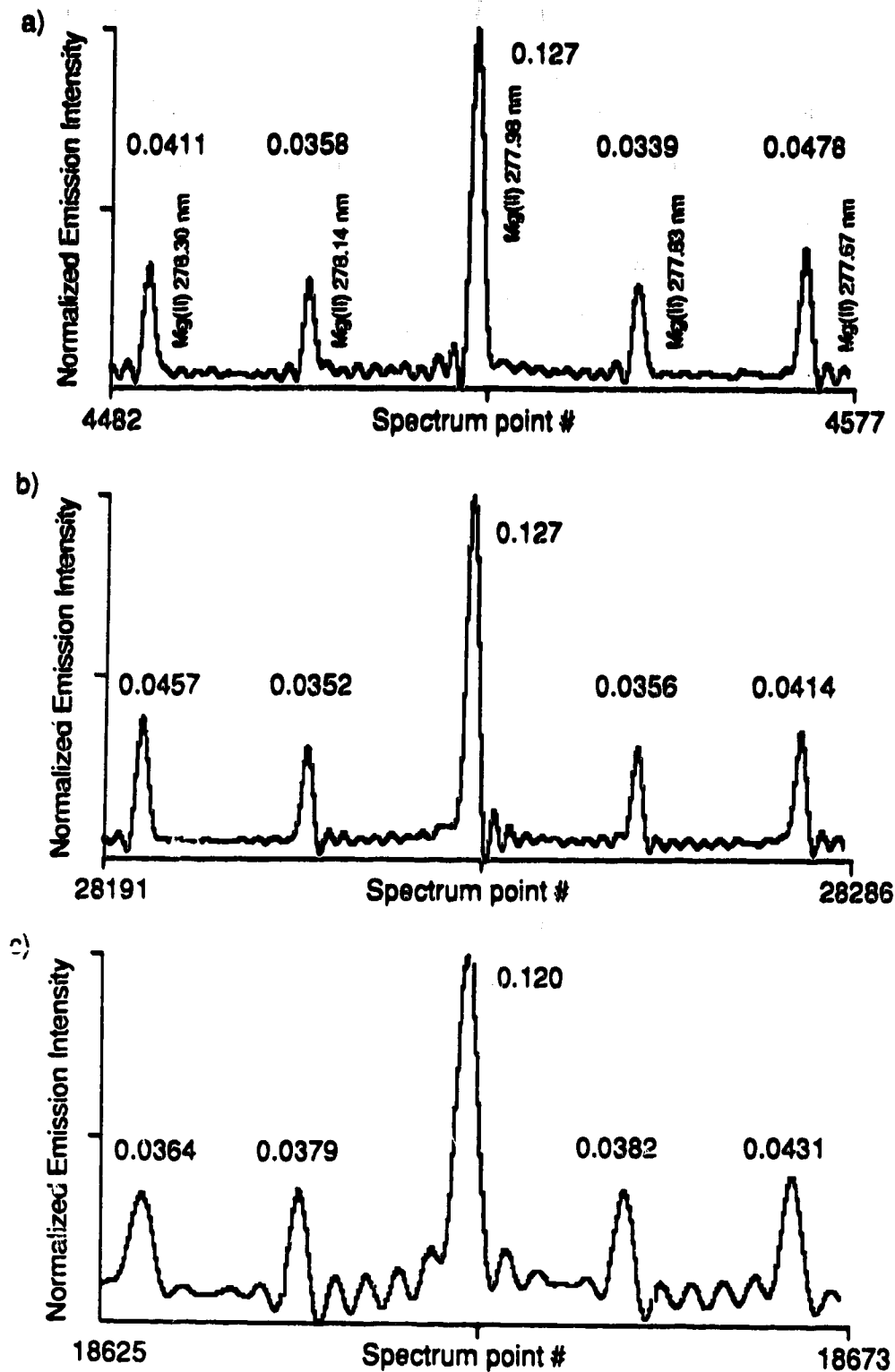


Figure 3-85. Expansions of ~278.5-277.5 nm region of aliased and de-aliased spectra. a) ADC CLK = 1x FRINJ. b) ADC CLK = 4x FRINJ. c) ADC CLK = 8x FRINJ. (See text for details.)

Chapter 4

Current Applications

The interferometer system developed in this thesis has opened up a wide range of studies by which the true capability of FTS for UV-VIS measurements can be applied and developed.

Dr. Greg King, a recently graduated co-worker in this laboratory, has developed an excellent software package with which the Fourier transform of the digitized interferogram is calculated to produce the spectrum of the interferogram [43]. This program, "Spectro-Plot", also displays the resultant spectrum, allowing a number of versatile manipulations of the data to be performed. Much of the data processing is custom-tailored for analytical spectro-chemical applications. Much of the development of this program occurred ahead of the development of the hardware. Upon completion of the hardware, Dr. King extensively tested the soft-ware and, in the process, the analytical capabilities of the overall system.

One of the oft-cited advantages of FTS over dispersive systems is the ease with which the wavelength axis in the final spectrum is calibrated. As described in Ch. 2, in theory the wavelength axis could be calculated from the HeNe reference laser wavelength. However, in practice a calibration procedure is used. The wave-length accuracy of the current system has typically been found to be $\pm 1\text{pm}$ [43]. Wavelengths of spectral peaks that are

obtained with this instrument show discrepancies that are on the order of the uncertainty of the literature values that are reported in the wavelength tables that are typically employed by workers in this field. [77-79].

The potential wavelength coverage of this instrument is from approximately 180 nm to 3 μm . To reach the low end, the instrument would have to be evacuated or purged. The various optical components are designed for (near) VUV operation. To operate at 3 μm , the beam-splitter would have to be changed. The collimation and focussing optics would not be optimal for work at 3 μm [14], however, the entire reflective optical path should be suitable for a number of studies where optimal sensitivity is not required.

As indicated in Ch. 2 the spectral resolution can be reasonably expected to be between 0.6 and 0.7 cm^{-1} . The measured value of 0.63 cm^{-1} for the 285.213 nm line of a Mg HCL corresponds to a FWHM of 2.52 nm at 200 nm. Practical examples of the resolution capabilities of this instrument are shown in Figs. 4-1 and 4-2.

Fig. 4-1 [43] is a portion of the spectrum of Fe when excited in an ICP. The interferogram from which this spectrum was derived, was acquired over a mirror travel of 65,536 periods of the reference laser interferogram. This is the highest resolution mirror travel for the present version of the instrument. The two lines at 234.810 nm and 234.830 nm, with a peak separation of 20 pm, are essentially base-line resolved.

A classic spectral interference in ICP spectroscopy is illustrated in Fig. 4-2 [80] That is, the overlap of the As 228.812 nm and Cd 228.802 nm peaks. The spectrum in part a) of this figure was derived from an interferogram

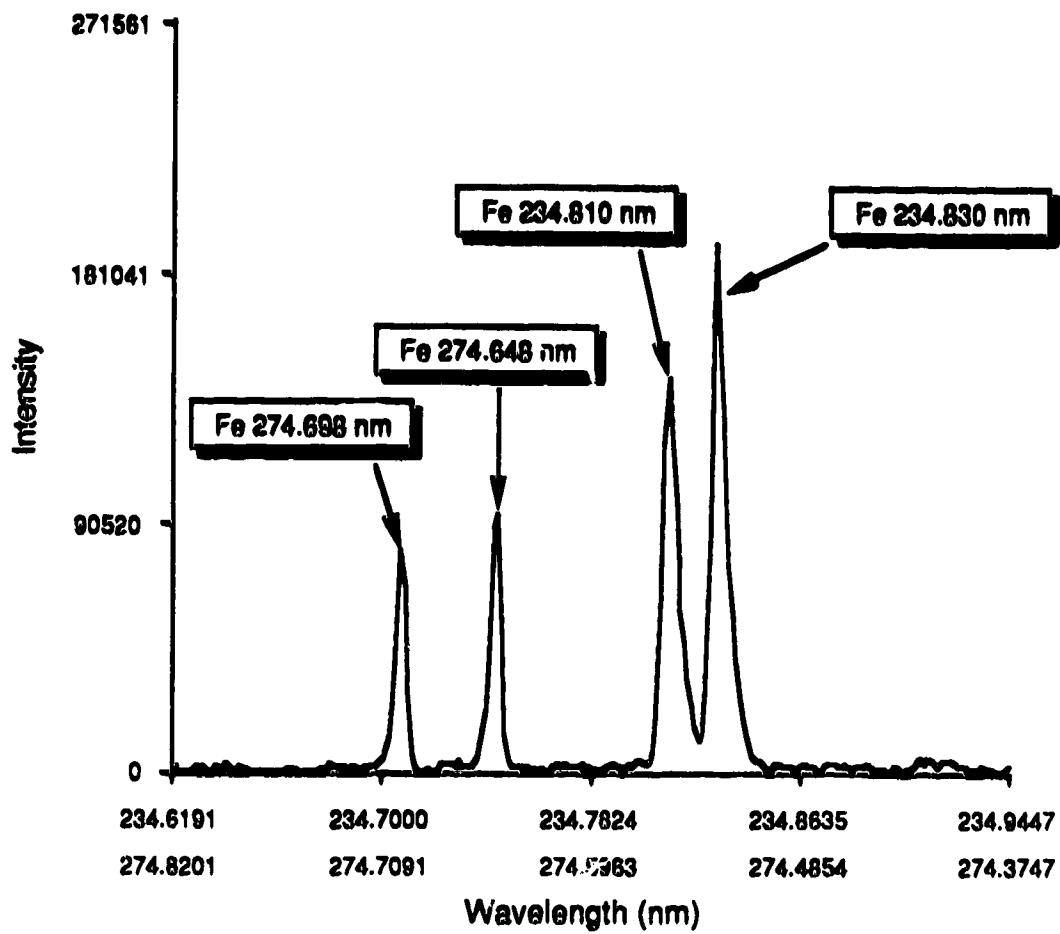


Figure 4-1. Practical resolution capability. 1000 µg/ml Fe in an ICP.

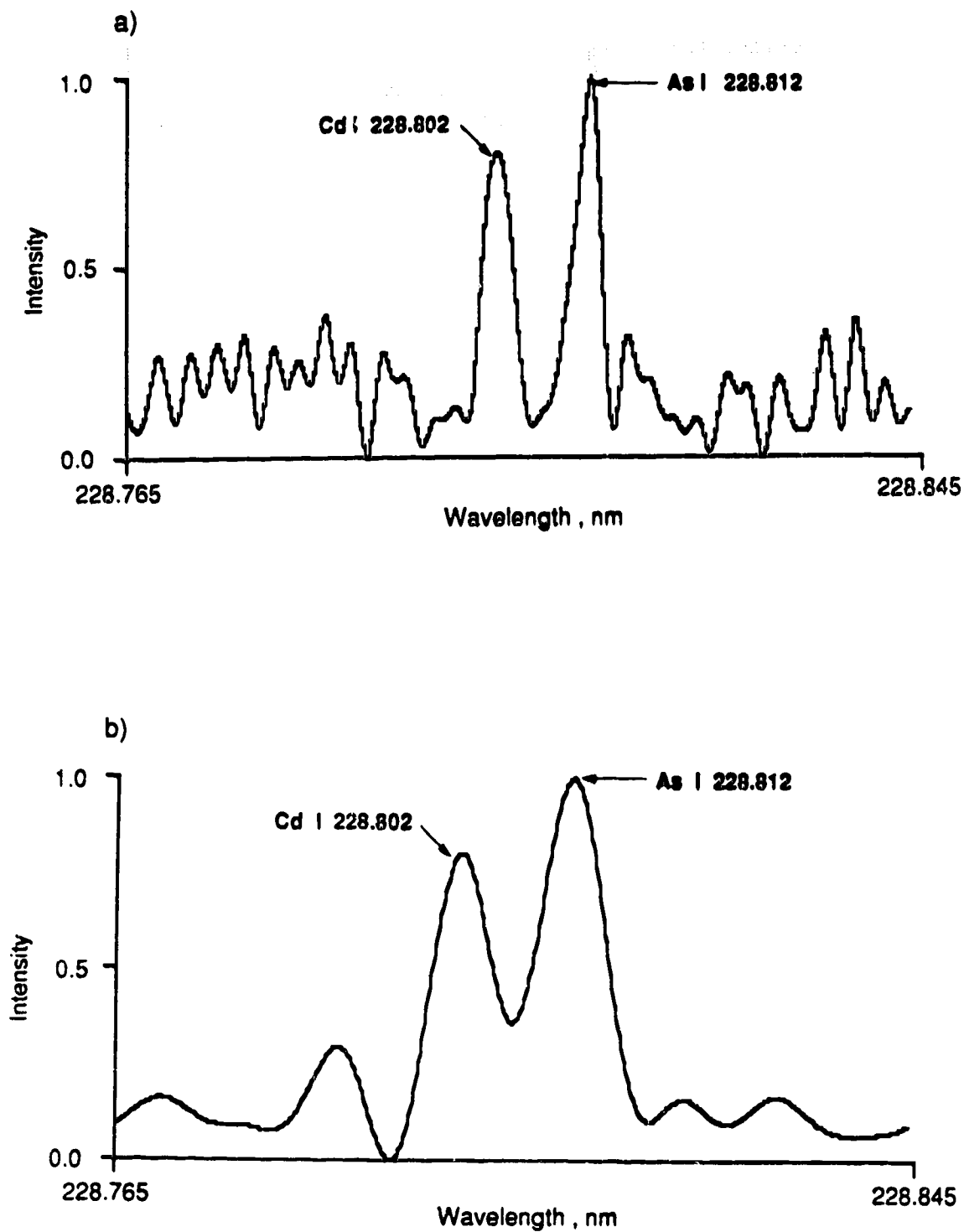


Figure 4-2. Practical resolution capability. Arsenic interfering with Cadmium. a) 16K interferogram. b) 64K interferogram. (See text for details.)

consisting of 16,384 periods of the reference laser fringe. In part b) the maximum resolution capability of the instrument was employed (65,536 periods of the reference laser fringe). The interfering peaks are fully base-line resolved.

By virtue of the true multi-line capability, and high achievable resolution, FTS is an almost ideal (not truly ideal because of the multiplex disadvantage problem) candidate for the measurement of peak wavelengths of spectral lines for compilation into wavelength tables. Researchers in the field of optical analytical spectroscopy are expressing a critical need for this information [81]. G. King has started work on a spectral atlas [43]. With this instrument he has measured the wavelengths of spectral lines of 21 elements that are excited within the ICP. This work is continuing.

The analytical capabilities of this instrument are the subject of on-going investigations. With the veritable plethora of information that is available in a single interferogram, an obvious technique to explore is automatic qualitative elemental analysis. A particularly fortunate feature of the practical implementation of this technique is that by definition the spectrum exists in digital form. A wide-range of mathematical techniques are available with which spectra can be processed, correlated, searched, and so on. As one might expect, it is important to have high spectral resolution such that closely spaced lines can be identified as such.

Using this instrument, an expert system has been developed which is designed to automatically identify spectral lines as to the emitting element [43]. This was tested on standard steel samples and the system correctly assigned to each line the element that was responsible for that line. However,

a number of known trace element lines were not assigned. That is, they were buried in the base-line noise and hence, they could not be assigned.

Again, by virtue of the continuous wave-length coverage, most elements will be represented by a number of lines in a spectrum. This allows one to pick either the best line, or a number of lines, for analysis of an element. The use of a number of lines of a particular element to improve the detection limit for that element has been investigated [43]. It was found that a modest improvement in the detection limit of Fe could be achieved when 15 Fe lines were used to produce each point on a calibration curve, versus only one line. However, it was clear that the multiplex disadvantage was still limiting the achievable detection limit.

As discussed in Ch 1, it would appear that in order to reduce the effect of the noise due to a large intensity component in the interferogram, on a small intensity component, the photons due to the large component must be prevented from reaching the detector. A method by which this can be achieved is pre-filtering of the source radiation prior to entry into the interferometer.

The concept of pre-filtering has been proven within this laboratory. E. Stubbley studied the coupling of a scanning monochromator with a Michelson interferometer [18, 23]. This system was dubbed a "window slew-scan Fourier transform" (WSS-FTS) system. In this system, the scanning monochromator was configured for low spectral resolution. By using 2mm entrance and exit slits the optical band-pass was set to be 4 nm. The idea here was to pass a selectable window of the spectrum and let the FTS part of the system achieve high resolution. By appropriately setting the position of the spectral window,

high intensity components of the source radiation could be blocked, prior to entering the interferometer.

The system was tested with a 16 component multi-element sample [18]. The same solution was tested with an ARL 34000 direct reading polychromator. A comparison of the detection limits for the elements in this solution, obtained with straight FTS and WSS-FTS, indicated a lowering of the detection limit in the latter case by two to ten times. Clearly, the situation was improved. The WSS-FTS detection limits were typically within an order of magnitude of those obtained with the ARL 34000.

A variation on this theme is now in the process of being tested. Instead of a scanning mono-chromator, the pre-disperser is that indicated in Fig. 4-3. The pre-dispersing element is essentially the optical system of a LECO PLASMARRAY® echelle/photo-diode array spectrometer, without the echelle grating and PDA. The basic operation of the pre-dispersion system is as follows.

The source radiation is focussed onto the entrance slit of a 0.5 m polychromator. The spherical grating (G1) disperses the source light and focusses the dispersed components onto a focal plane. Situated at the focal plane is a mask. The mask consists of slits that allow only the desired components of the source radiation through. The mask is positioned to be at the focal point of a spherical mirror (M1). Since the desired components that pass through the mask were focussed at the position of the slits, each component is collimated by the spherical mirror. The collimated components travel to a plane grating (G2). This is the recombining grating, in that it recombines the desired components into a collimated (quasi-white)

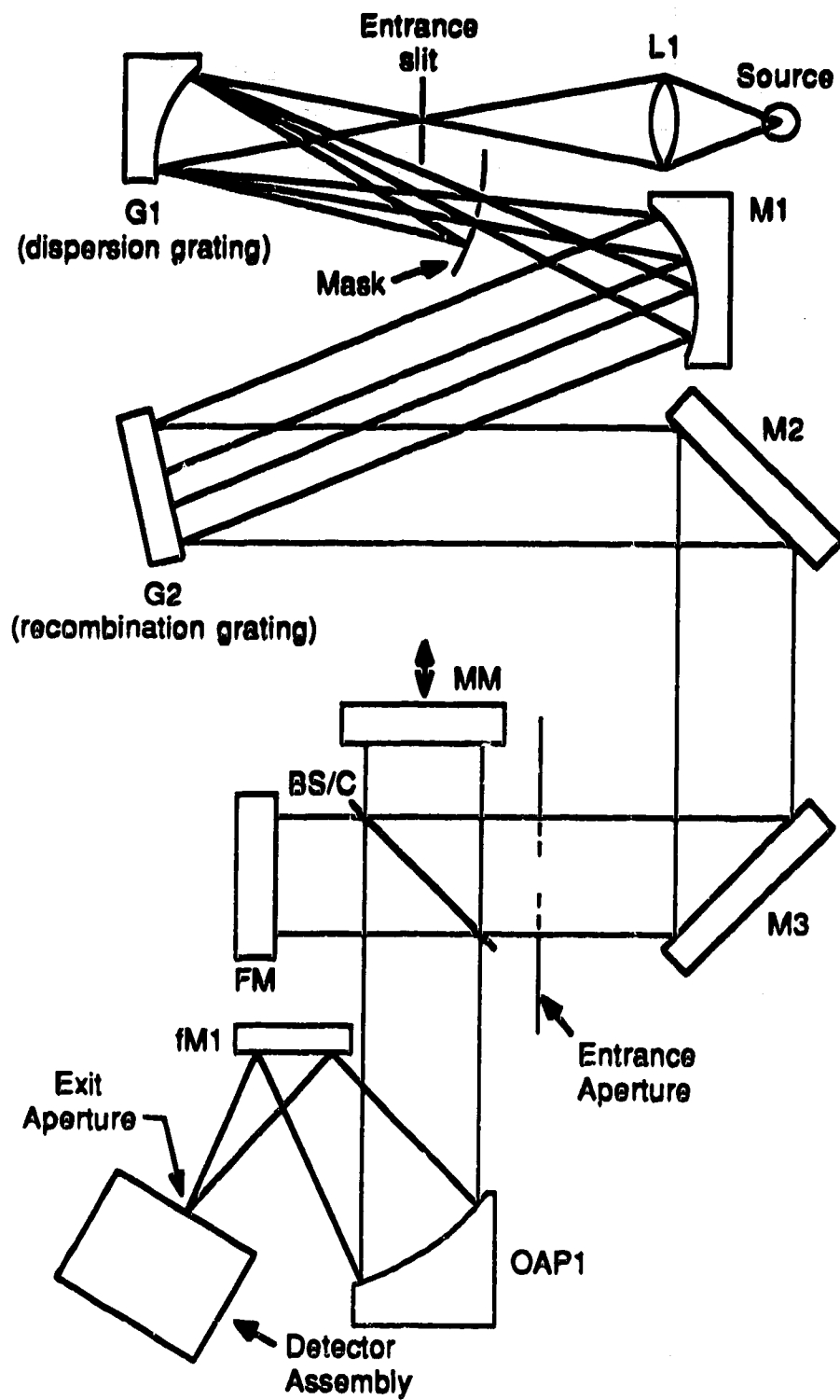


Figure 4-3. A pre-dispersion configuration.

beam. This collimated and re-combined radiation is folded with two plane mirrors (M1 and M2) such that it can enter the interferometer. Thus, by appropriately positioning the slits on the mask, one can choose the components of the source radiation that it is desired to have enter the interferometer. This allows the operator to remove large intensity components in the source radiation, thereby allowing small intensity components to be detected.

This system was built by the author and it is presently undergoing characterization. Data from a preliminary proof-of-concept experiment is presented in Fig. 4-4 [80]. The spectrum shown in part a) of this figure is that which was obtained when a solution containing Fe and Cr, in the ratio 100:1, was nebulized into an ICP. The spectrum has been expanded vertically in an attempt to recognize the three indicated Cr lines. It is not with extreme confidence that one could report that these lines were observed. The large number of emission lines due to the iron generate enough noise in the baseline that the Cr peaks are obscured. This measurement was made with no mask in the system. If a mask that is designed to pass only the three Cr lines is positioned appropriately within the system, the spectrum shown in part b) of this figure results. Now the three Cr lines are clearly in evidence. Again, this is only a proof-of-concept experiment. It is unlikely that the system is optimally configured, yet. However, this experiment clearly shows the viability of this approach to beating the multiplex advantage.

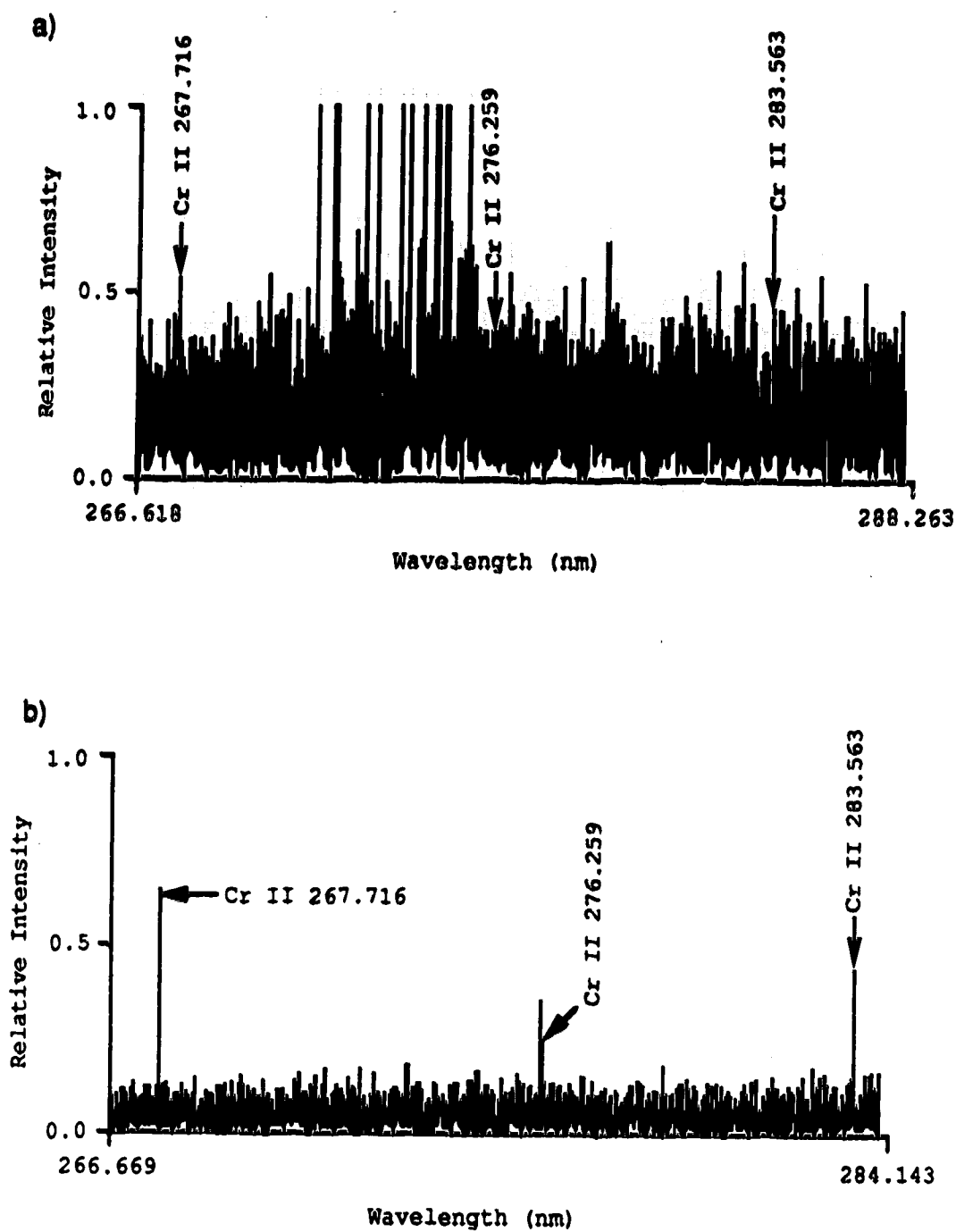


Figure 4-4. Reduction of the multiplex disadvantage via pre-dispersion.
a) No pre-dispersion. b) Pre-dispersion. (See text for details.)

Chapter 5

Conclusions and Future Directions

"The long and winding road..."

A Fourier transform spectrometer for use in the UV-VIS-NIR regions of the spectrum has been designed, constructed, and characterized (at least partially).

Most of the electronics systems have been completely re-designed-from the ground up. For the most part, the system is robust. However, as is always the case, further improvements and developments should be pursued. Alternative methods by which the direction of movement of the mirror can be sensed should be investigated, or the auxiliary coils method should be improved to be made less susceptible to noise and/or drift. Detection of whether or not the direction signal FWD/\overline{BWD} is situated within the brackets of a turn-around sequence should be automated. In fact, this is a difficult pattern recognition problem that was abandoned by the author as a result of excessive time spent. Ideally, if FWD/\overline{BWD} does not occur within the brackets, one would like to know how many fringe periods it is away from the brackets, and whether it occurs before or after the brackets. Presently, the situation has been left open loop. If the signal described above was available the loop could be closed. Then, if FWD/\overline{BWD} was not within the brackets, the computer would be alerted, at which point it would shift subsequent

interferograms by the appropriate number of fringe periods, prior to involving them in the signal average. This would relieve many of the stringent design requirements of the circuitry that generates FWD/\overline{BWD} .

As a development step, the electronics systems could be greatly reduced in size. The electronics was first bread-boarded and tested, then hard-wired into this prototype model. Much of the digital circuitry is small-scale integration (SSI). The functionalities of the various counters are available on medium, large, and very large scale (MSI, LSI, and VLSI) integration. One IC such as an Intel 8253 could perform a good deal of the fringe counting. In aid of simplicity in the design process, and with no apologies, SSI was utilized. Future models and/or designs should employ at least LSI. Similarly, the logic functionalities are in a form that is suitable for burning into programmable logic arrays. Again, this would significantly reduce the size of the electronics system.

In the opinion of the author, the interferometer system should be developed from the perspective that ultimately it will become a stand-alone intelligent peripheral device. It would receive information as to the desired resolution and number of signal averages. Upon acquisition of an interferogram it would calculate the spectrum via a hardware FFT processor and communicate that digital information to the computer for further processing. This then could be an interrupt driven system in that the computer would not have to be dedicated to the task of acquiring the interferogram. It would signal the interferometer to begin acquisition, and then proceed with other tasks. Upon completion of the calculation of the resultant spectrum, the interferometer would tug the coat-tails of the computer via an interrupt signal. In addition, if the interface was designed to

be general, then a number of different brands of computer could be easily interfaced to the system.

In particular, a stand-alone architecture would enable the use of this type of instrument in remote environments, for example, as an element in a process control system in an industrial setting, or for remote sensing in environmental testing sites. In the former, the interferometer could become a complex feed-back element that would allow previously open loops to be closed. In the latter, the instrument would return data to a central location for monitoring purposes.

The optical system of the interferometer has largely been re-vamped, and improved alignment procedures have been developed. The optical systems should be re-designed for the next generation of this instrument. Clearly, there is too much instrumental apodization. For our present purposes, this is of little concern. A resolution of 0.63 cm^{-1} is adequate resolution for most of the studies that we will pursue. However, in the future it may be decided to pursue fundamental studies of sources that will require line-profile data. For such studies the resolution would have to be improved. The present electronics systems could be easily adapted to allow for longer travel of the moving mirror. However, the optical system would have to be re-designed.

Various possibilities for the optical configuration of the next generation interferometer are illustrated in Fig. 5-1. In both of these designs, corner cube retro-reflectors are employed. These are so-called "tilt-insensitive" optical elements. If a beam of light enters the element with a particular angle of incidence, then the beam that is reflected from the element

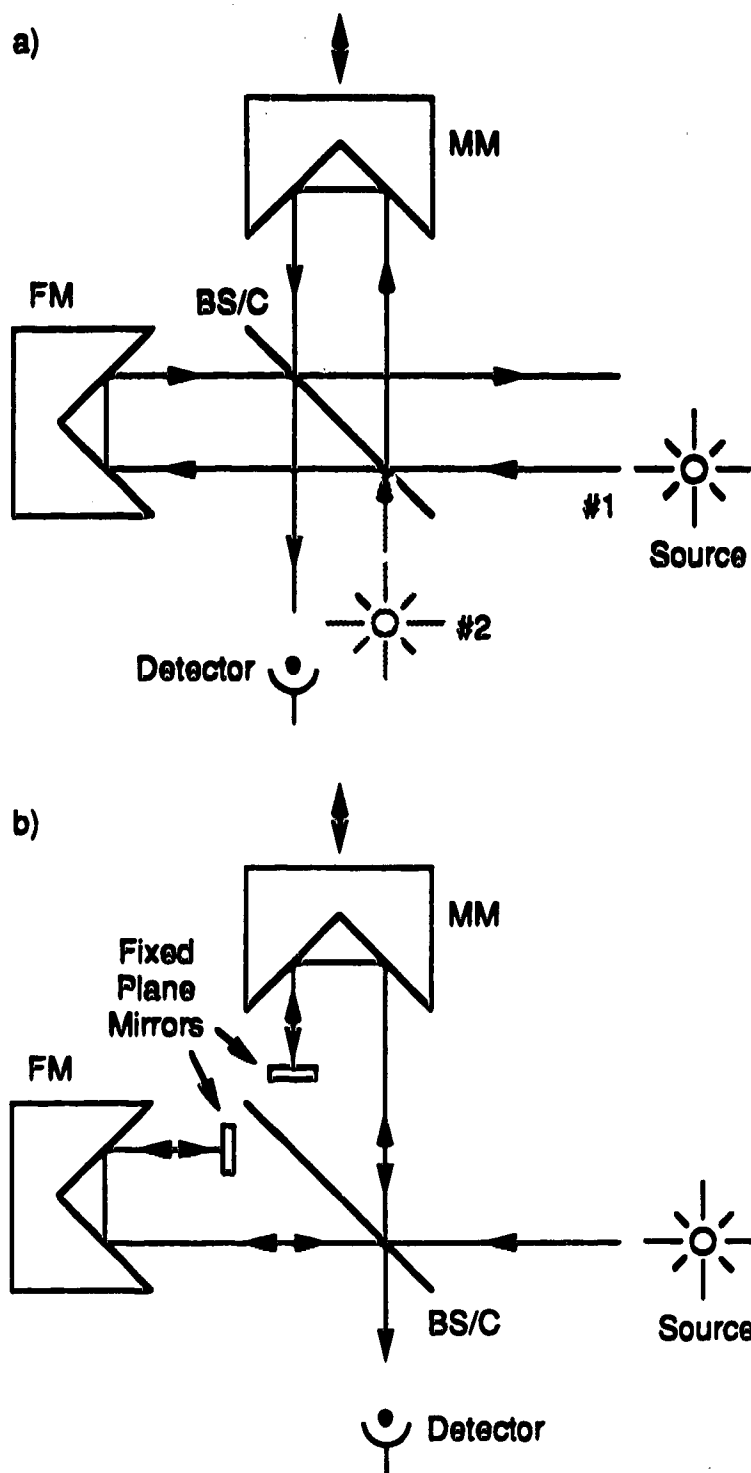


Figure 5-1. Alternative Michelson interferometer configurations.
 a) Separate optical paths. Tilt insensitive.
 b) Same optical paths. Tilt and shear insensitive.

returns with the same angle. That is the retro-reflector returns a beam upon itself, except with a lateral displacement. The important feature of these devices is that the retro-reflection is insensitive to tilt of the element (for moderate angular deviations). Note however, that these elements are shear sensitive, in that the return beam is shifted laterally if the element is shifted laterally. This can be contrasted with a plane mirror, which is insensitive to shear, but highly sensitive to tilt. By virtue of the complementarity of these two elements, the combination of the two can often result in both tilt and shear insensitivity.

In part a) of Fig. 5-1, the interferometer configuration is essentially the same as the present design, except that the plane mirrors have been replaced with corner cube retro-reflectors. It has only been in the last 5 years that these elements have become commercially available with the required precision for UV work, and at a reasonable price (the major manufacturer is Precision Lapping and Optical Co.). By replacing the plane mirrors with a pair of corner cubes, the tolerances that are required of the mirror drive mechanical components to maintain effective re-combination of the return beams throughout the mirror travel are lessened. The system is for the most part tilt insensitive. However, it is shear sensitive. An attractive aspect of this design is the fact that the interferogram that returns directly to the source in the plane mirror configuration is now displaced, and consequently, accessible. As described in Ch.1, this interferogram is 180° out of phase with the output interferogram.

A common practice in astronomical interferometry (where cat's eye retro-reflectors are often used) is to utilize this second detected interferogram to correct for scintillation noise which always results when viewing light

sources through the turbulent atmosphere. Scintillation noise is akin to flicker noise, hence this approach might aid in the battle against the multiplex disadvantage.

A particularly interesting experiment to try would be to build a pair of identical ICP sources. The analysis torch would be positioned at point #1 in this diagram. The null torch would be positioned at point #2 in this figure. Consider that it was desired to detect trace elements in a sample of iron. In this case, the large number of spectral lines from the iron would create a large multiplex disadvantage, thereby obscuring the lines of the trace elements.

The first step of this scheme would be to accurately determine the concentration of the iron in the sample solution. Then, a second solution containing the same concentration of iron would be made up. This is the null solution. This solution is aspirated into both the analysis and null ICPs. The parameters of each plasma are adjusted until equal dc-intensities are observed. This would be done with one arm of the interferometer blocked such that no interference occurs. The two PMT detectors will have been matched prior to this via adjustments of dynode voltages, amplifier gains, etc. At this point, one would know that the amount of iron radiation that is being emitted by both plasmas is equivalent.

Now the sample and null solutions are nebulized into the analysis and null ICPs, respectively. By virtue of the 180° phase shift between the two ports of the interferometer at which the ICPs are positioned, at the point at which the detector is positioned the radiation from the null plasma destructively interferes with that of the sample. Since the null plasma produces an equal amount of iron radiation as does the sample plasma, the

total iron radiation at the detector has an intensity of zero. The intensity of the various radiations have been re-distributed via interference such that no iron radiation impinges upon the detector. Clearly, this would go a long way towards beating the multiplex disadvantage in this situation.

The design shown in part b) of this figure has a pair of plane mirrors added to provide shear insensitivity. An attractive aspect of this design is that a mirror movement of Δx produces a change in the optical path difference of $4\Delta x$ (as opposed to $2\Delta x$ for the previously described design). Thus, the range of travel of the mirror could be limited. Not only would this allow for compactness of the instrument but also, translating the moving mirror less distance is desirable from the point of view of recombination of the return beams at the beam-splitter. Note however, that the return optical paths in the interferometer are no longer separate from the incident path. Thus, only the one output interferogram is readily accessible.

Alternative interferometer/disperser configurations can be envisioned. Instead of pre-dispersing the radiation as described in Ch. 4, a post-dispersing system could be employed. For instance, as indicated in Fig. 5-2, the LECO optical system could be positioned after the interferometer. The interferometer would then modulate the source radiation prior to entry into the LECO system. At the focal plane of the dispersing grating, each slit in the mask passes a band-width limited interferogram. These interferograms, sans large offending wavelength components, are recombined by the recombining grating. The collimated radiation from the recombining grating is focussed onto a single PMT.

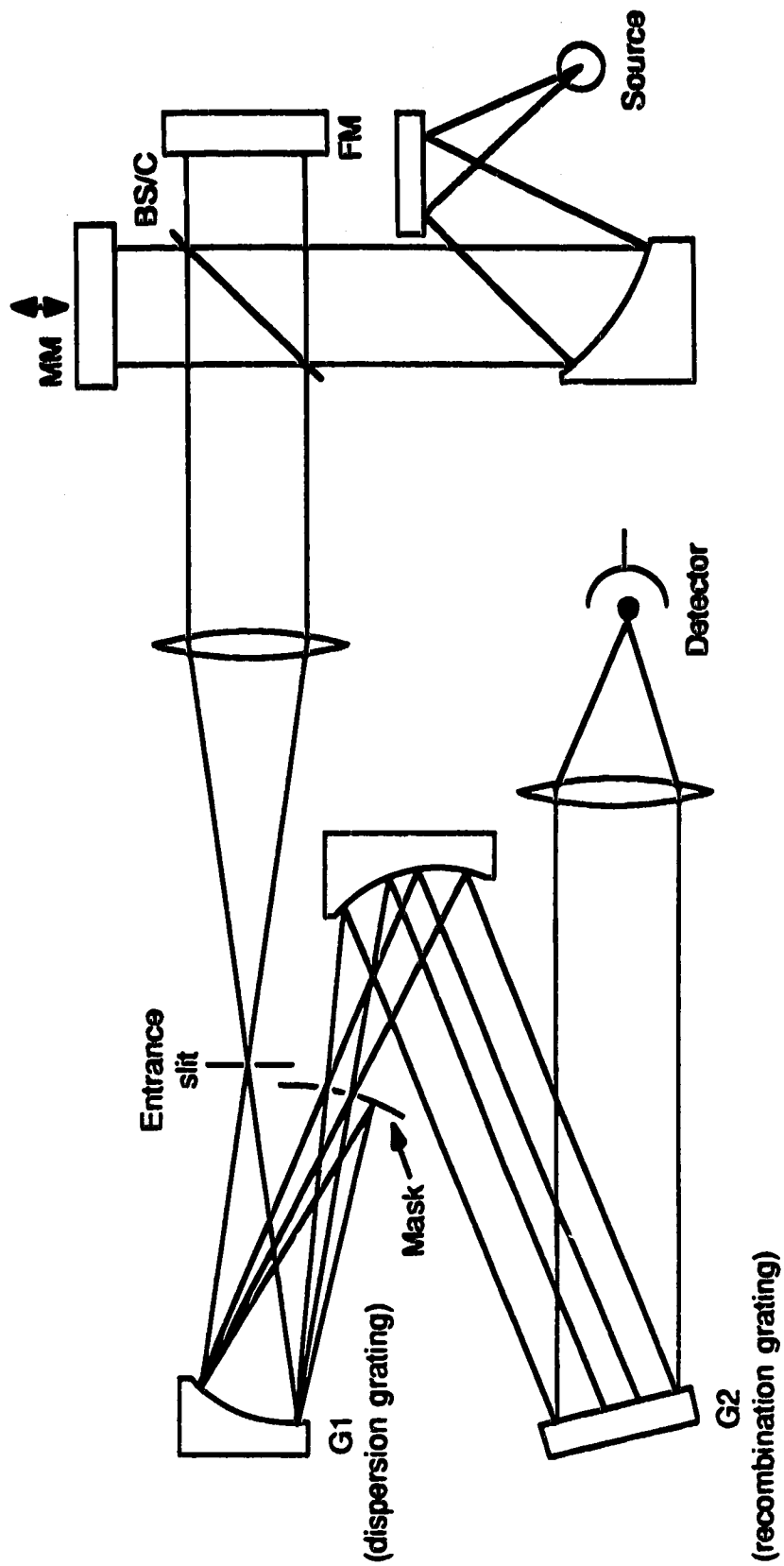


Figure 5-2. Post-dispersion configuration.

An alternative pre-dispersion design with intriguing possibilities is to short-circuit the recombining grating altogether. This is illustrated in Fig. 5-3. Band-width limited interferograms could be detected at the focal plane of the 0.5 m polychromator in several ways. In the simplest scheme, a single detector could be positioned to measure a particular desired band. An experiment that will be attempted in the very near future will be to couple positions in the focal plane of the polychromator to the interferometer entrance aperture via a slit to circle fibre optic cable. As discussed in Ch 2, the entrance off-axis parabolic mirror assembly is particularly well-suited to input via a fibre optic, since this represents a source of limited size. The interferogram that would be measured in this fashion would be produced from spectrally band-limited data. Hence, resolution could be obtained with a relatively small number of data points. Since each spectrum would cover a small spectral band-width, aliasing could be allowed to occur without overlap problems. Thus, the travel of the mirror could be lengthened for resolution while the interferogram could be under-sampled. Therefore, the interferogram would not contain a large number of points. With interferograms containing a relatively small number of points the possibility of utilizing hardware FFT processors for effectively real-time processing opens up.

Alternatively, a number of detectors could be placed at strategic points on the focal plane. In the simplest case, this would be akin to a conventional polychromator that is outfitted with several detectors in the focal plane. However, the resolution of the system is no longer dependent upon the geometry of the disperser system. Instead it is dependent upon the interferometer. A number of interesting multiplexing schemes can be

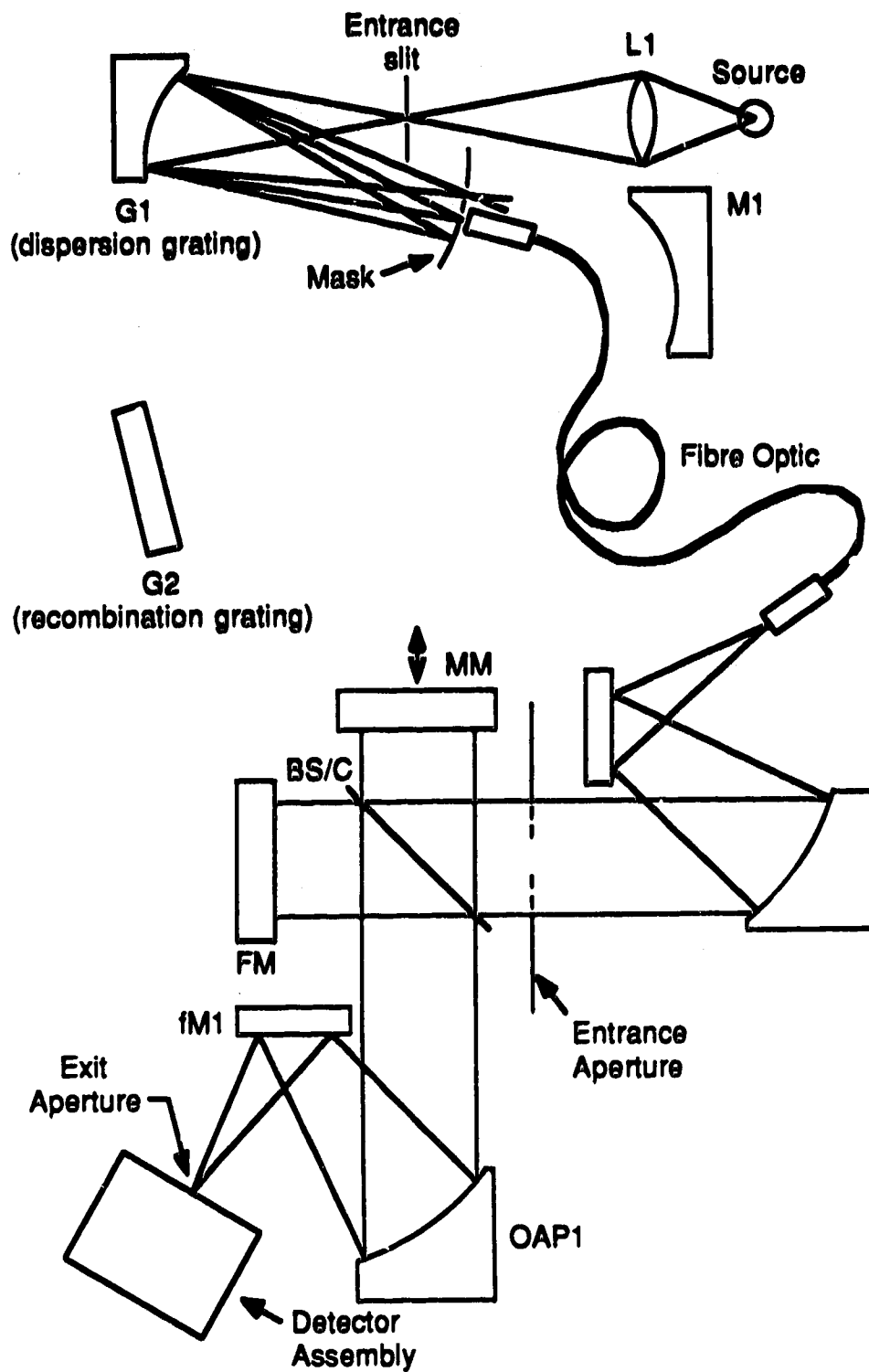


Figure 5-3. Pre-dispersion without recombination. Fibre optic coupling.

devised with which the information from each detector would be acquired and processed for most efficient operation.

Most of the studies involving the present version of the interferometer have involved either an ICP or HCL as a source of atomic emission. A Glow Discharge Lamp, for solid sample analysis, is currently being developed within our laboratory. Since this is being fabricated in-house, it is considered important that the spectral characteristics of this source may be measured in a simple and efficient manner. In this way the mechanical design of this source can proceed in an iterative manner. It is anticipated that this spectrometer will be particularly useful for this application.

In this thesis, the design and characterization of a Fourier transform spectrometer for use in the UV-VIS region has been described. Along the way, the reader has been made aware of some of the considerations involved in applying the FTS method within region of the spectrum. This is a problem of challenging complexity. Many of the problems requiring solutions are only now becoming understood. It is anticipated that the instrument described in this thesis will be the appropriate tool with which many of these problems may be elucidated and eliminated.

References.

- [1] J. Chamberlain, "The Principles of Interferometric Spectroscopy". John Wiley and Sons, New York, N.Y. (1979)
- [2] M. L. Forman, W. H. Steele, and G. A. Vanasse, J. Opt. Soc. Am., 56, 59 (1966)
- [3] P. R. Griffiths, "Fourier Transform Infrared Spectroscopy". John Wiley and Sons, New York, N.Y. (1986)
- [4] P. B. Felgett, J. Phys. Rad., 19, 187 (1958)
- [5] P. B. Felgett, Ph. D. Thesis. University of Cambridge, Cambridge, U. K. (1951)
- [6] A. Girard and P. Jacquinet, "Advanced Optical Techniques". North Holland, Amsterdam. (1967)
- [7] P. Luc and S. Gerstenkorn, Astron. Astrophys., 18, 209 (1972)
- [8] J. Pinard, J. Phys. C, 2, 142 (1967)
- [9] J. Connes and P. Connes, J. Opt. Soc. Am., 56, 896 (1966)
- [10] P. Luc and S. Gerstenkorn, Appl. Opt., 17, 1327 (1978)
- [11] J. W. Brault, "A High Precision Fourier Spectrometer for the Visible", in Proceedings, ESO/CERN Conference on Auxiliary Instrumentation for Large Telescopes, S. Lusten, and A. Reiz, Eds. CERN, Geneva. (1972)

- [12] J. W. Brault, *J. Opt. Soc. Am.*, **66**, 1081 (1976)
- [13] D. E. Jennings, R. Hubbard, and J. W. Brault, *Appl. Opt.*, **24**, 3438 (1985)
- [14] W. K. Yuen and G. Horlick, *Appl. Spectrosc.*, **32**, 38 (1978)
- [15] W. K. Yuen, Ph. D. Thesis. Department of Chemistry, University of Alberta, Edmonton, Alberta (1978)
- [16] G. Horlick, W. K. Yuen, and R. Hall, "Atomic Emission Spectrochemical Measurements with a Fourier Transform Spectrometer", in "Fourier Transform Infrared Spectroscopy", vol. 3, J. Ferraro, L. Basile, and A. Mantz, eds. Academic Press, New York, N.Y. (1982)
- [17] E. A. Stubley and G. Horlick, *Appl. Spectrosc.*, **39**, 805 (1985)
- [18] E. A. Stubley and G. Horlick, *Appl. Spectrosc.*, **39**, 811 (1985)
- [19] R. C. L. Ng and G. Horlick, *Appl. Spectrosc.*, **39**, 834 (1985)
- [20] S. Marra and G. Horlick, *Appl. Spectrosc.*, **40**, 804 (1986)
- [21] E. A. Stubley and G. Horlick, *Appl. Spectrosc.*, **38**, 162 (1984)
- [22] S. Marra, Ph. D. Thesis. Department of Chemistry, University of Alberta, Edmonton, Alberta (1985)
- [23] E. A. Stubley, Ph.D. Thesis, Department of Chemistry, University of Alberta, Edmonton, Alberta (1983)
- [24] R. C. L. Ng and G. Horlick, *Appl. Spectrosc.*, **39**, 841 (1985)

- [25] R. C. L. Ng, Ph. D. Thesis. Department of Chemistry, University of Alberta, Edmonton, Alberta (1985)
- [26] L. M. Faires, B. A. Palmer, R. Engleman Jr., and T. M. Niemczyk, *Spectrochim. Acta*, **39B**, 819 (1984)
- [27] L. M. Faires, B. A. Palmer, R. Engleman Jr., and T. M. Niemczyk, *Spectrochim. Acta*, **40B**, 545 (1985)
- [28] L. M. Faires, *Spectrochim. Acta*, **40B**, 1473 (1985)
- [29] L. M. Faires, B. A. Palmer, and J. W. Brault, *Spectrochim. Acta*, **40B**, 135 (1985)
- [30] D. E. Jennings, A. Weber, and J. W. Brault, *Appl. Opt.*, **25**, 284 (1986)
- [31] Los Alamos National Laboratory technical bulletin (no date-late 1986). Communication with G. Horlick at the University of Alberta, Edmonton, Alberta, Canada.
- [32] Los Alamos National Laboratory technical bulletin (May 11, 1987). Communication with G. Horlick at the University of Alberta, Edmonton, Alberta, Canada.
- [33] Los Alamos National Laboratory technical bulletin. LALP-8828. July 1988.
- [34] J. W. Brault, " High Resolution Fourier Transform Spectroscopy; Proceedings of the 15th Annual Advanced Course of the Swiss Society of Astrophysics and Astronomy", Geneva Observatory, Sauverny, Switzerland. (1985)

- [35] T. Hasegawa and H. Haraguchi, *Spectrochim. Acta* **40B**, 123 (1985)
- [36] J. A. C. Broekaert, K. R. Brushwyler, and G. M. Hieftje, *Mikrochim. Acta*, submitted for publication.
- [37] L. M. Faires, *J. Anal. At. Spectrom.*, **2**, 585 (1987)
- [38] A. P. Thorne, C. J. Harris, I. Wynne-Jones, R. C. M. Learner, and G. Cox, *J. Phys. E: Sci. Instrum.*, **20**, 54 (1987)
- [39] D. E. M. Spillane, R. D. Snook, A. P. Thorne, and J. E. G. Wheaton, *J. Anal. At. Spectrom.*, **2**, 591 (1987)
- [40] P. Hobbs, D. E. M. Spillane, R. D. Snook, and A. P. Thorne, *J. Anal. At. Spectrom.*, **3**, 543 (1988)
- [41] E. A. Stubbley and G. Horlick, *Appl. Spectrosc.*, **39**, 800 (1985)
- [42] R. Hall, Ph. D. Thesis. Department of Chemistry, University of Alberta, Edmonton, Alberta (1979)
- [43] G. King, Ph. D. Thesis. Department of Chemistry, University of Alberta, Edmonton, Alberta (1989)
- [44] E. R. Schildkraut and T. B. Hirschfeld, "Fourier Transform Raman Spectroscopy", in "Laser Raman Gas Diagnostics", M. Lapp and C. M. Penney, eds. Plenum, New York, N.Y. (1974)
- [45] H. Graener, A. Laubereau, *Springer Proc. Phys.*, **4**, 11 (1985)
- [46] T. Hirschfeld, D. B. Chase, *Appl. Spectrosc.*, **40**, 133 (1986)

- [47] D. B. Chase, *J. Am. Chem. Soc.*, **108**, 7485 (1986)
- [48] A. Simon and R. Rubinovitz, Paper #343 presented at the 1989 Pittsburgh Conference, Mar. 6-10, Atlanta, Georgia. (1989)
- [49] R. W. Hannah, Paper #344 presented at the 1989 Pittsburgh Conference, Mar. 6-10, Atlanta, Georgia. (1989)
- [50] H. Guy and H. Buijs, Paper #345 presented at the 1989 Pittsburgh Conference, Mar. 6-10, Atlanta, Georgia. (1989)
- [51] R. J. Rosenthal, Paper #346 presented at the 1989 Pittsburgh Conference, Mar. 6-10, Atlanta, Georgia. (1989)
- [52] B. W. Smith and J. D. Winefordner, Paper #E6.5 presented at the XXV Colloquium Spectroscopicum Internationale, June 21-26, Toronto , Ontario. (1987)
- [53] M. J. Smith, Paper #1095 presented at the 1989 Pittsburgh conference, Mar. 6-10, Atlanta, Georgia. (1989)
- [54] M. R. Glick, B. T. Jones, B. W. Smith, and J. D. Winefordner, *Appl. Spectrosc.*, **43**, 342 (1989)
- [55] "CRC Handbook of Chemistry and Physics, 57th ed.", R. Weast (ed.), CRC Press, Boca Raton, Florida. (1976)
- [56] E. Hecht and A. Zajac, "Optics". Addison-Wesley, Reading, Mass. (1979)
- [57] A.A Michelson, *Phil Mag.* **32**, 338. (1881)

- [58] E. Goldin, "Waves and Photons". John Wiley and Sons, New York, N.Y. (1982)
- [59] J. M. Stone, "Radiation and Optics". McGraw - Hill, New York, N.Y. (1963)
- [60] R. Loudon, "The Quantum Theory of Light". Clarendon Press, Oxford. (1973)
- [61] T. Hirschfeld, *Appl. Spectrosc.*, **30**, 234 (1976)
- [62] E. Voightman and J.D. Winfordner, *Appl. Spectrosc.*, **41**, 7 (1987)
- [63] J. Davies and R.D. Snook, *J Anal. At. Spectrom.*, **1**, 195 (1986)
- [64] R. L. A. Sing and J. Hubert, *J Anal. At. Spectrom.*, **3**, 835 (1988)
- [65] R. R. Williams, *Appl. Spectrosc.*, **43**, 235 (1989)
- [66] J. E. Meier and A. G. Marshall, Paper# 344 presented at the 37th ASMS Conference on Mass Spectrometry and Allied Topics. May 21-26, Miami Florida. (1989)
- [67] "Ealing Optics Catalog", Ealing, 1984.
- [68] Barry Arnold, Arnold Optics. Sherwood Park, Alberta, Canada.
- [69] "CRC Handbook of Laser Science and Technology, Vol. 2: Gas Lasers", M. Weber (ed.), CRC press, Boca Raton, Florida. (1982)
- [70] "Capability Brochure and Product Catalog", Space Optics Research Labs, 1979.

- [71] C. F. Bruce and P. Hannaford, *Spectrochim. Acta* 26B, 207 (1971)
- [72] P. Hammond, "Electromagnetics for Engineers". Pergamon Press, New York, NY. (1978)
- [73] D. Halliday and R. Resnick, "Fundamentals of Physics". John Wiley and Sons, New York, NY. (1972)
- [74] K. Ogata, "Modern Control Engineering". Prentice Hall, Englewood Cliffs, N.J. (1970)
- [75] J. Millman and C. C. Halkias, "Integrated Electronics: Analog and Digital Circuits and Systems". McGraw Hill, New York, NY. (1974)
- [76] "Data Conversion Products Databook", Analog Devices, Norwood, Mass. (1988)
- [77] M. Parsons, A. Forster, and D. Anderson, "An Atlas of Spectral Interferences in ICP Spectroscopy", Plenum, New York, N. Y. (1980)
- [78] R. Winge, V. Fassel, V. Peterson, and M. Floyd, "Inductively Coupled Plasma-Atomic Emission Spectroscopy. An Atlas of Spectral Information.", Elsevier, Amsterdam (1985)
- [79] A. Zaidel, V. Prokofjev, S. Raiskii, V. Slayni, and E. Shreider, "Tables of Spectral Lines", IFI/Plenum, New York, N.Y. (1970)
- [80] T. B. Wang, Personal communication.
- [81] A. Scheeline, *Spectrochim. Acta*, 43B, 1 (1988)

Appendix 1

Spectrometer Control System Electronics

This appendix contains the detailed documentation of the electronics systems described in Ch. 3 of this thesis. These systems consist of four main boards, housed in a card cage, and three modules that are attached to the interferometer itself.

The functionalities on each board have been organized such that the boards are designated as the: 1) coarse feed-back module, 2) fine feed-back module, 3) turn-around counter (T/A CNTR) board, and 4) scan counter (NCNTR) board. Each board is documented separately in the above order. Typically, for each board the documentation consists of the card cage front panel architecture, the IC and/or modules designation on the board, the board modules pin-outs, the block diagram describing the IC and/or modules interconnections, and finally, the detailed circuit diagrams of the modules and /or IC groups.

In particular, the coarse and fine feed-back modules boards have been built up in a modular fashion. For the most part large functionalities were prototyped separately, tested, and then made into a module. Subsequently, these modules were attached to the main board of the card cage to facilitate interconnection. This strategy proved to be effective for producing an

A2

intermediate level prototyped system, in which the circuitry is all hard-wired but etched boards have not been designed yet.

The reference laser and white light detection modules, as well as the auxiliary coils module, are all attached in some fashion to the body of the interferometer. Each module is a self-contained unit, with power brought in via cables. The outputs of all of these modules are amplified versions of the signal of interest. This is done in an attempt to reduce the effects of noise involved in the transmission and subsequent amplification of low level signals. For each of these modules, the layout of the particular module (with IC designations) and the detailed circuit diagram is provided.

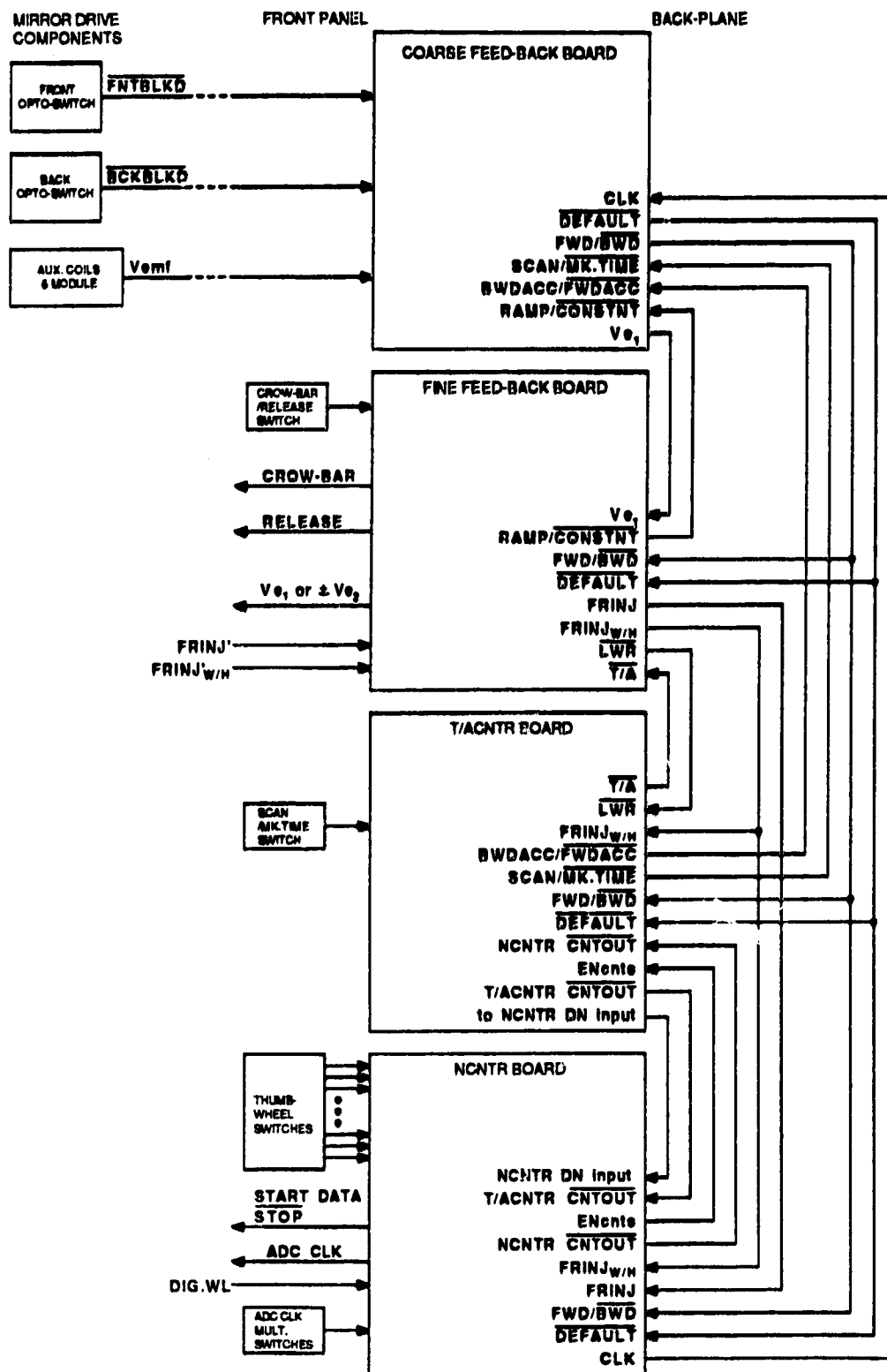


Figure A-1. Moving mirror control system connections.

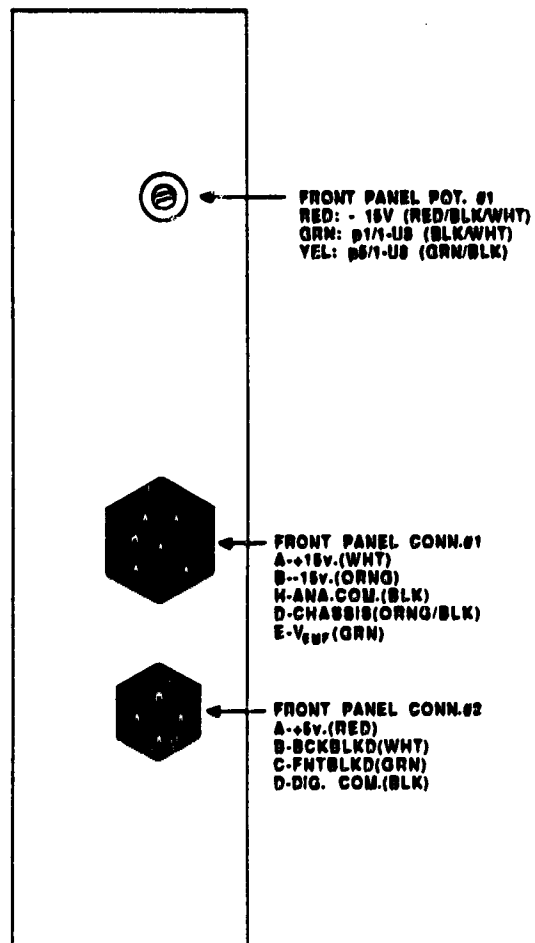


Figure A-2. Coarse feed-back module front panel.

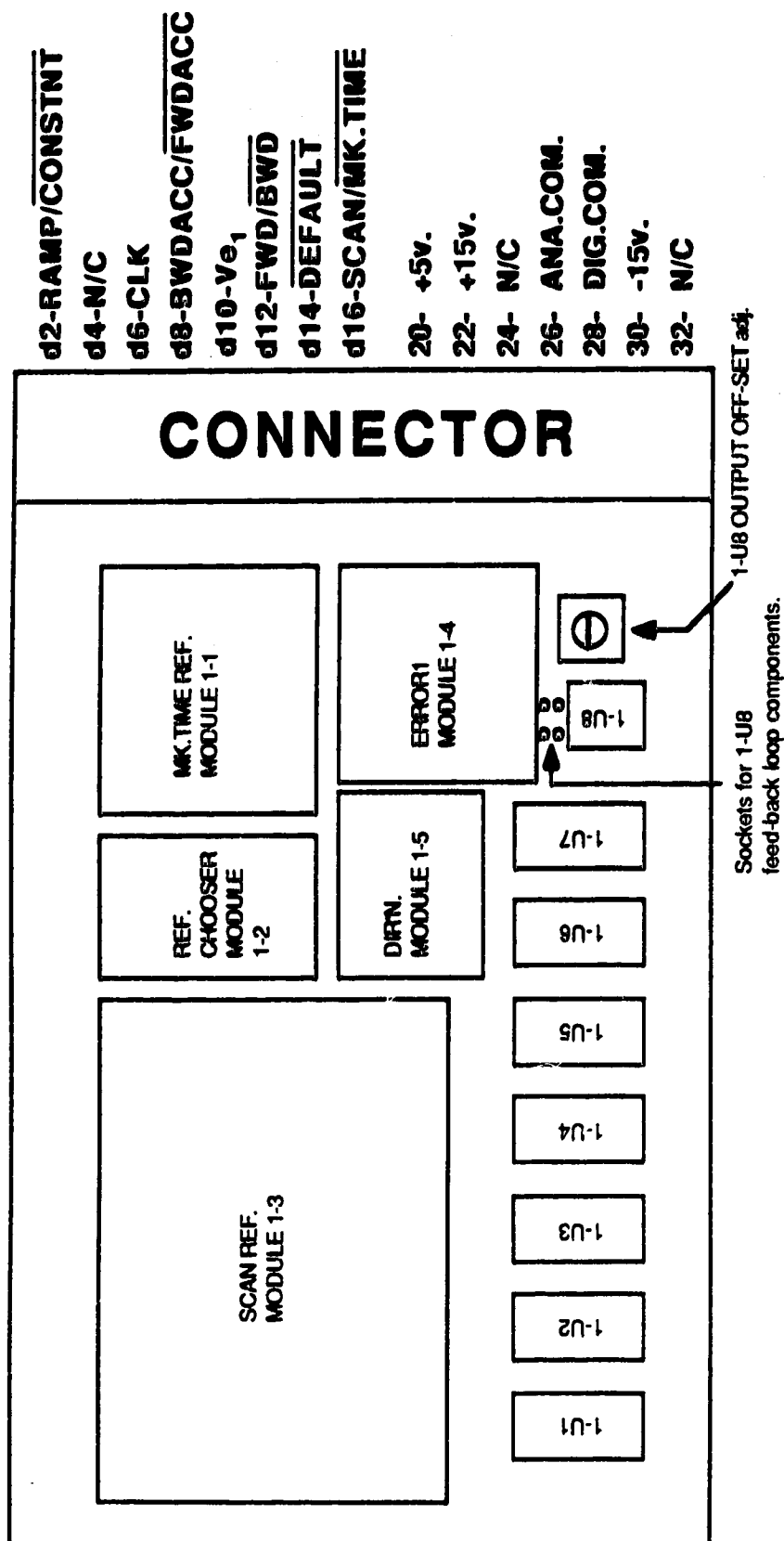
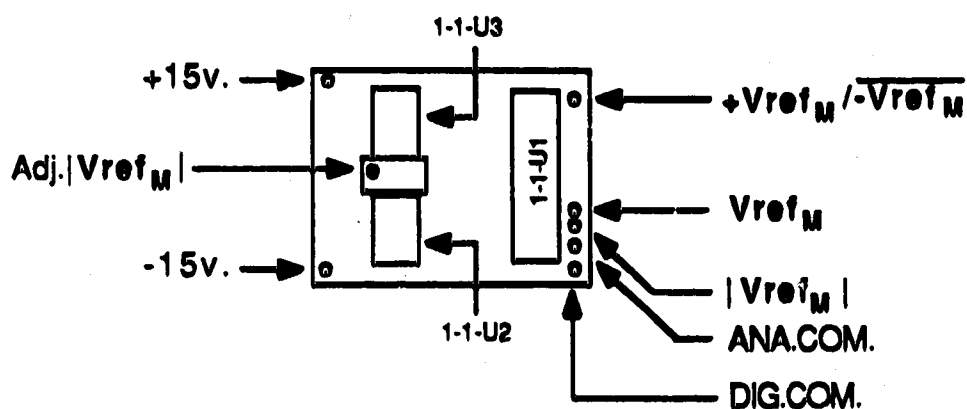
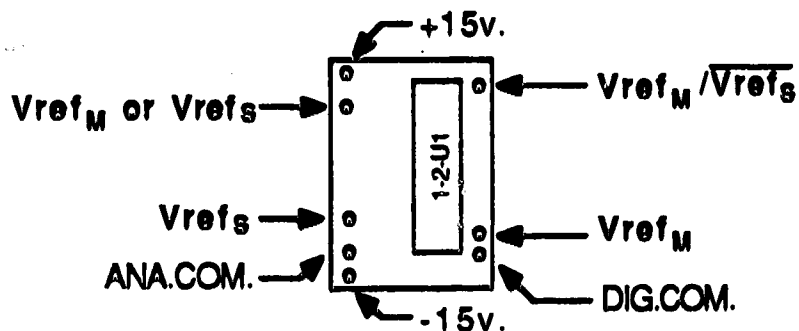


Figure A-3. Coarse feed-back board IC/module/connector assignments.

MODULE 1-1: MK. TIME REF. MODULE



MODULE 1-2: REF. CHOOSER MODULE



MODULE 1-3: SCAN REF. MODULE

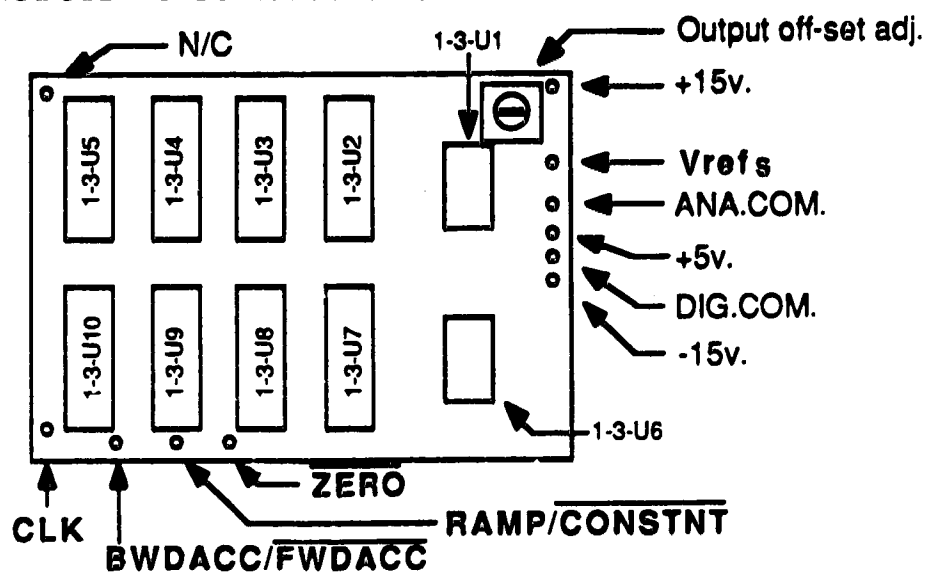
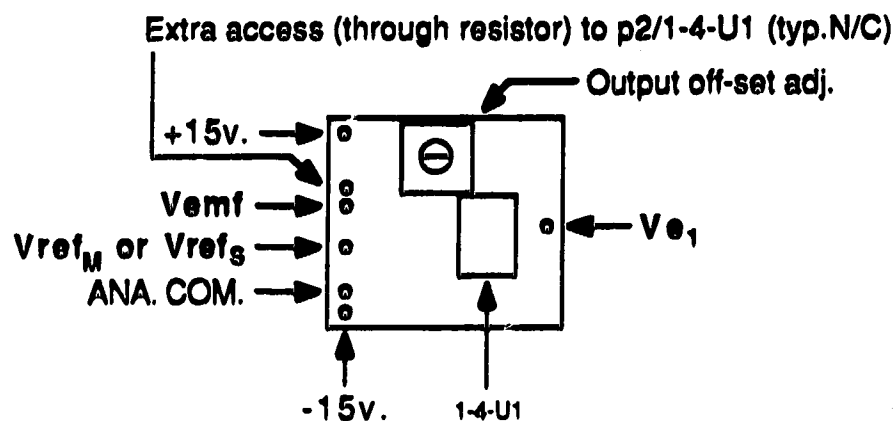


Figure A-4a. Coarse feed-back board modules pin-outs.

MODULE 1-4: ERROR1 MODULE



MODULE 1-5: DIR'N. MODULE

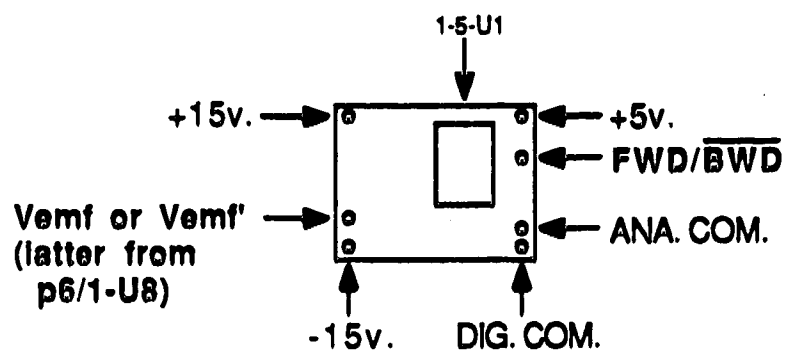


Figure A-4b. Coarse feed-back board modules pin-outs.

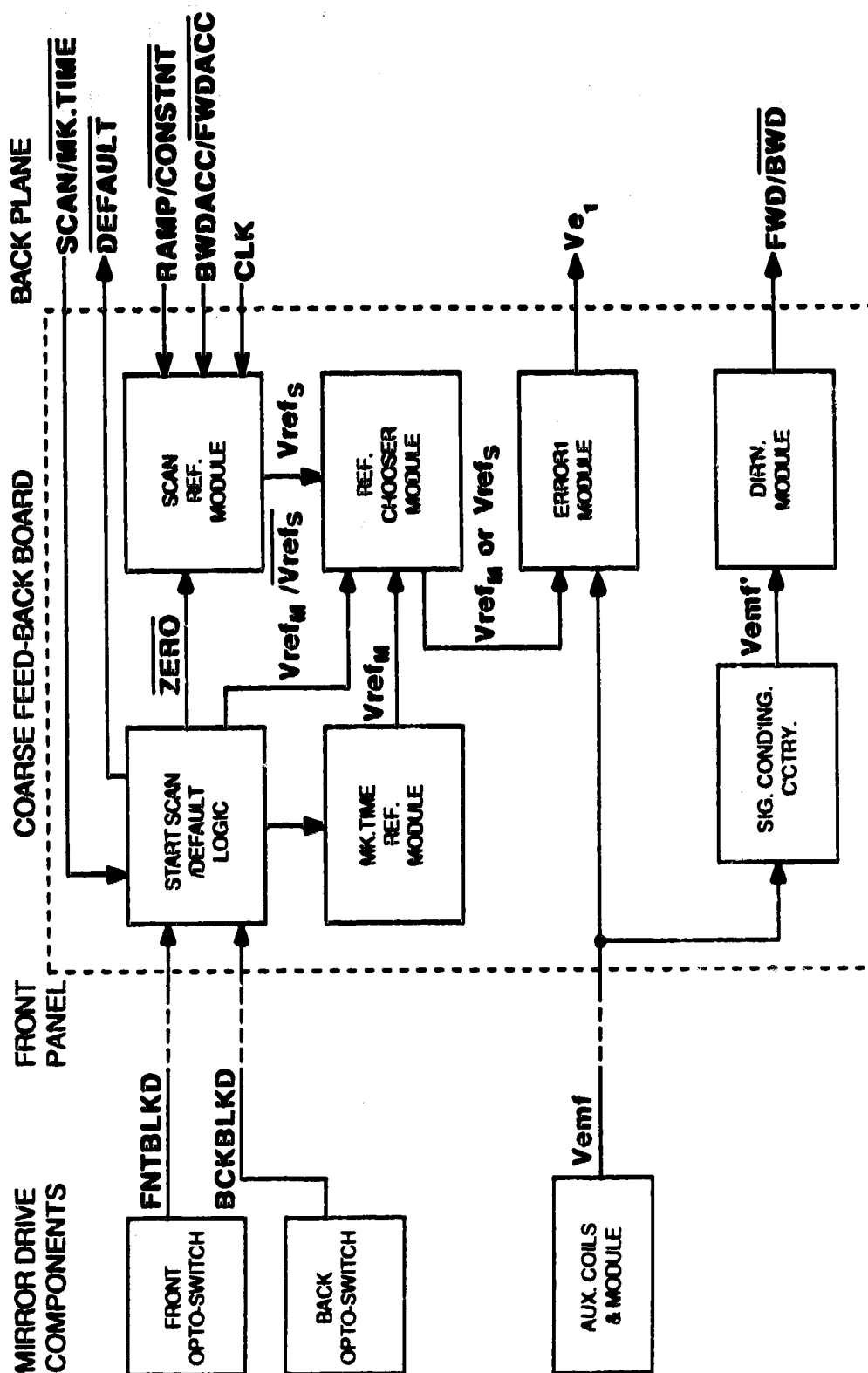


Figure A-5. Coarse feed-back board block diagram.

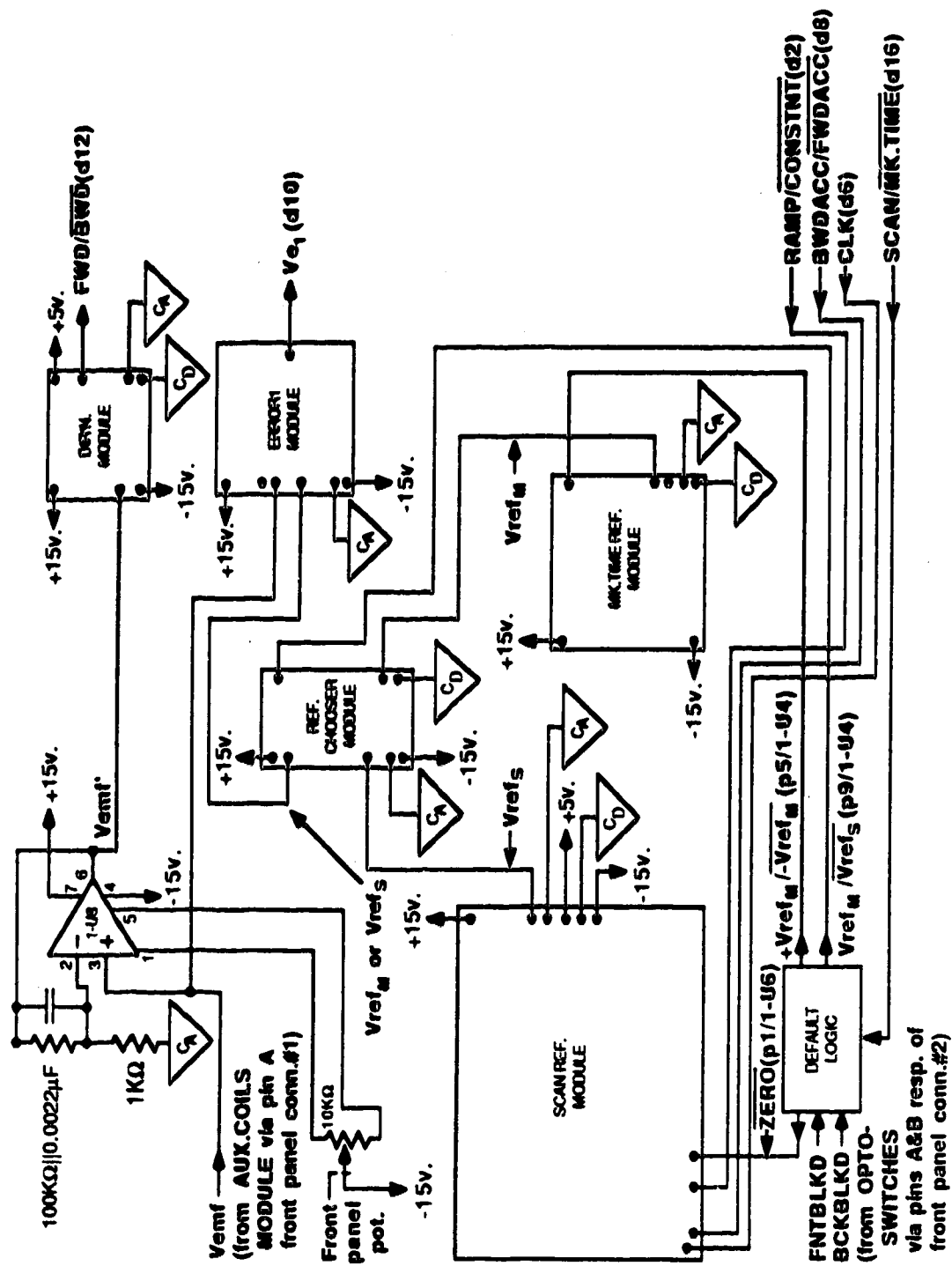


Figure A-6. Coarse feed-back board module inter-connections.

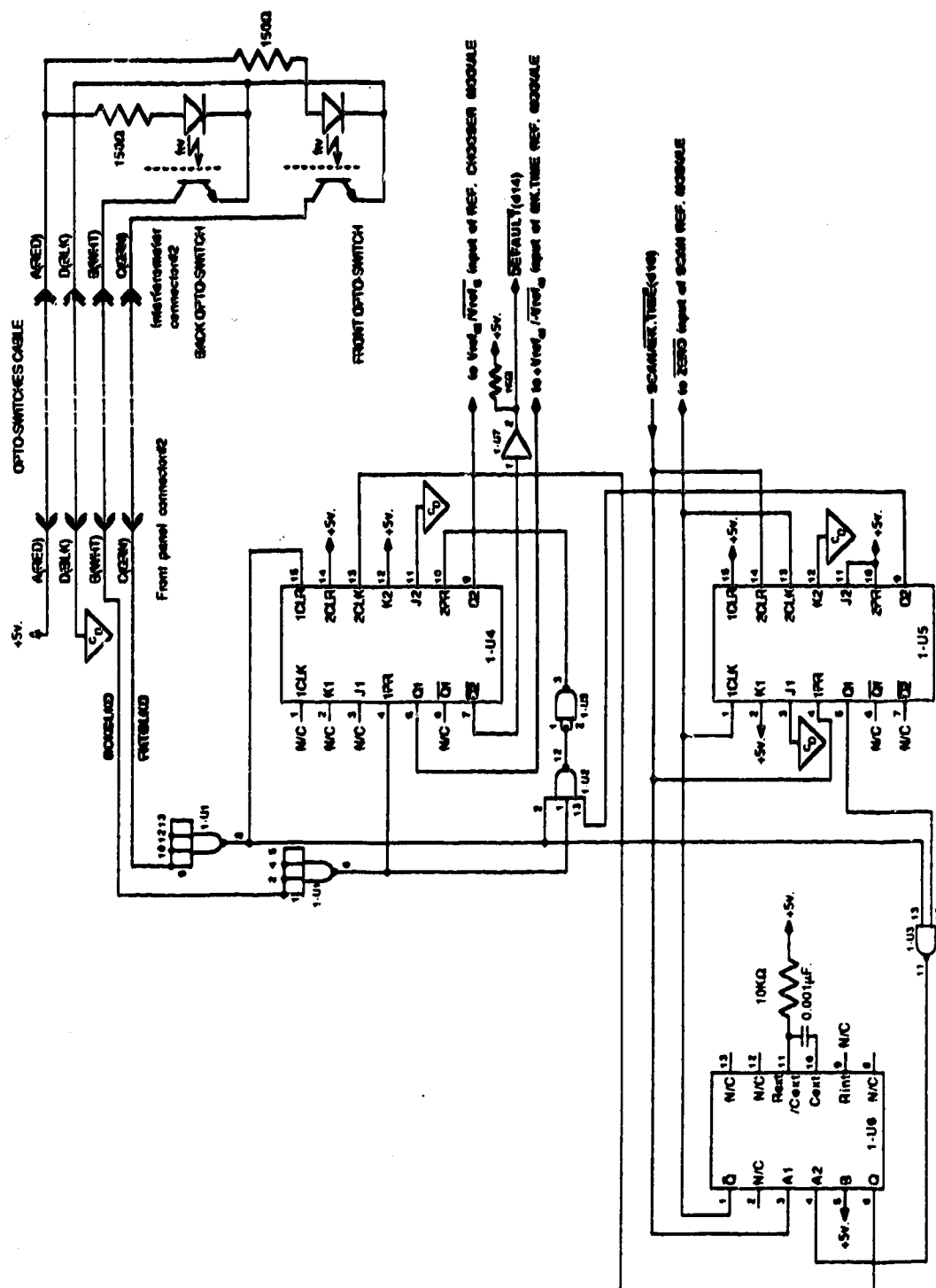
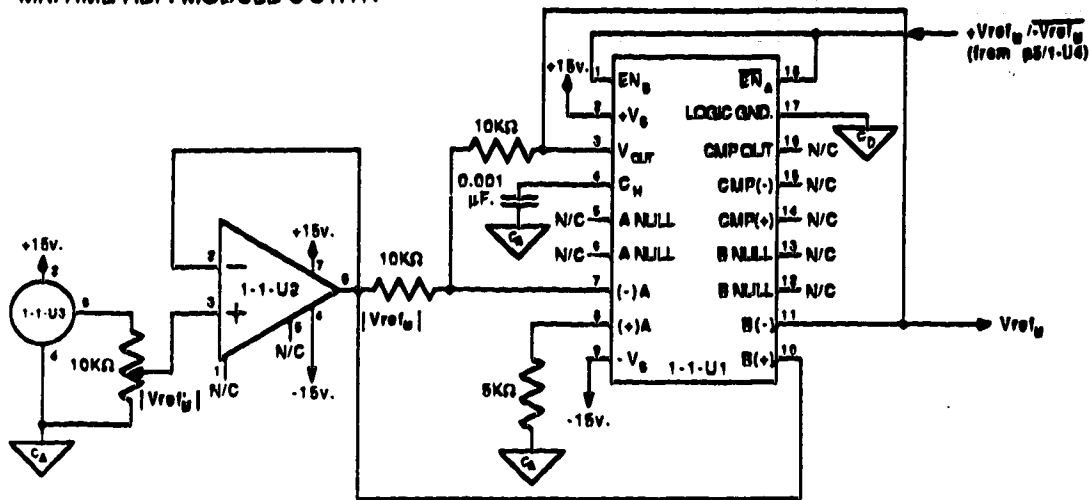


Figure A-7. Opto-switches and default logic.

MK.TIME REF. MODULE C'CTRY:



REF. CHOOSER MODULE C'CTRY:

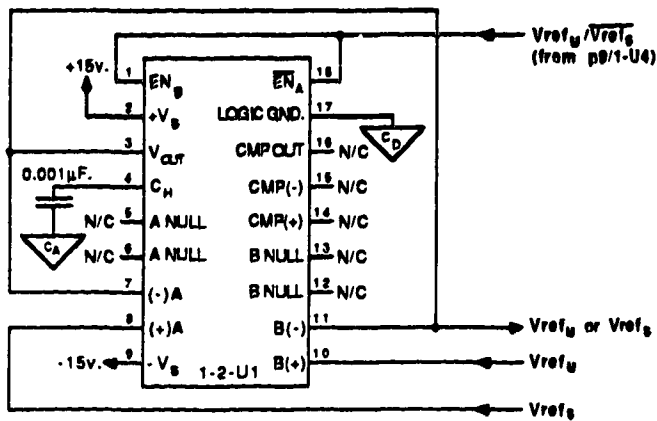
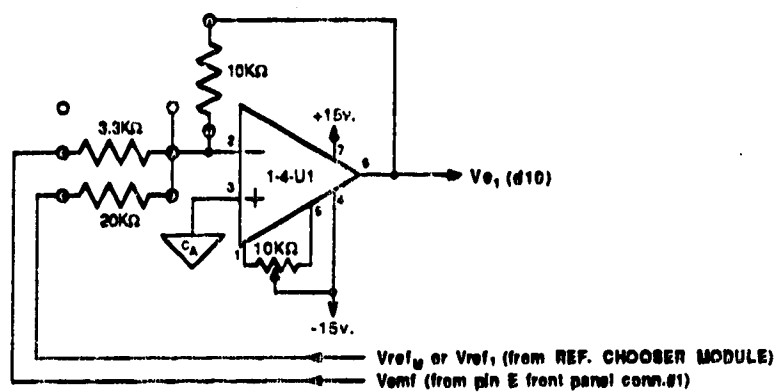


Figure A-8. Mark time reference and reference chooser modules circuitry.



Figure A-9. Scan reference module circuitry.

ERROR1 MODULE C'CTRY



DIR'N. MODULE C'CTRY

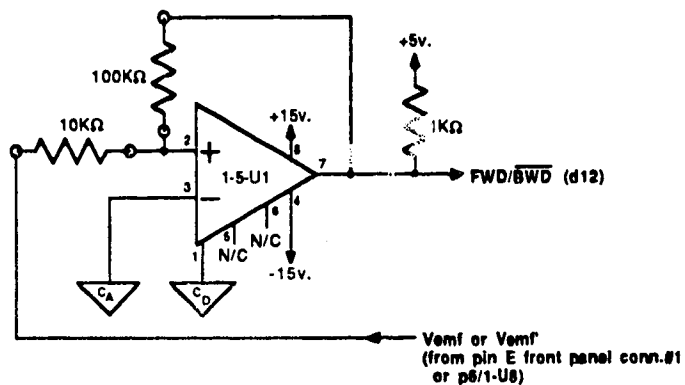


Figure A-10. Coarse feed-back error signal and direction modules circuitry.

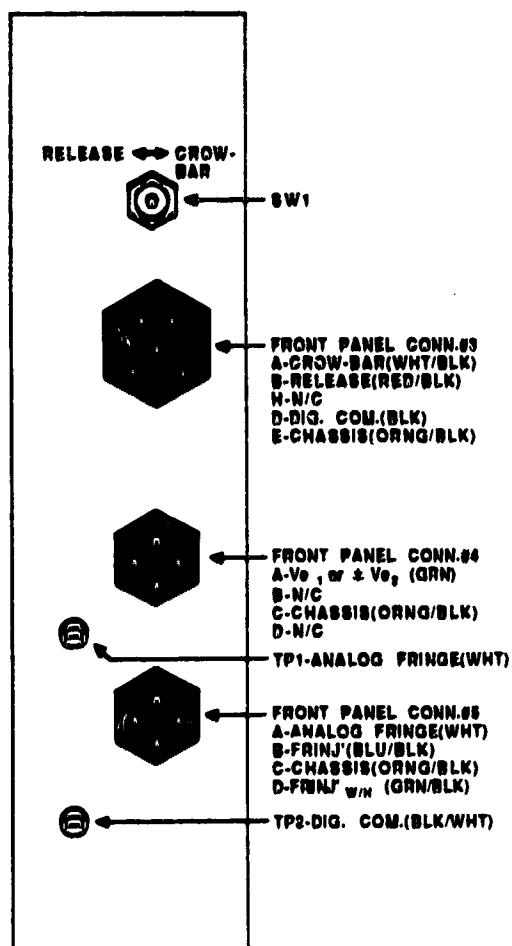


Figure A-11. Fine feed-back module front panel.

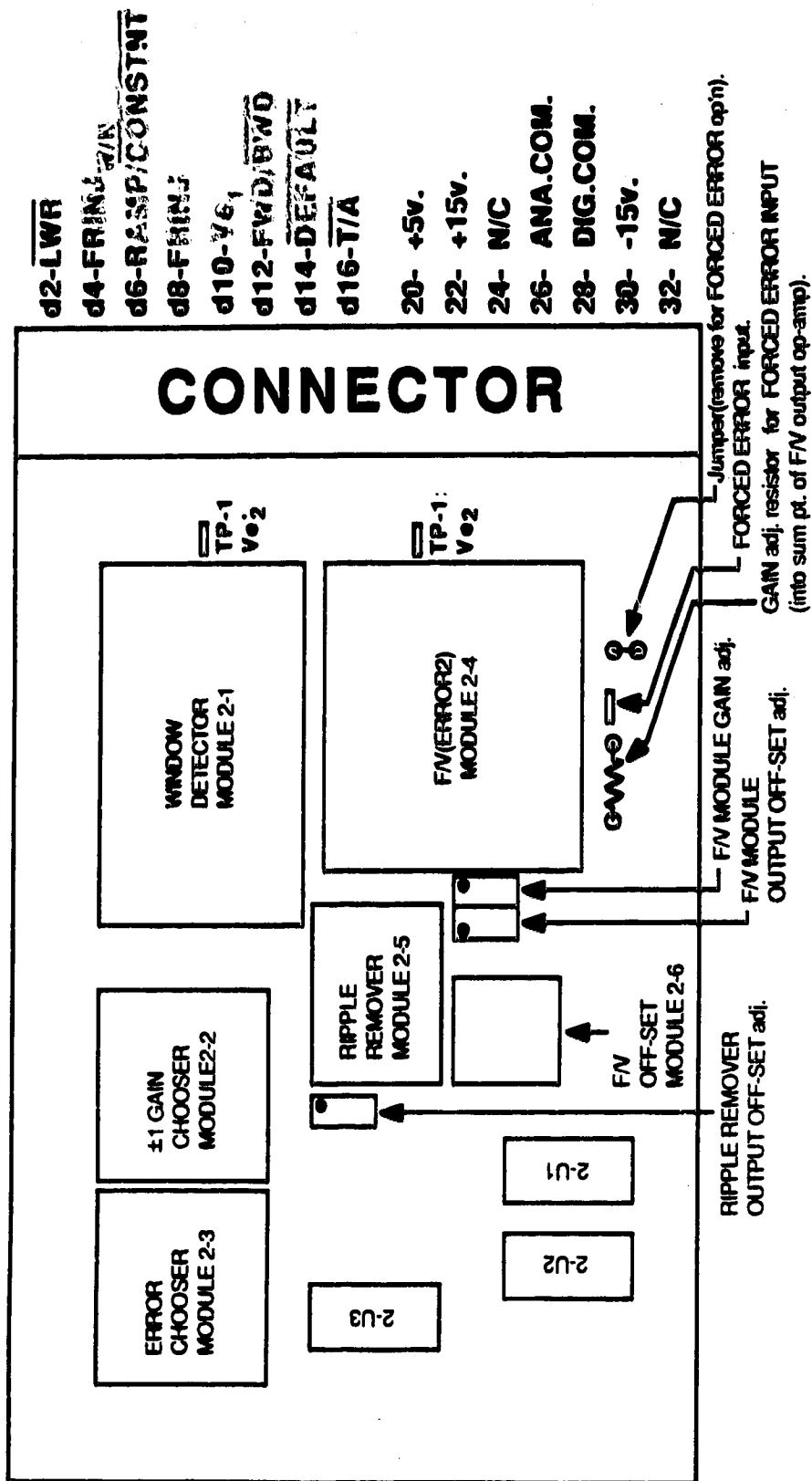
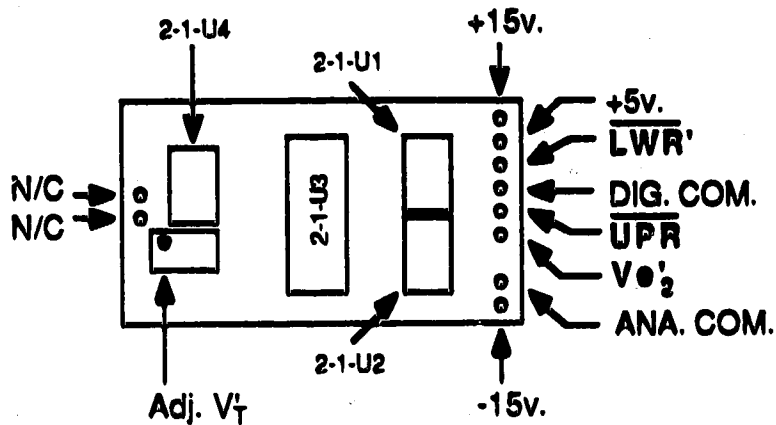
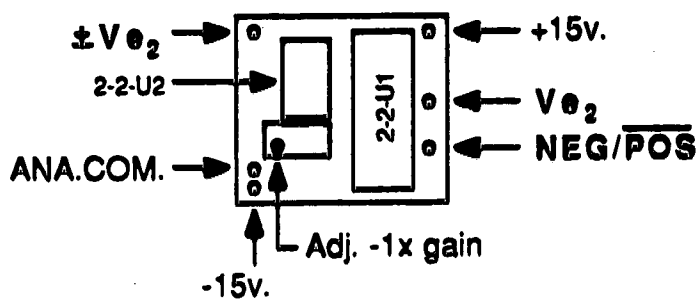


Figure A-12. Fine feed-back board IC/module/test points/connector assignments.

MODULE 2-1: WINDOW DETECTOR MODULE

MODULE 2-2: $\pm 1 \times$ GAIN CHOOSER MODULE

MODULE 2-3: ERROR CHOOSER MODULE

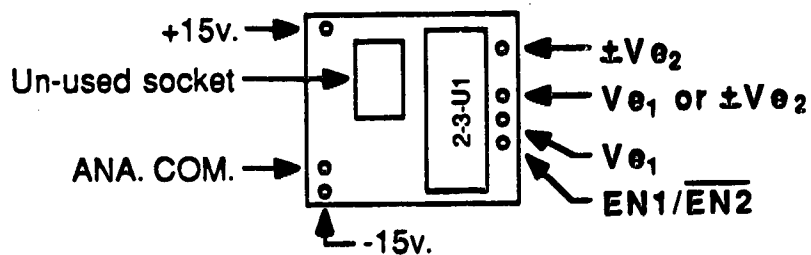
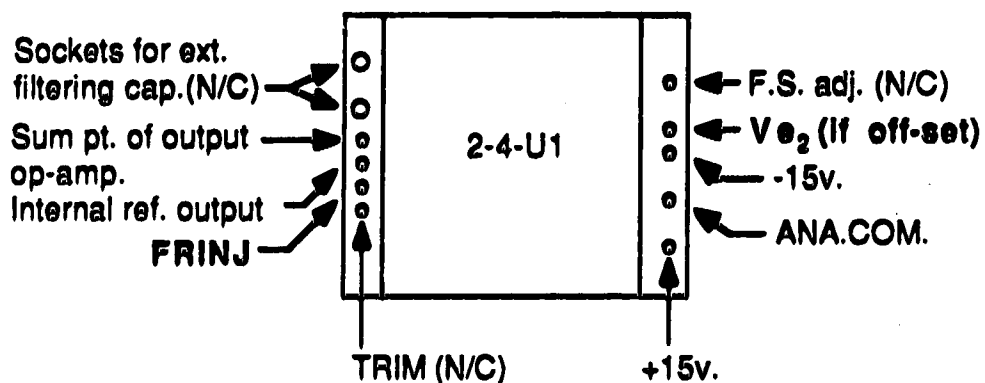
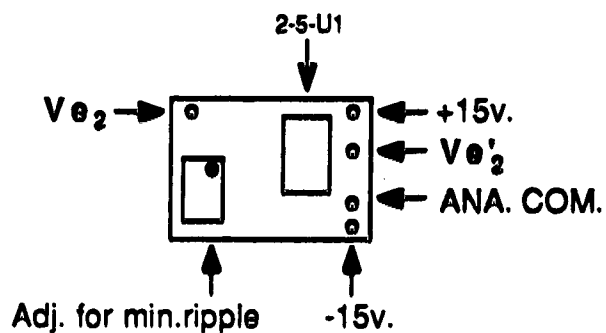


Figure A-13a. Fine feed-back board modules pin-outs.

MODULE 2-4: F/V(ERROR2) MODULE



MODULE 2-5: RIPPLE REMOVER MODULE



MODULE 2-6: F/V OFF-SET MODULE

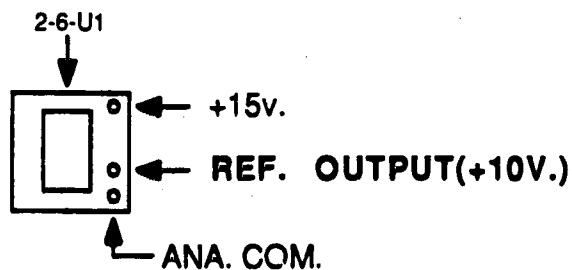


Figure A-13b. Fine feed-back board modules pin-outs.

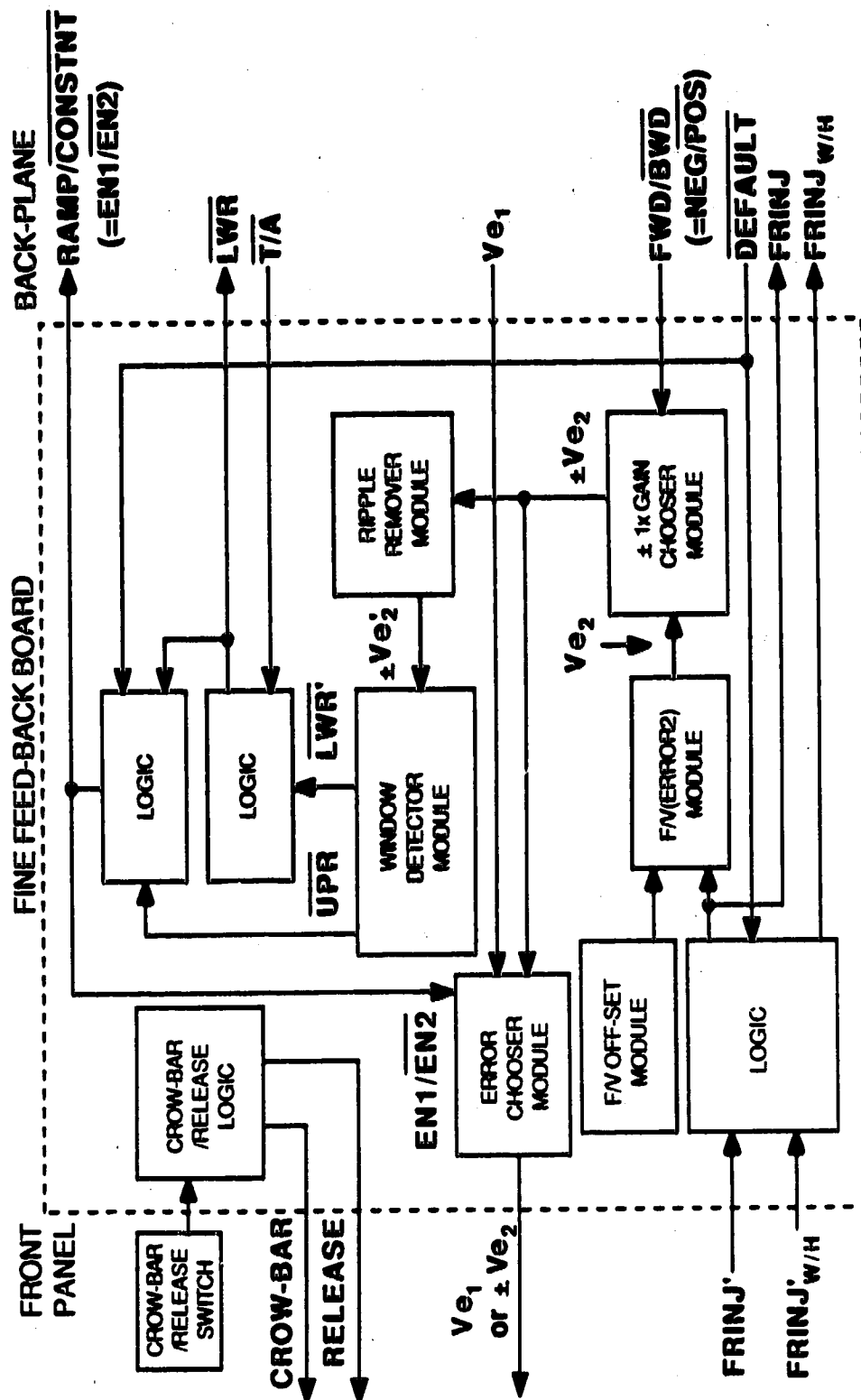


Figure A-14. Fine feed-back board block diagram.

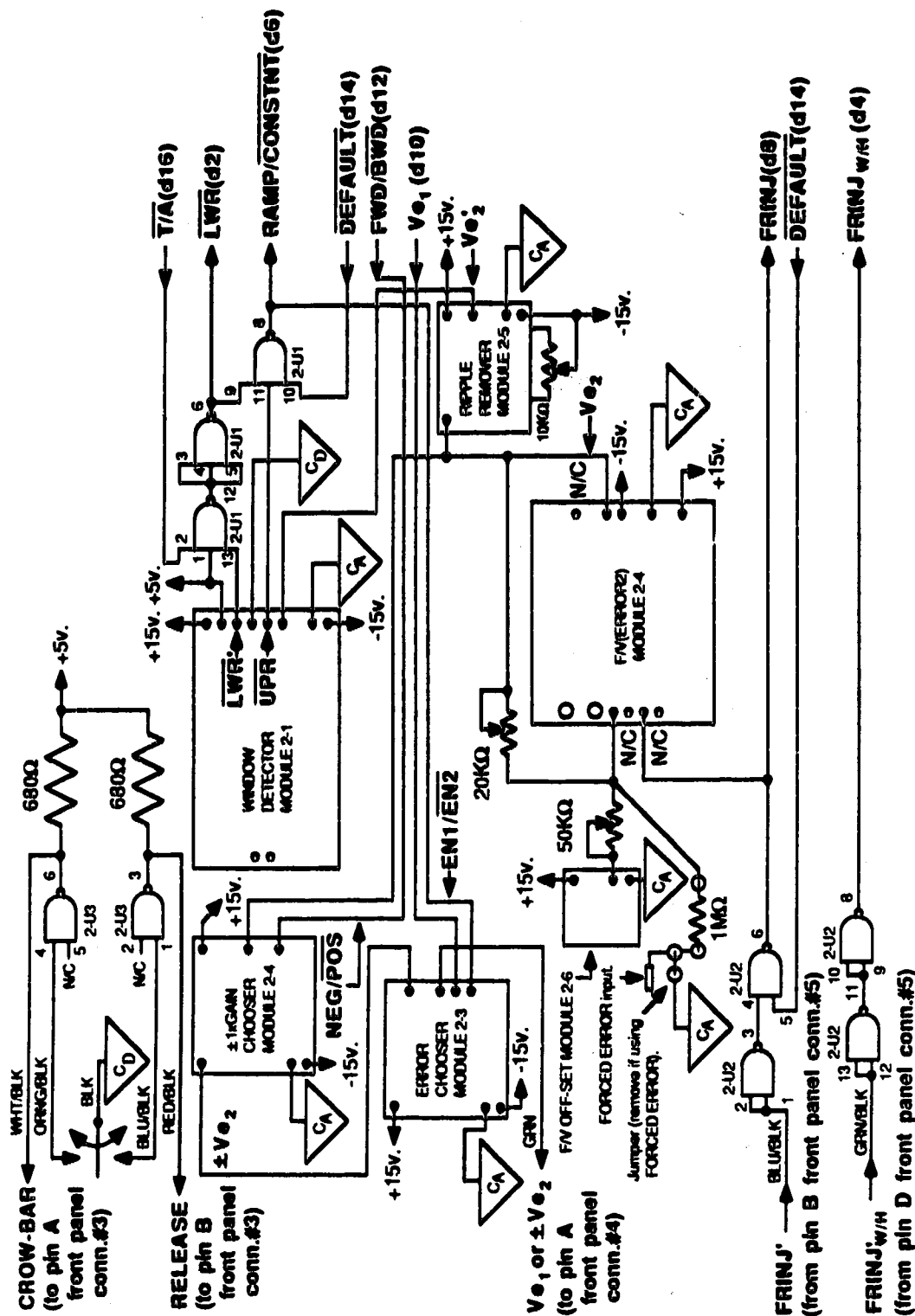
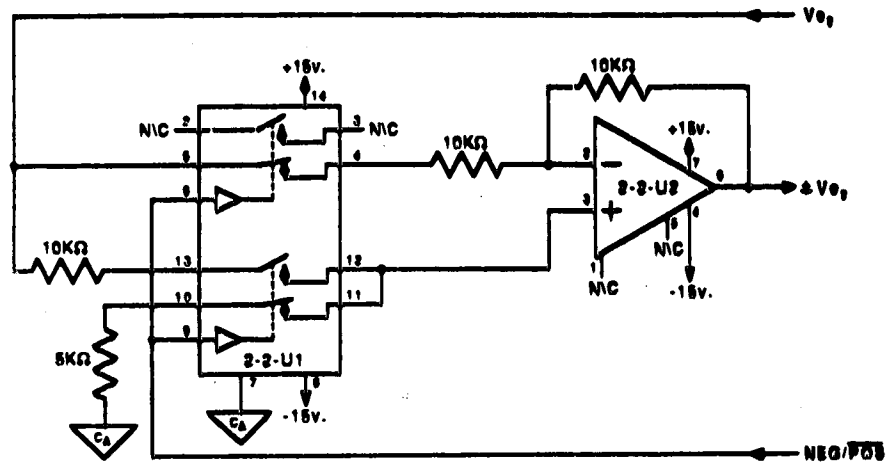
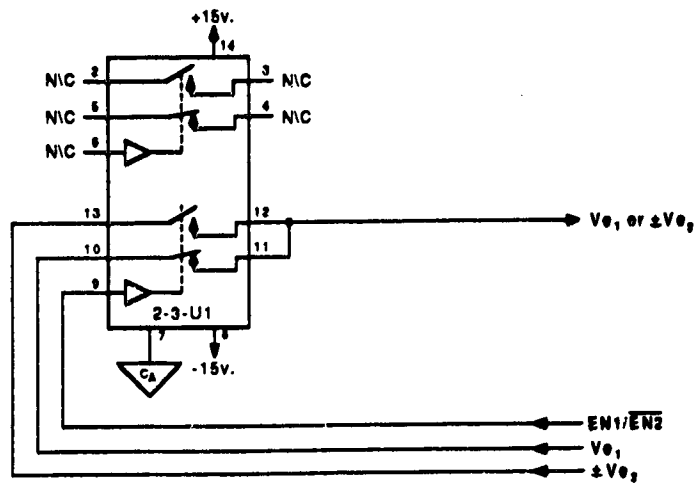


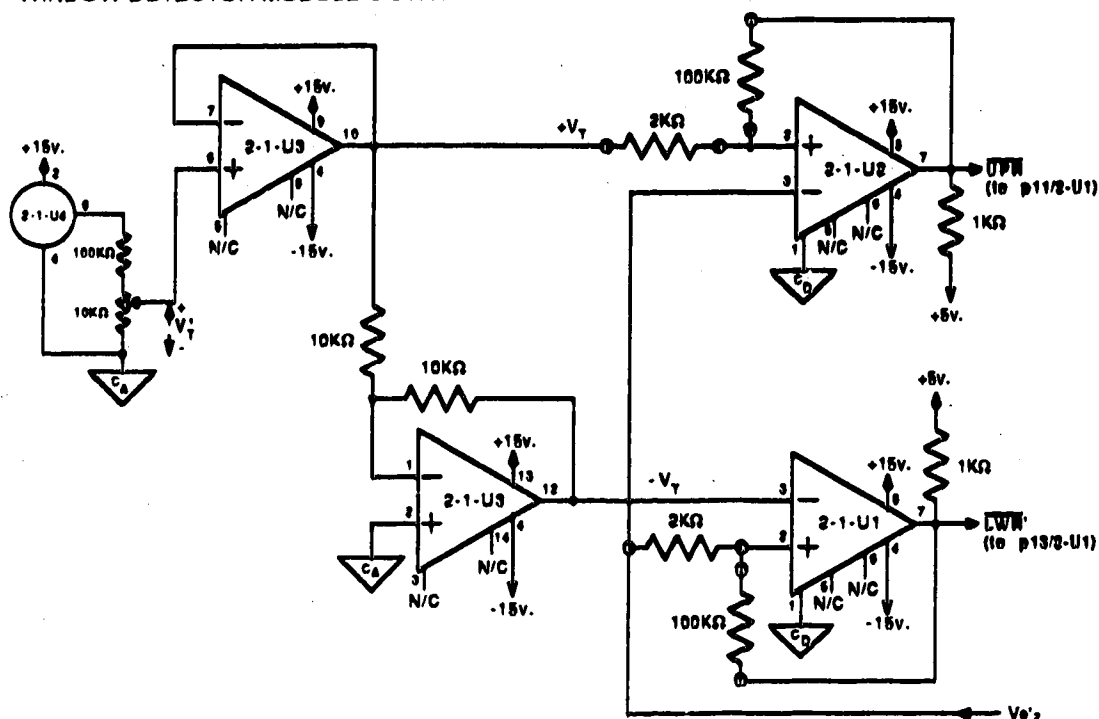
Figure A-15. Fine feed-back board modules inter-connections.

$\pm 1\times$ GAIN MODULE C'CTRY:

ERROR CHOOSER MODULE C'CTRY:

Figure A-16. $\pm 1\times$ Gain and error chooser modules circuitry.

WINDOW DETECTOR MODULE C'CTRY:



RIPPLE REMOVER MODULE C'CTRY:

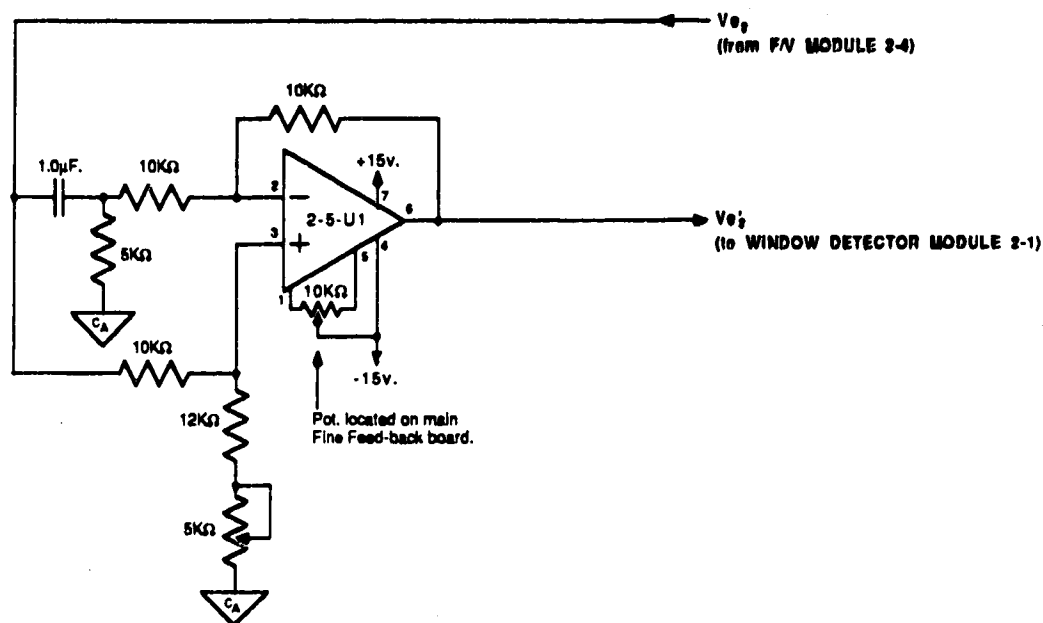


Figure A-17. Window detector and ripple remover modules circuitry.

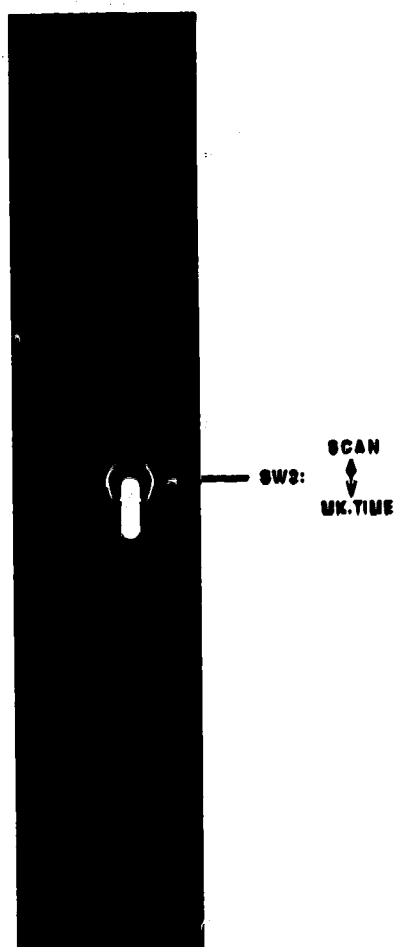


Figure A-18. Turn-around counter (T/A CNTR) board front panel.

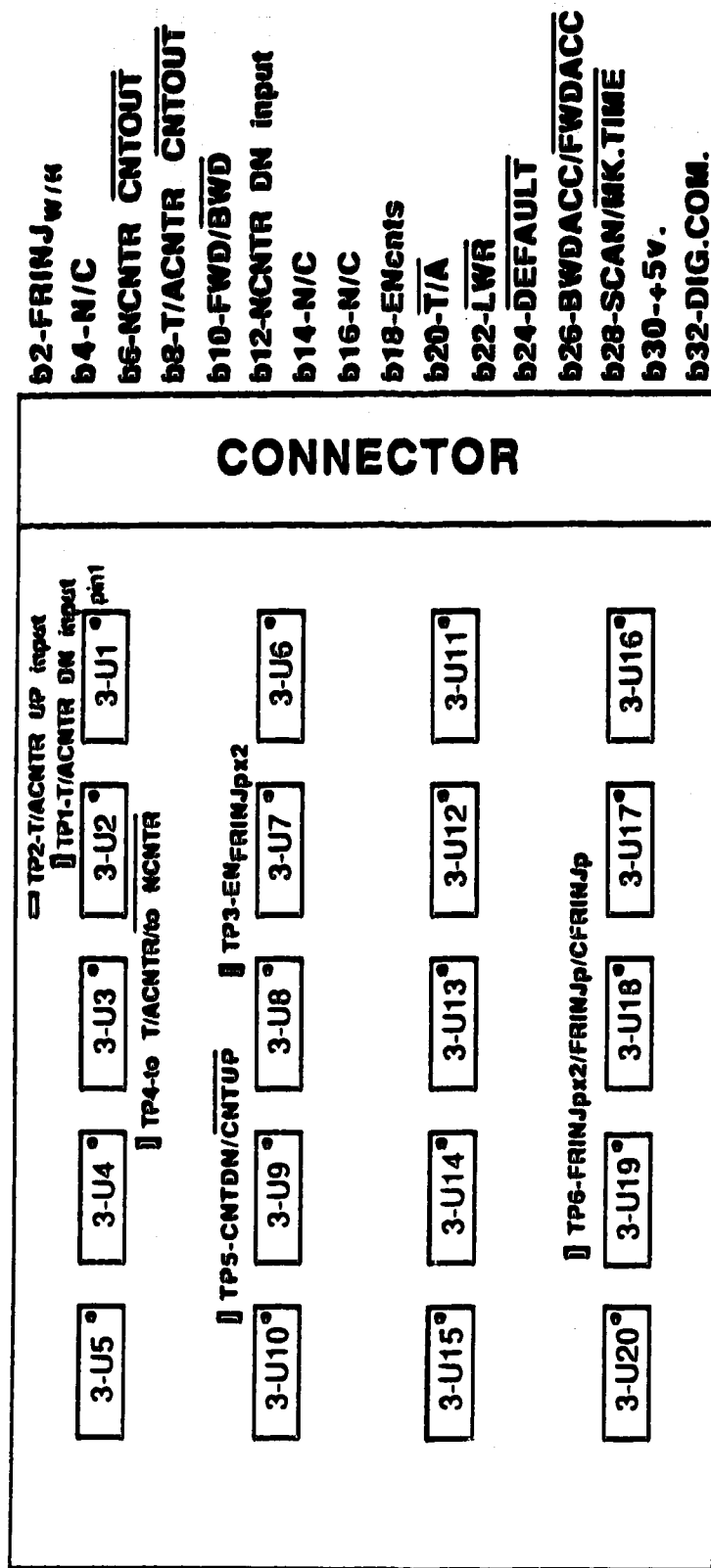


Figure A-19. T/A CNTR board IC/test points/connector assignments.

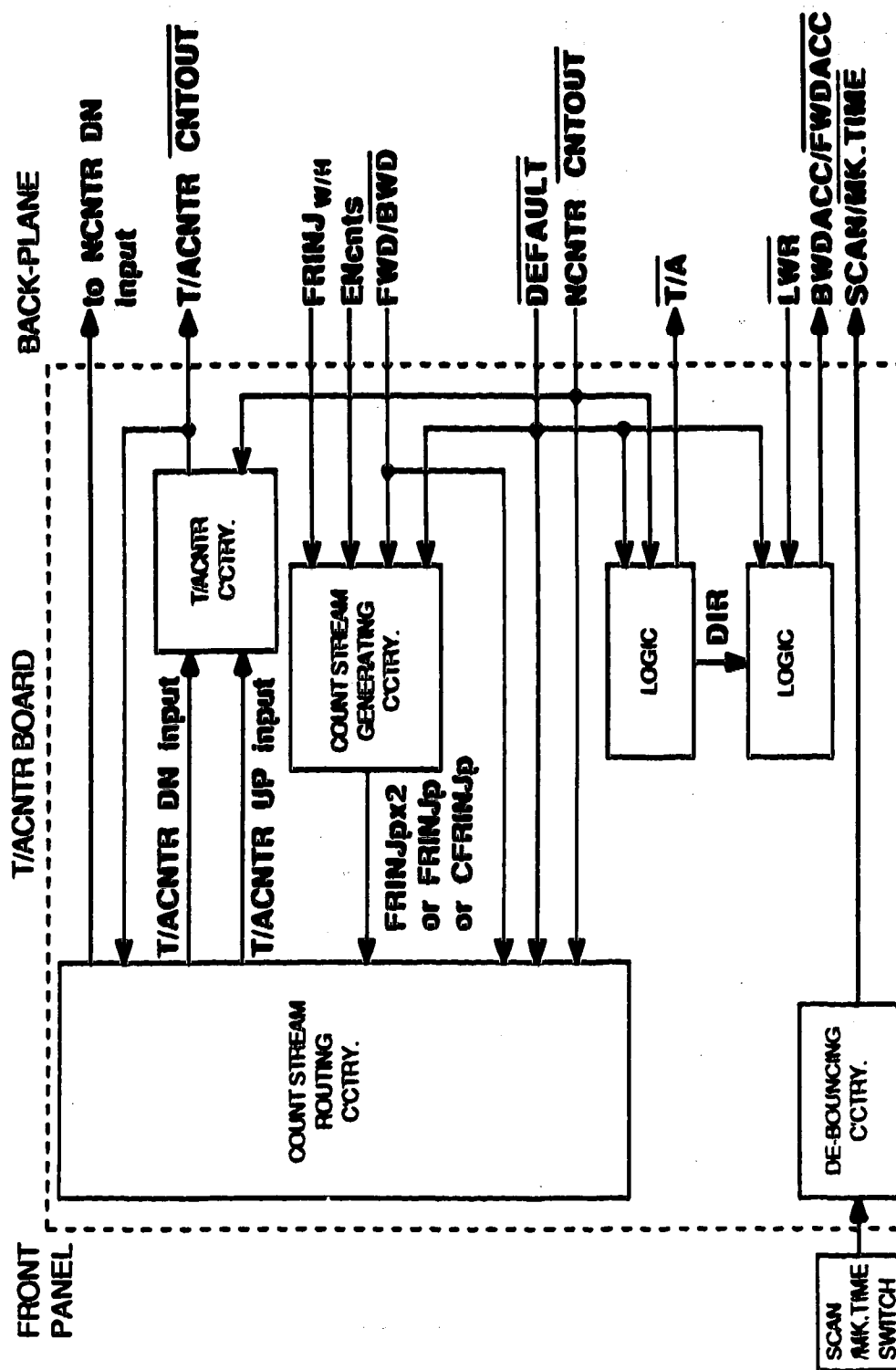


Figure A-20. T/A CNTR board block diagram.



Figure A-21. Count stream routing circuitry.

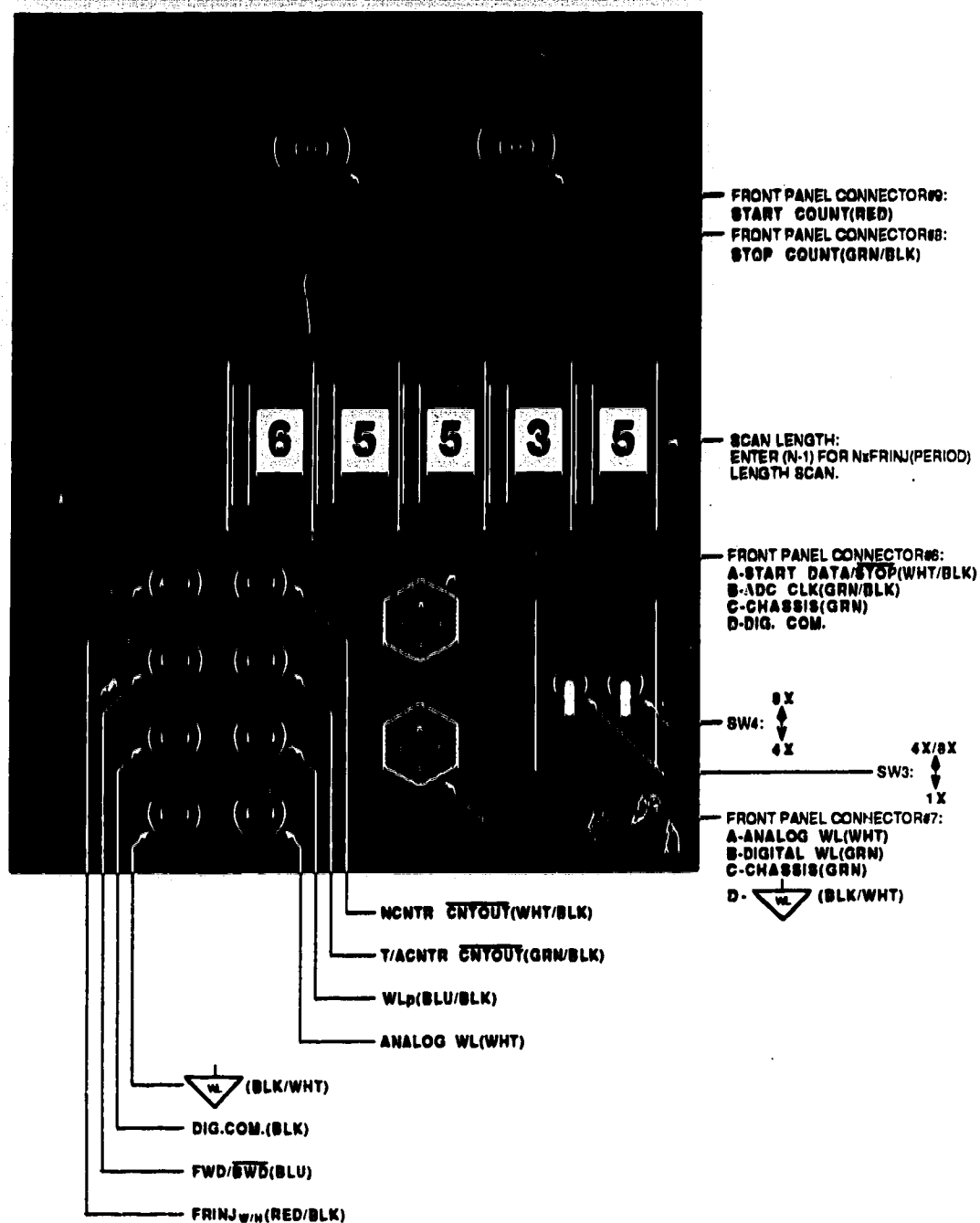


Figure A-23. Scan counter (NCNTR) board front panel.

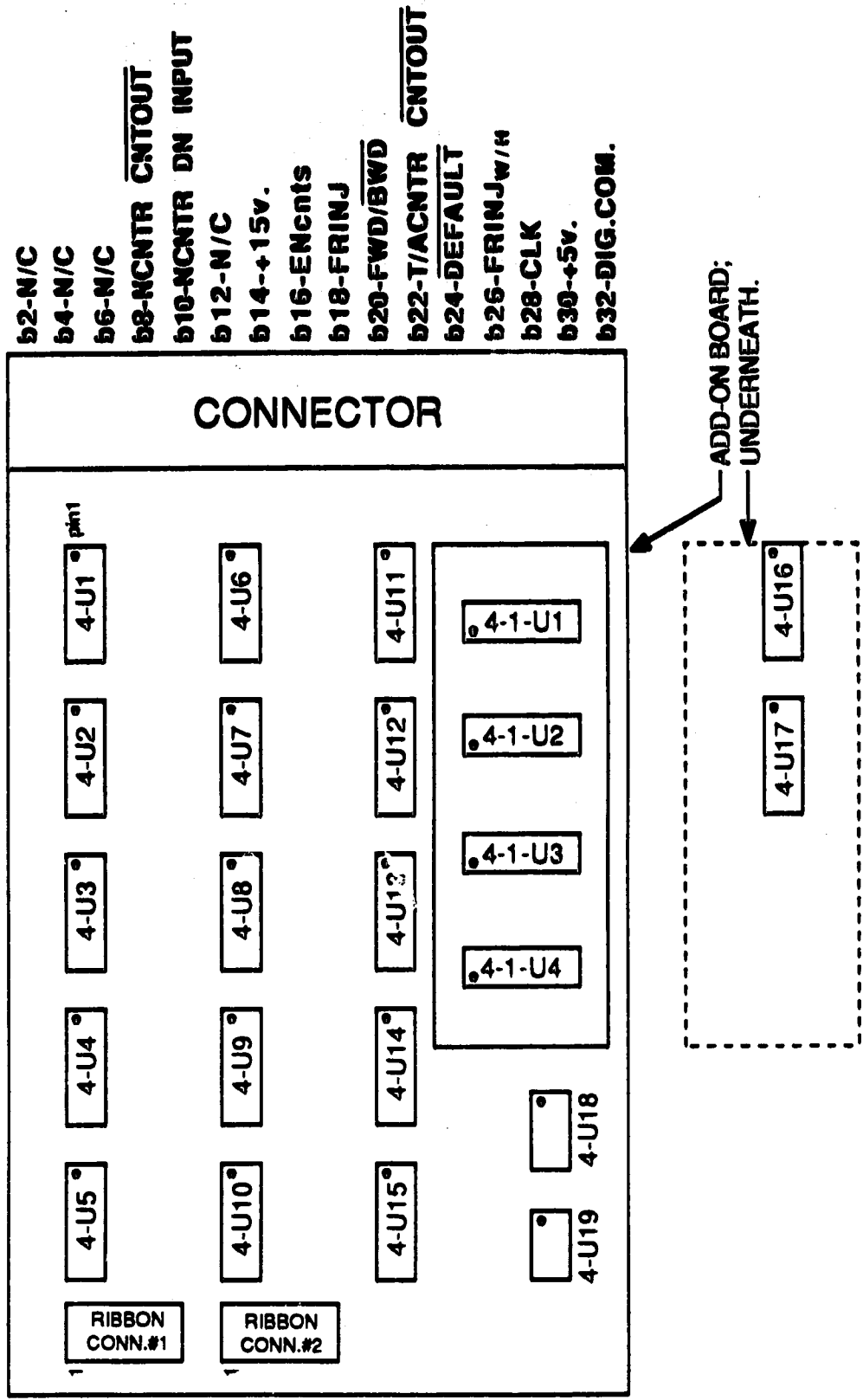


Figure A-24. NCNTR board IC/connector assignments.

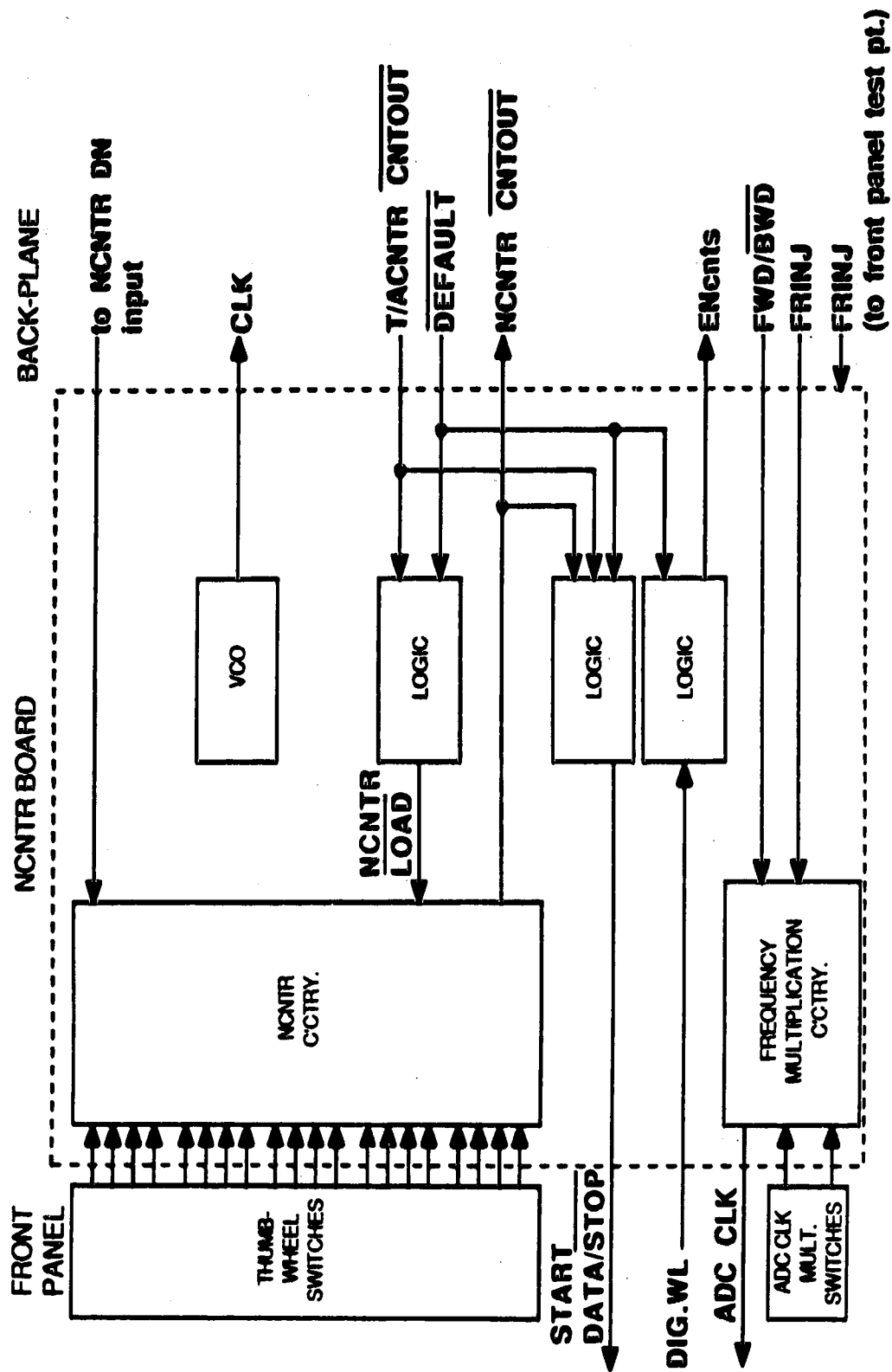


Figure A-75. NCNTR board block diagram.

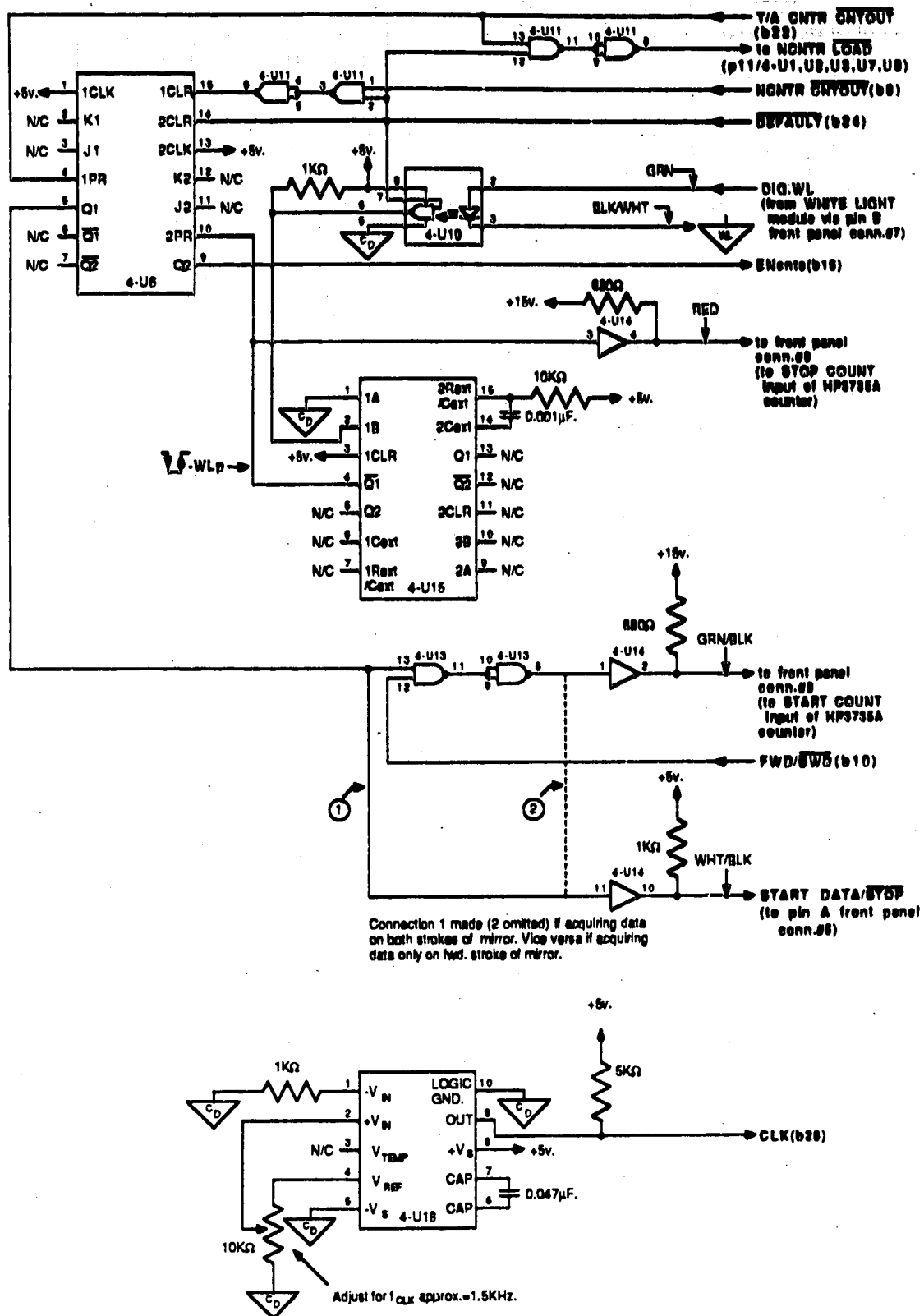


Figure A-26. NCNTR board miscellaneous logic.

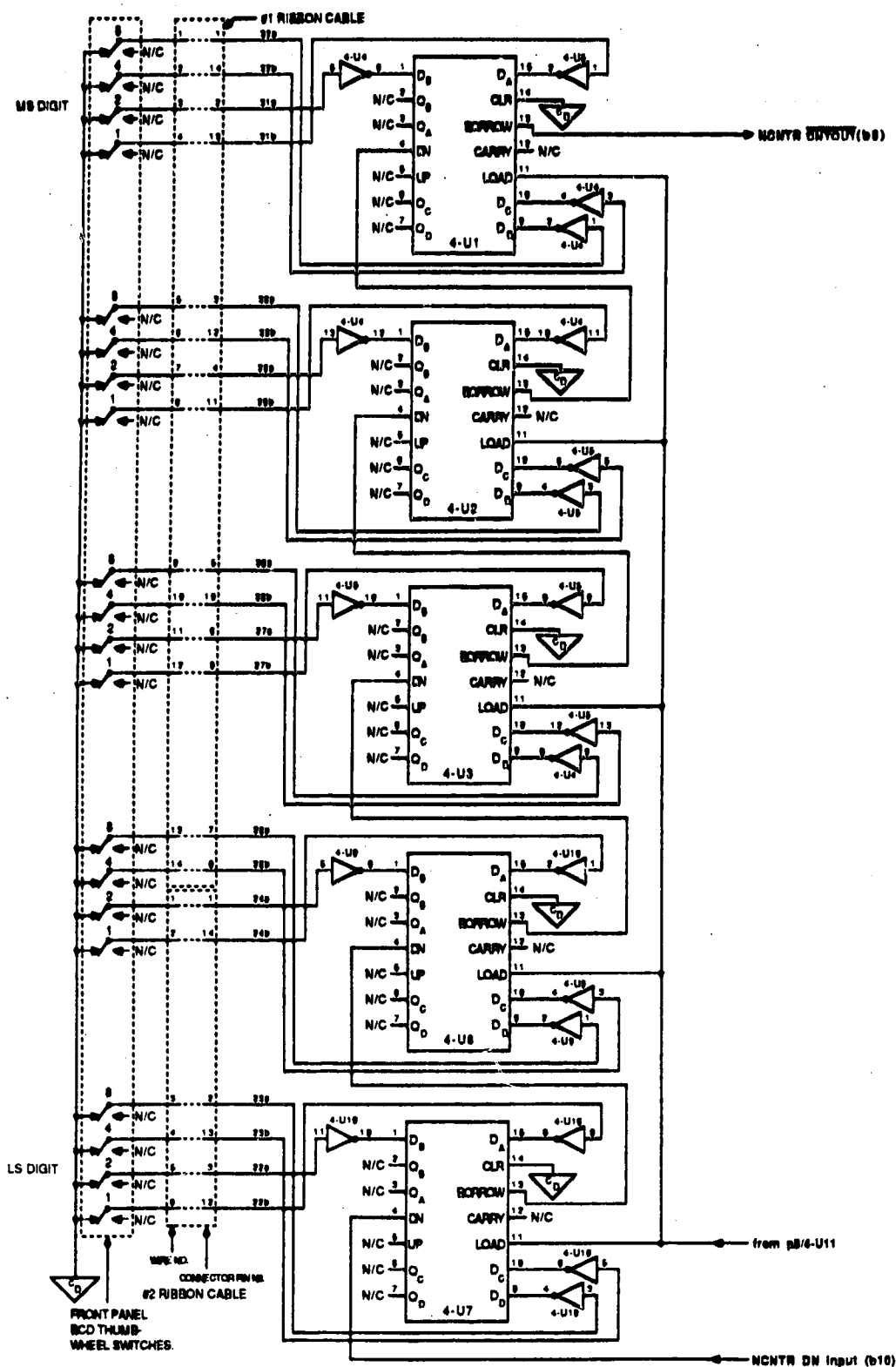


Figure A-27. NCNTR circuitry.

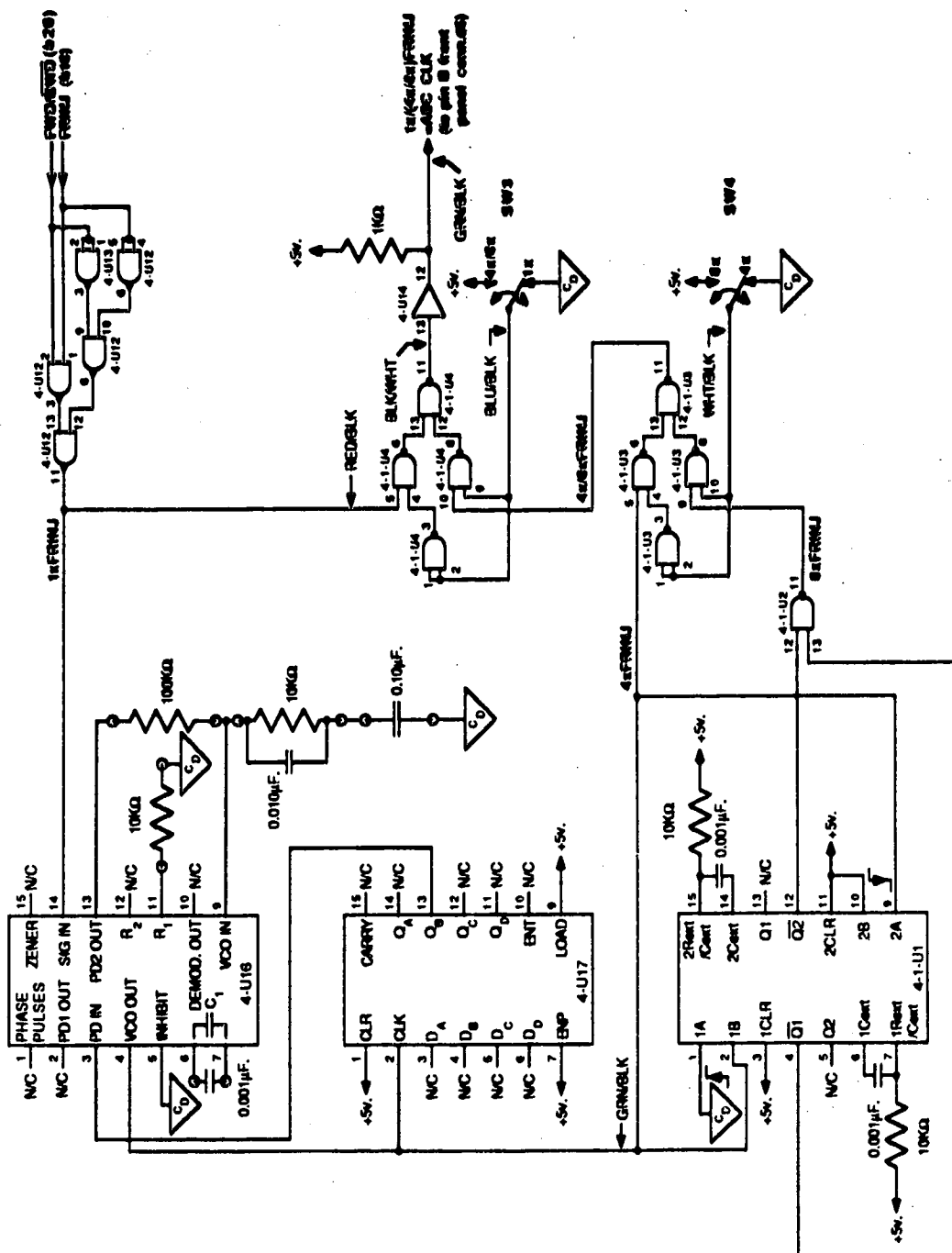


Figure A-28. ADC CLK frequency multiplication circuitry.